

208

SPRINGER TRACTS
IN MODERN PHYSICS

Ralf Röhlsberger

Nuclear Condensed Matter Physics with Synchrotron Radiation

Basic Principles, Methodology and Applications



Springer

Springer Tracts in Modern Physics

Volume 208

Managing Editor: G. Höhler, Karlsruhe

Editors: J. Kühn, Karlsruhe

Th. Müller, Karlsruhe

A. Ruckenstein, New Jersey

F. Steiner, Ulm

J. Trümper, Garching

P. Wölfle, Karlsruhe

Available online at
[SpringerLink.com](#)

Starting with Volume 165, Springer Tracts in Modern Physics is part of the [SpringerLink] service. For all customers with standing orders for Springer Tracts in Modern Physics we offer the full text in electronic form via [SpringerLink] free of charge. Please contact your librarian who can receive a password for free access to the full articles by registration at:

springerlink.com

If you do not have a standing order you can nevertheless browse online through the table of contents of the volumes and the abstracts of each article and perform a full text search.

There you will also find more information about the series.

Springer Tracts in Modern Physics

Springer Tracts in Modern Physics provides comprehensive and critical reviews of topics of current interest in physics. The following fields are emphasized: elementary particle physics, solid-state physics, complex systems, and fundamental astrophysics.

Suitable reviews of other fields can also be accepted. The editors encourage prospective authors to correspond with them in advance of submitting an article. For reviews of topics belonging to the above mentioned fields, they should address the responsible editor, otherwise the managing editor.

See also springeronline.com

Managing Editor

Gerhard Höhler

Institut für Theoretische Teilchenphysik

Universität Karlsruhe

Postfach 69 80

76128 Karlsruhe, Germany

Phone: +49 (7 21) 6 08 33 75

Fax: +49 (7 21) 37 07 26

Email: gerhard.hoehler@physik.uni-karlsruhe.de
www-ttp.physik.uni-karlsruhe.de/

Elementary Particle Physics, Editors

Johann H. Kühn

Institut für Theoretische Teilchenphysik

Universität Karlsruhe

Postfach 69 80

76128 Karlsruhe, Germany

Phone: +49 (7 21) 6 08 33 72

Fax: +49 (7 21) 37 07 26

Email: johann.kuehn@physik.uni-karlsruhe.de
www-ttp.physik.uni-karlsruhe.de/~jk

Thomas Müller

Institut für Experimentelle Kernphysik

Fakultät für Physik

Universität Karlsruhe

Postfach 69 80

76128 Karlsruhe, Germany

Phone: +49 (7 21) 6 08 35 24

Fax: +49 (7 21) 6 07 26 21

Email: thomas.mueller@physik.uni-karlsruhe.de
www-ekp.physik.uni-karlsruhe.de

Fundamental Astrophysics, Editor

Joachim Trümper

Max-Planck-Institut für Extraterrestrische Physik

Postfach 13 12

85741 Garching, Germany

Phone: +49 (89) 30 00 35 59

Fax: +49 (89) 30 00 33 15

Email: jtrumper@mpe.mpg.de

www.mpe-garching.mpg.de/index.html

Solid-State Physics, Editors

Andrei Ruckenstein

Editor for The Americas

Department of Physics and Astronomy

Rutgers, The State University of New Jersey

136 Frelinghuysen Road

Piscataway, NJ 08854-8019, USA

Phone: +1 (732) 445 43 29

Fax: +1 (732) 445-43 43

Email: andrei@physics.rutgers.edu

www.physics.rutgers.edu/people/pips/

Ruckenstein.html

Peter Wölflé

Institut für Theorie der Kondensierten Materie

Universität Karlsruhe

Postfach 69 80

76128 Karlsruhe, Germany

Phone: +49 (7 21) 6 08 35 90

Fax: +49 (7 21) 6 08 77 79

Email: woelfle@tkm.physik.uni-karlsruhe.de

www-tkm.physik.uni-karlsruhe.de

Complex Systems, Editor

Frank Steiner

Abteilung Theoretische Physik

Universität Ulm

Albert-Einstein-Allee 11

89069 Ulm, Germany

Phone: +49 (7 31) 5 02 29 10

Fax: +49 (7 31) 5 02 29 24

Email: frank.steiner@physik.uni-ulm.de

www.physik.uni-ulm.de/theo/qc/group.html

Ralf Röhlsberger

Nuclear Condensed Matter Physics with Synchrotron Radiation

Basic Principles, Methodology and Applications

With 152 Figures



Springer

Ralf Röhlsberger
HASYLAB@DESY
Notkestr. 85
22607 Hamburg, Germany
E-mail: Ralf.roehlsberger@desy.de

Library of Congress Control Number: 2004113131

Physics and Astronomy Classification Scheme (PACS):
76.80.+y, 75.70.-i, 63.22.+m

ISSN print edition: 0081-3869

ISSN electronic edition: 1615-0430

ISBN 3-540-23244-3 Springer Berlin Heidelberg New York

This work is subject to copyright. All rights are reserved, whether the whole or part of the material is concerned, specifically the rights of translation, reprinting, reuse of illustrations, recitation, broadcasting, reproduction on microfilm or in any other way, and storage in data banks. Duplication of this publication or parts thereof is permitted only under the provisions of the German Copyright Law of September 9, 1965, in its current version, and permission for use must always be obtained from Springer. Violations are liable for prosecution under the German Copyright Law.

Springer is a part of Springer Science+Business Media

springeronline.com

© Springer-Verlag Berlin Heidelberg 2004

Printed in Germany

The use of general descriptive names, registered names, trademarks, etc. in this publication does not imply, even in the absence of a specific statement, that such names are exempt from the relevant protective laws and regulations and therefore free for general use.

Typesetting: by the author and TechBooks using a Springer L^AT_EX macro package

Cover concept: eStudio Calamar Steinen

Cover production: *design & production* GmbH, Heidelberg

Printed on acid-free paper SPIN: 10876283 56/3141/jl 5 4 3 2 1 0

To Seher Aytül and Can Lukas,
Ursula and Karl-Heinz

Preface

The use of nuclei to probe condensed-matter properties has a long-standing history in physics. With the determination of magnetic and electric moments of nearly all stable nuclei they became eligible to be used as probes for external fields acting on them. Various experimental methods like nuclear magnetic resonance (NMR), perturbed angular correlation (PAC) and Mössbauer spectroscopy (MS) constitute the field of nuclear condensed matter physics. All of these techniques are microscopic methods that rely on the signals from individual nuclei in the sample.

Following a proposal by *Ruby* in 1974, a new method was established that probes the hyperfine interaction of nuclei via nuclear resonant scattering of synchrotron radiation. This is a time-based extension of the Mössbauer effect that became feasible with the availability of very brilliant synchrotron radiation sources. The fact that this method relies on coherent scattering rather than incoherent absorption opens new experimental possibilities compared to conventional Mössbauer spectroscopy. The combination of diffraction and spectroscopy allows one to study the interplay between structure and electronic properties in new classes of materials in the shape of thin films, multilayers, nanoparticles and more.

Meanwhile, nuclear resonant scattering of synchrotron radiation has become an established field of condensed-matter research. The use of synchrotron radiation for nuclear resonant spectroscopy has opened new applications. Its outstanding brilliance, transverse coherence and polarization have opened the field for many unique studies, especially in the field of materials science. This applies in particular for the electronic and magnetic structure of very small sample volumes like micro- and nanostructures and samples under extreme conditions of pressure and temperature. It is the virtue of this technique that elastic *and* inelastic scattering experiments can be performed in basically the same setup. These two fields constitute the main branches of this book. Besides that, new scattering methods are introduced that extend the existing limits for energy and time resolution.

This book is intended to give an introduction and a review of this field with special emphasis to applications in materials science. While the introductory parts are given on a tutorial level, many applications are discussed in detail so that the material should be useful also for lectures and courses.

Acknowledgments

This book would not be existing without the support, enthusiasm, and encouragement of many colleagues, coworkers and friends. The main body of this book was completed during my stay at the University of Rostock. I am grateful to Eberhard Burkhardt for his continuous support during that time. Moreover, I want to thank the members of his group during that time (in random order): Harald Sinn, Christian Seyfert, Uli Ponkratz, Stephan Flor, Radu Nicula, Heiko Thomas, Adrian Jianu, Christine Benkiser, Ulrike Schröder, Kai Schlage, Peter Dobbert, Axel Bernhard, Klaus Quast, Stefan Otto, Elvira Schmidt, Torsten Klein and others for their help and assistance in many respects, ranging from administration and computer problems to various aspects in scientific research and teaching.

It was a great pleasure for me to collaborate with Karl-Heinz Meiwes-Broer and the members of his group, in particular Joachim Bansmann, Volker Senz, Andreas Bettac, Karl-Ludwig Jonas and Armin Kleibert. I always enjoyed the stimulating atmosphere during our common projects.

The experiments described here were performed at the Advanced Photon Source (APS), Argonne National Laboratory, USA, the European Synchrotron Radiation Facility (ESRF), Grenoble, France and the Hamburger Synchrotronstrahlungslabor (HASYLAB), DESY, Hamburg. The results presented were only possible due to the hospitality and the support I have experienced at these facilities. At the APS, I am very grateful to Ercan Alp and his team, namely Wolfgang Sturhahn, Tom Toellner, Michael Hu, John Sutter, Phil Hession and Peter Lee for their various contributions during numerous beamtimes. At the ESRF, Rudolf Rüffer and his coworkers have always provided a very pleasant environment for experiments and discussions. My special thanks go also to Sasha Chumakov, Hermann and Hanne Grünsteudel, Olaf Leupold, Joachim Metge, and Thomas Roth. At HASYLAB and the II. Institut für Experimentalphysik, Universität Hamburg, I have benefitted greatly from the support of Erich Gerdau and his continuous enthusiasm. I am indebted to Yuri Shvyd'ko, Dierk Rüter, Olaf Leupold, Hans-Christian Wille, Martin Lucht, Michael Lerche, Barbara Lohl and Karl Geske for their help during several experiments.

The subject of this book is embedded in the wide range of x-ray physics. In this field I always enjoyed stimulating discussions with Sunil Sinha. Furthermore, it was a great pleasure to exchange ideas and collaborate with Uwe Bergmann, Caroline L'abbé, Johan Meersschaut, Uwe van Bürck, Werner Keune, Walter Potzel, Stan Ruby, Brent Fultz, Peter Høghøj, Sarvjet Shastri, and Gopal Shenoy. Special thanks go to Peter Becker (PTB Braunschweig) for his support with high-quality channel-cut crystals. A significant part of this book was completed during a one-year interim professorship at the Physikdepartment E13 of the Technical University of Munich. I thank W. Petry and the members of this group for their hospitality during that time.

The work presented here was in parts financially supported by the German *Bundesministerium für Bildung und Forschung* (BMBF) under contracts no. 05 643HRA 5 and 05 ST8HRA 0. Use of the Advanced Photon Source was supported by the U.S. Department of Energy, Basic Energy Sciences, Office of Science, under contract No. W-31-109-ENG-38.

Finally, I would like to acknowledge Brent Fultz and Erich Gerdau for a critical reading of the manuscript. Last but not least, I want to thank my wife Aytül for her love, patience und support that made this work possible.

Hamburg, September 2004

Ralf Röhlsberger

Contents

| | | |
|----------|---|-----------|
| 1 | Introduction | 1 |
| 1.1 | Elastic Nuclear Resonant Scattering | 2 |
| 1.2 | Inelastic Nuclear Resonant Scattering | 3 |
| 1.3 | Outline of this Book | 4 |
| | References | 6 |
| 2 | General Aspects of Nuclear Resonant Scattering | 7 |
| 2.1 | Classification of Scattering Processes | 7 |
| 2.1.1 | Coherent Elastic Nuclear Resonant Scattering | 8 |
| 2.1.2 | Coherent Inelastic Nuclear Resonant Scattering | 9 |
| 2.1.3 | Incoherent Elastic Nuclear Resonant Scattering | 10 |
| 2.1.4 | Incoherent Inelastic Nuclear Resonant Scattering | 11 |
| 2.2 | Features of Elastic Nuclear Resonant Scattering | 12 |
| 2.2.1 | X-ray Diffraction in Space and Time | 13 |
| 2.2.2 | The Nuclear Exciton | 14 |
| 2.2.3 | The Index of Refraction | 15 |
| 2.2.4 | Pulse Propagation | 19 |
| 2.2.5 | Speedup | 20 |
| 2.2.6 | Quantum Beats | 22 |
| 2.2.7 | Suitable Isotopes | 24 |
| 2.3 | Forward Scattering from a Single Target | 25 |
| 2.3.1 | Solution in the Time Domain | 26 |
| 2.3.2 | Solution in the Energy Domain | 28 |
| 2.4 | Forward Scattering from Separated Samples | 29 |
| 2.5 | Nuclear Bragg Scattering | 30 |
| 2.5.1 | Pure Nuclear Reflections | 30 |
| 2.5.2 | Electronically Allowed Reflections: Ta(110) | 31 |
| 2.5.3 | Applications in Materials Science | 32 |
| | References | 33 |
| 3 | Methods and Instrumentation | 37 |
| 3.1 | Synchrotron Radiation Sources | 37 |
| 3.1.1 | Historical Development | 37 |
| 3.1.2 | Properties of Synchrotron Radiation | 40 |
| 3.1.3 | Synchrotron Radiation for Mössbauer Experiments | 45 |

| | | |
|----------|--|-----------|
| 3.2 | Monochromatization | 46 |
| 3.2.1 | Heat-Load Monochromators | 47 |
| 3.2.2 | High-Resolution Monochromators | 47 |
| 3.2.3 | Polarization Filtering | 52 |
| 3.3 | Detection Schemes | 56 |
| 3.3.1 | Basic Requirements | 56 |
| 3.3.2 | Timing Electronics | 57 |
| 3.3.3 | Detectors | 58 |
| 3.4 | Beamlines | 61 |
| | References | 62 |
| 4 | Coherent Elastic Nuclear Resonant Scattering | 67 |
| 4.1 | The Dynamical Theory | 68 |
| 4.1.1 | The Scattering Amplitude | 70 |
| 4.1.2 | Forward Scattering | 73 |
| 4.1.3 | Total Reflection from Boundaries | 74 |
| 4.1.4 | Grazing-Incidence Reflection from Stratified Media | 76 |
| 4.1.5 | The Radiation Field in Layered Systems | 81 |
| 4.1.6 | Coherent Reflection from Ultrathin Layers | 81 |
| 4.1.7 | The Influence of Boundary Roughness | 84 |
| 4.1.8 | Calculation of Intensities | 87 |
| 4.2 | Nuclear Resonant Scattering | 88 |
| 4.2.1 | The Nuclear Scattering Amplitude | 90 |
| 4.2.2 | Polarization Dependence | 91 |
| 4.2.3 | Resonant Reflection from Surfaces | 96 |
| 4.2.4 | Resonant Reflection from Ultrathin Films | 96 |
| 4.2.5 | Determination of Magnetic Moment Orientations and Spin Structures | 98 |
| 4.2.6 | Comparison with Conventional Mössbauer Spectroscopy | 104 |
| 4.3 | Special Aspects | 106 |
| 4.3.1 | Kinematical vs. Dynamical Theory | 106 |
| 4.3.2 | Transverse Coherence: Influence of the Detector Aperture | 107 |
| 4.3.3 | Standing Waves in Thin Films | 110 |
| 4.4 | Magnetism of Multilayers, Thin Films, and Nanostructures | 115 |
| 4.4.1 | Depth Selectivity in Resonant X-Ray Reflection | 115 |
| 4.4.2 | Magnetic Superlattices | 117 |
| 4.4.3 | The Spin Structure of Exchange-Coupled Films | 123 |
| 4.4.4 | Magnetism of Fe Islands on W(110) | 130 |
| 4.4.5 | Perpendicular Magnetization in Fe Clusters on W(110) | 139 |
| 4.4.6 | Nuclear Resonant Small-Angle X-ray Scattering | 144 |
| 4.5 | Magnetism at High Pressures | 150 |
| 4.6 | Study of Dynamical Properties | 155 |
| 4.6.1 | Quasielastic Nuclear Resonant Scattering | 155 |

| | | |
|----------|--|------------|
| 4.6.2 | Diffusion in Crystalline Systems | 156 |
| 4.6.3 | Slow Dynamics of Glasses | 160 |
| 4.6.4 | Relaxation Phenomena | 162 |
| 4.7 | Data Analysis | 166 |
| 4.8 | Comparison with Other Scattering Methods | 167 |
| 4.8.1 | Resonant Magnetic X-ray Scattering | 168 |
| 4.8.2 | Polarized Neutron Reflectometry | 168 |
| | References | 171 |
| 5 | Inelastic Nuclear Resonant Scattering | 181 |
| 5.1 | Inelastic Nuclear Resonant Absorption | 182 |
| 5.2 | Extraction of the Phonon Density of States | 186 |
| 5.3 | Experimental Aspects | 189 |
| 5.3.1 | Lamb-Mössbauer Factor and Multiphonon Excitations | 189 |
| 5.3.2 | Temperature Dependence and Anharmonicity | 190 |
| 5.3.3 | Thermodynamic Quantities | 192 |
| 5.4 | Vibrational Properties of Thin Films and Nanostructures | 192 |
| 5.4.1 | Phonon Damping in Thin Films of Fe | 194 |
| 5.4.2 | Vibrational Modes in Nanoparticles | 198 |
| 5.4.3 | Phonons in Fe Islands on W(110) | 201 |
| 5.4.4 | Vibrational Excitations in Amorphous FeTb Alloys | 203 |
| 5.4.5 | Phonon Softening in Fe-Invar Alloys | 207 |
| 5.4.6 | Local Vibrational Density of States: Interface Phonons and Impurity Modes | 210 |
| 5.5 | Further Applications | 214 |
| 5.5.1 | Lattice Dynamics at High Pressures: Geophysical Aspects | 214 |
| 5.5.2 | Dynamics of Biomolecules | 219 |
| 5.6 | Comparison with Other Scattering Methods | 225 |
| | References | 226 |
| 6 | Advanced Scattering Techniques | 233 |
| 6.1 | Resonant Scattering from Moving Matter | 233 |
| 6.2 | The Nuclear Lighthouse Effect | 234 |
| 6.2.1 | Basic Principles | 234 |
| 6.2.2 | Observation of the Nuclear Lighthouse Effect | 236 |
| 6.2.3 | Space-Time Description | 238 |
| 6.2.4 | Imaging the Temporal Evolution of Nuclear Resonant Scattering | 240 |
| 6.2.5 | Observation of the 22.5-keV Resonance of ^{149}Sm | 243 |
| 6.2.6 | Practical Considerations | 246 |
| 6.3 | High-Resolution Filtering of Synchrotron Radiation | 248 |
| 6.3.1 | Energetic Bandwidth | 249 |
| 6.3.2 | Spectrometer Types | 251 |
| 6.3.3 | Considerations on Inelastic Spectroscopy | 254 |

| | | |
|----------|--|-----|
| 6.4 | Heterodyne and Stroboscopic Detection Schemes | 255 |
| 6.5 | Time-Domain Interferometry | 259 |
| 6.5.1 | General Considerations | 259 |
| 6.5.2 | Determination of the Intermediate Scattering Function | 260 |
| 6.5.3 | Application: Dynamics at the Glass Transition | 262 |
| 6.6 | SRPAC: Perturbed Angular Correlation with Synchrotron Radiation | 263 |
| | References | 268 |
| 7 | Outlook and Perspectives | 273 |
| 7.1 | Future Synchrotron Radiation Sources | 273 |
| 7.2 | Elastic Nuclear Resonant Scattering | 278 |
| 7.2.1 | Lighthouse Filtering | 278 |
| 7.2.2 | Picosecond Time-Resolution | 278 |
| 7.2.3 | Metrology | 279 |
| 7.3 | Inelastic Nuclear Resonant Scattering | 280 |
| 7.3.1 | Nuclear Inelastic Pump-Probe Experiments | 280 |
| | References | 282 |
| 8 | Concluding Remarks | 283 |
| A | Appendix | 285 |
| A.1 | Hyperfine Interactions | 285 |
| A.2 | Structure Function and Propagation Matrix | 288 |
| A.3 | Calculation of the Matrix Exponential $e^{i\mathbf{F}z}$ | 291 |
| A.4 | Transverse Coherence of X-rays | 293 |
| A.5 | Derivation of the Roughness Matrix | 296 |
| A.6 | The Projected and the Total Phonon Density of States | 297 |
| A.6.1 | Single-Crystalline Systems | 298 |
| A.6.2 | Polycrystalline Systems | 299 |
| A.7 | Table of Resonant Isotopes | 299 |
| | References | 312 |
| | Index | 313 |

List of Acronyms

| | |
|---------|--|
| ADC | Analog-to-Digital Converter |
| AF | antiferromagnetic |
| APD | Avalanche Photodiode |
| APS | Advanced Photon Source |
| BM | Bending Magnet |
| CEMS | Conversion Electron Mössbauer Spectroscopy |
| CFD | Constant-Fraction Discriminator |
| CONUSS | Coherent Nuclear Scattering from Single Crystals |
| CRL | Compound Refractive Lens |
| DAC | Diamond Anvil Cell |
| DFT | Density Functional Theory |
| DHO | Damped Harmonic Oscillator |
| DOS | Density of States |
| EELS | Electron Energy Loss Spectroscopy |
| EFG | Electric Field Gradient |
| ESRF | European Synchrotron Radiation Facility |
| FWHM | Full-Width at Half-Maximum |
| GISAXS | Grazing-Incidence Small-Angle X-ray Scattering |
| GMR | Giant Magnetoresistance |
| HASYLAB | Hamburger Synchrotronstrahlungslabor |
| HHLM | High-Heat-Load Monochromator |
| HRM | High-Resolution Monochromator |
| ID | Insertion Device |
| INS | Inelastic Neutron Scattering |
| IXS | Inelastic X-ray Scattering |
| LEED | Low-Energy Electron Diffraction |
| MAS | Magic-Angle Spinning |
| MBE | Molecular Beam Epitaxy |
| MCA | Multi-Channel Analyzer |
| MCF | Mutual Coherence Function |
| MOKE | Magneto-Optical Kerr Effect |

XVI List of Acronyms

| | |
|---------|---|
| NBS | Nuclear Bragg Scattering |
| NFS | Nuclear Forward Scattering |
| NIA | Nuclear Inelastic Absorption |
| NIS | Nuclear Inelastic Scattering ¹ |
| NLE | Nuclear Lighthouse Effect |
| NMR | Nuclear Magnetic Resonance |
| NRS | Nuclear Resonant Scattering |
| NRIXS | Nuclear Resonant Inelastic X-ray Scattering |
| NRSAXS | Nuclear Resonant Small-Angle X-ray Scattering |
| NRVS | Nuclear Resonant Vibrational Spectroscopy |
| PDOS | Phonon Density of States |
| PHOENIX | Phonon Excitation by Nuclear Inelastic Scattering of X-rays |
| PMT | Photomultiplier Tube |
| PCS | Photon Correlation Spectroscopy |
| PSD | Position-Sensitive Detector |
| QNFS | Quasi-Elastic Nuclear Forward Scattering |
| QNS | Quasi-Elastic Neutron Scattering |
| rf | radio-frequency |
| rms | root-mean-square |
| SANS | Small-Angle Neutron Scattering |
| SAXS | Small-Angle X-ray Scattering |
| SMR | Synchrotron Mössbauer Reflectometry |
| SPHINXS | Synchrotron-based Phonon Inelastic Nuclear X-ray Scattering |
| SPring8 | Super Photon ring 8 GeV |
| SR | Synchrotron Radiation |
| SRPAC | Synchrotron Radiation based Perturbed Angular Correlation |
| STM | Scanning Tunneling Microscopy |
| TAC | Time-to-Amplitude Converter |
| TDI | Time-Differential Interferometry |
| TDPAC | Time-Differential Perturbed Angular Correlation |
| UHV | Ultra-High Vacuum |
| VDOS | Vibrational Density of States |
| XFEL | X-ray Free Electron Laser |
| XPCS | X-ray Photon Correlation Spectroscopy |

¹ There is currently no unique acronym for inelastic spectroscopy involving excitation of nuclear resonances, i.e., the acronyms NIS, NIA, PHOENIX, NRIXS, NRVS are synonymous.

1 Introduction

The scattering of x-rays is a very powerful tool to investigate the structure and dynamics of condensed matter. The research in this field can be subdivided into three major classes: *Diffraction*, *Spectroscopy* and *Imaging*.

Diffraction experiments probe structural properties: If the photon momentum transfer matches typical reciprocal length scales (i.e. Fourier components of the structure factor), one finds enhanced intensity at the corresponding scattering angle. *Spectroscopy* experiments probe excitations in condensed matter by tuning the energy of the radiation relative to an energy reference: If the photon energy transfer matches an excitation energy, a peak in the scattered intensity is observed. *Imaging* methods are complementary to diffraction methods since they operate directly in real space rather than in reciprocal space. It depends on the desired resolution, what technique is the most suitable one. To obtain very high spatial resolution, one performs the measurement in reciprocal space, because in a diffraction experiment small length scales in real space are mapped to large scattering angles. The combination of various complementary techniques in this field allows to obtain information on practically all length scales.

However, the above list lacks full symmetry, since the reciprocal counterpart of *Spectroscopy* is missing. Because spectroscopy is always considered as the measurement of certain physical parameters as a function of energy, the counterpart should be a time-based technique. Since the operation on the time scale is restricted by causality, the transformation between energy and time domain and vice versa is not as straightforward as the transformation between spatial coordinates and momentum space.

This book is devoted to a particular technique in this field, namely the time-based analog of Mössbauer spectroscopy as it is realized via nuclear resonant scattering of synchrotron radiation. Applications are found in two major fields: *Hyperfine spectroscopy* proceeds via analysis of beat patterns in the temporal evolution of the nuclear decay after excitation by synchrotron radiation. *Vibrational spectroscopy* proceeds via phonon assisted nuclear resonant absorption, where time discrimination is applied to detect the decay of nuclei that were excited by synchrotron radiation. For comparison with other methods, several experimental techniques and their ranges in energy and time resolution are displayed in Fig. 1.1.

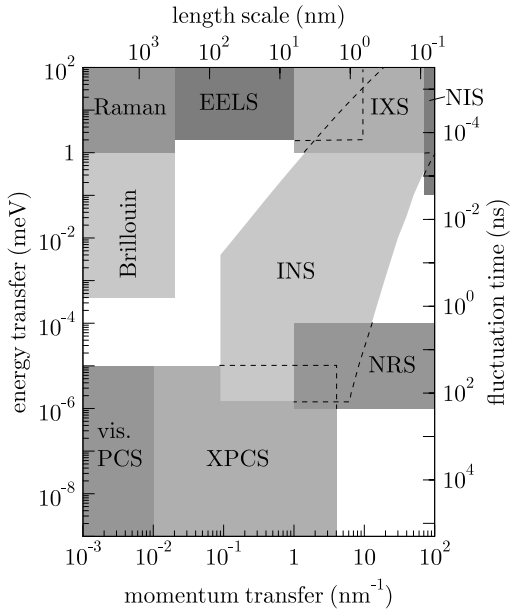


Fig. 1.1. Ranges in energy-momentum space accessible for various scattering techniques: inelastic neutron scattering (INS), nuclear resonant scattering (NRS), inelastic x-ray scattering (IXS), electron-energy loss spectroscopy (EELS), Brillouin light scattering, Raman scattering, photon correlation spectroscopy (PCS) in the visible and in the x-ray regime (XPCS). The wide range of energy transfers covered by INS results from the combination of spin-echo, backscattering and chopper-based spectroscopies. The technique of nuclear inelastic scattering (NIS) is based on an incoherent scattering process and thus does not allow for q -resolved measurements

1.1 Elastic Nuclear Resonant Scattering

To probe nuclear interactions in condensed matter, a number of spectroscopic methods are available, constituting the field of *nuclear condensed matter physics* [1, 2]. An outstanding method in this field is the Mössbauer effect that provides energy resolutions in the neV range. It probes internal fields in the sample that result in an energetic hyperfine splitting of the nuclear levels. In the time domain, the frequency differences of the resonance lines manifest as modulations (quantum beats) in the temporal evolution of the nuclear decay, very similar to the acoustic beats of slightly-detuned tuning forks. Due to the narrow nuclear resonance width, the scattering process takes place on time scales ranging from ns to μ s, depending on the lifetime of the corresponding isotope. This allows for a discrimination of the resonantly scattered radiation from the instantaneous nonresonant charge scattering that proceeds on time scales in the range of 10^{-15} s. The availability of pulsed synchrotron radiation sources has opened this field for many exciting experiments.

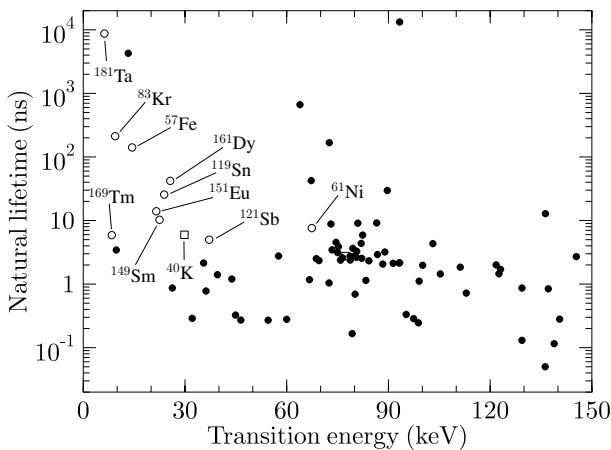


Fig. 1.2. Plot of all known Mössbauer isotopes as a function of resonance energy and lifetime. The open circles mark those isotopes that have been applied in *coherent* nuclear resonant scattering experiments with synchrotron radiation. The open squares are those isotopes where resonance excitation has been detected via *incoherent* scattering. The former and the latter isotopes are explicitly listed in Table 2.1. A complete listing of all stable Mössbauer isotopes is given in the appendix (Table A.1)

An important advantage of this technique over the conventional Mössbauer spectroscopy is the fact that it employs *coherent scattering* rather than *incoherent absorption*. Therefore it is sensitive to spatial phase factors. Thus, diffraction and interferometry experiments are possible to correlate information about internal fields with the spatial arrangement of the atoms in the sample. Together with the enormous brilliance of present-day synchrotron radiation sources this technique becomes a unique tool to investigate very small sample volumes like nanostructures, ultrathin films and clusters.

Figure 1.2 displays all known Mössbauer isotopes (here: stable isotopes with nuclear levels below 150 keV) as a function of resonance energy E_0 and lifetime τ_0 . The open circles mark those isotopes that have been used with synchrotron radiation so far, mostly confined to the energy range below 30 keV. Particular data about these isotopes are listed in Tables 2.1 and A.7. Other isotopes, especially in the range of 80 keV could be interesting candidates to extend this kind of spectroscopy to high energies.

1.2 Inelastic Nuclear Resonant Scattering

Inelastic nuclear resonant scattering relies on the fact that a certain fraction of resonant absorption events proceeds with transfer of recoil energy to the solid.

The spectroscopic method is thus based on *inelastic* nuclear resonant absorption in the sample under study. If the incident photon energy is off-resonance, excitation of the nuclear resonance can be achieved via energy exchange with vibrational modes in the sample. Therefore, the yield of nuclear fluorescence photons as a function of incident energy gives a direct measure of the number of phonon states. From such phonon spectra, the vibrational density of states in the sample can be determined model-independently in a straightforward manner. The energy resolution is determined by the bandwidth of the x-ray monochromator. Presently, vibrational spectra can be recorded with an energy resolution below 1 meV. Again, the outstanding brilliance of modern synchrotron radiation sources renders this technique very sensitive to small sample volumes.

The principal limit for the energy resolution is given by the resonance width of the Mössbauer isotope. This challenges the development of new techniques for inelastic x-ray scattering with μ eV resolution. With these techniques monochromatization to that level is achieved via elastic nuclear resonant scattering, and energy tuning over several meV is reached via high-speed Doppler motion. In this book two new techniques are introduced to realize this kind of spectroscopy.

The first technique relies on grazing-incidence reflection from a rotating mirror coated with ^{57}Fe . The narrow band of resonantly scattered radiation is discriminated against the nonresonant photons by polarization filtering. Due to the linear Doppler shift at the rotating mirror the reflected radiation can be tuned over a few meV around the resonance energy. The second approach relies on the *Nuclear Lighthouse Effect*: In a rotating medium the excited nuclear state rotates with the sample during the scattering process. As a result, the time spectrum of the nuclear decay is mapped to an angular scale. This allows for separation of the resonantly scattered photons from the intense primary beam and enables one to extract a μ eV-wide beam out of the broad band of synchrotron radiation. Tunability over several meV is achieved by transverse displacement of the rotating scatterer relative to the beam. Due to the strong bandwidth reduction in these techniques, their applicability is presently limited by the flux obtainable at current synchrotron radiation sources. Due to the steady improvement of insertion devices and optical elements, such inelastic experiments should be possible in the near future.

1.3 Outline of this Book

The book starts with an introduction to the basic principles of nuclear resonant scattering of synchrotron radiation. The method has found a multitude of applications in condensed matter physics, because many different scattering processes are possible, resulting from all combinations of coherent and incoherent with elastic and inelastic processes. The main processes that are

exploited presently are *coherent elastic* and *incoherent inelastic* scattering of synchrotron radiation. While the former one finds an important application in the determination of magnetic structures, the latter one allows determination of the vibrational density of states in condensed matter. Although these methods require Mössbauer atoms in the sample, they have found a vast number of applications in many fields of physics so far, ranging from high-pressure physics and magnetic nanostructures to biological macromolecules and quasicrystals.

The first chapter specifically deals with the features of coherent elastic scattering, in particular forward scattering and Bragg scattering. While most readers will be familiar with the transformation between momentum and space coordinates, this probably does not apply for the transformation between energy and time coordinates. The intriguing features of time-resolved resonant scattering will be discussed in detail because they greatly influence the appearance of the experimental data.

The use of synchrotron radiation for these experiments requires the application of highly elaborate instrumentation. In particular, high-resolution monochromators and detectors had to be developed specifically for these experiments. Chapter 3 gives an introduction to modern synchrotron radiation sources and their properties as they are relevant for nuclear resonant scattering experiments. The following section explains the basic principles of monochromatization that is mandatory for these experiments. The development has led to the routine operation of sub-meV monochromators that allow recording the vibrational dynamics in condensed matter with very high resolution. A similar development has taken place in the field of x-ray detectors. Avalanche photodiodes are used with time resolutions of a few hundred picoseconds. Since these devices are standard components of present-day beamlines, their basic principles will be explained here.

The next chapter is devoted to applications of coherent nuclear resonant scattering. The scattering theory is outlined with special emphasis to stratified media like thin films and multilayers. A number of experimental examples is given with recent results on the magnetic properties of thin films, two- and three-dimensional magnetic nanostructures, magnetism under high pressure, and dynamical processes in crystalline and disordered materials.

While the previous chapter was devoted to elastic nuclear resonant scattering, Chap. 5 will explain the principles of inelastic nuclear resonant scattering. As an incoherent method, this allows a direct determination of the partial phonon density of states of the resonant atoms in the sample. A number of experimental examples are given, again with emphasis on thin films and nanostructures as well as lattice dynamics under high pressure and vibrational properties of biomolecules. The high isotopic specificity enables one to study the vibrational properties with a very high spatial resolution and a sensitivity in the monolayer range.

The unique properties of resonant scattering still leave room for new developments. Two of these will be discussed in Chap. 6: The Nuclear Lighthouse Effect is observed when resonant scattering takes place in a sample that rotates with a frequency of several kHz. The corresponding mapping of the temporal response to an angular scale opens new possibilities for elastic nuclear resonant scattering. In particular, time resolutions can be expected to go beyond currently existing limits. Moreover, nuclear resonant scattering allows one to monochromatize synchrotron radiation down to bandwidths in the μeV range. This opens perspectives for inelastic x-ray spectroscopy in regions of phase space that have not been accessible so far. The book concludes with a chapter about future applications of these methods, also in view of the development of new x-ray sources, a process that will certainly continue in the future.

Throughout the text, the treatment is given at a level that should allow advanced students to obtain a basic introduction. Likewise, it should be suited to provide an easy access to researchers that want to enter this field. Software for data analysis is already available for most of the scattering methods discussed here. Nevertheless, the basic principles behind these procedures will be explicitly explained in this book. The methods discussed here can be used to complement the results obtained by other scattering methods like magnetic x-ray scattering or elastic and inelastic neutron scattering. For this reason, in many places a comparison with those methods is given.

References

1. G. Schatz, A. Weidinger : *Nukleare Festkörperphysik* (Teubner, Stuttgart 1985) 2
2. G. Schatz, A. Weidinger : *Nuclear Condensed Matter Physics : Nuclear Methods and Applications*, 2nd edition (Wiley, New York 1996) 2

2 General Aspects of Nuclear Resonant Scattering

Nuclear resonant scattering (NRS) unites a number of different scattering processes that can be used to investigate properties of condensed matter. The choice of a specific scattering channel determines what information about the system can be extracted. For that reason an overview over these processes will be given in this chapter.

2.1 Classification of Scattering Processes

Resonant light scattering as a quantum mechanical phenomenon can be treated as the absorption and subsequent reemission of photons. After excitation the subsequent decay may proceed along two different routes:

- The system returns to its ground state, or
- the system moves into an excited state.

Here the ‘excited state’ denotes a state of the atom that differs from the original ground state, e.g., caused by energy exchange with the electron shell or lattice excitations. The balance between the two routes is determined by the possible relaxation processes of the system. In case of nuclear excitations these are due to changes of the nuclear wavefunction (e.g., spin flip in the ground state), the electronic wavefunction (e.g., internal conversion, i.e., transfer of the excitation energy to an electron), or the vibrational wavefunction (i.e., transfer of recoil energy to the lattice).

Along the first route, the sample is in the same state as before the scattering process, thus it cannot be determined which particular atom in the sample was involved. In other words, the path of the system during the scattering process cannot be traced; all possible paths are indistinguishable and are thus equally probable. This is essentially the definition of a *coherent* scattering process. In most cases coherence implies that the energy of the system does not change, i.e., the scattering is *elastic*. The only, albeit important exception is the interaction with delocalized quasi-particle excitations like phonons during the scattering process. This is an inelastic process that does not violate the condition for coherence.

Along the second route, however, coherence is lost because a particular scattering path can be traced via the atom in the sample that did not return

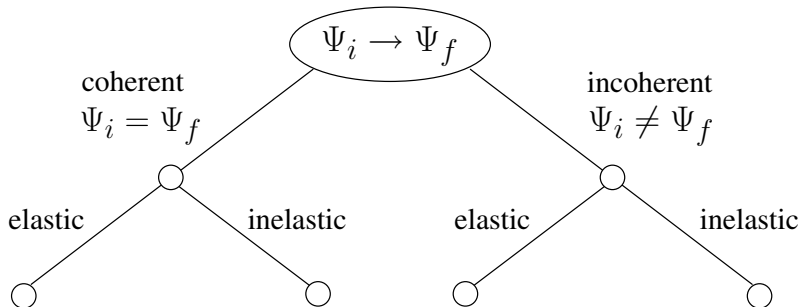


Fig. 2.1. Classification of resonant scattering processes with respect to coherence and elasticity. Ψ_i and Ψ_f are the wavefunctions of the initial and the final state, respectively

to its ground state. The scattering process is then called *incoherent*. Since all such processes involve individual atoms, there is no preferred direction anymore in space so that the reemission is isotropic. In most cases, incoherence implies an energy transfer to the system so that the scattering process is *inelastic*. Here the only exception occurs if the atom returns into a degenerate ground state, e.g., after spin flip.

Figure 2.1 displays the classification of the possible scattering processes that result from the combination of coherence and elasticity and their complements.

2.1.1 Coherent Elastic Nuclear Resonant Scattering

After the scattering process the system returns into its initial state. Thus, the probability amplitudes for scattering from all atoms in the sample have to be added coherently. The phased superposition of these all these amplitudes leads to a highly directional emission into Bragg or Laue reflections. In case of resonant scattering, however, the scattering process takes place on a time scale determined by the resonance width¹. The coherent nature of the scattering process influences the temporal evolution because the oscillators in the sample are coupled through the radiation field. A special situation arises when these oscillators are excited simultaneously, e.g., by a synchrotron radiation flash. Then the temporal *and* spatial coherence of the scattered wavefield leads to interesting phenomena like speedup and quantum beats in the time spectra of the decay. The latter phenomenon is illustrated in Fig. 2.2. The temporal response is very sensitive to the hyperfine interactions of the nuclei in the sample. Therefore, this kind of time-resolved spectroscopy with synchrotron radiation has found several applications in

¹ Electronic scattering, however, proceeds on a ‘fast’ time scale in the order of 10^{-15} s that is not resolvable by current detectors and is therefore treated as instantaneous.

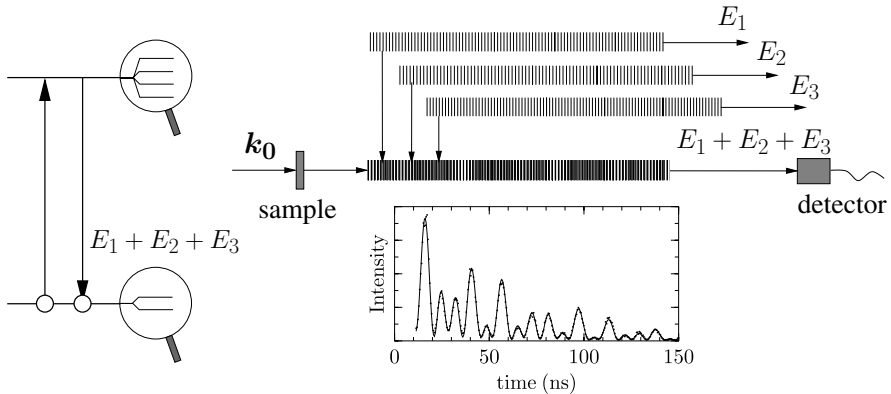


Fig. 2.2. Coherent elastic NRS in forward direction. The superposition of waves emitted from various hyperfine-split levels leads to quantum beats in the temporal evolution of the decay. This is illustrated by overlaying three wavetrains of slightly different frequencies, leading to a Moiré pattern that represents the quantum beats

condensed matter physics. The basic principles and applications particularly in the field of thin-film magnetism are treated in Sect. 4.4.

2.1.2 Coherent Inelastic Nuclear Resonant Scattering

This type of scattering is illustrated in Fig. 2.3. The excited nuclear state interacts with lattice vibrations in the sample that transfer energy to the reemitted photon. The energetic analysis of the scattered radiation as a function of momentum transfer allows the determination of phonon dispersion relations and the study of vibrational excitations in condensed matter. This is typically done via (nonresonant) electronic x-ray scattering which has been developed into a powerful method at modern synchrotron radiation sources [1, 2, 3, 4]. Unfortunately, this scattering process is much less favorable in case of nuclear resonant scattering. A detailed analysis was given by Sturhahn & Kohn [5]. One reason is that the lifetimes of thermal phonons are very short compared to the nuclear lifetime. Therefore, the coherence of the waves scattered by the nuclei in the sample is preserved only during a very short time. Then, in analogy to nuclear resonant scattering in the presence of diffusion (see Sect. 4.6), one expects an extremely fast decay ($\sim 10^{-12}$ s) of coherent inelastic NRS, which would make its observation extremely difficult. A closer inspection reveals that this type of scattering can be appreciable when a phonon is created upon absorption while during reemission the lattice state does not change. However, since the reemitted photon has the nuclear transition energy, it suffers strong resonant absorption. For that reason coherent

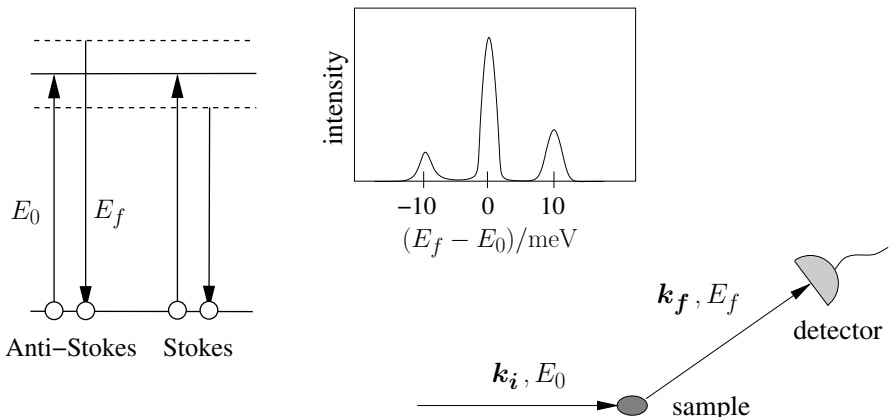


Fig. 2.3. Coherent inelastic NRS. The diagram on the left illustrates the case that the incident energy is fixed and the energy of the scattered photon is analyzed. The opposite case with a fixed exit energy while tuning the incident energy, is possible, too

inelastic NRS is indeed small, but may be appreciable for scattering from thin films where the escape depth of the reemitted photons is small.

A tacit assumption in these considerations was that the scattering takes place from thermally excited phonons. In cases where phonons are excited by external sources like ultrasound or pulsed laser irradiation, the population of phonon states may be sufficiently high to render the observation of coherent inelastic NRS feasible. This has been demonstrated for the excitation of phonons in stainless steel by ultrasound and subsequent energy analysis by a resonant absorber in forward direction [6].

2.1.3 Incoherent Elastic Nuclear Resonant Scattering

Incoherence is introduced if the decay of the excited nuclear state proceeds via resonance fluorescence or internal conversion, for example. In this case the atomic wavefunction changes so that the atom is ‘tagged’ and coherence is lost. This is indicated in Fig. 2.4 by the black circle in the final state. The subsequent reemission proceeds then into a solid angle of 4π . The reemitted particles can be either fluorescence photons or conversion electrons. Both can be used to measure the hyperfine interaction of the nuclei in the sample. The incident energy of a radioactive source is tuned while the yield of nuclear decay products is monitored. The inset shows a conversion electron Mössbauer (CEMS) spectrum from a Fe/Ag multilayer. Due to the small escape depth of the electrons, the technique is very sensitive to thin films in the monolayer regime.

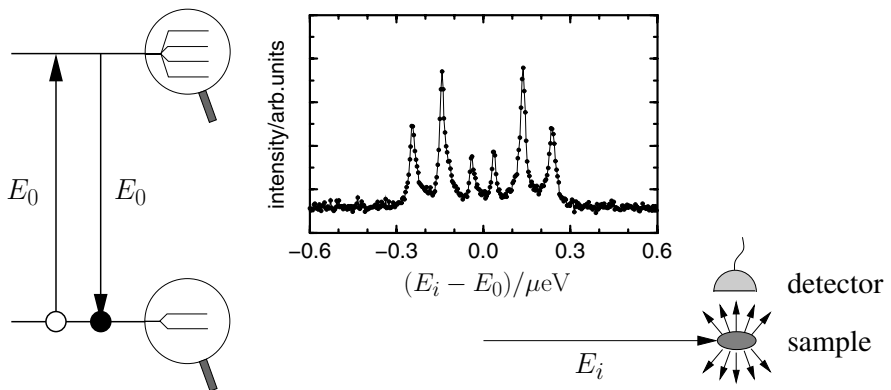


Fig. 2.4. Incoherent elastic NRS. The nucleus de-excites by emission of fluorescence radiation or internal conversion. The *black circle* in the diagram on the left indicates that the atomic wavefunction has changed. This process is applied in Mössbauer spectroscopy with detection of fluorescence radiation or conversion electrons (CEMS)

2.1.4 Incoherent Inelastic Nuclear Resonant Scattering

In this case nuclear resonant absorption proceeds via creation or annihilation of phonons, as symbolized in Fig. 2.5. The spectrum of vibrational excitations is recorded by tuning the energy of the incident radiation around the resonance while the yield of nuclear decay products is monitored². Due to the low cross sections and the detuning energies of several meV, a radioactive source and a Doppler drive are not suited to perform this kind of spectroscopy. Instead, highly monochromatized synchrotron radiation is used to record phonon spectra of bcc Fe as shown in the inset. This technique was first introduced by Seto *et al.* [10] in 1995 and applied to many fields in condensed matter physics since then.

While all possible combinations and their relevance have been reviewed in the preceding sections, the remainder of this book will focus on

- Coherent elastic nuclear resonant scattering (Chap. 4) and
- Incoherent inelastic nuclear resonant scattering (Chap. 5).

These two methods have gained significant momentum during the past years that is sustained by unique applications in condensed matter physics and the availability of high-brilliance synchrotron radiation.

² This method is conceptionally equivalent to the technique of vibronic sideband phonon spectroscopy, see, e.g., [7, 8, 9].

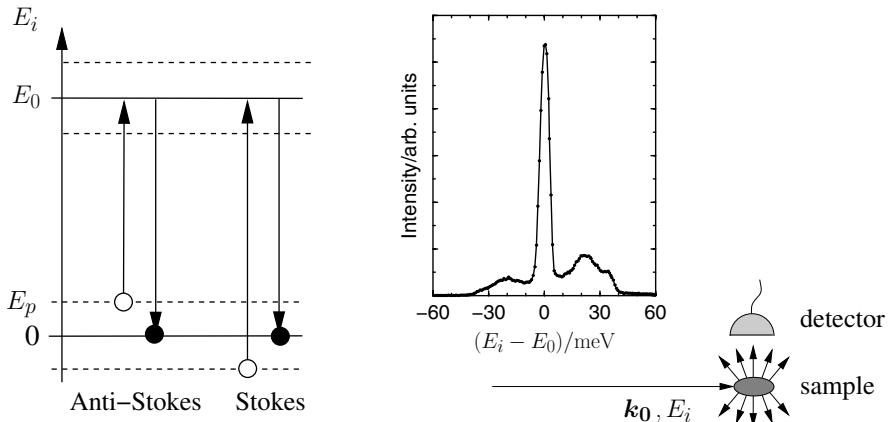


Fig. 2.5. Incoherent inelastic NRS. This method is often referred to as ‘phonon-assisted nuclear resonant absorption’: If the incident photon energy is off-resonance, excitation of the nuclear resonance is achieved via energy exchange with a phonon. The yield of nuclear fluorescence photons as a function of incident energy gives a measure of the number of phonon states

2.2 Features of Elastic Nuclear Resonant Scattering

The propagation of x-rays in a resonant system is affected by scattering processes that take place on a time scale given by $\tau_0 = \hbar/\Gamma_0$ where Γ_0 is the natural linewidth of the resonance. The presence of a resonance drastically changes the x-ray optical properties of the medium. This was demonstrated for total reflection from the surface of a resonant material [11] and nuclear Bragg diffraction from single crystals [12]. While classical optical theory proved to be sufficient to understand the behavior of resonant absorbers either on the energy scale [13] or on the time scale [14], a puzzling fact remained: The experimental observations could only be explained if not single nuclei but nuclear ensembles were involved in the scattering of single quanta. These apparently contradictory concepts could be successfully combined in a single physical picture, the *nuclear exciton*, that was introduced independently by *Hannon & Trammell* [15, 16] and *Kagan & Afanas’ev* [17, 18, 19, 20]. As a result, nuclear resonant scattering of synchrotron radiation can be treated basically via two approaches:

- If the duration of the synchrotron pulse and its transit time through the system are short compared to the lifetime of the nuclear resonance, the formation of the excited state and its subsequent decay can be treated as independent quantum-mechanical processes [21]. This concept leads to the notion of the ‘nuclear exciton’ as a description of a collectively excited nuclear state. In this formalism the influence of the spatial arrangement of the nuclei on the radiative decay can be conveniently evaluated.

- The interaction can be treated as a resonant scattering problem where the optical properties of the medium are expressed by an energy-dependent index of refraction. This approach provides a very convenient way to calculate the scattered amplitudes: The time-dependent amplitudes are simply given by the Fourier transform of the frequency dependent reflection or transmission amplitudes.

It should be noted that all the x-ray optical properties of resonant matter discussed here fall within the framework of linear (single-photon) optics. Even for the strongest present-day sources of hard x-rays the probability for more than one photon per mode of the radiation field does not exceed 10^{-4} [22]. Only x-ray sources like the projected x-ray free-electron laser (XFEL) are expected to be fully coherent sources with several hundred photons per mode [23]. Such sources will open the field for nonlinear optics, multiphoton scattering and quantum optics involving nuclear resonances.

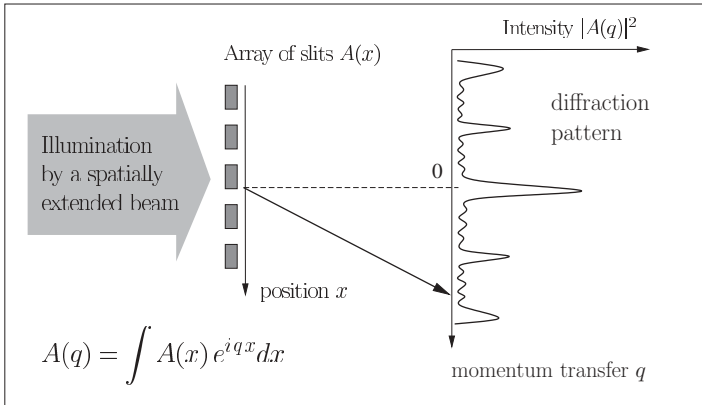
2.2.1 X-ray Diffraction in Space and Time

The coherence and the collective nature of the scattering process lead to interesting effects on the time scale:

- **Speedup** of the decay compared to that of an isolated nucleus, resulting from superradiance-like effects in the coherent decay channels.
- **Quantum beats** resulting from the coherent superposition of waves emitted from different nuclei at different frequencies.

The technique of time-resolved nuclear resonant scattering exhibits some striking similarities with diffraction from a set of slits, as shown in Fig. 2.6. In both cases an array of objects (slits/resonances) is illuminated by a (spatially/energetically) broad beam of radiation. While conventional x-ray diffraction works in position-momentum space, time-resolved nuclear resonant scattering works in energy-time space. Recording a diffraction pattern in reciprocal space allows to reconstruct the shape of the diffracting object. Likewise, recording a temporal quantum-beat pattern allows to determine the relative energetic positions and the shape of the resonance lines. In both methods the field amplitudes in the complementary representations are related by Fourier transformation. The only difference is that the transformation to the time scale is restricted by causality. Besides that, both methods can be united into one space-time formulation of x-ray diffraction, leading to the quantum theory of crystal optics [15, 16]. As a consequence, the spatial arrangement of resonant scatterers will influence the temporal evolution of the decay. This fact finds its expression in the speed-up of the radiative decay of an ensemble of nuclei that are coupled through the standing wave that builds up in a Bragg reflection. On the other hand, the energetic arrangement of resonant scatterers may influence the distribution of radiation in reciprocal space. This manifests in the appearance of pure nuclear Bragg

(a) Diffraction in position–momentum space



(b) Diffraction in energy–time space

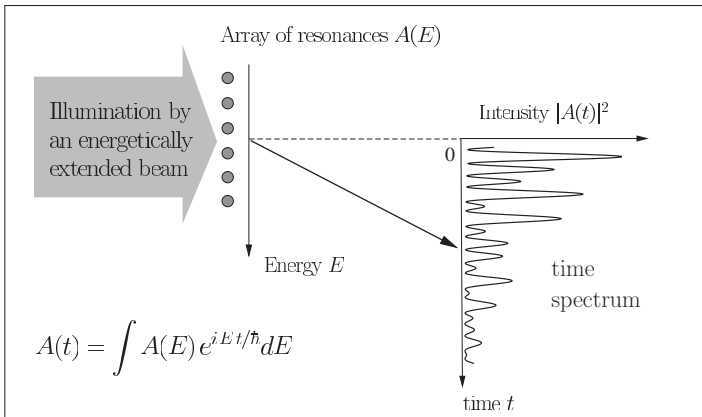


Fig. 2.6. Correspondence between diffraction from an array of slits and temporal beats resulting from simultaneous excitation of an array of resonances. In both cases these arrays are illuminated by a spatially viz. energetically extended incident beam. The diffraction pattern results from a Fourier transformation of the spatial/energetic arrangement of diffracting objects. The symmetry between both techniques is broken on the time scale, because causality has to be observed

reflections, for example. This discussion shows that the concept of diffraction naturally extends into the four-dimensional space-time continuum.

2.2.2 The Nuclear Exciton

Consider a single resonant photon incident on an ensemble of resonant nuclei. One may assume that this leads to a single excited nucleus within this ensemble. However, this is not the case in a *coherent* scattering process where

it is not possible to identify the scattering atom. Instead, for each individual nucleus in the sample there is a small probability amplitude that this nucleus is excited while all other nuclei remain in the ground state. The summation of all these small amplitudes then gives the total probability amplitude for a photon to interact resonantly with the nuclei. If the incident radiation pulse is short compared to the nuclear lifetime τ_0 , these probability amplitudes exhibit the same temporal phase. As a result, a collectively excited state is created, where a *single* excitation is coherently distributed over the atoms of the sample [24]. The wavefunction of this collectively excited state is thus given by a coherent superposition of states in which just one nucleus is excited while all the others are in their ground state:

$$|\Psi(\mathbf{k}_0)\rangle = \frac{1}{\sqrt{N}} \sum_i e^{i\mathbf{k}_0 \cdot \mathbf{r}_i} |g\rangle |e_i\rangle , \quad (2.1)$$

where $|g\rangle |e_i\rangle$ denotes the state in which the i th atom at the position \mathbf{r}_i is in its excited state $|e_i\rangle$ and all the remaining atoms are in their ground states $|g\rangle$. Such an excited state has been named *nuclear exciton*³. It exhibits remarkable optical properties resulting from the coherent superposition of states, that will be discussed in the following. However, these features will be discussed mainly in the index-of-refraction picture with referral to some results derived in the nuclear-exciton picture. A detailed elaboration of the nuclear-exciton picture is beyond the scope of this book. Instead, we refer to extended reviews on this subject in the literature [21, 25].

2.2.3 The Index of Refraction

In a macroscopic picture, a collectively excited nuclear state can be considered as a nuclear polariton, i.e., a coupled state between the ensemble of nuclei and the radiation field. Within this picture one finally obtains an effective description of the optical properties of the medium via the index of refraction. It has been shown by Lax that such a continuum approach is justified for x-rays in condensed matter, even though the mean distance of scattering centers is usually greater than the wavelength of the scattered radiation [26]. Since then, the index-of-refraction approach has been used extensively in neutron and x-ray optics. The polariton concept is applicable to the interaction of several quasiparticle excitations (phonons, magnons, plasmons, excitons) with electromagnetic radiation. The coupling of the radiation field with the atomic resonance into a polariton leads to a hybridization of the individual dispersion relations. This is illustrated in Fig. 2.7.

Remarkable features on the time scale are the speedup of the radiative decay compared to that of an isolated atom, and quantum beats resulting from interference of waves emitted from different resonances at different atoms.

³ This, however, is somewhat misleading compared to the widely accepted definition of an atomic exciton as an electron-hole pair in a solid.

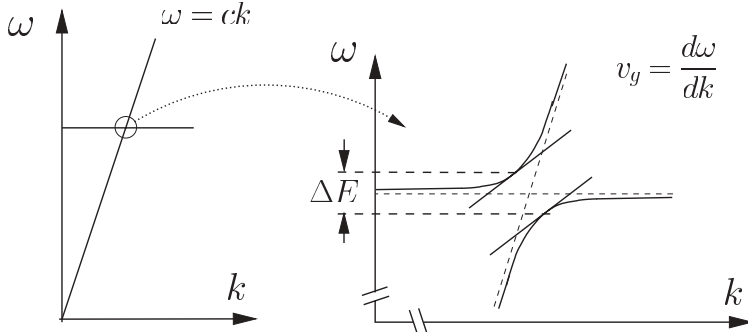


Fig. 2.7. Dispersion relation for photons, a (dispersionless) solid state excitation (left) and the coupled state between the atomic ensemble and the radiation field (right). The particular shape of the dispersion relation leads to propagation quantum beats in the time response of the coherent nuclear decay. They result from the superposition of waves with slightly different energy traveling with the same group velocity as illustrated on the right side

So far, such exciton states have been prepared by short-pulse laser radiation exciting long-lived electronic levels [27, 28] or by synchrotron radiation pulses recoillessly exciting nuclear levels [29, 30]. The analysis of the temporal evolution of the subsequent radiative decay provides valuable information about the environment of the atoms in the sample. Therefore, this type of time-resolved spectroscopy has generated several applications in condensed matter physics [28, 29, 30].

To derive the relation between the atomic scattering amplitude f and the index of refraction n , we consider the following case of forward transmission through a homogeneous slab of material with atomic density ϱ and thickness d , illustrated in Fig. 2.8. We consider the radiation amplitude A in depth z of the slab. At this position there is a platelet with a thickness dz . The platelet is thin enough so that its scattering response can be treated in the kinematical approximation. The change dA in the amplitude by proceeding into depth $z + dz$ is then given by

$$dA = i b f A(z) dz \quad \text{with} \quad b = 2\pi\varrho/k_0^2. \quad (2.2)$$

This leads to the differential equation

$$\frac{dA}{dz} = i b f A(z), \quad (2.3)$$

which has the solution

$$A(z) = A_0 e^{ibfz} e^{ik_0 z}, \quad (2.4)$$

where the geometric phase factor $e^{ik_0 z}$ for traveling in empty space has been appended. Finally, the transmitted amplitude assumes the well-known expression

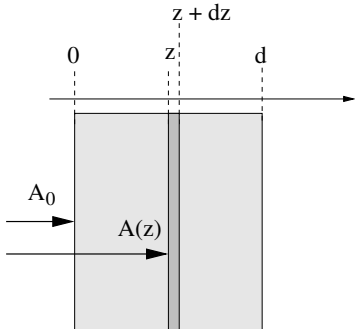


Fig. 2.8. Transmission of x-rays through a slab of homogeneous material to derive the relation between the atomic scattering amplitude f and the index of refraction n

$$A(z) = A_0 e^{i k_0 n z}, \quad (2.5)$$

with the index of refraction n :

$$n = 1 + \frac{2\pi\rho}{k_0^2} f. \quad (2.6)$$

Quite remarkably, this approach can be generalized to a multitude of scattering problems, ranging from simple forward scattering to anisotropic optics, thin-film reflection and Bragg diffraction from crystals and gratings. By definition, such an effective medium description of the material contains all multiple scattering events. The resulting radiation field is a self-consistent solution to the scattering problem within the dynamical theory. The treatment in more complex cases like reflection from thin films and multilayers is given in Sect. 4.1.

It is well known that optical properties of a system change dramatically if the photon energy approaches an atomic resonance. This is valid for the complete spectral range from the infrared into the hard x-ray regime. The remarkable features of x-ray scattering from inner-shell resonances have been discovered and exploited when high-brilliance synchrotron radiation became available [31, 32, 33]. This has occurred for x-ray scattering from nuclear resonances as well [29, 30, 34]. The special features of this type of scattering will be elaborated in the following.

The scattering amplitude for a nuclear-resonance polariton can be written as⁴:

$$f = f_e + f_n, \quad (2.7)$$

where f_e and f_n are the electronic and nuclear contributions to the scattering amplitude, respectively:

⁴ This equation is often written as

$$f = r_0 [-Z + f' + i f''].$$

The first term gives the free-electron Thomson scattering while f' and f'' are corrections describing the anomalous scattering from the bound electrons and the nuclear resonance.

$$f_e = f'_e + i f''_e = -Z r_0 + i \frac{k_0}{4\pi} \sigma_{tot} \quad (2.8)$$

$$f_n = f'_n + i f''_n = \frac{f_0 x}{x^2 + 1} + i \frac{f_0}{x^2 + 1}, \quad (2.9)$$

where Z is the atomic number, $r_0 = e^2/m_e c^2$ is the classical electron radius, and σ_{tot} is the total absorption cross section, consisting of contributions from photoelectric absorption and Compton scattering.

The nuclear scattering amplitude f_n is given for a single resonance line (i.e., no hyperfine interaction). $x = 2(E - E_0)/\Gamma_0$ denotes the deviation of the energy from the exact resonance energy E_0 measured in units of the natural linewidth Γ_0 of the transition. f_0 expresses the ‘oscillator strength’ of the nuclear resonance:

$$f_0 = \frac{f_{LM}}{2k_0} \frac{2I_e + 1}{2I_g + 1} \frac{1}{1 + \alpha}, \quad (2.10)$$

where f_{LM} is the Lamb-Mössbauer factor, I_e and I_g are the spins of the ground and excited nuclear state, respectively, and α is the coefficient of internal conversion. The strong variation of the nuclear scattering amplitude f_n around the resonance is plotted in the left panel of Fig. 2.9 for the 14.4 keV transition of ^{57}Fe . The vertical axis is scaled in units of r_0 . Remarkably, near the resonance the scattering strength of the nucleus corresponds to an

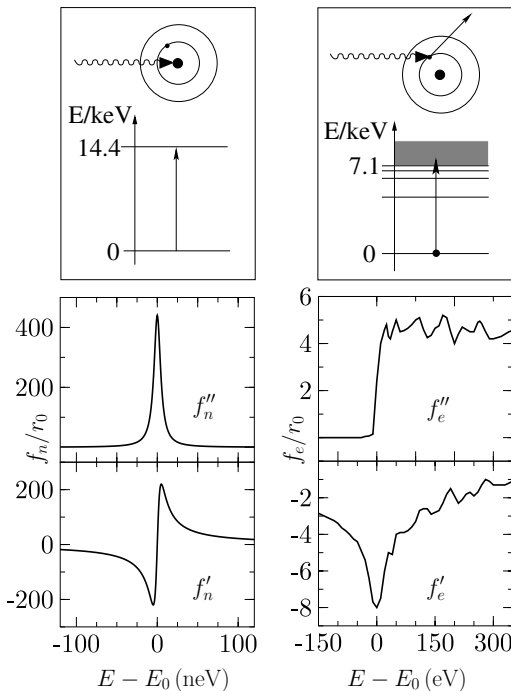


Fig. 2.9. Anomalous scattering amplitudes f' and f'' in case of a nuclear resonance, the 14.4 keV resonance of ^{57}Fe (left panel) and an electronic resonance, the 7.1 keV K-shell resonance of Fe (right panel). While nuclear resonant scattering proceeds between discrete nuclear levels, the excitation of an electronic resonance involves a continuum of final states

atom with $Z \approx 200$. This means that out of the small energy range around the resonance a very strong scattering signal can arise that exceeds that of electronic resonances. For comparison, the resonance behavior of the K-edge in Fe is shown. The basic difference is that the excitation of the K-shell electron involves continuum states, so that one obtains a superposition of resonances that leads to asymmetric resonance broadening [35].

Figure 2.10 shows the deviation of the index of refraction n from unity, $n - 1$, around the nuclear resonance of ^{57}Fe for the alloy $^{57}\text{Fe}_2\text{Cr}_2\text{Ni}$, in which ^{57}Fe behaves as a single line scatterer. Note that in certain regions around the resonance the real part of the index of refraction assumes even values greater than unity⁵. This gives rise to remarkable x-ray optical properties of materials that contain resonant isotopes.

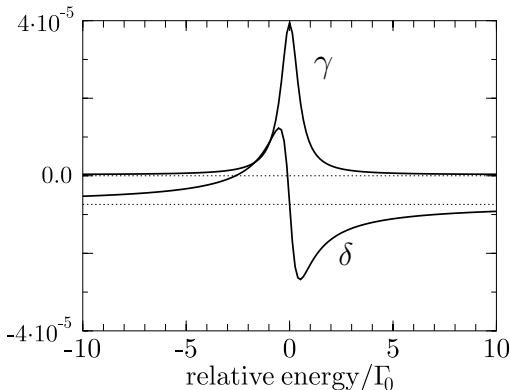


Fig. 2.10. Real increment δ and imaginary increment γ of the index of refraction $n = 1 - \delta + i\gamma$ around the nuclear resonance of $^{57}\text{Fe}_2\text{Cr}_2\text{Ni}$. In this alloy, ^{57}Fe behaves as a single-line scatterer. The energy is measured relative to the transition energy in units of the natural linewidth Γ_0 . The corresponding electronic values are shown as dashed lines

2.2.4 Pulse Propagation

The dispersion of the polaritons contains valuable information about the solid and its elementary excitations. Several methods have been developed to probe polariton dispersion relations [36]. One important method relies on the propagation of monochromatic radiation pulses in the material. If the spectral width of the radiation pulse is much smaller than the resonance width, the pulse propagates with the group velocity

$$v_g = \frac{d\omega}{dk} = \frac{c}{n + \omega \frac{dn}{d\omega}}, \quad (2.11)$$

that is given by the slope of the dispersion curve at that energy. Close to the resonance energy the slope gets very small and so does the group velocity (see Fig. 2.7). In Cu_2O , for example, values down to $10^{-5}c$ could be

⁵ Typically, in the x-ray regime the index of refraction of any material is smaller than one, see also Sect. 4.1.3.

observed [37]. In ultracold atomic gases like Bose-Einstein condensates with electromagnetically induced transparency [38], the velocity of light has been reduced to a few m/s [39].

A different situation arises if the spectral width of the pulse is much larger than the width of the resonance. This particularly applies for the excitation of nuclear resonances with synchrotron radiation, the case that will be discussed in the remainder of this paragraph. If a nuclear resonance is excited by a broad-band radiation pulse, propagating waves with different group velocities interfere and lead to a beat pattern in the temporal evolution of the transmitted intensity. In principle, the time dependent transmission can be treated in a similar way as outlined in the previous section. However, the time dependence introduces more complexity and (2.3) turns into an integro-differential equation:

$$\frac{dA}{dz} = \int_{-t}^{\infty} K(t, t') A(z, t) dt. \quad (2.12)$$

A very elegant solution of this problem was developed by *Shvyd'ko* [40]. This approach is outlined in more detail in Sect. 2.3 of this book. The solution of (2.12) for the time dependence of the transmitted amplitude in case of a single resonance leads to the following expression:

$$A(t) = \delta(t) - \gamma e^{-t/2\tau_0} \frac{J_1(2\sqrt{\gamma t})}{\sqrt{\gamma t}} \quad \text{with} \quad \gamma = \frac{k_0 d f_0}{\tau_0} \quad (2.13)$$

where τ_0 is the natural lifetime of the nucleus, d is the thickness of the material, and $J_1(z)$ is the first-order Bessel function. This function describes an aperiodic oscillation of the intensity that is often referred to as ‘propagation quantum beat’ or ‘dynamical beat’ [41, 42]. It should be noted that the apparent beat period increases with increasing time after excitation and decreases with increasing thickness of the sample. Besides nuclear resonant scattering, these propagation quantum beats have been observed in many other systems. An example is the propagation of light pulses in Cu₂O in the vicinity of an excitonic resonance, as shown in Fig. 2.11 [37].

2.2.5 Speedup

Radiative transitions in an excitonic state are enhanced by coherent effects. This has been investigated in detail by *Dicke* [44] who introduced the concept of superradiance. In a system of N atoms the transition probability is enhanced by a factor of N and, correspondingly, the lifetime of the excited level is reduced by a factor of N compared to a free atom. However, an important condition is that all contributions from different atoms have the same phase. This is possible as long as the wavelength of the radiation is long compared to the interatomic distances. For x-rays this condition is no longer fulfilled and therefore the concept of Dicke superradiance cannot be

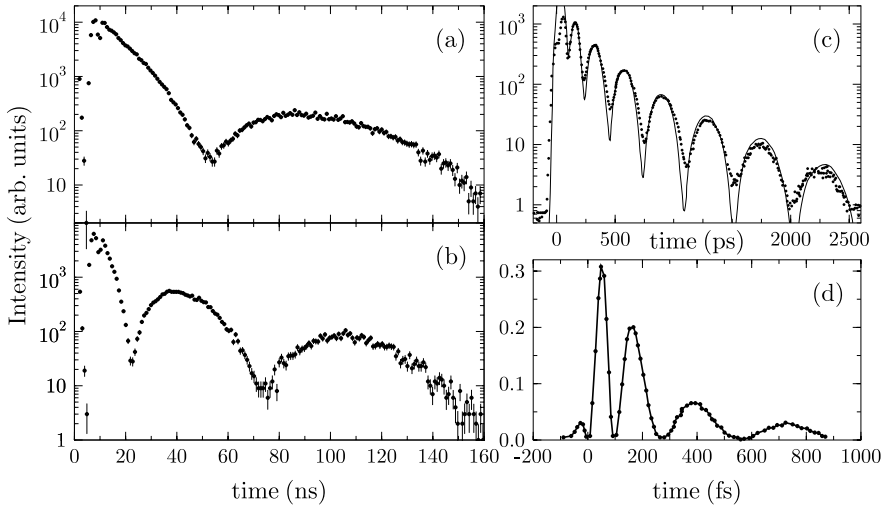


Fig. 2.11. Coherent pulse propagation in case of a single-line resonant medium. The time spectra exhibit characteristic propagation quantum beats: NFS from thin foils of stainless steel ($^{57}\text{Fe}_{55}\text{Cr}_{25}\text{Ni}_{20}$) with thicknesses of (a) $6\text{ }\mu\text{m}$ and (b) $12\text{ }\mu\text{m}$, (c) propagation of 30-fs pulses through a single crystal of Cu_2O with an exciton resonance at 2 eV (Figure adopted from Fröhlich *et al.* [37]), (d) propagation of 60-fs pulses at 1.48 eV in Cs vapor (Figure adopted from Matusovsky *et al.* [43])

simply transferred to the decay properties of nuclear excitons. Nevertheless, coherence effects for properly phased arrays of radiating nuclei have a drastic effect on the radiative decay rate [21, 45, 46].

The acceleration of the nuclear decay in a coherent scattering process has been called *speedup*. It has been observed in nuclear Bragg scattering from single crystals [47] as well as in forward scattering geometry [48] and results from the radiative coupling that is induced by the geometric phasing of the nuclei in the sample. For an isolated nucleus, the radiative decay is described by

$$I(t) = I_0 e^{-\Gamma_0 t/\hbar}. \quad (2.14)$$

$I_0 = \Gamma_\gamma + \Gamma_\alpha$ is the natural linewidth, where Γ_γ is the partial width for radiative decay and $\Gamma_\alpha = \alpha\Gamma_\gamma$ is the partial width for internal conversion decay. For the exciton state given in (2.1), the radiative decay width is significantly increased by the effect of spatial coherence:

$$\Gamma_\gamma = \Gamma_c + \Gamma'_\gamma, \quad (2.15)$$

where Γ'_γ is the partial width for spatially incoherent decay and Γ_c is the coherent decay width. In the absence of hyperfine splittings of the nuclei, Γ_c is given by [21]

$$\Gamma_c = \frac{\Gamma_{coh}}{4\pi N} \int d\Omega [1 - (\hat{k}_0 \cdot \hat{\varepsilon}_0)^2] |S(\mathbf{k} - \mathbf{k}_0)|^2 \quad (2.16)$$

with $\Gamma_{coh} = \frac{f_{LM}}{2} \frac{2I_e + 1}{2I_g + 1} \Gamma_\gamma$

and $S(\mathbf{k} - \mathbf{k}_0) = \sum_{i=1}^N e^{-i(\mathbf{k} - \mathbf{k}_0) \cdot \mathbf{r}_i}$,

where $S(\mathbf{k} - \mathbf{k}_0)$ is the structure factor of the ensemble of nuclei, and the factor $[1 - (\hat{k}_0 \cdot \hat{\varepsilon}_0)^2]$ describes the polarization dependence. The integration over the solid angle strongly depends on the dimensionality and the shape of the crystal. For a three-dimensional sample in forward scattering geometry one arrives at the following expression for the coherent enhancement:

$$\Gamma_c = \frac{\varrho \lambda^2 d}{4\pi} \Gamma_{coh} , \quad (2.17)$$

where ϱ is the density of resonant nuclei. Assuming $\lambda = 0.1 \text{ nm}$ and $\varrho = 10 \text{ nm}^{-3}$, one obtains a doubling of the decay rate already for sample thicknesses in the range of 10 nm. The linear dependence of Γ_c on the sample thickness has been experimentally demonstrated using ^{57}Fe foils [48]. The upper limit of the coherent enhancement is determined by photoabsorption in the sample to about $\Gamma_c \approx 1000 \Gamma_\gamma$. Very large values can be obtained in grazing incidence reflection geometry from thin films, as demonstrated in [49, 50].

Effectively, the envelope of the temporal evolution is often described as

$$I(t) = I_0 e^{-(1+\chi)t/\tau_0} , \quad (2.18)$$

with

$$\chi = \frac{1}{4} \varrho \sigma_0 f_{LM} d , \quad (2.19)$$

where σ_0 is the absorption cross section at resonance, tabulated in Table A.1 for all Mössbauer isotopes.

2.2.6 Quantum Beats

So far the discussion was focused on a system with a single isolated resonance. The dynamical beats encountered in that case resulted from *intraresonance* interference between different spectral components within the resonance line. If the nuclei are subject to hyperfine interactions, the degeneracy of the nuclear levels is lifted, leading to a splitting of the nuclear transition into several resonance lines. The flashlike synchrotron radiation pulses excite the various sublevels instantaneously and coherently, as illustrated in Fig. 2.6b, which then radiate at their various frequencies. The frequency differences lead to beats in the temporal evolution of the exciton decay. Since this results from the superposition of amplitudes from different resonances, this should be

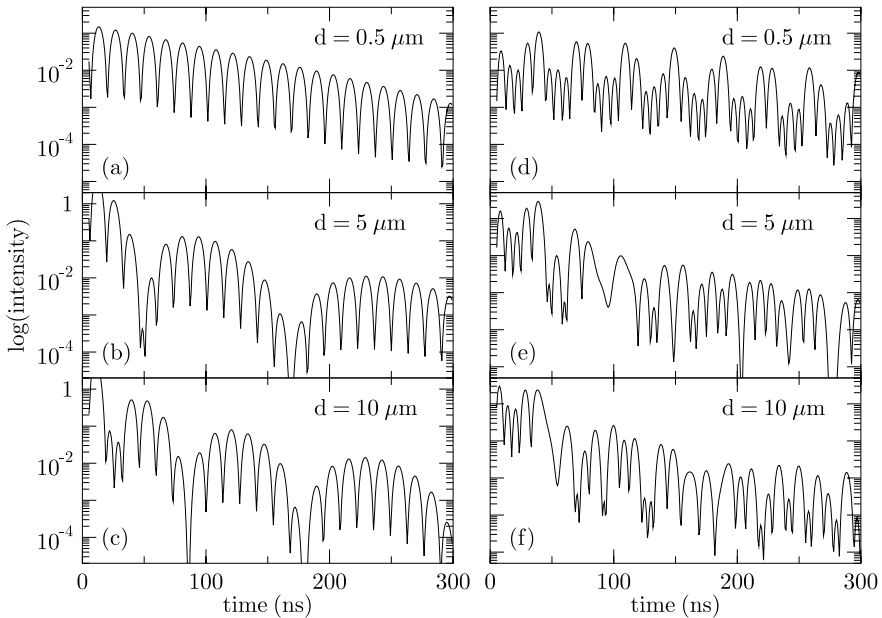


Fig. 2.12. Time spectra of nuclear forward scattering from α -Fe foils of $0.5\text{ }\mu\text{m}$, $5\text{ }\mu\text{m}$, and $10\text{ }\mu\text{m}$ thickness. (a–c) The foils are magnetized so that only the two $\Delta m = 0$ transitions are excited, leading to a quantum-beat period of 14 ns . (d–f) The foils are in a magnetically polycrystalline state where all six hyperfine transitions are excited

referred to as *interresonance* interference. Small energy differences are translated into large quantum beat periods, so that quantum beat measurements can be even more precise than conventional Mössbauer absorption measurements. In the case that the resonance lines are well separated, the time dependence of nuclear forward scattering (NFS) from a sample of thickness d can be expressed as (compare with (2.13)):

$$A(t) = \delta(t) - \sum_i \gamma_i e^{iE_i t / \hbar - t / 2\tau_0} \frac{J_1(2\sqrt{\gamma_i t})}{\sqrt{\gamma_i t}} \quad \text{with} \quad \gamma_i = \frac{k_0 d f_{0,i}}{\tau_0} \quad (2.20)$$

Accordingly, the temporal evolution comprises dynamical beats as well as quantum beats. To illustrate the nature of quantum beats in nuclear forward scattering, a number of examples is compared in Fig. 2.12. The samples were foils of α - ^{57}Fe with thicknesses of $0.5\text{ }\mu\text{m}$, $5\text{ }\mu\text{m}$ and $10\text{ }\mu\text{m}$, respectively. In Figs. 2.12a–c the two foils were magnetized so that only two of the six hyperfine transitions were excited, corresponding to two well-separated

resonances with an energy difference of $0.1 \mu\text{eV}$ ⁶. This leads to quantum beats with a period of $\Delta t = 10 \text{ ns}$. While the envelope of these beats decays monotonously, the envelope in Figs. 2.12b,c exhibits an additional modulation due to propagation quantum beats that have been discussed in Sect. 2.2.4. Thus, the typical appearance of NFS time spectra is a superposition of quantum beats and dynamical beats. The interplay of both often leads to more complex beat patterns referred to as ‘hybrid beat’ that has been studied in detail in [51]. The time spectra get more complex, when more than two resonance lines are involved. This is demonstrated in Figs. 2.12d–f, where the Fe foils were assumed to be polycrystalline. In this case all six transitions contribute with different weights. While the quantum beats of the thin foil still exhibit a regular pattern, the beat pattern of the thick foil lacks any periodicity. This is the result of the superposition of the quantum beats and the dynamical beats from each of the different resonances that blend into a rather complex pattern. Nevertheless, this can be used as a ‘fingerprint’ for a magnetically polycrystalline sample. An additional complexity arises if the hyperfine fields are not single-valued, but distributed over magnitude or direction. In many cases these distributions influence the time spectra in a characteristic way that allows to identify them. A detailed analysis of the quantum beat patterns that arise from distributed magnetic fields has been given by *Shvyd’ko et al.* [53].

An instructive view on quantum beats is provided by nuclear forward scattering at the 6.23-keV resonance of ^{181}Ta [54] which is an E1 transition. The ground and excited states exhibit a nuclear spin of $7/2$ and $9/2$, respectively, and the natural abundance of this isotope is 100%. An external magnetic field lifts the degeneracy of the nuclear levels and leads to a splitting into 8 and 10 sublevels, respectively, as sketched in Fig. 2.13. The right graph shows a time spectrum from a $6 \mu\text{m}$ thick Ta foil that was magnetized so that only the $\Delta m = 0$ transitions were excited. The quantum beats show up as pronounced peaks that result from the interference of 8 equidistant resonances. The time spectrum resembles quite closely the diffraction pattern in case of multi-slit interference. This highlights the analogy between diffraction (the Fourier transform from real space into reciprocal space) and time-resolved spectroscopy (the Fourier transform from the energy domain into the time domain), as illustrated in Fig. 2.6. The latter, however, is restricted by causality.

2.2.7 Suitable Isotopes

Most of the Mössbauer isotopes with resonance energies below 30 keV have been employed in experiments with synchrotron radiation. They are listed in Table 2.1. See also the review article by *Leupold et al.* [52].

⁶ These are the transitions belonging to a change in the magnetic quantum number of $\Delta m = 0$. A detailed account on the magnetic hyperfine interaction will be given in Sect. 4.2.2.

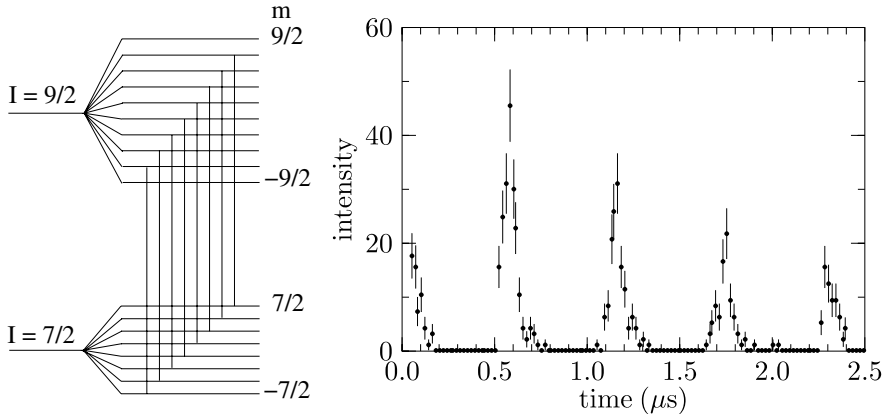


Fig. 2.13. Time spectrum of nuclear forward scattering from a Ta foil. The foil was magnetized so that only the $\Delta m = 0$ transitions were excited. The corresponding level scheme is shown on the left (Right figure adopted from Leupold *et al.* [52])

Table 2.1. Parameters of Mössbauer isotopes that are frequently used in experiments with synchrotron radiation. a is the natural abundance of the isotope, I_g and I_e are the spins of the ground and excited state, Γ_0 is the natural linewidth, and τ_0 is the lifetime. The reference points to the first reported excitation of the resonance by synchrotron radiation

| Isotope | E_γ [keV] | a [%] | Γ_0 [neV] | τ_0 [ns] | I_g | I_e | Multipolarity | Ref. |
|-------------------|---------------------|------------|---------------------|------------------|-------|-------|---------------|----------|
| ^{181}Ta | 6.23 | 99.9 | 0.067 | 9870 | 7/2 | 9/2 | E1 | [54] |
| ^{169}Tm | 8.41 | 100 | 114 | 5.8 | 1/2 | 3/2 | M1 | [55] |
| ^{83}Kr | 9.40 | 12.0 | 3.3 | 212 | 9/2 | 7/2 | M1 | [56, 57] |
| ^{57}Fe | 14.41 | 2.1 | 4.7 | 141 | 1/2 | 3/2 | M1 | [34] |
| ^{153}Eu | 21.53 | 47.8 | 47.0 | 14.1 | 5/2 | 7/2 | M1 | [58] |
| ^{149}Sm | 22.49 | 13.8 | 64.1 | 10.3 | 7/2 | 5/2 | M1 | [59] |
| ^{119}Sn | 23.87 | 8.6 | 25.7 | 25.7 | 1/2 | 3/2 | M1 | [60] |
| ^{161}Dy | 26.65 | 18.9 | 16.2 | 40.8 | 5/2 | 5/2 | E1 | [61] |
| ^{121}Sb | 37.13 | 57.25 | 130.0 | 5.0 | 5/2 | 7/2 | M1 | [62] |
| ^{40}K | 29.83 | 0.0117 | 160.5 | 4.13 | 4 | 3 | M1 | [63] |
| ^{61}Ni | 67.40 | 1.25 | 88.3 | 7.5 | 3/2 | 5/2 | M1 | [64] |

2.3 Forward Scattering from a Single Target

Two approaches can be formulated to calculate the time-resolved response of a coherently excited ensemble of nuclei. The first is based on the energy-dependent calculation of the amplitudes transmitted through the material.

This is the natural approach for the exact description of Mössbauer transmission spectra that led to the formulation of the so-called ‘transmission integral’ [13]. A subsequent Fourier transform of the energy-dependent amplitudes then yields the time-dependent amplitudes from which the intensities relevant for the experiment are calculated [65]. In the second approach the amplitudes are calculated in the time domain directly. This approach is particularly suited for the description of coherent scattering phenomena in the presence of time-dependent perturbations [40]. An important example are magnetic switching phenomena that have been studied in a series of experiments [66, 67, 68, 69].

2.3.1 Solution in the Time Domain

The propagation of a radiation pulse between two points in space-time can be described by an integral equation, which is essentially a generalized version of Huygens principle: If a wave function $\psi(\mathbf{r}', t')$ is known at a certain time t' then its shape at a later time t can be deduced by regarding every spatial point \mathbf{r}' at time t' as a source of a spherical wave that emerges from \mathbf{r}' . It is plausible to assume that the amplitude $\mathbf{A}(\mathbf{r}, t)$ of the wave, which arrives at \mathbf{r} at time t , is proportional to the initial exciting wave amplitude $\psi(\mathbf{r}', t')$. Let us call the constant of proportionality $-i\mathcal{N}(\mathbf{r}, t, \mathbf{r}', t')$. Then

$$\mathbf{A}(\mathbf{r}, t) = -i \int \mathcal{N}(\mathbf{r}, t, \mathbf{r}', t') \mathbf{A}(\mathbf{r}', t') d\mathbf{r}' dt', \quad \text{with } t > t'. \quad (2.21)$$

Written more explicitly, (2.21) reads:

$$\mathbf{A}(\mathbf{r}, t) = -i \int_V d\mathbf{r}' \int_0^t dt' \mathcal{N}(\mathbf{r}, t, \mathbf{r}', t') \mathbf{A}(\mathbf{r}', t'), \quad (2.22)$$

where the spatial integration extends over the whole volume V of the sample. Since nuclear resonant scattering is a second-order process, the integral kernel $\mathcal{N}(\mathbf{r}, t, \mathbf{r}', t')$ results from the evaluation of a two-point correlation function in space-time for the nuclei in the sample [15, 65]. This quantity represents a matrix to account for the polarization dependence of the scattering process. Note that (2.21) is valid only in the kinematical approximation, that describes single-scattering events, i.e. the first-order Born approximation. Therefore it is not applicable for thick samples, because it does not contain multiple scattering events. A solution for that case is to properly sum over parts of the sample (thin slices, platelets), for which the first-order Born approximation is valid. In the case of a homogeneous sample (i.e., \mathcal{N} does not depend explicitly on spatial coordinates; therefore the dependence on coordinates \mathbf{r}, \mathbf{r}' is dropped), the contribution from an infinitesimally thin platelet ($\mathbf{r} = \mathbf{r}'$) is given by

$$d\mathbf{A}(\mathbf{r}, t) = -i d\mathbf{r} \int_0^t dt' \mathcal{N}(t, t') \mathbf{A}(\mathbf{r}, t') . \quad (2.23)$$

Turning \mathbf{r} into a scalar coordinate z that denotes the depth in the sample measured from the entrance surface, this equation turns into the following integro-differential equation for the amplitude in depth z of the sample [40]:

$$\frac{d\mathbf{A}(z, t)}{dz} = -i \int_0^t dt' \mathcal{N}(t, t') \mathbf{A}(z, t') . \quad (2.24)$$

Introduction of the integral operator $\mathcal{D}(t, t') = \int_0^t dt' \mathcal{N}(t, t')$ facilitates to formally rewrite the above equation as follows:

$$\frac{d\mathbf{A}(z, t)}{dz} = -i \mathcal{D}(t, t') \mathbf{A}(z, t') . \quad (2.25)$$

To be a full solution of the problem this equation has to be supplemented by the boundary condition $\mathbf{A}(0, t) = \mathbf{A}_0(t)$, representing the incident radiation field at the entrance surface of the sample. This equation has the formal solution [40]:

$$\mathbf{A}(z, t) = \exp[-i \mathcal{D}(t, t') z] \mathbf{A}_0(t') . \quad (2.26)$$

In case of experiments with pulsed synchrotron radiation, the incident radiation field is given to a very good approximation by $\mathbf{A}_0(t) = \delta(t) \mathbf{A}_0$. Then the first terms of the series expansion of (2.26) read:

$$\begin{aligned} \mathbf{A}(z, t) &= \mathbf{A}_0 \left(\int \mathbf{1} \delta(t-t') \delta(t') dt' - z \int \mathcal{N}(t, t') \delta(t') dt' \right. \\ &\quad \left. + \frac{1}{2} z^2 \int \mathcal{N}(t, t') \mathcal{N}(t', t'') \delta(t'') dt' dt'' - \dots \right) \\ &= \mathbf{A}_0 \left(\mathbf{1} \delta(t) - z \mathcal{N}(t, 0) + \frac{1}{2} z^2 \int \mathcal{N}(t, t') \mathcal{N}(t', 0) dt' - \dots \right), \end{aligned} \quad (2.27)$$

where $\mathbf{1}$ is the unit matrix. This can be written in short form as:

$$\mathbf{A}(z, t) = (\mathbf{1} \delta(t) - \mathbf{G}(z, t)) \mathbf{A}_0 , \quad (2.28)$$

where $\mathbf{1} \delta(t)$ represents the prompt pulse that has passed the sample without interaction, while $\mathbf{G}(t)$ describes the delayed response from the collectively excited ensemble of nuclei in the sample.

Scattering from a Single-Line Sample

As an example (2.27) will be solved for a sample with a single resonance line. In this case the nuclear scattering operator simply reads:

$$\mathcal{N}(t, t') = e^{i\omega_0(t-t')} e^{-(t-t')/2\tau_0} \Theta(t-t') , \quad (2.29)$$

where τ_0 is the natural lifetime of the transition and $\Theta(t)$ is the unit step function. It is a characteristic property of elastic scattering that the propagator depends only on the time difference $t - t'$, i.e., $\mathcal{N}(t, t') = \mathcal{N}(t - t')$. Inserting (2.29) into (2.27) leads to the following series:

$$\mathbf{A}(z, t) = \delta(t) - e^{i\omega_0 t} e^{-t/2\tau_0} \gamma \sum_{n=1}^{\infty} \frac{(-\gamma t)^{n-1}}{(n-1)! n!}, \quad (2.30)$$

with

$$\gamma = \frac{1}{4} \varrho \sigma_0 f_{LM} z/\tau_0, \quad (2.31)$$

where σ_0 is the resonant absorption cross section and ϱ is the density of resonant nuclei in the sample. The comparison with the series representation of the first order Bessel function

$$J_1(z) = \frac{z}{2} \sum_{k=0}^{\infty} \frac{(-1)^k}{k!(k+1)!} \left(\frac{z}{2}\right)^{2k} \quad (2.32)$$

leads to the result

$$\mathbf{A}(z, t) = \delta(t) - \gamma e^{i\omega_0 t} e^{-t/2\tau_0} \frac{J_1(2\sqrt{\gamma t})}{\sqrt{\gamma t}}. \quad (2.33)$$

This function describes the propagation quantum beats that have been already discussed in Sect. 2.2.4.

2.3.2 Solution in the Energy Domain

In most experimental situations the hyperfine interactions are independent of time. In this case the scattering problem can be solved conveniently in the energy domain. This can be achieved by Fourier transform of (2.25) that turns into:

$$\frac{d\mathbf{A}(z, E)}{dz} = -\frac{1}{2\pi} \int_{-\infty}^{\infty} i\tilde{\mathcal{D}}(E, E') \mathbf{A}(z, E') dE', \quad (2.34)$$

where the operator $\tilde{\mathcal{D}}(E, E')$ is the Fourier image of $\mathcal{D}(t, t')$. This equation is very general because it also allows for inelastic scattering between two states with energy E and energy E' . While a closed solution is not possible in the general case, there is an important class of problems where a solution can be found. This applies for *elastic* nuclear resonant scattering. In that case the scattering operator has the property

$$\tilde{\mathcal{D}}(E, E') = \tilde{\mathcal{D}}_1(E) 2\pi \delta(E - E'). \quad (2.35)$$

Then the integro-differential equation in (2.34) turns into a linear differential equation:

$$\frac{d\mathbf{A}(z, E)}{dz} = -i \tilde{\mathcal{D}}_1(E) \mathbf{A}(z, E), \quad (2.36)$$

which has the simple solution

$$\mathbf{A}(z, E) = \exp[-iz\tilde{\mathcal{D}}_1(E)] \mathbf{A}(E). \quad (2.37)$$

As will be shown in the next chapter, this formalism does not only apply for forward scattering but can be extended to a large class of diffraction phenomena.

2.4 Forward Scattering from Separated Samples

We now consider nuclear resonant forward scattering from two separated samples as sketched in Fig. 2.14. Assume $f_1(t)$ and $f_2(t)$ to be the time responses of both samples which can be written as:

$$f_i(t) = \delta(t) - g_i(t) \quad (i = 1, 2) \quad (2.38)$$

The δ function accounts for the part of the radiation pulse that propagates through the sample without resonant interaction, and $g(t)$ describes the delayed resonant response. The time response of the whole system is then given by the convolution of both contributions:

$$\begin{aligned} F(t) &= \int_0^\infty f_1(\tau) f_2(t - \tau) d\tau \\ &= \int_0^\infty \{\delta(\tau) - g_1(\tau)\} \{\delta(t - \tau) - g_2(t - \tau)\} d\tau \\ &= \delta(t) - g_1(t) - g_2(t) + \int_0^\infty g_1(\tau) g_2(t - \tau) d\tau. \end{aligned} \quad (2.39)$$

The four parts of this expression correspond to the different scattering events: The first part describes the radiation that has passed through both samples without resonant interaction, the second and third part correspond to the resonant interaction with either one of the single absorbers, and the fourth term represents the radiative coupling of both absorbers via the coherent field propagating in the forward direction. The time response given in (2.39) corresponds to the coherent sum over the four paths that are displayed in Fig. 2.14a. It is also quite instructive to visualize the scattering process in a spacetime diagram as shown in Fig. 2.14b. The diagram shows the worldlines of the two foils at rest and the photons propagating between them for a fixed temporal delay Δt between the incident pulse and the scattered photon. The outer lines correspond to the two terms with a resonant interaction in only one of the two targets. The interference term, i.e., the convolution integral

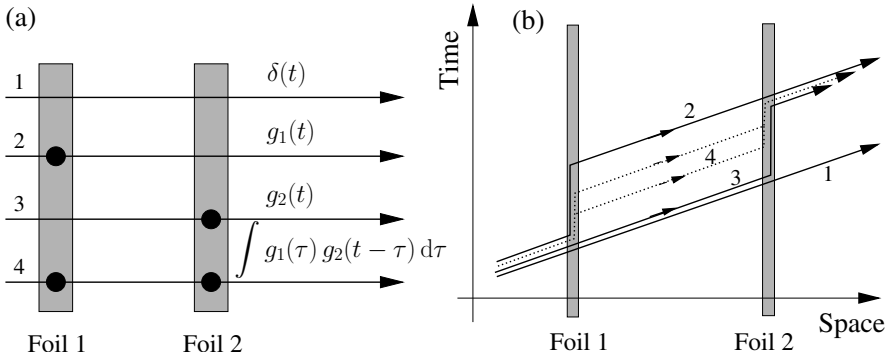


Fig. 2.14. Visualization of the scattering processes that build up the scattering response from two separated targets according to (2.39). The total signal is the sum over paths that can be attributed to four conceptually different scattering processes

in (2.39) is given by the sum over all the dashed lines in the diagram, from which only two are shown here. For better visibility, they are slightly displaced along the temporal axis. The outer lines of the spacetime diagram resemble a Mach-Zehnder interferometer, where one spatial axis has been replaced by the time axis. Since both arms are of equal length, there is no phase shift between the contributions from the various paths. Hence, the interference between both targets takes always place regardless of their spatial separation. Accordingly, the time response of such a two-target system is independent of the longitudinal coherence length of the incident radiation.

2.5 Nuclear Bragg Scattering

2.5.1 Pure Nuclear Reflections

Nuclear resonant diffraction of x-rays is sensitive to the spatial symmetry of the *nuclei* in the sample. The corresponding structure factor is not necessarily the same as for the electron shells. This difference is induced by the hyperfine interactions of the nuclei, leading to superstructure Bragg reflections. If the electronic structure factor vanishes at those angular positions, these reflections are called *pure nuclear reflections*. They have been observed so far in crystals like YIG (Yttrium Iron Garnet) [34, 70] and TIG (Thulium Iron Garnet) [55, 71], FeBO_3 [47, 72], Fe_3BO_6 [73], and Fe_2O_3 [74, 75]. A general prerequisite for pure nuclear reflections are at least two inequivalent lattice sites of the resonant nuclei. Correspondingly, one can classify the following mechanisms that lead to pure nuclear reflections:

- **Isotopic arrangement**

Here the inequivalence results from the difference between resonant and

nonresonant nuclei. Single crystals of such an arrangement are difficult to grow because the isotopic composition has to be controlled over hundreds or thousands of lattice planes. Instead, isotopic superstructures have been realized in artificial multilayer systems [76, 77].

- **Lattice sites distinguished by nuclear energy eigenvalues**

This may be induced by different hyperfine interactions at the nuclear sites. Typical examples are antiferromagnetic magnetic structures like in FeBO_3 [47], Fe_2O_3 [74], or layered structures like Fe/Cr multilayers [78].

- **Lattice sites distinguished by nuclear phases**

This leads to pure nuclear reflections even in the case of identical eigenvalues of the nuclei, i.e., the case of nuclear level crossing, as has been demonstrated in [79].

2.5.2 Electronically Allowed Reflections: Ta(110)

The investigation of nuclear scattering from electronically allowed reflections is affected by the presence of very strong charge scattering. An observation of such reflections thus requires a sufficient bandwidth reduction of the primary beam, as demonstrated by *Faigel et al.* [75]. At modern third-generation synchrotron radiation sources this issue became increasingly important, leading to the development of efficient monochromatization schemes with bandwidths below 1 meV (see Sect. 3.2).

It is interesting to extend the investigation of single crystals to other isotopes besides ^{57}Fe . This has been done for a Ta(110) single crystal, employing the 6.23-keV resonance of ^{181}Ta . This transition has a natural lifetime of 9800 ns that is one of the longest amongst all known Mössbauer isotopes⁷. Since the corresponding linewidth amounts to 67 peV, the resonance is extremely sensitive to external fields. This is particularly true for electrical field gradients that result from impurities and internal strains in the crystal. For that reason, special care had to be taken in the preparation of the crystal. To remove impurities from the lattice, the Ta crystal was heated under UHV conditions several times for a few minutes up to temperatures around 2600 K. For protection against oxidation in air, the crystal was finally coated with a few monolayers of Ag.

The experiment was performed at the nuclear-resonance beamline ID18 of the ESRF [80] with a bunch spacing of 2.8 μs (single-bunch mode). A Si(333) channel-cut crystal was used to monochromatize the incident radiation to a bandwidth of about 60 meV. This led to a prompt flux of approximately 10^9 ph/s reaching the detector via the Ta(110) reflection⁸ while the delayed count rate in a time window from 300 to 2500 ns was about 1 s^{-1} . The measured

⁷ Its first excitation by synchrotron radiation is reported in [54]. In that experiment forward scattering from a thin Ta foil was observed.

⁸ A special signal processing trick (baseline restoring) had to be applied to avoid the strong baseline shift of the detector signal at such high event rates.

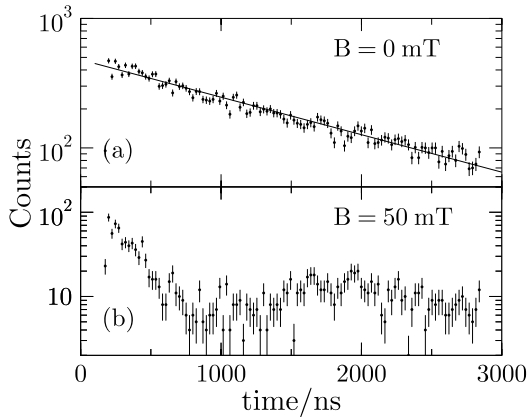


Fig. 2.15. Time spectra of the Ta(110) reflection. (a) without external field and (b) in a field of 50 mT perpendicular to the scattering plane

time spectra of the Ta(110) reflection are shown in Fig. 2.15 for zero external field (a) and an external field of 50 mT (b). The decay curve in Fig. 2.15a follows an exponential decay with a lifetime of $\tau = 1.5 \mu\text{s}$. Taking the intrinsic speedup of the Ta(110) reflection into account, one arrives at a linewidth of the resonance of 4 times the natural linewidth. This result proves the feasibility to prepare high-quality Ta single crystals by controlled annealing under UHV conditions. Such crystals may be used to probe external fields that are induced by magnetic deposits, for example. To check this we have applied an in-plane external field of 50 mT perpendicular to the incident beam. The corresponding time spectrum is shown in Fig. 2.15. It shows that the measured signal is very sensitive already to small external fields. This allows one to study almost arbitrary magnetic films and nanostructures of non-Mössbauer atoms by using the 6.23-keV resonance in a perfect Ta crystal as a probe. Instead of a bulk single crystal of Ta one also may use thin epitaxial Ta films (as they can be prepared on sapphire single crystal substrates, for example) as a probe for magnetism.

2.5.3 Applications in Materials Science

The observation of pure nuclear reflections is a very sensitive probe of magnetic order in the sample. While the first experiments on pure nuclear reflections required relatively large perfect single crystals, the enormous brilliance of present-day synchrotron radiation sources enables the investigation of very small crystals, e.g., individual crystallites in a polycrystalline sample. Therefore, the field of nuclear Bragg diffraction should get new momentum due to promising applications in materials science.

Nuclear diffraction studies allow to probe certain sublattices, as it has been demonstrated in case of the $a -$ sites of YIG, for example [81]. A possible application is the study of sublattice magnetization in new magnetic compounds. New experimental schemes could be designed like the observation

of nuclear Debye-Scherrer rings, i.e., nuclear resonant powder diffractometry, as proposed in [82]. This, however, requires the development of new detector setups with ns time resolution and high spatial resolution. Evaluation of such patterns would allow for a site-selective determination of atomic positions. This would be very important for structure determination, e.g., in case of quasicrystals like Al₆₂Cu_{25.5}Fe_{12.5}, where in particular the sites occupied by the Fe atoms are debated.

References

1. E. Burkhardt: *Inelastic Scattering of X-Rays with Very High Energy Resolution* (Springer, Berlin 1991) 9
2. E. Burkhardt: Rep. Prog. Phys. **63**, 171 (2000) 9
3. F. Sette, G. Ruocco, M. Krisch, C. Masciovecchio, U. Bergmann, V. Mazzacurati, G. Signorelli, and R. Verbeni: Phys. Rev. Lett. **75**, 850 (1995) 9
4. F. Sette, M. H. Krisch, C. Masciovecchio, G. Ruocco, and G. Monaco: Science **280**, 1550 (1998) 9
5. W. Sturhahn and V. G. Kohn: Hyperfine Interact. **123/124**, 367 (1999) 9
6. Yu. V. Shvyd'ko and G. V. Smirnov: J. Phys.: Condens. Matter **4**, 2663 (1992) 10
7. W. A. Tolbert, W. M. Dennis, and W. M. Yen: Phys. Rev. Lett. **65**, 607 (1990) 11
8. X. Wang, W. M. Dennis, and W. M. Yen: Phys. Rev. Lett. **67**, 2807 (1991) 11
9. X. Wang, J. Ganem, W. M. Dennis, and W. M. Yen: Phys. Rev. B **44**, 900 (1991) 11
10. M. Seto, Y. Yoda, S. Kikuta, X. W. Zhang, and M. Ando: Phys. Rev. Lett. **74**, 3828 (1995) 11
11. S. Bernstein and E. C. Campbell: Phys. Rev. **132**, 1625 (1963) 12
12. U. van Bürck, G. V. Smirnov, R. L. Mössbauer, H. J. Maurus, and N. A. Semioschkinina: J. Phys. C (Solid State Phys.) **13**, 4511 (1980) 12
13. S. Margulies and J. R. Ehrmann: Nucl. Instrum. Meth. **12**, 131 (1961) 12, 26
14. R. E. Holland, F. J. Lynch, G. J. Perlow, and S. S. Hanna: Phys. Rev. Lett. **4**, 181 (1960); F. J. Lynch, R. E. Holland, and M. Hamermesh: Phys. Rev. **120**, 513 (1960) 12
15. J. P. Hannon and G. T. Trammell: Phys. Rev. **169**, 315 (1968) 12, 13, 26
16. J. P. Hannon and G. T. Trammell: Phys. Rev. **186**, 306 (1969) 12, 13
17. A. M. Afanas'ev and Yu. Kagan: Zh. Eksper. Teoret. Fiz. **48**, 327 (1965) (Sov. Phys. JETP **21**, 215 (1965)) 12
18. A. M. Afanas'ev and Yu. Kagan: Zh. Eksper. Teoret. Fiz. **52**, 191 (1967) (Sov. Phys. JETP **25**, 124 (1967)) 12
19. Yu. Kagan and A. M. Afanas'ev: Zh. Eksper. Teoret. Fiz. **49**, 1504 (1965) (Sov. Phys. JETP **22**, 1032 (1966)) 12
20. Yu. Kagan, A. M. Afanas'ev, and I. P. Perstnev: Zh. Eksper. Teoret. Fiz. **54**, 1530 (1968) (Sov. Phys. JETP **27**, 819 (1968)) 12
21. J. P. Hannon and G. T. Trammell: Hyperfine Interact. **123/124**, 127 (1999) 12, 15, 21
22. T. S. Toellner: PhD thesis (Northwestern University, Evanston 1996) 13
23. TESLA Technical Design Report, Part V: The X-ray Free Electron Laser, edited by G. Materlik and Th. Tschenzsch (DESY 2001 - 011, ECFA 2001 - 209, TESLA Report 2001 - 23, TESLA - FEL 2001 - 05) 13

24. J. P. Hannon and G. T. Trammell: Physica B **159**, 161 (1989) **15**
25. Yu. Kagan: Hyperfine Interact. **123/124**, 83 (1999) **15**
26. M. Lax: Rev. Mod. Phys. **23**, 287 (1951) **15**
27. S. Haroche, in: *High Resolution Laser Spectroscopy*, edited by K. Shimoda (Springer, Berlin 1976), p. 253. **16**
28. H. Stoltz: *Time Resolved Light Scattering from Excitons* (Springer, Berlin 1993) **16**
29. E. Gerdau and H. de Waard: *Nuclear Resonant Scattering of Synchrotron Radiation, Part A*, Hyperfine Interact. **123/124** (1999) **16, 17**
30. E. Gerdau and H. de Waard: *Nuclear Resonant Scattering of Synchrotron Radiation, Part B*, Hyperfine Interact. **125** (2000) **16, 17**
31. D. Gibbs, D. R. Harshman, E. D. Isaacs, D. B. McWhan, D. Mills, and C. Vettier: Phys. Rev. Lett. **61**, 1241 (1988) **17**
32. J. P. Hannon, G. T. Trammell, M. Blume, and D. Gibbs: Phys. Rev. Lett. **61**, 1245 (1988) and Phys. Rev. Lett. **62**, 2644 (1989) (erratum) **17**
33. G. Materlik, C. J. Sparks, and K. Fischer (eds.): *Resonant Anomalous X-Ray Scattering*, Proceedings of the International Conference on Anomalous Scattering, Malente, Germany 1992 (Elsevier, Amsterdam 1994) **17**
34. E. Gerdau, R. Rüffer, H. Winkler, W. Tolksdorf, C. P. Klages, and J. P. Hannon: Phys. Rev. Lett. **54**, 835 (1985) **17, 25, 30**
35. R. W. James: *The Optical Principles of the Diffraction of X-rays* (G. Bell and Sons, London 1958), Chap. IV.1. **19**
36. C. Klingshirn: *Semiconductor Optics* (Springer, Berlin 1997) **19**
37. D. Fröhlich, A. Kulik, B. Uebbing, A. Mysyrowicz, V. Langer, H. Stoltz, and W. von der Osten: Phys. Rev. Lett. **67**, 2343 (1991) **20, 21**
38. K. J. Boller, A. İmamoğlu, and S. E. Harris: Phys. Rev. Lett. **66**, 2593 (1991) **20**
39. L. V. Hau, S. E. Harris, Z. Dutton, and C. H. Behroozi: Nature (London) **397**, 594 (1999) **20**
40. Yu. V. Shvyd'ko: Phys. Rev. B **59**, 9132 (1999) **20, 26, 27**
41. U. van Bürck: Hyperfine Interact. **123/124**, 483 (1999) **20**
42. G. V. Smirnov: Hyperfine Interact. **123/124**, 31 (1999) **20**
43. M. Matusovsky, B. Vaynberg, and M. Rosenbluth: J. Opt. Soc. Amer. B **13**, 1994 (1996) **21**
44. R. H. Dicke: Phys. Rev. **93**, 99 (1954) **20**
45. H. J. Lipkin: Phys. Rev. Lett. **58**, 1176 (1987) **21**
46. G. T. Trammell and J. P. Hannon: Phys. Rev. Lett. **61**, 653 (1988) **21**
47. U. van Bürck, R. L. Mössbauer, E. Gerdau, R. Rüffer, R. Hollatz, G. V. Smirnov, and J. P. Hannon: Phys. Rev. Lett. **59**, 355 (1987) **21, 30, 31**
48. U. van Bürck, D. P. Siddons, J. B. Hastings, U. Bergmann, and R. Hollatz: Phys. Rev. B **46**, 6207 (1992) **21, 22**
49. R. Röhlsberger, E. Gerdau, M. Harsdorff, O. Leupold, E. Lüken, J. Metge, R. Rüffer, H. D. Rüter, W. Sturhahn, and E. Witthoff: Europhys. Lett. **18**, 561 (1992) **22**
50. R. Röhlsberger, E. Gerdau, E. Lüken, H. D. Rüter, J. Metge, and O. Leupold: Z. Phys. B **92**, 489 (1993) **22**
51. U. van Bürck, W. Potzel, P. Schindelmann, Yu. V. Shvyd'ko, E. Gerdau, O. Leupold, and H. D. Rüter: Phys. Rev. A **61**, 013803 (2000) **24**
52. O. Leupold, A. I. Chumakov, E. E. Alp, W. Sturhahn, and A. Q. R. Baron: Hyperfine Interact. **123/124**, 611 (2000) **24, 25**

53. Yu. V. Shvyd'ko, U. van Bürck, W. Potzel, P. Schindelmann, E. Gerdau, O. Leupold, J. Metge, H. D. Rüter, and G. V. Smirnov: Phys. Rev. B **57**, 3552 (1998) [24](#)
54. A. I. Chumakov, A. Q. R. Baron, J. Arthur, S. L. Ruby, G. S. Brown, G. V. Smirnov, U. van Bürck, and G. Wortmann: Phys. Rev. Lett. **75**, 549 (1995) [24, 25, 31](#)
55. W. Sturhahn, E. Gerdau, R. Hollatz, R. Rüffer, H.D. Rüter, and W. Tolksdorf: Europhys. Lett. **17**, 821 (1991) [25, 30](#)
56. A. Q. R. Baron, A. I. Chumakov, S. L. Ruby, J. Arthur, G. S. Brown, G. V. Smirnov, and U. van Bürck: Phys. Rev. B **51**, 16384 (1995) [25](#)
57. D. E. Johnson, D. P. Siddons, J. Z. Larese, and J. B. Hastings: Phys. Rev. B **51**, 7909 (1995) [25](#)
58. O. Leupold, J. Pollmann, E. Gerdau, H. D. Rüter, G. Faigel, M. Tegze, G. Borstel, R. Rüffer, A. I. Chumakov, and A. Q. R. Baron: Europhys. Lett. **35**, 671 (1996) [25](#)
59. R. Röhlsberger: Hyperfine Interact. **125**, 69 (2000) [25](#)
60. E. E. Alp, T. M. Mooney, T. S. Toellner, W. Sturhahn, E. Witthoff, R. Röhlsberger, E. Gerdau, H. Homma, and M. Kentjana: Phys. Rev. Lett. **70**, 3351 (1993) [25](#)
61. Yu. V. Shvyd'ko, M. Gerken, H. Franz, M. Lucht, and E. Gerdau: Europhys. Lett. **56**, 309 (2001) [25](#)
62. H. C. Wille: private communication (2004) [25](#)
63. M. Seto, S. Kitao, Y. Kobayashi, R. Haruki, T. Mitsui, Y. Yoda, X. W. Zhang, and Yu. Maeda: Phys. Rev. Lett. **84**, 566 (2000) [25](#)
64. H. C. Wille, M. Gerken, E. Gerdau, Yu. V. Shvyd'ko, H. D. Rüter, and H. Franz: Hyperfine Interact. **5**, 1 (2002) [25](#)
65. W. Sturhahn and E. Gerdau: Phys. Rev. B **49**, 9285 (1994) [26](#)
66. Yu. V. Shvyd'ko, S. L. Popov, and G. V. Smirnov: Pis'ma Zh. Éksp. Teor. Fiz. **53**, 217 (1991) (JETP Lett. **53**, 231 (1991)) [26](#)
67. Yu. V. Shvyd'ko, S. L. Popov, and G. V. Smirnov: J. Phys.: Condens. Matter **5**, 1557 (1993) [26](#)
68. Yu. V. Shvyd'ko, S. L. Popov, and G. V. Smirnov: J. Phys.: Condens. Matter **5**, 7047 (1993) [26](#)
69. Yu. V. Shvyd'ko, T. Hertrich, U. van Bürck, E. Gerdau, O. Leupold, J. Metge, H. D. Rüter, S. Schwendy, G. V. Smirnov, W. Potzel, and P. Schindelmann: Phys. Rev. Lett. **77**, 3232 (1996) [26](#)
70. R. Rüffer, E. Gerdau, R. Hollatz, and J. P. Hannon: Phys. Rev. Lett. **58**, 2359 (1987) [30](#)
71. W. Sturhahn: PhD thesis (Universität Hamburg, 1991) [30](#)
72. H. D. Rüter, R. Rüffer, E. Gerdau, R. Hollatz, A. I. Chumakov, M. V. Zelepukhin, G. V. Smirnov, and U. van Bürck: Hyperfine Interact. **58**, 2473 (1990) [30](#)
73. A. I. Chumakov, G. V. Smirnov, M. V. Zelepukhin, U. van Bürck, E. Gerdau, R. Rüffer, and H. D. Rüter: Europhys. Lett. **17**, 269 (1991); Hyperfine Interact. **71**, 1341 (1992) [30](#)
74. G. Faigel, D. P. Siddons, J. B. Hastings, P. E. Haustein, and J. R. Grover: Phys. Rev. Lett. **58**, 2699 (1987) [30, 31](#)
75. G. Faigel, D. P. Siddons, J. B. Hastings, P. E. Haustein, J. R. Grover, and L. E. Berman: Phys. Rev. Lett. **61**, 2794 (1988) [30, 31](#)

76. A. I. Chumakov, G. V. Smirnov, A. Q. R. Baron, J. Arthur, D. E. Brown, S. L. Ruby, G. S. Brown, and N. N. Salashchenko : Phys. Rev. Lett. **71**, 2489 (1993) **31**
77. R. Röhlsberger, E. Witthoff, E. Gerdau, and E. Lüken : J. Appl. Phys. **74**, 1933 (1993) **31**
78. T. S. Toellner, W. Sturhahn, R. Röhlsberger, E. E. Alp, C. H. Sowers, and E. E. Fullerton : Phys. Rev. Lett. **74**, 3475 (1995) **31**
79. R. Rüffer, E. Gerdau, H. D. Rüter, W. Sturhahn, R. Hollatz, and A. Schneider : Phys. Rev. Lett. **63**, 2677 (1989) **31**
80. R. Rüffer and A. I. Chumakov : Hyperfine Interact. **97/98**, 589 (1996) **31**
81. R. Rüffer, J. Metge, H. D. Rüter, W. Sturhahn, and E. Gerdau : Hyperfine Interact. **71**, 1353 (1992) **32**
82. E. Gerdau and U. van Bürck, in: *Resonant Anomalous X-Ray Scattering*, Proceedings of the International Conference on Anomalous Scattering (Malente, Germany 1992), edited by G. Materlik, C. J. Sparks, and K. Fischer (Elsevier, Amsterdam 1994) **33**

3 Methods and Instrumentation

On the basis of the given brilliances of present-day synchrotron radiation sources one easily estimates that they should be ideally suited for nuclear resonant scattering: Their brilliance supercedes those of radioactive sources by several orders of magnitude. However, a real experiment will only succeed if the resonant radiation is transmitted efficiently from the source to the detector. Due to the small energetic bandwidth of the nuclear resonance, this is a very challenging task that has led to the development of unique instrumentation like monochromators with sub-meV energy resolution and efficient detectors with sub-ns time resolution.

Moreover, the time evolution of the nuclear decay can only be measured if the time structure of the radiation and the detector electronics allows for a sufficient time resolution. Since the first observation of coherent nuclear resonant scattering of synchrotron radiation in 1985 [1], a big effort has been undertaken in the development and optimization of all these components. This chapter shall give a brief review of the instrumentation that is required to perform this kind of spectroscopy.

3.1 Synchrotron Radiation Sources

It is beyond the scope of this book to give a comprehensive review about synchrotron radiation and its properties. For this case the reader is referred to a number of excellent books and review articles, e.g., [2, 3, 4, 5]. However, there are some aspects that crucially influence the performance of nuclear resonant scattering experiments. Because these aspects determine the actual choice of a storage ring or a beamline for such experiments, they should be reviewed here.

3.1.1 Historical Development

As charged particles are forced on a circular orbit while traversing a magnetic field, the centripetal acceleration causes them to emit electromagnetic radiation in a direction tangential to their path. This kind of radiation was first observed in 1947 from electrons orbiting in a synchro-cyclotron and henceforth called *synchrotron radiation* (SR) [6, 7]. In the first place it was considered

to be an unfortunate by-product of circular accelerators that were developed for high-energy physics experiments¹. Due to its broad energy distribution reaching from the infrared to the hard x-ray regime, it was considered as a unique source of radiation that can be advantageously used for spectroscopic investigations. By the late 1950s, synchrotron radiation itself was being used for experiments, but until the 1970s work was carried out in a parasitic mode with respect to high-energy physics experiments. Although not optimized for the production of synchrotron radiation, the first-generation synchrotron rings, such as DORIS at the Hamburger Synchrotronstrahlungslabor (HASYLAB), CESR at the Cornell High Energy Synchrotron Source (CHESS), and SPEAR at the Stanford Synchrotron Radiation Laboratory (SSRL), delivered photon densities (brilliances) around five orders of magnitude higher than conventional laboratory X-ray sources². At that time it was realized in 1974 by *Ruby* [8] that synchrotron radiation would be intense enough to be used as a source for Mössbauer experiments. Since then intense theoretical and experimental efforts were undertaken, initiating the field of nuclear resonant scattering (NRS) of synchrotron radiation that was started off by the first observation of coherent NRS by *Gerdau* and coworkers in 1985 [1].

In the late 1970s to early 1980s, dedicated second-generation storage rings were developed using a special arrangement of dipole, quadrupole, and sextupole magnets (the so-called Chasman–Green lattice [9]) that yielded an increase in brilliance by two orders of magnitude. Examples of such sources are the National Synchrotron Light Source (NSLS) at Brookhaven National Laboratory (BNL) on Long Island, New York, and the Photon Factory (KEK) in Japan.

The next improvement came with the implementation of insertion devices at SSRL around 1980 [10]. Insertion devices consist of linear arrays of dipole magnets alternating in orientation, see Fig. 3.1. When inserted into a straight section of the storage ring (between the bending magnets), they cause the particle beam to follow a sinusoidal path. The gap between the poles can be adjusted to tune the properties of the emitted radiation. Wigglers have a large amplitude for the sinusoidal electron path and produce a relatively wide fan of radiation, covering horizontal angles of a few degrees. Since the waves emitted at the n individual poles add up incoherently, one obtains approximately n times more photon flux compared to a single dipole magnet. Undulators lead to a low amplitude of the sinusoidal electron beam motion that produces a *coherent* superposition of the contributions from the individual poles.

¹ On the other hand, in some circumstances it is a desired by-product because the emission of synchrotron radiation damps oscillatory motions of the electrons.

² The brilliance of a radiation source is given in units of number of photons per second in a certain energy bandwidth, normalized to the source area and the solid angle of the radiation cone.

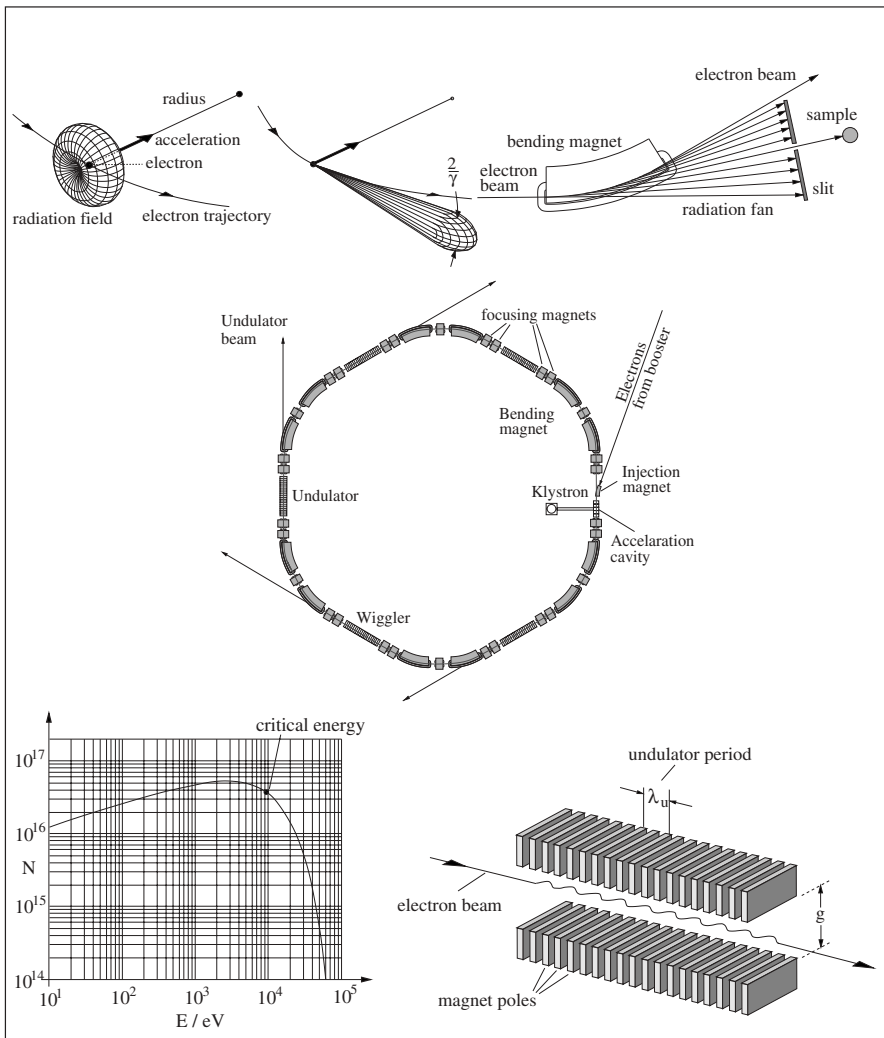


Fig. 3.1. Schematic layout and properties of a modern synchrotron radiation source. The central part displays the typical layout of a third-generation storage ring in the configuration of a ‘Chasman-Green lattice’. In the *upper left* part the transformation of the radiated field distribution from the rest frame of the electrons into the laboratory frame is shown, indicating the highly directional emission from relativistic electrons. The *upper right* part shows the emission of synchrotron radiation from a bending magnet and the *lower right* part an insertion device (wiggler or undulator) that forces the electrons on a sinusoidal trajectory. The *lower left* diagram shows the distribution of the spectral flux delivered by a bending magnet with a radius of 12.2 m for an electron energy of 5 GeV (Figures adopted from Wille [4]).

As a result, one obtains extremely well-collimated beams of radiation with approximately n^2 times more photon flux. A synopsis over the generation of synchrotron radiation and the typical layout of modern synchrotron radiation sources is given in Fig. 3.1.

Third-generation storage rings have been designed specifically to take advantage of insertion devices, primarily undulators. Storage rings such as the European Synchrotron Radiation Facility (ESRF) in Grenoble, the Advanced Photon Source (APS) at Argonne National Laboratory, and Super Photon ring-8 GeV (SPring-8) in Japan have long straight sections (to incorporate long insertion devices) and low-emittance lattices.

3.1.2 Properties of Synchrotron Radiation

Synchrotron Radiation is characterized by three important properties that distinguish it from all other sources of x-rays: Brilliance, time structure, and polarization. Since nuclear resonant scattering heavily relies on these properties, they will be briefly reviewed here.

Flux, Brightness and Brilliance

With increasing intensity of the incident radiation, samples can be examined more rapidly, and smaller, thinner, and more dilute samples become accessible. However, it is not only the enormous photon flux that renders synchrotron radiation so attractive. Since the emission is highly directional, highly collimated beams can be used, e.g., for the investigation of low-dimensional structures. For that reason a short summary of the basic characteristics and the nomenclature is given here.

The total number of photons per second emitted by an orbiting electron is proportional to the radiated power that is given by [2]:

$$P = \frac{e^2 c}{6\pi\varepsilon_0} \frac{1}{(m_0 c^2)^4} \frac{E^4}{R^2} = \frac{e^2 c}{6\pi\varepsilon_0} \frac{1}{R^2} \gamma^4, \quad (3.1)$$

with $\gamma = E/m_0 c^2$, where m_0 is the rest mass of the particles, E their total energy, and R the radius of curvature. This quantity determines the *total flux* of the source:

$$\text{Total flux} \equiv \frac{\text{Photons}}{\text{s}}. \quad (3.2)$$

The total flux includes all photons of all energies and is therefore only interesting for experiments that require ‘white’ radiation. In most spectroscopic applications, however, monochromatic radiation is required and one has to consider the spectral distribution of the synchrotron radiation. As shown in the top part of Fig. 3.1, the relativistic nature of the orbiting electrons leads to a sharp collimation of the radiation into a cone with an opening angle of

$$\sigma'_r = \frac{1}{\gamma} . \quad (3.3)$$

Moving on a circular path with radius R , an observer watching tangentially will see a radiation flash with a duration of

$$\Delta t = \frac{4R}{3c\gamma^3} . \quad (3.4)$$

This time is typically in the order of 10^{-17} – 10^{-19} s, so that the highest Fourier components extend into the hard x-ray regime and beyond. A typical spectral distribution emitted from a bending magnet is shown in Fig. 3.1 (bottom left). The energetic distribution of synchrotron radiation from a bending magnet usually follows a black-body curve with a critical energy E_c that is determined by the energy E of the orbiting electrons or positrons:

$$E_c = \frac{3\hbar c\gamma^3}{2R} = C \frac{E^3}{R} \quad \text{with} \quad C = 2.218 \times 10^{-6} \text{ m/GeV}^2 . \quad (3.5)$$

The critical energy determines roughly the upper energy limit of the useful radiation. Storage rings with electron energies below 2.5 GeV are more suited for experiments with soft x-rays (below 1.5 keV)³. Hard x-rays needed for excitation of nuclear resonances are most efficiently produced in storage rings with $E > 2.5$ GeV. To characterize the spectral distribution of the radiation one defines the *spectral flux*:

$$\text{Spectral flux} \equiv \frac{\text{Photons/s}}{0.1\%\text{bandwidth}} , \quad (3.6)$$

which is the flux normalized to a relative spectral bandwidth of $\Delta E/E = 10^{-3}$. As already mentioned above, the opening angle of the emitted radiation is given by $1/\gamma$. This value can be significantly reduced if insertion devices like wigglers or undulators are used. These devices consist of a number N of alternating magnet poles with a period λ_u , separated by a variable gap, as shown in Fig. 3.1 (bottom right). They are mounted in the straight sections of the storage ring. The electrons are forced to a sinusoidal orbit so that at every bend of this oscillation synchrotron radiation is emitted. The opening angle of the radiation cone is given by

$$\sigma'_r = \frac{1}{\gamma} \sqrt{\frac{1 + \frac{1}{2}K^2}{2Nn}} , \quad (3.7)$$

where N is the number of periods, n the order of the harmonic. K is the so-called deflection parameter that is derived from the magnetic period λ_u and the peak magnetic field B_0 :

$$K = 0.934 \lambda_u (\text{cm}) B_0 (\text{T}) . \quad (3.8)$$

³ However, the spectrum can be significantly extended into the hard x-ray regime by use of optimized insertion devices like high-field wigglers with superconducting magnets, as they are under commission in storage rings like ALS or BESSY II.

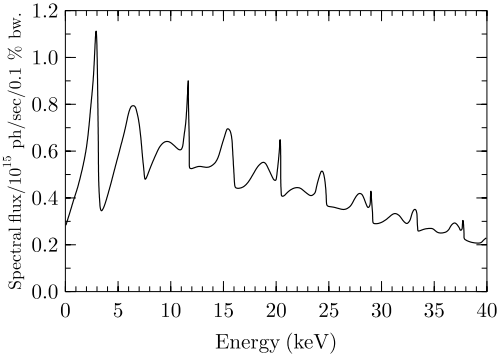


Fig. 3.2. Spectral flux (integrated over all angles) of APS undulator A at a gap of 11.5 mm ($K = 2.17$), calculated for an electron energy of 7 GeV and 100 mA beam current (Data taken from Lai *et al.* [11])

This parameter distinguishes a wiggler from an undulator: If $K \ll 1$ the radiation amplitudes emitted from the individual bends superpose coherently (undulator), while for $K \gg 1$ these contributions add incoherently (wiggler). As an example, the spectral flux delivered from a typical undulator of a third-generation source is shown in Fig. 3.2. The coherent superposition of the emitted amplitudes leads to sharp peaks (harmonics) in the energy spectrum that appear at energies given by:

$$E_n(\text{keV}) = \frac{0.95 n E^2(\text{GeV})}{\lambda_u(\text{cm})(1 + K^2/2)}, \quad (3.9)$$

where n is the order of the harmonic. The energetic position of these undulator harmonics can be tuned by variation of the undulator gap that acts on K via the magnetic field B_0 as described by (3.8). For a chosen photon energy the gap is tuned to one of the harmonic peaks to obtain maximum spectral flux.

In order to describe the angular collimation of the radiation one introduces the *brightness*:

$$\text{Brightness} \equiv \frac{\text{Photons/s}}{\text{mrad}^2 \cdot 0.1\%\text{bandwidth}}, \quad (3.10)$$

which is the spectral flux normalized to a solid angle of 1 mrad². The actual divergence of the radiation at the sample position is not only determined by the insertion device, but also by the size of the electron beam at the undulator. Since every electron beam in a ring is subject to transverse oscillations, the so-called betatron oscillations, the beamsize is given by the amplitude of these oscillations. The so-called beta function $\beta(s)$, defined for both transverse directions separately, is the maximum amplitude of particle oscillations around the stable orbit at a given point s around the circumference. The beta functions sensitively depend on the electron optics of the storage ring. Further fundamental parameters of a storage ring are the horizontal and vertical emittance $\varepsilon_{x,y}$. They give the area in phase space (position, angle) the

particle beam covers during its travel around the storage ring. Horizontal and vertical emittance are related to each other by a parameter called the coupling constant. At third-generation sources it is typically on the order of 0.01, i.e. $\varepsilon_y = 0.01 \varepsilon_x$. From the beta function and the emittance the spatial or angular source sizes can be calculated:

$$\sigma'_{x,y} = \sqrt{\frac{\varepsilon_{x,y}}{\beta_{x,y}}} \quad \text{and} \quad \sigma_{x,y} = \sqrt{\varepsilon_{x,y} \beta_{x,y}}. \quad (3.11)$$

Finally, the overall divergence of the x-ray beam is obtained by adding the particle and radiative divergences in quadrature:

$$\Sigma'_{x,y} = \sqrt{\sigma'^2_{x,y} + \sigma'^2_r}. \quad (3.12)$$

The x-ray divergence can be dominated by the divergence of the particle beam or the radiative divergence, depending on the emittance of the ring.

The x-ray source size is of great importance for many applications that rely on an efficient use of x-ray optical elements. The smaller the source size, the better the radiation at the sample position can be approximated by a plane wave, for example. To characterize the radiation source in this respect, one introduces the *brilliance*⁴:

$$\text{Brilliance} \equiv \frac{\text{Photons/s}}{\text{mrad}^2 \cdot \text{mm}^2 \cdot 0.1\%\text{bandwidth}}, \quad (3.13)$$

which is the spectral flux normalized to a solid angle of 1 mrad² and a source area of 1 mm². Currently, third-generation storage rings produce a maximum brilliance of $\approx 10^{20}$ photons/s/0.1%BW/mm²/mrad². Figure 3.3a shows the growth in brilliance of x-ray sources since 1955 [12]. Figure 3.3b compares the brilliance of several existing sources with those of projected future machines. On the way of further development, free-electron lasers driven by linear accelerators are planned that could reach an average brilliance of 10^{25} ph/s/mrad²/mm²/0.1%BW in the x-ray regime [13].

Time Structure

To compensate for the losses by emission of synchrotron radiation the orbiting particles have to be re-accelerated. This is achieved in resonators along the ring, the so-called cavities. To ensure a proper synchronization of the accelerating voltage with the revolution frequency f_0 of the particles, the operating frequency f_c of the cavity must be an integral multiple of f_0 :

$$f_c = m f_0 \quad \text{with} \quad m \geq 1. \quad (3.14)$$

This means, m is the number of stable orbit points along the circumference of the storage ring. Particles in the beam perform longitudinal harmonic oscillations around these points, the so-called synchrotron oscillations. The

⁴ Brilliance and brightness are often used synonymously in American literature.

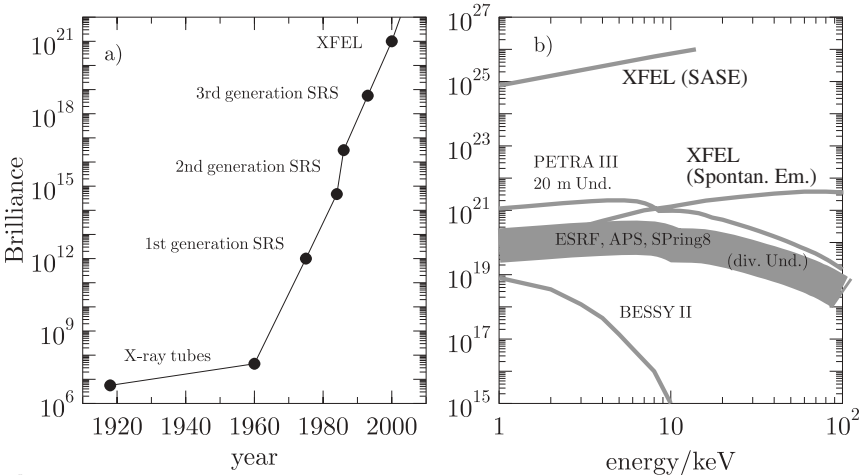


Fig. 3.3. (a) Evolution of spectral brilliance of sources for hard x-rays. (b) Spectral brilliance of existing synchrotron radiation sources (SRS) and projected future devices like the x-ray free electron laser (XFEL) (Data compiled from *Materlik & Tschentscher* [13] and *Balewski et al.* [14])

regions around the stable points to which the particles can be confined are called *buckets*. Depending on the operating mode, not all buckets are filled with particles. In particular, for time-resolved studies it is desired to fill only a few equidistant buckets. The temporal distance of the radiation pulses should be on the order of the lifetime of the resonant isotope. This requires a very elaborate filling procedure. Typically, the injection mechanism leads to dark currents with an intensity of 10^{-4} – 10^{-6} relative to the current of the main bunches. The corresponding electrons are mostly located in buckets around the main bunches. Such a high ratio of spurious bunches severely affects time resolved measurements, particularly at very short times after excitation⁵.

To achieve purities on the order of 10^{-7} – 10^{-8} , special procedures have been developed to clean the storage ring from these spurious bunches. These methods rely on the fact that the amplitude of the betatron oscillations depends on the current in the bunch. Bunches with low current can be selectively excited to betatron oscillations with large amplitude and then extracted by a catcher electrode [15].

The length of the bunches and thus the temporal duration of the radiation pulses is determined by the amplitude of the synchrotron oscillations within the buckets. Typically the bunch length is small compared to the bucket separation. It is usually in the range of 50–200 ps, compared to bucket

⁵ On the other hand, such a level of unwanted bunches is too low to be detected by pick-up coils in the ring. Instead, diagnostics of these bunches can be performed by detection of the emitted synchrotron radiation.

Table 3.1. Parameters of storage rings that are currently (2004) used for nuclear resonant scattering experiments. The data are taken from [16]

| Storage Ring, Location | Particle Energy [GeV] | Circumference [m] | Orbit Period [μs] | Bucket Separat. [ns] | Bunch Length [ps] |
|------------------------|-----------------------|-------------------|-------------------|----------------------|-------------------|
| ESRF, Grenoble, France | 6.0 | 844 | 2.816 | 2.84 | 70 |
| APS, Argonne, USA | 7.0 | 1104 | 3.683 | 2.84 | 60 |
| SPring8, Japan | 8.0 | 1436 | 4.790 | 1.97 | 100 |
| PETRA II, Hamburg | 12.0 | 2304 | 7.680 | 2.00 | 100 |

separations of a few ns. Values for some present-day synchrotron radiation sources are listed in Table 3.1.

Polarization

Synchrotron radiation by nature is completely polarized in the plane of the storage ring. This, however, is true only for radiation emitted exactly in that plane. Photons that are emitted out-of-plane from a bending magnet can exhibit a certain degree of ellipticity. Due to the finite angular acceptance of an experimental setup, every experiment will be in principle affected by contaminations from circularly polarized light. If that is not desired, these contributions can be filtered out by polarizing Bragg reflections, as will be discussed in Sect. 3.2.3. On the other hand, in many experiments it is highly desired to have circularly polarized radiation available. Various concepts have been developed to achieve this goal. One approach is the use of specially designed insertion devices like helical undulators [17]. Another solution is the application of quarter-wave plates for x-rays [18, 19, 20]. The latter have the advantage that the state of polarization can be switched very fast so that measurements of magnetic circular dichroism, e.g., can be performed easily.

3.1.3 Synchrotron Radiation for Mössbauer Experiments

It has been realized by Ruby in 1974 [8], that synchrotron radiation could be superior to radioactive sources for nuclear resonant absorption and scattering experiments. A quantitative comparison will be given in the following [21].

A commercially available ^{57}Co source with 100 mCi activity produces an equivalent spectral photon flux of approximately 2.5×10^{10} ph/s/eV into $2 \times 2 \text{ deg}^2$ solid angle (0.001 sr), taking into account that the energy range of the measurement extends over 200 natural linewidths Γ_0 . A typical third-generation undulator beamline, e.g., at the APS delivers about 2.5×10^{12} ph/s/eV into a solid angle of $0.001 \times 0.003 \text{ deg}^2$. If samples are small, i.e., they only accept radiation within a small spatial or angular range, it is particularly useful to know brightness and brilliance of the source. For the

Table 3.2. Comparison between a third-generation undulator source and a commercially available ^{57}Co source with 100 mCi activity (values taken from *Sturhahn* [22])

| Property | Synchrotron Radiation | Radioactive Source |
|--|--------------------------|-----------------------|
| Spectral flux (ph/s/eV) | 2.5×10^{12} | 2.5×10^{10} |
| Brightness (ph/s/(eV· sr)) | 2.8×10^{22} | 2.5×10^{13} |
| Brilliance (ph/s/(eV· sr ·mm ²)) | 2.8×10^{22} | 2.5×10^{11} |
| Typical beam size (mm ²) | 1×1 | 10×10 |
| Focused beam size (μm^2) | 6×6 | — |
| Energy resolution (neV) | — | 4.7 |
| Time resolution (ns) | 0.7 | — |
| Polarization | linear or circular | unpolarized |

radioactive source, we obtain a brightness of 2.5×10^{13} ph/s/(eV sr), and, at 30 cm distance, the brilliance is 2.8×10^{11} ph/s/(eV sr mm²). Synchrotron radiation achieves much higher values providing a brightness of 2.8×10^{22} ph/s/(eV sr) and a brilliance of typically 2.8×10^{22} ph/s/(eV sr mm²). Evidently, synchrotron radiation produces more useful intensity for Mössbauer experiments [21]. This comparison is summarized in Table 3.2. A detailed analysis of data collection times in forward scattering geometry has been given by *Alp et al.* [23]. It was shown that data collection times of a few seconds can be expected even for samples with natural Fe. However, a severe restriction is the very strong nonresonant intensity that has to be handled by the detector and the subsequent electronics. This limits the application of this technique at the undulator beams of third-generation storage rings, even if monochromatization to meV-bandwidth is performed. Here efficient techniques for background suppression like polarization filtering, as discussed in Sect. 3.2.3, have to be applied. Perhaps also the technique of grazing-incidence antireflection films [24, 25] should be reconsidered.

3.2 Monochromatization

The demand for suppression of the nonresonant radiation in NRS experiments has driven the development of high-resolution crystal optics with bandwidths of a few meV [26, 27]. It was then recognized that these devices are an excellent tool for inelastic spectroscopy of vibrational excitations [28, 29]. The further development of this technique pushed the development of monochromators with sub-meV resolution [30, 31, 32]. The principal limit for Si-based crystal optics was estimated to be about 0.3 meV at a photon energy of 14.4 keV [32], mainly determined by the finite extinction depth of the radiation in the crystal. At higher photon energies above 20 keV the limit can

be pushed to about $100\text{ }\mu\text{eV}$ by employing superpolished single crystals with a very large asymmetry angle [33]. The limit set by the laws of dynamical diffraction can only be overcome by employing other scattering mechanisms that are energetically much sharper. An evident choice is nuclear resonant scattering itself due to the very narrow nuclear linewidth [34]. A detailed description of this approach is given in Chap. 6 of this book.

3.2.1 Heat-Load Monochromators

The first optical element in almost every beamline is a monochromator that leads to an energetic bandwidth of a few eV. It typically consists of two subsequent reflections of low order, for example Si(111) or Diamond(111), in a non-dispersive setting. The two crystals are mounted on stages so that the monochromatized beam leaves the monochromator at a fixed height, independent of the chosen energy. Since the first crystal has to stand high heat loads in the order of several kW/cm^2 , a very efficient cooling scheme has to be applied. During the construction and commissioning of third-generation sources this was a very intense field of research and development. Several schemes have been developed, including liquid-gallium cooling [35] and cryogenic cooling with cold nitrogen or helium gas [36, 37]. While these approaches employ thick Si crystals with properly designed cooling channels, another very efficient scheme is the use of thin crystals that transmit most of the unwanted radiation rather than absorbing it [38]. In this case water cooling is sufficient even at high-power undulator beamlines.

It is of crucial importance for any subsequent high-resolution optics that no vibrations are introduced at this stage. The angular beam motions connected with such perturbations easily lead to a loss in flux by one order of magnitude at the sample position. After several years of development the cryogenic cooling with cold gases and the use of water-cooled thin diamond crystals have proven to be the most stable solutions. A review about the performance of cooling schemes for heat-load monochromators at third-generation facilities was given by Chumakov *et al.* [39].

3.2.2 High-Resolution Monochromators

The main task of a high-resolution monochromator is to minimize the energy bandwidth of the transmitted radiation while maintaining an acceptable transmission of the available spectral flux [32]. Depending on the type of experiment, the design considerations for the monochromator fall into two different categories:

- Transmission-optimized designs:

In this case an optimum transmission of the spectral flux is desired. This is important for all experiments involving *elastic nuclear resonant scattering*. The energetic bandwidth should be a few meV to reach a low prompt count rate without sacrificing the spectral flux at the sample.

- Energy-resolution-optimized designs:

Here the spectral flux may be sacrificed to some extend for reduction of the energy bandwidth. This quantity determines the energy resolution in experiments involving *inelastic nuclear resonant scattering*. In such designs energy resolutions in the sub-meV range have been reached.

In any case the spatial and angular acceptance of the monochromator have to be matched to the size and divergence of the incident radiation. This means, on the other hand, that the meaningful types of high-resolution monochromators are determined mainly by the characteristics of the radiation source. Such aspects have to be carefully taken into account when designing a beamline for nuclear resonant scattering experiments.

In the following, the basic principles are outlined that determine the design of high-resolution monochromators [32, 40]. Two basic aspects have to be combined in the design of such devices:

- Matching of the angular acceptance to the divergence of the incident radiation. This is achieved by employing asymmetric Bragg reflections. The angular acceptance of the crystal can be tuned by the asymmetry angle α .
- Bandpass reduction into the meV or sub-meV range. This is achieved by high-order Bragg reflections close to back-reflection.

The fulfillment of both conditions leads to a combination of both types of reflections in one monochromator setup. To explain this in more detail, the basic aspects of asymmetric Bragg reflection, as illustrated in Fig. 3.4, will be discussed. To characterize such a reflection one introduces the asymmetry parameter b :

$$b = \frac{\sin(\Theta + \alpha)}{\sin(\Theta - \alpha)} . \quad (3.15)$$

The asymmetry angle α is the angle between the reflecting planes and the surface of the crystal. A symmetric reflection implies that $b = 1$. The asymmetry changes the balance between the angular acceptance D_- and the angular emittance D_+ of a Bragg reflection:

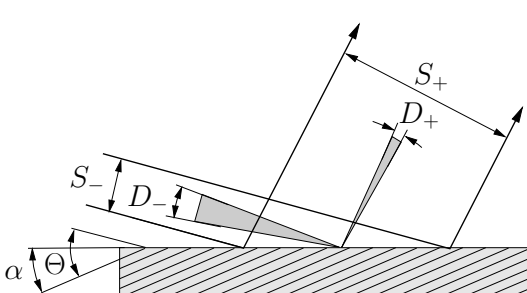


Fig. 3.4. Geometry of an asymmetric Bragg reflection with incident (-) and diffracted (+) beam. Θ is the Bragg angle and α is the angle of the lattice planes relative to the surface. S_{\pm} and D_{\pm} denote the size and the angular width of the incident and diffracted beam, respectively

$$D_{\pm} = \frac{2P|\chi_{rH}|}{\sin 2\Theta} b^{\pm 1/2}. \quad (3.16)$$

For $b = 1$, one obtains the Darwin width D of the reflection. χ_{rH} is the real part of the dynamic susceptibility:

$$\chi_{rH} = -\frac{r_e \lambda^2}{\pi V} \sum_j (f_H + f') \exp(2\pi i \mathbf{H} \cdot \mathbf{R}_j) f_{DW}^{(j)}(\mathbf{H}). \quad (3.17)$$

V is the volume of the unit cell, r_0 is the classical electron radius, \mathbf{H} is the reciprocal lattice vector, and \mathbf{R}_j is the atomic position within the unit cell. P is the polarization factor of the incident radiation⁶. It follows that the ratio between emittance and acceptance, as well as the ratio between the transverse beamsizes S_{\pm} is simply given by the asymmetry factor:

$$\frac{D_+}{D_-} = b \quad \text{and} \quad \frac{S_+}{S_-} = \frac{1}{b}, \quad \text{i.e.} \quad D_+ S_+ = D_- S_- . \quad (3.18)$$

The last equation expresses the fact that the product of angular divergence and beam size is constant for a given reflection⁷. This means, one either obtains a collimated beam with large size or a divergent beam with small size, as illustrated in Fig. 3.4. This is a very important aspect in the design of high-resolution monochromators. It should also be noted that for an asymmetric reflection the reflectivity curve is shifted relative to the nominal Bragg angle by an amount that is given by

$$\Delta_{\pm} = \frac{1}{2} \frac{|\chi_{r0}|}{\sin 2\Theta} (1 + b^{\pm 1}) , \quad (3.19)$$

where χ_{r0} is obtained from (3.17) for $\mathbf{H} = 0$.

The intrinsic energy width ΔE of a given reflection is intimately related to the angular spread $\Delta\Theta$ of the reflection, i.e., its Darwin width:

$$\frac{\Delta E}{E} = -\Delta\Theta \cot\Theta . \quad (3.20)$$

This relation follows directly from Bragg's law by differentiation for E . From the $\cot\Theta$ dependence it follows that the best energy resolution is achieved close to backscattering geometry, i.e., $\Theta \approx \pi/2$. The task is then to match the angular acceptance of the crystal optics with the divergence $\Delta\Theta$ of the incident radiation. At third-generation sources the undulator radiation is well collimated with a vertical divergence of about 15 µrad and a vertical beam size (central cone) smaller than 1 mm at the sample position. While high-order reflections provide a good energy resolution, the Darwin widths are exceedingly small, in the range of a few µrad around 10 keV. To overcome this

⁶ $P = 1$ if the polarization is perpendicular to the scattering plane (σ -polarization) radiation and $P = \cos 2\Theta$ for radiation that is polarized parallel to scattering plane (π -polarization).

⁷ This follows directly from Liouville's theorem which says that the phase space volume of a dynamic system under conservative forces is constant.

mismatch, two approaches are possible that result either in a transmission-optimized design or an energy-resolution-optimized design. In both cases, two subsequent reflections are employed that have to be placed in $(+, +)$ setting:

- Transmission-optimized designs:

The incident radiation is first collimated by a low-order asymmetric reflection with $b < 1$ that results in a large angular acceptance. The divergence of the reflected beam then matches the narrow angular acceptance of the second, high-order reflection. This was initially proposed as a means to achieve high-energy resolution and large angular acceptance to improve the signal-to-noise ratio in elastic nuclear resonant scattering experiments [26].

- Energy-resolution-optimized designs:

The radiation is reflected over two highly asymmetric, high-order reflections. This arrangement leads to some loss of spectral flux, but is capable of achieving energy resolutions in the sub-meV range. Such monochromator arrangements were developed for inelastic nuclear resonant scattering experiments [30, 31].

The basic principle of monochromatization along these lines is illustrated in Fig. 3.5. To obtain the angular and energetic width of a given sequence of reflections one plots the Bragg equations $\lambda = 2d_{hkl} \sin \Theta$ for each of the crystals. Reflectivity is achieved in the intersection areas of these graphs. Since this technique was first proposed by *DuMond* [41], these plots are called ‘DuMond-diagrams’. A modern implementation of such diagrams into a computer program was put forward by *Toellner* [32] to obtain the exact transmission of subsequent crystal reflections.

At very high energy resolutions, particular attention has to be paid to the temperature stability of the setup. A temperature drift δT of the monochromator is related to a relative energy shift that is given by

$$\frac{\delta E}{E} = \beta \delta T , \quad (3.21)$$

where β is the coefficient of thermal expansion of the crystal material ($\beta = 2.56 \times 10^{-6}$ for Si). Thus, at 14.4 keV an energetic detuning of 1 meV is caused by a temperature drift of 0.027 K. The tuning of the monochromator energy is achieved via tuning the relative angular orientation of the crystals while monitoring their temperatures. In case of an arrangement of two (channel-cut) crystals in $(+, +)$ setting like those shown in Figs. 3.3A–D, the energetic detuning is given by [32]

$$\frac{\delta E}{E} = \frac{\delta\Theta_1 - \delta\Theta_2 - \beta(\delta T_1 \tan \Theta_1 + \delta T_2 \tan \Theta_2)}{\tan \Theta_1 + \tan \Theta_2} , \quad (3.22)$$

where Θ_1 and Θ_2 are the Bragg angles of the two crystals. $\delta\Theta_1, \delta\Theta_2$ are the corresponding changes in the angular settings and $\delta T_1, \delta T_2$ are the temperature changes of the crystals.

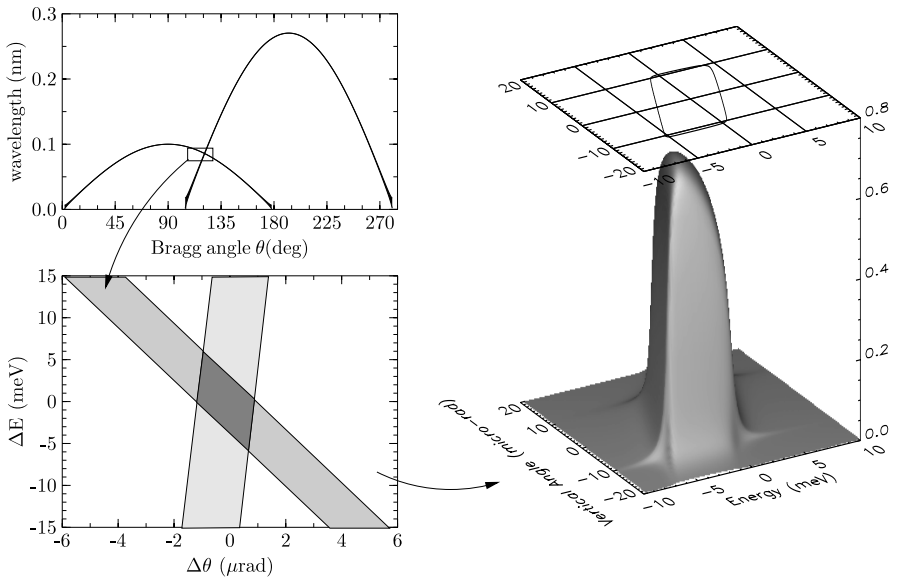


Fig. 3.5. A two-crystal arrangement for a transmission-optimized monochromator, consisting of a Si(4 2 2) and a Si(12 2 2) reflection in dispersive setting as shown in Table 3.3B. The *upper left* figure displays the Bragg equation $\lambda = 2d_{hkl} \sin \Theta$ plotted for both crystals, the *bottom left* figure shows the intersection area of both graphs enlarged so that the energy/angle widths can be read. The *right* figure finally displays the exact transmission of this setup as function of energy and angle (*Right* figure taken from Toellner [32])

The realization of these concepts has led to a number of monochromator arrangements that have been used in NRS experiments so far. They are summarized together with some other designs in Table 3.3. These high-resolution monochromators require a very good angular control and a very good temperature stability. Since crystals become very large at high asymmetry angles, the temperature homogeneity over the crystal surface plays an important role. This applies in particular for the sub-meV monochromators where the temperature stability should be better than 0.01 K. Angular positions of the crystals have to be controlled with a precision of a few nanorad, especially in the case of sub-meV monochromators where high-resolution interferometric encoders have been developed [45]. While transmission-optimized designs will be based on nested monochromators, the ultimate limit of the energy resolution will be achieved by the individual control of single, highly-polished crystals. In this field the construction of ‘artificial’ channel-cuts has been successfully applied [46]. The efficiency of such setups will improve further with the development of cryogenically cooled crystals, operated at a temperature of 123 K where the thermal expansion of Si is zero. This enhances the

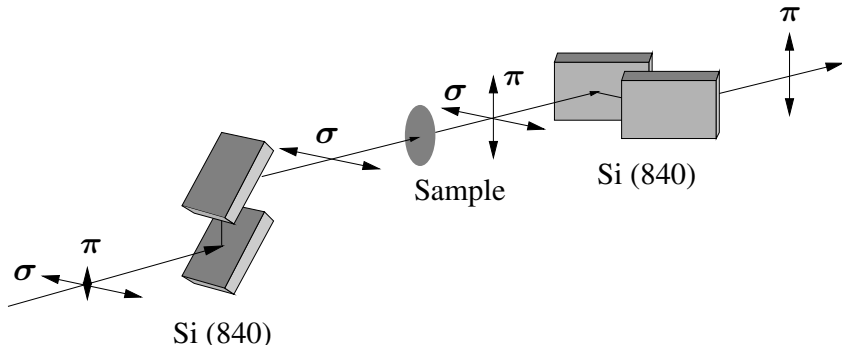


Fig. 3.6. Polarization filtering of 14.4 keV x-rays with two crossed Si(840) polarizers. The incident radiation is almost completely linearly polarized after leaving the first polarizer. A polarization-mixing scattering process in between yields a strong orthogonal polarization component that passes the second crystal while the original polarization is almost completely blocked. The arrows symbolize the polarization state present in the beam

throughput because of vanishing lattice distortions that result from thermal gradients imposed by the heat load of the incident eV-wide beam.

The throughput of high-resolution monochromators can be further enhanced by using collimating refractive lenses [47, 48]. This allows to match the divergence of the incident radiation to the angular acceptance of the monochromator crystals [49].

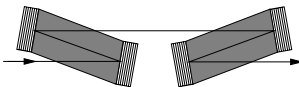
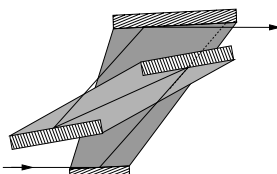
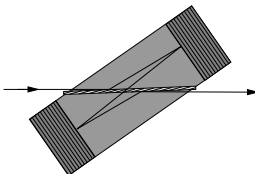
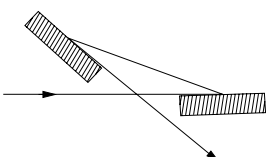
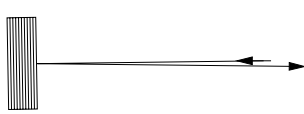
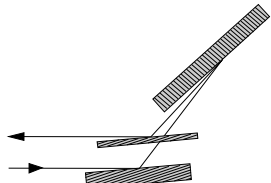
A very comprehensive review about high-resolution x-ray optics was given by *Shvyd'ko* [40].

3.2.3 Polarization Filtering

Monochromatization to energy widths in the μeV range can be achieved by employing nuclear resonant scattering itself. One approach uses the polarization dependence of the scattering process from (magnetically) anisotropic materials that results in strong orthogonal ($\sigma \leftrightarrow \pi$) scattering in the vicinity of the resonance. Separation of the nuclear resonant $\sigma \rightarrow \pi$ scattering from the nonresonant polarization-conserving scattering leads to beams with an energetic width below $1\,\mu\text{eV}$. This filtering is achieved by two polarizing reflections in crossed setting with a resonant scattering process in between, as shown in Fig. 3.6. The first crystal generates almost pure σ polarization. The second crystal is adjusted so that its scattering plane is at an angle of 90° relative to that of the first crystal. Then the polarization state transmitted by the first crystal is almost completely blocked while the $\sigma \rightarrow \pi$ scattering is transmitted.

This scheme resembles the principle of optical polarimetry where the optical activity of a substance is measured in a polarizer/analyzer setup. Visible

Table 3.3. High-resolution x-ray monochromators used for elastic and inelastic nuclear resonant scattering. See also the extensive review by *Shvyd'ko* [40]

| | Geometry | Characteristics | Refs. |
|---|---|--|------------------------|
| A |  | Symmetric reflections on two subsequent channel-cut crystals, relatively low angular acceptance | [42] |
| B |  | Nested monochromator consisting of two channel-cut crystals, asymmetric inner and outer crystals, high angular acceptance, meV energy resolution | [26], [27], [32] |
| C |  | Nested monochromator, very thin inner crystal, high angular acceptance and compact design at energies above 20 keV, sub-meV energy resolution | [43] |
| D |  | Two single crystals, highly asymmetric cut, high angular acceptance, sub-meV energy resolution | [30], [31], [32] |
| E |  | Four single crystals, highly asymmetric cut, high angular acceptance, 120 μeV energy resolution at 14.4 keV | [33] |
| F |  | Exact backreflection, reflection has to match resonance energy, high angular acceptance, meV energy resolution | [44] |
| G |  | Highly asymmetric reflection very close to backscattering, meV and sub-meV energy resolution at photon energies 5–10 keV | [40] |

light can be polarized by reflection at a dielectric mirror under the Brewster angle. In this case the reflected and the refracted beam enclose an angle of 90°. Due to the dipole emission characteristic, no radiation is reflected that is polarized parallel to the scattering plane. Only those components are reflected that are polarized perpendicularly to the scattering plane (σ -polarization). The same principle can be used for x-rays by using Bragg reflections with Bragg angles of 45°. This is the Brewster angle for x-rays since refraction effects are very small at these energies. However, at room temperature it is very unlikely to find a reflection with a Bragg angle of exactly 45° for a given wavelength of a nuclear transition. The deviation from 45° determines the suppression ratio of π -polarization relative to σ -polarization. At 14.4 keV the Si(840) reflection with $\Theta_B = 45.1^\circ$ is best suited to be used for a polarizing Bragg reflection [50, 51, 52, 53]. A disadvantage is the small Darwin width of 0.5 μrad that limits the angular acceptance. This value can be enlarged to 10.6 μrad by cutting the crystal with an asymmetry angle of 43.1°, i.e., the angle of incidence relative to the crystal surface is 2° [50, 52, 53]. This is illustrated in Fig. 3.7. Due to the small angular acceptance, experiments with such polarizing reflections can be efficient only at high-brilliance synchrotron radiation sources. Typical divergences at undulator beamlines of 3rd generation facilities are in the range of 15 μrad vertical and 50 μrad horizontal. Despite such a good collimation, there is still a mismatch with the angular acceptance of the polarizer-analyzer crystals, so that only a flux of approximately 10% of the incident flux can be used. However, this situation will significantly improve if the horizontal emittance of the storage ring can be further reduced, as it is presently being tested at the APS. Another approach is the use of compound refractive lenses for x-rays [54, 55, 56] that can be applied as collimators [47, 48] to improve the efficiency of subsequent x-ray optical elements [49].

Formally, the transmission through an arrangement of two crossed linear polarizers with an intermediate polarization mixing scattering process is described in the linear polarization basis (σ, π) by the following expression:

$$(A_\sigma, A_\pi) = (1, \xi) \begin{pmatrix} 1 & 0 \\ 0 & \delta \end{pmatrix} \begin{pmatrix} R_{\sigma\sigma} & R_{\sigma\pi} \\ R_{\pi\sigma} & R_{\pi\pi} \end{pmatrix} \begin{pmatrix} \delta & 0 \\ 0 & 1 \end{pmatrix} \approx (\delta R_{\sigma\sigma}, R_{\sigma\pi}) . \quad (3.23)$$

This is the description of the setup in Fig. 3.6 within the Jones-matrix formalism. The radiation from the undulator is almost completely σ -polarized with a small admixture ξ of π -polarization. The polarizer/analyzer crystals are represented by the corresponding matrices for linear polarizers with an imperfection of $\delta \approx 10^{-4}\text{--}10^{-5}$, resulting from the deviation of the Bragg angle from the optimum value of 45°. The middle matrix describes the polarization dependence of the nuclear scattering process that can be either forward scattering [51, 52] or grazing incidence reflection [57]. In the latter case remarkably large bandwidths can be obtained. As an example we

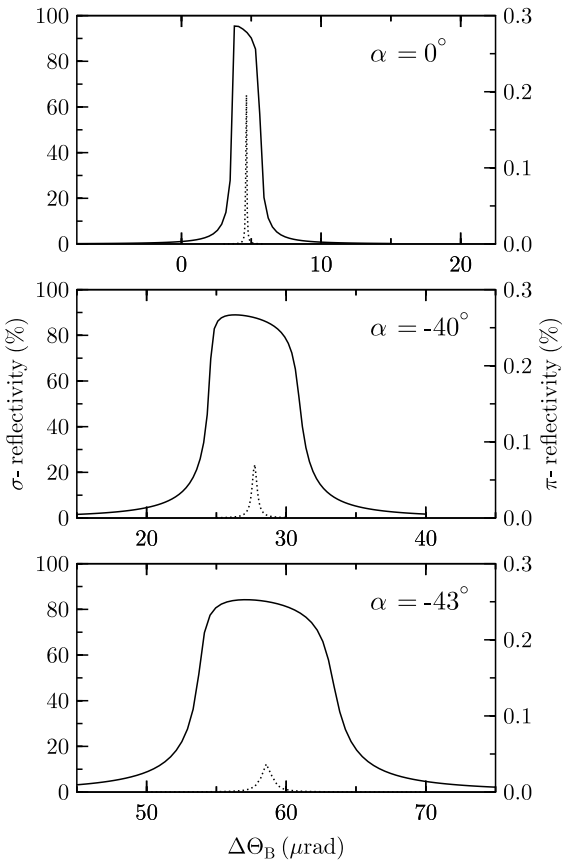


Fig. 3.7. Rocking curves of the Si(840) reflection for σ polarization (solid lines, left scale) and π polarization (dotted lines, right scale), calculated for various asymmetry angles α . $\Delta\Theta_B$ measures the deviation from the kinematical Bragg angle Θ_B . The ratio between the areas under the curves determines the suppression of π vs. σ polarization. This can be significantly increased by cutting the crystal asymmetrically. Note that the angular position of the reflections shifts with increasing asymmetry due to refraction

consider a 10-nm thick film of ^{57}Fe on a Pd substrate. The scattering takes place in Faraday geometry, i.e., the film is magnetized along the direction of \mathbf{k}_0 . This yields the strongest polarization mixing effects. A more detailed discussion is given in Sect. 6.3.1. The spectral response of the film within the polarizer/analyzer setup is shown in Fig. 3.8 where the width of the response is about $0.8 \mu\text{eV}$. This example shows that such a setup can be used very efficiently to obtain a spectrally very pure band of resonantly scattered radiation. On the other hand, it allows one to study magnetic phenomena that lead to optical activity with a very high sensitivity. This was first demonstrated to measure the Faraday rotation in magnetic x-ray scattering at the Fe and Co K absorption edges [58], and applied to investigate magnetic relaxation phenomena via nuclear forward scattering [59]. Due to almost complete suppression of electric charge scattering, time spectra can be recorded from very early times ($\approx 1 \text{ ns}$) after excitation.

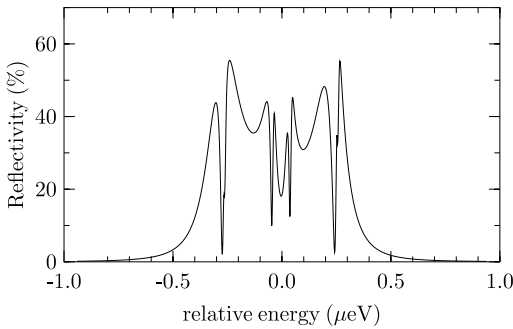


Fig. 3.8. Calculated energy spectrum of the reflected intensity $|R_{\sigma\pi}|^2$ of 10 nm ^{57}Fe on Pd, magnetized along \mathbf{k}_0 [34]

3.3 Detection Schemes

One of the main problems in nuclear resonant scattering experiments is the time-resolved detection of delayed events in the presence of a huge prompt data rate. While this can be alleviated to some extent by meV bandpass filtering using high-resolution monochromators, the detector system still has to tolerate a very high event rate. This is particularly true at the undulator beams of third-generation sources that seem to steadily gain in brilliance and flux by continuous improvement of instrumentation. In this section the basic requirements for the detectors and their realization in present-day experimental setups will be discussed.

3.3.1 Basic Requirements

For an efficient recording of time-resolved nuclear resonant scattering, a detection system has to satisfy the following demands:

- Single-photon counting in the energy range from 6 to 60 keV.
- High quantum efficiency, preferably greater than 50%.
- Low background noise, preferably $\leq 0.01 \text{ s}^{-1}$.
- High count-rate capability, preferably $\geq 10^8 \text{ s}^{-1}$.
- Good time resolution, preferably $\leq 1.0 \text{ ns}$.
- Fast recovery/large dynamic range.
- Large active area, preferably $\geq 1 \text{ cm}^2$.
- Operation at room temperature, radiation hardness, long-time stability.

Many of these points are certainly desirable for any detector. However, for nuclear scattering experiments where signal rates are often only in the range of $\sim 0.1 \text{ s}^{-1}$, their importance is enhanced.

According to the Nyquist theorem, the value of the time resolution should not be larger than twice the smallest quantum-beat period to be resolved. In case of coherent scattering at the ^{57}Fe resonance, a time resolution around 1 ns is sufficient to resolve beat periods of 5–10 ns. For other isotopes like

^{161}Dy with beat periods in the range of 200 ps this is not sufficient anymore. While time resolutions in that range are possible, one usually has to make trade-offs, e.g., sacrificing efficiency to gain time-resolution.

The fast recovery is of particular importance in case of high event rates like in case of inelastic absorption measurements or nuclear forward scattering experiments. If the recovery time exceeds the inverse of the event rate, then the dead time will be large and severely affects the signal rate.

3.3.2 Timing Electronics

The basic scheme of the electronics necessary for time resolved measurements of nuclear resonant scattering is shown in Fig. 3.9. The x-ray detector pulses are fed into a constant-fraction-discriminator (CFD) that generates very sharp timing signals independent of the pulse height of the incoming signals. These timing pulses are then used as a START signal for the time-to-amplitude converter (TAC). The measurement of the delay time then requires a STOP signal signal that is locked with a fixed phase relative to the arrival time of the photons at the sample. This reference signal can be generated by another fast x-ray detector looking at the radiation flashes from the orbiting bunches. A more convenient solution is the derivation of pulses from the master-oscillator that controls the radio-frequency (rf) operation of the storage ring. To facilitate time-resolved measurements, such a signal is provided at experimental stations of many facilities as so-called bunch-clock

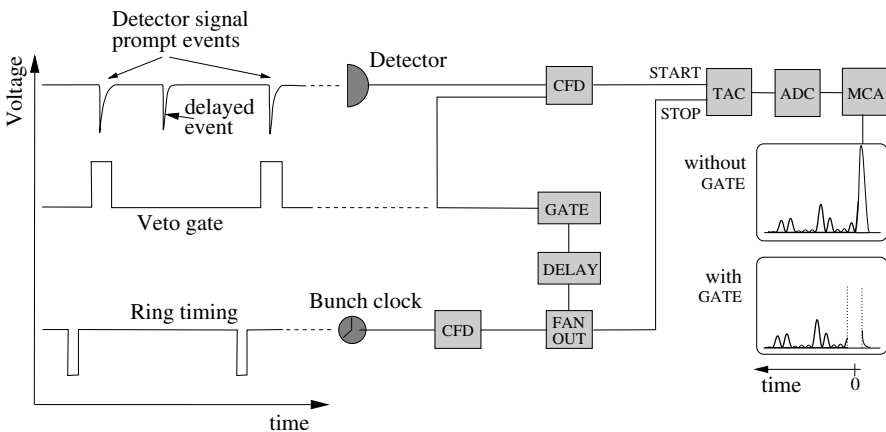


Fig. 3.9. Scheme of the timing electronics. The *left side* displays the input signals as a function of time, on the *right side* the wiring diagram of the electronic devices is shown. CFD = constant-fraction discriminator, TAC = time-to-amplitude converter, ADC = analog-to-digital converter, MCA = multichannel analyzer. The FAN OUT splits the signal from the bunch clock to generate the veto gate signal and the stop signal for the TAC

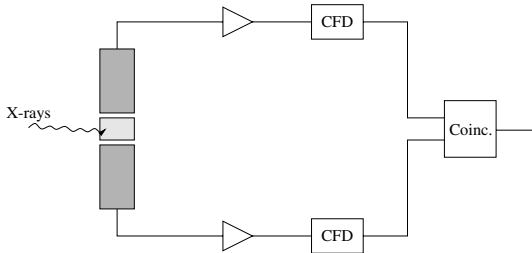


Fig. 3.10. Scheme of a plastic scintillation detector with two multiplier tubes in coincidence operation

or ring-timing signal. In addition to the STOP signal for the TAC this signal is used to generate a veto gate for the CFD that processes the signal from the detector. The gate signal is adjusted via the DELAY to arrive in coincidence with the detector signals and prevents the CFD from releasing a start pulse to the TAC. In that way the huge rate of prompt events cannot saturate the TAC (already at count rates of a few 10 kHz deadtime effects become significant). For the same reason the ring-timing signal is used as a stop signal instead of a start signal; otherwise the TAC would be started with the frequency of the orbiting bunches that would certainly overload this device. On the subsequent multi-channel-analyzer (MCA) the time spectrum is recorded as a histogram of counts versus a (inverted) time scale. Instead of this histogram format one might consider a data format like it is used in nuclear or high-energy physics, where each event is individually recorded, as proposed by *Baron* [60]. This yields a list of subsequent events containing the time of the event and other experimental parameters. Then the evaluation would be done afterwards, investigating correlations of the recorded events with the experimental parameters, for example. Such a scheme has been applied for the stroboscopic detection of nuclear resonant scattering as discussed in Sect. 6.4.

The overall time resolution of such a system is typically between 100 ps and 1 ns. It is limited by the synchrotron radiation pulse width, the time resolution of the x-ray detector and the jitter in the electronics. The main contribution usually comes from the detector, as will be discussed below.

3.3.3 Detectors

Early Detectors

In the first observation of coherent nuclear resonant scattering of synchrotron radiation, a germanium diode with a time resolution of 20 ns was used [1]. In order to observe quantum beat patterns in the nuclear decay, this detector was replaced with two plastic scintillation detectors in a fast-slow coincidence circuit, shown in Fig. 3.10. This was the standard detector for several years, providing about 1 ns time resolution, a background noise of about 0.5 s^{-1} and efficiencies around 40% at 14.4 keV [61].

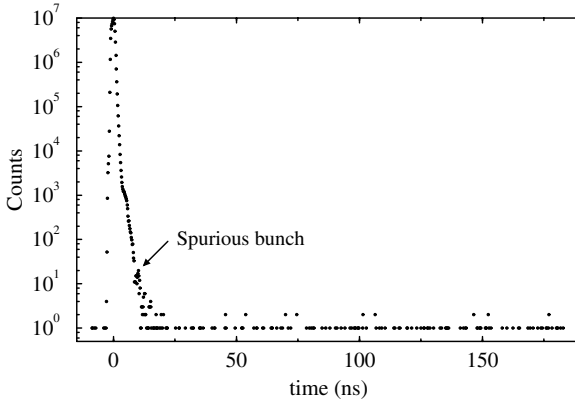


Fig. 3.11. Time spectrum of the bunch structure in DORIS III, taken with an APD detector over an acquisition time of 30 min. The spectrum shows the main bunch and a spurious bunch with a relative intensity of 10^{-6} . One clearly notices the large dynamic range of greater than 10^7 (Data taken from Metge [69])

Another type of detector was developed for the time-resolved detection of conversion electrons [62]. This detector is based on a system of micro-channel plates with an electron optics. It was successfully used, e.g., to investigate the interplay of coherent and incoherent decay channels in nuclear forward scattering from ^{57}Fe with a time resolution of 0.5 ns [63].

Avalanche Photodiodes (APD)

The most efficient detector to date used in almost all kinds of nuclear resonant scattering experiments is the avalanche photodiode (APD). It was first introduced into the field of x-ray physics by *Kishimoto* [64, 65] and *Baron & Ruby* [66] and thoroughly characterized [67, 68]. The main advantages compared to the plastic scintillator are their better count-rate capability (up to few GHz) and their lower noise (around 0.01 Hz). This leads to a very high dynamic range, as shown in the time spectrum displayed in Fig. 3.11. In addition, their relatively small size of about 0.5 cm^3 allows a much better handling. This is important in confined geometries where the detector has to be very close to the sample as it is the case for nuclear inelastic scattering from thin films and samples in high-pressure cells.

Avalanche photodiodes are based on the internal multiplication of charge carriers that are accelerated and lose their kinetic energy by formation of secondary electron-hole pairs. These charge carriers are accelerated themselves and create additional electron-hole pairs. This effect is usually responsible for the electric breakthrough in semiconductor diodes at high field strengths. However, if the diode is operated just below the breakthrough voltage, the avalanche effect is used to obtain an effective gain of the diode in the range of 100–1000. Avalanche photodiodes are made from a thin silicon wafer where doping and reverse biasing lead to a depletion region of 50–100 μm (active) thickness in which the x-ray absorption occurs. At present the most commonly used detectors are based on the so-called reach-through design shown

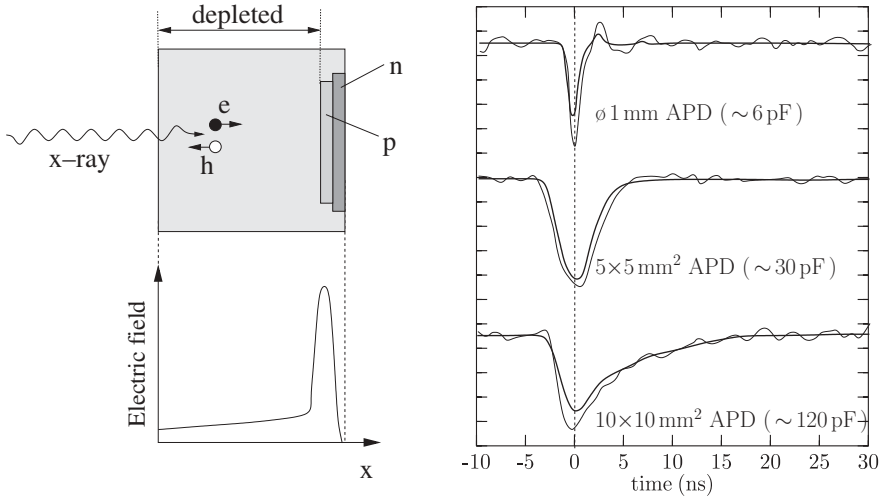


Fig. 3.12. *Left:* Scheme of a reach-through APD structure with low-field drift region and high-field gain region. *Right:* Signal shape from various diodes of different areas, generated by 14.4 keV photons. The *thick lines* are the average response while the *thin lines* are single photon events (Figure adopted from Baron [60])

in Fig. 3.12. The depletion layer consists of a relatively broad low-field (drift-) region and a narrow high-field (gain-) region on the back of the APD. The active thickness of this layer determines the quantum efficiency of the device and its time resolution. The time resolution is generally not better than the active thickness divided by the drift velocity, which is about $100 \mu\text{m}/\text{ns}$ in Si at high fields. The signal from the APD is amplified by a voltage amplifier preferably with about 1 GHz bandwidth. Typical pulse shapes for several diodes are shown in Fig. 3.12. While the rise time is determined by the charge transport within the device, the fall time is given by the RC time constant of the diode capacitance and the amplifier output impedance [70]. The shape of this signal is crucial for time gating of the prompt signal. Its width determines how long it takes until the detector recovers from a prompt pulse of several photons to detect a single delayed photon. Thus, for recording high-resolution time spectra like in NFS, smaller diodes are to be preferred. On the other hand, for recording delayed quanta in NIS, these requirements are more relaxed and larger-area APDs can be used.

The high gain of APD detectors facilitates the detection of low-energy photons below 10 keV which is of particular importance for measurement of delayed K-fluorescence photons in inelastic nuclear scattering experiments. The efficiency for high-energy photons can be increased, e.g., by using a high-Z material like GaAs instead of Si. First promising results in that direction have been reported [71, 72].

Another approach to increase the efficiency is the stacking of many APDs in a row [73], where, in addition, the active areas may be illuminated in grazing incidence geometry. This is particularly important for the observation of NRS at energies above 20 keV. An example is the 25.65 keV resonance of ^{161}Dy . Dy compounds are interesting because of their magnetic properties. In the ferromagnetic phase of Dy metal below 85 K the magnetic hyperfine field assumes values up to 580 T [74], and in compounds like $\text{Dy}_2\text{Fe}_{14}\text{B}$ magnetic hyperfine fields of up to 600 T at room temperature are reported [75]. The resulting hyperfine splitting leads to quantum beat periods below 100 ps. The development of a proper detector for this resonance is challenging because of the relatively low detector efficiency at high photon energies and the requirement for a very good time resolution. Both conditions are mutually exclusive in Si APDs because the ratio of the active thickness to the time resolution is equal to the (almost constant) drift velocity of the electrons in the APD ($\approx 100 \mu\text{m/ns}$). This means, an increase in the APD thickness to improve the efficiency automatically leads to a degradation of the time resolution. An approach to overcome this limitation is the use of an array of APDs that is illuminated at grazing angles, so that the path length of the radiation becomes large while the thickness of the active region can be kept small. This has been demonstrated successfully for nuclear resonant scattering at the 25.65 keV resonance of ^{161}Dy by *Shvyd'ko et al.* [76] and *Baron et al.* [77]. In the latter case, an array of 16 APDs with a surface area of $1 \times 2.5 \text{ mm}^2$ each was used, illuminated at a grazing angle of about 3° . A time resolution of 180 ps and an efficiency of about 17% at 25.6 keV was achieved [77].

It is beyond the scope of this book to cover all recent developments in x-ray APD technology. For a recent review and further references see, e.g., the article by *Baron* [60]. Certainly, a big part of the future progress in the field of nuclear resonant scattering will depend on the improvement of x-ray detectors.

3.4 Beamlines

Since the instrumentation for NRS experiments is highly specialized, the development of this field has led to dedicated beamlines at several synchrotron radiation sources. This begins with the station F4 at the DORIS storage ring [78] that was located at a bending magnet. It continues with the wiggler-based station BW4 at DORIS and merges into the present-day undulator based sources at the ESRF [79], APS [80, 81], and HASYLAB [82]. The given references provide a good overview over the technical challenges that had to be overcome to use synchrotron radiation for nuclear resonant scattering experiments. A typical layout of such a beamline is shown in Fig. 3.13. The given distances measured from the radiation source are typical values for beamlines at third-generation sources. The sketched elements are typically

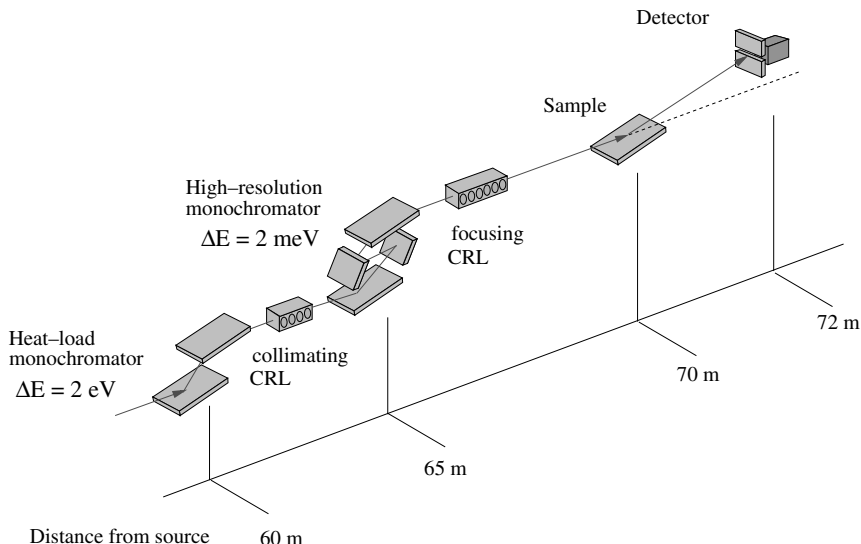


Fig. 3.13. Schematic layout of a typical beamline for nuclear resonant scattering. The dimensions given at the bottom are for a third-generation source like the ESRF, APS or SPring-8. In order to enhance the throughput of the high-resolution monochromator, a collimating compound refractive lens (CRL) is used. Behind the monochromator, a focusing device like a CRL or a Kirkpatrick-Baez mirror optics is used to match the beam cross section with the sample dimensions

located in separated hutches to ensure independent access and unperturbed operation during the experiments.

More information about beamlines and operation modes can be found on the corresponding web-pages of the facilities

- European Synchrotron Radiation Facility
ESRF (<http://www.esrf.fr>)
- Advanced Photon Source
APS (<http://www.aps.anl.gov>)
- Super Photon-ring 8 GeV
SPring8 (<http://www.spring8.or.jp>)
- Hamburger Synchrotronstrahlungslabor
HASYLAB (<http://www-hasylab.desy.de>)

References

1. E. Gerdau, R. Rüffer, H. Winkler, W. Tolksdorf, C. P. Klages, and J. P. Hannon : Phys. Rev. Lett. **54**, 835 (1985) **37**, **38**, **58**

2. J. D. Jackson : *Classical Electrodynamics* (Wiley, New York 1975) **37**, **40**
3. H. Wiedemann : *Particle Accelerator Physics I + II* (Springer, Berlin 1993) **37**
4. K. Wille : *Physik der Teilchenbeschleuniger und Synchrotronstrahlungsquellen* (Teubner, Stuttgart 1996) **37**, **39**
5. H. Winick : *Synchrotron Radiation Sources, a Primer* (World Scientific, 1994) **37**
6. W. Brefeld and P. Gürler in: *Handbook on Synchrotron Radiation*, edited by S. Ebashi, M. Koch, and E. Rubinstein (Elsevier Science Publishers, Amsterdam 1991) **37**
7. R. E. Watson and M. L. Perlman : *Science* **199**, 1295 (1978) **37**
8. S. L. Ruby : *J. de Physique* **35**, C6-209 (1974) **38**, **45**
9. R. Chasman and K. Green : *BNL Report*, BNL 50505 (1980) **38**
10. H. Winick : *Scientific American* **257**, No. 5, 88 (1987) **38**
11. B. Lai, A. Khounsary, R. Savoy, L. Moog, and E. Gluskin : Advanced Photon Source Technical Report ANL/APS/TB-3 (Argonne 1993) **42**
12. G. P. Williams : *Synch. Rad. News* **10**, 2 (1997) **43**
13. TESLA Technical Design Report, Part V: The X-ray Free Electron Laser, edited by G. Materlik and Th. Tschentscher (DESY 2001 - 011, ECFA 2001 - 209, TESLA Report 2001 - 23, TESLA - FEL 2001 - 05) **43**, **44**
14. K. Balewski, W. Brefeld, W. Decking, W. Drube, H. Franz, R. Gehrke, P. Gürler, U. Hahn, J. Pfleiger, H. Schulte-Schrepping, M. Tischer, and E. Weckert : DESY-HASYLAB, Internal Report (DESY 2002) **44**
15. R. J. Nawrocky, U. Bergmann, and D. P. Siddons : Proceedings of the 1993 Particle Accelerator Conference **3**, 2145 (1993) **44**
16. G. Mühlaupt and R. Rüffer : *Hyperfine Interact.* **123/124**, 13 (1999) **45**
17. J. C. Lang, G. Srayer, and R. J. Dejus : *Rev. Sci. Instrum.* **67**, 62 (1996) **45**
18. K. Hirano, T. Ishikawa, and S. Kikuta : *Nucl. Instrum. Methods Phys. Res. A* **336**, 343 (1993) **45**
19. J. C. Lang and G. Srayer : *Rev. Sci. Instrum.* **66**, 1540 (1995) **45**
20. J. Pollmann, G. Srayer, J. Maser, J. C. Lang, C. S. Nelson, C. T. Venkataraman, and E. D. Isaacs : *Rev. Sci. Instrum.* **71**, 2386 (2000) **45**
21. W. Sturhahn, E. E. Alp, T. S. Toellner, P. M. Hession, M. Hu, and J. Sutter : *Hyperfine Interact.* **113**, 47 (1998) **45**, **46**
22. W. Sturhahn : *J. Phys.: Condens. Matter* **16**, 497 (2004) **46**
23. E. E. Alp, W. Sturhahn, and T. S. Toellner : *Nucl. Instrum. Methods Phys. Res. B* **97**, 526 (1995) **46**
24. J. P. Hannon, N. V. Hung, G. T. Trammell, E. Gerdau, M. Mueller, R. Rüffer, and H. Winkler : *Phys. Rev. B* **32**, 5068 (1985) **46**
25. R. Röhlsberger, E. Gerdau, M. Harsdorff, O. Leupold, E. Lüken, J. Metge, R. Rüffer, H. D. Rüter, W. Sturhahn, E. Witthoff : *Europhys. Lett.* **18**, 561 (1992) **46**
26. T. Ishikawa, Y. Yoda, K. Izumi, C. K. Suzuki, X. W. Zhang, M. Ando, and S. Kikuta : *Rev. Sci. Instrum.* **63**, 1015 (1992) **46**, **50**, **53**
27. T. M. Mooney, T. S. Toellner, W. Sturhahn, E. E. Alp, and S. D. Shastri : *Nucl. Instr. Methods Phys. Res. A* **347**, 348 (1994) **46**, **53**
28. M. Seto, Y. Yoda, S. Kikuta, X. W. Zhang, and M. Ando : *Phys. Rev. Lett.* **74**, 3828 (1995) **46**
29. W. Sturhahn, T. S. Toellner, E. E. Alp, X. Zhang, M. Ando, Y. Yoda, S. Kikuta, M. Seto, C. W. Kimball, and B. Dabrowski : *Phys. Rev. Lett.* **74**, 3832 (1995) **46**

30. A. I. Chumakov, J. Metge, A. Q. R. Baron, H. Grünsteudel, H. F. Grünsteudel, R. Rüffer, and T. Ishikawa : Nucl. Instrum. Methods Phys. Res. A **383**, 642 (1996) **46, 50, 53**
31. T. S. Toellner, M. Y. Hu, W. Sturhahn, K. Quast, and E. E. Alp : Appl. Phys. Lett. **71**, 2112 (1997) **46, 50, 53**
32. T. S. Toellner : Hyperfine Interact. **125**, 3 (2000) **46, 47, 48, 50, 51, 53**
33. M. Yabashi, K. Tamasaku, and T. Ishikawa : Phys. Rev. Lett. **87**, 140801 (2001) **47, 53**
34. R. Röhlsberger, E. Gerdau, R. Rüffer, W. Sturhahn, T. S. Toellner, A. I. Chumakov, and E. E. Alp : Nucl. Instrum. Methods Phys. Res. A **394**, 251 (1997) **47, 56**
35. R. K. Smith : Nucl. Instrum. Methods Phys. Res. A **291**, 286 (1990) **47**
36. S. Joksch, G. Marot, A. Freund, and M. Krisch : Nucl. Instrum. Methods Phys. Res. A **306**, 386 (1991) **47**
37. G. S. Knapp, C. S. Rogers, M. A. Beno, C. L. Wiley, G. Jennings, P. L. Cowan : Rev. Sci. Instrum. **66**, 2138 (1995) **47**
38. A. K. Freund, G. Marot, H. Kawata, S. Joksch, E. Ziegler, L. E. Berman, and J. B. Hastings : Rev. Sci. Instrum. **63**, 442 (1992) **47**
39. A. Chumakov, R. Rüffer, O. Leupold, J. P. Celse, K. Martel, M. Rossat, and W. K. Lee : J. Synchrotron Rad. **11**, 132 (2004) **47**
40. Yu. V. Shvyd'ko: *X-Ray Optics: High-Energy-Resolution Applications* (Springer, Berlin 2004) **48, 52, 53**
41. J. W. M. DuMond : Phys. Rev. **52**, 872 (1937) **50**
42. J. B. Hastings, D. P. Siddons, U. van Bürck, R. Hollatz, and U. Bergmann : Phys. Rev. Lett. **66**, 770 (1991) **53**
43. A. Q. R. Baron, Y. Tanaka, D. Ishikawa, D. Miwa, M. Yabashi and T. Ishikawa : J. Synchrotron Rad. **8**, 1127 (2001) **53**
44. Yu. V. Shvyd'ko, E. Gerdau, J. Jäschke, O. Leupold, M. Lucht, and H. D. Rüter : Phys. Rev. B **57**, 4968 (1998) **53**
45. D. Shu, T. S. Toellner, and E. E. Alp in: *Proceedings of the 11th US National Conference on Synchrotron Radiation Instrumentation*, edited by P. Pianetta, AIP **521**, 219 (2000) **51**
46. D. Shu, T. S. Toellner, and E. E. Alp : Nucl. Instrum. Methods Phys. Res. A **467-468**, 771 (2001) **51**
47. A. Q. R. Baron, Y. Kohmura, Y. Ohishi, and T. Ishikawa : Appl. Phys. Lett. **74**, 1492 (1999) **52, 54**
48. A. Q. R. Baron, Y. Kohmura, V. V. Krishnamurthy, Yu. V. Shvydko, and T. Ishikawa : J. Synchrotron Radiat. **6**, 953 (1999) **52, 54**
49. A. I. Chumakov, R. Rüffer, O. Leupold, A. Barla, H. Thiess, T. Asthalter, B. P. Doyle, A. Snigirev, and A. Q. R. Baron : Appl. Phys. Lett. **77**, 31 (2000) **52, 54**
50. E. E. Alp, W. Sturhahn, and T. S. Toellner : Hyperfine Interact. **125**, 45 (2000) **54**
51. D. P. Siddons, J. B. Hastings, U. Bergmann, F. Sette, and M. Krisch : Nucl. Instrum. Methods Phys. Res. B **103**, 371 (1995) **54**
52. T. S. Toellner, E. E. Alp, W. Sturhahn, T. M. Mooney, X. Zhang, M. Ando, Y. Yoda, and S. Kikuta : Appl. Phys. Lett. **67**, 1993 (1995) **54**
53. T. S. Toellner : PhD thesis (Northwestern University, Evanston 1996) **54**
54. P. Elleaume : Nucl. Instr. Methods Phys. Res. A **412**, 483 (1998) **54**
55. B. Lengeler, J. Tümmler, A. Snigirev, I. Snigireva, and C. Raven : J. Appl. Phys. **84**, 5855 (1998) **54**

56. A. A. Snigirev, V. G. Kohn, I. I. Snigireva, and B. Lengeler: Nature (London) **384**, 49 (1996) 54
57. R. Röhlsberger: Hyperfine Interact. **123/124**, 301 (1999) 54
58. D. P. Siddons, M. Hart, Y. Amemiya, J. B. Hastings: Phys. Rev. Lett. **64**, 1967 (1990) 55
59. O. Leupold, A. Bernhard, E. Gerdau, J. Jäschke, H. D. Rüter, Yu. V. Shvydko, H. de Waard, E. E. Alp, P. Hession, M. Hu, W. Sturhahn, J. Sutter, T. Toellner, A. I. Chumakov, J. Metge, and R. Rüffer: Hyperfine Interact. **113**, 81 (1998) 55
60. A. Q. R. Baron: Hyperfine Interact. **125**, 29 (2000) 58, 60, 61
61. J. Metge, R. Rüffer, and E. Gerdau: Nucl. Instrum. Methods Phys. Res. A **292**, 187 (1990) 58
62. K. Quast: Diploma thesis (Universität Hamburg, 1993) 59
63. W. Sturhahn, K. W. Quast, T. S. Toellner, E. E. Alp, J. Metge, and E. Gerdau: Phys. Rev. B **53**, 171 (1996) 59
64. S. Kishimoto: Nucl. Instrum. Methods Phys. Res. A **309**, 603 (1991) 59
65. S. Kishimoto: Rev. Sci. Instrum. **63**, 824 (1992) 59
66. A. Q. R. Baron and S. L. Ruby: Nucl. Instrum. Methods Phys. Res. A **343**, 517 (1993) 59
67. A. Q. R. Baron: Nucl. Instrum. Methods Phys. Res. A **352**, 665 (1995) 59
68. T. S. Toellner, W. Sturhahn, E. E. Alp, P. A. Montano, and M. Ramanathan: Nucl. Instrum. Methods Phys. Res. A **350**, 595 (1994) 59
69. J. Metge: PhD thesis (Universität Hamburg, 1996) 59
70. G. F. Knoll: *Radiation Detection and Measurement*, 3rd ed. (Wiley, New York 1999) 60
71. J. Lauter, A. Förster, D. Protic, and H. Lüth: Nucl. Instrum. Methods Phys. Res. A **356**, 324 (1995) 60
72. J. Lauter, A. Förster, H. Lüth, K. D. Müller, and R. Reinartz: IEEE Trans. Nucl. Sci. **43**, 1446 (1996) 60
73. A. Q. R. Baron, R. Rüffer, and J. Metge: Nucl. Instrum. Methods Phys. Res. A **400**, 124 (1997) 61
74. S. Ofer, M. Rakavy, E. Segal, and B. Khurgin: Phys. Rev. **138**, A241 (1965) 61
75. P. C. M. Gubbens, A. M. van der Kraan, and K. H. J. Buschow: phys. stat. sol. (b) **130**, 575 (1985) 61
76. Yu. V. Shvyd'ko, M. Gerken, H. Franz, M. Lucht, and E. Gerdau: Europhys. Lett. **56**, 309 (2001) 61
77. A. Q. R. Baron, Y. Tanaka, and T. Ishikawa: SPring-8 Research Frontiers 2000/2001, edited by S. Kikuta, p.96, unpublished 61
78. R. Rüffer, D. Giesenbergs, H. D. Rüter, R. Hollatz, E. Gerdau, J. Metge, K. Ruth, W. Sturhahn, M. Grote, and R. Röhlsberger: Hyperfine Interact. **58**, 2467 (1990) 61
79. R. Rüffer and A. I. Chumakov: Hyperfine Interact. **97/98**, 589 (1996) 61
80. E. E. Alp, T. M. Mooney, W. Sturhahn, and T. Toellner: Hyperfine Interact. **90**, 323 (1994) 61
81. W. Sturhahn, T. S. Toellner, K. W. Quast, R. Röhlsberger, and E. E. Alp: Nucl. Instrum. Methods Phys. Res. A **372**, 455 (1996) 61
82. H. Franz, B. Hukelmann, and J. R. Schneider: Hyperfine Interact. **126**, 397 (2000) 61

4 Coherent Elastic Nuclear Resonant Scattering

In the field of x-ray diffraction, the intensity and the direction of scattered waves are determined by the properties of the individual scatterers and their arrangement in space. In the special case of forward scattering, the x-ray optical properties of solids do not depend on their microscopic structure, but are entirely determined by the properties of the individual constituting atoms. If the scattering is coherent elastic, i.e., the internal state of the scattering system is unmodified in the scattering process, then a macroscopic ensemble of scatterers can be replaced by a continuous medium with an index of refraction \mathbf{n} [1]:

$$\mathbf{n} = 1 + \frac{2\pi}{k_0^2} \sum_i \varrho_i \mathbf{M}_i , \quad (4.1)$$

where \mathbf{M}_i is the coherent forward scattering length of the i th atom and ϱ_i is the number density of these atoms. The sum runs over all atoms within the scattering volume. k_0 is the wavenumber of the radiation. The amplitude in depth z of a slab of material is then given by the well-known expression:

$$\mathbf{A}(z) = e^{ik_0 \mathbf{n} z} \mathbf{A}_0 . \quad (4.2)$$

This formula can be extended to describe the propagation of light in anisotropic media where the index of refraction is dependent on the polarization state of the light. This is the field of anisotropic optics where the index of refraction is a 2×2 matrix [2]. Remarkably, this concept can be extended further to describe not only forward scattering but also diffraction from single crystals and reflection from surfaces, thin films and multilayers. For that purpose it is convenient to rewrite (4.2) as:

$$\mathbf{A}(z) = e^{i\mathbf{F}z} \mathbf{A}_0 \quad \text{with} \quad \mathbf{F} = \mathbf{k}_0 + \mathbf{f} , \quad (4.3)$$

where \mathbf{f} is the forward scattering matrix given by

$$\mathbf{f} = \frac{2\pi}{k_0} \sum_i \varrho_i \mathbf{M}_i . \quad (4.4)$$

Comparison of (4.1) and (4.4) leads to the following relation between the index of refraction \mathbf{n} and the forward scattering matrix \mathbf{f} :

$$\mathbf{n} = 1 + \frac{\mathbf{f}}{k_0} . \quad (4.5)$$

In the general case of x-ray diffraction, \mathbf{F} is a multidimensional matrix with a dimension that is given by the number of the open scattering channels. The main problem is then the calculation of the matrix exponential $e^{i\mathbf{F}z}$. In general, this problem cannot be solved analytically, except for cases where the matrix \mathbf{F} exhibits special symmetries. Fortunately, this applies for the case of grazing incidence reflection, where an outline of the solution will be given here. In order not to obscure the basic principles, the main structure of the formalism will be described in the text, whereas detailed derivations will be given in the appendix.

While the structural arrangements of the scatterers determines the dimension and the symmetries of \mathbf{F} , the interaction of the photons with the atoms is given by the atomic scattering lengths \mathbf{M}_i . The scattering length contains contributions from nonresonant and resonant as well as electronic and nuclear scattering processes. These will be discussed in the following section with special emphasis given to nuclear resonant scattering.

In the kinematical approximation the scattering response is mainly determined by the atomic scattering amplitude. This approximation is encountered quite often in the case of scattering from surfaces and thin films where only a small amount of resonant material is present. For that reason, the polarization and energy dependence of the nuclear scattering amplitude, as well as the time dependence resulting from that will be discussed in detail.

4.1 The Dynamical Theory

The problem in the dynamical theory of x-ray scattering is to find a self-consistent solution for the radiation field in all scattering channels, taking all orders of multiple scattering into account. In general, every approach to describe this problem mathematically can be transformed into a set of coupled linear differential equations with constant coefficients, as shown, for example, in [3, 4]. After an appropriate transformation, the variation of the electric field amplitude along the depth z in the sample can be described by a first-order differential equation:

$$\frac{d\mathbf{A}}{dz} = i\mathbf{F}\mathbf{A}, \quad (4.6)$$

where \mathbf{F} is called the *propagation matrix* because it describes the modification of the wavefield \mathbf{A} upon propagation from coordinate z to coordinate $z + dz$. For a homogeneous material where \mathbf{F} does not depend on the coordinate z , the solution of (4.6) for the amplitude $\mathbf{A}(z)$ of the electromagnetic field in depth z is given by

$$\mathbf{A}(z) = e^{i\mathbf{F}z} \mathbf{A}(0), \quad (4.7)$$

which is, of course, of the same shape as (4.3). Here, the dimension of \mathbf{F} is determined by the number of available scattering channels. Correspondingly,

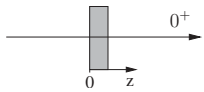
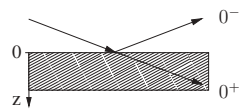
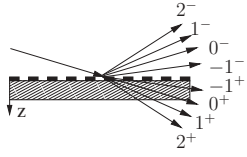
| Type of scattering | Scattering matrix | Scattering channels |
|---|---|---|
| A Forward scattering | $\mathbf{F} = \mathbf{k}_0 + \mathbf{f}_{0+0+}$ |  |
| B Grazing incidence reflection (2-beam diffraction) | $\mathbf{F} = \begin{pmatrix} \mathbf{f}_{0+0+} + \mathbf{k}_{0+z} & \mathbf{f}_{0+0-} \\ \mathbf{f}_{0-0+} & \mathbf{f}_{0-0-} + \mathbf{k}_{0-z} \end{pmatrix}$ |  |
| C N-beam grazing incidence diffraction | $\mathbf{F} = \begin{pmatrix} \mathbf{k}_{m+z} + \mathbf{f}_{m+m+} & \cdots & \mathbf{f}_{m+m-} \\ \vdots & \ddots & \vdots \\ \mathbf{f}_{m-m+} & \cdots & \mathbf{k}_{m-z} + \mathbf{f}_{m-m-} \end{pmatrix}$ |  |

Fig. 4.1. The propagation matrix \mathbf{F} for various scattering geometries. \mathbf{k}_{m+z} is the z component of the wavevector in the scattering channel m^+ and \mathbf{f}_{m+n-} is the scattering amplitude for the transition from the scattering channel n^- into scattering channel m^+ . These quantities are 2×2 matrices to take the polarization dependence into account

$\mathbf{A}(z)$ is a multidimensional vector that contains the field amplitudes in the open scattering channels. A few examples are illustrated in Fig. 4.1:

- (A) In forward scattering geometry only the scattering channel for forward transmission (0^+) is open. This scattering channel is always existent, regardless of the structure of the sample.
- (B) If the momentum transfer coincides with a reciprocal lattice vector, a Bragg reflection is excited and forward transmission (0^+) is accompanied by specular reflection (0^-), so that two scattering channels are open. This is the two-beam case of dynamical diffraction. The same applies if the angle of incidence approaches the critical angle of total reflection. This is a two-beam case as well which is essentially the (000) Bragg reflection. It is independent of the atomic structure of the reflecting medium like in the case of forward scattering. Each matrix element of \mathbf{F} describes the transition amplitude for scattering between two open scattering channels. The derivation of the propagation matrix from the structure function is shown in detail in appendix A.2.
- (C) If the radiation illuminates a reflection grating, several diffraction orders are excited.

It was shown that this formalism can be used to include more than 30 diffraction orders and describe the diffraction pattern of laminar gratings of various

shapes [5]. In principle, this concept can be extended to an arbitrary number of scattering channels.

The central element in the dynamical theory is the matrix exponential $e^{i\mathbf{F}d}$ that relates the field amplitudes $\mathbf{A}(d)$ in depth z to the amplitudes $\mathbf{A}(0)$ of the incident field [6]. Analytic expressions can be found only if the scattering amplitude matrices $\mathbf{f}_{ss'}$ that constitute \mathbf{F} can be diagonalized simultaneously. This is possible in the following cases:

- (1) They are diagonal in every polarization basis. This occurs for
 - a) pure electronic scattering,
 - b) single-line nuclear resonant scattering,
 - c) certain averagings over the directions of the hyperfine fields, e.g. in the case of polycrystalline samples where the directions of the hyperfine fields are equally distributed in space.

In these cases the scattering is isotropic and every incident polarization is an eigenpolarization of the medium, i.e. the matrices $\mathbf{f}_{ss'}$ are already diagonal. If the scattering length is the same for σ and π polarization, as in grazing incidence geometry, the matrices \mathbf{f} and \mathbf{k}_{0z} reduce to scalars. For oblique angles of incidence φ one has to take into account an additional factor of $\gamma = \mathbf{k} \cdot \mathbf{k}' / k k' = \cos 2\varphi$ for π polarization. Then \mathbf{f} is a diagonal (2×2) matrix with $f_{\pi\pi} = \gamma f_{\sigma\sigma}$.

- (2) They are equal (except for the sign). This occurs for nuclear scattering with scattering angles 2φ of 0° , 90° and 180° . Of special interest in this work is grazing-incidence scattering that can be treated in the limit $\varphi \rightarrow 0^\circ$, where

$$\mathbf{f}_{0+0+} = \mathbf{f}_{0+0-} = -\mathbf{f}_{0-0+} = -\mathbf{f}_{0-0-} =: \mathbf{f}. \quad (4.8)$$

- (3) Only one channel is open. This applies to a very good approximation in the case of off-Bragg scattering, where the angle of incidence is far away from any Bragg angle of the scatterer. Then only the 0^+ channel is open (forward scattering) and we have:

$$\mathbf{f}_{0+0-} = \mathbf{f}_{0-0+} = \mathbf{f}_{0-0-} = 0, \quad \mathbf{f}_{0+0+} =: \mathbf{f}. \quad (4.9)$$

The case of nuclear Bragg diffraction has to be solved numerically. For this purpose the program package CONUSS (=COherent NUclear Scattering from Single crystals) has been developed [7]. In the case of purely electronic scattering, this formalism leads to the Darwin–Prins equations of x-ray diffraction [8], if the structure function of a perfect single crystal is used.

4.1.1 The Scattering Amplitude

So far, the algebraic structure of the scattering theory was outlined. Since no assumptions were made about the scattering mechanism, the formalism can be applied to a multitude of problems. The physics of the interaction

of the electromagnetic wave with the atoms is contained in the scattering length \mathbf{M} . In the following, the evaluation of this quantity with particular emphasis on resonant scattering processes will be discussed. To account for polarization-mixing effects, the energy dependent scattering length $\mathbf{M}(\omega)$ is treated as a 2×2 matrix. It is convenient to decompose $\mathbf{M}(\omega)$ into a nonresonant part $\mathbf{E}(\omega)$ that describes electronic charge scattering and a part $\mathbf{N}(\omega)$ that contains all contributions from nonresonant scattering processes:

$$\mathbf{M}(\omega) = \mathbf{E}(\omega) + \mathbf{N}(\omega). \quad (4.10)$$

The electronic scattering length $\mathbf{E}(\omega)$ is given by

$$[\mathbf{E}(\omega)]_{\mu\nu} = (\boldsymbol{\varepsilon}_\mu \cdot \boldsymbol{\varepsilon}_\nu) \left[-Z r_0 + i \frac{k_0}{4\pi} \sigma_t(\omega) \right], \quad (4.11)$$

where Z is the atomic number, r_0 is the classical electron radius, and σ_t is the total absorption cross section. $\mathbf{N}(\omega)$ contains the contributions from resonant scattering processes like resonant magnetic x-ray scattering [9, 10] or nuclear resonant scattering [7, 11, 12]. For an electric 2^L -pole resonance this scattering length is given by [9]

$$[\mathbf{N}(\omega)]_{\mu\nu} = \frac{4\pi f_R}{k_0} \sum_{M=-L}^L [\boldsymbol{\varepsilon}_\nu \cdot \mathbf{Y}_{LM}(\mathbf{k}_0)] [\mathbf{Y}_{LM}^*(\mathbf{k}_0) \cdot \boldsymbol{\varepsilon}_\mu] F_{LM}(\omega). \quad (4.12)$$

$f_R < 1$ describes the degree of elasticity of the scattering process, expressed by the Debye-Waller factor in the fast-relaxation limit and by the Lamb-Mössbauer factor in the slow-relaxation limit. The two dot products between the polarization basis vectors $(\boldsymbol{\varepsilon}_\nu, \boldsymbol{\varepsilon}_\mu)$ and the vector spherical harmonics $\mathbf{Y}_{LM}(\mathbf{k}_0)$ describe the anisotropy of photon absorption and reemission, respectively. The energy dependence of the scattering process is contained in the functions $F_{LM}(\omega)$. These functions are the energy-dependent resonant strengths for transitions with a change of M in the magnetic quantum number. In the general case they are given by [9]

$$F_{LM}(\omega) = \sum_{\alpha,\eta} \frac{p_\alpha p_\alpha(\eta) \Gamma_x(\alpha M \eta; L)}{[E(\eta) - E(\alpha) - \hbar\omega] - i\Gamma(\eta)/2}, \quad (4.13)$$

where the sum runs over all initial (ground) states labeled by α and the intermediate excited states labeled by η . p_α is the probability that the initial state α is occupied and $p_\alpha(\eta)$ is the probability that the state η is unoccupied in the initial state. $E(\alpha)$ and $E(\eta)$ are the energies of the ground-state and excited-state levels, respectively. $\Gamma_x(\alpha M \eta; L)$ is the partial resonance width of the transition between α and η with a change of M in the magnetic quantum number, $\Gamma(\eta)$ denotes the full resonance width. Since $\Gamma(\eta) \approx 1 - 10$ eV for electronic resonances, the scattering proceeds on a time scale $\hbar/\Gamma(\eta)$ of $\approx 10^{-16}$ s which is essentially prompt. In contrast, the width of nuclear resonances is in the range of $10^{-6} - 10^{-12}$ eV so that the scattering proceeds on

comparatively long timescales. For that case, the functions $F_{LM}(\omega)$ will be evaluated explicitly in Sect. 4.2.

It is convenient to expand (4.12) in powers of the unit vector \mathbf{m} that defines the magnetic quantization axis of the atom in the sample. The resonant scattering length for an electric dipole transition ($L = 1$) can then be written as [12]:

$$\begin{aligned} [\mathbf{N}(\omega)]_{\mu\nu} = & \frac{3}{16\pi} \{ (\boldsymbol{\varepsilon}_\mu \cdot \boldsymbol{\varepsilon}_\nu) [F_{+1} + F_{-1}] \\ & - i(\boldsymbol{\varepsilon}_\mu \times \boldsymbol{\varepsilon}_\nu) \cdot \mathbf{m} [F_{+1} - F_{-1}] \\ & + (\boldsymbol{\varepsilon}_\mu \cdot \mathbf{m})(\boldsymbol{\varepsilon}_\nu \cdot \mathbf{m}) [2F_0 - F_{+1} - F_{-1}] \} . \end{aligned} \quad (4.14)$$

For convenience, we have dropped the subscript L .

In case of a magnetic dipole transition the role of the electric and magnetic fields of the radiation are interchanged. Then one has to transform the polarization vectors in (4.14) according to $\boldsymbol{\varepsilon} \rightarrow \boldsymbol{\varepsilon} \times \mathbf{k}_0$, where \mathbf{k}_0 is a unit vector along the photon wavevector. The three terms in (4.14) represent different polarization dependences. The first term is not sensitive to the sample magnetization. Its polarization dependence given by $\boldsymbol{\varepsilon}_\mu \cdot \boldsymbol{\varepsilon}_\nu$ is that of non-resonant charge scattering. The second term describes circular dichroism because it depends on the difference between the resonant scattering amplitudes F_{+1} and F_{-1} . Since its polarization dependence is $\boldsymbol{\varepsilon}_\mu \times \boldsymbol{\varepsilon}_\nu$, it describes orthogonal scattering, e.g., $\boldsymbol{\sigma} \rightarrow \boldsymbol{\pi}$ and $\boldsymbol{\pi} \rightarrow \boldsymbol{\sigma}$. The third term that is proportional to $2F_0 - F_{+1} - F_{-1}$ describes linear magnetic dichroism. Its polarization dependence allows for all scattering processes within the given polarization basis.

For a linear polarization basis, as it is frequently used in case of scattering experiments with synchrotron radiation, the matrix elements can be explicitly written as:

$$\begin{aligned} [\mathbf{N}]_{\sigma\sigma} &= \frac{3}{16\pi} [F_{+1} + F_{-1} + (\boldsymbol{\pi} \cdot \mathbf{m})^2 (2F_0 - F_{+1} - F_{-1})] \\ [\mathbf{N}]_{\sigma\pi} &= \frac{3}{16\pi} [-i(\mathbf{k}_0 \cdot \mathbf{m})(F_{+1} - F_{-1}) - \\ &\quad (\boldsymbol{\sigma} \cdot \mathbf{m})(\boldsymbol{\pi} \cdot \mathbf{m})(2F_0 - F_{+1} - F_{-1})] \\ [\mathbf{N}]_{\pi\sigma} &= \frac{3}{16\pi} [i(\mathbf{k}_0 \cdot \mathbf{m})(F_{+1} - F_{-1}) - \\ &\quad (\boldsymbol{\sigma} \cdot \mathbf{m})(\boldsymbol{\pi} \cdot \mathbf{m})(2F_0 - F_{+1} - F_{-1})] \\ [\mathbf{N}]_{\pi\pi} &= \frac{3}{16\pi} [F_{+1} + F_{-1} + (\boldsymbol{\sigma} \cdot \mathbf{m})^2 (2F_0 - F_{+1} - F_{-1})] . \end{aligned} \quad (4.15)$$

These matrix elements express the strong polarization-mixing effects that are observed in resonant scattering from magnetized samples. The occurrence of optical activity crucially depends on the orientation of \mathbf{m} relative to the incident wavevector and its polarization state. The off-diagonal elements

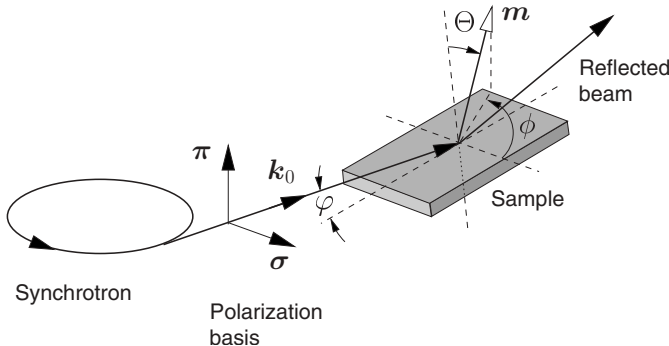


Fig. 4.2. Geometry used in nuclear resonant scattering of synchrotron radiation from thin films and surfaces, defining the relative orientation (Θ, ϕ) of the incident wavevector \mathbf{k}_0 to the direction of a unidirectional magnetization \mathbf{m} of the sample. ($\hat{\sigma}, \hat{\pi}$) are the linear polarization basis vectors

describe the orthogonal scattering that turns incident σ -polarization into π -polarization and vice versa. The formulation given by (4.15) allows one in a convenient way to discuss polarization effects in scattering experiments with synchrotron radiation, as sketched in Fig. 4.2.

4.1.2 Forward Scattering

Conceptually, the most simple case is forward scattering in a homogeneous medium where only one scattering channel is open, thus $\mathbf{F} = \mathbf{k}_0 + \mathbf{f}$, with \mathbf{f} being the forward scattering amplitude. Equation (4.6) then has the familiar solution:

$$\mathbf{A}(z) = e^{i\mathbf{n}\mathbf{k}_0 z} \mathbf{A}(0) =: \mathbf{T}(z) \mathbf{A}(0), \quad (4.16)$$

with $\mathbf{n} = \mathbf{1} + \mathbf{f}/k_0$ being the index of refraction of the medium as given by (4.1). The matrix exponential in the above equation constitutes the transmission matrix $\mathbf{T}(z)$ of the sample. In the case of an anisotropic medium, \mathbf{n} is represented by a 2×2 matrix to describe the polarization dependence of the scattering process. To evaluate the matrix exponential in (4.16) the scattering matrix \mathbf{f} is diagonalized:

$$\mathbf{f} = \begin{pmatrix} f_{xx} & f_{xy} \\ f_{yx} & f_{yy} \end{pmatrix} = \mathbf{g} \mathbf{f}_d \mathbf{g}^{-1} \quad \text{with} \quad [\mathbf{f}_d]_{ij} = \delta_{ij} f_i, \quad (4.17)$$

where f_1 and f_2 are the eigenvalues of this matrix. They are given by

$$f_{1,2} = \frac{1}{2}(f_{xx} + f_{yy}) \pm \frac{1}{2}\sqrt{(f_{xx} - f_{yy})^2 + 4f_{xy}f_{yx}}. \quad (4.18)$$

The eigenvalues are the scattering amplitudes for the two eigenpolarizations which are eigenvectors of \mathbf{f} . Finally, the transmission matrix is given by

$$\mathbf{T}(z) = e^{ik_0 z} e^{i\mathbf{f}z} = e^{ik_0 z} [\mathbf{g} e^{i\mathbf{f}_d z} \mathbf{g}^{-1}]. \quad (4.19)$$

Introducing $T_{\pm}(z) := e^{if_1 z} \pm e^{if_2 z}$ and dropping the phase factor $e^{ik_0 z}$, $\mathbf{T}(z)$ takes the form

$$\mathbf{T}(z) = \begin{pmatrix} \frac{1}{2} \left(T_+ + T_- \left(\frac{f_{xx} - f_{yy}}{f_1 - f_2} \right) \right) & T_- \left(\frac{f_{xy}}{f_1 - f_2} \right) \\ T_- \left(\frac{f_{yx}}{f_1 - f_2} \right) & \frac{1}{2} \left(T_+ - T_- \left(\frac{f_{xx} - f_{yy}}{f_1 - f_2} \right) \right) \end{pmatrix}. \quad (4.20)$$

Nuclear forward scattering of synchrotron radiation was first observed after employing meV monochromatization to suppress the enormous intensity of nonresonant radiation [13], followed by detailed studies [14]. Equation (4.20) was investigated in detail by *Siddons et al.* [15] using polarization filtering to study the individual matrix elements. An early application of the technique was the determination of the temperature dependence of the magnetic hyperfine field in Fe [16].

In many experiments, the time-integrated intensity in forward direction is an important figure of merit. It should be noted that this quantity is a non-monotonous function of the sample thickness. At very small thickness values, the time-integrated intensity increases with increasing thickness. Due to photoabsorption, this increase saturates at some thickness L_0 and then turns into a decrease with increasing thickness. This behavior is displayed in Fig. 4.3 for a foil of natural Fe. In the case that multiple scattering can be neglected, the value of L_0 is close to the photoabsorption length of the material. For highly enriched samples, multiple scattering leads to a strong speedup of the decay, so that most of the intensity is concentrated at very early times. In this case, L_0 depends on the time after excitation where the time gating begins, as shown in the inset of Fig. 4.3.

4.1.3 Total Reflection from Boundaries

In the x-ray regime, the index of refraction of any material is very close to and slightly below unity. To discuss this quantitatively, resonant scattering processes will be neglected in the following. Then $\mathbf{M} = \mathbf{E}$ and after inserting (4.11) into (4.1), one obtains

$$n = 1 + \frac{2\pi\varrho}{k_0^2} \left(-Zr_0 + i \frac{k_0}{2\pi} \sigma \right) =: 1 - \delta + i\gamma \quad (4.21)$$

for a material consisting of a single atomic species, where $\delta \approx 10^{-5}$ and $\gamma \approx 10^{-7}$ for hard x-rays. Since the index of refraction is smaller than 1, every material is optically thinner than vacuum. Thus, at the boundary between the vacuum and the material total reflection occurs for angles below the critical angle φ_c that is given by the condition $\cos \varphi_c = n$. Expanding the cosine for angles of incidence $\varphi \ll 1$ and neglecting the imaginary part of (4.21), one obtains:

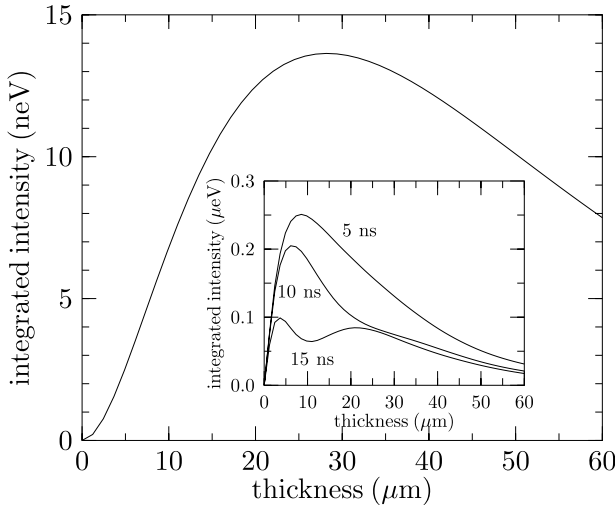


Fig. 4.3. Time-integrated intensity of nuclear forward scattering from an α -Fe foil with natural content of ^{57}Fe . The inset shows the same quantity for a Fe foil, highly enriched (95%) in ^{57}Fe , with the integration starting at different times after excitation, as labeled in the figure

$$\varphi_c = \sqrt{2\delta} = \sqrt{\frac{Z\varrho r_0 \lambda^2}{2\pi}} . \quad (4.22)$$

Typical values for φ_c are in the range of a few mrad. To illustrate this, for some selected materials the reflectivity curves are shown in Fig. 4.4a. Above the critical angle, the radiation deeply penetrates into the material and the reflectivity drops according to $|R|^2 \sim \varphi^{-4}$. Even below the critical angle the radiation must penetrate into the material. Otherwise the condition for the tangential component of the electric field across a boundary being continuous could not be fulfilled. This leads to the existence of an evanescent wave in the material, the amplitude of which is exponentially damped as function of depth. Figure 4.4b shows the angular dependence of the penetration depth for these materials. Below the critical angle, the penetration depth is only a few nm, depending strongly on the photoabsorption coefficient σ .

After a reflection in grazing incidence geometry, the beam is often used in subsequent scattering experiments. In some cases like in interference processes, it is important to know the phase of the scattered waves. For this reason, the angular dependence of the reflection phase relative to the phase of the incident wave is shown in Fig. 4.4c. With increasing angle of incidence the relative phase increases and approaches π near the critical angle.

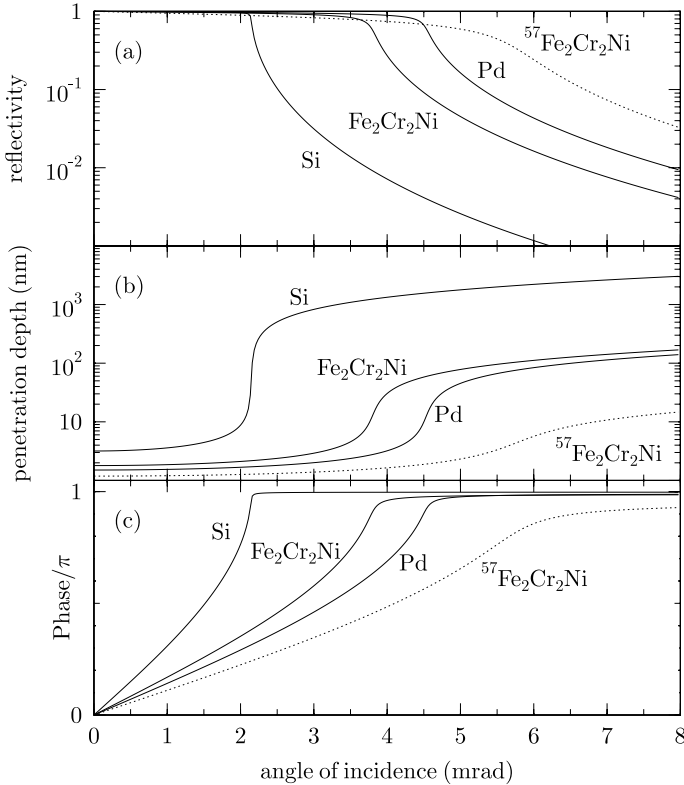


Fig. 4.4. (a) Reflectivity, (b) penetration depth, and (c) phase of the reflection coefficient for grazing incidence reflection from surfaces of Si, Pd, Fe₂Cr₂Ni (solid lines) at 14.4 keV. The dashed lines are calculated for ⁵⁷Fe₂Cr₂Ni near the resonance at $\Delta E/\Gamma_0 = 2$

4.1.4 Grazing-Incidence Reflection from Stratified Media

Here we apply the dynamical theory to the case of grazing incidence reflection from stratified media. Grazing incidence reflection from smooth surfaces and layer systems represents the (000) Bragg reflection. It is a two-beam case that can be treated in the forward-scattering approximation, i.e., it does not rely on the crystalline structure of the sample. In this geometry two scattering channels are open, i.e., specular reflection (+) and forward transmission (-). The basic geometry and nomenclature to describe this situation is introduced in Fig. 4.5. In a single layer, labeled by the index i , the field amplitude $\mathbf{A}(z) = (A_+(z), A_-(z))$ in depth z is related to the field amplitude $\mathbf{A}(0)$ at the surface by

$$\mathbf{A}(z) = e^{i\mathbf{F}_i z} \mathbf{A}(0) =: \mathbf{L}_i(z) \mathbf{A}(0) , \quad (4.23)$$

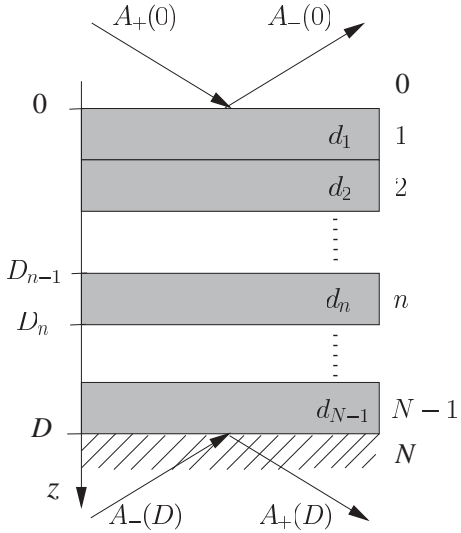


Fig. 4.5. Scheme of a layer system to describe x-ray propagation in stratified media. The incident wave is divided into two scattering channels, corresponding to specular reflection (−) and forward transmission (+). The layers labeled by 0 and N denote vacuum and substrate, respectively

with the propagation matrix

$$\mathbf{F} = \begin{pmatrix} \mathbf{f} + \mathbf{k}_{0z} & \mathbf{f} \\ -\mathbf{f} & -\mathbf{f} - \mathbf{k}_{0z} \end{pmatrix}, \quad (4.24)$$

and \mathbf{f} given by¹

$$\mathbf{f} = \frac{2\pi}{k_{0z}} \sum_i \varrho_i \mathbf{M}_i. \quad (4.25)$$

The matrix $\mathbf{L}_i(z)$ is called the *layer matrix* of layer i . In the general case of multiple layers (N layers on a substrate), the field amplitude in depth z of the sample (located in the n th layer) is given by the product of the corresponding layer matrices:

$$\mathbf{A}(z) = \mathbf{L}(z) \mathbf{A}(0), \quad (4.26)$$

with

$$\mathbf{L}(z) = \mathbf{L}_n(z - D_{n-1}) \mathbf{L}_{n-1}(d_{n-1}) \dots \mathbf{L}_2(d_2) \mathbf{L}_1(d_1), \quad (4.27)$$

where the d_i are the thicknesses of the individual layers, $D := \sum_{i=1}^N d_i$, and $D_n := \sum_{i=1}^n d_i$.

This formalism can be applied to a variety of phenomena like Bragg- and Laue diffraction from single crystals [7], diffraction from planar gratings and

¹ Note that this expression is different compared to the case of forward scattering as described by (4.4). Since the sample exhibits translational invariance along in-plane directions, only the z -component k_{0z} of the wave vector k_0 becomes effective.

grazing-incidence reflection from thin-film systems [17]. It allows in a natural way to accommodate the polarization dependence of the scattering as it arises in magnetic x-ray scattering or nuclear resonant scattering. The mathematical problem in any of these cases is the calculation of the exponential of the propagation matrix \mathbf{F} . Since there is no analytic solution in general, this problem often has to be solved numerically. However, in special cases a closed solution can be found that reduces the computational effort and provides physical insight. This applies for scattering in grazing incidence geometry which shall be considered in the following.

The solution of the scattering problem becomes comparatively easy in the system of eigenpolarizations of the sample. Those are the polarization states that remain unchanged in the scattering process. They are obtained by diagonalization of the forward scattering matrix \mathbf{f}_i :

$$\mathbf{f}_{i,D}(\omega) = \mathbf{g} \mathbf{f}_i(\omega) \mathbf{g}^{-1} \quad \text{with} \quad [\mathbf{f}_D(\omega)]_{\mu\nu} = \delta_{\mu\nu} f_{i,\mu}(\omega), \quad (4.28)$$

with the diagonalizing matrix \mathbf{g} and the eigenvalues $f_{i,\mu}(\omega)$ of the matrix \mathbf{f}_i . After this diagonalization, the (4×4) propagation matrix \mathbf{F} can be written as the direct product of two (2×2) matrices, one for each eigenpolarization, as shown in appendix A.3. Correspondingly, the propagation matrix \mathbf{F} and the layer matrix $\mathbf{L}(z)$ decompose into two (2×2) matrices. In the following, \mathbf{F} is treated as a (2×2) matrix for each eigenpolarization (see (A.34)). For better readability we drop the polarization index from here on.

The reflectivity of the layer system can now be calculated for each eigenpolarization separately. Subscripts are used to label the individual layers of the layer system. The layer matrix for layer no. (1) can then be written in a very compact form²:

$$\mathbf{L}_1(z) = e^{i\mathbf{F}z} = \frac{1}{t_{01}} \begin{pmatrix} 1 & r_{01} \\ r_{01} & 1 \end{pmatrix} \begin{pmatrix} e^{ik_{1z}z} & 0 \\ 0 & e^{-ik_{1z}z} \end{pmatrix} \begin{pmatrix} 1 & r_{10} \\ r_{10} & 1 \end{pmatrix} \frac{1}{t_{10}}. \quad (4.29)$$

k_{1z} is the z -component of the wavevector in the film, which is through Snell's law related to the z -component of the incident wavevector by

$$k_{1z} = k_{0z}\beta_1 \quad \text{with} \quad \beta_1 = \sqrt{1 + \frac{2f_1}{k_{0z}}}. \quad (4.30)$$

r_{ij} and t_{ij} are the Fresnel reflection and transmission coefficients of the boundary between the media i and j , respectively:

$$r_{ij} = \frac{\beta_i - \beta_j}{\beta_i + \beta_j}, \quad t_{ij} = \frac{2\beta_i}{\beta_i + \beta_j}. \quad (4.31)$$

Equation (4.29) represents a very intuitive description of the scattering process that can be read from right to left: The right matrix describes the transition of the wavefield at the boundary from the vacuum (0) into the medium

² A detailed derivation of this equation is given in the appendix A.3.

(1), the middle matrix describes the free propagation of the eigenpolarizations in the medium in (+) and (-) directions, and the left matrix describes the transition of the wavefield back into vacuum.

To calculate the specularly reflected field $A_-(0)$ and the forward transmitted field $A_+(D)$ of an arbitrary layer system, we decompose (4.26) into its components in the various scattering channels:

$$\begin{pmatrix} A_+(z) \\ A_-(z) \end{pmatrix} = \begin{pmatrix} L_{++}(z) & L_{+-}(z) \\ L_{-+}(z) & L_{--}(z) \end{pmatrix} \begin{pmatrix} A_+(0) \\ A_-(0) \end{pmatrix}, \quad (4.32)$$

with $L_{++}(z)$, $L_{+-}(z)$, $L_{-+}(z)$, $L_{--}(z)$ being the matrix elements of \mathbf{L} . For a unique solution, two boundary conditions have to be supplied that describe the radiation field at the surface and the substrate boundary of the layer stack:

$$A_+(0) = A_0, \quad A_-(D) = 0. \quad (4.33)$$

While the first equation describes the incident amplitude, the second equation means that there is no wave incident on the substrate boundary from below. To solve for $A_-(0)$ and $A_+(D)$, (4.32) has to be evaluated at the coordinate $z = D$, i.e., the matrix product for the whole layer system shown in Fig. 4.5 has to be calculated:

$$\mathbf{A}(D) = \mathbf{L}(D) \mathbf{A}(0) \quad (4.34)$$

$$\text{with } \mathbf{L}(D) = \mathbf{L}_N \mathbf{L}_{N-1}(d_{N-1}) \dots \mathbf{L}_2(d_2) \mathbf{L}_1(d_1).$$

Due to its very large thickness, the layer matrix \mathbf{L}_N of the substrate requires a special treatment, resulting in

$$\mathbf{L}_N = \begin{pmatrix} 0 & 0 \\ 0 & 1 \end{pmatrix} \begin{pmatrix} 1 & r_{N0} \\ r_{N0} & 1 \end{pmatrix} \frac{1}{t_{N0}}. \quad (4.35)$$

The left matrix reflects the fact that the wave propagating into the substrate vanishes with increasing depth so that only waves in the specular direction remain. Inserting the boundary conditions given by (4.33) into (4.32), we obtain for the specularly reflected field $A_-(0)$ and the forward transmitted field $A_+(D)$:

$$A_-(0) = - \left(\frac{L_{-+}(D)}{L_{--}(D)} \right) A_0 =: R A_0 \quad (4.36)$$

$$A_+(D) = \left(L_{++}(D) - \frac{L_{+-}(D) L_{-+}(D)}{L_{--}(D)} \right) A_0 =: T A_0. \quad (4.37)$$

This defines the reflectivity R and the transmission T of the layer system for the corresponding eigenpolarization. As an example, we calculate the reflectivity R for a single layer of thickness D on a semi-infinite substrate, a situation that is encountered quite frequently. According to (4.34), the field amplitudes at the substrate boundary are given by

$$\mathbf{A}(D) = \mathbf{L}_N \mathbf{L}_1(d) \mathbf{A}(0). \quad (4.38)$$

Inserting (4.29) and (4.35) into this equation results in³

$$\mathbf{A}(D) = \frac{1}{t_{21} t_{10}} \begin{pmatrix} 0 & 0 \\ 0 & 1 \end{pmatrix} \begin{pmatrix} 1 & r_{21} \\ r_{21} & 1 \end{pmatrix} \begin{pmatrix} e^{ik_1 z D} & 0 \\ 0 & e^{-ik_1 z D} \end{pmatrix} \begin{pmatrix} 1 & r_{10} \\ r_{10} & 1 \end{pmatrix} \mathbf{A}(0) \quad (4.39)$$

$$= \begin{pmatrix} L_{++}(D) & L_{+-}(D) \\ L_{-+}(D) & L_{--}(D) \end{pmatrix} \mathbf{A}(0). \quad (4.40)$$

The reflectivity R according to (4.36) is then given by

$$R = -\frac{L_{-+}(D)}{L_{--}(D)} = \frac{r_{01} + r_{12} e^{i2k_1 z D}}{1 + r_{01} r_{12} e^{i2k_1 z D}}. \quad (4.41)$$

This is, of course, the classical formula for multibeam interference from a single film on a substrate, in the field of x-ray physics often referred to as Parratt formula [18].

Once the reflectivities for each eigenpolarization have been calculated, the (2×2) reflectivity matrix \mathbf{R} in the original polarization basis is then obtained via the backtransformation

$$\mathbf{R} = \mathbf{g}^{-1} \mathbf{R}_D \mathbf{g} \quad \text{with} \quad [\mathbf{R}_D]_{\mu\nu} = \delta_{\mu\nu} R_\mu, \quad (4.42)$$

where the R_μ are the reflectivities for both eigenpolarizations, given by (4.41). Evaluation of (4.42) then leads to the following closed expression for the reflectivity matrix \mathbf{R} :

$$\mathbf{R} = \begin{pmatrix} \frac{1}{2} \left(R_+ + R_- \left(\frac{f_{xx} - f_{yy}}{f_1 - f_2} \right) \right) & R_- \left(\frac{f_{xy}}{f_1 - f_2} \right) \\ R_- \left(\frac{f_{yx}}{f_1 - f_2} \right) & \frac{1}{2} \left(R_+ - R_- \left(\frac{f_{xx} - f_{yy}}{f_1 - f_2} \right) \right) \end{pmatrix}, \quad (4.43)$$

with $R_\pm = R_I \pm R_H$.

The formalism outlined in this section can be applied to layer systems with an arbitrary spin arrangement along the surface normal. This is particularly interesting for the study of magnetic spin structures at interfaces between soft- and hard-magnetic films (exchange-spring layer systems [19, 20]), between antiferromagnetic and ferromagnetic films (exchange-bias layer systems [21]), and between two ferrimagnetic films [22, 23]. A slightly different supermatrix formalism was used by Deák *et al.* to treat nuclear resonant scattering from multilayers in the presence of polarization mixing [24]. A similar approach has been applied for the description of polarized neutron reflectometry from arbitrary spin structures [25].

³ Note that

$$\begin{pmatrix} 1 & r_{02} \\ r_{02} & 1 \end{pmatrix} \begin{pmatrix} 1 & r_{10} \\ r_{10} & 1 \end{pmatrix} = - \begin{pmatrix} 1 & r_{21} \\ r_{21} & 1 \end{pmatrix} \quad \text{and} \quad \frac{r_{10} + r_{02}}{t_{02} t_{10}} = \frac{1}{t_{21}}.$$

4.1.5 The Radiation Field in Layered Systems

In many applications, the amplitude of the radiation field within the layer system has to be known. This applies for the calculation of the coherent reflectivity from ultrathin layers, as outlined in the following section, and the incoherent fluorescence yield as discussed in Sect. 5.4.1.

The amplitude $A(z)$ of the electric field in depth z of the layer system results from the superposition of the waves in depth z traveling in (+) and (-) directions, i.e.,

$$A(z) = A_+(z) + A_-(z). \quad (4.44)$$

Inserting (4.36) into (4.32), we obtain for the normalized field amplitude $a(z) = A(z)/A_0$ in depth z of the layer system:

$$a(z) = L_{++}(z) + L_{-+}(z) - [L_{+-}(z) + L_{--}(z)] \frac{L_{-+}(D)}{L_{--}(D)}. \quad (4.45)$$

Using the above formula, the field intensity $I(z) = |a(z)|^2$ in arbitrary layer systems can be calculated. This is particularly interesting for the discussion of standing waves that form in layered systems, as it is the case in x-ray waveguides. The most simple case of such a structure is a single layer of thickness d on a total reflecting semi-infinite substrate. The normalized field amplitude inside the layer is then given by

$$a(z) = t_{02} \frac{e^{igz} + r_{12} e^{2igd} e^{-igz}}{1 + r_{01} r_{12} e^{2igd}}. \quad (4.46)$$

This example is illustrated in Fig. 4.20b and will be discussed amongst others in Sect. 4.3.3. In the following section we use (4.45) to calculate the amplitude of the radiation that is coherently scattered from ultrathin films that are embedded in layer systems.

4.1.6 Coherent Reflection from Ultrathin Layers

Ultrathin films are often used as probe layers to investigate the internal magnetic, electronic, or structural properties of stratified media with very high spatial resolution. This has been exploited in a number of applications where incoherent fluorescence radiation from a probe layer was detected. The signal in this case scales *linearly* with the intensity of the electric field at the probe layer position. A different situation is encountered for the radiation that is coherently scattered from the probe layer. In this case one observes an intensity enhancement that scales *quadratically* with the normalized intensity at the probe layer position [26]. It is obvious that this can lead to a very strong signal enhancement from smallest amounts of material, especially if applied in combination with x-ray waveguide structures. This effect can be exploited in any case where the signal from the probe layer is discriminated against the signal from the surrounding layer system, as it is the case for scattering

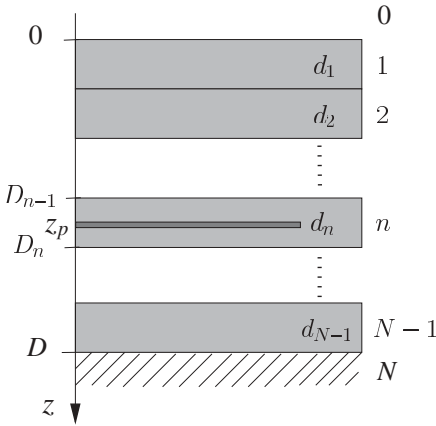


Fig. 4.6. Scheme of a layer system that contains an ultrathin probe layer in depth z_p within the n th layer

processes that rely on elemental or isotopic specificity. Due to the broad range of applications in magnetic x-ray scattering and nuclear resonant scattering, for example, this effect will be described here in detail.

For the following calculations, we assume such a probe layer of infinitesimal thickness d being located in depth z_p of the layer system within the n th layer of the system, as shown schematically in Fig. 4.6. To calculate the reflectivity of this system, we write the field amplitude in depth D of the layer system as follows:

$$\mathbf{A}(D) = \mathbf{L}(D - z_p) \mathbf{L}_n(d) \mathbf{L}(z_p) \mathbf{A}_0 . \quad (4.47)$$

This equation expresses the fact that the probe layer is sandwiched between two layer stacks of total thickness z_p and $D - z_p$. It follows from the definition in (4.27) that

$$\mathbf{L}(D - z_p) = \mathbf{L}(D) \mathbf{L}^{-1}(z_p) . \quad (4.48)$$

Accordingly, (4.47) can now be written as:

$$\mathbf{A}(D) = \mathbf{L}(D) \mathbf{L}^{-1}(z_p) \mathbf{L}_n(d) \mathbf{L}(z_p) \mathbf{A}_0 . \quad (4.49)$$

For an ultrathin layer, the matrix $\mathbf{L}_n(d) = e^{i\mathbf{F}_n d}$ can be approximated by

$$\mathbf{L}_n(d) \approx 1 + i\mathbf{F}_n d , \quad (4.50)$$

with the propagation matrix being the following 2×2 matrix:

$$\mathbf{F}_n = \begin{pmatrix} f_n + k_{0z} & f_n \\ -f_n & -f_n - k_{0z} \end{pmatrix} , \quad (4.51)$$

where f_n is the scattering amplitude of the probe layer material for each of the eigenpolarizations. Equation (4.49) then turns into:

$$\begin{aligned} \mathbf{A}(D) &= [\mathbf{L}(D) \mathbf{L}^{-1}(z_p) (1 + i\mathbf{F}_n d) \mathbf{L}(z_p)] \mathbf{A}_0 \\ &= \mathbf{L}(D) [1 + id \mathbf{L}^{-1}(z_p) \mathbf{F}_n \mathbf{L}(z_p)] \mathbf{A}_0 , \end{aligned} \quad (4.52)$$

with $\mathbf{L}(z_p)$ as defined in (4.32) and $\mathbf{L}(D)$ written as:

$$\mathbf{L}(D) =: \begin{pmatrix} D_{++} & D_{+-} \\ D_{-+} & D_{--} \end{pmatrix}. \quad (4.53)$$

The inverse of the matrix $\mathbf{L}(z_p)$ is given by

$$\mathbf{L}^{-1}(z_p) = \begin{pmatrix} L_{--} & -L_{+-} \\ -L_{-+} & L_{++} \end{pmatrix}, \quad (4.54)$$

where we have already used the fact that $\det(\mathbf{L}_i) = 1$, as can be easily verified via (4.29). This implies that also the determinant of $\mathbf{L}(z)$, i.e., any product of matrices \mathbf{L}_i equals 1. Performing the matrix multiplications in (4.52), the reflectivity is given according to (4.36) by

$$R = -\frac{D_{-+}(1 + idE_{++}) + idD_{--}E_{-+}}{D_{--}(1 + idE_{--}) + idD_{-+}E_{+-}}, \quad (4.55)$$

with

$$\begin{aligned} E_{++} &= (L_{++} + L_{-+})(L_{--} + L_{+-}) f_n + (L_{++}L_{--} + L_{+-}L_{-+}) k_{0z} \\ E_{+-} &= (L_{--} + L_{+-})^2 f_n + 2L_{--}L_{+-} k_{0z} \\ E_{-+} &= -(L_{++} + L_{-+})^2 f_n - 2L_{++}L_{-+} k_{0z} \\ E_{--} &= -E_{++}. \end{aligned} \quad (4.56)$$

Expanding (4.55) up to first order in (*id*) leads to

$$R \approx R_0 + id(2R_0E_{++} + E_{-+} - R_0^2E_{+-}), \quad (4.57)$$

with $R_0 = -(D_{-+}/D_{--})$ being the reflectivity of the layer system without the probe layer. Inserting (4.56) into (4.57), one obtains:

$$\begin{aligned} R &= R_0 + id[(L_{++} + L_{-+}) + (L_{+-} + L_{--})R_0]^2 f_n \\ &\quad - 2id(R_0L_{--} + L_{-+})(R_0L_{+-} + L_{++})k_{0z}. \end{aligned} \quad (4.58)$$

By comparison with (4.32) and taking into account that $A_-(0) = R_0 A_0$, this equation can be written as:

$$\begin{aligned} R(\omega) &= R_0 + idf_n(\omega)[A_+(z_p) + A_-(z_p)]^2/A_0^2 \\ &\quad + 2idA_+(z_p)A_-(z_p)k_{0z}/A_0^2. \end{aligned} \quad (4.59)$$

To indicate the energy dependence of these quantities, they were written as function of frequency ω . The expression in the square brackets is exactly the normalized field amplitude $a(z_p)$ at the position z_p of the probe layer, as given by (4.45). The last term in (4.59) is a geometric contribution that does not depend on energy. Thus, the energy dependent contribution $R_n(\omega)$ of the probe layer to the reflectivity is given by the term that is proportional to $f_n(\omega)$. Performing the transformation back into the original polarization basis according to (4.42), we obtain [26]:

$$\mathbf{R}_n(\omega) = id a(z_p)^2 \mathbf{f}_n(\omega), \quad (4.60)$$

where \mathbf{R}_n and \mathbf{f}_n appear as 2×2 matrices. A similar relation was suggested by Andreeva *et al.*, for the special case of an ultrathin film on the surface of a layer system [27]. This case will be studied experimentally in Sect. 4.2.4.

In the case of nuclear resonant scattering, the signal from the probe layer is discriminated against the nonresonant scattering from the layer system by recording its delayed response on the time scale. The time response from the isotopic probe layer is obtained by Fourier transformation of (4.60):

$$\tilde{\mathbf{R}}_n(t) = id a(z_p)^2 \tilde{\mathbf{f}}_n(t). \quad (4.61)$$

For calculation of the scattered intensity $I(t)$ (see (4.75) we take into account the scattering geometry shown in Fig. 4.2, assuming the standard situation with incident σ polarization and no polarization analysis in the detection process. This leads to:

$$I(t) = d^2 I_p^2 I_n(t), \quad (4.62)$$

where $I_p = |a(z_p)|^2$ is the normalized intensity of the electric field at the position of the probe layer.

The central result of this section, (4.60), can be compared with the description of nuclear resonant specular reflection in the distorted-wave Born approximation (DWBA) [28], where the reflectivity of a surface is given by

$$R(\omega) = R_0 + T(\mathbf{k}_i) T(\mathbf{k}_f) R_n(\omega). \quad (4.63)$$

$T(\mathbf{k}_i)$ and $T(\mathbf{k}_f)$ are the Fresnel coefficients for transmission into the material (wavevector \mathbf{k}_i) and transmission back out (wavevector \mathbf{k}_f), respectively. These coefficients can be related to the reflection coefficients via $T = 1 + R$. This equation expresses the superposition of the incident amplitude a_0 and the reflected amplitude $R a_0$, resulting in the field amplitude $a = (1 + R) a_0$ at the boundary between the two media. Thus, in a more general approach, T should be replaced by the amplitude of the electric field at the layer boundary. In the special case of $\mathbf{k}_i = \mathbf{k}_f$ (specular reflection), the product $T(\mathbf{k}_i) T(\mathbf{k}_f)$ merges into $a(z)^2$ as in (4.60).

The strong enhancement of the signal from an ultrathin layer, as described by (4.60) can be used to determine the in-depth magnetic structure of thin films with very high spatial resolution. This is experimentally demonstrated in Sects. 4.3.3 and 4.4.3.

4.1.7 The Influence of Boundary Roughness

So far we have assumed that the boundaries of the layer system were perfectly smooth. This, however, is not true for real samples. Figure 4.7 shows a model of a thin film on a substrate that exhibits a step-like corrugation. Due to the spatial displacement of the surface elements, the amplitude scattered from each of them contributes to the total scattered amplitude with a spatial phase factor.

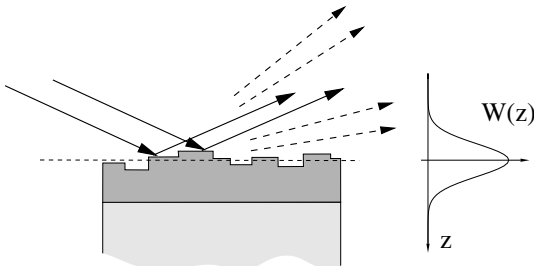


Fig. 4.7. A rough surface introduces relative phases between the scattered waves that result in a reduction of the specularly reflected intensity and scattering into diffuse directions. $W(z)$ is the distribution function of the surface elements along z

Kinematical Approximation

In the kinematical approximation, coherent summation over all contributions from laterally displaced surface elements yields for the reflected amplitude:

$$r'_{012} = r_{012} \int W(z) \exp\{2ik_{0z}z\} dz , \quad (4.64)$$

where the distribution function $W(z)$ describes the probability to find an element of the surface in depth z . If $W(z)$ is a Gaussian with standard deviation σ , the integral in (4.64) can be calculated exactly and we finally obtain for the intensity scattered from the sample:

$$I(t) = |r_{012}|^2 \exp\{-8k_0^2\varphi^2\sigma^2\} . \quad (4.65)$$

Thus, surface roughness leads to a damping of the reflected intensity that is given by an expression which is the Fourier transform of the height distribution function $W(z)$.

For a numerical example, we assume a sample with a roughness of $\sigma = 1.5 \text{ nm}$, illuminated with 14.4-keV radiation ($k_0 = 7.3 \text{ \AA}^{-1}$) at an angle of 5 mrad. According to (4.65) the reflected specular intensity is reduced by a factor of 10. The example shows that a smooth substrate is an important condition for a high reflectivity. This is especially important if samples with low coverages in the sub-monolayer range are investigated. It should be noted that the coherent summation performed in (4.64) is justified only if the lateral dimension of the surface elements is smaller than the in-plane transverse coherence length L_t of the radiation. This will be discussed in more detail in Sect. 4.3.2.

Dynamical Treatment

In the preceding section the matrix exponential $e^{i\mathbf{F}z}$ was evaluated in order to calculate the field of a wave at depth z of a material characterized by the scattering matrix \mathbf{F} . The calculation of the field in layered media is accomplished by multiplication of the corresponding matrix exponentials. This

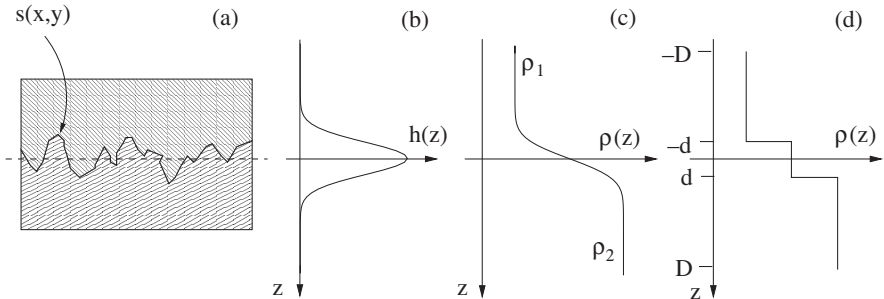


Fig. 4.8. Density variation around a rough interface between two layers with density ϱ_1 and ϱ_2 . (a) Rough boundary between two materials with densities ϱ_1 and ϱ_2 . $s(x, y)$ is the surface profile function. (b) height distribution function $h(z)$, describes the probability to find an element of the surface in depth z . (c) density transition $\rho(z)$ as obtained from integration over the height distribution function. (d) simplified model of (c), leading to (A.49) [6]

procedure is only valid for layers of homogeneous density, i.e. where \mathbf{F} is independent of z . However, in the case of boundary roughness we encounter a situation where the density may vary continuously over a certain range. In this case the above formalism can be applied again if the layer system is subdivided into thin slices of homogeneous density. A drawback is the increase in computational effort which accompanies such a procedure. Therefore a closed solution is attempted which replaces the effect of the transition region by one single ‘roughness matrix’ $e^{\mathbf{W}}$. The transition from the case of a smooth boundary to a rough boundary shall be accomplished by inserting this matrix $e^{\mathbf{W}}$ between the two exponential matrices of the adjacent layers:

$$e^{i\mathbf{F}_2 d_2} e^{i\mathbf{F}_1 d_1} \longrightarrow e^{i\mathbf{F}_2 d_2} e^{\mathbf{W}} e^{i\mathbf{F}_1 d_1}. \quad (4.66)$$

\mathbf{W} is expected to be a function of the scattering matrices $\mathbf{F}_1, \mathbf{F}_2$ and d , a parameter characterizing the thickness of the transition region.

In the following, only the specularly reflected radiation is considered⁴, and the roughness will be treated as a continuous density transition along the surface normal. In grazing incidence geometry this assumption is justified as long as the condition $k_z d \ll 1$ holds. The rough boundary shall be located around $z = 0$, surrounded by two layers with densities ϱ_1 and ϱ_2 and equal thickness $D \gg d$, see Fig. 4.8. The boundary plane is defined as the average smooth surface for which $\int s(x, y) dx dy = 0$ holds, where $s(x, y)$ is the surface profile function, measured relative to that plane. For derivation of the roughness matrix we subdivide the density transition region into thin

⁴ Fluctuations of the optical properties perpendicular to the surface normal lead to diffuse scattering. A corresponding theory for x-ray diffuse scattering including polarization effects has just been developed on basis of the distorted-wave Born approximation [29]. This, however, is beyond the scope of this book.

slices of constant density and multiply the layer matrices of all these layers. A sketch of the computational procedure is given in appendix A.5. The result is:

$$\mathbf{W} = \sum_{n=1}^{\infty} \frac{\langle h(z) \rangle_{2n}}{(2n)!} [\mathbf{F}_1, \mathbf{F}_2]_{2n}, \quad (4.67)$$

where $\langle h(z) \rangle_{2n}$ is the $(2n)$ th moment of the height distribution function $h(z)$ and $[\mathbf{F}_1, \mathbf{F}_2]_{2n}$ is the commutator of order $2n$ between \mathbf{F}_1 and \mathbf{F}_2 , i.e. $[\mathbf{F}_1, \mathbf{F}_2]_2 = [\mathbf{F}_1, \mathbf{F}_2]$, $[\mathbf{F}_1, \mathbf{F}_2]_4 = [[[F_1, F_2], F_1], F_2]$, and so on.

This is the general result for taking into account roughness described by a density transition which follows from a height distribution. In this limit it is valid for all kinds of scattering phenomena that are described in the exponential matrix formalism, especially grazing incidence reflection with polarization mixing and diffraction from laterally structured surfaces. In the special case of a Gaussian height distribution we have:

$$h(z) = \frac{1}{\sqrt{2\pi}\sigma} e^{-z^2/(2\sigma^2)} \quad \text{and} \quad \langle h(z) \rangle_{2n} = (2n-1)!! \sigma^{2n}, \quad (4.68)$$

so that the roughness matrix is given by

$$\mathbf{W} = \sum_{n=1}^{\infty} \frac{1}{n!} \left(\frac{\sigma^2}{2} \right)^n [\mathbf{F}_1, \mathbf{F}_2]_{2n}. \quad (4.69)$$

A closed expression for this series has so far been found only in the special case that the eigenpolarizations for all layers are the same. It has been shown [6] that in this limit the above result is equivalent to the widely used formula that was obtained by *Nevot & Croce* [30].

4.1.8 Calculation of Intensities

The information that can be revealed in x-ray scattering from magnetic films depends on the polarization state of the incident radiation and the polarization properties of the detector system. These polarization properties are not necessarily given by pure states like (σ, π) linear polarization or (left,right) circular polarization. In the general case, the calculation of the reflected intensity I from the reflectivity matrix \mathbf{R} is most conveniently performed within the quantum mechanical density matrix formalism, see e.g. [31]. In this language, the measured intensity is the modulus squared of the expectation value $\langle a_f | \mathbf{R} | a_i \rangle$, averaged over all initial and final states:

$$I = \overline{|\langle a_f | \mathbf{R} | a_i \rangle|^2}, \quad (4.70)$$

where $|a_i\rangle$ is the state vector of the incident wave (after the polarizer) and $|a_f\rangle$ the state vector of the detector (after the analyzer). Given the density matrices $\boldsymbol{\varrho}_i$ and $\boldsymbol{\varrho}_f$ of the initial and final states, respectively,

$$\boldsymbol{\varrho}_i = \overline{|a_i\rangle\langle a_i|} \quad \text{and} \quad \boldsymbol{\varrho}_f = \overline{|a_f\rangle\langle a_f|}, \quad (4.71)$$

the measured intensity can be expressed as:

$$I = \overline{\langle a_f | \mathbf{R} | a_i \rangle \langle a_i | \mathbf{R}^* | a_f \rangle} = \overline{\langle a_f | \mathbf{R} \boldsymbol{\varrho}_i \mathbf{R}^* | a_f \rangle}. \quad (4.72)$$

Thus, the final result is

$$I = \text{Tr} [\boldsymbol{\varrho}_f \mathbf{R} \boldsymbol{\varrho}_i \mathbf{R}^*]. \quad (4.73)$$

If the reflectivity is a scalar quantity, i.e. $\mathbf{R} = R$, then the intensity is simply given by $I = |R|^2$ because $\text{Tr}(\boldsymbol{\varrho}_i) = \text{Tr}(\boldsymbol{\varrho}_f) = 1$. Equation (4.73) is the generalization of this expression to a matrix-valued reflectivity.

The density matrices of the polarizer and the analyzer can be expressed by the three real Stokes parameters ξ_1, ξ_2 , and ξ_3 :

$$\boldsymbol{\varrho}_{i,f} = \frac{1}{2} \begin{pmatrix} 1 + \xi_1 & \xi_2 - i\xi_3 \\ \xi_2 + i\xi_3 & 1 - \xi_1 \end{pmatrix}. \quad (4.74)$$

The ξ_i assume values between -1 and $+1$ to describe a state within a basis of orthogonal polarizations: ξ_1 refers to a linear polarization basis, ξ_2 to a linear basis rotated by an angle of 45° relative to the previous one, and ξ_3 refers to a circular polarization basis. In the following we assume an arbitrary degree of linear polarization of the incident beam, i.e. $|\xi_1| \leq 1$ and $\xi_2 = \xi_3 = 0$. The extreme values of $\xi_1 = +1$ and $\xi_1 = -1$ represent the pure states of σ - and π -polarization, respectively. Further we assume no polarization analysis of the scattered beam, i.e. $[\boldsymbol{\varrho}_f]_{\mu\nu} = \delta_{\mu\nu}$. In this configuration we obtain for the scattered intensity:

$$I = \frac{1}{2}(1 + \xi_1)(|R_{11}|^2 + |R_{12}|^2) + \frac{1}{2}(1 - \xi_1)(|R_{21}|^2 + |R_{22}|^2), \quad (4.75)$$

where the R_{ij} are the matrix elements of \mathbf{R} .

4.2 Nuclear Resonant Scattering

So far the formalism was quite general, i.e., no assumptions were made about the type of scattering that enters into the functional shape and the energy dependence of the functions F_{+1}, F_0 and F_{-1} . In the following the focus will be on *nuclear* dipole transitions, in particular nuclear resonant scattering from the 14.4 keV resonance of ^{57}Fe . Due to its large cross section, large recoilless fraction and its relevance in many fields of the natural sciences, this resonance is one of the most widely applied Mössbauer transitions. The resonance is a magnetic dipole transition with spins $I_g = 1/2, I_e = 3/2$, magnetic moments $\mu_g = 0.091 \mu_N, \mu_e = -0.153 \mu_N$ of the ground and excited state, respectively, and a natural lifetime of $\tau_0 = 141$ ns. In magnetic materials the spin-polarized $3d$ electrons create a spinpolarization of the s-electrons via the exchange interaction. This leads to a strong magnetic field at the nuclear position, which, for example, amounts to $B = 33.3$ T in the case of ferromagnetic α -Fe. In this magnetic field the energetic degeneracy of ground-

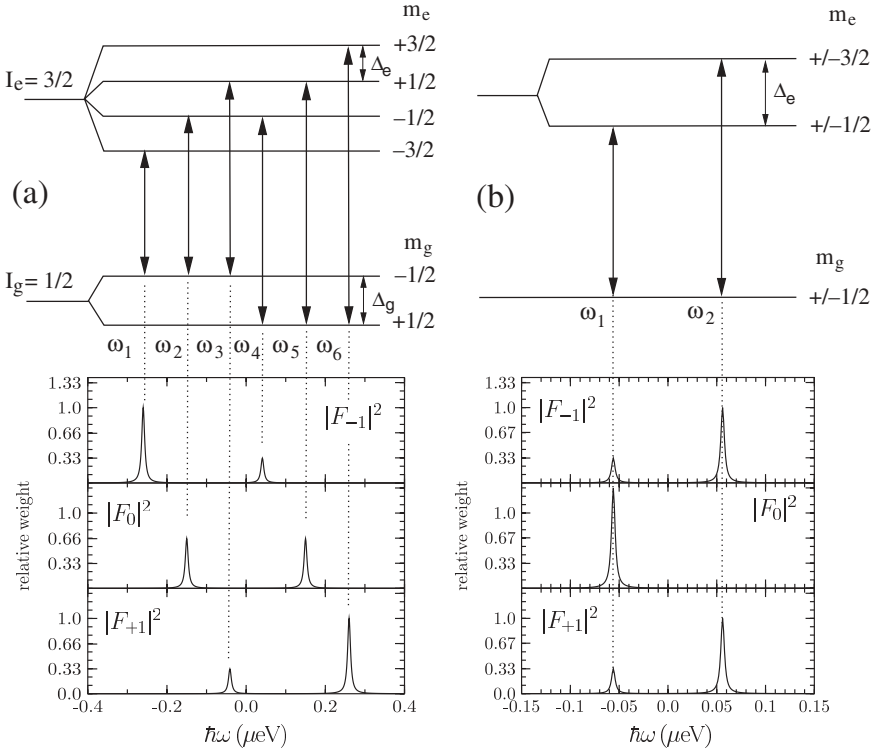


Fig. 4.9. Energy dependence of the functions F_M in the case of nuclear resonant scattering from a magnetic dipole resonance between nuclear spins $I_g = 1/2$ and $I_e = 3/2$. (a) Pure magnetic hyperfine interaction. The energetic positions apply to the case of $\alpha^{57}\text{Fe}$ with a magnetic hyperfine field of 33.3 T. The six dipole allowed transitions decompose into three different polarization dependencies: The functions F_{-1} , F_0 , and F_{+1} describe the scattering of right-circular, linear, and left-circular polarization, respectively. (b) Pure electric hyperfine interaction. The energetic positions of the resonances correspond to those of Fe in ferrocene [32]

and excited states is lifted, resulting in a Zeeman-splitting of the nuclear levels. The dipole selection rule $M = m_e - m_g = 0, \pm 1$ leads to 6 allowed transitions, corresponding to 6 energetically well separated resonances. The resulting energy dependence of the functions F_M for $M = -1, 0, +1$ is shown in Fig. 4.9. In the case of a pure magnetic hyperfine interaction the energetic positions of the resonance lines are given by

$$E = E_0 - \left(\mu_e \frac{m_e}{I_e} - \mu_g \frac{m_g}{I_g} \right) B = E_0 - (m_e g_e - m_g g_g) B, \quad (4.76)$$

where m_g and m_e are the magnetic quantum numbers and g_g and g_e are the g-factors of the ground and excited states, respectively. For a pure electric

hyperfine interaction, the resonance lines are found at the energetic positions given by

$$E = E_0 \pm \frac{eQ_n V_{zz}}{2} \quad (4.77)$$

for a $3/2 \rightarrow 1/2$ transition like in ^{57}Fe . Q_n is the quadrupole moment of the nucleus and V_{zz} is the electric field gradient at the nucleus. The calculation of the energy eigenvalues for the hyperfine interactions is described in detail in the appendix A.1. The case of mixed interactions where m_j is not conserved is not treated explicitly here. For these cases we refer to corresponding review articles [33, 34].

4.2.1 The Nuclear Scattering Amplitude

It is one virtue of nuclear resonant scattering that optical constants can be calculated analytically. The reason is that the nuclear transitions proceed between isolated nuclear levels with a well-defined transition amplitude, whereas electronic resonances involve continuum states with a density of states that strongly depends on the chemical surroundings. For nuclear resonant scattering the functions $F_M(\omega)$ in (4.14) and (4.15) are given by

$$F_M(\omega) = K \sum_{m_i} \frac{C^2(I_g 1 I_e; m_i M)}{\hbar(\omega - \omega_{m_i M}) + i\Gamma_0/2} \quad (4.78)$$

$$\text{with } K = \frac{2\pi f_{LM} \Gamma_0}{k_0(1+\alpha)(2I_g + 1)},$$

where I_g and I_e are the nuclear spins of the ground- and excited states, f_{LM} is the Lamb-Mössbauer factor, Γ_0 the natural linewidth of the transition, and α the coefficient of internal conversion. The sum runs over all ground state levels with magnetic quantum numbers m_i . $\omega_{m_i M}$ is the resonance energy of the transition with the quantum numbers m_i and M . This is illustrated for the 14.4 keV resonance of ^{57}Fe in Fig. 4.9. The $C(I_g 1 I_e; m_i M)$ are the Clebsch-Gordan coefficients in the notation of Rose [35] that describe the relative strength of the transitions.

Let us assume in the first place that the degeneracy of the nuclear levels is not lifted, so that the whole resonance strength is concentrated in one single transition. Then the summation in (4.12) reduces to a sum over the Clebsch-Gordan coefficients and one obtains for the nuclear scattering length:

$$[\mathbf{N}(\omega)]_{\mu\nu} = (\boldsymbol{\varepsilon}_\mu \cdot \boldsymbol{\varepsilon}_\nu) \frac{k_0 \sigma_0 f_{LM}}{2\hbar(\omega - \omega_0)/\Gamma_0 + i}, \quad (4.79)$$

with

$$\sigma_0 = \frac{2\pi}{k_0^2} \frac{2I_e + 1}{2I_g + 1} \frac{1}{1 + \alpha} \quad (4.80)$$

being the nuclear absorption cross section at resonance, that is tabulated for the Mössbauer isotopes in Table A.7 of the appendix. As already outlined in Sect. 2.2, the resonance strength around the nuclear transition energy can be extraordinarily high. A quantitative picture for the case of ^{57}Fe was given in Fig. 2.9.

4.2.2 Polarization Dependence

In this section, the polarization dependence of nuclear resonant scattering is discussed for the cases of a purely magnetic and a purely electric hyperfine interaction. While the general case is that of a mixed hyperfine interaction, there is a significant number of situations where strictly one of these cases is encountered.

Magnetic Hyperfine Interaction

As already mentioned, a magnetic hyperfine field lifts the degeneracy of the nuclear levels and leads to a multiplet of hyperfine transitions, as shown in Fig. 4.9. The corresponding angular emission characteristics for the transitions with $M = 0$ and $M = \pm 1$ are shown in Fig. 4.10 as polar diagrams. In this example, a thin film is magnetized perpendicular to the incident wavevector \mathbf{k}_0 . The direction of the quantization axis given by \mathbf{m} determines the orientation of the polar diagrams. For a magnetic (electric) dipole transition the excitation probability is given by the value of the polar diagram along the direction of the magnetic field vector \mathbf{B} (electric field vector \mathbf{E}) of the incident wave. Thus, in case of the 14.4 keV magnetic dipole transition of ^{57}Fe , the $M = 0$ transitions cannot be excited, if the magnetization \mathbf{m} is in

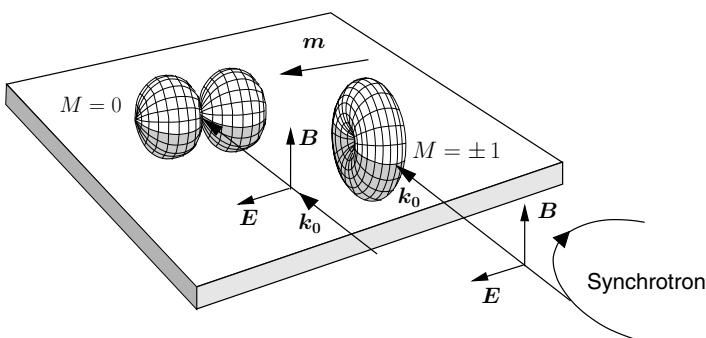


Fig. 4.10. Orientation of the vector spherical harmonics for a magnetic dipole transition in the case of an in-plane magnetization \mathbf{M} . The magnetic field \mathbf{B} of the incident electromagnetic wave is parallel to the surface normal. The $M = 0$ transitions cannot be excited because there is no amplitude of the corresponding spherical harmonics along the direction of \mathbf{B}

the plane of the sample as sketched in Fig. 4.10. This plays an important role for the shape of the time spectra that are recorded. The analysis of a given scattering problem becomes particularly simple in the frame of eigenpolarizations of the system that are obtained by diagonalization of \mathbf{f} . In general, \mathbf{f} is not hermitian, so that the eigenpolarizations are not orthogonal and depend explicitly on energy through the functions F_1, F_{-1} and F_0 . However, there are a number of important cases where \mathbf{f} is hermitian and a system of orthogonal eigenpolarizations can be found so that

$$\mathbf{f}(\omega) = \mathbf{g} \mathbf{f}_D(\omega) \mathbf{g}^{-1}. \quad (4.81)$$

\mathbf{f}_D is a diagonal matrix, and the diagonalizing matrix \mathbf{g} does not depend on ω . Those are the cases where \mathbf{k}_0 and \mathbf{m} are perpendicular or parallel to each other. This is illustrated in Fig. 4.11, where the scattering matrices and typical time spectra are displayed. The time spectra were calculated according to (4.75) for incident σ polarization and unpolarized detection, i.e., $I(t) = |R_{11}|^2 + |R_{12}|^2$. The sample assumed here was a 2 nm thick ^{57}Fe film on W. The following geometries are often encountered experimentally:

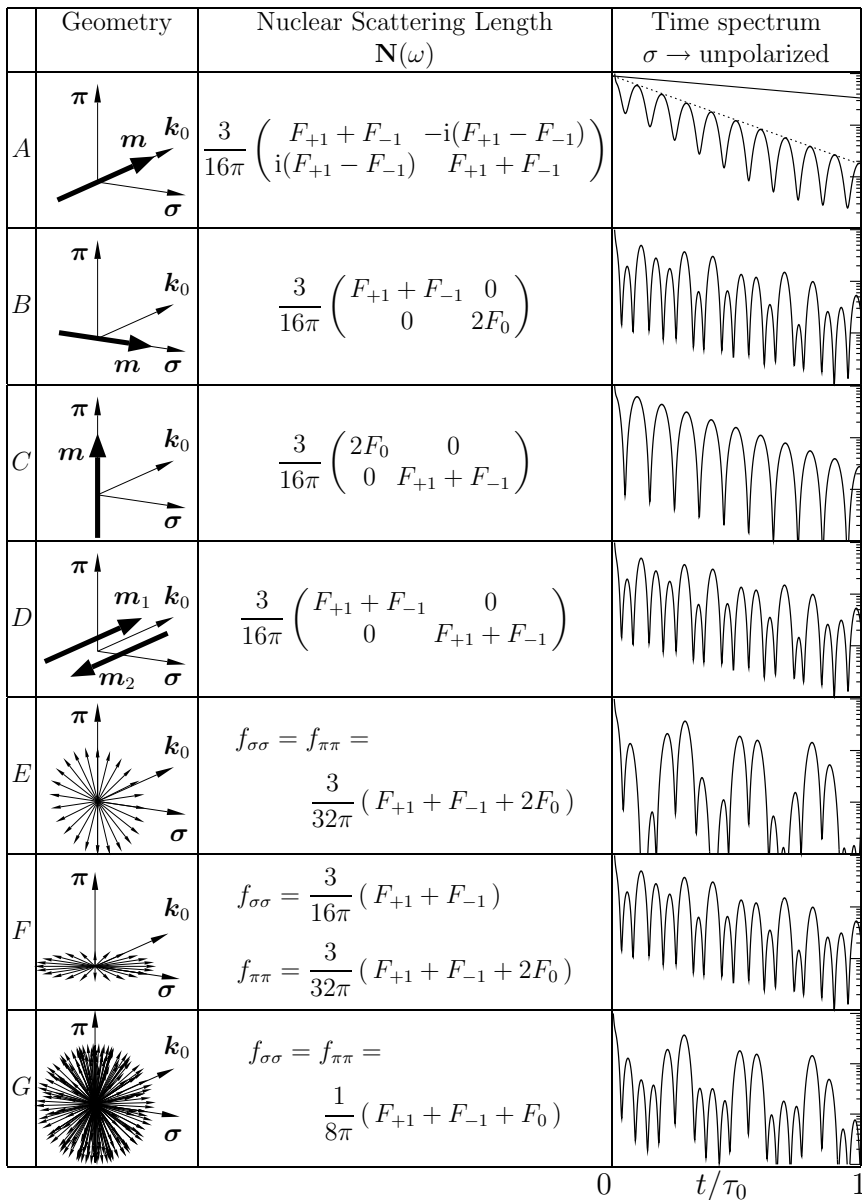
- \mathbf{k}_0 and \mathbf{m} are **perpendicular** ($\mathbf{k}_0 \cdot \mathbf{m} = 0$):

$$\mathbf{f}_D = \frac{3}{16\pi} \begin{pmatrix} F_1 + F_{-1} & 0 \\ 0 & 2F_0 \end{pmatrix} \quad \text{and} \quad \mathbf{g} = \begin{pmatrix} \cos\Theta & \sin\Theta \\ -\sin\Theta & \cos\Theta \end{pmatrix}. \quad (4.82)$$

In this case the linear polarizations are eigenpolarizations of the system. The scattering matrix $\mathbf{f}(\omega)$ is diagonal for $\phi = 0, \Theta = 0$ and $\phi = 0, \Theta = \pi/2$ (modulo π), which corresponds to the geometries sketched in Figs. 4.11B and C, respectively.

- \mathbf{k}_0 and \mathbf{m} are **parallel** or **antiparallel** ($\mathbf{k}_0 \cdot \mathbf{m} = \pm 1$):

Fig. 4.11. Time spectra of nuclear resonant scattering for selected orientations of the magnetic hyperfine field \mathbf{m} relative to the incident wave vector \mathbf{k}_0 . The scattering matrix is given in a linear polarization basis (σ, π) . The time spectra are calculated for a 2 nm thick, ferromagnetic $\alpha-^{57}\text{Fe}$ film on a tungsten substrate, assuming purely σ polarized incident radiation and unpolarized detection. This is the most frequently used scattering geometry in experiments with synchrotron radiation. **A–C** display the results for a unidirectional magnetization of the sample. **D** results from the superposition of two magnetic sublattices in antiparallel alignment as it is the case in antiferromagnets, for example. **E** and **F** display results for 2-dimensional random distributions of spin directions. **G** shows the result for a 3D polycrystalline distribution. Since the scattering matrix in these cases is diagonal, only the diagonal elements are shown. The time scale in the right column covers one natural lifetime of the 14.4-keV transition, i.e. 141 ns. The envelope of the time spectra (*dashed line* in the *upper right* figure) indicates that the time response of the film is considerably speeded up compared to the natural decay (*solid straight line*)



$$\mathbf{f}_D = \frac{3}{16\pi} \begin{pmatrix} F_{\pm 1} & 0 \\ 0 & F_{\mp 1} \end{pmatrix} \quad \text{and} \quad \mathbf{g} = \begin{pmatrix} 1 & \pm i \\ \pm i & 1 \end{pmatrix}, \quad (4.83)$$

where the upper signs are for parallel orientation, the lower signs for antiparallel orientation. Here the circular polarizations are the eigenpolarizations of the system. Note that the off-diagonal elements in (4.15) change sign if the relative orientation between \mathbf{k}_0 and \mathbf{m} changes from parallel to antiparallel. For that reason, the geometries shown in Figs. 4.11A and D lead to different scattering matrices.

– **Polycrystalline directional distributions of fields:**

Of particular relevance are situations where the directions of magnetic moments are distributed uniformly in space or over certain subspaces that are generated by magnetic anisotropies. In case of thin films, for example, the large magnetic shape anisotropy forces the magnetic moments to be aligned in the plane of the film. In case of unmagnetized multi-domain films one often encounters a two-dimensional random distribution of magnetic moments. In these cases the scattering amplitude can be calculated analytically by integration over the corresponding angle variables. The results are summarized in Figs. 4.11E–G. In all these cases the scattering matrix \mathbf{N} is diagonal in a linear polarization basis [36].

Obviously, the beat pattern in the spectra characteristically reflects the underlying spin structure. However, there are degenerate cases (B, D, F) in Fig. 4.11 where the time spectra are identical for different spin structures. For that reason, a single time spectrum is not sufficient to determine the spin structure unambiguously. Instead, to avoid such degeneracies, a set of time spectra has to be taken at different orientations in a tomographic-like measurement. It will be shown in Sect. 4.4.4 that a reconstruction of the magnetic structure is possible by recording time spectra at a number of sample orientations, e.g., by varying the azimuthal angle ϕ .

Electric Hyperfine Interaction

In some cases the nuclear level splitting is determined by a pure electric hyperfine interaction. This applies, e.g., for Fe in metallorganic complexes like ferrocene [32], biomolecules [37, 38], or for Fe monolayers on surfaces like W(110) [39]. The nuclear level scheme in such cases is shown in Fig. 4.9b together with the energy dependence of the functions F_M . The nuclear scattering amplitude matrix $\mathbf{N}(\omega)$ follows from the evaluation of (4.15) with \mathbf{m} being replaced by the unit vector \mathbf{v}_{zz} that gives the direction of the principal axis of the electric field gradient tensor. The scattering matrices for different geometries together with the corresponding time spectra in a typical scattering experiment are shown in Fig. 4.12. The spectra were calculated according to (4.75) with $\xi_1 = 1$. The energy dependence of the functions F_0, F_{+1} , and F_{-1} for this case is shown in Fig. 4.9. Since $F_{+1} = F_{-1}$ it follows that there is no circular dichroism which is observed in the case of a magnetic hyperfine

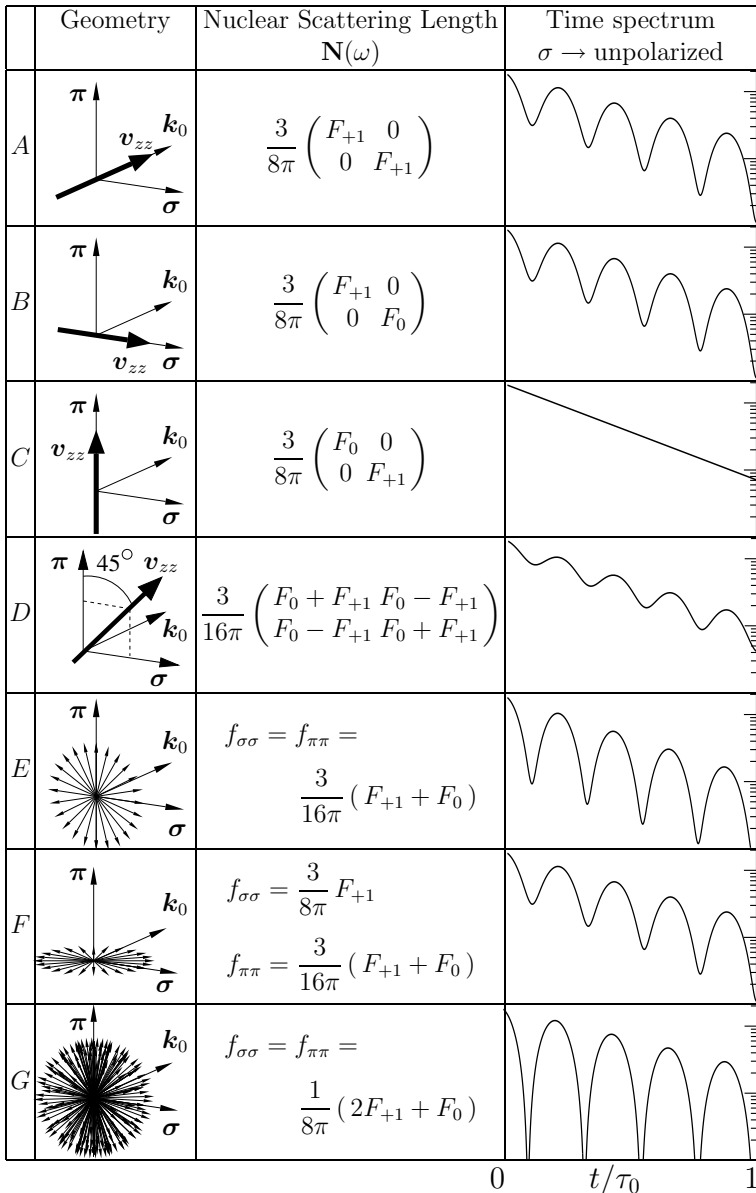


Fig. 4.12. Time spectra of nuclear resonant scattering for selected orientations of the principal axis v_{zz} of the electric field gradient relative to the incident wave vector k_0 . Calculations were performed along the same lines as for Fig. 4.11. The beat period in the time spectra corresponds to a quadrupole splitting as observed in the ferrocene molecule [32]

interaction. However, optical activity can occur due to linear dichroism, as illustrated in Fig. 4.12D.

4.2.3 Resonant Reflection from Surfaces

The resonant nature of the scattering process changes the optical properties of a material in a characteristic way. This has been exemplified already in case of the critical angle of total reflection. An important figure of merit in the discussion of resonant scattering experiments is the time-integrated signal that is reflected from a surface or a layer system. This was studied in detail by *Baron et al.* [28]. The analysis shows that the delayed signal is large at angles where the electronic reflectivity varies rapidly with angle. Therefore, in case of a reflection from a surface, a maximum in the time-integrated signal is observed at the critical angle of total reflection. This is illustrated in Fig. 4.13a where the electronic and nuclear reflectivity of the surface of ^{57}Fe is shown around the critical angle of 3.8 mrad. Figure 4.13b shows the situation for a 30 nm thick film of ^{57}Fe on Si. Maxima in the delayed reflectivity occur at positions with the steepest negative slope in the electronic reflectivity. In the following section we will see that the maximum in the delayed signal is closely related to the formation of standing waves in the sample.

4.2.4 Resonant Reflection from Ultrathin Films

In many cases the sample under study consists of nanostructures that are deposited on a smooth surface like that of a single crystal. Such a system can be considered as an ultrathin film on a semi-infinite substrate. For a calculation of the reflected amplitudes we apply the formalism outlined in Sect. 4.1.6, resulting in the evaluation of (4.59). The reflectivity R_0 of the layer system without the ultrathin layer is then given by $R_0 = r_{02}$, which is the Fresnel reflectivity of the vacuum-substrate boundary. The normalized field amplitudes $A_+(z_p)$ and $A_-(z_p)$ are

$$A_+(z_p) = 1 \quad \text{and} \quad A_-(z_p) = r_{02}. \quad (4.84)$$

Taking into account that $1 + r_{02} = t_{02}$, (4.59) can be written as

$$\begin{aligned} \mathbf{R}(\omega) &\approx r_{02} (1 + i\mathbf{f}_1(\omega)|t_{02}|^2 d) \\ &\approx r_{02} e^{i\mathbf{f}_1(\omega)|t_{02}|^2 d}. \end{aligned} \quad (4.85)$$

Equation (4.85) is an expression very similar to the description of nuclear forward scattering (NFS) where the scattered field is given by⁵ $\mathbf{A}(\omega) = \mathbf{A}_0 e^{i\mathbf{f}(\omega)d}$. Thus, the reflection from an ultrathin film can be treated like forward scattering with an ‘effective’ thickness of

⁵ Note that in grazing incidence geometry, $\mathbf{f}_1(\omega) = (k_0/k_{0z}) \mathbf{f}(\omega) = \mathbf{f}(\omega)/\varphi$, where $f(\omega)$ is the forward scattering amplitude.

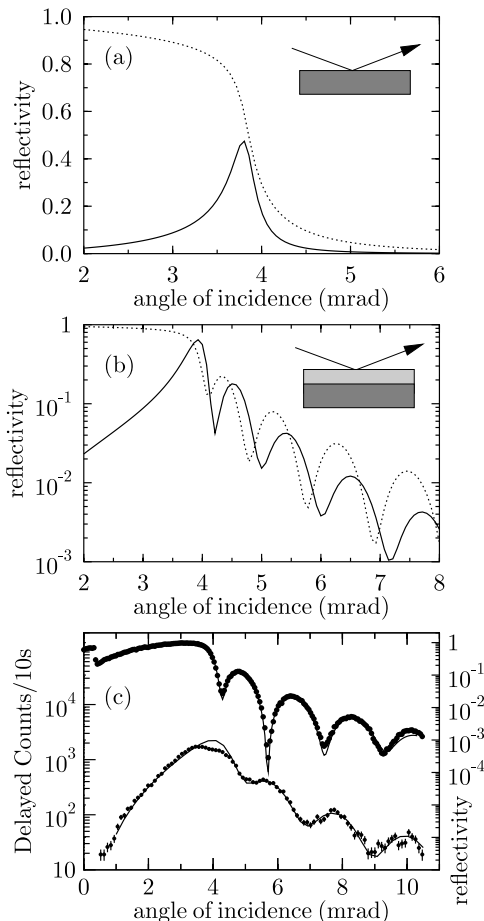


Fig. 4.13. Angular dependence of the delayed resonant reflectivity from surfaces and thin films (solid lines). Calculations have been performed (a) for the surface of ^{57}Fe and (b) for a 30 nm thick film of ^{57}Fe on Si. The dashed lines are the corresponding electronic reflectivity curves. (c) Measured reflectivity from a 30 nm thick film of ^{57}Fe on Si. The top curve shows the electronic reflectivity, the bottom curve displays the delayed signal counted within a time window reaching from 12 ns to 170 ns after excitation. Solid lines are simulations

$$d' = d |t_{02}|^2 / \varphi . \quad (4.86)$$

While d is enhanced by a factor $|t_{02}|^2$ resulting from x-ray interference effects, an additional enhancement is given by the factor $1/\sin \varphi \approx 1/\varphi$. This simply describes the increase in path length for radiation that travels under an angle φ through a film of thickness d . $|t_{02}|^2$ is the relative intensity of the standing wave with amplitude A_S that results from the superposition of incident and reflected wave, i.e., $A_S = (1 + r_{02})A_0 = t_{02}A_0$. This enhanced interaction with the radiation field thus mimics an increased film thickness.

The time response $\mathbf{R}(t)$ of the system is obtained by Fourier transformation of $\mathbf{R}(\omega)$ in (4.85):

$$\mathbf{R}(t) \approx \delta(t) - \tilde{\mathbf{f}}(t) \chi e^{-\chi t/2\tau_0} , \quad (4.87)$$

with

$$\chi = \frac{1}{4} \varrho \sigma_0 f_{LM} |t_{02}|^2 \frac{d}{\varphi}, \quad (4.88)$$

where $\tilde{\mathbf{f}}(t)$ is the Fourier transform of $\mathbf{f}(\omega)$. The δ -function describes the instantaneous radiation pulse that has passed the sample without resonant interaction. Since the time dependence of $\tilde{\mathbf{f}}(t)$ is governed by the natural lifetime τ_0 , the envelope $I_e(t)$ of the intensity $I(t)$, as determined from (4.87) by application of (4.73), can be described to a good approximation by

$$I_e(t) \approx \chi^2 e^{-(1+\chi)t/\tau_0}. \quad (4.89)$$

These results allow for a number of conclusions:

- Already for very thin layers the time response of the scattering exhibits a speedup compared to the natural decay (see Sect. 2.2.5). According to (4.86) a monolayer of ^{57}Fe on W ($d = 2 \text{ \AA}$) illuminated at $\varphi = 4 \text{ mrad}$ acts with an effective thickness of $d' = 0.2 \mu\text{m}$, leading to a speedup of $\chi = 1.5$.
- The maximum contribution emerges at the critical angle of the substrate, where $|t_{02}|^2$ peaks. At this angle the interference between incident and reflected wave forms a standing wave with an antinode exactly at the boundary. A similar effect has been observed for nuclear resonant scattering from thick Fe layers [28].
- The scattered amplitude from the film is strongest if the photoabsorption in the substrate is lowest. This is illustrated in Fig. 4.14 where the time-integrated delayed intensity has been calculated for one monolayer ^{57}Fe on different substrate materials.

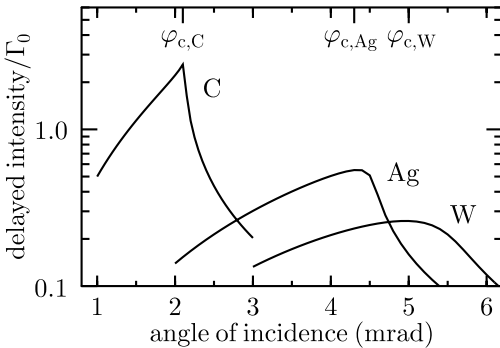


Fig. 4.14. Angular dependence of delayed nuclear resonant scattering from 0.3 nm ^{57}Fe on various substrates: The intensity peaks at the critical angle of the substrate material

4.2.5 Determination of Magnetic Moment Orientations and Spin Structures

The time spectra shown in Fig. 4.11 may be taken as fingerprints for the spin structure of the sample. This suggests to extract this information directly

from the time spectra. In fact, in the kinematical approximation this can be accomplished even for more complicated spin structures. In the following we introduce an algorithm to derive information about the magnetic structure of the sample from a Fourier analysis of the measured data [40].

Calculation of Time Spectra

Assuming no polarization analysis in the detection process, we obtain for the resonantly reflected intensity according to (4.75):

$$I(t) = |R_{11}|^2 + |R_{12}|^2 . \quad (4.90)$$

Taking only the delayed part of (4.87) into account, this equation turns into

$$I(t) = \{ |\tilde{f}_{11}(t)|^2 + |\tilde{f}_{12}(t)|^2 \} \chi^2 e^{-\chi t/\tau_0} , \quad (4.91)$$

where the $\tilde{f}_{ij}(t)$ are matrix elements of $\tilde{\mathbf{f}}(t)$ which results from evaluation of (4.15) and Fourier transform into the time domain. Since the electronic contribution $\mathbf{E}(\omega)$ to the scattering length is energetically broad, it contributes only to the prompt response and need not be considered here. Thus, we evaluate the nuclear contributions $\mathbf{N}_i(\omega)$ of each magnetic sublattice \mathbf{m}_i given by (4.14). We set $\Theta = \pi/2$, because the magnetization is in the plane of the sample and obtain

$$\mathbf{N}_i(\omega) = \frac{3}{16\pi} \begin{pmatrix} F_{+1} + F_{-1} & -i(\mathbf{k}_0 \cdot \mathbf{m}_i)(F_{+1} - F_{-1}) \\ i(\mathbf{k}_0 \cdot \mathbf{m}_i)(F_{+1} - F_{-1}) & F_{+1} + F_{-1} \end{pmatrix} . \quad (4.92)$$

To account for the general case of a directional distribution of in-plane magnetizations, one has to calculate the weighted sum over all these contributions:

$$\mathbf{N}(\omega) = \sum_i p_i \mathbf{N}_i = \frac{3}{16\pi} \begin{pmatrix} F_{+1} + F_{-1} & -iS(\phi)(F_{+1} - F_{-1}) \\ iS(\phi)(F_{+1} - F_{-1}) & F_{+1} + F_{-1} \end{pmatrix} , \quad (4.93)$$

with

$$S(\phi) = \mathbf{k}_0 \cdot [\mathbf{D}(\phi) \mathbf{M}] . \quad (4.94)$$

\mathbf{M} is the magnetic structure function of the sample:

$$\mathbf{M} = \sum_i p_i \mathbf{m}_i e^{i\mathbf{q} \cdot \mathbf{R}_j} \quad \text{with} \quad \sum_i p_i = 1 , \quad (4.95)$$

where the sum runs over all magnetic sublattices, represented by unit vectors \mathbf{m}_j and the phase factor accounts for the position \mathbf{R}_j of the atoms. $\mathbf{q} = \mathbf{k} - \mathbf{k}'$ is the momentum transfer in the scattering process. The rotation matrix

$$\mathbf{D}(\phi) = \begin{pmatrix} \cos \phi & \sin \phi \\ -\sin \phi & \cos \phi \end{pmatrix} \quad (4.96)$$

describes the azimuthal rotation of the sample about an angle ϕ relative to the incident beam.

Inserting the corresponding matrix elements of (4.93) into (4.91), we obtain for the scattered delayed intensity:

$$I(t) = \{ |\tilde{F}_{+1} + \tilde{F}_{-1}|^2 + S^2(\phi) |\tilde{F}_{+1} - \tilde{F}_{-1}|^2 \} \chi^2 e^{-\chi t/\tau_0}. \quad (4.97)$$

The functions $\tilde{F}_{\pm 1}(t)$ are the Fourier transforms of $F_{\pm 1}(\omega)$ as given by (4.78). They are given by

$$\tilde{F}_{+1}(t) = (a_1 e^{i\omega_1 t} + a_4 e^{i\omega_4 t}) e^{-t/2\tau_0} \quad (4.98)$$

$$\tilde{F}_{-1}(t) = (a_3 e^{i\omega_3 t} + a_6 e^{i\omega_6 t}) e^{-t/2\tau_0}. \quad (4.99)$$

The evaluation of (4.97) using these expressions leads to the appearance of frequency differences $\omega_i - \omega_j$ that can be related to splittings $\Delta_g = \mu_g B/I_g$ and $\Delta_e = \mu_e B/I_e$ of ground and excited state⁶, respectively (see Fig. 4.2):

$$\Omega_1 = \omega_4 - \omega_1 = (\Delta_e + \Delta_g)/\hbar \quad (4.100)$$

$$\Omega_2 = \omega_3 - \omega_1 = 2\Delta_e/\hbar.$$

Observing that $a_3 = a_4, a_1 = a_6$ and thus $|F_{+1}(t)|^2 = |F_{-1}(t)|^2$, (4.97) can now be written as:

$$I(t) = e^{-\chi t/\tau_0} [G(0, 0, \Omega_1) (1 + S^2(\phi)) + G(\Omega_1 + \Omega_2, \Omega_1 - \Omega_2, \Omega_2) (1 - S^2(\phi))], \quad (4.101)$$

where the function G is given by

$$G(\omega_1, \omega_2, \omega_3) = \cos \omega_1 t + a^2 \cos \omega_2 t + 2a \cos \omega_3 t, \quad (4.102)$$

with $a = a_1/a_4 = a_6/a_3 = 1/3$ being the amplitude ratio of the two resonance lines that comprise the functions $F_{\pm 1}(\omega)$.

To illustrate this, we consider a sample with a unidirectional magnetization, i.e., $S(\phi) = \cos \phi$. Figure 4.15 shows calculated time spectra $I(t)$ according to (4.101) for ϕ assuming various angles between 0° and 90° . Such a situation is frequently encountered when thin films and nanostructures with a uniaxial in-plane anisotropy are investigated. An inspection of the time spectra shows that the shape of the beat pattern is rather insensitive to changes of the moment orientation around $\phi = 0$. Moreover, it should be noted that the time-integrated intensity changes with the relative angle ϕ as shown on the right side of Fig. 4.15.

Extraction of the Spin Structure from Time Spectra

A fit of (4.101) to the experimental data can be used to determine $S(\phi)$ and reconstruct the underlying spin structure M . In the following we give an outline of a different procedure for determination of $S(\phi)$ that relies on a harmonic analysis of the measured time spectra. Since (4.101) is a superposition

⁶ In case of ⁵⁷Fe with $B = 33.3$ T the splittings of ground and excited state are $\Delta_g = 190.25$ neV and $\Delta_e = 108.70$ neV.

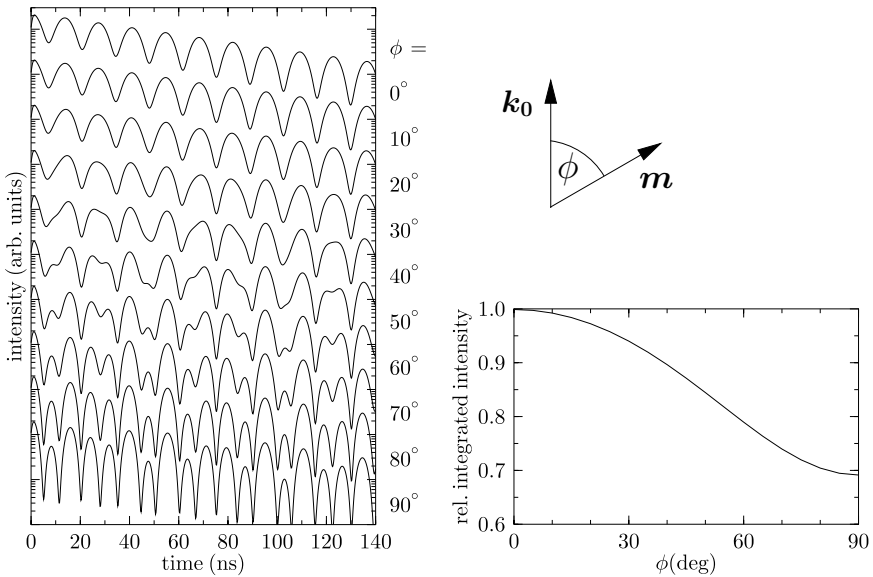


Fig. 4.15. Evolution of the time spectra for magnetic film with an in-plane moment orientation varying from $\mathbf{m} \parallel \mathbf{k}_0(\phi = 0^\circ)$ to $\mathbf{m} \perp \mathbf{k}_0(\phi = 90^\circ)$. The spectra were calculated using (4.101). The right figure shows the dependence of the time-integrated intensity as function of ϕ

of damped harmonic functions, its Fourier transform is a superposition of Lorentzians $L(\Omega_i)$ centered around frequencies Ω_i with weight factors $g(\Omega_i)$:

$$I(\omega) = \sum g(\Omega_i) L(\Omega_i) \quad (4.103)$$

$$\begin{aligned} &= (1 + S^2)(1 + a^2) L(0) \\ &\quad + 2a(1 + S^2) L(\Omega_1) + 2a(1 - S^2) L(\Omega_2) \\ &\quad + (1 - S^2) L(\Omega_1 + \Omega_2) \\ &\quad + a^2 (1 - S^2) L(\Omega_1 - \Omega_2). \end{aligned} \quad (4.104)$$

This means, $S(\phi)$ can be determined from the weights of the Lorentzians $L(\Omega_1)$ and $L(\Omega_2)$ as follows:

$$S = \sqrt{\frac{g(\Omega_1) - g(\Omega_2)}{g(\Omega_1) + g(\Omega_2)}}. \quad (4.105)$$

In grazing incidence geometry, the momentum transfer q is very small so that the condition $\mathbf{q} \cdot \mathbf{R} \ll 1$ is fulfilled and $e^{i\mathbf{q} \cdot \mathbf{R}} \approx 1$. Then, with $\mathbf{k}_0 = (1, 0)$ and $\mathbf{M} := (m_x, m_y)$ the function $S(\phi)$ according to (4.94) is given by

$$S(\phi) = m_x \cos \phi + m_y \sin \phi. \quad (4.106)$$

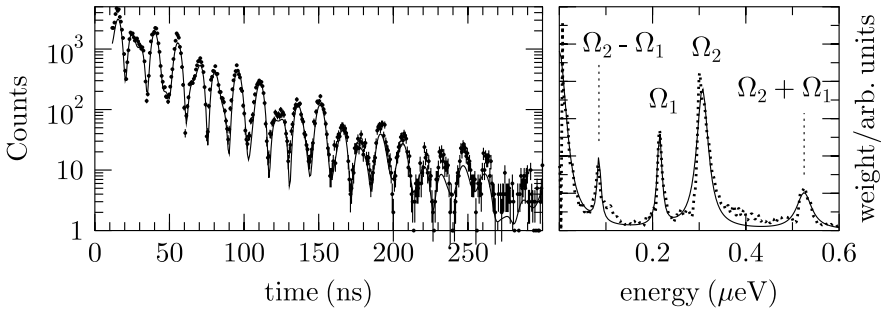


Fig. 4.16. *Left:* Time spectrum of nuclear resonant scattering from a 0.7 nm thick film of ^{57}Fe embedded in an x-ray waveguide. The sample is magnetized at an in-plane angle ϕ (see Fig. 4.2) relative to the photon wavevector. *Right:* Fourier transform of the measured data to reveal the spectral components that contribute to the temporal beat pattern. The solid lines are Lorentzian fits to the peaks. According to (4.107), ϕ is determined from the weights of the frequency components at Ω_1 and Ω_2 to be $54(3)^\circ$. The solid line in a) is a fit according to (4.101)

In the most simple case of a unidirectional magnetization of the sample with $\mathbf{m} = (1, 0)$ and $\mathbf{k}_0 = (1, 0)$ one obtains $S(\phi) = \cos \phi$. From (4.101) it follows that the time spectrum $I(t)$ at $\phi = 0$ is a beat pattern with a single frequency Ω_1 , as shown in Fig. 4.11A. With ϕ increasing towards $\pi/2$ the modulation becomes more complex due to the admixture of three more frequencies. This corresponds to a rotation of \mathbf{M} in the (σ, \mathbf{k}_0) plane (see Fig. 4.2) where upon a transition between the time spectra shown in Figs. 4.11A and 4.11B takes place, as shown in Fig. 4.15. In this case the in-plane rotation angle can be derived from the weights of the frequency components Ω_1 and Ω_2 according to

$$\phi = \arccos \sqrt{\frac{g(\Omega_1) - g(\Omega_2)}{g(\Omega_1) + g(\Omega_2)}}. \quad (4.107)$$

An example is shown in Fig. 4.16. It shows a time spectrum of nuclear resonant scattering from a thin film of ^{57}Fe magnetized at an in-plane angle ϕ relative to the photon wavevector. The Fourier transform of the measured data reveals the spectral components that contribute to the temporal beat pattern. Applying (4.107), one determines a planar rotation angle of $\phi = 54(3)^\circ$. A detailed discussion of the sample used here is given in Sect. 4.4.3.

The algorithm presented here can be applied to determine the magnetic structure of thin films and nanoparticles on surfaces. In many cases an unambiguous reconstruction can be performed. With increasing degree of complexity, however, the reconstruction becomes less unique and the analysis has to be guided by additional information about the sample.

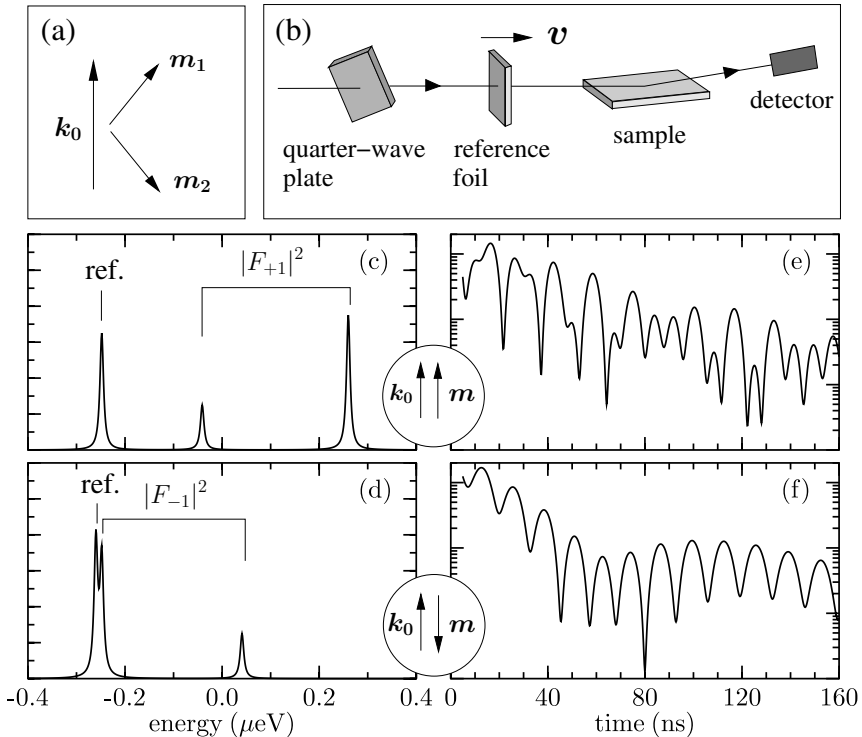


Fig. 4.17. Nuclear resonant scattering with circularly polarized radiation to determine the sign of the moment orientation in the sample. This allows one to distinguish between the orientations \mathbf{m}_1 and \mathbf{m}_2 in (a). (b) Experimental setup. Circularly polarized radiation is generated by a quarter-wave plate for x-rays. The sample is a quintalayer with the sequence Fe/Cr/Fe/Cr/Fe and the center layer enriched in ^{57}Fe . A single-line reference foil of $0.5\ \mu\text{m}$ ^{57}Fe -stainless steel at a constant velocity of $v = 5.6\ \text{mm/s}$ is used to break the inversion symmetry of the resonance lines [41]. (c, d) Energy spectra for parallel or antiparallel alignment of \mathbf{k}_0 and the sample magnetization \mathbf{m} . (e, f) Time spectra corresponding to the energy spectra shown in c, d

The Sign of the Moment Orientation

Using linearly polarized light, one cannot distinguish between magnetization orientations with antiparallel components along the direction of \mathbf{k}_0 as those shown in Fig. 4.17a. Sensitivity to the sign can be obtained by using circularly polarized light as has been demonstrated by *L'abbé et al.* [41].

Photons with left- (right-) circular polarization have a helicity of +1 (−1). Provided the magnetization is parallel (antiparallel) to \mathbf{k}_0 ⁷, these photons couple only to nuclear transitions with a change in angular momentum of $M = +1$ ($M = -1$). The energy dependence is given by the functions $F_+(\omega)$ ($F_-(\omega)$) as shown in Fig. 4.9a. Since the energetic separation and the relative intensities of the two lines that comprise the functions $F_{\pm 1}(\omega)$ are identical, the time spectra in both cases are the same, and the sensitivity to the sign of the orientation is lost. It can be restored if the inversion symmetry of the functions $F_{+1}(\omega)$ and $F_{-1}(\omega)$ is broken. This is achieved, for example, by introduction of a single-line reference sample that is energetically shifted relative to the center of the inversion symmetry. The corresponding experimental setup is sketched in Fig. 4.17b. A quarter-wave plate is used to prepare a circularly polarized beam [42, 43, 44], and a single-line absorber is mounted on a constant-velocity drive to break the inversion symmetry. Figures 4.17c,d show the energy spectra of this arrangement for parallel and antiparallel alignment of the sample magnetization relative to \mathbf{k}_0 , and Figs. 4.17e,f show the corresponding time spectra. The difference in both time spectra underlines the high sensitivity for the sign of the magnetic moment orientation. This method has been applied to investigate the interlayer coupling in (50 Å Fe)/(11 Å Cr) quintalayers where three Fe layers are antiferromagnetically coupled through two Cr layers [41]. To probe the coupling while excluding surface effects, only the center Fe layer is enriched to 95% in ⁵⁷Fe. It was shown in that experiment that the coupling is not purely antiferromagnetic, but contains noncollinear contributions.

4.2.6 Comparison with Conventional Mössbauer Spectroscopy

Source Brilliance

An explicit comparison between the properties of synchrotron radiation and radioactive sources has been given in Sect. 3.1.3. It should be emphasized again that the brilliance of the undulator radiation at a third-generation source exceeds that of a radioactive source by several orders of magnitude. This results in a corresponding reduction of data acquisition times and allows for systematic studies under conditions that could be hardly kept stable over long data acquisition times. One example is the investigation of diffusion at high temperatures as described in Sect. 4.6.

Coherence

Due to the coherence of the scattering process, the delayed intensity scales quadratically with the amount of resonant nuclei in the sample. This can be

⁷ In noncollinear arrangements this reasoning has to be applied for the corresponding components parallel or antiparallel to \mathbf{k}_0 .

seen in (4.62) and (4.89) where the intensity $I(t)$ is proportional to the square of the layer thickness d . This dependence leads to a strong gain (loss) in intensity with increasing (decreasing) amount of resonant nuclei in the sample. In conventional Mössbauer spectroscopy the contribution to the measured spectrum scales linearly with the amount of resonant nuclei.

These considerations have to be applied to *all* resonant nuclei in the sample. This is particularly important if isotopically enriched layers are used to probe selected parts of the sample which contains the isotope in its natural abundance. In a coherent scattering process the measured signal is then proportional to the square of the ratio between the amount a_p of resonant nuclei in the probe layer and the amount of resonant nuclei a_r in the remainder of the sample:

$$I(t) \sim \left(\frac{a_p}{a_r} \right)^2. \quad (4.108)$$

Thus, if $a_p \gg a_r$, the contribution from the surrounding material can be neglected. In thin films that are illuminated in grazing incidence geometry the parameters a_p and a_r have to be weighted with the average intensity of the radiation at the position of the nuclei in the layer. This may strongly affect the relative contributions from both parts.

In any experiment such considerations have to be performed to estimate the contribution from resonant nuclei in the surrounding materials. In any case the use of materials that are depleted from the resonant isotope will significantly increase the ratio a_p/a_r .

Spin Structures

In ferromagnetic samples that contain Fe with a magnetically split sextet of hyperfine lines, the spin structure can be inferred from the intensity ratio between the second (or fifth) and the third (or fourth) line, $R_{23} = I_2/I_3 = I_5/I_4$ [45]. If the hyperfine field \mathbf{B}_{hf} of an Fe atom, which is antiparallel to the spin direction, forms an angle θ with the wavevector of the incident photon, this intensity ratio is given by

$$R_{23} = 4 \frac{1 - \cos^2 \theta}{1 + \cos^2 \theta}. \quad (4.109)$$

Since in conventional Mössbauer spectroscopy the incident photon makes an angle of $\theta = 90^\circ$ with the plane of the sample, one obtains $R_{23} = 4$ for the case that the sample exhibits an in-plane magnetization. Accordingly, the method is insensitive to variations of the spin structure in the plane of the sample. Such configurations may be analyzed only in a non-perpendicular geometry, with the radiation incident at an angle φ relative to the sample plane. If the in-plane spin directions are distributed according to a function $P(\phi)$, with ϕ being the azimuthal angle of \mathbf{B}_{hf} relative to the projection of \mathbf{k}_0 on the surface, the intensity ratio is given by

$$R_{23} = 4 \int_0^{2\pi} \frac{1 - \cos^2 \varphi \cos^2 \phi}{1 + \cos^2 \varphi \cos^2 \phi} P(\phi) d\phi \quad \text{with} \quad \int_0^{2\pi} P(\phi) d\phi = 1. \quad (4.110)$$

For an analysis of the in-plane spin structure, Mössbauer spectra are taken for different azimuthal orientations of the sample relative to the incident beam. This technique was applied to analyze the magnetic structure of ion-beam irradiated magnetic films [46] and to investigate the spiral magnetic spin structure in Fe/SmCo exchange-spring bilayers [47]. A detailed study for various distribution functions $P(\phi)$ is reported in [48]. Early theoretical work to evaluate the spin texture by Mössbauer spectroscopy goes back to *Pfannes & Fischer* [49] and *Greeneche & Varret* [50].

4.3 Special Aspects

4.3.1 Kinematical vs. Dynamical Theory

The procedure for determination of the magnetic structure function as outlined in Sect. 4.2.5 is valid for ultrathin films in the limit of kinematical scattering. With increasing film thickness, however, multiple scattering processes have to be taken into account. The time spectra are then modulated by a long-period temporal oscillation, the so-called dynamical beat, that imposes restrictions on the applicability of the numerical algorithm described here. Here we want to quantify the validity limit of this algorithm in terms of film thickness d and number density ϱ of resonant nuclei.

The first minimum of the dynamical beat is located at time

$$t_M \approx \frac{16\varphi}{f_{LM}\sigma_0\varrho d} \tau_0 \approx \frac{4\varphi\tau_0}{\chi}, \quad (4.111)$$

where σ_0 is the nuclear absorption cross section as given in Table A.1 and χ is given by (2.19). For times $t < t_M$ the envelope of the time spectra is given by $e^{-(1+\chi)t/\tau_0}$. After multiplication with $e^{\chi t/\tau_0}$ the speedup of the envelope is corrected for and the numerical algorithm can be reliably applied. On the other hand, in the region around $t = t_M$ the time spectra are strongly perturbed. This is illustrated in Fig. 4.18. Time spectra of grazing incidence reflection from Fe films on W have been calculated according to the full dynamical theory. It is obvious that with increasing thickness the first minimum of the dynamical beat, indicated by the shaded region, shifts to earlier times. In the corresponding Fourier spectra the lines are broadened and their relative intensities are changed so that the spectral weights $g(\Omega_i)$ cannot be determined reliably anymore. According to (4.111) the area density ϱd of the resonant nuclei determines the time range Δt that is not perturbed by dynamical beats. If one asks for $\Delta t = 300$ ns as displayed here, the critical area density is given by $1.8 \times 10^{20} \text{ m}^{-2}$ (assuming that $f_{LM} = 0.8$

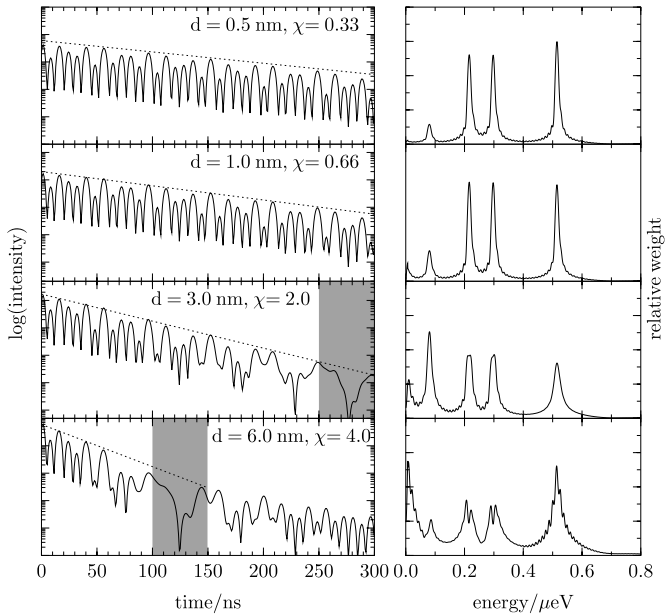


Fig. 4.18. Time spectra of grazing incidence reflection from ^{57}Fe films of various thicknesses on W at an angle of incidence of $\varphi = 4.4 \text{ mrad}$ in the magnetization geometry of Fig. 4.11B. The *dashed lines* mark the envelope that is characterized by the speedup χ . The *right panel* shows the Fourier spectra of the time spectra in the *left panel*

and $\varphi = 5 \text{ mrad}$). For pure ^{57}Fe with $\varrho = 8.46 \times 10^{28} \text{ m}^{-3}$ this limit is exceeded already for $d > 2.2 \text{ nm}$. If films of larger thicknesses should be studied by this method, the degree of enrichment should be decreased. On the other hand, one could decrease the time range Δt that is subject to the Fourier transform. This goes, however, at the expense of energetic resolution in the Fourier spectra. Thus, for best results, the speedup should be below $\chi = 1$ and the time spectra should extend over a large temporal range.

4.3.2 Transverse Coherence: Influence of the Detector Aperture

The transverse coherence length L_T describes the degree of coherence between laterally separated points within the radiation field at the sample position. This is explained in detail in the appendix, Sect. A.4. Transverse coherence plays an important role in the interpretation of x-ray scattering experiments with synchrotron radiation [51, 52]. Due to the small source size of undulator synchrotron radiation sources, for example, the transverse coherence length at the sample position can amount to several μm [53]. In grazing incidence geometry, these values increase to L_T/φ , so that coherent illumination may

occur over in-plane distances of several hundred μm . To observe the corresponding diffraction pattern one needs a detector with a sufficiently high resolution in momentum space. With increasing detector aperture, an increasing part of the diffraction pattern contributes to the signal so that the effective coherence length decreases [51]. Then it appears that contributions from laterally separated parts of the surface have to be added with a decreasing degree of coherence. This is illustrated in Fig. 4.19 where two islands with a projected separation g are coherently illuminated and the diffraction pattern is recorded by a detector in a distance L . Assuming that $L \gg g$, the path length difference between the waves scattered from the islands is given by $\Delta x = g \tan \alpha = 2gy/L$, where y is the linear coordinate in the detector plane. Thus, up to a phase factor, the amplitude at the detector position is given by

$$A(y) = r_1 + r_2 e^{ik_0(2g/L)y}, \quad (4.112)$$

where r_1 and r_2 are the reflected amplitudes at the two islands. The intensity in the detector plane is then given by

$$I(y) = |A(y)|^2 = |r_1|^2 + |r_2|^2 + 2|r_1 r_2| \cos[k_0(2g/L)y]. \quad (4.113)$$

The finite detector aperture is taken into account by convolution of this expression with the corresponding aperture function. In the extreme case where the detector aperture is much larger than the spacing of the diffraction peaks, i.e., $D > L/(2k_0 g)$, the cosine function averages to zero and one obtains:

$$I(y) = |r_1|^2 + |r_2|^2. \quad (4.114)$$

In this limit, one observes a fully incoherent superposition of the contributions from different parts of the sample. Therefore, depending on the size D of the

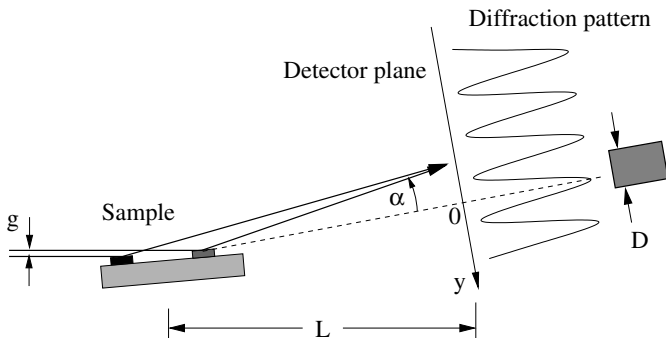


Fig. 4.19. Coherent x-ray scattering from a sample with lateral inhomogeneities, represented by two islands on a flat surface. The detector plane is located in a distance L from the sample. The diffraction pattern has a $\cos^2 \alpha$ dependence. D is the detector aperture

detector aperture, one observes a superposition of scattered amplitudes with a different degree of coherence.

These considerations have to be taken into account if the samples exhibit lateral inhomogeneities. This is of particular relevance for the investigation of magnetic systems with an in-plane domain structure. For a numerical estimate, we assume two domains/islands separated by $d = 1\text{ }\mu\text{m}$, the sample being illuminated under an angle of $\varphi = 4\text{ mrad}$ and the detector in a distance of $L = 1\text{ m}$. Then $g = d\varphi = 4 \cdot 10^{-9}\text{ m}$ so that $L/(2k_0 g) = 3.4\text{ mm}$. This matches the typical aperture of APD detectors as they are used in such experiments. The arguments presented here underline the importance to carefully control these parameters, because the degree of coherent superposition may mimic other effects that could be ascribed to the spin structure of the sample. For example, the incoherent superposition of the contributions from two sets of in-plane magnetic domains can be mistaken for a uniaxial magnetization of the sample. This can be understood by inspection of (4.101) that describes the intensity scattered from a sample with an in-plane magnetization. In the case of a unidirectional magnetization and $\mathbf{k}_0 = (1, 0)$ we have $S(\phi) = \cos\phi$. Abbreviating the functions $G(0, 0, \Omega_1) =: G_a$ and $G(\Omega_1 + \Omega_2, \Omega_1 - \Omega_2, \Omega_2) =: G_b$, and assuming two sets of domains (with equal weights), oriented at angles ϕ_1 and ϕ_2 , we obtain for the scattered intensity:

$$I(t) = e^{-\chi t/\tau_0} [G_a(1 + (\cos^2 \phi_1 + \cos^2 \phi_2)/2) + G_b(1 - (\cos^2 \phi_1 + \cos^2 \phi_2)/2)]. \quad (4.115)$$

This is the same intensity as scattered from a sample with a unidirectional magnetization oriented at an angle ϕ defined by $\cos^2 \phi = (\cos^2 \phi_1 + \cos^2 \phi_2)/2$. In contrast, for a coherent superposition of these contributions, one obtains a unidirectional magnetization at an effective angle ϕ defined by $\cos \phi = (\cos \phi_1 + \cos \phi_2)/2$. Thus, in the case of a lateral domain structure, one obtains different results depending on the degree of coherence in the superposition of the individual contributions. It can be shown that for a relatively narrow distribution of moment orientations ($\text{FWHM} \approx 20^\circ$) one obtains still the average moment direction, in either case of coherent or incoherent superposition. In the case of a much broader orientational distribution one has to extend the investigations by measurement of nuclear small-angle scattering (see Sect. 4.4.6) or taking data at several different orientations of the sample (see Sect. 4.4.4) in order to obtain information about the spin structure of the sample.

The previous considerations illuminate some difficulties that may arise from the partial coherence of the radiation when the sample exhibits lateral heterogeneities. On the other hand, the control of the effective transverse coherence length via the detector aperture may give an interesting handle to reveal in-plane correlations of the magnetic structure.

4.3.3 Standing Waves in Thin Films

Thin-film x-ray waveguide structures have a longstanding history in the field of x-ray analysis [54]. They are typically realized as thin-film systems consisting of a low-density guiding layer coated on a substrate with higher electron density. The standing wave that forms as a result of multi-beam interference between the incident and the reflected wave can be used as primary wave for probing the properties of the guiding layer. First experiments of this kind were reported by Wang *et al.* [55] who used the standing waves that formed in a macromolecular film on a metal substrate to obtain structural information about the film. The strong enhancement of the field intensity in the guiding layer was used to probe the vibrational properties of thin films via inelastic x-ray scattering [56, 57]. Moreover, it was shown that the strong enhancement of the fluorescence yield from ultrathin probe layers can be used for structural characterization of metallic multilayers [58, 59]. The intensity in the antinodes of the wavefield can be even more enhanced by sandwiching the guiding layer between two layers of higher electron density. This approach was systematically investigated by Sinha and coworkers [60]. Recently, x-ray waveguides received a renewed interest for the analysis of liquid films [61, 62], biomolecular layers [63] and the production of x-ray nanobeams [64].

Calculation of Field Intensities

Some typical situations that are encountered quite frequently in thin-film x-ray interference shall be discussed now. They are illustrated in Fig. 4.20. The right side shows the intensity of the radiation as a function of depth in the sample, calculated according to (4.45) derived in Sect. 4.1.5. At the critical angle, for example, an antinode of the standing wave coincides with the surface, where the intensity peaks with up to four times the incident intensity, see Fig. 4.20a. Such standing waves can be created inside of thin films if they are coated on a highly reflective substrate, i.e., a material of higher electron density. A substantial intensity enhancement inside the layer is achieved if the layer thickness d is an integer multiple of the standing wave period, because waves that are repeatedly reflected at the boundaries then add up constructively [55, 65], see Fig. 4.20b. The intensity enhancement is most pronounced if the film under study is sandwiched between two highly reflecting layers, as shown in Fig. 4.20c. Since the energy transport takes place parallel to the layer boundaries, such layer systems can be regarded as x-ray waveguides [60]. Depending on the film thickness, a certain number of guided modes can be excited, which show up as minima in the reflectivity of the layer system between the critical angles of the layer and the substrate material⁸.

⁸ This effect has been exploited to produce grazing-incidence antireflection (GIAR) films for x-rays [66, 67, 68, 69, 70]. Such films have been used for nuclear resonant filtering of synchrotron radiation [71, 72].

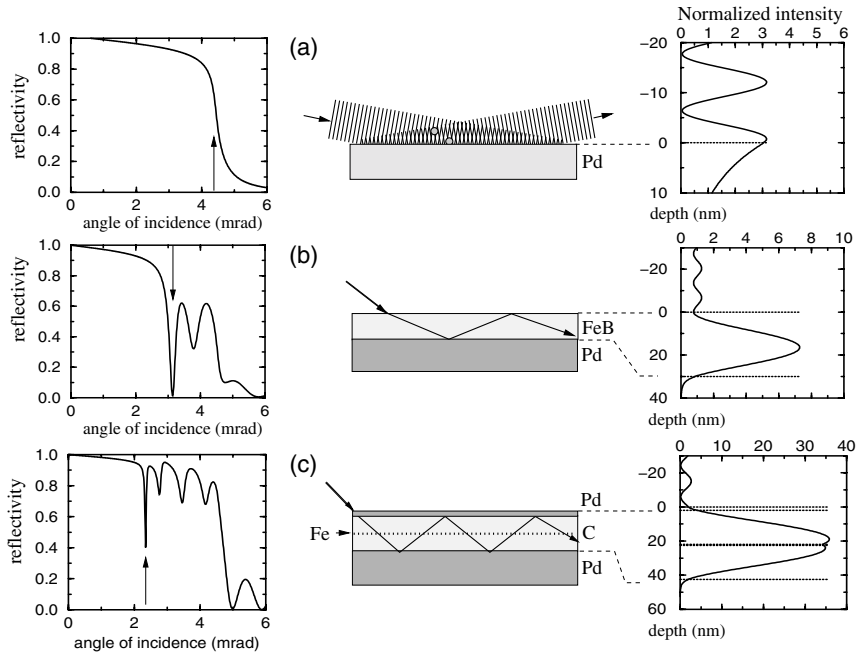


Fig. 4.20. Thin-film interference effects in grazing incidence geometry, calculated for a photon energy of 14.4 keV. The graphs show the specular reflectivity of the structures (*left column*) and the field intensity as a function of depth (*right column*). The superposition of incident and reflected waves leads to the formation of standing waves (**a**) above a total-reflecting Pd surface at the critical angle. An antinode of the standing wave coincides with the surface, (**b**) inside a thin film of FeB on a total – reflecting Pd substrate, (**c**) inside a Pd/C/Pd sandwich structure that acts as x-ray waveguide structure. Due to a very strong intensity enhancement, this geometry allows one to probe nanoparticles that are placed in the center of the C-spacer layer, for example

The angles at which the guided modes appear can be derived from the following consideration: Inside a medium with a critical angle φ_c , the z component of the wavevector is $k_{1,z} = \beta_1 k_{0,z} \approx k_0 \sqrt{\varphi^2 - \varphi_c^2}$, so that the period of the standing wave that forms inside such a medium above a total reflecting surface is given by

$$L = \frac{\lambda}{2\sqrt{\varphi^2 - \varphi_c^2}} . \quad (4.116)$$

If the film thickness is an integer multiple of this period, the incident radiation couples into guided modes.

Since the standing wave extends evanescently into the adjacent media, the number of periods within the guiding layer is reduced by about half a period.

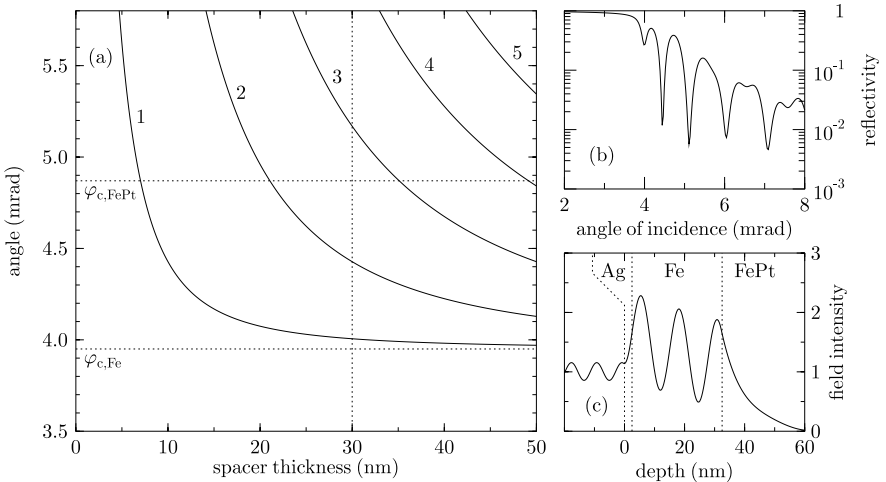


Fig. 4.21. (a) Angular position of modes inside an Ag/Fe/FePt x-ray waveguide as function of the Fe spacer layer thickness. With increasing layer thickness, more and more guided modes can be excited inside the spacer. The dashed horizontal lines are at the critical angles of total reflection φ_c for Fe and FePt at 14.4 keV. (b) Angular dependence of the reflectivity of the layer system, consisting of 2 nm Ag on 25 nm Fe on FePt. Three guided modes can be excited, appearing as minima in the reflectivity at 4.0 mrad, 4.3 mrad and 5.0 mrad. (c) Depth dependence of the radiation intensity inside the layersystem for the third-order guided mode at 5.0 mrad

Thus, the angles φ at which the guiding modes are excited follow from the condition $d \approx nL - L/2$. Inserting (4.116) into this expression, one obtains:

$$\varphi \approx \sqrt{\varphi_c^2 + \left[\frac{(2n-1)\lambda}{4d} \right]^2}. \quad (4.117)$$

This relation is shown in Fig. 4.11a for various orders n , assuming a layersystem consisting of 11 nm Fe sandwiched between a 3 nm thick Ag layer and a FePt substrate. Every signal that is derived from the electric field inside the layer can be increased by designing the layer system as an x-ray waveguide and coupling the incident beam into a guided mode by proper adjustment of the angle of incidence. This can be exploited to study the magnetism as well as the lattice dynamics of thin films and nanoparticles, as demonstrated in Sects. 4.4.3 and 5.4.1, respectively.

Intensity Enhancement from Ultrathin Probe Layers

The intensity of x-rays that are coherently scattered from an ultrathin layer is proportional to the 4th power of the normalized radiation amplitude at the position of this layer. This was the result of the theoretical considerations in

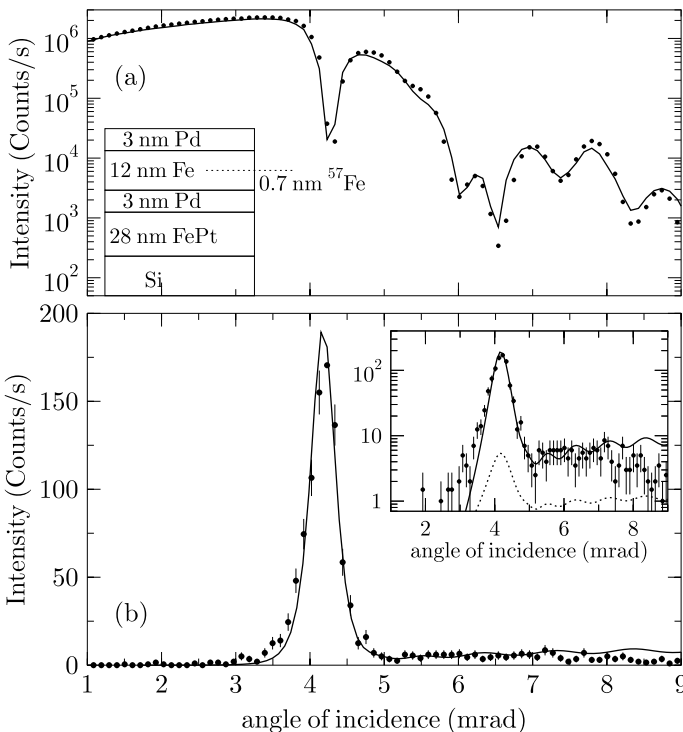


Fig. 4.22. (a) Measured electronic reflectivity from the layer system shown in the inset. In the center of the guiding layer (Fe), an ultrathin film of 0.7 nm ^{57}Fe is deposited. At the minimum at $\varphi_m = 4.3$ mrad, the radiation couples into the first-order guided mode. (b) Time-integrated delayed intensity from the layer system, recorded within a time window from 20–160 ns after excitation. The inset shows the same data on a logarithmic scale. The *dashed line* is the normalized intensity of the electric field at the position of the ^{57}Fe layer [26]

Sect. 4.1.6. Here we verify the validity of this relation, expressed by (4.62), experimentally. For this purpose, we use a thin layer of ^{57}Fe that is embedded in the guiding layer of a Pd/Fe/Pd single-mode x-ray waveguide, where the guided mode is excited at an angle of incidence of 4.3 mrad, as shown in Fig. 4.22a. Figure 4.22b shows the resonant signal from the ^{57}Fe probe layer as obtained by taking the time-integrated delayed signal within a time window ranging from 12 ns to 160 ns after excitation. Its angular dependence shows a strong peak at the angular position where the waveguide mode is excited. One observes a 36-fold enhancement of the intensity relative to the value obtained at large angles of incidence. For better illustration of relative intensities, the same data are shown in the inset on a logarithmic scale. The dashed line in the inset displays the normalized intensity of the electric field at the position

of the ^{57}Fe layer. In the antinode of this TE_0 mode the intensity is almost 6-fold enhanced relative to the intensity of the incident beam. Correspondingly, the coherently scattered signal from the probe layer experiences a 36-fold enhancement. The solid line in both graphs is obtained by squaring the values of this dashed curve and scaling them to the measured data. The very good agreement verifies the quadratic dependence on the normalized intensity at the probe layer position as established by (4.62).

To demonstrate the impact of this method for measurements using ultra-thin probe layers, a time spectrum was recorded with the sample aligned to the maximum of the delayed intensity, shown in Fig. 4.23. In this geometry the average delayed count rate was about 250s^{-1} so that a time spectrum with a very good statistical quality could be obtained within 1 hour at the NRS beamline ID18 of the ESRF. The solid line is a fit to the data according to (4.101), from which an azimuthal angle of $\phi = 22^\circ$ as defined in Fig. 4.2 was derived. In contrast, data acquisition times in conventional Mössbauer spectroscopy with a radioactive source of 50 mCi activity that lead to a comparable statistical quality are in the range of several days to weeks.

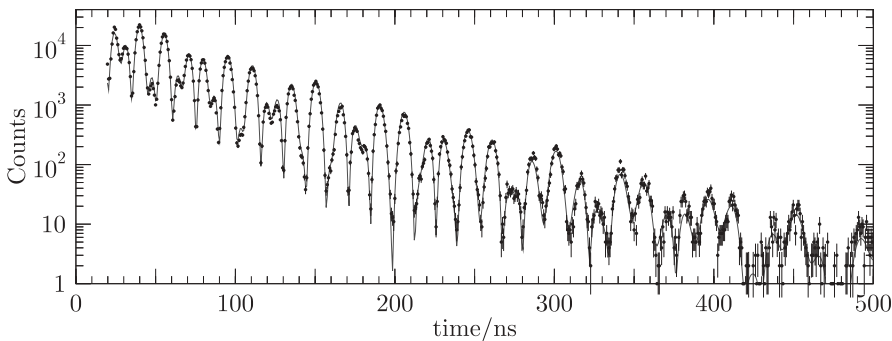


Fig. 4.23. Time spectrum of a 0.7 nm thick layer of ^{57}Fe embedded in an x-ray waveguide structure. Due to the strong intensity enhancement, this spectrum could be obtained within 1 h in single-bunch mode at beamline ID18 of the ESRF. The *solid line* is a fit according to (4.101) from which an in-plane angle $\phi = 22^\circ$, as defined in Fig. 4.2, was derived

4.4 Magnetism of Multilayers, Thin Films, and Nanostructures

4.4.1 Depth Selectivity in Resonant X-Ray Reflection

Two approaches are described in the following that enable one to obtain depth dependent information about hyperfine interactions in thin films and multilayers. While the first one relies on controlling the penetration depth via the angle of incidence, the second one is based on the placement of isotopic probe layers in the regions of the sample to be investigated, as illustrated in Fig. 4.24. While the former method still integrates over a significant part of the sample, the latter one becomes a true differential probe if the thickness of the probe layer approaches the monolayer regime.

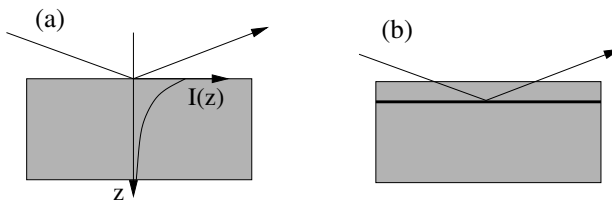


Fig. 4.24. Controlling the spatial origin of the reflected signal (a) via the penetration depth of the radiation or (b) via the placement of isotopic probe layers in the region of interest within the sample

Depth-Sensitive Spectroscopy Using Evanescent Waves

X-ray scattering in grazing incidence geometry allows one to control the thickness of the irradiated surface layer. The penetration depth of x-rays varies strongly around the critical angle and decreases to a few nanometers in the regime of total reflection, see Fig. 4.4. Therefore, measurements of the time spectra of nuclear scattering as a function of increasing grazing angle enables one to probe hyperfine interactions in surface layers of increasing thickness. Roughly speaking, the measured signal is proportional to the Laplace transform of the hyperfine interaction profile along the surface normal.

An example of such depth-sensitive hyperfine spectroscopy of an oxidized thin film is shown in Fig. 4.25. Time spectra of nuclear resonant scattering at various grazing angles were recorded from an originally 20 nm thick ^{57}Fe film oxidized for 4 h at 170°C in air [73]. For the bottom three spectra the penetration depth is comparable to the total thickness of the film. The fast beats are characteristic for $\alpha\text{-Fe}$ and a magnetic iron oxide, probably Fe_3O_4 . For the upper three spectra the penetration depth was about 2–3 nm, corresponding to about ten atomic layers. No magnetic interaction is seen in

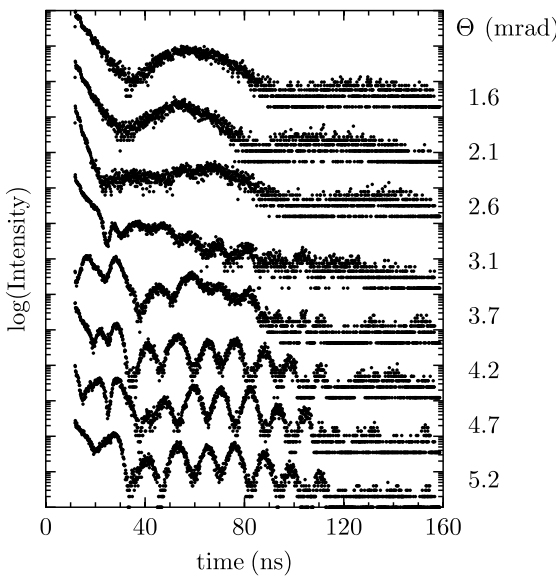


Fig. 4.25. Time spectra of grazing incidence nuclear resonant scattering from a ^{57}Fe film that was annealed in air at 170°C for 4 h. The angle of incidence is plotted on the right. (Data taken from Nagy *et al.* [73])

these spectra. The upper layer could probably be assigned to paramagnetic $\beta\text{-FeOOH}$ and to superparamagnetic $\alpha\text{-Fe}_2\text{O}_3$. The clear difference of the time spectra of nuclear scattering for the same sample at different grazing angles demonstrates the high sensitivity of this technique. Due to the short data collection times at third-generation synchrotron radiation sources, such investigations can be performed while external parameters are varied. A possible application is the in-situ study of chemical reactions in thin films, for example.

Depth-Selective Spectroscopy Using Ultrathin Probe Layers

A much higher depth resolution than in the previous example can be achieved by deposition of ultrathin resonant probe layers in the layer system under study. This approach is used since a long time to study the depth dependence of magnetic properties in thin films by conversion electron Mössbauer spectroscopy [74, 75, 76, 77, 78]. While such measurements are time consuming even with the use of strong radioactive sources, the enormous brilliance of modern synchrotron radiation sources has opened new avenues in this field [79, 80]. It has been shown that the sensitivity of this method is in the range of a single monolayer [79] or even below [80]. An advantage of this method compared to the conventional technique are the short data acquisition times, the high signal-to-noise ratio and the access to external conditions like high magnetic fields and extreme temperatures. An important application of this technique is the imaging of spiral magnetic spin structures in exchange coupled films. This will be discussed in detail in Sect. 4.4.3.

Reconstruction Methods

The determination of spatial structures from diffraction methods is closely related to the solution of the phase problem in crystallography. This can be partly solved if additional information from the sample is available. In the preceding examples this was achieved by controlling the spatial origin of the reflected radiation. But also the presence of interfaces at different depths in a layer system may provide enough phase information so that a reconstruction of depth information can be achieved. This was shown for the determination of electron density profiles of thin films [81]. The reconstruction algorithm relies on the theory of logarithmic dispersion relations [82]. In the same way as the real and imaginary part of an analytic function are connected by the Kramers-Kronig relations, one can establish a similar relation for the modulus and the phase of an analytic function. Thus, from the measurement of the scattered intensity, which is in the kinematical limit the modulus-squared of the structure function, the phase of the structure function can be reconstructed under certain conditions [83]. This method has been advantageously applied to soft-matter thin films like polymers, liquids or layered bio-organic structures like membranes [83, 84, 85]. It should be checked if this method can also be applied to determine the depth profile of hyperfine parameters from a set of measurements shown in Fig. 4.25.

4.4.2 Magnetic Superlattices

Ferromagnetic layers in magnetic layer systems like multilayers or superlattices experience a magnetic interaction that is mediated by the spacer layer between them. As a result of this coupling, such layer systems exhibit a richness of magnetic properties that is not found in bulk materials. One of the first striking discoveries in this field was the antiferromagnetic (AF) coupling of Fe layers in a Fe/Cr multilayer [86]. In some systems, a 90° orientation of successive magnetic layers is observed as a result of biquadratic coupling [87, 88, 89]. Since the exchange coupling energy between adjacent films can be of similar magnitude as the dipolar energy in modest external fields, one observes complex magnetic phase diagrams [90]. Moreover, the temperature dependence of the magnetic coupling gives rise to remarkable spin reorientation phenomena [91]. Technologically most relevant was the discovery of the giant magnetoresistance (GMR) effect that was first observed in antiferromagnetically coupled Fe/Cr superlattices [92]. This enabled a significant miniaturization of magnetic read heads and thus promoted a dramatic increase of the magnetic storage density.

Interlayer Exchange Coupling

In a phenomenological description, the interlayer coupling energy per unit area between two ferromagnetic layers is given by

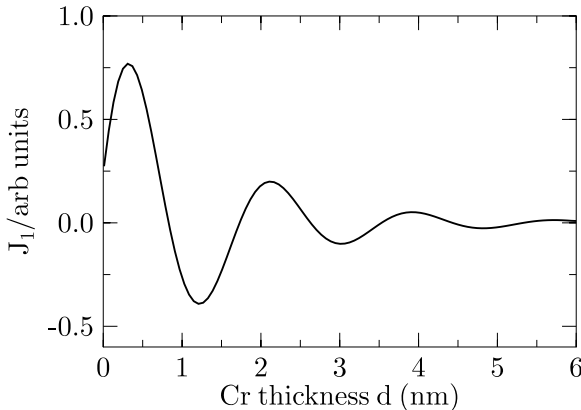


Fig. 4.26. Oscillation of the interlayer coupling strength J_1 between two Fe layers coupled through a Cr spacer layer of thickness d

$$\frac{E}{A} = -J_1 \mathbf{m}_1 \cdot \mathbf{m}_2 - J_2 (\mathbf{m}_1 \cdot \mathbf{m}_2)^2 = -J_1 \cos \theta - J_2 \cos^2 \theta , \quad (4.118)$$

where \mathbf{m}_1 and \mathbf{m}_2 are the magnetizations of the films on both sides of the spacer layer and θ is the coupling angle between both magnetizations. J_1 and J_2 describe the type and the strength of the coupling. If the first term in (4.118) dominates, then the coupling is ferromagnetic (antiferromagnetic) for positive (negative) values of J_1 . Since this term is linear in the magnetizations of the adjacent layers, this coupling is called bilinear coupling. If the second term dominates and is negative one obtains 90° -coupling, also referred to as biquadratic coupling. In general, the equilibrium configuration is determined by the condition $\partial E / \partial \theta = 0$.

Soon after the discovery of the antiferromagnetic interlayer coupling it was found that the coupling strength J_1 is an oscillatory function of the thickness of the nonmagnetic spacer layer [93]. For the Fe/Cr system, this function is shown in Fig. 4.26. The oscillatory interlayer exchange coupling is the result of an indirect exchange interaction mediated by the conduction electrons of the spacer layer. It is closely related to the Ruderman-Kittel-Kasuya-Yoshida (RKKY) interaction [94] between localized moments that is mediated by the conduction electrons of the host metal. For ferromagnetic transition metal layers separated by paramagnetic spacer layers, the description of the coupling needs to be modified. The oscillatory coupling between magnetic layers can qualitatively be explained by the formation of spin-polarized standing electron waves resulting from the spin-dependent reflection of the electrons at the boundaries of the spacer layer [95, 96]. According to this model the period of the oscillations is given by the π/k_F where k_F is the Fermi wave vector of the electrons in the spacer material. This period, however, is usually not observed in layered magnetic structures. The experimental value is typically much larger, probably due to a kind of aliasing effect [97]. Remarkably, the oscillation period for almost all paramagnetic spacer materials is around the same value of 1.0 nm [98]. The only exception is Cr with an oscillation

period of about 1.8 nm independent of the crystallographic orientation [99]. In this case the first maximum in the antiferromagnetic coupling is observed for a Cr thickness of about 1.3 nm.

Antiferromagnetic Coupling in Fe/Cr Multilayers

Antiferromagnetic multilayers can be used as model systems to study the behavior of low-dimensional magnetic structures. Scattering methods like neutron scattering, magnetic x-ray scattering or nuclear resonant scattering are particularly suited to probe the internal magnetic structure of such systems. Here we focus on the archetypal Fe/Cr multilayer with the Cr thickness adjusted to the maximum of the antiferromagnetic coupling around $d = 1.3$ nm. Due to the AF coupling of the Fe layers, the magnetic unit cell is twice as large as the chemical unit cell. This gives rise to half-order Bragg reflections that are located between the Bragg peaks of the chemical structure [100, 101]. The observation of such reflections can be used to probe antiferromagnetic interlayer coupling. For example, half-order reflections from periodic Fe/Cr multilayers were observed via neutron reflectometry [102], which served as evidence for their antiferromagnetism. Nuclear resonant scattering exhibits a similar sensitivity to magnetic superstructures as neutron scattering does.

The Fe/Cr multilayer in this experiment consisted of 20 bilayers of (1.3 nm Fe/1.0 nm Cr) on a Si wafer, produced by sputter deposition in an Argon atmosphere from a Cr target and a Fe target enriched to 95% in ^{57}Fe . The angular dependence of the electronic and nuclear reflectivity is shown in Fig. 4.27. The chemical periodicity of the multilayer with a period of 2.3 nm results in the first-order electronic Bragg reflection at a grazing angle of 0.75° . The same peak is seen also in the nuclear reflectivity. However, in contrast to the electronic reflectivity, the nuclear reflectivity shows peaks also at the angular positions of the half-order reflections, which corresponds to a spatial period of 4.6 nm. This is the period of the magnetic superstructure that results from the antiferromagnetic coupling of the neighboring iron layers.

Time spectra of the nuclear resonant reflectivity were taken at the critical angle, the half-order Bragg reflection and the first-order Bragg reflection. These spectra are shown in Fig. 4.28. The shape of the spectra can be qualitatively explained by considering the distribution of the intensity of the radiation field inside the layer stack. This is illustrated on the right side of Fig. 4.28. While at the critical angle the intensity decays exponentially with increasing depth, at the Bragg reflections one observes a standing wave with the period of the diffracting lattice planes. Thus, at the critical angle and the first-order peak the reflected signal is a coherent superposition of the contribution from all layers. Correspondingly, the time spectrum resembles to some degree the spectrum from two sites with opposite magnetization, as for the case displayed in Fig. 4.11D. For the half-order reflection, the time spectrum contains mostly the contribution from layers with the same magnetization direction, since the other layers are located in the nodes of the radiation field.

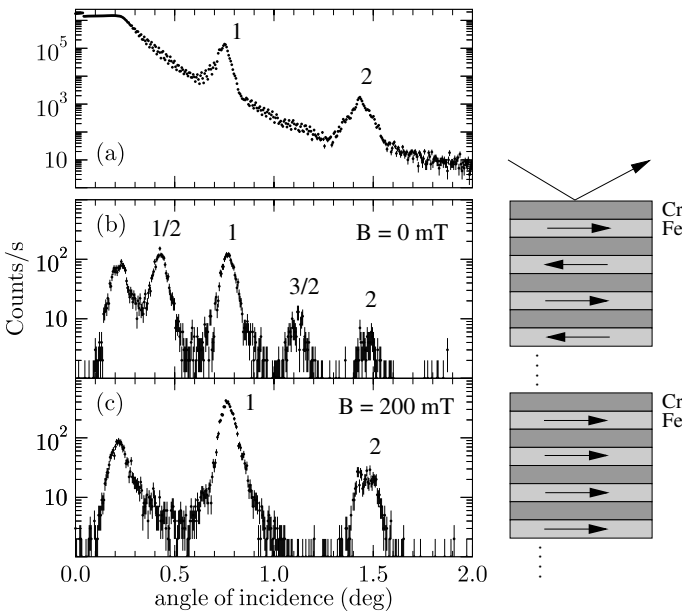


Fig. 4.27. Reflectivity of a multilayer consisting of $20 \times (1.3 \text{ nm Fe}/1.0 \text{ nm Cr})$. Numbers denote the order of the reflection. (a) Electronic charge scattering, (b) delayed nuclear resonant scattering in remanence after magnetization perpendicular to the incident wavevector. The Fe layers couple antiferromagnetically. (c) delayed nuclear resonant scattering in an external field of 0.2 T with the moments of the Fe layers aligned parallel to each other

Therefore, the corresponding time spectrum contains to a good approximation only a single frequency, as shown in Fig. 4.11A. A theoretical simulation of these data, however, is only possible with exact knowledge of the magnetic hyperfine field distribution of the Fe atoms in the vicinity of the Fe/Cr boundary [101, 103].

The Bulk Spin-Flop in a Fe/Cr Superlattice

If a uniaxial antiferromagnet is subjected to an external field, it may undergo a magnetization reorientation transition that is referred to as bulk spin-flop transition. Below a critical field \mathbf{H}_{SF} the magnetic moments are ordered in two sublattices with opposite magnetization \mathbf{M} oriented along the easy axis. If an external field above \mathbf{H}_{SF} is applied along this direction, the anisotropy-stabilized AF order becomes energetically unfavorable and a sudden magnetization reorientation takes place after which the magnetic sublattices are canted relative to the external field \mathbf{H} . Thus, the bulk spin flop constitutes an abrupt decoupling between the axis of the antiferromagnet and the easy

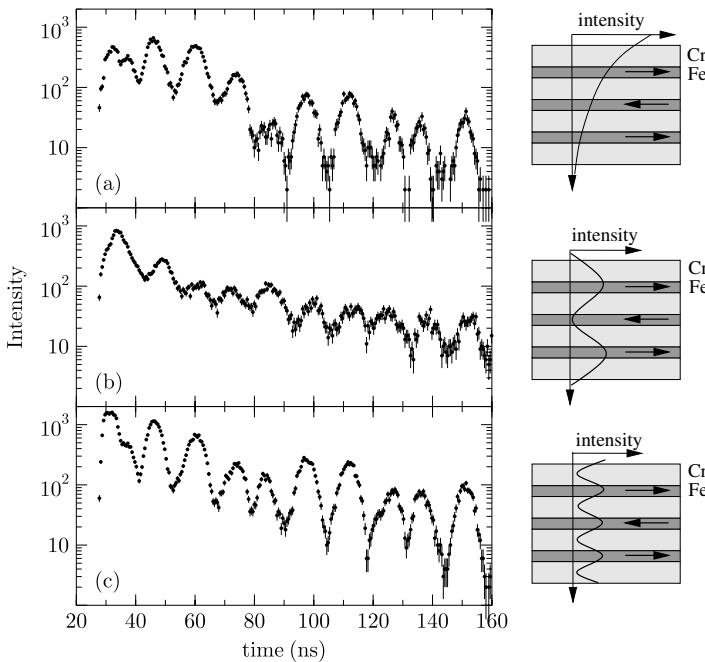


Fig. 4.28. Time spectra of nuclear resonant scattering from a Fe/Cr antiferromagnetic multilayer at three different angular positions: (a) the critical angle, (b) the half-order Bragg peak and (c) the first-order Bragg peak. On the right side the intensity of the electric field as a function of depth in the layer system is shown

axis. This first-order phase transition to the spin-flop phase was predicted by Neél [105] and experimentally confirmed almost 30 years later for a bulk antiferromagnet [106].

In artificially layered structures like AF multilayers, the spin-flop transition is modified due to the finite size of the system. It was predicted [107] and experimentally confirmed [108] that the surface undergoes a spin-flop instability at a field well below the bulk spin flop if the surface layer of the spins is antiparallel to the external magnetic field. The magnetic structure during the surface spin-flop transition was investigated via polarized neutron reflectometry for a Fe/Cr(001) multilayer [109] and a Fe/Cr(211) multilayer [110], revealing in both cases a nonuniformly canted state of the spin-flop phase.

Due to its pronounced sensitivity to the orientation of magnetic hyperfine fields relative to the photon wave vector \mathbf{k}_0 , nuclear resonant scattering is a well-suited tool to investigate such spin-flop phenomena. Here the technique was applied to study the bulk spin flop in a Fe/Cr(001) superlattice [112]. The sample consisted of 20 bilayers of (2.5 nm ^{57}Fe /1.4 nm Cr) on MgO(001).

To probe the magnetic order, the angle of incidence was adjusted to the first AF Bragg peak, and the time-integrated delayed reflectivity was recorded.

Above the critical field \mathbf{H}_{SF} , a bulk spin flop occurs with the layer magnetizations oriented $\pm 90^\circ$ relative to the external field. To study this spin flop transition, the sample was saturated in an external field parallel to the direction of the incident photon wavevector \mathbf{k}_0 . Then the external field was decreased to zero. The resulting remanent spin configuration of two AF sublattices perpendicular to \mathbf{k}_0 does not give rise to half-order Bragg peaks. This changes when an external field \mathbf{H}_S is applied perpendicular to \mathbf{k}_0 . Figure 4.29 shows a number of time-integrated reflectivity curves for increasing values of \mathbf{H}_S . The curves are normalized to the peak intensity of the first-order electronic Bragg peak. At field values above 10 mT one observes the appearance of half-order Bragg peaks, indicating the existence of AF sublattices that are aligned along the direction of \mathbf{k}_0 . Figure 4.30 displays the normalized AF peak intensity vs. the magnitude of the external field. The solid line is a guide to the eye. From this plot one derives a critical field of $H_{SP} = 13$ mT, as marked by the dashed vertical line [111].

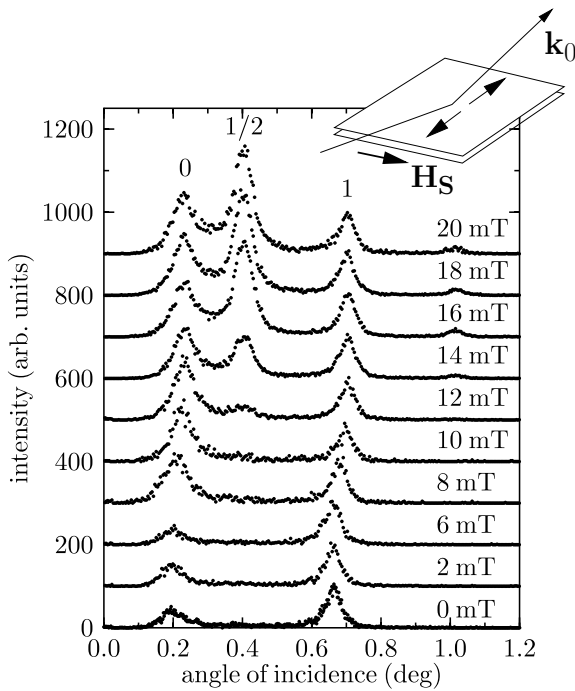


Fig. 4.29. Time-integrated nuclear resonant reflectivity of a MgO(001)/[2.5 nm $^{57}\text{Fe}/1.4 \text{ nm Cr}]_{20}$ superlattice for increasing external field \mathbf{H}_S after saturation along \mathbf{k}_0 . The experimental geometry is shown on the top. The appearance of the half-order antiferromagnetic reflections shows the re-orientation of the layer magnetizations during the bulk spin-flop transition (Data taken from Bottyán *et al.* [104])

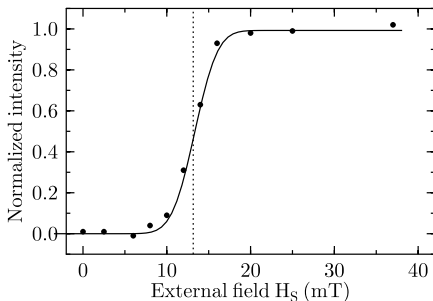


Fig. 4.30. Normalized intensity of the antiferromagnetic Bragg peak as function of the external field H_S in the geometry shown in Fig. 4.29. The *solid line* is a guide to the eye. The *dashed line* at 13 mT defines the critical field H_{SP} of the spin-flop transition (Data taken from Nagy *et al.* [111])

4.4.3 The Spin Structure of Exchange-Coupled Films

The experiment described here deals with the direct measurement of the depth-dependent spin rotation in an exchange-coupled bilayer by using ultrathin probe layers of ^{57}Fe . The samples consist of a soft-magnetic film like Fe on a hard-magnetic substrate like FePt.

Scientific Background

The magnetic properties of exchange-coupled thin films are an active field of research presently. The exchange coupling between different magnetic phases within thin films, multilayers and nanoparticles plays an important role in the development of novel functional magnetic nanostructures [113, 114]. The functionality of such systems relies critically on the magnetic spin structure that develops in external magnetic fields, in particular, if (spin-dependent) electronic transport is considered [115]. A very prominent example is the giant magnetoresistance effect that is observed in exchange-coupled magnetic multilayers [92, 116], and its application in high-density magnetic storage media. Moreover, nanocomposite materials consisting of exchange-coupled soft- and hard-magnetic phases are promising candidates for new permanent magnetic materials with magnetic energy products beyond 1 MJ/m³ [117]. Thin bilayers consisting of a hard- and a soft-magnetic material are ideal model systems to investigate the fundamental properties of this coupling mechanism. As a result of the exchange interaction, the magnetization of the soft-magnetic film at the interface is pinned to the hard-magnetic film which is assumed to exhibit a unidirectional anisotropy (e.g., the remanent state after saturation). With increasing distance from the interface, the exchange coupling becomes weaker and the magnetization may rotate under the action of an external field. If, for example, the external field is applied perpendicularly to the magnetization direction of the hard layer, the magnetic moments in the soft layer arrange in a spiral structure along the normal, as shown schematically in Fig. 4.31. Due to the reversible nature of this alignment, this is called the exchange-spring effect [19, 118]. While a number of micromagnetical models

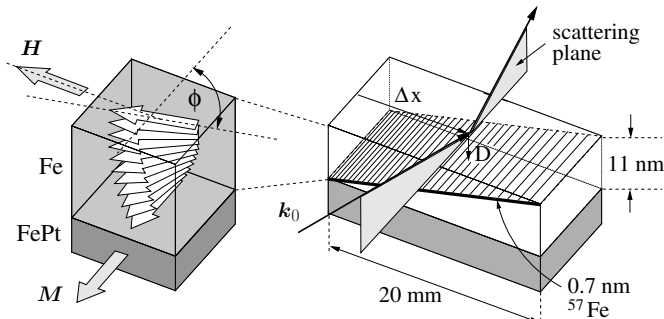


Fig. 4.31. *Left:* Scheme of the spin structure in an exchange-spring bilayer consisting of a soft-magnetic layer (Fe) on a hard-magnetic layer (FePt) with uniaxial anisotropy. An external field \mathbf{H} is applied perpendicularly to the remanent magnetization \mathbf{M} of the hard layer. *Right:* To image the resulting magnetic spiral, a tilted ultrathin probe layer of ^{57}Fe is deposited within the soft layer. The magnetic properties in depth D of the film are probed by adjusting the transverse coordinate Δx of the sample relative to the incident beam

have been developed to describe this behavior [19, 119, 120], direct measurements of the actual spin structure are scarce. Methods applied so far like polarized neutron scattering either probe the whole volume of the sample⁹ or they are too surface sensitive as in case of electron scattering.

Sample Preparation and Characterization

The sample is an exchange-coupled bilayer consisting of 11 nm Fe on 30 nm hard-magnetic $\text{Fe}_{55}\text{Pt}_{45}$ (further denoted as FePt) with unidirectional magnetization. A schematic view of the sample is shown in Fig. 4.31. The layers were deposited by rf-magnetron sputtering in an Ar atmosphere of 1.5×10^{-2} mbar on a superpolished Si wafer. FePt was sputtered from a composite target consisting of a number of Pt chips on a high-purity Fe foil to obtain the desired composition. After deposition, the layer was annealed for 30 min at 800 K to form the hard-magnetic tetragonal L1₀ phase [122, 123]. The rms surface roughness of the FePt layer was determined by x-ray reflectivity to be less than 0.5 nm, indicating that the grain size did not increase too much upon annealing. The x-ray reflectivity of a 30 nm thick FePt film is shown in Fig. 4.32. The pronounced shape of the Kiessig fringes over a large angular interval indicates the good structural quality of the FePt film. Hysteresis loops were measured via the magneto-optical Kerr effect (MOKE), as shown in Fig. 4.32, from which a coercivity of 0.96 T at room temperature was determined. The hysteresis loop of the Fe/FePt bilayer shows the coupling of

⁹ In this case, however, special reconstruction techniques allow one to extract depth-resolved spin structures [121].

both layers that allows for a reversible cycling of the loop below the switching field of the hard layer. To image the magnetic spin structure within the Fe layer, a tilted probe layer is embedded in the Fe, as shown schematically in Fig. 4.31. Such a sample is prepared in the following way: First, a wedge-shaped Fe film with a slope of 0.5 nm/mm is produced by linear variation of the exposure during sputter deposition of Fe. After growth of a 0.7 nm thick ^{57}Fe probe layer the same wedge was deposited with opposite slope. Different depths D in the sample can thus be probed by adjusting the displacement Δx of the sample transversely to the incident beam. Finally, the layer system was coated with 3 nm Ag to prevent oxidation.

Experiment

The experiment was performed in single-bunch filling mode at the Nuclear Resonance beamline ID18 of the ESRF [124]. At the sample position the beam cross section was $150 \mu\text{m}$ (vertical) $\times 200 \mu\text{m}$ (horizontal). The sample was magnetically saturated in an external field of 2.3 T so that the remanent magnetization of the FePt layer was oriented along \mathbf{k}_0 , as shown in Fig. 4.31. It was mounted in a cryo-magnet system with an in-plane external field perpendicular to \mathbf{k}_0 where it was cooled to 4 K to increase the coercivity and the remanence of the hard-magnetic layer [125]. The angle of incidence was then adjusted to maximize the delayed intensity via coupling of the radiation into

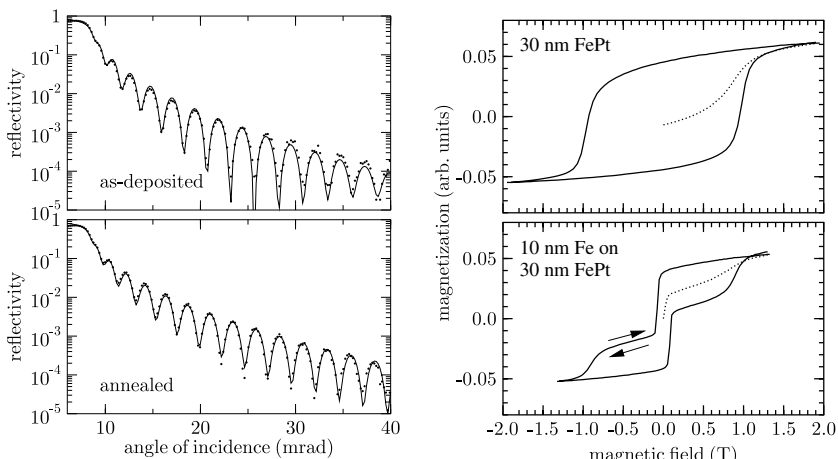


Fig. 4.32. Characterization of the samples. *Left:* X-ray reflectivity at 8.4 keV measured before and after annealing for 30 min at 800 K . Solid lines are simulations of the data, yielding a rms-roughness of 0.42 nm and 0.49 nm before and after annealing, respectively. *Right:* Hysteresis loops of a 30 nm thick hard-magnetic FePt film (*top*) and a layer system consisting of 10 nm Fe on 30 nm FePt (*bottom*), recorded via the magneto-optical Kerr effect (MOKE)

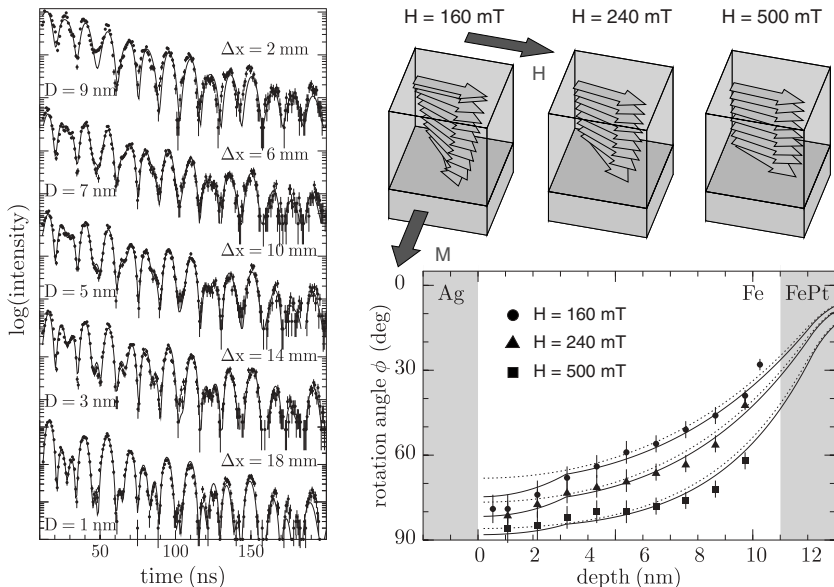


Fig. 4.33. *Left:* Measured time spectra of grazing incidence reflection in a perpendicular magnetic field of $H = 160$ mT at various lateral positions Δx . The change in the beat pattern reflects the rotation of the magnetization direction as a function of depth D . *Solid lines* are theoretical simulations. *Right:* Depth dependence of the spin rotation in the Fe layer for external magnetic fields of 160 mT (●), 240 mT (▲), and 500 mT (■). *Dashed lines* are simulations according to the model outlined in the text, assuming homogeneous magnetic properties throughout the layer. The *solid lines* are simulations assuming a reduced exchange coupling constant within a 3 nm wide region of the Fe layer close to the Ag/Fe boundary

a waveguide mode of the layer system. The superposition of waves that are multiply reflected at the Ag/Fe/FePt boundaries led to a significant x-ray flux enhancement inside the Fe layer [20], as described in Sect. 4.3.3. This resulted in an average resonant (delayed) count rate of up to 200 s^{-1} , so that time spectra with very good statistical quality were obtained within only 15 min. A series of time spectra taken at selected transverse displacements Δx is shown in Fig. 4.33. The beat pattern in the spectra undergoes characteristic changes that reflect the rotation of the magnetization as function of depth. With increasing Δx the time spectra probe the Fe layer from the FePt interface up to the Ag interface. At $\Delta x = 2$ mm the time spectrum exhibits almost only a single beat frequency due to the alignment of the magnetization almost along the incident wavevector. With increasing Δx the rotation angle ϕ increases and the modulation becomes more complex due to the admixture of three more frequencies.

Results and Discussion

From the fit of the measured data according to (2.27) the planar rotation angle ϕ of the magnetization in depth D of the Fe layer was derived¹⁰. The evolution of the magnetization rotation between these positions is plotted in Fig. 4.33. Data were recorded for external fields of $H = 160$ mT, 240 mT and 500 mT, all within the reversibility range of the hysteresis loop shown in Fig. 4.32. This behavior can be simulated by application of a one-dimensional micromagnetic model [19]. The layer system is divided into N sublayers of thickness $d = (d_{\text{Fe}} + d_{\text{FePt}})/N$. The total magnetic energy of this layer system is given by the sum of the magnetic exchange and anisotropy energies and the dipolar interaction with the external field, respectively:

$$E = - \sum_{i=1}^{N-1} \frac{A_{i,i+1}}{d^2} \cos(\phi_i - \phi_{i+1}) - \sum_{i=1}^N (K_i \cos^2 \phi_i + H M_i \cos(\phi_i - \phi_H)) \quad (4.119)$$

In this experiment the external field H is oriented at an angle $\phi_H = \pi/2$. $A_{i,i+1}$ is the exchange constant between sublayers i and $i + 1$, K_i the anisotropy constant and M_i the magnetization of the i th sublayer. To find the equilibrium spin configuration, the magnetic energy has to be minimized for each of the ϕ_i . For a given sublayer i the new orientation ϕ'_i is determined from the condition $\partial E / \partial \phi_i = 0$:

$$\tan \phi'_i = \frac{A_{i,i+1} \sin \phi_{i+1} + A_{i-1,i} \sin \phi_{i-1} + d^2 H M_i \sin \phi_H}{A_{i,i+1} \cos \phi_{i+1} + A_{i-1,i} \cos \phi_{i-1} + 2d^2 K_i \cos \phi_i + d^2 H M_i \cos \phi_H} \quad (4.120)$$

This procedure is repeated all over until equilibrium for all sublayers is reached¹¹. Solid lines in Fig. 4.33 are the results of the simulation, showing a reasonable agreement with the measured data. For the FePt layer we have used the parameters $K_h = 4.0 \cdot 10^7$ erg/cm³, $M_h = 1100$ emu/cm³, and $A_h = 1.0 \cdot 10^{-6}$ erg/cm, as given in [126]. For the Fe layer we have assumed $K_s = 1.0 \cdot 10^3$ erg/cm³, $M_s = 1900$ emu/cm³, and $A_s = 1.0 \cdot 10^{-6}$ erg/cm. For the exchange constant at the interface we have assumed $A_{int} = (A_h + A_s)/2$. The anisotropy constant K_s was estimated from the coercivity of a single Fe layer. Due to the polycrystalline nature of the Fe layer the volume anisotropy becomes negligible, resulting in an anisotropy constant that is more than two orders of magnitude smaller than the bulk value [19]. The exchange constant A_s of the Fe layer was the only parameter that had to be adjusted in

¹⁰ The magnitude of the magnetic hyperfine field at 4 K is 33.8 T. Its temperature dependence as measured by nuclear forward scattering [16] is displayed in Fig. 4.42.

¹¹ Note, that $A_{0,1} = A_{N,N+1} = 0$.

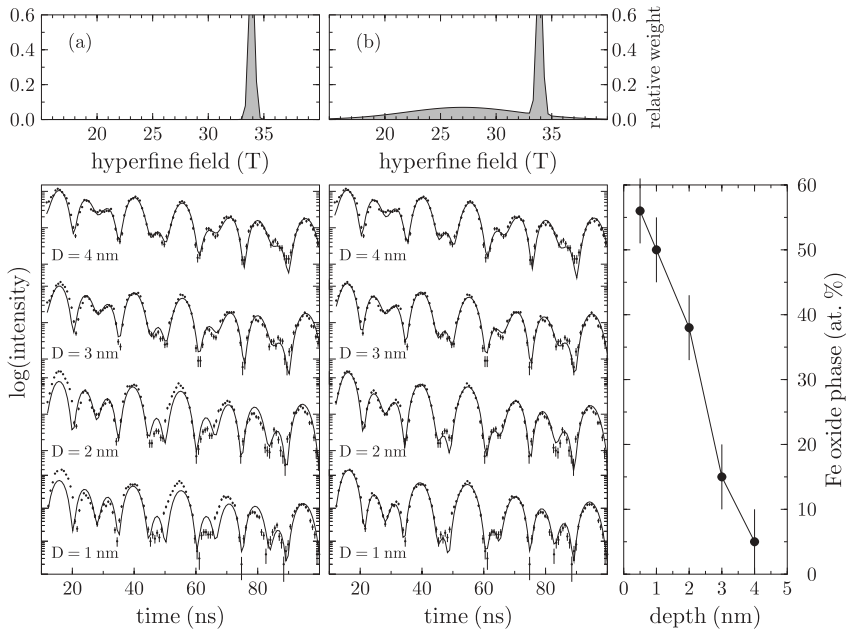


Fig. 4.34. Effect of a hyperfine field distribution on the measured time spectra. In the *left column* the time spectra were simulated assuming a single hyperfine field of 33.8 T. Big discrepancies between the data and the best fits can be seen, especially close to the Ag/Fe interface (small values of D). The *middle column* shows the same time spectra that were simulated with an additional field distribution around 27 T, as shown in the diagram *above*. The relative amount of Fe in this phase decreases with increasing distance from the surface, as shown on the *right*

the simulation procedure¹². Other parameters like A_{int} cannot account for the observed behavior of the magnetization. Very likely, A_s depends on the microstructure of the film that is determined by the deposition process. In regions close to the top of the Fe layer the measured rotation angle deviates significantly from the simulations. The dashed lines are simulations under the assumption that the exchange constant is reduced to $A_s = 3.0 \cdot 10^{-7}$ erg/cm in the top 3 nm of the Fe layer. This may be due to diffusion of oxygen through the Ag and the formation of a native Fe oxide or due to interdiffusion of Ag and Fe. To support this interpretation, the time spectra from the probe layer close to the Ag/Fe interface are evaluated in two different ways: a) With a single, unidirectional hyperfine field of 33.8 T, and b) with an additional broad hyperfine field distribution at lower fields. Both cases are displayed in Fig. 4.34. The broad component around 27 T (a Gaussian with $\sigma = 5$ T) is

¹² Values quoted in the literature are $A_s = 2.8 \cdot 10^{-6}$ erg/cm [19] and $A_s = 1.9 \cdot 10^{-6}$ erg/cm [127].

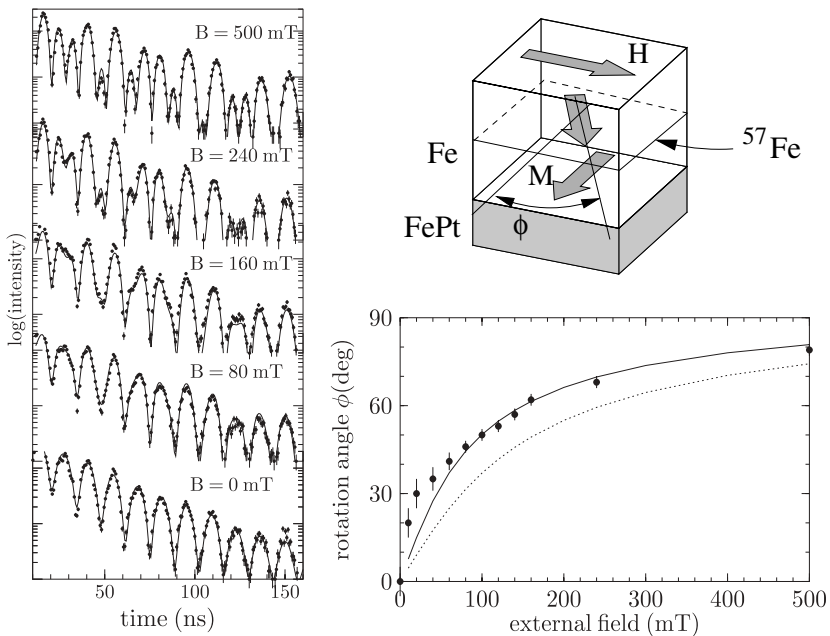


Fig. 4.35. *Left:* Measured time spectra of grazing incidence reflection at various external magnetic fields. With increasing field the magnetic moment of the Fe aligns towards the external field. *Solid lines* are theoretical simulations. *Right:* Rotation angle in the center of the Fe layer as function of the external magnetic field with simulations for $A_s = 1.0 \cdot 10^{-6}$ erg/cm (*solid line*) and $A_s = 2.8 \cdot 10^{-6}$ erg/cm (*dashed line*)

characteristic for a native Fe oxide [128], that is ferromagnetic and aligned with the magnetization of the Fe. One clearly sees a significant discrepancy between the data and the simulation for case a), particularly in regions very close to the interface. The assumption of the hyperfine field distribution of case b) leads to a much better agreement. From the evaluation of the time spectra we obtain a decreasing fraction of the interface phase with increasing distance from the Ag/Fe boundary, as shown in the right column of Fig. 4.34.

To confirm the validity of our model, we have measured the rotation angle in the center of the Fe layer as function of external field, shown in Fig. 4.35. The simulation (solid line) demonstrates the significance of the exchange constant of the soft layer as the relevant parameter for the exchange spring behavior in this system. For comparison, the dashed line represents the simulation for an exchange constant of $A_s = 2.8 \cdot 10^{-6}$ erg/cm as given in [19]. The remaining discrepancies are most likely due to the formation of magnetic domains at low fields.

Conclusion

The experiment described here has shown that ultrathin probe layers can be used to determine magnetic properties in thin films with very high depth resolution. An intrinsic advantage of this technique is that isotopic probe layers do not disturb the electronic and magnetic configuration of the system. The enormous brilliance of third-generation synchrotron radiation sources allows to obtain data with very good statistical quality in short data acquisition times. X-ray interference effects that take advantage of the sample geometry can provide an additional boost of the intensity at the location of the probe layer. This allows one to decrease the probe-layer thickness even further to obtain almost atomic resolution. In this case, however, one has to ensure that the signal is not contaminated by contributions from the residual content of the resonant isotope in the surrounding material. In this case, the surrounding material should be depleted from the resonant isotope. If these conditions are fulfilled, the method can also be applied to Mössbauer isotopes like ^{149}Sm , ^{161}Dy and ^{151}Eu , for example, that are particularly interesting as constituents of new magnetic materials.

4.4.4 Magnetism of Fe Islands on W(110)

The magnetism of self-organized nanostructures and clusters is an active field of research due to a rich variety of novel properties that are not found in the bulk [129, 130]. An understanding of these properties is highly desirable because of fundamental aspects of nanoscale magnetic ordering in general and possible applications in high-density magnetic recording devices and magnetoelectronics in particular. A particular route for production of nanosized particles is the growth via condensation from the gas phase [131], colloidal agglomeration in solution [132] or the self-organized formation on single-crystalline surfaces [130, 133]. In this experiment, the latter route was taken to produce single-crystalline, island-shaped Fe particles on a W(110) surface [40]. These islands, enriched to 95% in ^{57}Fe , were prepared under ultrahigh-vacuum conditions by thermal evaporation. Deposition of a few monolayers and subsequent heating to about 700 K leads to the formation of separated and well ordered 3D islands [134], shown in Fig. 4.36. The surface of the islands is atomically flat, their long axis is aligned along the in-plane W[001] direction. They are of bcc(110) type with the lattice constant of bulk Fe, as confirmed via x-ray diffraction, shown in Fig. 4.37a. To prevent oxidation, the samples were capped with about 5 monolayers of Ag.

Spin Structure of the Fe Islands

To determine the magnetic ordering in the Fe islands, time spectra of nuclear resonant scattering in grazing incidence geometry were taken. The sample was illuminated at an angle of 5 mrad that is close to the critical angle of the W substrate where the resonant signal acquires its maximum, as

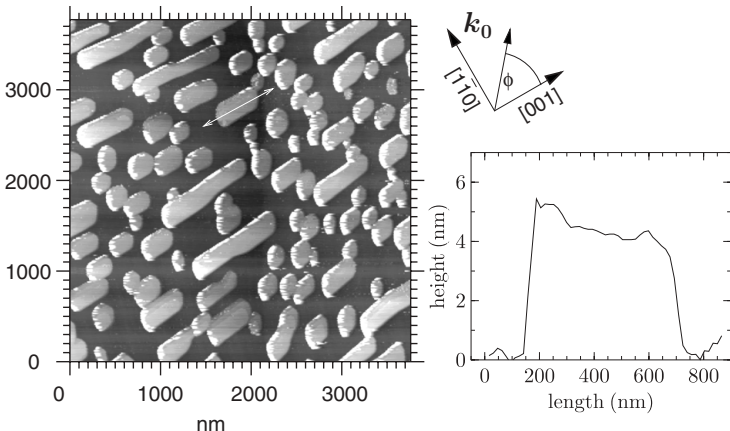


Fig. 4.36. STM image of Fe Islands on W(110). The long axis of the islands points along the W[001] in-plane direction. On the *right side* a cross section of a typical island as marked by the *white arrow* is shown

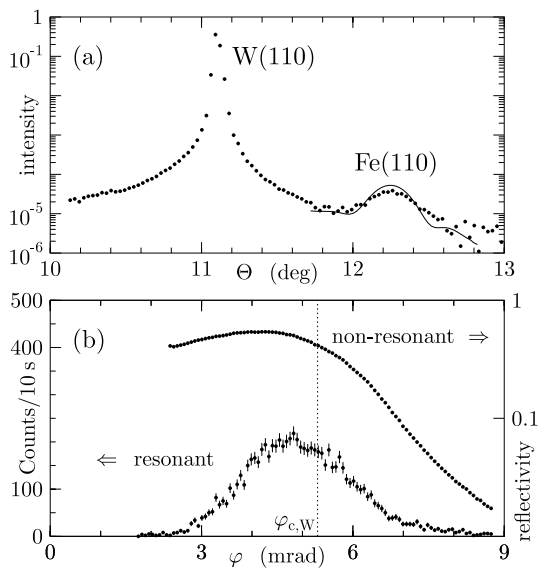


Fig. 4.37. (a) X-ray diffraction from the (110) reflection of the W substrate and the Fe islands. The *dotted line* is a calculation according to the dynamical theory of x-ray diffraction, proving the good crystalline quality of the Fe islands. (b) Non-resonant (*upper curve*) and resonant reflectivity (*lower curve*) of the sample

shown in Fig. 4.37b. A total delayed count rate of about 40s^{-1} was obtained on average so that time spectra with very good statistical quality could be obtained in about 30 min¹³. Before the measurements, the sample was remanently magnetized along the in-plane [001] direction by a pulsed

¹³ The experiment was performed in single-bunch mode at the Nuclear Resonance beamline (ID18) of the ESRF [124].

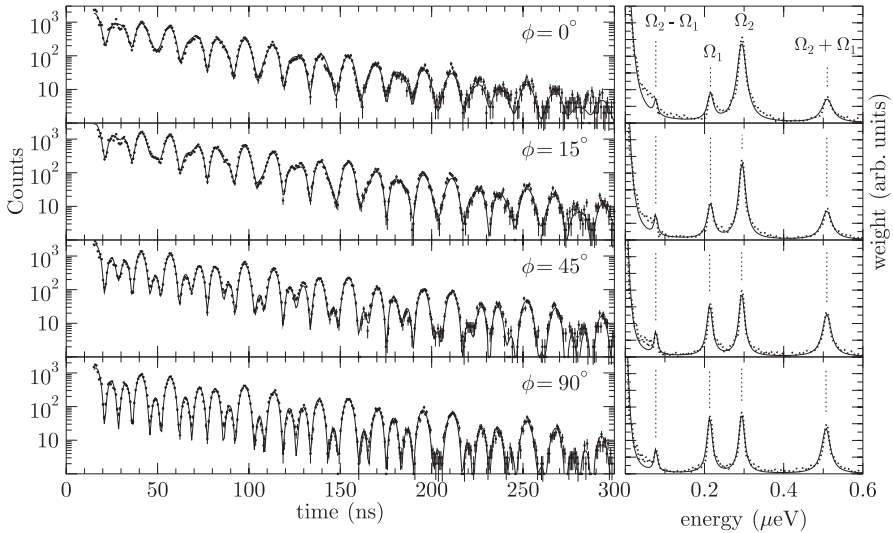


Fig. 4.38. *Left:* Time spectra of NFS from Fe Islands on W(110) at various azimuthal angles of the in-plane [001] direction relative to the incident wavevector. The *solid lines* are theoretical simulations. *Right:* Fourier transforms of the measured data, fitted with Lorentzian functions (*solid lines*) [40]

magnetic field of about 50 mT. As discussed in Sect. 4.2.2, a single measurement is not sufficient to determine the magnetic structure in the sample uniquely. For that reason time spectra were taken at various azimuthal orientations ϕ of the sample, as shown in Fig. 4.38. The beat pattern undergoes characteristic changes that reflect the rotation of the sample magnetization. Based on the elongated shape of the islands one would expect the magnetization of the islands to point along the in-plane [001]-directions. Then, upon azimuthal rotation a transition between the geometries shown in Figs. 4.11A and C takes place, where $\phi = 90^\circ$ corresponds to Fig. 4.11C. However, the measured time spectra for $\phi = 0^\circ$ and $\phi = 90^\circ$ slightly deviate from those displayed in Figs. 4.11A, C. This indicates that the spin structure of the islands cannot be simply unidirectional.

For a detailed analysis, the reconstruction algorithm derived in Sect. 4.2.5 will be applied here. In the right panel of Fig. 4.38 the Fourier transform of the measured time spectra is shown. The peaks at the frequencies Ω_1 , Ω_2 , $\Omega_1 - \Omega_2$, and $\Omega_1 + \Omega_2$ clearly display the dependence of the various spectral components on the azimuthal angle. Their energetic positions correspond to those of the $\Delta M = \pm 1$ transitions for a magnetic hyperfine field of 33.3 T, as described by (4.76). From these energy spectra one can already exclude an admixture of a perpendicular spin orientation. This would lead to Fourier components at $\omega = 1/2\Omega_1$, $\Omega_1 - 1/2\Omega_2$, and $\Omega_1 + 1/2\Omega_2$. Within the statistical quality of the data, such contributions are below a relative weight of

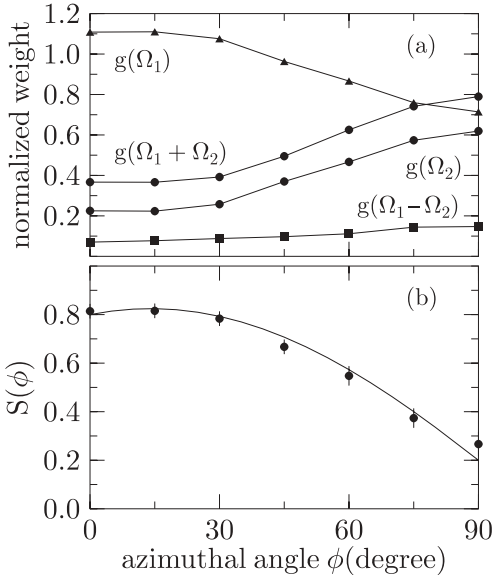


Fig. 4.39. (a) Dependence of the normalized Fourier components shown in Fig. 4.38 on the azimuthal angle ϕ . (b) The function $S(\phi)$ as obtained from the data in a) according to (4.105). The solid line is a fit of (4.106) to the data [40]

0.03. The angular dependence of the weights $g(\Omega_i)$ is shown in Fig. 4.39a, from which the function $S(\phi)$ was derived as shown in Fig. 4.39b. From a fit of (4.106) to the measured function $S(\phi)$, the components m_x and m_y are determined to be $m_x = 0.19(3)$ and $m_y = 0.77(3)$. These values are the result of a linear combination of magnetic sublattices:

$$(m_x, m_y) = \sum_i p_i \mathbf{m}_i \quad (4.121)$$

that has to fulfill the conditions

$$\sum_i p_i = 1 \quad \text{and} \quad |\mathbf{m}_i| = 1 \quad (4.122)$$

From these constraints it immediately follows that the data cannot be described by a single magnetic sublattice only. The assumption of two sublattices allows the following reconstruction:

$$\mathbf{m} = 0.8 \hat{\mathbf{u}}_{[001]} + 0.2 \hat{\mathbf{u}}_{[1\bar{1}0]} \quad (4.123)$$

where $\hat{\mathbf{u}}_{[001]}$ and $\hat{\mathbf{u}}_{[1\bar{1}0]}$ are unit vectors along the in-plane $[001]$ and $[1\bar{1}0]$ directions, respectively. It can be shown that this is a unique reconstruction for this particular case. Other configurations like closure domains with more than two magnetic sublattices can be excluded here. We can therefore conclude that the Fe islands are laterally separated, single magnetic domains.

There are two types of islands, the magnetization of which is aligned in the in-plane $[001]$ direction and $[1\bar{1}0]$ direction, with relative weights of 0.8 and 0.2, respectively. Most probably, this distribution of magnetization directions

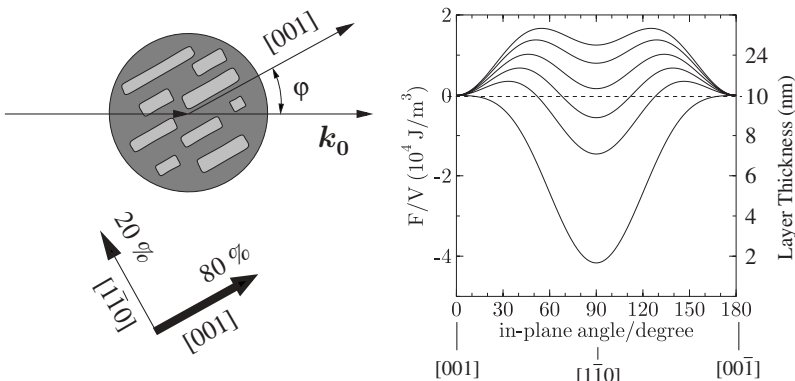


Fig. 4.40. Spin structure of the Fe islands on W(110). 80% of the moments are oriented along the in-plane [001] direction while 20% are along the [1 $\bar{1}$ 0] direction. The graph on the right shows the free magnetic energy as a function of azimuthal (in-plane) orientation. The minimum of the curve indicates the easy direction of magnetization. The reorientation of the easy magnetization direction is a function of the Fe thickness (after *Gradmann et al.* [135])

results from the interplay of different anisotropy energy terms. In this case we have to consider the contributions of the magneto-crystalline, the magneto-elastic and the surface anisotropy. However, in the first experimental study of the magnetic anisotropy of closed Fe films on W(110) only the contributions of magneto-crystalline and surface anisotropy had been taken into account [135]. In that case the total free energy F per volume V in the (110) plane depending on the Fe film thickness d can be written as

$$\frac{F}{V} = \frac{K_1}{4} (\sin^2 2\varphi + \sin^4 \varphi) - \frac{1}{d} (K_{s,p}^{(1)} + K_{s,p}^{(2)}) \sin^2 \varphi$$

with K_1 being the first order magneto-crystalline anisotropy constant and $K_{s,p}^{(1)}$ and $K_{s,p}^{(2)}$ describing the surface anisotropies of both interfaces of the film, respectively. Whereas the surface anisotropy, favoring the easy axis along [1 $\bar{1}$ 0], dominates for very small film thicknesses, the magneto-crystalline part forces the magnetization parallel to the in-plane [001] direction. Both contributions are balanced at around a thickness of 50 monolayers where the magnetization rotates from [1 $\bar{1}$ 0] for thin films to the bulk easy axis [001]. In case of a Ag capping layer on top of the iron film the surface anisotropy constant is smaller compared to the iron-vacuum interface, leading to the spin reorientation already at around 36 Fe monolayers ($K_{s,p}^{\text{Fe/Ag}} = 4.0 \cdot 10^{-5} \text{ J/m}^2$, $K_{s,p}^{\text{Fe/UHV}} = 6.5 \cdot 10^{-5} \text{ J/m}^2$ [135]). A continuation of this experimental study revealed, however, that due to the quite large Fe-W lattice mismatch of 9.1%, the contribution of the magneto-elastic anisotropy is in the same range as the first-order magneto-crystalline energy [136, 137]. However, in our case the structural characterization of the islands using LEED and X-ray diffraction

(see Fig. 4.36) shows that the Fe lattice is completely relaxed and strain-free both in horizontal and vertical direction, respectively, leading to the expectation that the magneto-elastic energy is negligible.

In the case of separated islands which exhibit a direction of preferred growth, the in-plane shape anisotropy has additionally to be taken into account. The magnetization along the orientation of the islands ([001]) should energetically be favored, particularly in islands with high aspect ratios. Since this shape anisotropy is a function of the aspect ratio, it exhibits a statistical distribution. Thus, the distribution of magnetization directions directly reflects the statistics of island shapes and the corresponding contributions of the magnetic shape anisotropy. It turns out, that this contribution is of no relevance in smaller, spherically shaped islands, where the easy magnetization axis points along the [1 $\bar{1}$ 0] direction as in the case of closed thin iron films on W[110]. In islands with higher aspect ratios the magneto-crystalline and the shape anisotropy, which favor the [001] axis, may together overcome the surface anisotropy. Due to the additional contribution of the pronounced shape anisotropy the reorientation of the magnetization from the [1 $\bar{1}$ 0] to the [001] axis takes place at lower thicknesses than in the closed film.

Spinwave Quantization in Fe Islands

In any magnetic material, the decay of the spontaneous magnetization with increasing temperature is the result of two types of magnetic excitations: a) One-electron excitations from the majority spin band into an empty state in the minority spin band (Stoner excitations) and b) spin waves or magnons which are propagating collective excitations of the precessing spin moments. At low temperatures the density of magnon states is much larger than that of Stoner excitations. Therefore, the temperature dependence of the spontaneous magnetization in this range is completely determined by the spin-wave spectrum.

It is to be expected that propagating excitations are strongly influenced by the geometry of the sample when its dimensions are comparable to their wavelength. In this section we investigate the temperature dependence of the spontaneous magnetization in the Fe islands on W(110) shown in Fig. 4.36. A number of selected time spectra taken at various temperatures is shown in Fig. 4.41. With decreasing temperature one observes an increasing temporal beat frequency, as indicated by the dashed vertical line in Fig. 4.41. Due to the very good statistical quality of the data, the value of the hyperfine field could be determined with an accuracy of about 1%. The solid lines are fits to the data, assuming the spin structure of the islands as determined in the previous section. No indication was found that the orientation of the magnetic fields in the islands changed as a function of temperature. Thus, the data were fitted with the magnetic hyperfine field and the recoilless fraction as the only free parameters. The resulting temperature dependence of the hyperfine field is shown in Fig. 4.42.

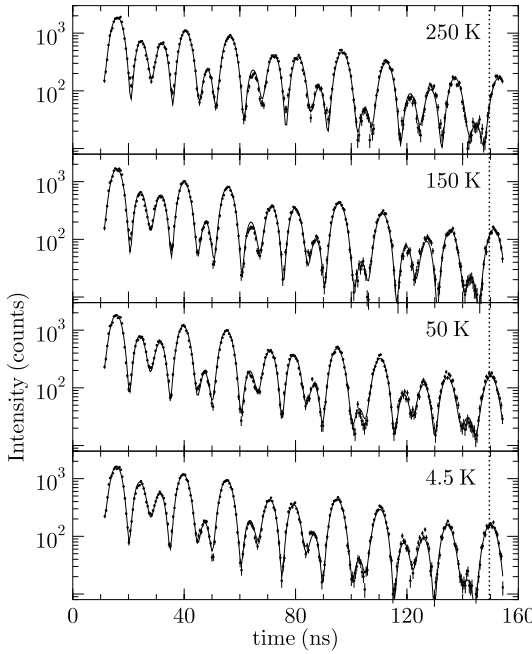


Fig. 4.41. Time spectra of the Ag-capped Fe islands as a function of temperature. The evaluation shows that the spin structure does not change as a function of temperature. The magnetic hyperfine field derived from the data is shown in Fig. 4.42. (Figure adopted from Senz *et al.* [138])

Spin waves in cubic crystals are most easily excited perpendicularly to the most dense lattice planes, i.e. the (111) planes in fcc lattices and the (110) planes in bcc lattices [139]. We assume that the spinwave eigenstates depend on the square of the wavenumber as in the bulk metal, i.e.,

$$E = Dq^2, \quad (4.124)$$

where $D = 2JSa^2 = 2.8 \text{ meV nm}^2$ is the spin-wave stiffness parameter for bcc Fe [140] with $J = 11.9 \text{ meV}$ being the exchange constant, $S = 1.5$ the atomic spin, and $a = 2.87 \text{ \AA}$ being the cubic lattice constant. The quadratic approximation is well justified for bulk iron, where no optical spin-wave branch evolves and the occupation number for high-energy spin-waves is relatively small, particularly at low temperatures [141, 142, 143]. With increasing temperature, the decrease of the magnetization is proportional to the number of excited magnons:

$$M(T) = M(0) - \int P(E) n(E, T) dE, \quad (4.125)$$

where $P(E)$ is the density of spin-wave states and $n(E, T)$ is the Bose occupation number. In case of a continuous distribution of spin-wave states as in the bulk with $P(E) = (V_0/4\pi^2) D^{-3/2} \sqrt{E}$, this equation leads to the well-known temperature dependence given by Bloch's law [144], i.e.,

$$M(T) = M(0)(1 - B T^{3/2}) \quad \text{with} \quad B = 2.6149 V_0 \left(\frac{k_B}{4\pi D} \right)^{3/2}, \quad (4.126)$$

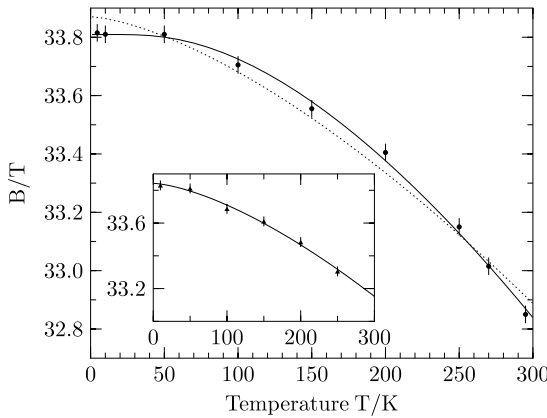


Fig. 4.42. Temperature dependence of the magnetic hyperfine field in the Fe(110) islands as determined from the evaluation of the data in Fig. 4.41. The *solid line* is a fit of the data according to (4.129). The *dashed line* is the best fit to the data assuming Bloch’s $T^{3/2}$ law. The inset shows the corresponding data for bulk bcc Fe, taken from Bergmann *et al.* [16], fitted with the $T^{3/2}$ law

where V_0 is the volume per atom and $B = 3.5 \cdot 10^{-6} \text{ K}^{-3/2}$ for bcc bulk Fe.

In a confined space with linear dimension d only discrete wavenumbers are possible where the largest value is $q = 2\pi/d$. The first excited level of the quantized spin wave spectrum is then given by [139, 145]:

$$\Delta E = D \left(\frac{\pi}{d} \right)^2. \quad (4.127)$$

In the low-temperature limit only the first few eigenstates are populated. To describe the gap in the spin wave spectrum at low energies, the Bose occupation number is written as:

$$n(E, T) = \frac{1}{\exp[(E + \Delta E)/k_B T] - 1}. \quad (4.128)$$

Evaluation of (4.125) then leads in a good approximation to [138]:

$$M(T) = M(0) \left[1 - B T^{3/2} \sum_{k=1}^{\infty} \frac{e^{-k\Delta}}{k^{3/2}} \right], \quad (4.129)$$

with $\Delta = \Delta E/k_B T$. The series assumes limiting values of $e^{-\Delta}$ for $\Delta E \gg k_B T$ and 2.6149 for $\Delta E \ll k_B T$ which is the case of Bloch’s law. We have applied this equation to fit the temperature dependence in Fig. 4.42 and obtained values of $D = 1.26(10) \text{ meV nm}^2$ and $\Delta E = 6.7 \pm 1 \text{ meV}$. Inserting these values into (4.127) we find that a linear dimension of $d = 1.4 \text{ nm}$ reproduces the measured energy gap. This is in the range of the island height shown in Fig. 4.36 which is a reasonable agreement within our simple model.

Obviously, the finite size of the islands has significant influence on the temperature dependence of the magnetization. At low temperatures the magnetization of the islands decays slower with temperature than does the magnetization in the bulk. This is a consequence of the energy gap in the spinwave spectrum. At elevated temperatures the softening of the eigenstates becomes dominant and the spontaneous magnetization of the islands decays faster with temperature than the bulk magnetization [139]. As long as $K a^3 \ll JS^2$, the influence of surface anisotropies on the spin-wave spectrum can be neglected [139]. Thus, magnetic anisotropies in this case are far too small to account for a gap of sufficient magnitude in the spectrum of the spin waves [146]. We admit that it is difficult to derive details of the spin dynamics such as quantization effects by measuring an integral quantity like the temperature dependence of the spontaneous magnetization.

While the magnetic hyperfine field is derived from the quantum beat period, the recoilless fraction is determined from the speed-up of the decay, i.e., the slope of the envelope of the time spectrum. Thus, both parameters are independent of each other. The temperature dependence of the f-factor is shown in Fig. 4.43. Although the error bars are relatively large, the f-factor is almost constant over the whole temperature range. For comparison the temperature dependence of the f-factor for bulk Fe is also shown. The f-factor provides a bridge to the dynamical properties of the system (see Sect. 5.3). It is determined mainly by the low-energy part of the vibrational spectrum. Thus, any anomaly in the f-factor may point to unusual properties of low-energy excitations that lead to a deviation from the Debye behavior. While no conclusive explanation can be given at this stage the presentation of these data should motivate investigations of the spectrum of spinwave excitations in thin films and nanoparticles [147].

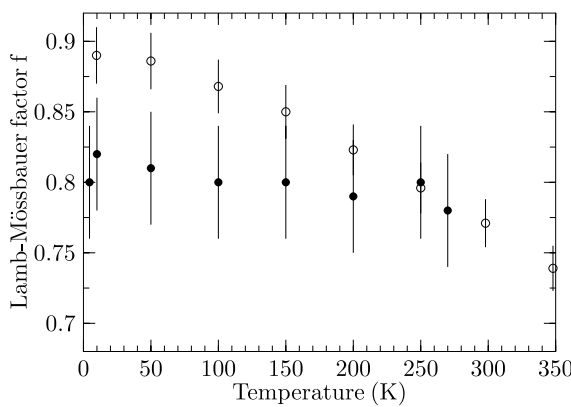


Fig. 4.43. Temperature dependence of the Lamb-Mössbauer factor for the Fe islands (solid circles). For comparison, the data for bulk bcc Fe (open circles) are shown, taken from Bergmann et al. [16]

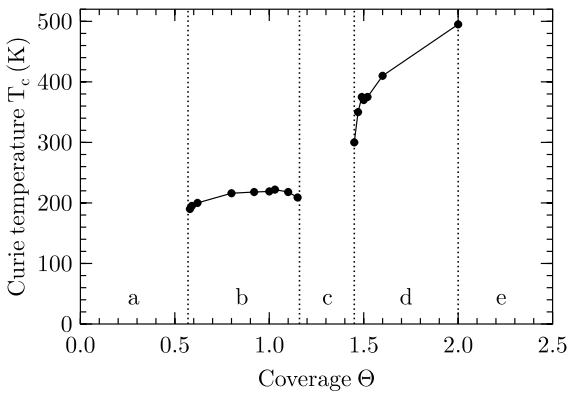


Fig. 4.44. Curie temperatures of Fe films on W(110) vs. coverage. Depending on the coverage, five magnetically different regions (**a–e**) can be identified, as explained in the text (Data taken from Elmers *et al.* [152])

4.4.5 Perpendicular Magnetization in Fe Clusters on W(110)

A very interesting phenomenon in low-dimensional magnetism is the perpendicular spin orientation in ultrathin films. Despite extensive experimental and theoretical efforts, a complete understanding of the relevant anisotropies has not been achieved so far.

Magnetic order in low-dimensional systems is typically induced by anisotropies that result from broken local symmetries. Qualitatively, the magnetization direction is determined by the interplay of surface and shape anisotropies and usually forces the magnetic moment into the film plane. If, however, the balance between these quantities is changed, e.g., by altering the structure of the film, a spin-reorientation transition into the out-of-plane direction can occur. Several investigations in this field have been reported so far [148, 149].

One of the first systems in which two-dimensional ferromagnetic ordering has been observed was the Fe(110) monolayer on W(110) [150]. Since then it has been used as a model system for two-dimensional magnetism because it displays a rich variety of magnetic phenomena due to the interplay of bulk, surface, and shape anisotropies. Magnetic ordering in this system has been studied by Mössbauer spectroscopy [77, 150, 151], spin-polarized low-energy electron diffraction [152, 153, 154] and magnetometry [155]. Due to the high surface energy of the W substrate in comparison with that of the film, Fe on W(110) is thermodynamically stable, in contrast to other layer/substrate systems like Fe/Cu and Fe/Ag. The first monolayer of Fe on W(110) grows pseudomorphically, i.e. with the lattice constant of the substrate. Depending on the coverage Θ , (measured in units of one bulk Fe(110) monolayer), five different magnetic regimes can be identified, illustrated in Fig. 4.44:

- (a) A submonolayer region for $\Theta < 0.58$. Deposition at ambient temperatures leads to the formation of stable and well-separated pseudomorphic

islands [156]. Above 100 K the islands appear to be nonmagnetic due to superparamagnetic relaxation [157].

- (b) A ferromagnetic one-monolayer region where the magnetization is confined to the film plane with a pronounced twofold anisotropy, the easy axis pointing along the $[1\bar{1}0]$ directions [135, 137]. Due to the large misfit between the Fe and W lattices of -9.4% , the pseudomorphic Fe(110) monolayer on W(110) is completed at a coverage of $\Theta = 0.82$.
- (c) A region for $1.20 < \Theta < 1.48$, consisting of second-layer islands on top of a single monolayer, with perpendicular spin orientation and antiferromagnetic coupling between islands.
- (d) The region for $\Theta > 2.0$ that exhibits the two-fold in-plane magnetic anisotropy. The Curie temperature increases with the coverage according to a finite-size scaling law [158].
- (e) The easy magnetization axis switches in-plane from the $[1\bar{1}0]$ direction into the $[001]$ direction for films thicker than about 8 nm.

While a large number of studies were devoted to the cases b)–e), investigations of the separated islands that form in region a) are scarce. To some extent the relation between magnetism and morphology of these islands was investigated by Elmers *et al.* [157] down to temperatures of 115 K. However, it remained an unresolved question what kind of magnetic ordering the islands would undergo at low temperatures. In this experiment the magnetic ordering of the ultrasmall Fe islands in region a) at temperatures as low as 4.5 K has been studied. The data provide strong evidence for a perpendicular spin orientation [80].

Experiment

The samples were prepared under ultrahigh-vacuum conditions by thermal evaporation of Fe, enriched to 95% in ^{57}Fe , on an atomically clean W(110) crystal at 450 K. The cleanliness of the W(110) surface and the pseudomorphic growth of the Fe islands was controlled by low-energy electron diffraction (LEED). The morphology of the islands was then inspected by scanning tunneling microscopy (STM). An STM image of the sample studied here is shown in Fig. 4.45. From this image the coverage was determined to be $\Theta = 0.57$ which is slightly below the percolation limit. The effective radius of the islands was determined to be $r_{ave} = 1.0$ nm. After preparation the sample was coated with about five monolayers of Ag to prevent contamination in the subsequent ex-situ experiment. The sample was mounted in a He cryostat with the in-plane $[001]$ direction aligned parallel to the incident beam. It was illuminated in a vertical scattering geometry at an angle of 5 mrad, the critical angle of total reflection of the W substrate at 14.4 keV.

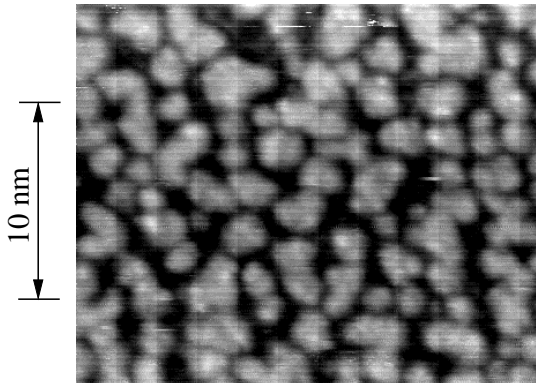


Fig. 4.45. STM image of Fe(110) islands on W(110) prepared at 300 K. The Fe coverage corresponds to $\Theta = 0.57$ pseudomorphous monolayers [80]

Results

A series of time spectra taken at various temperatures is shown in Fig. 4.46. The decay of the time-resolved reflectivity is considerably faster than the natural decay that is shown as the dotted line in the top picture. With decreasing temperature an additional modulation appears in the time spectra that results in distinct peaks at $t_1 = 34$ ns and $t_2 = 68$ ns at 4.5 K. For a theoretical description of the measured data a layer system consisting of a 0.2 nm thick film of ^{57}Fe on W was assumed. The right panel in Fig. 4.46 shows the distribution of magnetic fields that was obtained from the simulations. The strongly accelerated decay at 300 K is attributed to a broad distribution of hyperfine interactions around $B = 0$ T and a weak component around $B = 4$ T, as it was already observed in the single monolayer Fe on W(110) [77, 150]. The former component is found at all temperatures and is most likely related to parts of the sample that do not order magnetically in the temperature range investigated here. With decreasing temperature a non-zero magnetic component appears due to magnetic ordering of the Fe islands. The modulation in the time spectra points to a perpendicular magnetization that is characterized by a single quantum-beat frequency as shown in Fig. 4.11D¹⁴. Taking the time difference of $t_2 - t_1 = 34$ ns of the maxima at 4.5 K as quantum-beat period Δt , one obtains for the magnetic field

$$B = \frac{\hbar}{\Delta t (\mu_g/I_g - \mu_e/I_e)} = 13.5 \text{ T} . \quad (4.130)$$

This value is slightly larger than the value of $B = 11.9(2)$ T that was extrapolated for the Ag-coated Fe monolayer on W(110) at 0 K [150]. Since the Curie temperature is very likely dependent on the island size, the size distribution leads to a distribution of magnetic hyperfine fields that accounts for the width of the magnetic component at a given temperature.

¹⁴ The electric quadrupole interaction in this system is negligible [151].

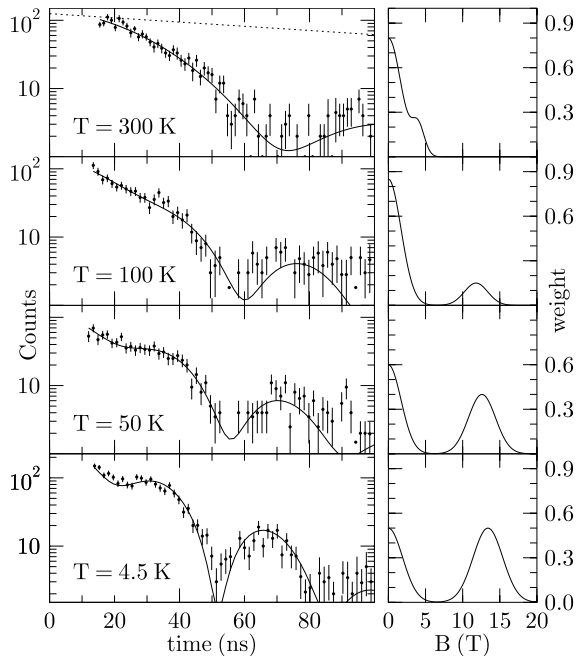


Fig. 4.46. Time spectra of grazing-incidence reflection from the ^{57}Fe islands on W(110) shown in Fig. 4.45 [80]. The modulation of the intensity is attributed to a perpendicular magnetization of the Fe islands. The *solid lines* are the results of simulations according to the formalism outlined in Sect. 4.1.4. For comparison, the natural decay of the ^{57}Fe level is shown in the *top graph* as *dotted line*. The *right panel* displays the probability density for the hyperfine field distribution that was used in the simulations [80]

The right panel in Fig. 4.46 shows that the weight of the magnetic component increases with decreasing temperature. This is attributed to superparamagnetic relaxation of the magnetic moments [159]. At high temperatures the magnetization of small particles is subject to fast thermal fluctuations so that the effective magnetic hyperfine field averages to zero. In the most simple model of a two-state relaxation, originally developed by *Bean and Livingston* [159], the relaxation time is given by

$$\tau = \tau_0 \exp\left(\frac{KV}{k_B T}\right), \quad (4.131)$$

where K is the magnetic anisotropy constant and V is the particle volume. The transition from the fast-relaxation regime to the magnetically ordered state occurs at a temperature that is roughly given by the condition $KV = k_B T$. However, due to the size distribution of the islands, as shown in Fig. 4.45, this transition is smeared out over a rather broad temperature

range. The temperature dependence of the magnetic component points to an average blocking temperature around 50 K. Taking an average island volume of $V = 0.6 \text{ nm}^3$, we estimate an anisotropy constant of $K \approx 1.0 \times 10^6 \text{ J/m}^3$. This is about 20 times the anisotropy constant of bulk Fe. Such an enhancement is attributed to the reduced symmetry of the system [160] and has been observed for other ultrathin films and nanoparticles as well [161, 162].

An in-plane magnetization of the Fe islands can be excluded, because it cannot reproduce the relative intensities of the quantum-beat peaks observed here. In that geometry the four resonance lines belonging to the $\Delta m = \pm 1$ transitions contribute to the scattered amplitude. It should be noted here that a magnetization along exclusively one of the in-plane [001] directions could explain the measured data, too. However, this can be ruled out because the [001] and [00 $\bar{1}$] directions should be equally populated due to the superparamagnetic relaxation. Even after cooling below the superparamagnetic blocking temperature in a zero external field, such a configuration would be energetically more favorable since it minimizes the magnetic stray field by flux closure of adjacent islands. The scattered amplitude is then again given by the above expression with contributions from four resonance lines.

As a result of the above considerations, the data strongly indicate a perpendicular spin orientation of the islands. The solid lines in the left panel of Fig. 4.46 are the results of the simulation, assuming an incoherent superposition of the amplitudes scattered from the magnetic and the nonmagnetic component. This is reasonable if the lateral separation of these components on the sample is larger than the transverse coherence length of the radiation, which is estimated to be in the range of 30 nm in the scattering geometry and detector aperture used here (see also the discussion in Sect. 4.3.2).

Discussion

The perpendicular magnetization of the Fe islands is quite remarkable because Fe films on W(110) are known to be magnetized in plane for coverages $\Theta > 0.6$ [149]. In general, the anisotropy energy per atom for perpendicular magnetization is given by $f_{\perp} = f_{Sh} + f_{MC} + f_{ME}$, where f_{Sh} is the shape anisotropy, f_{MC} the magneto-crystalline surface anisotropy, and f_{ME} the magneto-elastic anisotropy that is proportional to the in-plane strain of the film [163]. If $f_{\perp} < 0$, a perpendicular magnetization of the film is preferred. For the Ag-covered Fe monolayer on W(110), a total anisotropy of $f_{\perp} = +0.6 \text{ meV}$ has been determined experimentally [155]. There is strong evidence that this value results from a giant perpendicular strain anisotropy of $f_{ME} \approx -1 \text{ meV}$ that is overcompensated by an in-plane anisotropy contribution of $f_{Sh} + f_{MC} \approx +1.6 \text{ meV}$ [164]. Note that the shape anisotropy of $f_{Sh} = 0.14 \text{ meV}$ is only a small contribution compared to the magnetocrystalline anisotropy f_{MC} in this system. It is reasonable that the interface with the heavy metal W results in magnetocrystalline monolayer anisotropies that

are huge in comparison with typical metallic interface anisotropies (for example, $f_{MC}^{Fe/Ag} = -0.30 \text{ meV}$ (at 300K) [165]).

If a continuous film breaks up into separated islands, the balance between these contributions will be changed. Moreover, an additional contribution to the total anisotropy has to be considered: The magnetic step anisotropy. As magnetic anisotropies are induced by broken symmetries, it is evident that symmetry breaking due to surface steps changes the total anisotropy of nanoscale magnetic systems. This has been investigated experimentally [166, 167, 168] as well as theoretically [169, 170]. The morphological basis for this kind of anisotropy are broken or missing bonds at the step edges as well as strain in the remaining bonds. Since the 2.0 nm diameter islands in this sample contain roughly 50% atoms in step (or edge) positions, the magnetic step anisotropy must be a significant contribution. In fact, magnetic (excess) step anisotropies of -0.39 meV (at 300 K) have been found experimentally for the case of steps on Fe(110) surfaces oriented along the [001] direction [166]. A step anisotropy of this magnitude obviously would not explain the overcompensation of $+0.6 \text{ meV}$ in the islands. It should be noted that the steps investigated in these studies were homo-atomic steps, i.e. steps within the same atomic species. On the other hand, the anisotropy of hetero-atomic steps that form at coverages below one monolayer as in our experiment have not been studied yet. Since the Fe islands grow pseudomorphically on the W(110) substrate, as evidenced by LEED investigations, they are laterally strained. The resulting stress can be lowered by relaxation of the iron atoms at the island edges. This may form the morphological basis for the step anisotropy in this system (in addition to missing neighbors and/or those replaced by Ag). A strong hint for this relaxation is the hindered coalescence of the islands at coverages around $\Theta = 0.6$ [171]. In the STM image shown in Fig. 4.45 this behavior manifests indirectly as narrow channels between adjacent islands. For hetero-atomic steps as in the case of Fe on W(110) the resulting step anisotropies may be even larger than those for homo-atomic steps of Fe on Fe [166].

In conclusion, the interplay between the huge and counteracting perpendicular strain and in-plane intrinsic contributions, the tendency towards strong anisotropies near the W surface, and the considerable dependence of surface anisotropies on temperature make it a reasonable preposition that the perpendicular magnetization of the islands results from step anisotropies [172]. In a detailed analysis also the influence of the nonmagnetic coating has to be taken into account that is known to contribute to magnetic hyperfine fields [173] as well as to magnetic anisotropies [174].

4.4.6 Nuclear Resonant Small-Angle X-ray Scattering

Small-angle scattering of x rays (SAXS) and neutrons (SANS) are techniques that are routinely used to study inhomogeneities and disorder in matter on

length scales ranging from nm to μm . If the polarization dependence of the scattering process is exploited, both techniques become sensitive to fluctuations of the magnetic structure. This is due to the interaction of the angular momentum of the probing particle with the magnetic moments in the sample. In the case of x-rays the sensitivity to the magnetic structure is strongly enhanced if the photon energy is resonantly tuned to an absorption edge of an element in the sample that contributes to the magnetic moment. This applies equally well for the case of nuclear resonance excitation in the presence of a magnetic hyperfine interaction. Nuclear resonant small-angle x-ray scattering became feasible with the availability of high-brilliance synchrotron radiation at third-generation sources.

NRSAXS in Forward Scattering Geometry

A first experiment of this kind was performed with magnetized and unmagnetized ^{57}Fe foils in transmission geometry [175]. The foils were illuminated by a 6.4 meV wide beam from a high-resolution monochromator and the angular distribution of the scattered radiation was analyzed with a Si(111) channel-cut crystal. Figure 4.47 shows the experimental data. The angular resolution function of the setup was determined by recording the nonresonant prompt signal, shown as solid line in Fig. 4.47a. Its full width at half maximum of $\Delta\delta = 20\mu\text{rad}$ defines the resolution in reciprocal space of $\delta Q = k_0 \Delta\delta = 1.5\mu\text{m}^{-1}$. The nuclear resonant signal was obtained by counting delayed quanta within a time window ranging from 15–160 ns after excitation. Figure 4.47a shows the angular distribution of NRSAXS from a foil magnetized in-plane by an external field of 0.55 T. These data coincide with the resolution function, indicating that there are no magnetic inhomogeneities within the resolution range of the setup. In contrast, the angular distribution from unmagnetized foils of various thicknesses displays a significant broadening, as shown in Fig. 4.47b. This broadening results from the formation of domains and domain walls after the removal of the external magnetic field. It is remarkable that the broadening is approximately the same for all foils. This indicates that NRSAXS might be considered in a first approximation as a single scattering process, although NFS from these foils is dominated by multiple scattering processes due to their large effective thickness.

The angular dependence of the nuclear resonant signal can be written as:

$$N(\Theta) = I(\Theta) + \int_{-\infty}^{+\infty} S(\Theta - \Theta') I(\Theta') d\Theta' , \quad (4.132)$$

where $I(\Theta)$ and $S(\Theta)$ are the angular distribution functions of the incident radiation and the NRSAXS, respectively. A good fit to the data is achieved via a Lorentzian distribution function:

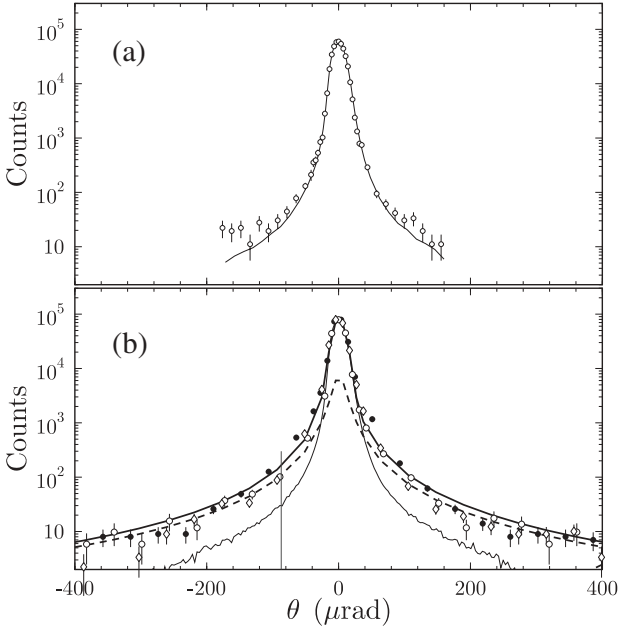


Fig. 4.47. (a) Angular distribution of the nonresonant prompt radiation, representing the resolution function of the setup. (b) Angular distribution of NRSAXS from unmagnetized ⁵⁷Fe foils with a thickness of 2.5 μm, 10 μm, and 36 μm. The *solid line* is a fit according to (4.132). (Data taken from Shvyd'ko *et al.* [175])

$$S(\Theta) = D \frac{\Delta\Theta}{2\pi} \frac{1}{\Theta^2 + (\Delta\Theta)^2} \quad (4.133)$$

with $\Delta\Theta = 23 \pm 5 \mu\text{rad}$ and $D = 0.16 \pm 0.03$. Assuming that the measured response $S(\Theta)$ is related to the real response function $R(Q)$ of NRSAXS via

$$S(Q_x) \sim \int R(Q) dQ_y \quad \text{with} \quad Q = \sqrt{Q_x^2 + Q_y^2} \quad \text{and} \quad Q_x = k_0\Theta, \quad (4.134)$$

one obtains for the response function:

$$R(Q) \sim \frac{1}{[Q^2 + (q/2)^2]^{3/2}} \quad \text{with} \quad q = k_0\Delta\Theta. \quad (4.135)$$

In a single-scattering model the function $R(Q)$ is the Fourier transform of the spatial distribution function of the magnetization in the sample, where q^{-1} is the correlation length. In this case one obtains $q^{-1} = 0.6 \mu\text{m}$. This is in accordance with the domain wall width in Fe, being typically in the range of 0.3 ... 1 μm [176]. The domain size of around 10 μm for polycrystalline Fe does not enter into the data due to the resolution limit in reciprocal space.

It should be noted that the Lorentzian angular dependence of NR-SAXS differs from the Gaussian dependence of small-angle neutron scattering (SANS) observed in bulk samples of Fe [177]. The Gaussian dependence originates from multiple scattering processes in SANS, which precludes to determine the magnetic domain size directly from experimental data. In contrast, NRSAXS allows one to directly extract the correlation function of the spatial distribution of the magnetization.

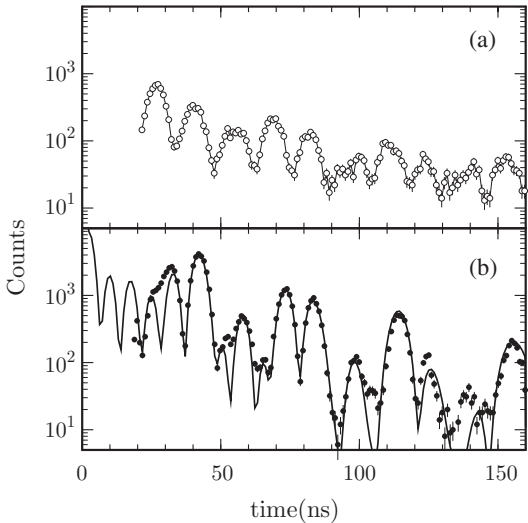


Fig. 4.48. Time spectra of nuclear resonant scattering from a 2.5 μm thick unmagnetized ^{57}Fe foil with the Si(111) analyzer crystal set at (a) $\Theta = -87 \mu\text{rad}$ and (b) $\Theta = 0 \mu\text{rad}$. The *solid line* in b) is a fit assuming nuclear forward scattering from polycrystalline Fe. (Data taken from *Shvyd'ko et al.* [175])

Information about the magnetic correlation is not only contained in the angular distribution of the resonantly scattered radiation, but also in the time spectra recorded at different transverse momentum transfers Q_x . This is illustrated in Fig. 4.48, where two time spectra from a 2.5 μm thick ^{57}Fe foil are shown, recorded at angles $\Theta = 0.0 \mu\text{rad}$ and $\Theta = -87 \mu\text{rad}$, respectively. While the spectrum at $\Theta = 0.0 \mu\text{rad}$ can be explained by the theory of nuclear forward scattering (NFS) from a polycrystalline material (solid line), this is not the case for the spectrum taken at $\Theta = -87 \mu\text{rad}$. A simulation of this spectrum has to take into account the angular correlation function of the moments within the sample. For a complete reconstruction of this function, several time spectra over a large Q_x range have to be taken. A suitable algorithm for this purpose still has to be developed.

An important implication of this observation is that NRSAXS may have significant impact on time spectra that are recorded in forward scattering geometry, because typically no angular analyzer is used and the detector integrates over a wide range of scattering angles viz. momentum transfers Q_x . This should be taken into account especially in cases when the relative amount of NRSAXS, as described by the parameter D in (4.133), is large.

NRSAXS in Grazing Incidence Geometry

To investigate spatial inhomogeneities in thin films and nanostructures, small-angle x-ray scattering is applied in grazing incidence geometry and is then called GISAXS [178]. This technique is used in many fields of thin-film physics like structure formation in soft-matter thin films [179] or particle layering in ceramic-metal films [180], for example. Combined with microfocusing

techniques, this method can be applied to study the local structure of low-dimensional systems [181].

The GISAXS technique can be advantageously combined with nuclear resonant scattering for the study of the domain structure in magnetic layer systems. Very often this domain structure influences the electric transport properties in device applications, e.g., it may strongly limit sensor applications based on the giant magnetoresistance (GMR) effect [182]. It is therefore of great interest to understand the formation of domains in antiferromagnetically coupled multilayers in external magnetic fields [183]. The archetypal system in this field is the Fe/Cr multilayer that exhibits oscillatory interlayer coupling [93, 184] and giant magnetoresistance [92]. In remanence, an antiferromagnetic multilayer is in a multidomain state where the domain structure of the individual ferromagnetic layers is strictly correlated through the layer stack from the substrate to the surface, as sketched in Fig. 4.49.

In the experiment described here, an epitaxial layer stack with 20 bilayers of (2.6 nm $^{57}\text{Fe}/1.3\text{ nm Cr}$) was grown on a MgO(001) single crystal. The Cr thickness was chosen to match the first antiferromagnetic maximum of the oscillatory interlayer exchange coupling [93]. Due to the crystalline structure of the sample, one observes a fourfold in-plane anisotropy with the easy axes along the [100] and [010] directions. In remanence, the magnetization vectors of the Fe layers always point along these directions. To study the magnetic domain structure, the off-specular scattering was measured at the first-order antiferromagnetic Bragg peak for a fixed scattering angle of 0.8° . Resonant and nonresonant photons were recorded as a function of the angle of incidence ω , shown in Fig. 4.50.

Such AF coupled multilayers exhibit a remarkable magnetic structure after exposition to external magnetic fields: Releasing the magnetic field parallel to one of the easy axes from saturation, the magnetizations settle solely in the perpendicular easy direction. This leads to interesting magnetic domain configurations as illustrated in Fig. 4.50. In Figs. 4.50a,b the sample

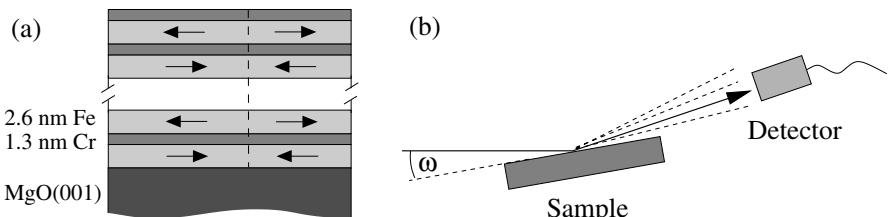


Fig. 4.49. (a) Schematic cross section of the chemical and magnetic structure of the Fe/Cr multilayer in the vicinity of a domain wall. (b) Scattering geometry. The diffuse scattering was measured by variation of the angle of incidence (here: ω) with the detector position fixed in q -space at the position of the first-order AF Bragg peak (ω -scan)

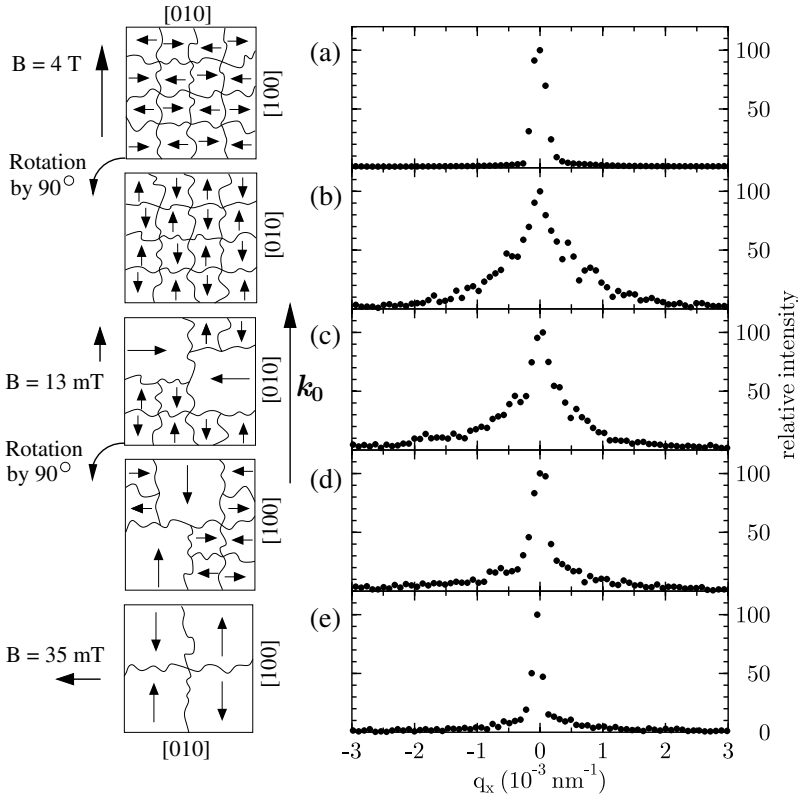


Fig. 4.50. Off-specular ω scans of nuclear resonant scattering from an antiferromagnetically coupled multilayer consisting of 20 bilayers of (2.6 nm ^{57}Fe /1.3 nm Cr) on MgO(001). (a) after saturation in an external field of 4 T along the in-plane [100] direction. (b) same as (a) but after rotation of the sample so that $k_0 \parallel [010]$. (c) after application of a 13 mT field along the [010] direction. (d) same as (c) but after sample rotation so that $k_0 \parallel [100]$. (e) after application of a 35 mT field along the [010] direction. The drawings on the left side schematically show the corresponding lateral domain state of the sample, displaying the magnetic structure of one of the Fe layers in the stack (Data taken from Nagy *et al.* [183])

was saturated in an external field of 4 T along the [100] direction and then kept in remanence. In Fig. 4.50a the layer magnetizations are perpendicular to the incident wavevector. In this geometry the ω scan is not sensitive to the magnetic domain structure because there is no phase contrast between the two classes of domains. Therefore, no additional broadening beyond the instrumental resolution function is observed. This changes drastically upon rotation of the sample by 90° , as shown in Fig. 4.50b. In this case the relative phase between the two types of domains is π , so that strong scattering into off-specular directions is observed. From the width of the peak one derives a

magnetic correlation length (\approx domain size) of $\xi \approx 2.6 \mu\text{m}$. If now an external field is applied along the easy axis where the layer magnetizations actually lie, an irreversible bulk spin-flop (BSF) transition takes place where the layer magnetizations jump into the perpendicular easy axis [112]. This occurs at a critical field of $H_{SF} \approx 13 \text{ mT}$ where the magnetic Zeeman energy overcomes the magnetocrystalline anisotropy (see Sect. 4.4.2). The resulting domain configuration is retained in remanence. This is shown in Figs. 4.50c,d where ω scans for two different sample orientations are shown after the sample was subjected to a field of 13 mT along the [010] direction. Remarkably, the peak width of both scans is considerably smaller than the width in Fig. 4.50b which points to a significantly larger domain size. The ω scan in Fig. 4.50d probes the domains that are aligned along the [001] direction. The peak width is only slightly larger than that of the instrumental resolution function, indicating a domain size of $\xi > 16.5 \mu\text{m}$. Well beyond the BSF transition, e.g., at a field of 35 mT, the magnetic structure of the sample has transformed into a state of much larger domains than before. This domain coarsening is described in detail in [183].

The mechanism of domain formation in this system can qualitatively be explained as follows: The primary domain structure, displayed in Figs. 4.50a,b originates by decreasing the external field from saturation along the [100] direction to zero. The formation of the AF domains nucleates in regions where the exchange coupling is strongest (there is always a distribution of the coupling strength due to thickness fluctuations), resulting in layer magnetizations in either the [010] or the [0 $\bar{1}$ 0] direction. The energy of the 180° walls between the adjacent AF domains is minimized by lateral growth of the domains. This process, however, is limited by domain-wall pinning (coercivity), so that the balance with the gain in domain-wall energy determines the average domain size. The formation of the large secondary domains as displayed in fig 4.50e proceeds along a different route. These domains form during the bulk spin flop and they result from the annihilation of primary 180° domain walls. Thus, this growth is not limited by coercivity and, consequently, the size of the secondary domains may become comparable to the sample size [183].

These studies show that nuclear resonant small angle scattering is a valuable tool for the study of the magnetic domain structure, especially in low-dimensional systems. Due to the isotopic sensitivity, such studies can be focused on individual layers in a multilayer by selectively depositing probe layers of the resonant isotope. This is particularly interesting to reveal the impact of interfaces on the properties of magnetic layer systems.

4.5 Magnetism at High Pressures

The very high brilliance of modern synchrotron radiation sources allows for efficient focusing of x-rays to spot sizes in the range from a few $10 \mu\text{m}$ down

into the sub- μm range. This is achieved via x-ray optical devices like refractive lenses, zone plates, Kirkpatrick-Baez mirrors or waveguides, for example. Thus, tiny samples in high-pressure cells can be very effectively studied by using micro-focused x-ray beams at modern synchrotron radiation sources. This applies in particular for nuclear resonant scattering studies. Figure 4.51 displays a typical diamond anvil cell (DAC) used for such experiments [185]. Due to the very compact design it is suited to be used in cryomagnet systems at low temperatures and in high magnetic fields. While in this case the DAC was made from a CuBe alloy, for high-temperature applications the DAC was made from a special Ti alloy with very small thermal expansion, allowing for heating up to 670 K. Depending on the surface area of the diamond anvils, pressures beyond 100 GPa (1.0 Mbar) can be reached. For entering and leaving the sample volume, the radiation has to pass about 5 mm of diamond. At 14.4 keV, the transmission is still 25%. It increases to about 60% at 21.5 keV, the resonance energy of ^{151}Eu .

One of the first applications in this field was the study of magnetic properties under high pressure [186, 187]. Due to the large pressure range of a DAC, the interatomic spacing is significantly changed, which is an important parameter for magnetic ordering. Interesting candidates for such studies are the Laves phases RFe_2 with $\text{R} = (\text{Y}, \text{Lu}, \text{Sc})$ that show a strong variation of the magnetic ordering temperature T_m with pressure. A series of NFS time spectra of LuFe_2 is shown in Fig. 4.52. The left panel shows data taken at 295 K and various pressures. The increase of the beat period with increasing pressure indicates a decreasing magnetic hyperfine field that has vanished at the highest pressure of 80 GPa. Time spectra taken at a pressure of 18 GPa and various temperatures are shown in the right panel of Fig. 4.52. From these data an ordering temperature of $T_m = 573$ K was derived by plotting

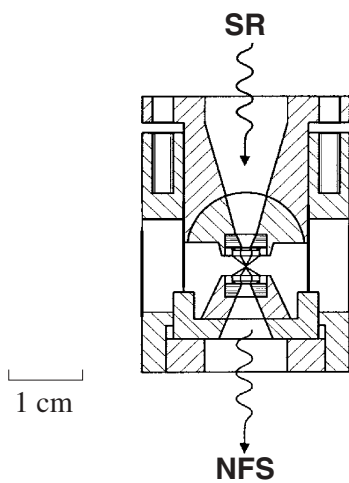


Fig. 4.51. Schematic drawing of high-pressure cells for nuclear forward scattering (left) and nuclear inelastic scattering (right). (Figure adopted from Wortmann *et al.* [185])

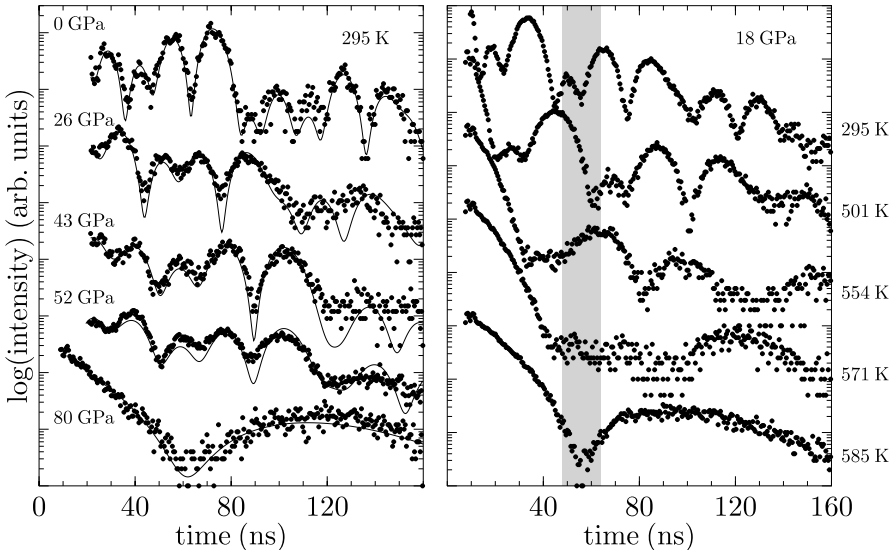


Fig. 4.52. *Left:* NFS spectra of LuFe₂ at T = 295 K and pressures up to 80 GPa. The increase of the beat period with increasing pressure indicates a decreasing magnetic hyperfine field. *Right:* NFS spectra of LuFe₂ at a pressure of 18 GPa and various temperatures. The delayed count rate within the shaded time window was used to calculate the count rate ratio displayed in Fig. 4.53a. (Data taken from Wortmann *et al.* [185])

the inverse of the count rate within the shaded area vs. temperature, as shown in Fig. 4.53a. The vanishing of the magnetic hyperfine field B_{hf} and the appearance of a pronounced Bessel minimum in the time spectrum leads to a peak at $T = T_m$. The decrease with increasing temperatures is due to the shift of the minimum resulting from the decreasing Lamb-Mössbauer factor.

It is instructive to plot the measured values for T_m and B_{hf} versus the interatomic Fe-Fe distance d_{Fe-Fe} , as shown in Fig. 4.53b,c. This allows for a direct comparison of the different structures, since the local surroundings of the Fe sites are very similar. Accordingly, the observed temperature dependencies are very similar for the three compounds. This behavior can be discussed within the model for 3d ferromagnetic band moments as developed by Wohlfahrt [188]: The Stoner criterion ($ID(E_F) > 1$) for the occurrence of ferromagnetic ordering in itinerant electron systems contains two conditions for this ordering: a) the strength of the exchange interaction, which is described by the Stoner parameter I , and a high density of states $D(E_F)$ at the Fermi energy. Although developed for ground state properties at $T = 0$ K, it can be extended to finite temperatures and provides a description of the two competing pressure effects on the ordering temperature T_m . First, pressure enhances the overlap of the atomic wave functions giving rise to an increase

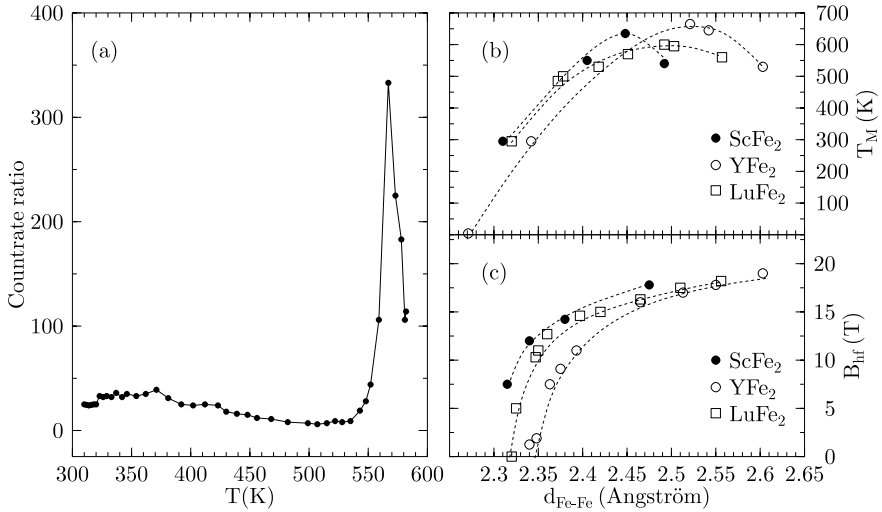


Fig. 4.53. (a) Normalized inverse delayed count rate for LuFe₂ at 18 GPa, taken within the time window indicated by the grey area in Fig. 4.52. (b) magnetic ordering temperatures T_m and (c) magnetic hyperfine fields B_{hf} in ScFe₂, YFe₂, and LuFe₂ at room temperature and various pressures as function of the Fe-Fe distance d_{Fe-Fe} that was determined by x-ray diffraction. Dashed lines are guides to the eye. (Data taken from Wortmann et al. [185])

of the exchange interaction I . This leads to an increased stability of the magnetic phase, i.e., to a higher T_m . This behavior is well known for systems with localized magnetic moments, e.g., pure 4f systems. However, in itinerant magnetism the band moment is affected by pressure. The 3d-bandwidth increases with decreasing interatomic distance and consequently $D(E_F)$ is lowered. Both effects lead to a smaller 3d band moment, as observed by the decrease of the magnetic hyperfine fields with pressure [186].

More quantitatively, the pressure dependence of the magnetic ordering temperature can be qualitatively described by the equation

$$\frac{dT_m}{dP} = \frac{5\kappa T_m}{3} - \frac{\kappa\alpha}{T_m} \quad (4.136)$$

where κ is the compressibility and α describes the variation of the band moment with the lattice spacing. At low pressures the first term dominates which describes the increase of T_m with increasing pressure due to the RKKY mechanism. With increasing pressure and decreasing interatomic spacing, the second term becomes dominant so that dT_m/dp changes sign, as observed.

The experiments discussed so far have shown how magnetic ordering changes and eventually vanishes with increasing pressure. In strongly correlated 4f electron systems like Kondo-lattice compounds one can observe the opposite behavior, i.e., magnetic order can be induced by pressure. Due to

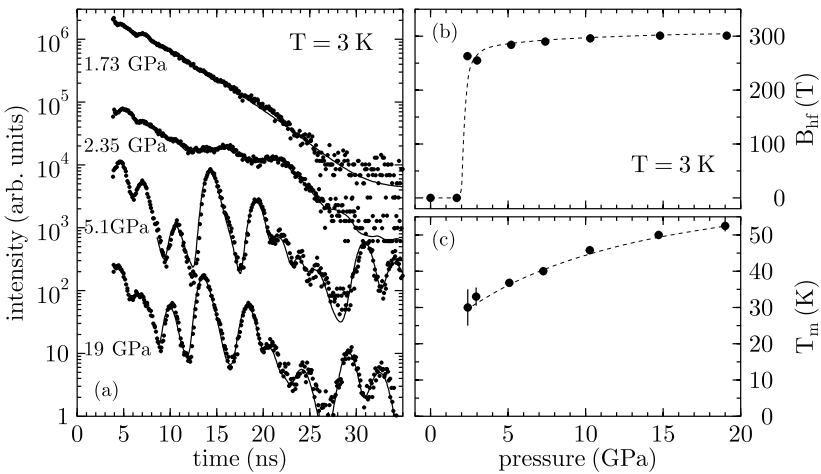


Fig. 4.54. (a) ^{149}Sm time spectra of nuclear forward scattering from SmS at 3 K and various pressures up to 19 GPa. (b) magnetic hyperfine field B_{hf} and (c) magnetic ordering temperature T_m as function of pressure. *Dashed lines* are guides to the eye (Data taken from Barla *et al.* [192])

the electronic correlations, the hybridization strength between the localized $4f$ electrons and the conduction electrons decreases with increasing pressure, thus enabling the system to develop long range magnetic order. This has been demonstrated for Yb-based heavy-fermion compounds like $\text{Yb}_2\text{Ni}_2\text{Al}$ via ^{179}Yb Mössbauer spectroscopy, electrical resistance and x-ray diffraction [189]. Another class of materials known as Kondo insulators or narrow-gap semiconductors show a similar behavior at low temperatures. Among these materials, SmS is particularly interesting because it shows a semiconductor-to-metal transition at a surprisingly low pressure of 0.65 GPa at room temperature [190] that goes along with an isostructural (NaCl-type) first-order phase transition. At low temperatures, the insulating gap collapses at a pressure of about 2 GPa. For this low-temperature high-pressure phase a magnetically ordered ground state was predicted [191]. Clear evidence for this behavior could be provided via nuclear resonant scattering of synchrotron radiation [192].

For this experiment SmS crystals, enriched to 97% in ^{149}Sm , were prepared by the Bridgman technique. A powder sample was placed in a diamond anvil cell with nitrogen as a pressure transmitting medium and cooled to a temperature of 3 K. Time spectra of nuclear forward scattering at pressures up to 19 GPa are shown in Fig. 4.54a. The spectrum at 1.73 GPa is characteristic for unsplit nuclear levels. Quantum beats in the spectrum at 2.35 GPa indicate the onset of hyperfine interactions with increasing pressure. At 5.1 GPa the hyperfine interaction is fully developed throughout the

sample. The Sm nuclei experience a combined magnetic and electric hyperfine interaction with $B_{hf} = 284(10)$ T and $\Delta E_Q = -1.56(6)$ mm/s [192]. These values undergo only slight changes upon increasing the pressure to 19 GPa. The pressure dependence of the magnetic hyperfine field B_{hf} and the magnetic ordering temperature T_m are displayed in Figs. 4.54b,c. The steep variation of B_{hf} underlines the first-order character of the transition. T_m was determined by recording the temperature dependence of the magnetic hyperfine field at different pressures. The values measured here are significantly higher than those determined by specific heat and resistivity measurements [192].

These observations clearly show the short-range magnetic order that exists within the Sm sublattice. Further experiments like magnetic x-ray or neutron scattering are necessary to reveal the magnetic structure of this compound at high pressures. Moreover, these experiments demonstrate that nuclear resonant scattering can be a very sensitive probe for the observation of magnetic ordering in highly correlated electron systems. In combination with the high brilliance of modern synchrotron radiation sources, smallest amounts of material in thin films and nanostructures become accessible.

4.6 Study of Dynamical Properties

So far the experiments discussed here were dealing with static samples whose structure did not change in time. For a more general treatment one has to take the time dependence of the atomic positions into account. This is particularly relevant for NRS where the duration of the scattering process is determined by the nuclear lifetime τ_0 . Dynamical processes on a timescale comparable to τ_0 thus may influence the temporal evolution of NRS.

4.6.1 Quasielastic Nuclear Resonant Scattering

A coherent scattering experiment measures the scattering function $S(\mathbf{q}, \omega)$, also called the dynamic structure factor. It describes the probability for the scattered particle to acquire a momentum transfer $\mathbf{q} = \mathbf{k}_1 - \mathbf{k}_0$ and an energy transfer $\omega = \omega_0 - \omega_1$ during the scattering process. On the other hand, the (dynamic) structure of the sample is described by the correlation function $G(\mathbf{r}, t)$ which describes the probability to find any particle at position \mathbf{r} and time t when the particle was at $\mathbf{r} = 0$ and $t = 0$ before. Both quantities are related by

$$G(\mathbf{r}, t) = \frac{1}{(2\pi)^3} \int S(\mathbf{q}, \omega) e^{-i(\mathbf{q} \cdot \mathbf{r} - \omega t)} d\mathbf{q} d\omega . \quad (4.137)$$

This relation was derived in 1954 by *van Hove* [193] and became the foundation of all modern scattering experiments. For a general review, see the article by *Sinha* [194], for example.

In time-resolved experiments like NRS or XPCS one measures the so-called intermediate scattering function $S(\mathbf{q}, t)$ which is defined as a single Fourier transform of $G(\mathbf{r}, t)$ in space:

$$S(\mathbf{q}, t) = \int G(\mathbf{r}, t) e^{i\mathbf{q} \cdot \mathbf{r}} d\mathbf{r}. \quad (4.138)$$

In the kinematical approximation, the intensity $I(\mathbf{q}, t)$ measured in NRS is proportional to the modulus squared of the intermediate scattering function:

$$I(\mathbf{q}, t) = I_0(\mathbf{q}, t) |S(\mathbf{q}, t)|^2, \quad (4.139)$$

where $I_0(\mathbf{q}, t)$ is the response of the sample under static conditions, i.e., the time dependence is solely determined by the resonant scattering process and the hyperfine interactions.

If the motion of the atoms in the sample is ergodic, a closed expression for the intermediate scattering function can be given [195, 196]. This applies, e.g., for the Markovian diffusion of atoms in crystalline or amorphous systems. It is particularly interesting to apply NRS to the study of diffusion, because typical time scales are in the range of nuclear lifetimes τ_0 .

An important aspect arises from the resonant nature of the scattering process. In NRS using synchrotron radiation, the pulse length of the incoming radiation is very short compared to the scattering process itself. For that reason, NRS probes the self-correlation part $G_S(\mathbf{r}, t)$ of the correlation function $G(\mathbf{r}, t)$, i.e., the probability to find the same atom at the spacetime coordinates (\mathbf{r}, t) when it was at $(0,0)$ before. This self-correlation function plays an important role in the theory of diffusion because it describes the wandering of atoms. In other methods like XPCS, QNS or TDI, where the scattering process is very short compared to the pulse length of the radiation, one probes the full pair correlation function $G(\mathbf{r}, t)$.

4.6.2 Diffusion in Crystalline Systems

The most common methods for the study of diffusion are quasielastic neutron scattering (QNS) and quasielastic Mössbauer spectroscopy (QMS). In both cases, diffusion manifests as an energetic broadening of the scattering response, because the motion of the atoms leads to an energy transfer to the scattered particle. The theoretical description of this mechanism was elaborated in 1960 by *Singwi & Sjölander* [197].

For Markovian diffusion on a single crystalline lattice, the intermediate scattering function can be written as:

$$S(\mathbf{q}, t) = \exp\left(-\frac{t}{\tau}\alpha(\mathbf{q})\right), \quad (4.140)$$

with

$$\alpha(\mathbf{q}) = \frac{1}{N} \sum_{i=1}^N (1 - e^{-i\mathbf{q} \cdot \mathbf{l}_i}), \quad (4.141)$$

where the \mathbf{l}_i are the jump vectors to N possible sites and τ is the residence time of the atoms on this type of site. According to the Einstein-Smoluchovski equation the residence time τ is intimately related to the diffusion coefficient D :

$$D = \frac{\langle x^2 \rangle}{6\tau}, \quad (4.142)$$

where $\langle x^2 \rangle$ is the mean square displacement during the time τ . The function $\alpha(\mathbf{q})$ is often called the ‘jump function’ because it contains all information on the sites that are visited by a jumping atom during the scattering time. Inserting (4.140) into (4.139) one obtains for the intensity in forward direction:

$$I(\mathbf{q}, t) = I_0 \frac{L^2}{4\tau_0} \exp\left(-\frac{t}{\tau_0}\right) \exp\left(-\frac{t}{\tau} \alpha(\mathbf{q})\right), \quad (4.143)$$

where we have assumed a single-line scatterer with an effective thickness of L and negligible speedup, i.e., $I_0(\mathbf{q}, t) = I_0(L^2/4\tau_0) \exp(-t/\tau_0)$. With $\Gamma_0 = \hbar/\tau_0$ and $\Gamma_d(\mathbf{q}) := (2\hbar/\tau) \alpha(\mathbf{q})$, (4.143) can be written as:

$$I(\mathbf{q}, t) = I_0 \frac{L^2}{4\tau_0} \exp\left(\frac{-t(\Gamma_0 + \Gamma_d(\mathbf{q}))}{\hbar}\right). \quad (4.144)$$

This illustrates that the diffusion leads to an effective broadening of the resonance line, resulting in an accelerated decay of the nuclear exciton. In other words, if diffusion jumps occur within the ensemble of resonant atoms during the scattering process, the spatial coherence between the waves scattered from the atoms is partially destroyed. This leads to increasing destructive interference with increasing time after excitation, as it is expressed by the factor $(1 - e^{-i\mathbf{q} \cdot \mathbf{l}_i})$ in (4.141).

An example is shown in Fig. 4.55 where the NFS time spectra from a single crystal of FeAl are shown for three different temperatures [198, 199, 200]. The incident beam was aligned parallel to the [110] direction of the crystal. With increasing temperature one observes an increasing acceleration of the nuclear decay. Deviations from the exponential decay at low temperatures are due to violations of the kinematical approximation resulting from a relatively large Lamb-Mössbauer factor at low temperatures. The maximum diffusivity D that can be determined by this method is limited by the accessibility of early times after excitation within which the fast decay can be observed. Currently, this limit is $D < 10^{-13} \text{ m}^2/\text{s}$ if the time spectra start at 20 ns. Access to decay times as short as 2 ns after excitation will push this limit up to values of $10^{-13} \text{ m}^2/\text{s}$.

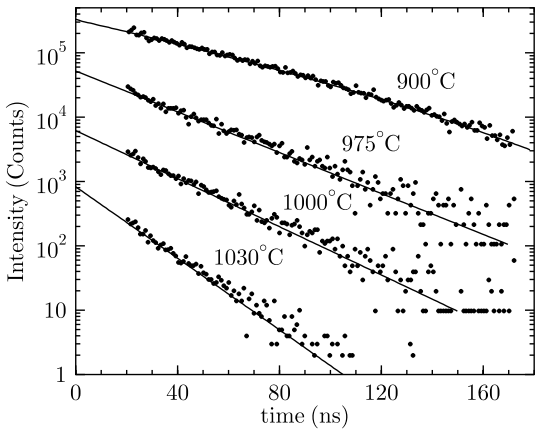


Fig. 4.55. Time spectra of NFS from a FeAl single crystal aligned with the [110] direction along \mathbf{k}_0 for different temperatures. (Figure adopted from Sepiol *et al.* [198])

Orientational dependence

Besides the determination of diffusion coefficients, this method can be applied to reveal the diffusion mechanism on an atomic scale, i.e., the atomic jumps that occur in the diffusion process. This is achieved by exploiting the orientational dependence of the time-integrated intensity (ODIN) that is given by

$$I_{ODIN}(\mathbf{q}) \sim \int_0^\infty I(\mathbf{q}, t) dt \sim \frac{1}{\Gamma_0 + \Gamma_d(\mathbf{q})}. \quad (4.145)$$

This is particularly interesting in intermetallic alloys like FeAl. The stoichiometric alloy FeAl crystallizes in the B2 structure (CsCl structure) shown in Fig. 4.56, where all nearest neighbors of Fe atoms are Al atoms. It is thus interesting whether the Fe atoms jump directly from one Fe site to the other (despite the relatively large distance) or whether the jump proceeds via a brief occupation of the Al sites. In this case, several independent jump sites have to be taken into account, and (4.145) has to be modified accordingly, resulting in:

$$I_{ODIN}(\mathbf{q}) \sim \left[\Gamma_0 + \frac{2\hbar}{\tau} \sum_j w_j \alpha_j(\mathbf{q}) \right]^{-1}, \quad (4.146)$$

where the w_j are the weights of the individual jump paths and $\alpha_j(\mathbf{q})$ are the corresponding jump functions as given by (4.141).

For investigation of the jump mechanism in FeAl, a single crystal was oriented with its $(\bar{1}\bar{1}0)$ plane coinciding with the plane of the storage ring. It was kept at a temperature of 1030°C , about 30°C below the melting point of FeAl. The time-integrated intensity over a time interval from 2 ns to 165 ns

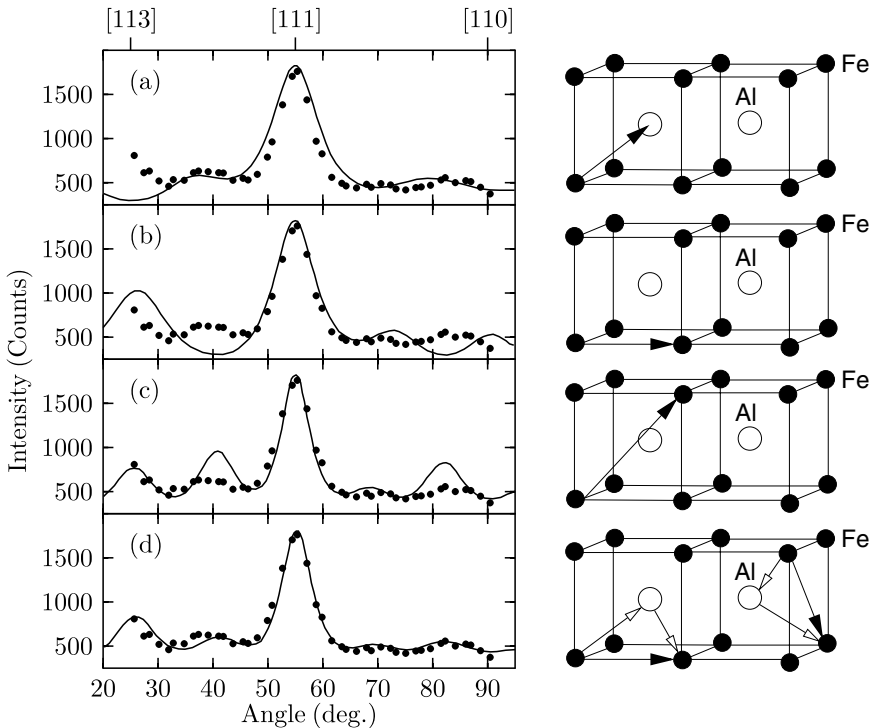


Fig. 4.56. Orientational dependence of time-integrated NFS from an FeAl single crystal at a temperature of 1030°C . Solid lines are model calculations assuming different types of jumps viz. jump sequences. (a) jumps of the Fe atoms to nearest neighbor sites, (b) jumps into second-nearest neighbor sites, (c) jumps to third-nearest neighbor sites, (d) a combination of [110] and [001] jumps at a ratio of 1.9:1 (Figure adopted from Vogl & Sepiol [199])

was recorded while the crystal was rotated around the $[0\bar{1}0]$ axis. The experimental data are shown in Fig. 4.56. Solid lines are model calculations assuming different jump models that are sketched on the right side. While the simulations (a)–(c) assume direct jumps to first, second, and third-nearest neighbors, the jump model in (d) is a combination of [110] and [001] jumps in the ratio of 1.9:1 [199, 201]. The latter simulation constitutes the best simulation of the data. In addition, the simulations displayed in Fig. 4.56 illustrate how different jump models can be discriminated against each other. The model in (d) is in agreement with data obtained previously via QMS [202], but the accuracy of the NRS data is much higher because the angular resolution is significantly better. Moreover, the data acquisition time is a few hours instead of several months, which makes it much easier to keep the crystal under well defined conditions close to the melting temperature. Although the jump to the Al antistructure site seems to be the elementary jump, the

details of this mechanism remain under debate, because first-principles calculations [203] indicate this jump to be energetically very unfavorable.

4.6.3 Slow Dynamics of Glasses

The description of diffusion and atomic transport in disordered materials is more complicated than in perfect crystals. In the latter case the structure is determined by a few Fourier components and the thermal properties are determined by well-defined collective excitations like phonons. In contrast, an amorphous solid requires an infinite number of Fourier components to define its structure, and various types of excitations are found on a wide range of energies. While in crystalline solids diffusion takes place via jumps to neighboring lattice sites, the long-range transport of atoms in disordered solids is very complex and still a subject of debate [204].

Of particular interest in this field is the liquid-to-glass transition as a crossover from an ergodic (liquid) to non-ergodic (solid) state on a microscopic scale. During this transition, no significant structural changes are observed. Instead, the internal mobilities of the atoms undergo drastic changes. For a theoretical description of this behavior, a fully atomistic formalism has been developed, the so-called mode coupling theory (MCT) [205]. A key element is the introduction of a critical temperature T_c that marks the transition from localized mobility into long-range structural relaxation with increasing temperature. Typically, T_c lies about 20–50% above the calorific glass temperature T_g which is defined, e.g., by the excess in specific heat that accompanies the onset of structural relaxation. Since the measurement of this quantity depends on the time scale of the corresponding experiment, T_g is not a unique transition temperature [206].

Due to the structural complexity of a disordered solid, its dynamical properties are more complex than that of crystalline solids. This is illustrated by the time-dependent density-density correlation function which is equivalent to the intermediate scattering function $S(\mathbf{q}, t)$ that has been introduced

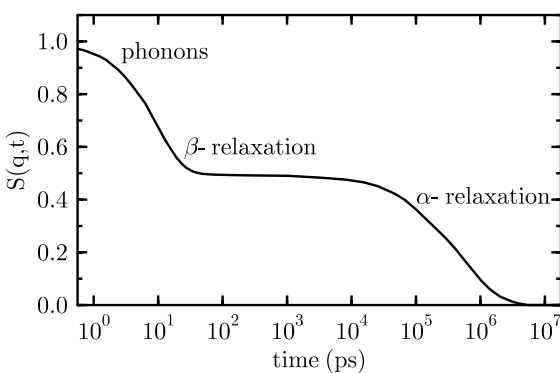


Fig. 4.57. Schematic shape of the density-density correlation function (intermediate scattering function) of an amorphous solid

above. The typical shape of this function for an amorphous solid is shown in Fig. 4.57. In a glass one finds three qualitatively different regimes on significantly different time scales:

(a) **The phononic region:**

At time scales of picoseconds or less dynamical behavior is dominated by lattice vibrations, giving rise to the initial decay of the correlation function.

(b) **β -relaxation**

In this region one identifies a local rattling of atoms in the cage that is formed by their neighbors. Due to confinement of atoms to a limited space, no long-range transport takes place.

(c) **α -relaxation**

In this region the final decay of $S(\mathbf{q}, t)$ to zero takes place. This decay results from long-range motion of the atoms.

The temporal dependence in the α -relaxation regime is well described by a stretched exponential, the so-called Kohlrausch function [207]:

$$S(\mathbf{q}, t) = f(\mathbf{q}) \exp \left[- (t/\tau_K)^{\beta} \right], \quad (4.147)$$

with the stretching parameter $\beta < 1$. In the limit of large momentum transfers, this function coincides with the MCT relaxation function [208]. The value $f(\mathbf{q})$ is the Debye-Waller factor which describes the height of the plateau in the correlation function.

The glass transition as described by the mode coupling theory occurs when the long-range structural α -relaxation decouples from the localized β -relaxation. In the region around T_c , the relaxation times are typically in the range of a few 10 ns. Therefore, nuclear resonant scattering can contribute to a better understanding of this phenomenon. However, one should be aware of the following aspects if the results from NRS measurements are to be compared with results from other techniques:

- Due to the large momentum of the photon, one probes the dynamical properties on sub-atomic length scales (in NRS, scattering phases are determined by the photon wavevector \mathbf{k}_0 rather than the momentum transfer \mathbf{q}). Most other techniques probe relaxation times on macroscopic or intermolecular distances. On the other hand, the momentum transfer in NRS experiments cannot be adjusted by selection of the scattering angle.
- Nuclear resonant scattering measures the single-particle dynamics rather than the dynamics of the pair-correlation function.

Thus, the access to single-particle dynamics on sub-atomic length scales constitutes a space-time region that is hardly accessible by other scattering methods. It is to be expected that at such short length scales the hydrodynamic scaling of relaxation times and diffusion coefficients no longer holds and new phenomena show up. Neutron scattering has contributed a great deal to the

atomistic interpretation of the glass transition, but most data were collected in the regime above T_c .

A certain drawback for the application of NRS is the fact that the sample has to contain resonant nuclei, and it may be a problem to find glass-forming systems containing iron. None of the model systems used so far to study glassy dynamics like glycerol, ortho-terphenyl, polymers, etc., contains iron or an element that may be substituted by iron. The only approach is to choose a composite system where the iron-containing compound reflects the dynamics of the host glass former. There are good reasons to assume that this applies for the system ferrocene ($\text{Fe}(\text{C}_5\text{H}_5)_2$) in dibutylphthalate [209]. In the following, an experiment involving this substance is discussed to illustrate the application of the method.

The sample was a solution of 4.4% ^{57}Fe -ferrocene in dibutylphthalate. The Fe nucleus in ferrocene experiences an electric field gradient that leads to a beat frequency of 27 MHz in the NFS time spectra, being only slightly dependent on temperature. Selected NFS time spectra at various temperatures are shown in Fig. 4.58a. From the envelope of the time spectra, the normalized decay rate λ_K/λ_0 is deduced as a function of temperature, shown in Fig. 4.58b. In the low-temperature regime it decreases with increasing temperature, because of a decrease of the Lamb-Mössbauer factor and a corresponding decrease of the effective thickness. When diffusion sets in around a temperature of 185 K, the decay is accelerated and the curve bends up again. The relaxation times τ_K determined from these data are shown in Fig. 4.58c (diamonds). The comparison with data from viscosity measurements [210] and dielectric spectroscopy [210, 211] reveals a striking difference by orders of magnitude. Moreover, the temperature dependence as measured by QNFS is much weaker than that determined by the other methods. The reason for this behavior goes back to the small length scale on which the motion is observed ($q = k_0 = 7.3 \text{ \AA}^{-1}$): For large values of q the relaxation times decay proportional to q^{-2} or even stronger.

In a recent investigation of ferrocene/dibutylphthalate in the undercooled state by NRS, a critical temperature of $T_c = 202 \text{ K}$ and a temperature-independent stretching exponent $\beta = 0.47$ was obtained [213]. Due to the isotopic specificity of the scattering process, the method is particularly suited to probe the dynamics of glasses in confined systems [214]. The signal is derived only from parts of the sample that contain the resonant nuclei, i.e., it is free of contributions from the surrounding materials.

4.6.4 Relaxation Phenomena

Time spectra of nuclear forward scattering are strongly affected when the state of the system changes during the nuclear lifetime. This can happen either via external influences like magnetic switching or ultrasound modulation or by intrinsic mechanisms like thermal excitation. In any case the the

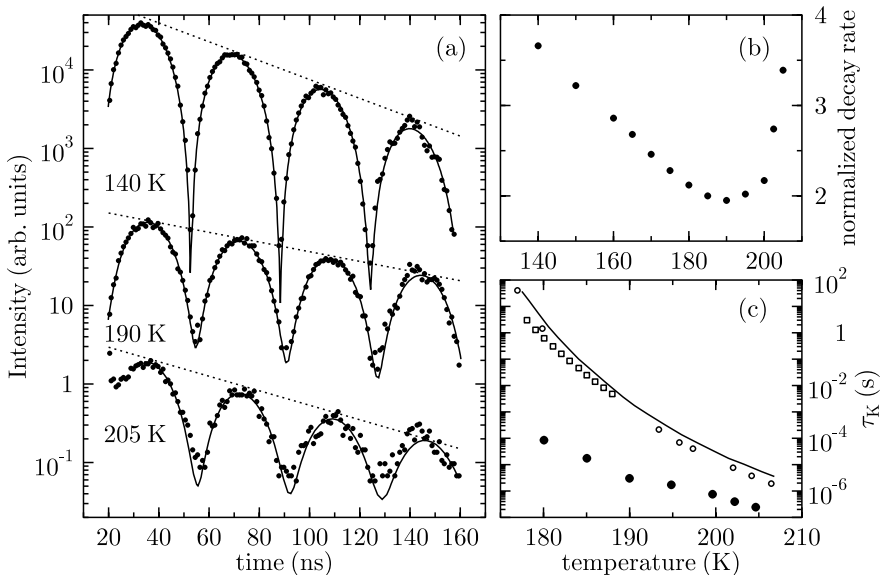


Fig. 4.58. (a) NFS time spectra from a solution of ferrocene in dibutylphthalate at different temperatures. The structural relaxation is reflected in the accelerated decay of the intensity as indicated by the dashed lines. (b) Effective decay rate of the NFS intensity as function of temperature, (c) Kohlrausch relaxation times for ferrocene/dibutylphthalate as derived from the NFS data (diamonds) in comparison with data from other methods: viscosity measurements (solid line) [210] and dielectric spectroscopy (circles and squares) [210, 211]. (Figure adopted from H. Franz et al. [212])

system fluctuates between different states. This phenomenon is called *relaxation*. It may occur between the electronic states of one atom or between different orientations of the magnetization in small superparamagnetic particles. In conventional Mössbauer spectroscopy, relaxation phenomena show up via line broadening. In the time domain, nuclear resonant forward scattering provides particularly valuable information on relaxation mechanisms. In both cases, the technique becomes sensitive to relaxation phenomena if the relaxation times are comparable to the Larmor precession times of the nuclei. The evaluation of the corresponding spectra can be achieved by adopting the stochastic theory by Blume and coworkers [215, 216]. In this theory the hyperfine interaction is described in terms of effective hyperfine fields acting on the nuclei. These effective fields either originate from the magnetization in small particles as in the case of superparamagnetism, or from the electronic states of a paramagnetic ion. In the latter case the concept of effective hyperfine fields is a very good approximation if the energy splittings in the electron shell (due to crystal fields, spin orbit coupling or external magnetic fields)

are large compared to the hyperfine interaction energies. Generally, one can distinguish between three time regimes:

- (a) The relaxation time τ_R is much larger than the Larmor precession time, i.e., $\tau_R \ll 1/\omega_{hf}$ (slow relaxation limit), where $E_{hf} = \hbar\omega_{hf}$ is the hyperfine interaction energy. In this case the nuclei experience the hyperfine field of each electronic state. In the spectrum this appears as a superposition of various subspectra with sharp resonance lines. The relative intensities of the subspectra are governed by the Boltzmann population of the electronic levels. The NFS time spectra exhibit pronounced quantum beats.
- (b) The relaxation time τ_R is much larger than the Larmor precession time, i.e., $\tau_R \gg 1/\omega_{hf}$ (fast relaxation limit). In this case the nucleus experiences a hyperfine field which is the weighted average of the individual fields of all electronic levels, leading to quantum beats and dynamical beats in the time spectra.
- (c) The relaxation time τ_R is comparable to $1/\omega_{hf}$ (intermediate relaxation regime). Energy spectra exhibit significant line broadenings and time spectra are characterized by a strong speed-up.

In the following, a specific example will be given to illustrate these relaxation regimes.

Superparamagnetic Relaxation of Fe_2O_3 Clusters

As already discussed in Sect. 4.4.5, the magnetization of small particles is subject to thermally excited fluctuations if the thermal energy is equal to or larger than the magnetic anisotropy energy. The method of time resolved nuclear resonant scattering is particularly sensitive to such fluctuations. This is demonstrated in the experiment described here. The sample was a Cu foil with ultrasmall precipitates of Fe that were oxidized mostly into Fe_2O_3 particles, as revealed by conventional Mössbauer spectroscopy. The estimated size of these particles is in the range of about 2 nm. Time spectra of NFS, recorded at the beamline ID18 of the ESRF at various temperatures are shown in Fig. 4.59. Clearly, the shape of the time spectra changes drastically between 10 K and 15 K. While the spectra above 15 K correspond to a single resonance line in the energy domain, the spectra below 10 K clearly exhibit a beat pattern that results from magnetically ordered particles. In the intermediate temperature range, the fluctuation rate of the magnetization is on the order of the Larmor precession time of the nuclear moments. To describe the influence of the relaxation on the lineshape of the resonance, a stochastical model was developed by Blume & Tjon [217]. This model has been implemented into the program package CONUSS [7, 218] to calculate time spectra of NFS under relaxation conditions. However, for an exact simulation the directions between which the fluctuations of the magnetic moments take place have to be known. On the other hand, even if these data are missing and the

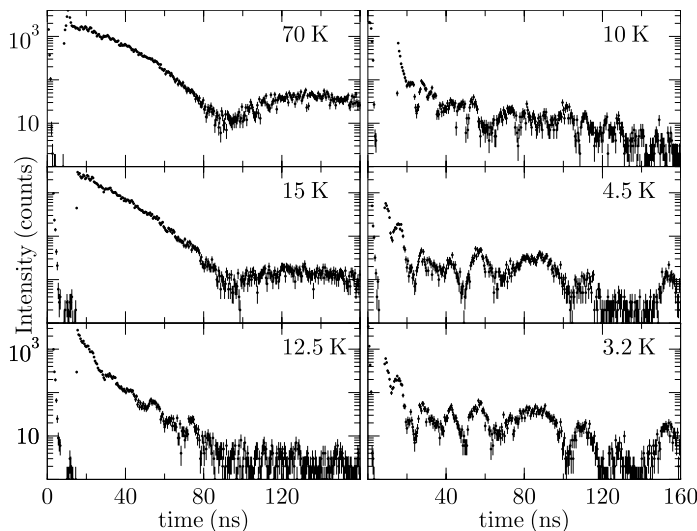


Fig. 4.59. Time spectra of nuclear resonant forward scattering from Fe_2O_3 clusters in Cu as function of temperature

exact shape of the time spectra cannot be calculated, valuable information can be obtained from monitoring the total delayed intensity. This is shown in Fig. 4.60, where the delayed signal within a time window from 15 ns to 160 ns is plotted as a function of temperature. Quite remarkably, one observes a drop in intensity over almost two orders of magnitude between 15 K and 5 K. This indicates the very strong sensitivity of this method to relaxation phenomena that can be used as a strong indicator for the presence of dynamical processes in the sample [219, 220, 221].

While the information that is contained in the shape of the time spectra can in principle be obtained by conventional Mössbauer spectroscopy as well, this is not the case for the time-integrated signal. The reason is that the relaxations are in fact stochastic fluctuations of the hyperfine fields that destroy the coherence between the nuclei. The resulting dephasing reduces the probability amplitude for creation of the nuclear exciton. Thus, on the time scale this dephasing manifests as a strong drop in intensity that is absent in incoherent methods like conventional Mössbauer spectroscopy. This particularly pronounced behavior in NFS is caused by the coherence of the scattering process that implies an enhanced sensitivity to relative phases between scattering sites. The temperature dependence observed here is unusual because it does not show a pronounced minimum as it is typically the case in the presence of relaxation phenomena. Therefore, this specific temperature dependence of the delayed intensity remains to be explained.

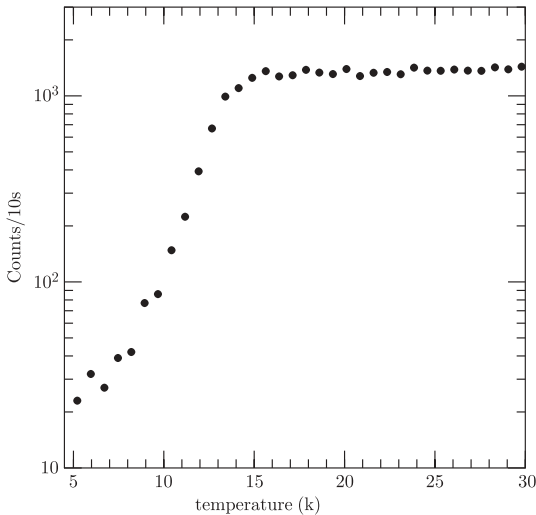


Fig. 4.60. Time-integrated signal of NFS from Fe_2O_3 clusters in Cu as function of temperature

Another example for relaxation in magnetic systems has been discussed in Sect. 4.4.5 where the magnetic dynamics of ultrathin Fe islands on W(110) is investigated.

4.7 Data Analysis

It appears that hyperfine interaction parameters or field distributions cannot be extracted in a straightforward manner from the measured time spectra. A simple inversion of the data is not possible because the phase information is lost by measuring intensities. This is the well-known phase problem of x-ray scattering that applies for the evaluation of time spectra as well. An inversion is only possible when some knowledge of the system is used as an initial guess. With this set of parameters, one calculates the response of the system to compare it with the measured data; the result of this comparison is then used to improve the initial guess, and so on. In any case this is an iterative procedure that does not necessarily lead to a unique solution; uniqueness can only be achieved via additional knowledge about the system.

For the analysis of coherent nuclear scattering experiments, a number of software packages are freely available. The first package that became available is CONUSS [7, 218, 222] that was developed originally for evaluation of nuclear Bragg scattering. It also includes routines to calculate nuclear forward scattering and an additional package to treat grazing-incidence reflection from thin films and multilayers [6]. While CONUSS calculates the reflected or transmitted amplitudes as a function of energy and performs a Fourier transform into the time domain, the program package MOTIF [223, 224] works in the time domain based on the formalism described in Sect. 2.3.1. While

the program was originally developed to treat time-dependent phenomena of magnetic switching [225, 226, 227] it is very powerful to treat NFS, but it does not include Bragg diffraction and thin-film reflection. Other packages to calculate NFS are SYNPOS [228, 229] and EFFINO [230], where SYNPOS is particularly specialized to handle paramagnetic iron complexes in biological macromolecules, while EFFINO also contains routines for thin-film reflection.

However, there exist experimental procedures like interferometry or tomography that enable to solve the phase problem under certain conditions. A promising interferometric approach to determine the phase of the quantum beat pattern has been proposed by *Sturhahn* [231]. In this technique the signal from the sample is brought to interference with the signal from a well-known reference absorber by using an Bonse-Hart interferometer. In another method, ambiguities in the determination of magnetic fields in thin films or single crystals can be removed by application of a tomographic-like technique where time spectra are recorded for a number of orientations of the sample. This is demonstrated in Sect. 4.4.4 of this book. Moreover, it should be checked whether inversion routines that are applied to determine the density profiles of thin films [81, 83] can be used to evaluate quantum beat patterns. In cases where the kinematical approximation is valid, procedures for data inversion can be found. However, the validity of the kinematic limit does not automatically imply that the problem can be inverted. It remains to be checked if this applies in case of NRS from very thin or dilute samples.

4.8 Comparison with Other Scattering Methods

It has been shown in the previous sections how nuclear resonant scattering can be employed to retrieve information about the magnetic structure of thin films. This information is extracted from the analysis of the temporal beat pattern in the time spectra. Due to its isotopic specificity, nuclear resonant scattering can be used to determine magnetic properties with very high spatial resolution, e.g., by employing isotopic probe layers. This renders it an ideal tool to complement other techniques that deliver macroscopic magnetic properties. Examples for such techniques are resonant magnetic x-ray scattering and polarized neutron scattering that will be briefly discussed in the following. While in the first case the magnetic information (orbital and spin magnetic moments) is obtained from spectroscopic measurements, the latter technique employs polarization analysis of scattered neutrons to determine magnetization profiles and spin structures. Despite the different scattering mechanisms, the same formalism for anisotropic optics as outlined in Sect. 4.1.4 can be employed to describe specular reflection from surfaces and layered structures.

4.8.1 Resonant Magnetic X-ray Scattering

Resonant scattering processes occur in any kind of bound systems. A very prominent example is x-ray scattering from inner-shell resonances [9]. The sample magnetization leads to an exchange splitting of the levels that results in a strong sensitivity of the scattering process to magnetic fields. For comparison, the level schemes for electronic and nuclear resonant x-ray scattering are shown in Fig. 4.61. In the case of magnetic x-ray scattering the transition takes place between the exchange split electronic levels and empty states above the Fermi level. The resonant contribution to the forward scattering amplitude is given by (4.12) with the energy dependence of the scattering process (due to the multiplet structure of the energy levels) described by (4.13). The polarization dependence of the scattering process is described by (4.14) or equivalently by (4.15). Specular reflection from magnetic layer systems can then be treated by application of the matrix formalism outlined in Sect. 4.1.4. A different type of algorithm for the description of resonant x-ray reflection from magnetic multilayers has been given by *Stepanov & Sinha* [243].

Due to the delocalized nature of the empty states, the scattering process probes the macroscopic magnetic properties of the sample. Sum rules can be applied to the absorption spectra taken for different photon polarization states (left/right-circular, σ/π -linear) to determine spin and orbital magnetic moments [232, 233]. While these dichroic methods rely on incoherent scattering processes, also coherent scattering channels like specular reflection can be exploited, especially for the study of magnetic thin films, multilayers and nanostructures on surfaces [234, 235, 236, 237, 238].

In contrast to this type of magnetic x-ray scattering, nuclear resonant scattering proceeds between levels that are belonging to strictly localized nuclei. Thus, nuclear resonant absorption and scattering is a probe of local magnetic properties. The splitting of the nuclear levels is determined by the magnetic hyperfine field at the nucleus. Although there is no direct way to determine the magnetic moment from the hyperfine field, in most cases they are proportional to each other. However, in ultrathin films and other low-dimensional systems there may be deviations from this proportionality when contributions to the local hyperfine field change with temperature, for example. In this case, the temperature dependence of the hyperfine field does not reflect the temperature dependence of the magnetization any longer.

4.8.2 Polarized Neutron Reflectometry

Neutron reflectometry is a very sensitive tool for the study of magnetic thin films and surfaces [239, 240]. Since the scattering process has no intrinsic energy dependence, the magnetic information is obtained through polarization dependent reflectivity measurements with polarization analysis. Typically

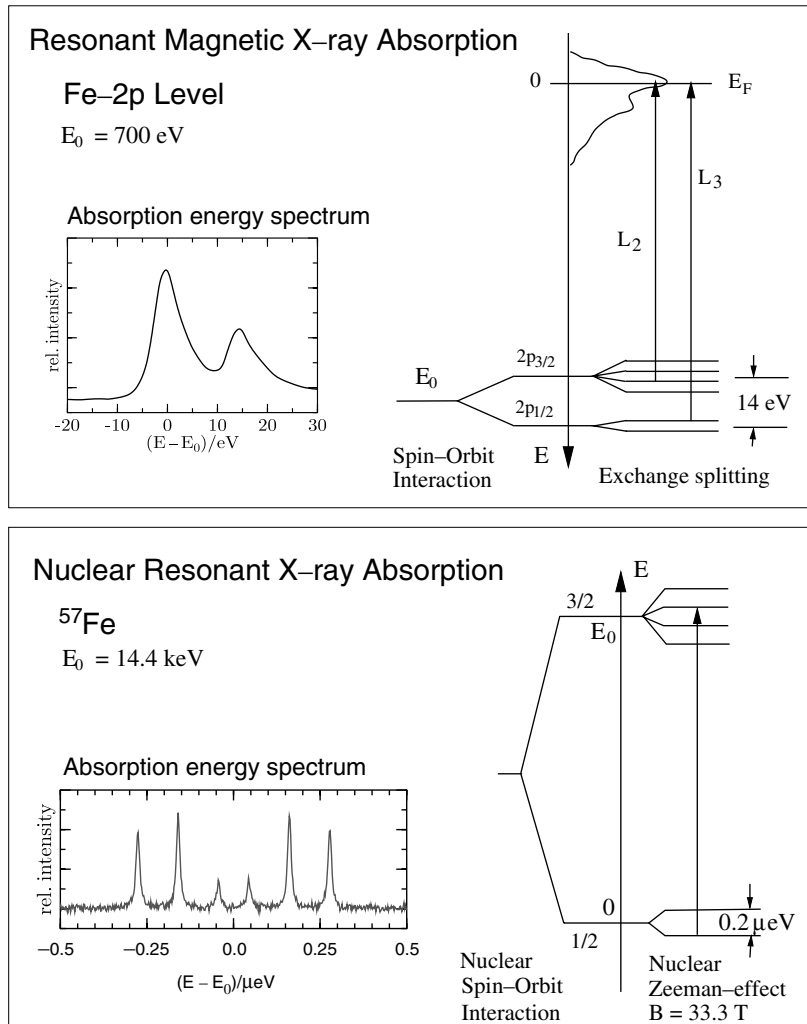


Fig. 4.61. Comparison between resonant magnetic x-ray scattering from the Fe - 2p level with a resonance energy of $E_0 = 710 \text{ eV}$ and nuclear resonant scattering from ^{57}Fe at $E_0 = 14.4 \text{ keV}$. Besides the level diagram, shown on the right, a typical absorption energy spectrum is shown on the left. In case of the Fe - 2p level, the yield of photoelectrons was measured, while in case of ^{57}Fe the yield of conversion electrons was recorded as function of the detuning energy relative to the resonance energy position E_0

four reflectivities are recorded which are R_{++} and R_{--} for the two non-spin-flip channels and R_{+-} and R_{-+} for the two spin-flip channels. These channels are selected by adjustment of the neutron polarizer and analyzer before and behind the sample, respectively [239]. In order to discuss the

polarization dependence of the scattering process, we briefly develop the expression for the coherent forward scattering amplitude in the following. A common algorithm for the calculation of nuclear resonant and polarized neutron reflectivity from stratified media was given by *Deák et al.* [241].

Neutrons in magnetic materials interact with the magnetic induction fields \mathbf{B} of the atoms via the neutron dipole moment $\boldsymbol{\mu}_n$. Together with the nuclear contribution to the interaction, which is of the same order of magnitude, the interaction potential can be written as [242]:

$$\mathbf{V} = \frac{\hbar^2}{2m_n} \sum_i \varrho_i b_i - \boldsymbol{\mu}_n \cdot \mathbf{B}, \quad (4.148)$$

where m_n is the neutron mass. The sum runs over all isotopic constituents in the sample with atomic density ϱ_i and coherent nuclear scattering length b_i . The interaction potential is related to the coherent neutron forward scattering amplitude \mathbf{f}_n via ¹⁵

$$\mathbf{f}_n = \frac{m_n}{\hbar^2 k_{0z}} \mathbf{V}, \quad (4.149)$$

where k_{0z} is the normal component of the incident wavevector relative to the surface. The operator of the neutron magnetic moment can be expressed as

$$\boldsymbol{\mu}_n = \mu_n \boldsymbol{\sigma}, \quad (4.150)$$

where μ_n is the magnetic moment of the neutron, and $\boldsymbol{\sigma}$ is a 3-component vector consisting of the Pauli spin matrices:

$$\sigma_x = \begin{pmatrix} 0 & 1 \\ 1 & 0 \end{pmatrix}, \quad \sigma_y = \begin{pmatrix} 0 & -i \\ i & 0 \end{pmatrix}, \quad \sigma_z = \begin{pmatrix} 1 & 0 \\ 0 & -1 \end{pmatrix}. \quad (4.151)$$

Inserting this together with (4.150) into (4.148), and writing the magnetic field as $\mathbf{B} = (B_x, B_y, B_z)$, the forward scattering amplitude can now be expressed as:

$$\mathbf{f}_n = \frac{1}{2k_{0z}} \left[\sum_i \varrho_i b_i - \frac{2\mu_n m_n}{\hbar^2} \begin{pmatrix} B_z & B_x - iB_y \\ B_x + iB_y & -B_z \end{pmatrix} \right]. \quad (4.152)$$

From this expression the polarization dependence of neutron scattering experiments can be derived. A typical scattering geometry is shown in Fig. 4.62 with linearly polarized neutrons incident on a sample. The polarization direction of the neutrons typically defines the quantization axis z relative to which the direction of the magnetization is measured. With \mathbf{B} being aligned along the z -direction, i.e., $B_x = B_y = 0$, \mathbf{f}_n is diagonal with different values for the two non-spin-flip channels. In the case that \mathbf{B} is aligned along the x -direction, one observes strong spin-flip scattering because of the non-zero

¹⁵ Treating the scattering process by the one-dimensional Schrödinger equation, one obtains for the normal component of the neutron wavevector in the material $k_{1z} = [k_{0z}^2 - 2m_n V/\hbar^2]^{1/2}$ [242]. Comparison with (4.30) then leads to (4.149).

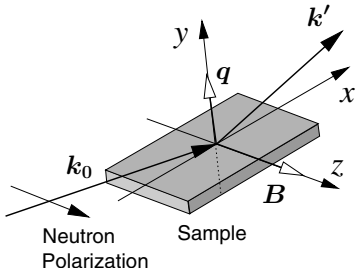


Fig. 4.62. Scattering geometry and coordinates for evaluation of the neutron scattering amplitude given in (4.152). The z -direction coincides with the quantization axis that is given by the neutron polarization direction. The incident neutron beam is linearly polarized parallel to the sample surface

off-diagonal elements of \mathbf{f}_n . From the intensities in the different scattering channels one determines spin directions as well as absolute magnetic moments [242]. However, it should be noted that the scattering is insensitive to the sample magnetization if \mathbf{B} is aligned along the y -direction because the magnetic induction is continuous across the boundary. In this case only the nuclear contribution is observed. In general, magnetic neutron scattering takes place only if the sample magnetization has a component perpendicular to the scattering vector (momentum transfer) $\mathbf{q} = \mathbf{k}' - \mathbf{k}_0$. Therefore, \mathbf{B} should always be taken as the component of the magnetization perpendicular to \mathbf{q} . For calculation of the neutron reflectivity of arbitrary layered systems \mathbf{f}_n can now be plugged into the matrix formalism developed in Sect. 4.1.4. An alternative formulation for polarized neutron reflectometry has been given by Rühm *et al.* [25].

References

1. M. Lax: Rev. Mod. Phys. **23**, 287 (1951) [67](#)
2. R. M. A. Azzam and N. M. Bashara: *Ellipsometry and Polarized Light* (Elsevier Science Publishers, Amsterdam 1987) [67](#)
3. B. W. Batterman and H. Cole: Rev. Mod. Phys. **36**, 681 (1964) [68](#)
4. Z. G. Pinsker: *Dynamical Scattering of X-rays in Crystals* (Springer, Berlin 1978) [68](#)
5. C. Kolbeck: Diploma thesis (Universität Hamburg, 1995) [70](#)
6. R. Röhlsberger: Hyperfine Interact. **123/124**, 301 (1999) [70, 86, 87, 166](#)
7. W. Sturhahn and E. Gerdau: Phys. Rev. B **49**, 9285 (1994) [70, 71, 77, 164, 166](#)
8. B. E. Warren: *X-ray diffraction* (Dover Publications, New York 1990) [70](#)
9. J. P. Hannon, G. T. Trammell, M. Blume, and D. Gibbs: Phys. Rev. Lett. **61**, 1245 (1988) and Phys. Rev. Lett. **62**, 2644 (1989) (erratum) [71, 168](#)
10. S. W. Lovesey and S. P. Collins: *X-ray Scattering and Absorption by Magnetic Materials* (Clarendon Press, Oxford 1996) [71](#)
11. J. P. Hannon and G. T. Trammell: Phys. Rev. **169**, 315 (1968) [71](#)
12. J. P. Hannon and G. T. Trammell: Hyperfine Interact. **123/124**, 127 (1999) [71, 72](#)
13. J. B. Hastings, D. P. Siddons, U. van Bürck, R. Hollatz, and U. Bergmann: Phys. Rev. Lett. **66**, 770 (1991) [74](#)

14. U. van Bürck, D. P. Siddons, J. B. Hastings, U. Bergmann, and R. Hollatz : Phys. Rev. B **46**, 6207 (1992) **74**
15. D. P. Siddons, U. Bergmann, and J. B. Hastings : Phys. Rev. Lett. **70**, 359 (1993) **74**
16. U. Bergmann, S. D. Shastri, D. P. Siddons, B. W. Batterman, and J. B. Hastings : Phys. Rev. B **50**, 5957 (1994) **74, 127, 137, 138**
17. R. Röhlsberger : Hyperfine Interact. **123/124**, 455 (1999) **78**
18. L. G. Parratt : Phys. Rev. **95**, 359 (1954) **80**
19. E. Fullerton, J. S. Jiang, M. Grimsditch, C. H. Sowers, and S. D. Bader : Phys. Rev. B **58**, 12193 (1998) **80, 123, 124, 127, 128, 129**
20. R. Röhlsberger, H. Thomas, K. Schlage, E. Burkel, O. Leupold, and R. Rüffer : Phys. Rev. Lett. **89**, 237201 (2002) **80, 126**
21. F. Nizzoli and J. R. Sandercock : *Dynamical Properties of Solids*, Vol. 6 (North-Holland, Amsterdam 1990) **80**
22. S. Mangin, F. Montaigne, and A. Schuhl : Phys. Rev. B **68**, 140404 (2003) **80**
23. F. Montaigne, S. Mangin, and Y. Henry : Phys. Rev. B **67**, 144412 (2003) **80**
24. L. Déák, L. Bottyán, D. L. Nagy, and H. Spiering : Phys. Rev. B **53**, 6158 (1996) **80**
25. A. Rühm, B. P. Toperverg, and H. Dosch : Phys. Rev. B **60**, 16073 (1999) **80, 171**
26. R. Röhlsberger, T. Klein, K. Schlage, O. Leupold, and R. Rüffer : Phys. Rev. B **69**, 235412 (2004) **81, 83, 113**
27. M. A. Andreeva and B. Lindgren : Pis'ma v ZhETF **76**, 833 (2002) **84**
28. A. Q. R. Baron, J. Arthur, S. L. Ruby, A. I. Chumakov, G. V. Smirnov, and G. S. Brown : Phys. Rev. B **50**, 10354 (1994) **84, 96, 98**
29. R. M. Osgood III, S. K. Sinha, J. Freeland, Y. U. Idzerda, and S. D. Bader : J. Magn. Magn. Mater. **198-199**, 698 (1999) **86**
30. L. Nevot and P. Croce : Rev. Phys. Appl. **15**, 761 (1980) **87**
31. L. I. Schiff : *Quantum Mechanics* (McGraw-Hill, London 1968) **87**
32. N. N. Greenwood and T. C. Gibb : *Mössbauer Spectroscopy* (Chapman and Hall, London 1971), p. 233ff. **89, 94, 95**
33. E. Matthias, W. Schneider, and R. M. Steffen : Phys. Rev. **125**, 261 (1962) **90**
34. E. Matthias, W. Schneider, and R. M. Steffen : Arkiv för Fysik **24**, 97 (1963) **90**
35. M. E. Rose : *Elementary Theory of Angular Momentum* (Wiley, New York 1957) **90**
36. R. Röhlsberger, O. Leupold, J. Metge, H. D. Rüter, W. Sturhahn, and E. Gerdaus : Hyperfine Interact. **92**, 1107 (1994) **94**
37. V. Schünemann and H. Winkler : Rep. Prog. Phys. **63**, 263 (2000) **94**
38. A. X. Trautwein and H. Winkler : Hyperfine Interact. **123/124**, 561 (1999) **94**
39. M. Sladeczek, B. Sepiol, J. Korecki, T. Slezak, R. Rüffer, D. Kmiec, and G. Vogl : Surf. Sci. **566-568**, 372 (2004) **94**
40. R. Röhlsberger, J. Bansmann, V. Senz, A. Bettac, K. L. Jonas, K. H. Meiwes-Broer, and O. Leupold : Phys. Rev. B **67**, 245412 (2003) **99, 130, 132, 133**
41. C. L'abbé, J. Meerschaut, W. Sturhahn, J. S. Jiang, T. S. Toellner, E. E. Alp, and S. D. Bader : Phys. Rev. Lett. **93**, 037201 (2004) **103, 104**
42. K. Hirano, T. Ishikawa, and S. Kikuta : Nucl. Instrum. Methods Phys. Res. A **336**, 343 (1993) **104**
43. J. C. Lang and G. Srayer : Rev. Sci. Instrum. **66**, 1540 (1995) **104**

44. J. Pollmann, G. Srajer, J. Maser, J. C. Lang, C. S. Nelson, C. T. Venkataraman, and E. D. Isaacs: Rev. Sci. Instrum. **71**, 2386 (2000) 104
45. G. K. Wertheim: *Mössbauer Effect: Principles and Applications* (Academic Press, New York and London, 1964) 105
46. P. Schaaf, A. Müller, E. Carpene, and M. Kahle: Hyperfine Interact. **144/145**, 129 (2002) 106
47. V. E. Kuncser, M. Doi, W. Keune, M. Askin, H. Spies, J. S. Jiang, A. Inomata, and S. D. Bader: Phys. Rev. B **68**, 064416 (2003) 106
48. V. Kuncser, W. Keune, M. Vopsaroiu, and P. R. Bissell: Nucl. Instrum. Methods Phys. Res. B **196**, 135 (2002) 106
49. H. D. Pfannes and H. Fischer: Appl. Phys. **13**, 317 (1977) 106
50. J. M. Greeneche and F. Varret: J. Phys. C: Solid State Phys. **15**, 5333 (1982) 106
51. A. Q. R. Baron, A. I. Chumakov, H. F. Grünsteudel, H. Grünsteudel, L. Niesen, and R. Rüffer: Phys. Rev. Lett. **77**, 4808 (1996) 107, 108
52. S. K. Sinha, M. Tolan, and A. Gibaud: Phys. Rev. B **57**, 2740 (1998) 107
53. E. Gluskin, E. E. Alp, I. McNulty, W. Sturhahn, and J. Sutter: J. Synchrotron Rad. **6**, 1065 (1999) 107
54. E. Spiller and A. Segmüller: Appl. Phys. Lett. **24**, 60 (1974) 110
55. Y. Wang, M. Bedzyk, and M. Caffrey: Science **258**, 775 (1992) 110
56. R. Röhlsberger, W. Sturhahn, T. S. Toellner, K. W. Quast, P. Hession, M. Hu, J. Sutter, and E. E. Alp: J. Appl. Phys. **86**, 584 (1999) 110
57. R. Röhlsberger, W. Sturhahn, T. S. Toellner, K. W. Quast, E. E. Alp, A. Bernhard, J. Metge, R. Rüffer, and E. Burkert: Physica B **263-264**, 581 (1999) 110
58. S. K. Ghose and B. N. Dev: Phys. Rev. B **63**, 245409 (2001) 110
59. S. K. Ghose, B. N. Dev, and A. Gupta: Phys. Rev. B **64**, 233403 (2001) 110
60. Y. P. Feng, S. K. Sinha, H. W. Deckman, J. B. Hastings, and D. P. Siddons: Phys. Rev. Lett. **71**, 537 (1993) 110
61. M. J. Zwanenburg, F. Peters, J. H. Bongaerts, S. A. de Vries, D. L. Abernathy, and J. F. van der Veen: Phys. Rev. Lett. **82**, 1696 (1999) 110
62. M. J. Zwanenburg, J. H. Bongaerts, F. Peters, D. O. Riese, and J. F. van der Veen: Phys. Rev. Lett. **85**, 5154 (2000) 110
63. F. Pfeiffer, T. Salditt, P. Høghøj, and C. David: SPIE Proceedings **4145**, 193 (2001) 110
64. F. Pfeiffer, T. Salditt, P. Høghøj, I. Anderson, and N. Schell: Phys. Rev. B **62**, 16939 (2000) 110
65. A. Krol, C. J. Sher, and Y. H. Kao: Phys. Rev. B **38**, 8579 (1989) 110
66. J. P. Hannon, G. T. Trammell, M. Mueller, E. Gerdau, H. Winkler, and R. Rüffer: Phys. Rev. Lett. **43**, 636 (1979) 110
67. J. P. Hannon, N. V. Hung, G. T. Trammell, E. Gerdau, M. Mueller, R. Rüffer, and H. Winkler: Phys. Rev. B **32**, 5068 (1985) 110
68. J. P. Hannon, N. V. Hung, G. T. Trammell, E. Gerdau, M. Mueller, R. Rüffer, and H. Winkler: Phys. Rev. B **32**, 5081 (1985) 110
69. J. P. Hannon, G. T. Trammell, M. Mueller, E. Gerdau, R. Rüffer, and H. Winkler: Phys. Rev. B **32**, 6363 (1985) 110
70. J. P. Hannon, G. T. Trammell, M. Mueller, E. Gerdau, R. Rüffer, and H. Winkler: Phys. Rev. B **32**, 6374 (1985) 110

71. R. Röhlsberger, E. Gerdau, M. Harsdorff, O. Leupold, E. Lüken, J. Metge, R. Rüffer, H. D. Rüter, W. Sturhahn, and E. Witthoff: *Europhys. Lett.* **18**, 561 (1992) [110](#)
72. R. Röhlsberger, E. Gerdau, E. Lüken, H. D. Rüter, J. Metge, O. Leupold: *Z. Phys. B* **92**, 489 (1993) [110](#)
73. D. L. Nagy, L. Bottyán, L. Deák, J. Dekoster, G. Langouche, V. G. Semenov, H. Spiering and E. Szilágyi, in: *Proc. Mössbauer Spectroscopy in Materials Science*, edited by M. Miglierini and D. Petridis (Kluwer Academic Press, Amsterdam 1999) p. 323. [115](#), [116](#)
74. J. Tyson, A. H. Owens, J. C. Walker, and G. Bayreuther: *J. Appl. Phys.* **52**, 2487 (1981) [116](#)
75. J. Korecki and U. Gradmann: *Phys. Rev. Lett.* **55**, 2491 (1985) [116](#)
76. G. Lugert and G. Bayreuther: *Phys. Rev. B* **38**, 11068 (1988) [116](#)
77. M. Przybylski, I. Kaufmann, and U. Gradmann: *Phys. Rev. B* **40**, 8631 (1989) [116](#), [139](#)
78. T. Shinjo: *Surf. Sci. Rep.* **21**, 49 (1991) [116](#)
79. B. Niesen, M. F. Rosu, A. Mugarza, R. Coehoorn, R. M. Jungblut, F. Rooseboom, A. Q. R. Baron, A. I. Chumakov, and R. Rüffer: *Phys. Rev. B* **58**, 8590 (1998) [116](#)
80. R. Röhlsberger, J. Bansmann, V. Senz, A. Bettac, K. L. Jonas, O. Leupold, R. Rüffer, E. Burkel, and K. H. Meiwes-Broer: *Phys. Rev. Lett.* **86**, 5597 (2001) [116](#), [140](#), [141](#), [142](#)
81. K.-M. Zimmermann, M. Tolan, R. Weber, J. Stettner, A. K. Doerr, and W. Press: *Phys. Rev. B* **62**, 10377 (2000) [117](#), [167](#)
82. W. L. Clinton: *Phys. Rev. B* **48**, 1 (1993) [117](#)
83. M. Tolan: *X-ray Scattering from Soft-Matter Thin Films* (Springer, Berlin 1999) [117](#), [167](#)
84. F. Pfeiffer, U. Mennicke, and T. Salditt: *J. Appl. Cryst.* **35**, 163 (2002) [117](#)
85. O. H. Seeck, I. D. Kaendler, M. Tolan, K. Shin, M. H. Rafailovich, J. Sokolov and R. Kolb: *Appl. Phys. Lett.* **76**, 2713 (2000) [117](#)
86. P. A. Grünberg, R. Schreiber, Y. Pang, M. B. Brodsky, and H. Sowers: *Phys. Rev. Lett.* **57**, 2442 (1986) [117](#)
87. M. Rührlig, R. Schäfer, A. Hubert, R. Mosler, J. A. Wolf, S. Demokritov, and P. Grünberg: *Phys. Status Solidi A* **125**, 635 (1991) [117](#)
88. J. C. Slonczewski: *Phys. Rev. Lett.* **67**, 3172 (1991) [117](#)
89. J. C. Slonczewski: *J. Magn. Magn. Mater.* **150**, 13 (1995) [117](#)
90. N. S. Almeida and D. L. Mills: *Phys. Rev. B* **52**, 13504 (1995) [117](#)
91. R. E. Camley, J. Kwo, M. Hong, and C. L. Chien: *Phys. Rev. Lett.* **64**, 2703 (1990) [117](#)
92. M. N. Baibich, J. M. Broto, A. Fert, F. Nguyen Van Dau, F. Petroff, P. Etienne, G. Creuzet, A. Friederich, and J. Chazelas: *Phys. Rev. Lett.* **61**, 2472 (1988) [117](#), [123](#), [148](#)
93. S. S. P. Parkin, N. More, and K. P. Roche: *Phys. Rev. Lett.* **64**, 2304 (1990) [118](#), [148](#)
94. M. A. Ruderman and C. Kittel: *Phys. Rev.* **96**, 99 (1954); T. Kasuya: *Prog. Theor. Phys.* **16**, 45, 58 (1956); K. Yosida: *Phys. Rev.* **106**, 893 (1957) [118](#)
95. P. Bruno: *Phys. Rev. B* **52**, 411 (1995) [118](#)
96. M. D. Stiles: *Phys. Rev. B* **48**, 7238 (1993) [118](#)
97. R. Coehorn: *Phys. Rev. B* **44**, 9331 (1991) [118](#)
98. S. S. P. Parkin: *Phys. Rev. Lett.* **67**, 3598 (1991) [118](#)

99. E. E. Fullerton, M. J. Conover, J. E. Mattson, C. H. Sowers, and S. D. Bader : Phys. Rev. B **48**, 15755 (1993) [119](#)
100. A. I. Chumakov, B. Niesen, D. L. Nagy, and E. E. Alp : Hyperfine Interact. **123/124**, 427 (1999) [119](#)
101. T. S. Toellner, W. Sturhahn, R. Röhlsberger, E. E. Alp, C. H. Sowers, and E. E. Fullerton : Phys. Rev. Lett. **74**, 3475 (1995) [119, 120](#)
102. N. Hossoito, S. Araki, K. Mibu, and T. Shinjo : J. Phys. Soc. Japan **59**, 1925 (1990) [119](#)
103. J. Landes, Ch. Sauer, R. A. Brand, W. Zinn, and Z. Kajcsos : Hyperfine Interact. **57**, 1941 (1990) [120](#)
104. L. Bottyán, J. Dekoster, L. Deák, B. Degroote, E. Kunnen, C. L'abbé, G. Langouche, O. Leupold, M. Major, J. Meersschaut, D. L. Nagy, and R. Rüffer in : ESRF Highlights 1999 [122](#)
105. L. Neél : Ann. Phys. (Paris) **5**, 232 (1936) [121](#)
106. Y. Shapira and S. Foner : Phys. Rev. B **1**, 3083 (1970) [121](#)
107. D. L. Mills : Phys. Rev. Lett. **20**, 18 (1968) [121](#)
108. R. W. Wang, D. M. Mills, E. E. Fullerton, J. E. Mattson, and S. D. Bader : Phys. Rev. Lett. **72**, 920 (1994) [121](#)
109. V. Lauter-Pasyuk, H. J. Lauter, B. P. Toperverg, L. Romashev, and V. Ustinov : Phys. Rev. Lett. **89**, 167203 (2002) [121](#)
110. S. G. E. te Velthuis, J. S. Jiang, S. D. Bader, and G. P. Felcher : Phys. Rev. Lett. **89**, 127203 (2002) [121](#)
111. D. L. Nagy, L. Bottyán, L. Deák, and M. Major : Proceedings of the XXXVI. Zakopane School of Physics, (Zakopane 2001) [122, 123](#)
112. L. Bottyán, L. Deák, J. Dekoster, E. Kunnen, G. Langouche, J. Meersschaut, M. Major, D. L. Nagy, H. D. Rüter, E. Szilágyi, and K. Temst : J. Magn. Magn. Mater. **240**, 514 (2002) [121, 150](#)
113. A. Ludwig and E. Quandt : J. Appl. Phys. **87**, 4691 (2000) [123](#)
114. J. Nogués and I. K. Schuller : J. Magn. Magn. Mater. **192**, 203 (1999) [123](#)
115. K. Mibu, T. Nagahama, T. Shinjo, and T. Ono : Phys. Rev. B **58**, 6442 (1998) [123](#)
116. G. Binasch, P. Grünberg, F. Saurenbach, and W. Zinn : Phys. Rev. B **39**, 4828 (1989) [123](#)
117. R. Skomski and J. M. D. Coey : Phys. Rev. B **48**, 15812 (1993) [123](#)
118. E. F. Kneller and R. Hawig : IEEE Trans. Magn. **27**, 3588 (1991) [123](#)
119. R. E. Camley : Phys. Rev. B **35**, 3608 (1987) [124](#)
120. J. S. Jiang, H. G. Kaper, and G. K. Leaf : Discrete and Continous Dynamical Systems - Series B **1**, 219 (2001) [124](#)
121. K. V. O'Donovan, J. A. Borchers, C. F. Majkrzak, O. Hellwig, and E. E. Fullerton : Phys. Rev. Lett. **88**, 067201 (2002) [124](#)
122. C. M. Kuo, P. C. Kuo, H. C. Wu, Y. D. Yao, and C. H. Lin : J. Appl. Phys. **85**, 4886 (1999) [124](#)
123. J. P. Liu, C. P. Luo, Y. Liu, and D. J. Sellmyer : Appl. Phys. Lett. **72**, 483 (1998) [124](#)
124. R. Rüffer and A. I. Chumakov : Hyperfine Interact. **97/98**, 589 (1996) [125, 131](#)
125. S. Jeong, Y. Hsu, D. E. Laughlin, and M. E. McHenry : IEEE Trans. Magn. **37**, 1299 (2001) [125](#)
126. J.-U. Thiele, L. Folks, M. F. Toney, and D. K. Weller : J. Appl. Phys. **84**, 5686 (1998) [127](#)

127. M. B. Stearns, in: *Magnetic Properties of Metals*, edited by H. P. J. Wijn, Landolt-Börnstein, New Series, III/19a (Springer, Berlin 1986) **128**
128. G. S. D. Beach, A. E. Berkowitz, V. G. Harris, F. T. Parker, B. Ramadurai, and D. J. Smith: *J. Appl. Phys.* **91**, 7526 (2002) **129**
129. F. J. Himpsel, J. E. Ortega, G. J. Mankey, and R. F. Willis: *Adv. Phys.* **47**, 511 (1998) **130**
130. K. H. Meiwes-Broer (ed.): *Metal Clusters at Surfaces*, (Springer, Berlin 2000) **130**
131. R. H. Kodama and A. S. Edelstein: *J. Appl. Phys.* **85**, 4316 (1999) **130**
132. S. Sun, C. B. Murray, D. Weller, L. Folks, and A. Moser: *Science* **287**, 1989 (2000) **130**
133. S. Padovani, J. Chado, F. Scheurer, and J. P. Bucher: *Phys. Rev. B* **59**, 1887 (1999) **130**
134. M. Bode, R. Pascal, and R. Wiesendanger: *J. Vac. Sci. Techn. A* **15**, 1285 (1997) **130**
135. U. Gradmann, J. Korecki, and G. Waller: *Appl. Phys. A* **39**, 101 (1986) **134**, **140**
136. P. Baumgart, B. Hillebrands, and G. Güntherodt: *J. Magn. Magn. Mater.* **93**, 225 (1991) **134**
137. H. J. Elmers and U. Gradmann: *Appl. Phys. A* **51**, 255 (1990) **134**, **140**
138. V. Senz, R. Röhlsberger, J. Bansmann, O. Leupold, and K. H. Meiwes-Broer: *New. J. Phys.* **5**, 47 (2003) **136**, **137**
139. P. V. Hendriksen, S. Linderoth, and P. A. Lindgård: *Phys. Rev. B* **48**, 7259 (1993) **136**, **137**, **138**
140. M. Pajda, J. Kudrnovský, I. Turek, V. Drchal, and P. Bruno: *Phys. Rev. B* **64**, 174402 (2001) **136**
141. C. K. Loong, J. M. Carpenter, J. W. Lynn, R. A. Robinson, and H. A. Mook: *J. Appl. Phys.* **55**, 1895 (1984) **136**
142. J. W. Lynn: *Phys. Rev. B* **11**, 2624 (1975) **136**
143. S. Y. Savrasov: *Phys. Rev. Lett.* **81**, 2570 (1998) **136**
144. N. W. Ashcroft and N. D. Mermin: *Solid State Physics* (Holt-Saunders, Philadelphia 1976) **136**
145. R. H. Kodama: *J. Magn. Magn. Mater.* **200**, 359 (1999) **137**
146. D. Mauri, D. Scholl, H. C. Siegmann, and E. Kay: *Phys. Rev. Lett.* **62**, 1900 (1989) **138**
147. U. Köbler: *J. Phys.: Condens. Matter* **14**, 8861 (2002) **138**
148. J. A. C. Bland and B. Heinrich (eds.): *Ultrathin Magnetic Structures I, II* (Springer, Berlin 1994) **139**
149. U. Gradmann, in: *Handbook of Magnetic Materials*, Vol. 7, edited by K. H. J. Buschow (Elsevier, Amsterdam 1993) **139**, **143**
150. M. Przybylski and U. Gradmann: *Phys. Rev. Lett.* **59**, 1152 (1987) **139**, **141**
151. M. Przybylski: *Hyperfine Interact.* **113**, 135 (1998) **139**, **141**
152. H. J. Elmers, J. Hauschild, H. Fritzsche, G. Liu, U. Gradmann, and U. Köhler: *Phys. Rev. Lett.* **75**, 2031 (1995) **139**
153. H. J. Elmers, J. Hauschild, and U. Gradmann: *Phys. Rev. B* **54**, 15224 (1996) **139**
154. W. Weber, D. Kerkemann, D. Pescia, D. A. Wesner, and G. Güntherodt: *Phys. Rev. Lett.* **65**, 2058 (1990) **139**
155. H. J. Elmers, G. Liu, and U. Gradmann: *Phys. Rev. Lett.* **63**, 566 (1989) **139**, **143**
156. M. Przybylski and U. Gradmann: *J. Phys. Colloq. C* **8**, 1705 (1988) **140**

157. H. J. Elmers, J. Hauschild, H. Höche, U. Gradmann, H. Bethge, D. Heuer, and U. Köhler: Phys. Rev. Lett. **73**, 898 (1994) [140](#)
158. F. Huang, G. J. Mankey, M. T. Kief, and R. F. Willis: J. Appl. Phys. **73**, 6760 (1993) [140](#)
159. C. P. Bean and J. D. Livingston: J. Appl. Phys. **30**, 120S (1959) [142](#)
160. J. G. Gay and R. Richter: Phys. Rev. Lett. **56**, 2728 (1986) [143](#)
161. F. Bødker, S. Mørup, and S. Linderoth: Phys. Rev. Lett. **72**, 282 (1994) [143](#)
162. Y. Park, S. Adenwalla, G. P. Felcher, and S. D. Bader: Phys. Rev. B **52**, 12779 (1995) [143](#)
163. A. Enders, D. Sander, and J. Kirschner: J. Appl. Phys. **85**, 5279 (1999) [143](#)
164. N. Weber, K. Wagner, H. J. Elmers, J. Hauschild, and U. Gradmann: Phys. Rev. B **55**, 14121 (1997) [143](#)
165. H. Fritzsché, H. J. Elmers, and U. Gradmann: J. Magn. Magn. Mater. **135**, 343 (1994) [144](#)
166. M. Albrecht, T. Furubayashi, M. Przybylski, J. Korecki, and U. Gradmann: J. Magn. Magn. Mat. **113**, 207 (1992) [144](#)
167. J. Chen and J. L. Erskine: Phys. Rev. Lett. **68**, 1212 (1992) [144](#)
168. Z. Q. Qiu and S. D. Bader: Surf. Sci. **438**, 319 (1999) [144](#)
169. D. S. Chuang, C. A. Ballentine, and R. C. O'Handley: Phys. Rev. B **49**, 15084 (1994) [144](#)
170. A. B. Shick, Yu. N. Gornostyrev, and A. J. Freeman: Phys. Rev. B **60**, 3029 (1999) [144](#)
171. H. Bethge, D. Heuer, Ch. Jensen, K. Reshöft, and U. Köhler: Surf. Sci. **331-333**, 878 (1995) [144](#)
172. U. Gradmann: private communication (2002) [144](#)
173. S. C. Hong, A. J. Freeman, and C. L. Fu: Phys. Rev. B **38**, 12156 (1988) [144](#)
174. H. J. Elmers and U. Gradmann: Surf. Sci. **304**, 201 (1994) [144](#)
175. Yu. V. Shvyd'ko, A. I. Chumakov, A. Q. R. Baron, E. Gerdau, R. Rüffer, A. Bernhard, and J. Metge: Phys. Rev. B **54**, 14942 (1996) [145](#), [146](#), [147](#)
176. S. Müller-Pfeiffer, M. Schneider, and W. Zinn: **49**, 15746 (1994) [146](#)
177. D. J. Hughes, M. T. Burgoy, R. B. Heller, and J. W. Wallace: Phys. Rev. **75**, 565 (1949) [146](#)
178. A. Naudon in: *Modern Aspects of Small-Angle Scattering*, edited by H. Brumberger (Kluwer Academic Publishers, Amsterdam 1995), p. 191. [147](#)
179. P. Müller-Buschbaum, M. Casagrande, J. Gutmann, T. Kuhlmann, M. Stamm, S. Cunis, G. von Krosigk, U. Lode, and R. Gehrke: Europhys. Lett. **42**, 517 (1998) [147](#)
180. A. Gibaud, S. Hazra, C. Sella, P. Laffez, A. Désert, A. Naudon, and G. Van Tendeloo: Phys. Rev. B **63**, 193407 (2001) [147](#)
181. S. V. Roth, M. Burghammer, C. Riekel, P. Müller-Buschbaum, A. Diethert, P. Panagiotou, and H. Walter: Appl. Phys. Lett. **82**, 1935 (2003) [148](#)
182. H. T. Hardner, M. B. Weissmann, and S. S. P. Parkin: Appl. Phys. Lett. **67**, 1938 (1995) [148](#)
183. D. L. Nagy, L. Bottyán, B. Croonenborghs, L. Deák, B. Degroote, J. Dekoster, H. J. Lauter, V. Lauter-Pasyuk, O. Leupold, M. Major, J. Meersschaert, O. Nikonorov, A. Petrenko, R. Rüffer, H. Spiering, and E. Szilágyi: Phys. Rev. Lett. **88**, 157202 (2002) [148](#), [149](#), [150](#)
184. J. Unguris, R. J. Celotta, and D. T. Pierce: Phys. Rev. Lett. **67**, 140 (1991) [148](#)

185. G. Wortmann, K. Rupprecht, and H. Giefers: Hyperfine Interact. **144/145**, 103 (2002) **151, 152, 153**
186. R. Lübbbers, G. Wortmann, and H. F. Grünsteudel: Hyperfine Interact. **123/124**, 529 (1999) **151, 153**
187. R. Lübbbers, K. Rupprecht, and G. Wortmann: Hyperfine Interact. **128**, 115 (2000) **151**
188. E. P. Wohlfahrt: Metallic Magnetism Under High Pressure, in: *Physics of Solids Under High Pressure*, edited by J. S. Shilling, R. N. Shelton (North-Holland, Amsterdam 1981) **152**
189. H. Winkelmann, M. M. Abd-Elmeguid, H. Micklitz, J. P. Sanchez, C. Geibel, and F. Steglich: Phys. Rev. Lett. **81**, 4947 (1998) **154**
190. A. Jayaraman, V. Narayananamurti, E. Bucher, and R. G. Maines: Phys. Rev. Lett. **25**, 1430 (1970) **154**
191. V. N. Antonov, B. N. Harmon, and A. N. Yaresko: Phys. Rev. B **66**, 165208 (2002) **154**
192. A. Barla, J. P. Sanchez, Y. Haga, G. Lapertot, B. P. Doyle, O. Leupold, R. Rüffer, M. M. Abd-Elmeguid, R. Lengsdorf, and J. Flouquet: Phys. Rev. Lett. **92**, 066401 (2004) **154, 155**
193. L. van Hove: Phys. Rev. **95**, 249 (1954) **155**
194. S. K. Sinha: J. Phys. Condens. Matter **13**, 7511 (2001) **155**
195. V. G. Kohn and G. V. Smirnov: Phys. Rev. B **57**, 5788 (1998) **156**
196. G. V. Smirnov and V. G. Kohn: Phys. Rev. B **52**, 3356 (1995) **156**
197. K. S. Singwi and A. Sjölander: Phys. Rev. **120**, 1093 (1960) **156**
198. B. Sepiol, C. Czihak, A. Meyer, G. Vogl, J. Metge, and R. Rüffer: Hyperfine Interact. **113**, 449 (1998) **157, 158**
199. G. Vogl and B. Sepiol: Hyperfine Interact. **123/124**, 595 (1999) **157, 159**
200. G. Vogl and M. Hartmann: J. Phys.: Condens. Matter **13**, 7763 (2001) **157**
201. B. Sepiol, A. Meyer, G. Vogl, H. Franz, and R. Rüffer: Phys. Rev. B **57**, 10433 (1998) **159**
202. G. Vogl and B. Sepiol: Acta Metall. Mater. **42**, 3175 (1994) **159**
203. J. Mayer and M. Fähnle: Defect and Diffusion Forum **143 - 147**, 285 (1997) **160**
204. H. Ehmler, A. Heesemann, K. Rätzke, and F. Faupel: Phys. Rev. Lett. **80**, 4919 (1998) **160**
205. W. Götze and L. Sjögren: Rep. Prog. Phys. **55**, 241 (1992) **160**
206. W. Götze in: *Liquids, Freezing and the Glass Transition* (Les Houches), edited by J. P. Hansen, D. Levesque and D. Zinn-Justin (North-Holland, Amsterdam 1991) **160**
207. R. Kohlrausch: Ann. Phys. (Leipzig) **91**, 56 and 179 (1854) **161**
208. M. Fuchs: J. Non-Cryst. Sol. **172-174**, 241 (1994) **161**
209. A. Meyer, H. Franz, J. Wuttke, W. Petry, N. Wiele, R. Rüffer, and C. Hübsch: Z. Phys. B **103**, 479 (1997) **162**
210. N. Menon, S. R. Nagel, and D. C. Venerus: Phys. Rev. Lett. **73**, 963 (1994) **162, 163**
211. J. Dufour, L. Jorat, A. Bondeau, A. Sibilini, and G. Noyel: J. Mol. Liq. **62**, 75 (1994) **162, 163**
212. H. Franz, W. Petry, and A. Q. R. Baron: Hyperfine Interact. **123/124**, 865 (1999) **163**

213. I. Sergueev, H. Franz, T. Asthalter, W. Petry, U. van Bürck, and G. V. Smirnov: Phys. Rev. B **66**, 184210 (2002) [162](#)
214. T. Asthalter, I. Sergueev, H. Franz, R. Rüffer, W. Petry, K. Messel, P. Härter, and A. Huwe: Eur. Phys. J. B **22**, 301 (2001) [162](#)
215. M. Blume: Phys. Rev. **174**, 351 (1968) [163](#)
216. M. J. Clauser and M. Blume: Phys. Rev. B **3**, 583 (1971) [163](#)
217. M. Blume and J. A. Tjon: Phys. Rev. **165**, 446 (1968) [164](#)
218. W. Sturhahn: Hyperfine Interact. **125**, 149 (2000) [164](#), [166](#)
219. O. Leupold, A. Bernhard, E. Gerdau, J. Jäschke, H. D. Rüter, Yu. V. Shvydko, H. de Waard, E. E. Alp, P. Hession, M. Hu, W. Sturhahn, J. Sutter, T. Toellner, A. I. Chumakov, J. Metge, and R. Rüffer: Hyperfine Interact. **113**, 81 (1998) [165](#)
220. O. Leupold and H. Winkler: Hyperfine Interact. **124/125**, 571 (1999) [165](#)
221. H. Winkler, W. Meyer-Klaucke, S. Schwendy, A. X. Trautwein, B. F. Matzanke, O. Leupold, H. D. Rüter, M. Haas, E. Realo, D. Mandon, and R. Weiss: Hyperfine Interact. **113**, 443 (1998) [165](#)
222. W. Sturhahn, E. E. Alp, T. S. Toellner, P. M. Hession, M. Hu, and J. Sutter: HyperfineInteract. **113**, 47 (1998) [166](#)
223. Yu. V. Shvyd'ko: Phys. Rev. B **59**, 9132 (1999) [166](#)
224. Yu. V. Shvyd'ko: HyperfineInteract. **123/124**, 173 (1999) [166](#)
225. Yu. V. Shvyd'ko, S. L. Popov, and G. V. Smirnov: J. Phys. Condens. Matter **5**, 1557 (1993) [167](#)
226. Yu. V. Shvyd'ko, S. L. Popov, and G. V. Smirnov: J. Phys. Condens. Matter **5**, 7047 (1993) [167](#)
227. Yu. V. Shvyd'ko, T. Hertrich, U. vanBürck, E. Gerdau, O. Leupold, J. Metge, H. D. Rüter, S. Schwendy, G. V. Smirnov, W. Potzel, and P. Schindelmann: Phys. Rev. Lett. **77**, 3232 (1996) [167](#)
228. M. Haas, E. Realo, H. Winkler, W. Meyer-Klaucke, A. X. Trautwein, O. Leupold, and H. D. Rüter: Phys. Rev. B **56**, 14082 (1997) [167](#)
229. M. Haas, E. Realo, H. Winkler, W. Meyer-Klaucke, and A. X. Trautwein: HyperfineInteract. **125**, 189 (2000) [167](#)
230. H. Spiering, L. Deák, and L. Bottyán: HyperfineInteract. **125**, 197 (2000) [167](#)
231. W. Sturhahn: Phys. Rev. B **63**, 094105 (2001) [167](#)
232. P. Carra, B. T. Thole, M. Altarelli, and X. Wang: Phys. Rev. Lett. **70**, 694 (1993) [168](#)
233. B. T. Thole, P. Carra, F. Sette, and G. vanderLaan: Phys. Rev. Lett. **68**, 1943 (1992) [168](#)
234. J. Geissler, E. Goering, M. Justen, F. Weigand, G. Schütz, J. Langer, D. Schmitz, H. Maletta, and R. Mattheis: Phys. Rev. B **65**, 020405 (2002) [168](#)
235. D. Haskel, G. Srajer, J. C. Lang, J. Pollmann, C. S. Nelson, J. S. Jiang, and S. D. Bader: Phys. Rev. Lett. **87**, 207201 (2001) [168](#)
236. D. R. Lee, S. K. Sinha, D. Haskel, Y. Choi, J. C. Lang, S. A. Stepanov, and G. Srajer: Phys. Rev. B **68**, 224409 (2003) [168](#)
237. H. C. Mertins, D. Abramsohn, A. Gaupp, F. Schäfers, W. Gudat, O. Zaharko, H. Grimmer, and P. M. Oppeneer: Phys. Rev. B **66**, 184404 (2002) [168](#)
238. K. Starke, F. Heigl, A. Vollmer, M. Weiss, G. Reichardt, and G. Kaindl:Phys. Rev. Lett. **86**, 3415 (2001) [168](#)

- 239. J. F. Anknerand G. P. Felcher: *J. Magn. Magn. Mater.* **200**, 741 (1999) [168](#), [169](#)
- 240. G. P. Felcher: *Phys. Rev. B* **24**, 1595 (1981) [168](#)
- 241. L. Deák, L. Bottyán, D. L. Nagy, and H. Spiering: *Physica B* **297**, 113 (2001) [170](#)
- 242. S. J. Blundelland J. A. C. Bland: *Phys. Rev. B* **46**, 3391 (1992) [170](#), [171](#)
- 243. S. A. Stepanov and S. K. Sinha: *Phys. Rev. B* **61**, 15302 (2000) [168](#)

5 Inelastic Nuclear Resonant Scattering

Soon after the discovery of the Mössbauer effect it became clear that nuclear resonant absorption would be a very sensitive tool for the investigation of atomic motion. The influence of lattice dynamics on the absorption of γ -quanta by nuclei was extensively studied by *Singwi & Sjölander* [1]. *Visscher* predicted that lattice vibrations should manifest as sidebands of the absorption line [2]. However, in a conventional Mössbauer experiment it is very difficult to observe such vibrational sidebands. One reason is that Doppler velocities of hundreds of m/s are necessary to tune the energy of the probing photon by typical phonon energies¹. Another limit results from the broadening of the resonance line due to the finite lifetime of the vibrational excitations. This reduces the peak absorption cross section by 6 to 7 orders of magnitude compared to the elastic peak. Despite of these difficulties a first experiment confirming the ideas of *Visscher* was performed in 1979, where the phonon spectrum and localized modes in TbO_x were measured [4, 5, 6] by using the 58-keV radiation of the ^{159}Tb Mössbauer isotope. Doppler shifts of up to 30 meV were achieved by employing high-speed rotational motion of the radioactive source. The phonon density of states of TbO_x obtained by this method is shown in Fig. 5.1. However, due to the low count rates in such experiments, this technique could not compete with the upcoming method of inelastic neutron scattering and the idea was neglected for a long time. Instead, lattice dynamics using nuclear resonant absorption was studied indirectly via the Lamb-Mössbauer factor and the second-order Doppler shift, see e.g. [7, 8]. The situation changed drastically with the advent of a) synchrotron radiation sources that surpassed the brilliance and spectral flux of radioactive sources by several orders of magnitude and b) x-ray optics that allowed for an energy tuning around the resonance with a resolution in the meV range. It was in 1995 when three groups almost simultaneously reported the first phonon spectra recorded by inelastic nuclear resonant absorption [9, 10, 11]. The experiments were performed at undulator-based beamlines with energy resolutions in the range of 6 meV. Since then the technique has made an impressive progress and nowadays phonon spectra are routinely recorded with sub-meV energy resolution [12]. It soon also became

¹ Such high-speed motion was indeed employed in the pre-Mössbauer era to overcome recoil energies and achieve nuclear resonant absorption [3].

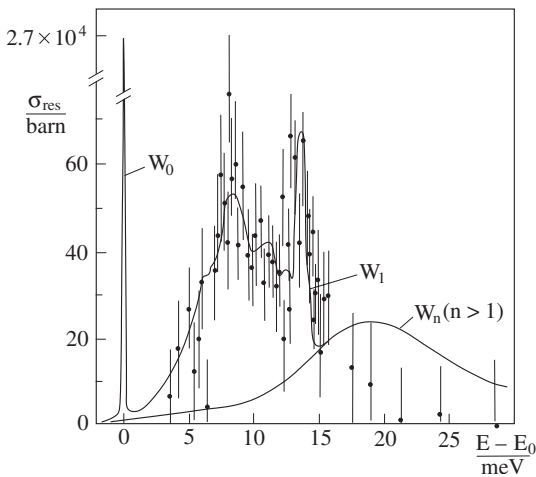


Fig. 5.1. Phonon spectrum of ^{159}Tb recorded with the radiation from a radioactive source (Figure adopted from Weiss *et al.* [5])

clear that the enormous brilliance of undulator radiation at third-generation synchrotrons renders this technique sensitive to very small sample volumes. In the following, the basic features of inelastic nuclear resonant scattering will be described and applications of this method to study vibrational properties of thin films and nanostructures will be demonstrated.

5.1 Inelastic Nuclear Resonant Absorption

Resonant nuclei in condensed matter provide a very accurate energy reference with a resolution that is limited only by the natural linewidth of the transition. If the energy of the incident radiation is off resonance, excitation of nuclei may be assisted by the creation or annihilation of phonons in the sample. Resonance excitation takes place if the energy of the photon plus the energy transfer involved in the interaction equals the resonance energy E_0 . This is shown schematically for the case of an Einstein solid in Fig. 5.2. The phonon energy spectrum of the sample is obtained by tuning the incident photon energy relative to the nuclear resonance² and recording the yield of nuclear decay products like fluorescence photons or conversion electrons. This yield gives a direct measure of the number of phonon states in the sample from which the phonon density of states can be derived [11]. A synopsis of the experimental method is shown in Fig. 5.3. The pulsed time structure of synchrotron radiation permits the use of timing techniques to efficiently discriminate the weak delayed nuclear response from the intense electronic scattering.

² In contrast, in conventional inelastic x-ray scattering [13, 14] one tunes the incident photon energy relative to the energy of the scattered photon.

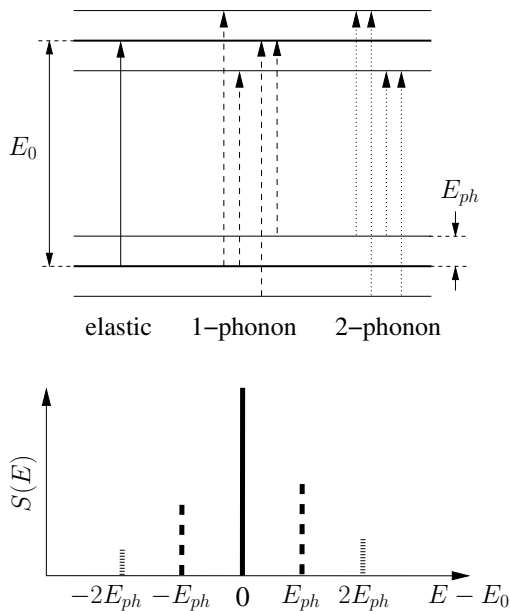


Fig. 5.2. Excitation processes upon resonant scattering from an Einstein solid and the corresponding excitation probability density $S(E)$. Direct excitation of the transition with resonance energy E_0 leads to the central elastic line in $S(E)$. Additional transitions (*dashed lines*) include the creation or annihilation of one phonon with the energy E_{ph} . Multiphonon transitions involve excitation of more than one phonon like the 2-phonon transitions shown as *dotted lines*. The strength of the vibrational transitions is determined by the number of phonon states at a given energy (DOS) and their thermal occupation number

An excited nucleus may decay via two channels: Radiative decay and internal conversion. The relative probability of these channels is $1/(1 + \alpha)$ and $\alpha/(1 + \alpha)$, respectively, where α is the internal conversion coefficient. Since for most Mössbauer isotopes $\alpha > 1$, the dominating channel is internal conversion. Depending on the experimental situation, the following decay channels can be used as the inelastic signal:

- **Nuclear resonant fluorescence**
The incident photon is absorbed and a photon is reemitted.
- **Conversion electron emission**
The excitation energy of the nucleus is transferred to the electron shell, so that an electron is emitted. Due to the small escape depth of the electrons, this method has a potentially high surface sensitivity.
- **Atomic fluorescence following internal conversion**
After emission of a conversion electron, the electronic recombination leads to emission of a fluorescence photon³.

The outstanding brilliance of modern synchrotron radiation sources allows one to probe the dynamical properties of very small sample volumes. In the following some quantitative aspects of this method will be elaborated.

In an incoherent scattering process the total yield of delayed K-fluorescence photons is given by

³ If the nuclear transition energy is below the K-edge, K-fluorescence is not possible, as it is the case for ^{119}Sn [15, 16]. Since L-fluorescence photons are often too low in energy to be detected, nuclear resonant fluorescence has to be used then.

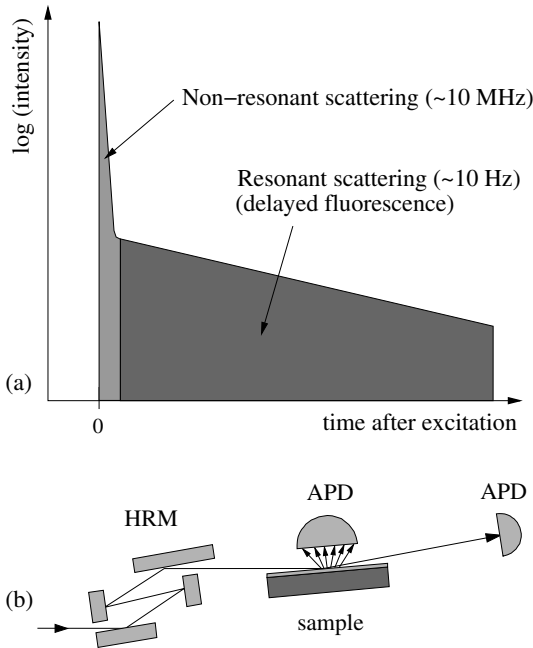


Fig. 5.3. Synopsis of the method of inelastic nuclear resonant scattering: (a) Time discrimination of the delayed nuclear resonant scattering after excitation at $t = 0$. The ratio of the nonresonant prompt photons and the resonant delayed counts is about 10^6 . (b) Scheme of the experimental setup with high-resolution monochromator (HRM) and detection of fluorescence quanta over the solid angle with a large-area avalanche photodiode (APD). The detector in forward direction monitors the energy dependence of the elastically scattered quanta which gives the resolution function of the setup

$$I(E) = I_0 \rho \eta_K \frac{\Gamma_K}{\Gamma_0} \sigma(E), \quad (5.1)$$

where I_0 is the incident flux, ρ the effective area density of the nuclei, and η_K the K-fluorescence yield. The ratio of the nonradiative (internal conversion) linewidth Γ_K to the natural linewidth Γ_0 of the nuclear transition is given by

$$\frac{\Gamma_K}{\Gamma_0} = \frac{\alpha_K}{1 + \alpha}, \quad (5.2)$$

where α and α_K are the total and partial internal conversion coefficients, respectively. $\sigma(E)$ is the cross section for nuclear resonant absorption of a photon with energy E :

$$\sigma(E) = \frac{\pi}{2} \sigma(E_0) \Gamma_0 S(E - E_0), \quad (5.3)$$

where $\sigma(E_0) = \sigma_0$ is the nuclear absorption cross section at the resonance energy E_0 ⁴. $S(E)$ is the normalized probability of absorption per unit energy interval at the energy E that depends also on the incident wavevector \mathbf{k}_0 . According to *Singwi & Sjölander* [1] it can be written as:

$$S(\mathbf{k}_0, E) = \frac{1}{2\pi} \int_0^\infty dt e^{-iEt - \Gamma_0 t/2} F(\mathbf{k}_0, t), \quad (5.4)$$

⁴ σ_0 is tabulated for all Mössbauer isotopes in Table A.1 of the appendix.

with

$$F(\mathbf{k}, t) = \langle e^{-i\mathbf{k} \cdot \mathbf{r}(0)} e^{i\mathbf{k} \cdot \mathbf{r}(t)} \rangle_T . \quad (5.5)$$

The angular brackets indicate thermal averaging over all initial lattice states. The function $F(\mathbf{k}, t)$ is often referred to as the self-intermediate scattering function. It describes the correlation between the positions of one and the same nucleus at different moments separated by the time interval t . The concept of the self-intermediate scattering function provides a very general description of the influence of lattice dynamics on resonant absorption.

It should be noted that $S(\mathbf{k}_0, E)$ does not depend on the direction of the wavevector \mathbf{k}_S of the scattered photon and is thus independent of the momentum transfer $\mathbf{q} = \mathbf{k}_S - \mathbf{k}_0$. However, inelastic nuclear resonant absorption depends on the direction of the incident wavevector \mathbf{k}_0 and is therefore anisotropic in general [17, 18]. The anisotropy vanishes only in the spherical symmetric limit, i.e., for cubic crystals and polycrystalline samples. In this case the true phonon density of states can be determined from the measured $S(E)$. Otherwise it always depends on the projection of the phonon polarization vectors along the direction of the incident beam. This is explained in detail in appendix A.6. Since the experiments discussed in this chapter are not affected by anisotropies of this kind, the explicit dependence on \mathbf{k}_0 will be dropped in the following. Inserting (5.2) and (5.3) into (5.1), we finally obtain for the phonon spectrum:

$$I(E) = I_0 \rho \sigma_0 \frac{\eta_K \alpha_K}{1 + \alpha} \frac{\pi}{2} \Gamma_0 S(E) . \quad (5.6)$$

In the approximation of a harmonic lattice, $S(E)$ can be expanded into contributions from multi-phonon excitations as follows [1, 20]:

$$S(E) = f_{LM} \left(\delta_\Gamma(E) + \sum_{n=1}^{\infty} S_n(E) \right) , \quad (5.7)$$

where f_{LM} is the Lamb-Mössbauer factor of the nuclei and $\delta_\Gamma(E)$ is a Lorentzian of width Γ . Since the nuclear linewidth Γ is orders of magnitude smaller than typical phonon energies, this term can be approximated by the Dirac δ -function because $\lim_{\Gamma \rightarrow 0} \delta_\Gamma(E) = \delta(E)$.

The function $S(E)$ exhibits a number of interesting properties that are expressed by its various moments, often referred to as Lipkin's sum rules [21, 22]:

$$\int E S(E) dE = E_R , \quad (5.8)$$

$$\int (E - E_R)^2 S(E) dE = 4 E_R T , \quad (5.9)$$

$$\int (E - E_R)^3 S(E) dE = \frac{\hbar^2}{m} E_R K , \quad (5.10)$$

where $E_R = E_0^2/2Mc^2$ is the recoil energy of the free atom, M is the nuclear mass, T is the average kinetic energy of the resonant nuclei and K is the mean force constant of the bound nuclei. The first of these sum rules expresses the remarkable fact that the average energy transfer to the lattice per photon emission is just the recoil energy of the free atom. These sum rules are of great importance for the decomposition of $S(E)$ into the multiphonon contributions. An outline of this procedure is given in the following section.

5.2 Extraction of the Phonon Density of States

In this section it is shown how to extract the phonon density of states $D(E)$ from a measured phonon spectrum. This procedure is the basis for a number of evaluation programs and has been described in detail in [16, 23, 24]. According to (5.1) and (5.7), the measured phonon spectrum $I(E)$ can be decomposed into an elastic part that is described by a δ function and an inelastic part $S'(E)$ ⁵:

$$I(E) = a S'(E) + b f_{LM} \delta(E). \quad (5.11)$$

The most important aspect for a quantitative data evaluation is the determination of the normalization constants a and b . Unfortunately, due to saturation effects that occur at resonance, those constants are not equal and a common normalization of elastic and inelastic contributions is not possible. The normalization constant a is determined via Lipkin's sum rule (5.8) for the first moment of the measured spectrum:

$$a = \frac{1}{E_R} \int I(E) E \mathrm{d}E. \quad (5.12)$$

The subtraction of the elastic contribution yields the inelastic part of the measured spectrum $I'(E) := a S'(E)$. Since $\int S'(E) \mathrm{d}E = 1 - f_{LM}$, we immediately obtain for the Lamb-Mössbauer factor⁶:

$$f_{LM} = 1 - \frac{1}{a} \int I'(E) \mathrm{d}E. \quad (5.13)$$

With this information the measured spectrum can be decomposed into multiphonon contributions, as shown in Fig. 5.4. In the harmonic approximation, the one-phonon contribution $S_1(E)$ is directly related to the phonon density of states $D(E)$:

$$S_1(E) = \frac{E_R D(E)}{E (1 - e^{-\beta E})}. \quad (5.14)$$

⁵ For a better view on the basic concepts, the instrumental resolution function was not included here. It enters as an additional convolution over energy.

⁶ This procedure is much more precise than the determination of the Lamb-Mössbauer factor via conventional Mössbauer spectroscopy or nuclear forward scattering. For a detailed discussion, see [8].

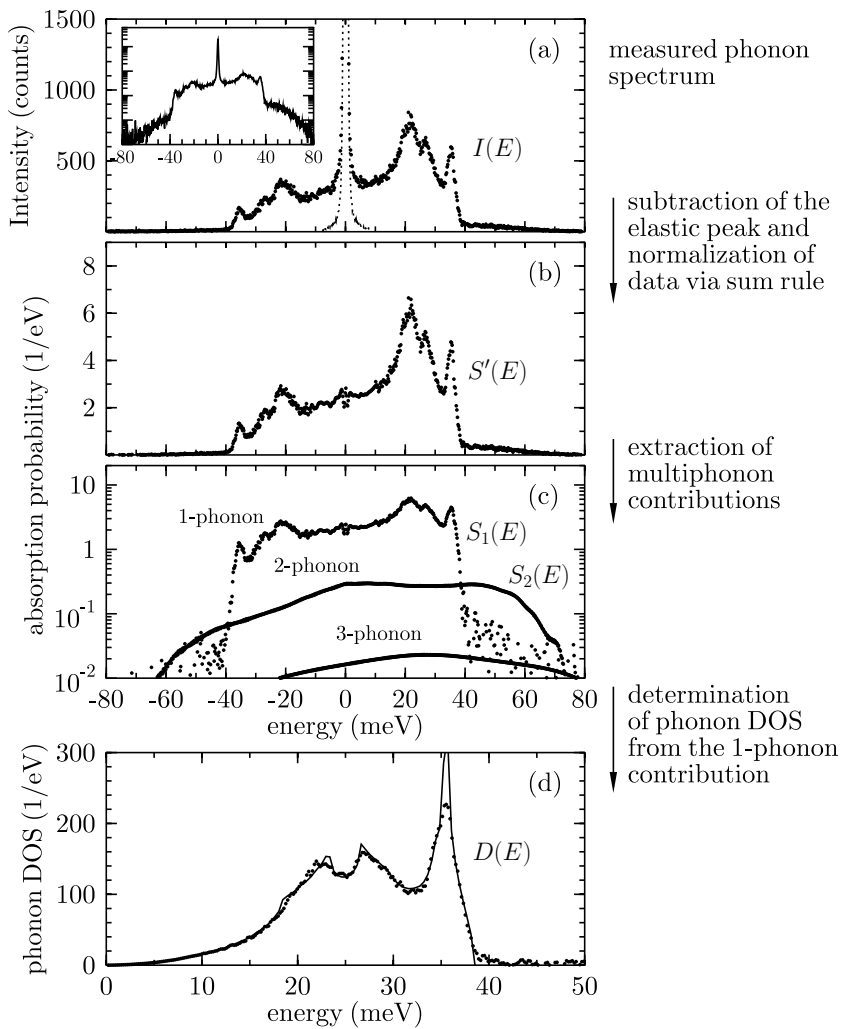


Fig. 5.4. Derivation of the phonon density of states from the measured data. (a) Phonon spectrum of bcc Fe, $I(E)$, recorded with an energy resolution of 0.66 meV [12]. The inset shows the same data on a logarithmic scale to illustrate the relative intensities within the spectrum. The *dotted line* is the resolution function $R(E)$ of the setup. (b) Normalized phonon spectrum, $S'(E)$, after removal of the elastic peak. Integration of this spectrum gives $1 - f_{LM}$. (c) Extraction of the 1-, 2-, and 3-phonon terms, $S_{1,2,3}(E)$ after an iterative procedure using (5.15). (d) Phonon density of states, $D(E)$, as determined from the one-phonon term via (5.23). The *solid line* is the phonon DOS as derived from neutron measurements [25] (Data taken from Toellner *et al.* [12])

The higher-order contributions are given by successive convolutions with the one-phonon term:

$$S_n(E) = \frac{1}{n} \int S_{n-1}(E - E') S_1(E') dE', \quad n > 1. \quad (5.15)$$

Using the convolution theorem, this equation has a very simple expression in Fourier space:

$$\tilde{S}_n(t) = \frac{1}{n!} \tilde{S}_{n-1}(t) \tilde{S}_1(t). \quad (5.16)$$

This recursive relation has the closed solution:

$$\tilde{S}_n(t) = \frac{1}{n!} [\tilde{S}_1(t)]^n. \quad (5.17)$$

Thus, taking the Fourier transform of (5.7) and performing the summation over the multiphonon contributions, one obtains:

$$\tilde{S}(t) = f_{LM} e^{\tilde{S}_1(t)}. \quad (5.18)$$

Finally, this expression can now be resolved for the one-phonon contribution:

$$S_1(E) = \int dt e^{-iEt} \ln \left[\frac{\tilde{S}(t)}{f_{LM}} \right]. \quad (5.19)$$

This method is known as the Fourier-Log decomposition [26].

Now we include the resolution function $R(E)$ into the formalism, i.e., (5.1) is replaced by

$$I(E) = \int R(E - E') \{aS(E') - b f_{LM} \delta(E')\} dE'. \quad (5.20)$$

$R(E)$ can be measured very accurately by monitoring the intensity of elastic forward scattering while tuning the energy. Including the convolution with $R(E)$ into the above formalism, the expression (5.19) for the single-phonon contribution turns into:

$$S_1(E) = \int dt e^{-iEt} \ln \left[1 + \frac{\tilde{I}'(t)}{a f_{LM} \tilde{R}(t)} \right], \quad (5.21)$$

where $\tilde{I}'(t)$ denotes the Fourier image of the measured phonon spectrum with the elastic peak subtracted. The finite width of the resolution function introduces a number of problems that should be discussed here briefly. It is obvious from (5.13) that the determination of f_{LM} and the single-phonon contribution depends critically on the subtraction of the elastic peak. Then an assumption has to be made how to describe the region under the elastic peak. In many cases it is reasonable to insert a one-phonon contribution from a Debye solid. However, this procedure has its limits in the case of samples with non-Debye behavior or a strong contribution from multiphonon terms under the elastic peak. The latter case applies for samples with small f_{LM} .

and can be cured to some extent by an iterative algorithm [24]. Also the numerical problems that arise from the deconvolution, i.e. the division by $\tilde{R}(t)$, are elaborated in [24].

Once $S_1(E)$ has been obtained, the phonon density of states $D(E)$ can be obtained via (5.14). Taking the condition of detailed balance into account, i.e.,

$$S_1(E) = e^{-\beta E} S_1(-E), \quad (5.22)$$

one can use both wings of the phonon spectrum to determine $D(E)$, resulting in:

$$D(E) = \frac{E}{E_R} (S_1(E) + S_1(-E)) \tanh\left(\frac{\beta E}{2}\right) \quad \text{with } E \geq 0. \quad (5.23)$$

The computational procedure outlined in this section has been illustrated in Fig. 5.4 for the case of bcc Fe.

The above formalism has been implemented into two program packages that are available for evaluation of phonon spectra, i.e., the package PHOENIX by *W. Sturhahn* [24] and DOS by *A. I. Chumakov* [23]. Both packages are available from the authors.

5.3 Experimental Aspects

In contrast to other methods like inelastic neutron, X-ray, and Raman scattering, inelastic nuclear resonant scattering gives direct access to the phonon density of states. The rapid development of this technique since 1995 became possible due to several distinct advantages [27]. Due to the resonant nature of the interaction the count rate of inelastic nuclear scattering is large enough to perform a complete measurement in a few hours. The combination of the large scattering cross-section and the small size of the synchrotron radiation beams allows one to use tiny samples like ultrathin films and nanoparticles and materials that are available only in small quantities. The experimental aspects of this method have been described in a comprehensive review by *Chumakov & Sturhahn* [27]. In the following we summarize a few selected aspects that are relevant for most experiments.

5.3.1 Lamb-Mössbauer Factor and Multiphonon Excitations

The Lamb-Mössbauer factor, also called f-factor or recoilless fraction, determines the fraction of recoilless events in nuclear resonant scattering. It was shown in the previous section that it can be directly derived from the measured data via (5.13). On the other hand, it is related to the phonon density of states via [1]:

$$f_{LM} = \exp \left(-E_R \int_0^{\infty} \frac{D(E)}{E} \frac{1 + e^{-E/k_B T}}{1 - e^{-E/k_B T}} dE \right). \quad (5.24)$$

This allows one to check the derivation of the phonon DOS for consistency with the Lamb-Mössbauer factor. Inspection of the above equation reveals that in the low-temperature limit the integrand in the exponential is weighted by $1/E$ and by $1/E^2$ in the high-temperature limit. This shows that the Lamb-Mössbauer factor is determined mainly by the low-energy part of the phonon DOS, that can be described for most solids by the Debye-model. Thus, the Lamb-Mössbauer factor is only sensitive to the phonon DOS if the spectrum of low-energy excitations undergoes changes.

The Lamb-Mössbauer factor can be used to estimate the relative contribution of multi-phonon excitations. The relative contribution of the n -phonon term is given by

$$\int S_n(E) dE = \frac{(-\ln f_{LM})^n}{n!}. \quad (5.25)$$

Thus, if the Lamb-Mössbauer factor is close to 1, only a few multiphonon contributions are significant, as shown for bcc Fe in Fig. 5.4a. In this case the expansion in (5.7) converges rapidly. If the Lamb-Mössbauer factor is small, e.g., at high transition energies or weakly bound nuclei, many multiphonon terms contribute and the separation between them is difficult. In such cases the extraction of the phonon DOS becomes difficult, as it is the case for biomolecules [28] or β -Sn [15, 29], for example.

5.3.2 Temperature Dependence and Anharmonicity

The phonon spectra recorded via nuclear inelastic absorption show a pronounced temperature dependence that is determined by the thermal occupation of phonon states. This is shown for bcc Fe in Fig. 5.5. The ratio between the absorption probability with energy gain and energy loss is determined by the detailed balance⁷, see (5.22). Because the recoil may excite phonons even at the lowest temperatures, inelastic absorption with energy loss is possible at all temperatures. Inelastic absorption with energy gain, on the other hand, depends on the occupation number of thermally excited phonons. At $T = 24$ K the thermal energy is only 2 meV, so that phonon states with higher energies have a very low occupation and practically only phonon creation takes place. Therefore inelastic absorption on the low-energy side of the spectrum is almost impossible. At $T = 400$ K the energy spectrum of inelastic absorption is much less asymmetric because the thermal energy

⁷ This is essentially a consequence of time-reversal invariance of the scattering process. In circumstances where this is not fulfilled, e.g., for spinwave excitations, the detailed balance does not hold.

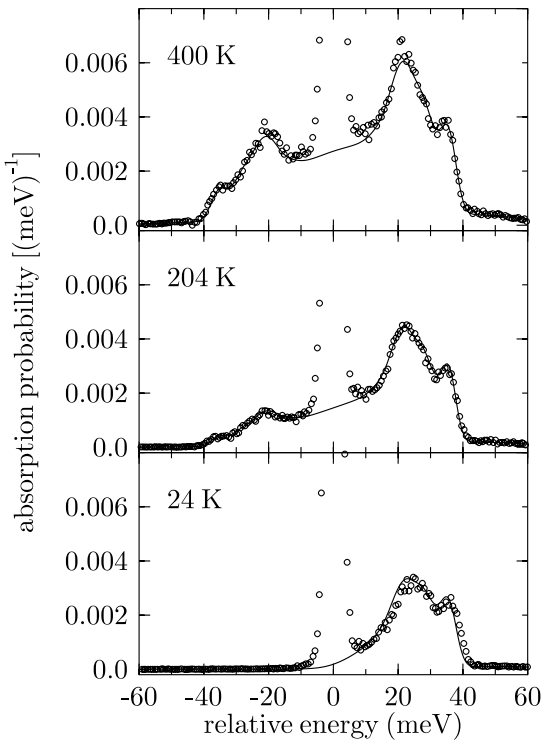


Fig. 5.5. Phonon spectra of bcc Fe recorded at temperatures of 24 K, 204 K, and 400 K. With decreasing temperature phonon annihilation becomes less probable due to decreasing thermal population of phonon states (Data taken from Chumakov & Rüffer [30])

$k_B T = 34 \text{ meV}$, so that the occupation is relatively high for all phonon states and phonon creation as well as phonon annihilation can take place.

While the phonon density of states in the harmonic approximation is solely a property of the crystalline lattice and does not depend on temperature, this is not the case if anharmonic effects are considered. This is particularly significant in the vicinity of phase transitions where interatomic distances and forces change [30]. But even in the absence of a phase transition the phonon DOS may show a temperature dependence due to the anharmonicity of lattice vibrations, as it has been shown for bcc Fe [31].

Even though the scattering process is fully incoherent, the measured signal may be affected by contributions from coherent scattering channels. This was investigated in detail by Sturhahn & Toellner [32] who showed that those contributions do not exceed 0.001 of the incoherent channel in case of ^{57}Fe . The only assumption made here was that of a harmonic lattice that enables one to perform the deconvolution of the multiphonon contributions. In the case of inelastic neutron scattering it can be very difficult to obtain the phonon DOS directly, in particular if the isotopes under investigation do not exhibit a significant incoherent scattering cross section (which is just the case for Fe).

5.3.3 Thermodynamic Quantities

Once $D(E)$ has been determined for a particular material, a number of thermodynamic quantities can be derived. As a first example we consider the phonon contribution to the lattice specific heat. The contribution of lattice excitations to the internal energy is given by

$$U = N \int E n(E) D(E) dE , \quad (5.26)$$

where N is the number of particles and $n(E) = 1/(e^{E/k_B T} - 1)$ is the Bose occupation number. From this expression the lattice specific heat follows immediately:

$$c_v(T) = \frac{dU}{dT} = \frac{N}{k_B T^2} \int_0^\infty E^2 e^{E/k_B T} n(E)^2 D(E) dE . \quad (5.27)$$

It is the virtue of this technique to be sensitive to very small amounts of material as in thin films and nanostructures. This allows one to investigate thermodynamic quantities on microscopic length scales, thus allowing study of, for example, dissipation phenomena in confined systems. The high isotopic specificity may be used to enhance the spatial resolution to the atomic level by selectively doping the system with monolayers of the resonant isotope.

Another important thermodynamic quantity derived from the PDOS is the vibrational entropy:

$$S_{vib}(T) = R \int_0^\infty D(E) [E n(E)/k_B T + \ln(1 + n(E))] dE . \quad (5.28)$$

Recent experiments indicate that the relative stability of the ordered and the disordered states of a compound may be significantly affected by their difference in vibrational entropy [33]. Thus, changes in vibrational entropy can be important for the thermodynamics of solid-state phase transitions [34] or diffusion and nucleation on surfaces [35].

It should be noted that the quantities in (5.27) and (5.28) give only the contributions of the resonant atoms. This may not be representative for the thermodynamic behavior of the material. Thus, the experimental data have to be complemented by data from other methods and calculations. Nevertheless, the vibrational entropies derived from the VDOS have been successfully used to explain order-disorder effects in Fe alloys [33, 36].

5.4 Vibrational Properties of Thin Films and Nanostructures

A multitude of studies on the vibrational properties of semiconductor superlattices and nanostructures has been reported [37]. Several novel effects

have been observed that are induced by the broken translational symmetry of these systems [38]:

- **Phonon Folding**

Folding of acoustical phonon dispersion relations into the first Brillouin zone due to the superlattice periodicity.

- **Phonon Confinement**

Quantization of optical phonons due to restriction of the propagation to certain layers.

- **Interface Phonons**

Vibrational states arising at the interface between different materials.

For metallic layer systems, however, only a few investigations about phonon folding [39] or phonon confinement [40] have been reported. The reason is that most elemental metals are not Raman active or only weakly so. Therefore it is highly desirable to develop characterization methods that are more suitable for metallic systems.

The investigation of collective excitations in reduced dimensions by means of advanced x-ray scattering techniques will be an important field in materials science in the future. With further progress in deposition and structuring techniques, the variety of materials as well as their complexity will rapidly increase. Such systems will exhibit large deviations from bulk behavior. Those deviations either limit the desired properties of new materials or they form the basis for a new functionality. A few key areas shall be identified here:

- **Thermal Transport in Microstructures**

In a confined geometry the vibrational spectrum is altered if the film thickness or the multilayer period is comparable to the phonon mean free path. This leads to novel features like *phonon zone-folding* in periodic layer structures and *phonon confinement* due to the restriction of phonon propagation to certain layers [38]. Such size effects on the vibrational properties will be of particular technical relevance for the thermal properties of thin films that are part of micromechanic and microelectronic devices [41]. Properties like thermal conductivity become more and more critical with increasing power level and decreasing time scales of electronic and mechanical processes in those devices.

- **Nanoscale Tribology**

The microscopic origin of friction is a subject of intense research presently [42, 43]. It became clear that frictional behavior is not only determined by structural properties like surface roughness, but is also influenced by dynamical properties: The density of vibrational states (VDOS) at a certain frequency determines how much energy can be dissipated in that particular mode. The design of solids, (e.g., nanostructured materials) with a gap in the VDOS over a critical region of frequencies could prevent energy losses through friction. Since these processes are naturally located at

buried interfaces, inelastic x-ray spectroscopy with its great penetration power and high surface sensitivity is the ideal tool for this purpose.

- Smart Materials Based on Lattice Instabilities

'Smart Materials' rely on structural phase transitions, which allow the material to modify the domain structure or the band structure to respond to external parameters like temperature, pressure, electric or magnetic fields [44]. The underlying physics of these phase transitions is intimately related to lattice instabilities with soft phonon modes. In the future new materials with a transformation behavior based on strongly modified phonon dispersion relations will emerge. Particular examples are ferroelastic and martensitic transformations as the origin of the shape-memory effect. These phenomena are frequently employed in sensor/actuator systems. It will be important to determine how the confined geometry of thin films and microstructures affects the fundamental properties of such devices.

This list indicates that tuning or even tailoring of phononic spectra to specific purposes will be of increasing importance in the future, and a field of 'phonon engineering' can be envisaged with many similarities to the common 'band gap engineering' of electronic properties. However, a full tunability of these properties will be possible only with a thorough understanding of the underlying processes. The increasing miniaturization of structures requires the further development of existing spectroscopic techniques or the development of new, particularly suited techniques. The measurement of vibrational properties of thin films is conceptually difficult because neither inelastic neutron scattering nor inelastic x-ray scattering are feasible for such small amounts of material. On the other hand, energy-loss spectroscopy with electrons or He atoms [45] or point-contact methods [46] may be too surface sensitive. Therefore, inelastic scattering of infrared or visible light accounts for the largest fraction of spectroscopic data on vibrational excitations in thin films [47]. However, the limited momentum transfer usually prohibits the determination of the full vibrational density of states.

5.4.1 Phonon Damping in Thin Films of Fe

In this experiment, inelastic nuclear resonant scattering is applied to determine the vibrational density of states of thin ^{57}Fe films. The aim is to identify effects of the confined geometry on the vibrational spectrum [48]. To enhance the inelastic signal, the films are illuminated in grazing incidence geometry, preferably under conditions where a waveguide mode inside the film can be excited. The measured yield $I(E)$ of delayed fluorescence photons is then proportional to the average intensity of the radiation field inside the film of thickness d . This can be expressed by an extension of (5.6) as follows:

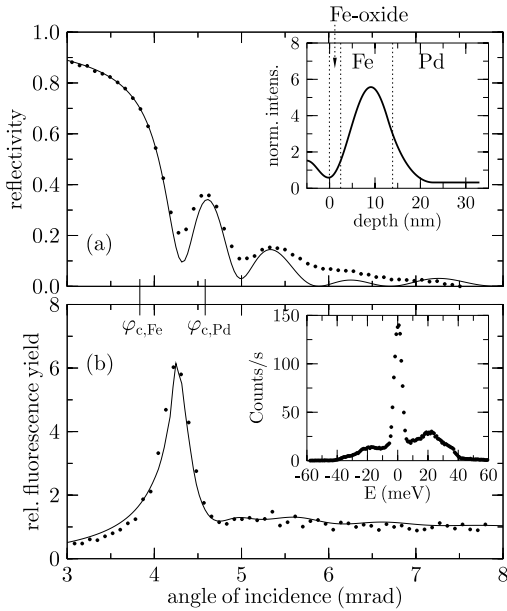


Fig. 5.6. (a) Electronic reflectivity of 13 nm Fe on Pd. A guided mode is excited at an angle of 4.2 mrad that appears as a minimum in the reflectivity between the two critical angles of Fe and Pd. The inset shows the depth dependence of the intensity inside the layer. (b) Angular dependence of the yield of delayed fluorescence from the Fe film, with the photon energy 20 meV above the resonance. The yield is maximum at the angle where the guided mode is excited. The inset shows the phonon spectrum that was recorded at this angle. *Solid lines* are simulations according to (5.29) [48]

$$I(E) = I_0 \varrho \sigma_0 \frac{\eta_K \alpha_K}{1 + \alpha} \frac{\pi}{2} \Gamma_0 S(E) \frac{1}{d} \int_0^d I(z) dz, \quad (5.29)$$

where $I(z)$ is calculated as explained in Sect. 4.1.5.

Two films were prepared, consisting of polycrystalline α -Fe (enriched to 95% in ^{57}Fe) with thicknesses of 13 nm and 28 nm, respectively. They were deposited at room temperature by sputtering in an Ar atmosphere onto a superpolished glass-ceramics substrate (ZERODUR). The 13-nm-thick film was deposited onto a 20-nm-thick Pd layer to obtain a significant intensity enhancement via x-ray interference in the film, as illustrated in Fig. 5.6. The DOS for both films is shown in Figs. 5.7c,d. For comparison, the DOS of bulk α - ^{57}Fe , obtained from a 10- μm -thick foil under the same experimental conditions, is shown in Fig. 5.7b. Figure 5.7a shows the DOS of bulk bcc Fe as calculated in a Born von-Karman model with force constants obtained from neutron data [25]. The peak at 35 meV corresponds to longitudinal phonons

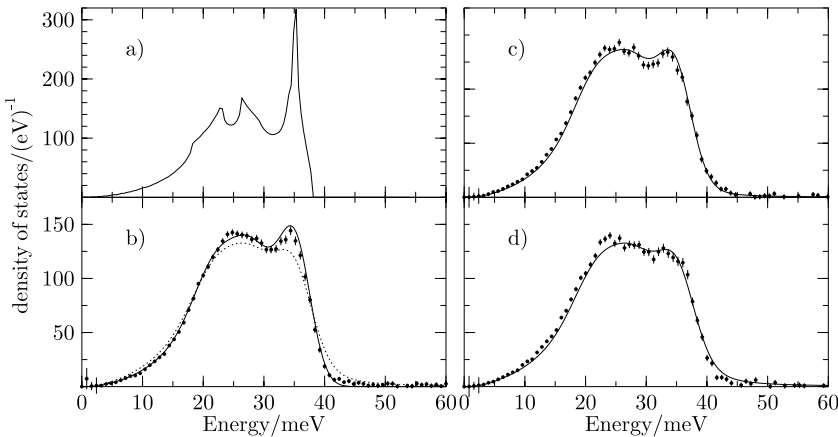


Fig. 5.7. (a) DOS of bcc Fe, from which the calculations (*solid lines*) for the following experimental data were derived: (b) DOS of bulk Fe, (c) DOS of 28-nm Fe on ZERODUR, (d) DOS of 13-nm Fe on 20-nm Pd on ZERODUR. The dotted line in b) corresponds to the solid line in d). The energy resolution in the experiments was 5.5 meV [48]

close to the boundary of the first Brillouin zone, while the two peaks at 23 meV and 27 meV mainly belong to the van-Hove singularities of transverse phonons [49]. The most obvious feature in the DOS is the shape of the peak at 35 meV, which suggests phonon damping in the Fe films.

In order to describe the measured DOS of the films, $D(E)$, we have applied the model of a damped harmonic oscillator (DHO) [50] as it was used in a similar study on Fe nanocrystals [51]. This model contains as the only adjustable parameter the quality factor Q that describes the damping of vibrational modes. Comparing the results of the Fe films with that of bulk Fe, the most obvious feature is the shape of the peak at 35 meV, which suggests phonon damping in the Fe films. At each energy E' of the calculated DOS $D_0(E)$ of bulk Fe, we have assumed an energy distribution given by $h(E', E)$ [50]:

$$D(E') = \int_0^{\infty} h(E', E) D_0(E) dE \quad (5.30)$$

$$h(E', E) = \frac{1}{\pi Q E'} \frac{1}{(E'/E - E/E')^2 + 1/Q^2} . \quad (5.31)$$

The physical basis for this choice is that the DHO model resembles the inelastic part of the dynamical structure factor of a system with anharmonic interactions that lead to phonon decay [52]. It is frequently applied in inelastic neutron [53] and x-ray scattering [54] and seems to be reasonable if the

damping is not too large. In the evaluations presented here, the quality factor Q was the only parameter used to fit the data.

The DOS of the 28-nm-thick Fe film shown in Fig. 5.7c was described with $Q = 25(2)$, while for the 13-nm-thick Fe film a value of $Q = 13(1)$ was obtained [48]. For a direct comparison with bulk bcc Fe, the calculated DOS of the 13-nm Fe film is drawn as dotted line in Fig. 5.7b. The discrepancies between both calculated DOS reveal the features that are introduced by the damping: The high-energy tail is smeared out over a wide range of energies, the peaks due to the van-Hove singularities are smoothed, and there is a slight increase of the DOS at low energies, caused by the long tails of the DHO function.

In spite of the good agreement, there remains an excess in the measured DOS over the calculated curve at low energies. Low-energy excitations are often linked to vibrational states in regions with low density or a high degree of disorder. A strong excess of such modes compared to bulk Fe has been observed in nanocrystalline Fe with an average particle size of 10 nm, where a large fraction of the Fe is close to or within surface oxide layers [51]. For the Fe films, the excess at low energies is considerably smaller, probably because the relative contribution from surface and interface regions is small: In case of the 28-nm film, the thickness of the surface oxide layer is small compared to the total thickness; in case of the 13-nm film on Pd, the electromagnetic field intensity peaks inside the Fe layer with a relatively small intensity at the interfaces. This is supported by the observation that the DOS of the Fe films does not show modes above 50 meV, which reflects the response of the Fe atoms to high-energy vibrations of oxygen atoms in surface oxides [51].

An enhancement of low energy modes is often found in systems with structural irregularities and is attributed to softening of transverse phonons. The phonon DOS in this energy region for both samples is shown in Fig. 5.8, plotted versus E^2 . The DOS is to a good approximation quadratic in energy, as expected from the Debye model. The slope indicates the sound velocity in the Fe films to be smaller than in the bulk, as described by (5.36).

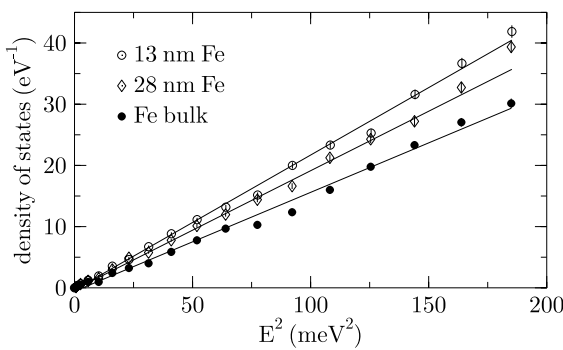


Fig. 5.8. Low-energy region of the phonon DOS of the Fe thin films and bulk Fe from Fig. 5.7 plotted vs. E^2

The observed differences in the Q values for both films are most likely related to the layer thickness d . Taken as the phonon mean free path, the layer thickness then limits the phonon lifetime in the films. Since the average crystallite size in polycrystalline thin films is in the same range as the layer thickness, this consideration holds also for in-plane phonons scattered at grain boundaries. Stresses originating at the layer boundaries, especially from the surface oxide, may propagate into the layer and give rise to additional scattering processes that shorten the phonon lifetime even more. It should also be noted that in Pd metal there are no phonon modes above 29 meV [49], resulting in a strong confinement of the high-energy modes in the Fe film on Pd.

Although the microscopic origin for the damping could not be discerned here, it is a remarkable fact that the DOS of two different films can be described within the same model with a single parameter. Remaining discrepancies may be due to extra soft modes and slightly different damping of transverse and longitudinal modes. The measurement of the effective phonon damping may be applied, e.g., to estimate the thermal resistivity of thin films in novel microstructures [41].

5.4.2 Vibrational Modes in Nanoparticles

The vibrational properties of clusters, nanoparticles, and nanocrystalline are of considerable interest because remarkable deviations from bulk behavior have been found [37]. These properties are of great importance for the understanding of thermodynamic properties like thermal expansion, heat capacity, thermal conductivity and vibrational entropy. An important ingredient for the determination of these quantities is the vibrational density of states (VDOS). The VDOS of metallic nanostructures has been measured by inelastic neutron scattering [55, 56, 57, 58, 59, 60] and inelastic nuclear resonant scattering [51, 61, 62]. In addition, computer simulations have been performed to calculate the VDOS of nanocrystalline materials [63, 64, 65, 66]. The experiments and the simulations reveal that the VDOS of nanocrystalline materials exhibits an excess of low- and high-energy modes that are not observed in the bulk or coarse-grained counterparts. These modes have been related to vibrations of atoms with reduced coordination and a modified local environment. Systematic studies, however, of the nature of these modes are scarce. In the center of such studies will be the following questions: (i) how does the VDOS depend on the crystallite size and (ii) does the high fraction of interfaces and surfaces lead to a deviation of the low-energy VDOS from the Debye-behavior? A systematic study in this field has been reported [62], as described in the following.

Fe nanoparticles were produced by inert gas condensation (IGC) [67] of Fe evaporated from a tungsten crucible in He gas (purity 99.9999%) with a pressure of 133 Pa. The IGC technique invariably leads to a certain oxidation of the nanoparticles due to reaction of iron with residual oxygen and

Table 5.1. Parameters of the nanocrystalline samples investigated here. $d_{\alpha\text{-Fe}}$ is the diameter of the $\alpha\text{-Fe}$ part of the crystallites, $X_{\alpha\text{-Fe}}$ is the relative fraction of the $\alpha\text{-Fe}$ phase of the crystallite, and Γ is the damping parameter used in (5.32) to describe the phonon lifetime broadening (Data taken from Pasquini *et al.* [62])

| Sample | $d_{\alpha\text{-Fe}}$ (nm) | $X_{\alpha\text{-Fe}}$ | Γ (meV) |
|--------|-----------------------------|------------------------|----------------|
| NC-a | 6.6(5) | 0.67(9) | 1.1(1) |
| NC-b | 9.3(5) | 0.74(8) | 0.7(1) |
| NC-c | 13.2(5) | 0.82(12) | 0.5(1) |
| NP-a | | 0.0(1) | |
| NP-b | 6(1) | 0.15(10) | |

water vapor introduced by the He gas. Size control of the nanoparticles was achieved by adjusting the heating current. At the end of the process the initial UHV conditions were restored and the nanoparticles were scraped off the deposition surface. Afterwards, nanocrystalline (NC) samples were prepared by in-situ compaction at a pressure of 1.5 GPa. Moreover, nanopowder (NP) samples were produced by extracting the nanoparticles without compaction. The structure of the samples was controlled by x-ray diffraction (XRD) and transmission electron microscopy (TEM), from which the average $\alpha\text{-Fe}$ crystallite diameter $d_{\alpha\text{-Fe}}$ and the relative fraction $X_{\alpha\text{-Fe}}$ of the $\alpha\text{-Fe}$ phase were determined. Correspondingly, $1 - X_{\alpha\text{-Fe}}$ can be taken as the degree of oxidation of the samples. Three NC samples were prepared with different degrees of oxidation, labeled by a,b,c. In one of the two NP samples (NP-a) no trace of $\alpha\text{-Fe}$ was detected in the XRD measurement. Therefore, this sample can be considered completely oxidized. The parameters for the various samples used in this experiment are compiled in Table 5.1. The VDOS of the samples was measured via inelastic nuclear resonant scattering with an energy resolution of 0.6 meV, shown in Fig. 5.9. Compared to the DOS of bulk $\alpha\text{-Fe}$, the following characteristic features can be identified:

- (1) An enhancement of low-energy modes below ≈ 15 meV,
- (2) a broadening of the peaks in the VDOS, and
- (3) additional high-energy modes in the range of 40–50 meV above the cutoff energy for bulk $\alpha\text{-Fe}$.

Features (2) and (3) can be described by the combined effect of oxidation and phonon confinement. The latter reduces the phonon lifetime, corresponding to a damping and a broadening of the features in the VDOS. This effect is taken into account by convolution of the VDOS of $\alpha\text{-Fe}$ with a Lorentzian of width Γ , resulting in the function $g_{\alpha\text{-Fe}}^{\Gamma}(E)$. The effects of damping and oxidation on the VDOS are then described by the function

$$g_{\text{comb}}(E) = X_{\alpha\text{-Fe}} g_{\alpha\text{-Fe}}^{\Gamma}(E) + (1 - X_{\alpha\text{-Fe}}) g_{\text{NP-a}}(E), \quad (5.32)$$

where $g_{\text{NP-a}}(E)$ is the VDOS of the nanopowder sample NP-a, which is completely oxidized. Solid lines in Fig. 5.9 are fits according to (5.32) with Γ as

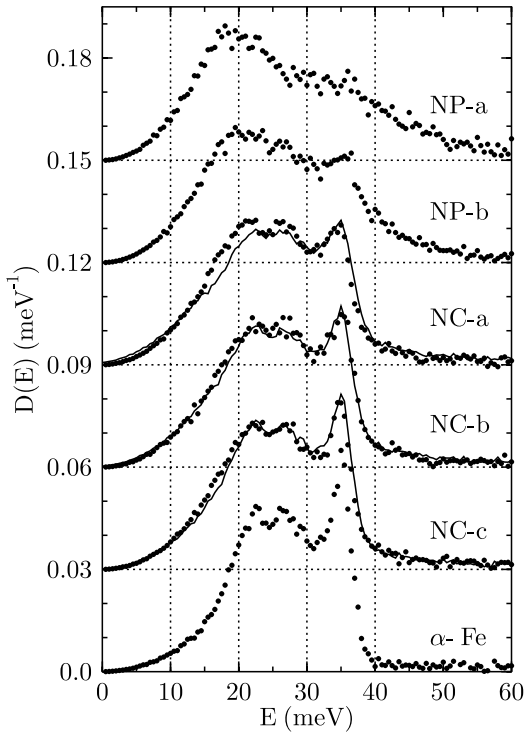


Fig. 5.9. Vibrational density of states (VDOS) for the nanocrystalline (NC) samples and the nanopowder (NP) samples, together with the VDOS of a α -Fe foil as reference. The energy resolution is 0.6 meV. Solid lines are fits according to (5.32) with parameters given in Table 5.1 (Data taken from Pasquini *et al.* [62])

free parameter, listed in Table 5.1. The width Γ increases continuously with decreasing particle size $d_{\alpha\text{-Fe}}$. This indicates that the phonon confinement in the nanocrystals is mainly responsible for the reduced phonon lifetime that is given by $\tau = 2\hbar/\Gamma$. However, the mixture of vibrational contributions as expressed by (5.32) does not properly describe the VDOS at low energies. In fact, (5.32) does not take into account the atoms that are located at interfacial sites, i.e., atoms experiencing a modified local environment. Since their number scales with $1/d$, the increase of the low-energy VDOS with decreasing d strongly suggests that this enhancement (or softening) is caused by vibrational modes of interface atoms. This conclusion is supported by computer simulations [68].

In order to investigate the dispersion of low-energy modes, the VDOS of all samples was fitted with a power law $D(E) \sim E^n$ over an energy range from 1.5 meV to 10 meV. Best fits for all data are obtained with $n = 2$ [62]. Thus, there are no indications that the interface modes deviate from the law $D(E) \sim E^2$ which is characteristic for 3-dimensional bulk crystals. This is in agreement with previous reports [51, 56]. In computer simulations, however, the power-law exponent was found to be $n = 1$ [63, 65] and $n \approx 1.5$ [68]. It should be noted that these results are not directly applicable to the

nanocrystalline samples investigated here, because these simulations were assuming isolated nanoparticles with free surfaces.

The experiments have shown that the excess of low-energy vibrational modes in nanocrystalline systems result from interface vibrational modes and oxidation. The excess of high-energy modes, on the other hand, results from oxidation only. Confinement of the phonons leads to a significant damping of modes. Similar results have been found for thin Fe films, as it has been shown in Sect. 5.4.1. In the case of Ag-capped single-crystalline Fe islands, as discussed in Sect. 5.4.3, oxidation effects can be excluded. Correspondingly, one finds extra vibrational modes only in the low-energy regime.

5.4.3 Phonons in Fe Islands on W(110)

While nanocrystalline materials typically exhibit a multitude of interfacial configurations, no such investigations have been reported so far on nanoscale systems with well-defined interfacial structures. In the experiment described here we have investigated three-dimensional Ag-capped Fe islands on W(110) that have already been introduced in Sect. 4.4.4. These islands typically have a thickness of a few nm and a lateral extension of several hundred nm, as shown in Fig. 4.36.

The experiment was carried out at the nuclear resonance beamline ID18 of the ESRF [69] where a high-resolution monochromator provided an energy resolution of 4.4 meV. The sample was illuminated in grazing incidence geometry under an angle of 5 mrad, close to the critical angle of W. Due to formation of standing waves above the surface, maximum fluorescence yield is expected at this angular position. A phonon spectrum was recorded by tuning the incident energy over a range of ± 60 meV around the resonance, while monitoring the yield of delayed K-fluorescence photons. The data are shown in Fig. 5.10, taken during an acquisition time of 12 h. The vibrational density of states as derived from the phonon spectrum is shown in Fig. 5.11a. For comparison, the VDOS of bulk bcc Fe, convoluted with the same energy

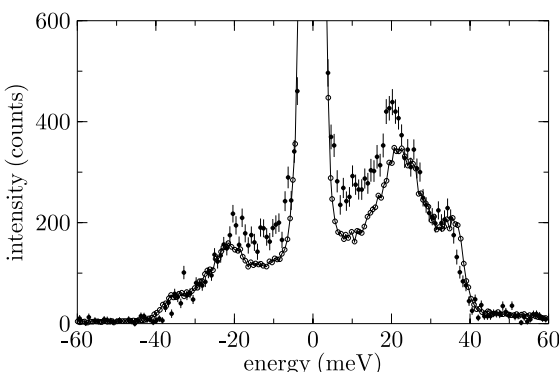


Fig. 5.10. Phonon spectrum of Fe islands on W(110) recorded with an energy resolution of 4.4 meV. Open circles display the phonon spectrum of bulk bcc Fe. Both spectra are normalized on the high-energy regime

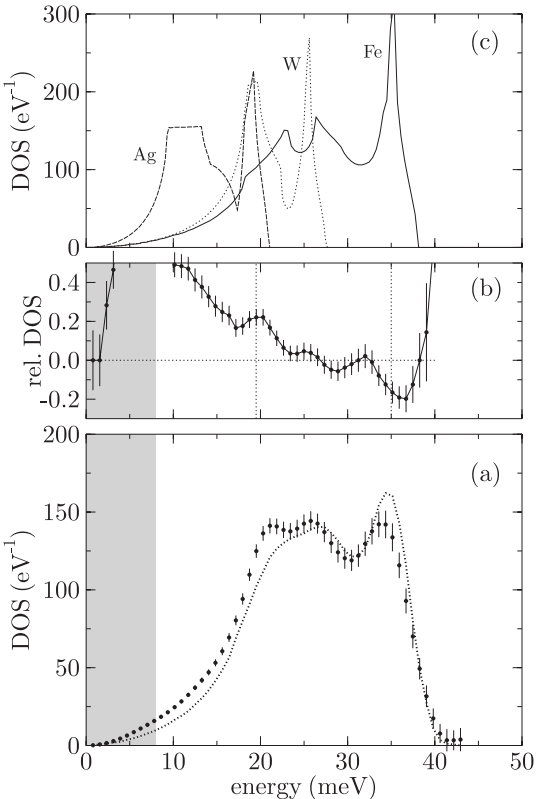


Fig. 5.11. (a) Vibrational density of states of Fe islands on W(110) as derived from the phonon spectrum in Fig. 5.10. The *dashed line* is the phonon DOS of bulk bcc Fe, obtained from the theoretical data [25, 49] by convolution with the energy resolution function. The *grey area* has to be excluded from the evaluation because it is covered by the resolution function. (b) Relative difference $(D(E) - D_0(E))/D_0(E)$ of the measured DOS and the bulk DOS of Fe. (c) Comparison of the phonon density of states for Ag, Fe and W [49]. The high-frequency modes of Fe cannot propagate in the neighboring materials Ag and W

resolution function, is drawn as dotted line. Pronounced differences appear especially at low phonon energies, where an excess of the island VDOS over the bulk VDOS can be observed. Similar structures have been observed also in metallic multilayers where the Fe layer thickness is comparable to the thickness of the Fe islands [70]. It has to be considered in these cases that the crystalline lattice of the surrounding material is coupled strongly to the Fe so that a hybridization of the vibrational DOS is to be expected.

To emphasize the differences more clearly, the relative difference $\Delta D(E) = (D(E) - D_0(E))/D_0(E)$ between the DOS of bulk Fe, $D_0(E)$, and the measured DOS, $D(E)$, is displayed in Fig. 5.11b. For a qualitative investigation, the corresponding phonon DOS of bulk Fe, W, and Ag are shown in Fig. 5.11c⁸. Remarkably, $\Delta D(E)$ goes through zero around 27 meV where

⁸ It should be noted that a direct comparison of the density of states is meaningful, because a) the islands are relaxed i.e., they exhibit the bcc Fe lattice constant and no residual strain has to be considered and b) the lattice is cubic so that no projection effects of the photon wavevector on the phonon polarization vectors are encountered. This is the isotropic limit where the ‘true’ DOS is obtained, as explained in the appendix, Sect. A.6.

the DOS of W terminates. At energies above 27 meV the Fe phonons cannot propagate in the neighboring materials and are essentially confined to the islands. Due to enhanced scattering at the boundaries and accompanying anharmonic interactions the phonon lifetime is shortened, leading to lifetime-broadening and damping of the high-frequency Fe modes, so that $\Delta D(E) < 0$. A similar behavior has been observed in thin films of Fe [48], as described already in Sect. 5.4.1. At low energies the DOS of W and Ag is larger than that of Fe, so that Fe vibrations can propagate freely into these materials. It is quite remarkable that at energies around 19 meV, where the DOS of Ag and W is strongly peaked, the DOS of the Fe islands is enhanced, too. This suggests a strong coupling of the lattices in this Ag/Fe/W sandwich structure. In contrast to nanocrystalline Fe (see Sect. 5.4.2), an enhanced DOS at high energies is not observed for the Fe islands. In the nanocrystals this is attributed partly to a shrinkage of the bond length and a corresponding increase in the interatomic force constants [64]. Here, however, the Fe islands exhibit the bulk bcc Fe lattice constant, so that no shrinkage effects are found here. The high-energy tail of the VDOS thus resembles quite closely that of bcc Fe.

Although a quantitative treatment cannot be given at this stage, these investigations open a way for an understanding of vibrational interactions in nanostructured metallic systems. Further investigations with other substrate materials and capping layers should be performed to deepen this understanding. This could be a first step on the way to a controlled manipulation of vibrational properties ('phonon engineering'), particularly in novel nanostructured materials. While the system Fe on W is already an established model system for low-dimensional magnetism it also has a potential as a model system for the lattice dynamics of nanostructures.

5.4.4 Vibrational Excitations in Amorphous FeTb Alloys

The dynamical properties of amorphous materials have attracted considerable attention because they show an anomalous behavior in the low-energy part of the vibrational spectrum [71, 72, 73, 74]. Of particular interest in this field is the so called boson peak [72], which appears in the vibrational density of states (VDOS), $D(E)$, as an excess contribution with respect to the usual Debye behavior $D(E) \sim E^2$. Such a behaviour was observed, for example, by coherent inelastic neutron scattering on bulk samples of binary metallic glasses, such as a-Mg₇₀Zn₃₀ [75]. Typically, the amorphous state is metastable and can only be stabilized by rapid quenching. Common techniques are melt-spinning, splat-cooling or condensation from the vapor phase, as it occurs, e.g., during the deposition of thin films. This is the case for Fe_xTb_{1-x} alloys, which can be prepared over a wide composition range by vapor quenching. In this experiment, FeTb alloys in the thickness range between 175 Å and 800 Å were found to be metastable at room temperature in the regime 0.20 < $x < 0.82$.

All a- $\text{Fe}_x\text{Tb}_{1-x}$ alloy thin films were prepared in ultrahigh vacuum (base pressure $\sim 5 \times 10^{-10}$ mbar) by thermal co-evaporation of Tb metal and metallic Fe (enriched to 95.5% in ^{57}Fe) from two independently controlled Knudsen cells [76]. The pressure during evaporation was below 1×10^{-10} mbar. The desired alloy composition was adjusted by selecting the corresponding ratio of the Tb and ^{57}Fe deposition rates. All alloy compositions given here are the nominal compositions as determined from the ratio of the two deposition rates with an error of ± 0.01 . The films were grown at 300 K on oxidized Si(001) wafers that were initially coated by a 200 Å thick polycrystalline Pt buffer layer in order to exploit the formation of x-ray standing waves for intensity enhancement [48]. All samples were coated with a 50 – 100 Å thick Si layer for protection against oxidation. The structure of the samples was characterized by x-ray diffraction (XRD) and ^{57}Fe conversion electron Mössbauer spectroscopy (CEMS).

Some typical XRD diagrams are shown in Fig. 5.12a, where only Bragg peaks of the 200 Å thick polycrystalline Pt buffer layer are present. The absence of Bragg reflections from hcp-Tb or intermetallic Tb-Fe compounds confirms the amorphous structure of the $\text{Fe}_x\text{Tb}_{1-x}$ thin films. Typical CEM spectra of a- $\text{Fe}_x\text{Tb}_{1-x}$ films are shown in Fig. 5.12b. Also these spectra confirm the amorphous structure, as evidenced by the broad hyperfine field distribution that is necessary to fit the data (solid lines). From the relative line intensities one deduces that the average Fe spin direction is preferentially perpendicular to the film plane. This is in agreement with earlier reports [76, 78, 79]. Moreover, a- $\text{Fe}_x\text{Tb}_{1-x}$ films with $x < 0.50$ are paramagnetic at room temperature, as indicated by the quadrupole split spectrum in Fig. 5.12b. This hyperfine structure results from a distribution of electric quadrupole splittings which is a typical feature of nonmagnetic amorphous binary Fe alloys [80, 81].

Vibrational spectra of the films were recorded at the undulator beamline 3-ID at the Advanced Photon Source with an energy resolution of 2.3 meV, shown in Fig. 5.13a. The incident beam illuminated the films under a grazing angle of about 4 mrad. Data acquisition times were 2–10 h per spectrum, depending on film thickness and Fe content.

The partial VDOS as deduced from the measured vibrational spectra is shown in Fig. 5.13b for $\text{Fe}_x\text{Tb}_{1-x}$ films of different composition. The VDOS represents a structureless broad peak, as anticipated for such structurally and atomically disordered materials, where van Hove singularities are smeared out. There is a tendency that the maximum energy of the VDOS in Fig. 5.13b shifts to lower energies with decreasing Fe content x of the amorphous films, i.e., the Fe vibrations soften with decreasing x . The low-energy modes in $D(E)$ below 10 meV in Fig. 5.13b are of particular interest because of the boson-peak phenomenon [71, 73, 74]. The usual way to observe a deviation from Debye-like behavior is to plot the reduced VDOS, $D(E)/E^2$, versus E . In this representation, strict Debye-like behavior is reflected by a horizontal

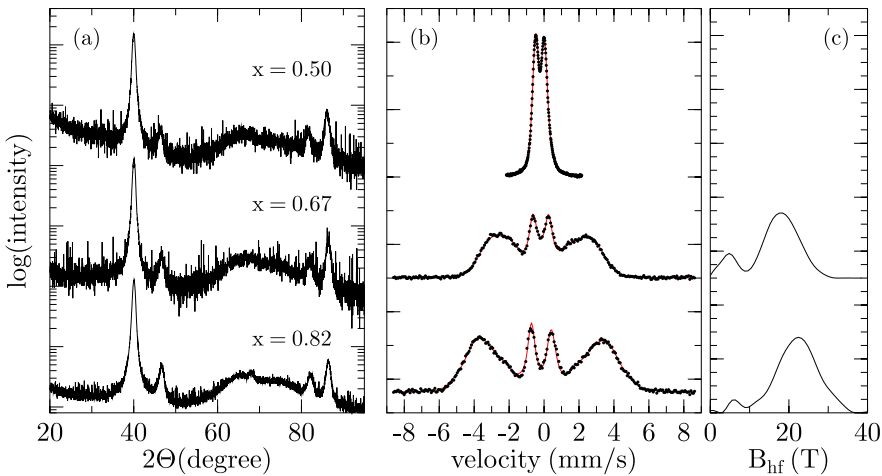


Fig. 5.12. (a) X-ray diffraction diagrams (Cu-K_α-radiation) of a-Fe_xTb_{1-x} films on a Pt-coated Si(001) substrate for $x = 0.5, 0.67, 0.82$. The film thickness was about 20 nm. (b) Room-temperature CEM-spectra of these films with the corresponding hyperfine-field distribution, shown in (c), that was derived from a fit to the spectra (*solid lines*). (Data are taken from Ruckert *et al.* [77])

line which intersects the $D(E)/E^2$ axis at a value that is proportional to c_S^3 (c_S = sound velocity) [30]. In Fig. 5.14 we have plotted $D(E)/E^2$ versus E for some representative examples: for two a-⁵⁷Fe_xTb_{1-x} films and, for comparison, for two crystalline systems, i.e. a 800 Å-thick cubic ⁵⁷Fe₂Tb(110) epitaxial film and bulk bcc Fe. In Fig. 5.14 a striking and unambiguous rise in $D(E)/E^2$ up to about 2.5/at.vol./eV/meV² below ~ 10 meV is observed for the Tb-rich a-⁵⁷Fe_{0.30}Tb_{0.70} film. Furthermore, a peak near 3 meV seems to exist for this sample. However, because of the limited energy resolution of 2.3 meV (FWHM) it is not clear at present whether this peak is real or an artifact of the data evaluation, which includes subtraction of the elastic peak⁹. For the less Tb-containing a-⁵⁷Fe_{0.67}Tb_{0.33} film, the rise in $D(E)/E^2$ below ~ 10 meV is clearly much weaker than for the Tb-rich sample. By contrast, the crystalline ⁵⁷Fe₂Tb film shows a value of ~ 0.5 /at.vol./eV/meV² near ~ 3 meV that is much smaller than that of the amorphous films, see Fig. 5.14¹⁰. Debye-like behavior seems to occur below ≈ 5 meV in cubic TbFe₂. For bulk bcc Fe, Debye-like behavior is observed in $D(E)/E^2$ below ~ 15 meV, with $D(E)/E^2 < 0.13$ /at.vol./eV/meV².

⁹ A much clearer evidence for this peak was found for amorphous Fe_xZr_{1-x} alloys [82], where the boson peak is located at higher energies around 4 meV.

¹⁰ The peaks at ~ 22.5 meV and ~ 16 meV and the dip near 10 meV, result from extrema in the VDOS due to optical and acoustic phonons of the cubic Laves phase [84], and are not related to low-energy excitations leading to a boson peak.

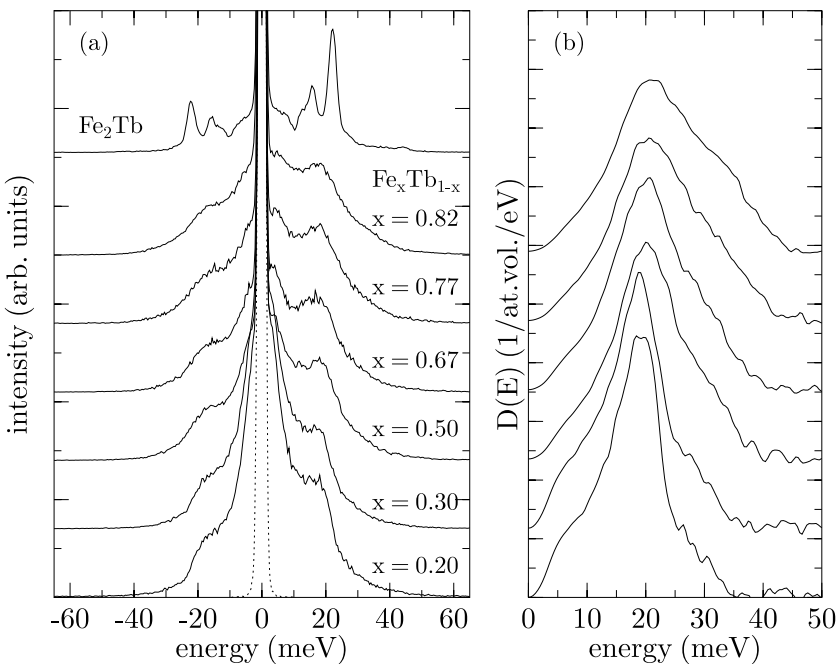


Fig. 5.13. (a) Phonon spectra measured at 300 K for $a\text{-}^{57}\text{Fe}_x\text{Tb}_{1-x}$ films of various compositions with $x = 0.20, 0.30, 0.50, 0.67, 0.77, 0.82$, and for the epitaxial, cubic Laves phase $\text{Fe}_2\text{Tb}(110)$ (from bottom to top). The dashed line is the instrumental resolution function with a FWHM of 2.3 meV. The spectra are vertically displaced for better visibility. (b) Partial vibrational density of states, $D(E)$, as derived from the phonon spectra shown in a). Neighbouring curves are vertically displaced by 50/at.vol./eV (Data are taken from Ruckert et al. [77])

Although the boson peak could not be fully resolved, Fig. 5.14 clearly demonstrates the existence of non-Debye-like vibrational excitations below about 10 meV in quench-condensed $a\text{-}^{57}\text{Fe}_x\text{Tb}_{1-x}$ alloy films. The excitation probability of these anomalous atomic vibrations increases with decreasing excitation energy and rising Tb content. They are not observed in crystalline systems such as cubic Fe_2Tb and bcc Fe. The microscopic origin of the observed anomalous low-energy excitations is unclear at present. For metallic glasses, either movements of atoms on the surface of very small voids or movements in lower density ‘defect’ regions of the metallic glass have been suggested [75] as an explanation for low-energy excitations in these systems. We speculate that the larger atomic diameter of Tb (3.52 Å) as compared to that of Fe (2.48 Å) might be an important factor in the $a\text{-}\text{Fe}_x\text{Tb}_{1-x}$ system. In the structurally disordered network of large Tb atoms in Tb-rich amorphous alloys, voids on an atomic scale might exist, which, when occupied by

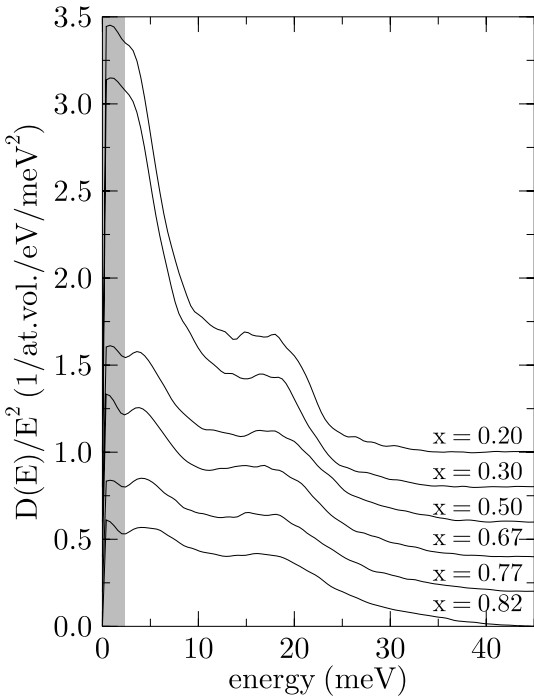


Fig. 5.14. Reduced partial VDOS, $D(E)/E^2$, for the $a\text{-}^{57}\text{Fe}_x\text{Tb}_{1-x}$ films, and for the epitaxial, cubic Laves phase $\text{Fe}_2\text{Tb}(110)$, taken at 300 K. Neighbouring curves are vertically displaced by $0.2/\text{at.vol./eV/meV}^2$. Due to the finite width of the energy resolution function, data points below 2.3 meV are physically irrelevant (Data are taken from Keune *et al.* [83])

Fe atoms, provide enough space for the smaller Fe atoms to vibrate in shallow potentials with low frequencies. Such voids do not exist in crystalline systems [77, 83].

5.4.5 Phonon Softening in Fe-Invar Alloys

Phase Transitions and Lattice Instabilities

The physics of several phase transitions is intimately related to lattice instabilities with soft phonon modes. Figure 5.15 displays schematically one transverse optic (TO) and one transverse acoustic (TA) phonon branch of a hypothetical crystal with several types of phonon anomalies labeled I–IV. The softening of an infrared-active mode at the zone center (I) is well known to be the driving force of ferroelectric transitions of usually (nearly) second-order character. The elastic analog is found in ferroelastic transformations; it is closely related to the famous Zener instability of bcc lattices. Its signature is a soft shear modulus with a small slope in the acoustic limit and the upward curvature at the zone center (II). Phonon anomalies of type III and IV are frequently found in shape memory materials, where the minima at finite wave vector represent intracell atomic displacements that essentially ‘freeze’ at the phase transition [86].

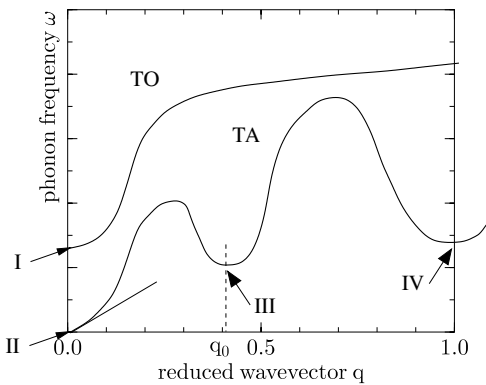


Fig. 5.15. Schematic diagram of phonon branches of a hypothetical crystal with various soft phonon anomalies associated with lattice instabilities (Figure taken from Krumhansl & Barsch [85])

Investigation of Disordered Fe-Pd

Disordered FePd with a Pd concentration between 25 and 30 at% is an Invar alloy like the more familiar FeNi and FePt compounds. The Invar-effect, i.e., an anomalously low thermal expansion coefficient over a wide temperature range, is attributed to magneto-volume instabilities occurring in 3d-transition-element rich systems. For an overview of the Invar problem and its relation to moment-volume instabilities see, e.g., [88]. In FePd the Invar effect is attributed to a softening of the [110] TA₁ phonon branch which starts at the Curie temperature $T_C \approx 575$ K, gets stronger with decreasing temperature and finally drives structural transformations of the crystal lattice. There are three structural phases involved in the Invar composition region of FePd. At higher Pd concentrations and temperatures the lattice is in the γ (fcc) phase, at lower Pd concentrations and temperatures in the α (bcc) phase and in the intermediate region in a γ' (fct) phase. The phase diagram based on the measurements by Matsui *et al.* [87] is shown schematically in Fig. 5.16. The $\gamma \rightarrow \gamma'$ transition is reversible of weakly first order, the $\gamma' \rightarrow \alpha$ transition is irreversible of first order. In Fe-Pd Invar the magneto-volume instabilities become critical at low temperatures (about 200 K) leading to a fcc-fct-phase transition which is also responsible for the appearance of the shape memory effect in this alloy [87, 89].

The phonon DOS has been measured via inelastic nuclear resonant scattering at the beamline 3-ID of the APS with an energy resolution of about 2.2 meV. The sample was a single crystal of nominal composition Fe₂₈Pd₇₂, grown by the zone-melting method (provided by Dr. T. Lograsso from AMES Laboratories, USA). Measurements of the modified DOS $G(E) = D(E)/E^2$ at different temperatures are shown in Fig. 5.17. In this plot deviations from the Debye-law $D(E) \sim E^2$ at low energies become visible, i.e., for a Debye - solid $G(E)$ should be constant at low energies. At $T = 300$ K an enhancement of low-energy modes is visible that displays a strong deviation from the

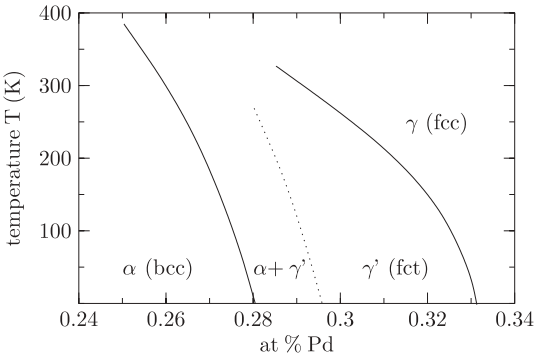


Fig. 5.16. Phase diagram of the structural phases in disordered FePd, as published in [87]

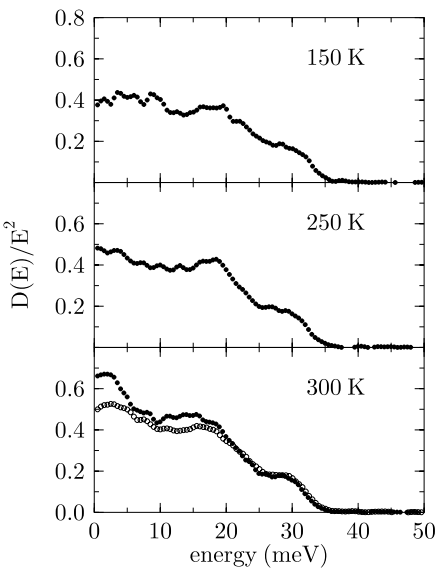


Fig. 5.17. Plot of $D(E)/E^2$ for the Fe-Pd crystal as a function of temperature, measured with an energy resolution of 2.2 meV. $D(E)$ is the partial phonon density of states of the Fe atoms. In this plot deviations from the Debye-law $D(E) \sim E^2$ become visible. The crystal was cooled down from 300 K to 150 K (solid circles) and then warmed up again to 300 K (open circles)

Debye behavior. Remarkably, with decreasing temperature the crystal becomes more and more Debye-like. If the temperature is raised to 300 K, the original deviations partly reappear again. This behavior cannot be explained by the softening of single phonon branches like in FePt [90]. Unfortunately, the energy resolution in this experiment is not sufficient to decide whether the observed enhancement merges into a true peak at energies below 3 meV. In that case it is possible that the observed behavior is related to the so-called ‘Boson peak’ [71, 91]. It has been shown that such enhancement of low-energy modes occurs for systems with force-constant disorder [73], either due to a distribution of bond-lengths or lattice disorder [92] like in this case. In addition, it should be checked how vibrational properties are influenced by collective magnetic excitations. This should play a vital role especially in materials like Invar with prominent moment-volume instabilities. It was

suggested that hybridization between phonon and magnon branches leads to an enhancement of low-energy modes in FeO [93].

5.4.6 Local Vibrational Density of States: Interface Phonons and Impurity Modes

Very often, the electronic, magnetic and thermal properties of materials are strongly influenced by the presence of impurity atoms. Vibrational properties are affected by the coupling of the impurity atoms to the surrounding lattice. The vibrational dynamics of impurity atoms was described theoretically by Green's function techniques [94]. In these theories, the vibrational density of states (VDOS) of the impurity atoms is derived from the unperturbed VDOS of the host crystal. Two kinds of vibrational modes are distinguished:

- **Resonance Modes:** The energies of these modes lie within the vibrational spectrum of the host lattice. This is to be expected when the mass of the impurity atom is larger than that of the host atom. Example: Fe in Al.
- **Localized Modes:** The energies of these modes are larger than the largest vibrational frequency of the host lattice. These modes appear when the mass of the impurity is smaller than that of the host atoms. Example: Fe in Cu.

This coupling was investigated by inelastic nuclear resonant scattering [95] from Fe as the impurity atom. Nuclear resonant scattering is an ideal tool to investigate this dynamics because the signal comes exclusively from the impurity atoms.

Figure 5.18 shows the VDOS of two samples: a) 0.017 at.% ^{57}Fe in Al and b) 0.01 at.% ^{57}Fe in Cu [95]. The VDOS of Fe in Al shows a strong peak around 15 meV that is very likely due to resonance modes, because its energy is well below the Al cutoff energy of about 40 meV. On the other hand, for Fe in Cu one observes additional modes above the Cu cutoff energy of 30.6 meV that may be localized modes. For a theoretical description of the data, the theory developed by Mannheim *et al.* [96, 97, 98] was applied here. This theory treats isolated impurities bound by central forces that are limited to the first-nearest neighbors. It contains as the only free parameter the ratio A/A' of the host-host force constant A and the host-impurity force constant A' . Together with the ratio M/M' of the average mass M of the host atoms and the mass M' of the impurity atom, the VDOS $D'(\omega)$ of the impurity is expressed in terms of the VDOS $D(\omega)$ of the host lattice:

$$D'(\omega) = \frac{M}{M'} \left[\frac{D(\omega)}{[1 + \varrho(\omega) S(\omega)]^2 + [\pi \omega \varrho(\omega) G(\omega)/2]^2} + \frac{\delta(\omega - \omega_L)}{\varrho(\omega)^2 T(\omega) + M/M' - [1 + \varrho(\omega)]^2} \right], \quad (5.33)$$

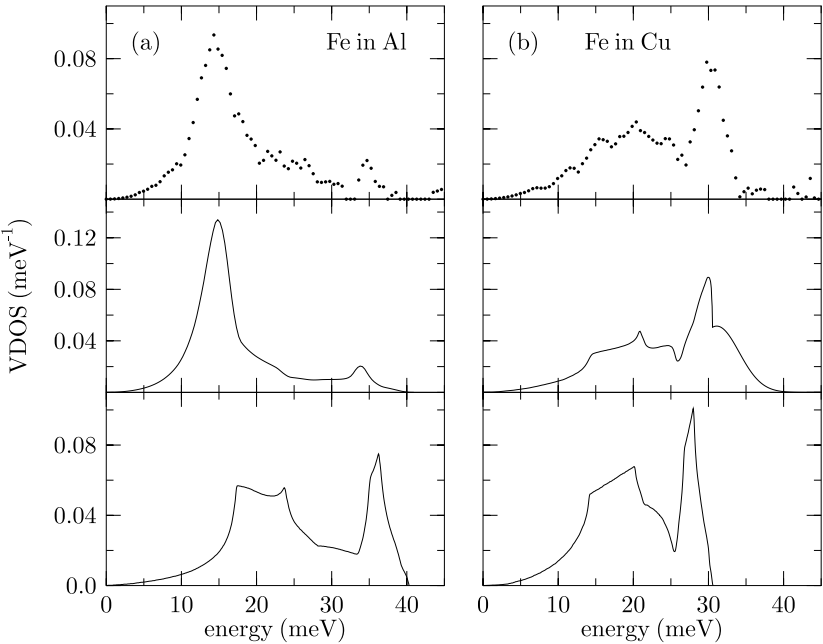


Fig. 5.18. Vibrational density of states of Fe impurity atoms, measured via inelastic nuclear resonant scattering. (a) VDOS of 0.017 at.% ^{57}Fe in Al, (b) VDOS of 0.01 at.% ^{57}Fe in Cu. The *middle panels* show calculations of the VDOS according to (5.33), assuming force-constant ratios $A/A' = 0.94$ for Fe in Al and $A/A' = 0.79$ for Fe in Cu. The *lower panels* show the phonon DOS of the host lattices for comparison. (Data taken from Seto *et al.* [95])

where

$$\varrho(\omega) = \frac{M}{M'} - 1 + \frac{\omega^2 [1 - A/A']}{\mu(2)}, \quad S(\omega) = \mathcal{P} \int_0^\infty \frac{\omega'^2 D(\omega')}{\omega'^2 - \omega^2} d\omega' \quad (5.34)$$

$$T(\omega) = \omega^4 \int_0^\infty \frac{D(\omega')}{\omega'^2 - \omega^2} d\omega', \quad \text{and} \quad \mu(n) = \int_0^\infty \omega^n D(\omega) d\omega. \quad (5.35)$$

\mathcal{P} denotes the principal value of the integral. The localized mode at ω_L only exists if $1 + \varrho(\omega_L) S(\omega_L) = 0$ and $\omega_L > \omega_{max}$. In this formalism, the localized mode is represented by a Dirac δ -function. In real cases, however, such a mode has a finite lifetime due to anharmonic effects, resulting in a broadening of the line.

From simulations according to this formalism, one obtains an effective force-constant ratio of $A/A' = 0.94(3)$ for Fe in Al and $A/A' = 0.79(3)$ for Fe in Cu. The resulting vibrational DOS of the Fe impurity atoms are shown as

solid lines in Fig. 5.18. For comparison, the dashed lines show the VDOS of the host lattices as determined from inelastic neutron scattering experiments and compiled in [49]. Due to the considerable mass difference between Fe and Al ($M/M' = M(\text{Al})/M(\text{Fe}) = 0.47$), the resonance mode around 15 meV is very pronounced. In case of Fe in Cu, the mass ratio is $M/M' = 1.1$, so that localized modes can be expected. In this experiment, however, their existence is not very conclusive, because the spectral features in the phonon spectrum are strongly broadened. It is therefore hard to distinguish possible localized modes from the tails of the broadened phonon lines close to the cutoff energy at 30 meV. Systems in which the mass ratio M/M' is larger may be better candidates to observe these modes.

Another example demonstrates the transition from bulk (3-dimensional) lattice dynamics via thin-film (2-dimensional) vibrational behavior to vibrational modes of impurity atoms (1-dimensional). Figure 5.19 shows the development of the VDOS along this route. The samples were Fe/Cr multilayers containing ^{57}Fe monolayers in various environments [99]. While the density of states of bcc Fe is basically the same as that of a ^{57}Fe monolayer within Fe, significant changes can be observed when the monolayer is located at the interface between Fe and Cr: While the high-energy modes around 35 meV are damped, the modes around 25 meV are strongly enhanced. This tendency continues drastically, if the ^{57}Fe probe layers are embedded within Cr: The VDOS of the Fe atoms around 25 meV is now twice as large compared to the region around 35 meV. In the case of ^{57}Fe impurities in Cr, this peak merges into a strong resonance mode around 22 meV. This can be described by the formalism outlined above: The solid line is a theoretical simulation according to (5.33) assuming a force-constant ratio of $A/A' = 1.6$.

The measurements discussed here demonstrate the high sensitivity of the method to very small amounts of material. While this is not only an interesting testbed for lattice dynamical theories of impurity atoms, it may also lead to further applications: The impurity atoms may be used to probe the dynamics of the host lattice, as shown in the following.

Determination of Sound Velocities

An interesting application of the vibrational spectroscopy of impurities in solids is the determination of the sound velocity of the host matrix [100]. For an isotropic or a polycrystalline sample, the low-energy part of the phonon density of states can be approximated by

$$D(E) = \left(\frac{M'}{M} \right) \frac{E^2}{2\pi^2 \hbar^3 \varrho v_D^3}, \quad (5.36)$$

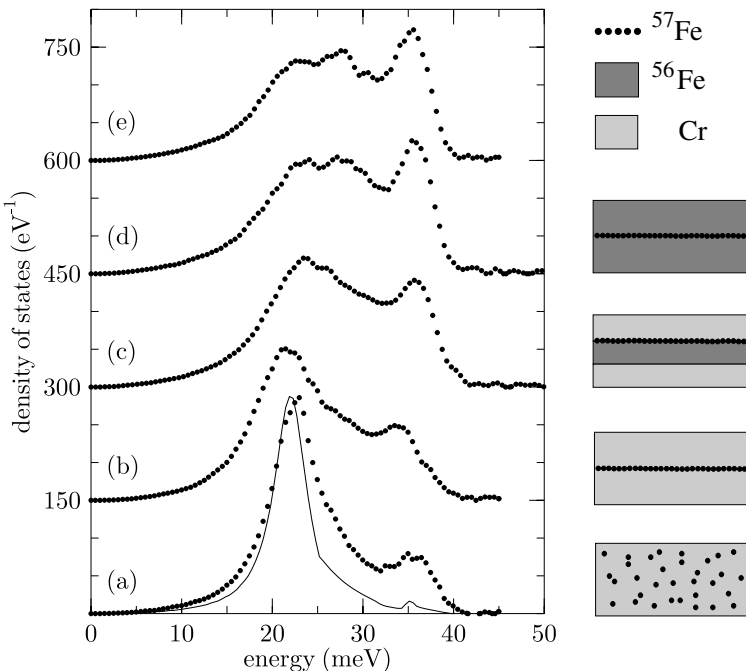


Fig. 5.19. Development of the vibrational density of states of ^{57}Fe with increasing dilution in Cr, recorded with an energy resolution of 4.4 meV. (a) bulk ^{57}Fe (b) ^{57}Fe monolayer in Fe, (c) ^{57}Fe monolayer at the Fe/Cr interface (d) ^{57}Fe monolayer in Cr (e) dilute ^{57}Fe in Cr. The ^{57}Fe monolayers were stacked up to 200 times in periodic multilayer structures. The solid line in e) is a simulation according to the theory outlined in the text assuming a force-constant ratio of $A/A' = 1.6$. (Experimental data taken from Alp et al. [70])

where ϱ is the number density of the atoms¹¹. v_D is the Debye sound velocity that is defined as an average over all sound velocities $c(\mathbf{q}, s)$, depending on propagation wave vector \mathbf{q} and polarization index s :

$$\frac{1}{v_D^3} = \frac{1}{3} \sum_{s=1}^3 \int \frac{d\Omega_q}{4\pi} \frac{1}{c^3(\mathbf{q}, s)} . \quad (5.37)$$

This method was applied to determine the sound velocity in Pd via nuclear inelastic scattering from $^{119}\text{Sn}_{0.01}\text{Pd}_{0.99}$ [100]. The quantity $D(E)/E^2$ is shown in Fig. 5.20, recorded with an energy resolution of 0.85 meV. Within the statistical accuracy, the sample shows Debye-like behavior up to an energy of about 5 meV. From these data the sound velocity v_D in Pd was determined to

¹¹ Equation (5.36) has also appeared in a recent study of the vibrational properties of myoglobin and related biological compounds [28].

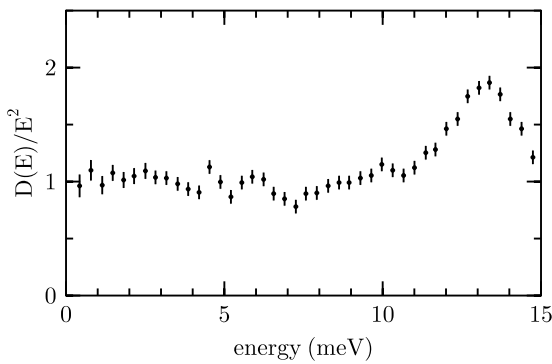


Fig. 5.20. Reduced vibrational DOS $D(E)/E^2$ of 1% ^{119}Sn in Pd, measured with an energy resolution of 0.85 meV. (Figure adopted from *Hu et al. [100]*)

be 2193 ± 35 m/s, which is well in the range of values given in the literature [101].

This method relies critically on the Debye behavior at small phonon energies as well as on the accurate determination of the phonon DOS in this region. One should also keep in mind that the extraction of the DOS relies on the assumption of the sample being a harmonic solid. Systematic uncertainties can thus be introduced by nonlinearities and unharmonicities in the low-energy part of the frequency spectrum. While these effects can be hardly avoided, the instrumental influences can be reduced by further improving the energy resolution and by an accurate measurement of the shape of the resolution function.

An application of this method is the determination of sound velocities in solids under extreme conditions of high pressure and temperature. This will have significant impact in the field of geophysics where the access to elastic properties under conditions of planetary cores is of great interest.

The experiments shown here are an impressive example of the high sensitivity of nuclear resonant inelastic scattering at modern synchrotron radiation facilities. Vibrational properties of low-dimensional systems and highly dilute systems can be studied with very high energy resolution. The drastic changes of the phonon spectra as function of the surrounding matrix opens perspectives to tailor vibrational properties of condensed matter by micro- and nanostructuring techniques (phonon engineering).

5.5 Further Applications

5.5.1 Lattice Dynamics at High Pressures: Geophysical Aspects

The inner core of the Earth consists almost entirely of Fe or Fe-rich alloys, subjected to temperatures of several 1000 K and pressures of several 100 GPa, as sketched in Fig. 5.21. Seismic models of the Earth's interior crucially rely

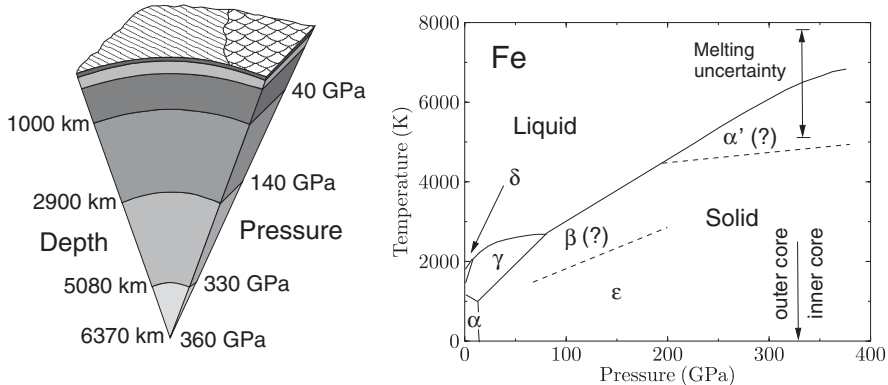


Fig. 5.21. *Left:* Model of the Earth's interior, illustrating the typical pressures at the transition between different regions. (Figure adopted from Lübbbers [107]). *Right:* High-pressure p - T phase diagram of Fe, including the established phases α (magnetic bcc), γ (nonmagnetic fcc), δ (nonmagnetic bcc), and ε (nonmagnetic hcp). The phases β (dhcp) and α' (bcc) are theoretically predicted [103], but not experimentally established yet. The *vertical arrow* indicates the pressure at the boundary between the Earth's inner and outer core at a depth of about 5080 km (Figure adopted from Lübbbers [107] in a modified version from Söderlind *et al.* [103])

on the knowledge of sound velocities as a function of depth [102]. This geo-physical aspect constitutes a strong motivation to study the elastic properties of iron [103], and its alloys over a wide range of pressures and temperatures. The p - T phase diagram of Fe is shown in Fig. 5.21b for the pressure and temperature range of the Earth's interior. Of particular interest is the hcp high-pressure phase of Fe (ε -Fe), as it is considered to be the most relevant phase for the inner core [104]. A striking feature is an anisotropy of 4–5% in the elastic properties of ε -Fe with respect to the c-axis that is comparable to the anisotropy of the sound velocity in the Earth's core with respect to its rotation axis [105]. This observation was speculatively attributed to a highly textured ε -Fe core [106].

Instrumentation

For nuclear inelastic scattering at high pressures a different type of diamond anvil cell is required compared to the design used in high-pressure NFS studies of Sect. 4.5. This is due to the fact that the incoherent nuclear decay products like Fe K_{α} fluorescence photons are emitted into the full solid angle. Accordingly, the cell has to be modified so that this radiation can be collected very efficiently. For this purpose, a gasket material has to be chosen that allows for a high transmission of the fluorescence radiation. A suitable replacement for the Ta₉₀W₁₀ alloy used in the NFS studies (see Sect. 4.5) turned out to be high-strength Be. Moreover, the geometry of the DAC had

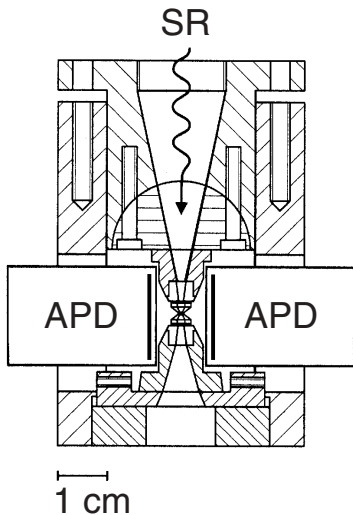


Fig. 5.22. Schematic drawing of a high-pressure cell for nuclear inelastic scattering scattering. The cell is specially designed to accommodate APD detectors as close as possible to the pressurized sample. (Figure adopted from Wortmann *et al.* [108])

to be extended so that APD detectors could be mounted as close as possible to the pressurized sample. This requires a freestanding mount of the diamond anvils so that the reemitted radiation on the way to the detectors is not obstructed.

High-Pressure Lattice Dynamics of Fe

Early high-pressure studies of the phonon DOS of Fe via nuclear resonant scattering were performed at pressures up to 40 GPa [109, 110]. While such pressures are far below of those found in the Earth's core, these investigations were extended up to pressures of 153 GPa in a subsequent experiment, as described in the following. The corresponding phonon DOS of Fe are shown in Fig. 5.23, measured with an energy resolution of 2 meV at beamline 3-ID of the APS (Argonne, USA) [111]. The pressures were calibrated via the method of ruby fluorescence [112] and confirmed by x-ray diffraction using the equation of state of Fe [113]. With increasing pressure, the phonon energies shift to higher energies, reflecting an increase in the Debye temperature from 400 K under ambient conditions to 670 K at 153 GPa [114]. Solid lines are theoretical simulations based on ab-initio electronic structure calculations [114]. While reasonable agreement is achieved in the low-pressure regime, significant discrepancies are observed above 13 GPa where the pressure induced transition into the ε -phase takes place. These discrepancies may be partly related to the magnetic structure of the hcp phase which could be in an antiferromagnetic state [115]¹². From a parabolic fit to the low-energy part of

¹² A strong influence of magnetic properties on the vibrational properties under high pressure has been observed in FeO [93].

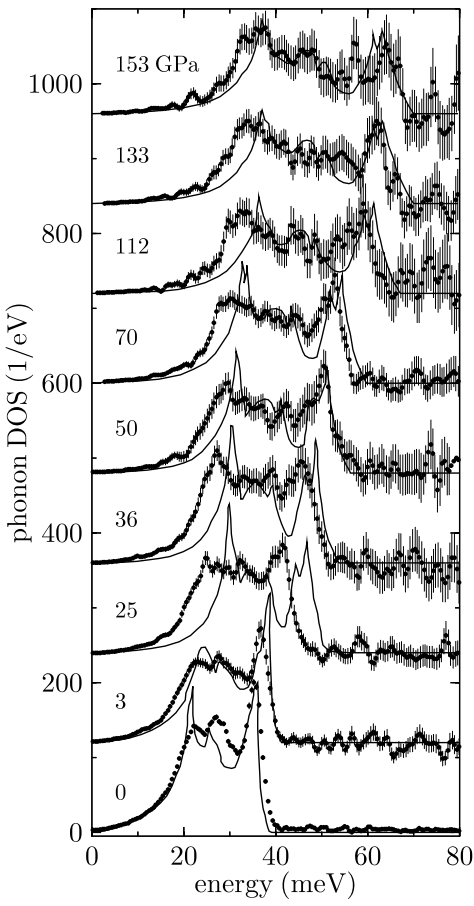


Fig. 5.23. The phonon DOS of metallic Fe at pressures up to 153 GPa, measured via inelastic nuclear resonant scattering with an energy resolution of 2 meV. The curves are displaced by 120 eV^{-1} relative to each other. Solid lines are calculations using an ab-initio theory. (Figure adopted from Mao *et al.* [111])

the phonon DOS the average (Debye) sound velocity v_D can be derived:

$$D(E) = \frac{E^2}{2\pi^2 \hbar^3 \varrho v_D^3}, \quad (5.38)$$

where ϱ is the number density of the atoms. v_D is related to the compressional sound velocity v_P and the shear velocity v_S as

$$\frac{3}{v_D^3} = \frac{1}{v_P^3} + \frac{2}{v_S^3}. \quad (5.39)$$

The numerators on the right side reflect the degeneracies of the longitudinal and transverse phonon modes, respectively. v_P and v_S are related to each other via

$$\frac{K}{\rho} = v_P^2 - \frac{4}{3} v_S^2 \quad \text{and} \quad \frac{G}{\rho} = v_S^2, \quad (5.40)$$

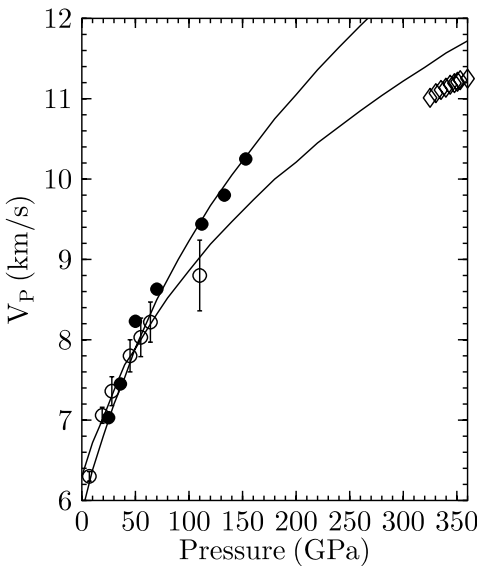


Fig. 5.24. Acoustic sound velocity V_P as derived from the phonon DOS shown in Fig. 5.23 (solid circles) [111] and from phonon dispersion relations measured by inelastic x-ray scattering (open circles) [116]. The solid lines are Birch fits to the measured data. In both cases the extrapolation to pressures in the Earth's core leads to values above the PREM data (open diamonds) [102]

where ρ is the density, K the bulk modulus and G the shear modulus. With ρ and K determined by x-ray diffraction and v_D determined from the phonon DOS, the above equations can be solved for v_P , v_S and G . On the other hand, v_P can be determined directly from the initial slope of the LA phonon dispersion relation, as determined via inelastic x-ray scattering up to a pressure of 110 GPa [116]. This measurement was performed on polycrystalline Fe¹³ and thus yielded the orientationally averaged dispersion curves of the LA phonon branch. Figure 5.24 displays the acoustic sound velocities derived from the phonon DOS together with the data from IXS measurements [116]. The solid line is a fit assuming a linear relation between the density ρ and the sound velocity v_P (Birch's law [117]). While the experimental data are in good agreement, the extrapolation to pressures at the inner core deviates from seismic data according to the *Preliminary Reference Earth Model* (PREM) [102]. This indicates that the Earth's inner core may be of slightly lower density than hcp Fe. This finding, however, is at variance with the conclusion derived in [111], where a heavier alloy, e.g., containing 5–10% Ni was suggested.

It should be noted that all the experiments reported here were performed at ambient temperatures. More reliable data can be only obtained if also the temperature can be adjusted to match conditions of the inner Earth. First studies in this field have been made with laser heating of the pressurized sample [118]. Another interesting aspect is the pressure-induced texturing of

¹³ Any single crystal of Fe transforms into a polycrystal upon the phase transition from α - to ε -Fe.

ε -Fe with the c-axis aligned along the direction of uniaxial compression [119]. This effect allows one to investigate the sound propagation along different directions in ε -Fe [108] and the anisotropy of its elastic parameters.

The experiments discussed here have shown that inelastic nuclear resonant scattering is a valuable method for the determination of sound velocities, which has significant impact for understanding the properties of planetary cores, for example. The measurements indicate the importance to obtain accurate data in the low-energy region of the phonon spectrum. This can be achieved by employing spectrometers with energy resolutions ΔE below 2 meV or better. Uncertainties related to the subtraction of the elastic peak then affect only a very small part of the phonon spectrum. For that reason, sound velocity data obtained in a previous study [110] ($\Delta E = 6.4$ meV) were deviating by 20% from those remeasured with better energy resolution ($\Delta E = 3.5$ meV) [109].

Another interesting approach in this field is the use of impurities of a resonant isotope to determine the sound velocity of the host material, as described in Sect. 5.4.6. This would allow one to determine sound velocities in materials that do not contain resonant isotopes [100].

5.5.2 Dynamics of Biomolecules

Several metallic species play a crucial role in the function of biological macromolecules. Prominent examples are Mg in chlorophyll and Fe in haemoglobin that constitute essential components of plant and animal metabolism, respectively. Fe in physiologically essential proteins is most often found in the center of a planar heme group, particularly in such proteins as haemoglobin and cytochrome c oxidase that mediate the transport and usage of molecular oxygen. The function of such molecules is closely related to their dynamics and conformational changes during reaction. Since these reactions often take place at a localized site, a route towards understanding the protein function is the synthesis and investigation of small molecules that mimic the structure of the active site. Model systems for the investigation of heme proteins are the iron-tetraphenylporphyrin Fe(TPP) compounds. For example, the heme model compound Fe(TPP)(2-MeHIm) mimics the active site of deoxymyoglobin, while Fe(TPP)(CO)(1-MeIm) represents the active site of carbonmonoxy myoglobin (MbCO). A useful model for heme proteins with fivefold coordinated Fe (with a ligand bound to the Fe), is Fe(TPP)(NO) [120, 121]. A model of this molecule is shown in Fig. 5.25. The Fe is located in the center of the planar heme group that consists of four pyrrole rings (I–IV), bridged by carbon atoms to which four phenyl groups are bound. It is believed that the out-of-plane motion of the Fe plays a fundamental role in the binding and transport of O₂ by haemoglobin [122]. This motion is a result of the dynamics of the surrounding protein matrix that controls the access to and the reactivity of the heme group. Peripheral substituents seem to have a large effect on the dynamics of the iron, especially for out-of-plane motions

[123]. In particular, low-energy vibrations directly couple to the binding of diatomic ligands like CO and NO to the Fe [124, 125].

Inelastic nuclear resonant scattering (NIS) is particularly suited to study biologically active iron modes that are not observed by other spectroscopic techniques. Unlike Raman or FTIR spectroscopy where observable modes are determined by optical selection rules, NIS detects all modes that have a sufficient displacement of the iron atom. A number of investigations in this field have been reported so far [28, 120, 121, 123, 126, 127, 128].

Figure 5.26a shows the vibrational density of states (VDOS) of Fe in Fe(TPP)(2-MeHIm) for a polycrystalline and a single-crystalline sample [121]. Since inelastic nuclear resonant absorption is sensitive to the projection $\langle \mathbf{k}_0 \cdot \mathbf{u} \rangle$ of the displacement vector \mathbf{u} of the atom on the photon wave vector, one is able to identify the directional character of individual modes by proper adjustment of the crystal. In this experiment the single crystal was oriented with the heme planes perpendicular and parallel to the wavevector \mathbf{k}_0 . The corresponding VDOS thus displays those modes with out-of-plane and with in-plane components, respectively, and the VDOS of the polycrystalline sample is a superposition of both. In this compound no further modes are observed beyond 55 meV. Figure 5.26b shows a comparison of the VDOS of heme protein model compounds with CO and NO ligands as well as the VDOS of carbonmonoxy myoglobin, MbCO. A striking feature is the large number of well-resolved vibrational resonances up to 80 meV. These modes indicate the localized character and the vanishing dispersion of vibrational excitations in molecular crystals, contrasting the broad phonon bands observed in simpler crystalline systems such as metals and oxides.

The comparison of the VDOS shown in Fig. 5.26b indicates the activation of several iron modes due to binding of CO or NO to the iron atom. In contrast, the VDOS of Fe(TPP)(2-MeHIm) in Fig. 5.26a without a ligand has only a few distinct peaks. Thus, it is very likely that the reduced symmetry

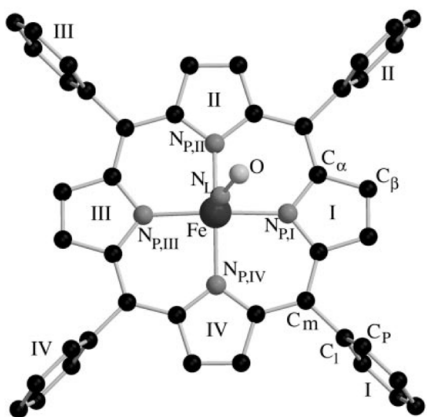


Fig. 5.25. Structure of the model compound Fe(TPP)(NO) in a perpendicular view on the porphyrin plane. Note the asymmetric binding of the NO ligand to the Fe (Figure adopted from Rai *et al.* [126])

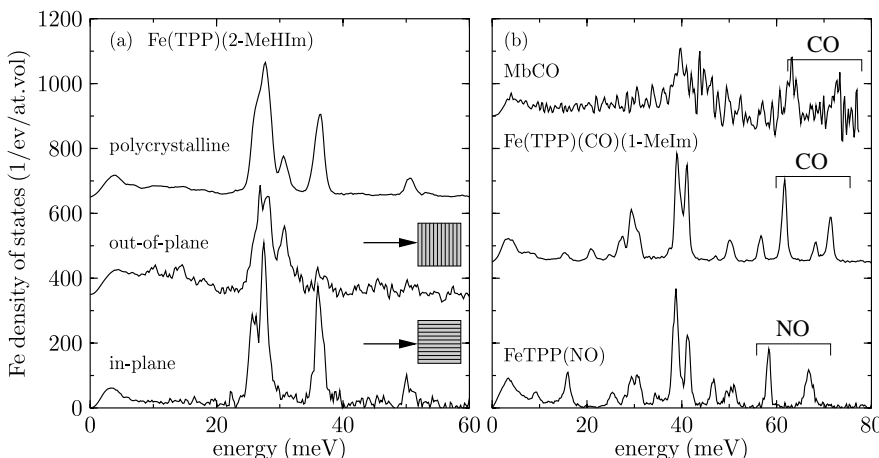


Fig. 5.26. (a) Vibrational spectra of $\text{Fe}(\text{TPP})(\text{2-MeHIm})$ at 20 K for a polycrystalline sample and a single crystal with the porphyrin plane oriented parallel or perpendicular to the incident beam. This allows for identification of in-plane or out-of-plane vibrations of the Fe, respectively. (b) Comparison of the Fe VDOS for various model compounds and the heme protein carbonmonoxy-myoglobin (MbCO) (Figures adopted from Rai *et al.* [123])

of the Fe environment induced by the asymmetric binding of the ligands (see Fig. 5.25) contributes to the activation of these modes. The strongest feature in the VDOS of the CO and NO ligated compounds is the pair of modes at 39.6 and 42.3 meV. These modes are associated to in-plane vibrations of the core porphyrin. The modes indicated by the brackets are NO and CO bend and stretch modes, as will be discussed later.

The extraction of the VDOS from the measured vibrational spectra assumes a harmonic lattice. This was confirmed by monitoring the temperature dependence of the vibrational modes in several different species of myoglobin up to 300 K [28]. In these studies no shift in the energetic positions of the lines has been observed. Therefore, it has been proven that the harmonic dynamics observed at low temperatures is present also in the physiological temperature regime above 180 K.

A confident assignment of the observed vibrational modes, however, requires a normal mode analysis. For molecular systems that exhibit discrete vibrational resonances, this approach provides a convenient basis for comparison of the experimental vibrational spectra with normal-mode calculations. This procedure is described, e.g., in [120, 121, 129]. In the case of $\text{Fe}(\text{TPP})(\text{CO})(\text{1-MeIm})$ the corresponding calculations allowed for a very good simulation of the measured VDOS and thus for an identification of individual vibrational modes [123].

Normal Mode Analysis

In the following we summarize the procedure how to extract mean-square displacements of individual vibrational modes from the measured vibrational spectrum [120]. In the low-temperature limit¹⁴ the normalized excitation probability is given by

$$S(\omega) = fL_0(\omega) + \sum_{\alpha} \phi_{\alpha} L(\omega - \omega_{\alpha}) , \quad (5.41)$$

with f being the recoilless fraction, i.e., the area fraction of the recoilless line. $L_0(\omega)$ and $L(\omega)$ are the lineshape functions of the elastic line and the vibrational modes, respectively. ϕ_{α} is the area fraction of the mode α with frequency ω_{α} in the spectrum. It can be expressed as:

$$\phi_{\alpha} = \frac{\omega_R}{\omega_{\alpha}} (\mathbf{k}_0 \cdot \mathbf{e}_{j\alpha})^2 (n_{\alpha} + 1) f , \quad (5.42)$$

where $\hbar\omega_R$ is the recoil energy of the free atom¹⁵, \mathbf{k}_0 is the unit photon wavevector, and $\mathbf{e}_{j\alpha}$ is the eigenvector of the normal mode α of atom j . n_{α} is the mean occupation number of mode α at temperature T that is given by

$$n_{\alpha} = \frac{1}{\exp(\hbar\omega_{\alpha}/k_B T) - 1} . \quad (5.43)$$

In the polycrystalline samples investigated here the orientational averaging of the projection factor in (5.42) yields:

$$\langle (\mathbf{k}_0 \cdot \mathbf{e}_{j\alpha})^2 \rangle = \frac{1}{3} e_{j\alpha}^2 , \quad (5.44)$$

so that

$$\phi_{\alpha} = \frac{1}{3} \frac{\omega_R}{\omega_{\alpha}} e_{j\alpha}^2 (n_{\alpha} + 1) f . \quad (5.45)$$

The quantity $e_{j\alpha}^2$ is the so-called *mode composition factor* which plays a central role in this analysis. It is closely related to the magnitude of the atomic fluctuations. In a harmonic system, the mean square deviation of atom j from its equilibrium position is given by

$$\langle r_j^2 \rangle = \sum_{\alpha} (2n_{\alpha} + 1) \langle r_{j\alpha}^2 \rangle_0 \quad \text{with} \quad \langle r_{j\alpha}^2 \rangle_0 = \frac{\hbar}{2m_j \omega_{\alpha}} e_{j\alpha}^2 . \quad (5.46)$$

$\langle r_{j\alpha}^2 \rangle_0$ is the contribution of mode α to the zero-point fluctuations of atom j in the ground state. This means, the mode composition factor $e_{j\alpha}^2$ is proportional to the contribution of mode α to the mean square fluctuations of atom j . For some simple cases, $e_{j\alpha}^2$ can be calculated directly. For example, $e_{j\alpha}^2 = m_j/M$ for an atom j with mass m_j , participating in a translational mode of

¹⁴ We consider only the one-phonon transitions $n_{\alpha} \rightarrow n_{\alpha} \pm 1$ in the occupation number of the vibrational states.

¹⁵ $\hbar\omega_R = 1.96$ meV for the 14.4 keV transition in ^{57}Fe .

a molecule with total mass M . Another simple case is a two-body oscillator consisting of two groups of atoms with masses M_1 and M_2 , where we have

$$e_{j\alpha}^2 = \frac{m_j}{M_1} \frac{M_2}{M_1 + M_2}. \quad (5.47)$$

For an experimental determination of the mode composition factors we use the normalization of (5.41), and the fact that the line-shape functions have unit area, to obtain

$$1 = \int S(\omega) d\omega = f + \sum_{\alpha} \phi_{\alpha}. \quad (5.48)$$

This equation is used to calculate the recoilless fraction f after determination of all values ϕ_{α} from the measured spectrum:

$$f = 1 - \sum_{\alpha} \phi_{\alpha}. \quad (5.49)$$

With this value (5.45) is solved for the mode composition factor $e_{j\alpha}^2$. For a test of the accuracy one takes these values to calculate the recoilless fraction via $f = \exp[-\langle (\mathbf{k}_0 \cdot \mathbf{r}_{Fe})^2 \rangle_T]$. Assuming again a polycrystalline sample, i.e., $\langle (\mathbf{k}_0 \cdot \mathbf{r}_{Fe})^2 \rangle = k_0^2 \langle r_{Fe}^2 \rangle / 3$, we use (5.46) together with the expression for the recoil energy $E_R = \hbar\omega_R = \hbar^2 k_0^2 / 2m_j$ and obtain:

$$f = \exp \left[-\frac{1}{3} \sum_{\alpha} \frac{\omega_R}{\omega_{\alpha}} (2n_{\alpha} + 1) e_{Fe,\alpha}^2 \right]. \quad (5.50)$$

While f is dominated by low-energy modes, a more convincing test is the comparison of the average kinetic energy

$$T = \frac{1}{12} \sum_{\alpha} \hbar\omega_{\alpha} (2n_{\alpha} + 1) e_{Fe,\alpha}^2 \quad (5.51)$$

with the model-independent value

$$T = \frac{\langle E^2 \rangle - E_R^2}{4E_R} \quad (5.52)$$

that follows from Lipkin's sum rules [22, 130], where $\langle E^2 \rangle$ denotes the second moment of the absorption probability $S(E)$, defined in (5.8). The results of the mode composition analysis for the compound Fe(TPP)(NO) at $T = 80$ K are shown in Fig. 5.27. The upper panel (a) shows the measured excitation probability, while the lower panel (b) displays the mode composition factors derived via the procedure described above. In this case (5.49) and (5.50) yield consistent values of $f = 0.948$ and $f = 0.944$, respectively. Also the average kinetic energy determined via (5.51) and (5.52) is in good agreement with values of $T = 9.17$ meV and $T = 9.42$ meV, respectively.

The peak at 67 meV is associated with a Fe-NO stretching mode. In fact, the value $e_{Fe}^2 = 0.34$ observed here is very close to the value $e_{Fe}^2 = 0.31$ predicted by (5.47) for a two-body Fe-NO oscillator. Moreover, the value

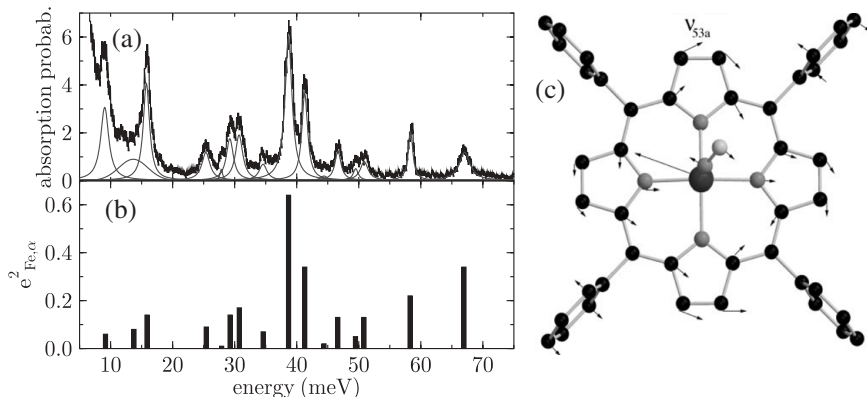


Fig. 5.27. (a) Measured excitation probability for the compound $\text{Fe}(\text{TPP})(\text{NO})$ at $T = 80 \text{ K}$. The *dashed lines* are Lorentzian fits to the peaks, the area of which was used to determine the weights ϕ_α . (b) Mode composition factors derived via the procedure described in the text. (c) Vibrational eigenvectors of the in-plane mode at a frequency of 38.7 meV . The lengths of the arrows indicate relative magnitudes of atom displacements (Figures (a), (b) adopted from *Sage et al.* [120], Figure (c) taken from *Rai et al.* [126])

$\sum_\alpha e_{Fe,\alpha}^2 = 2.62$ is close to the value $3 - 3m_{Fe}/M = 2.72$ that results from excluding acoustic modes from the normalization condition $\sum_\alpha e_{Fe,\alpha}^2 = 3$ for all modes. This observation suggests a partitioning of the Fe VDOS into discrete vibrational modes of the isolated molecule and acoustic phonon bands that lead to the broad feature below 4 meV . Vibrational modes that participate in biochemical reactions like Fe out-of-plane motions (doming mode) are assumed to lie in the range of $6\text{--}9 \text{ meV}$ [128].

The aim of a detailed computational analysis is the construction of the normal mode spectrum in terms of the Fe displacements. A recent approach is the application of ab-initio methods based on density functional theory (DFT) [129, 131]. In the traditional normal coordinate analysis, however, an empirical force field is developed consisting of force constants that are adjusted to fit the vibrational data [131]. Although this problem is strongly underdetermined due to the large number of normal modes, reliable results can be obtained by analyzing related model compounds in a consistent manner. Figure 5.27c shows the result for the vibrational eigenvectors of the mode at 38.7 meV [123]. The lengths of the arrows indicate relative magnitudes of atom displacements. This type of analysis has been performed for a number of heme proteins [121, 123].

It is the great virtue of inelastic nuclear resonant scattering from biomolecules and molecular crystals that it provides quantitative information on mode composition. This serves as important input for normal-mode calculations to reveal eigenvectors of vibrational modes. Such investigations are

not only of great importance to understand the function of physiologically relevant molecules, but also for molecules like $(\text{CN}_3\text{H}_6)_2\text{Fe}(\text{CN})_5\text{NO}$ (guanidinium nitroprusside) and $\text{Fe}(\text{tpa})(\text{NCS})_2$ that are promising materials for high-density optical information storage [132, 133].

5.6 Comparison with Other Scattering Methods

The traditional method for measuring vibrational properties of condensed matter are inelastic neutron scattering (INS) [134] and inelastic x-ray scattering (IXS) [13, 14]. Both methods provide measurements of the fundamental relationship between the vibrational excitation frequency and the momentum transfer, i.e., the dispersion relations, in bulk solids. From the dispersion relations of single crystals the phonon density of states can be calculated by integration over momentum space [135]. Therefore, inelastic nuclear resonant scattering and INS or IXS provide complementary information.

In the following the most important differences between INS, IXS and nuclear inelastic scattering (NIS) shall be reviewed. Inelastic nuclear resonant absorption of x-rays relies on the detection of decay products from internal conversion that is an incoherent process with a very large nuclear cross section [30]. Since the phase relation between different detected waves (e.g., x-ray fluorescence radiation) is uncorrelated, the measured signal reflects only single particle vibrations of the Mössbauer nuclei. This allows the direct determination of the partial VDOS with a minimum of modeling, only assuming a harmonic lattice [11, 30]. The data treatment resembles that for incoherent inelastic neutron scattering. However, in contrast to the latter technique, averaging over phonon momenta is not achieved by the specific location of detectors. Momentum integration in inelastic nuclear scattering is assured by monitoring the yield of the nonradiative channel of the nuclear de-excitation, where the atomic fluorescence radiation does not enter the momentum conservation law. Furthermore, the instrumental function of high-resolution monochromators is constant, and the energy transfer scale is defined with high precision. Therefore, even variations of the density of states of only a few percent can be accurately determined [31].

Moreover, the measured signal in INS generally contains contributions from coherent scattering (which allows the study of collective atomic vibrations, i.e., dispersion relations) and incoherent scattering (which is related to single-particle vibrations and the VDOS) [75]. Direct measurements of VDOS from incoherent INS or IXS are difficult (if not impossible) due to the small incoherent cross sections usually involved. In the case of coherent INS, a generalized VDOS can be determined with partial contributions according to the scattering power of each element in the sample. However, the data analysis is not straightforward due to interference scattering and coherent multiphonon scattering [75]. A comparison between the VDOS measured via

inelastic nuclear resonant scattering and the generalized VDOS determined from neutron scattering has been given for a bulk AlCuFe quasicrystal [136].

Compared with INS, a significant advantage of inelastic nuclear resonant absorption is the small amount of material required. Due to the small scattering cross sections, INS can be performed on bulk samples only; for instance, several grams of sample material are necessary [75]. This makes INS unsuitable for the investigation of atomic dynamics in thin films. However, the situation will improve with the next generation of pulsed neutron sources.

Other methods to probe dynamical properties like energy loss spectroscopy with electrons or He atoms [45] or point-contact methods [46] are intrinsically too surface sensitive. Moreover, phonons with larger wave vectors q are difficult to measure with electrons because the cross-section depends on q^{-4} [75]. Inelastic scattering of visible or infrared light (Brillouin or Raman scattering) has been used extensively to study vibrational excitations in (mostly semiconducting) thin films and multilayers [38, 47], but the limited momentum transfer does not allow a derivation of the VDOS. Further, the penetration depth of light in metals is small, and thus the scattered intensity is very low and difficult to measure. Accordingly, inelastic nuclear resonant absorption is the most promising method at present for deriving VDOS in thin films and nanoscale structures.

It should be noted again that inelastic nuclear resonant absorption intrinsically exhibits a unique sensitivity to the probe nucleus. This is particularly promising for biological applications, because it is possible to selectively probe vibrations of a single atom at the active site of a complex biomolecule, while avoiding interference from the vibrations of thousands of other atoms [127, 128, 137]. Moreover, inelastic nuclear resonant scattering does not face limitations due to selection rules and solvent interference that hamper traditional site-selective vibrational spectroscopies [120].

References

1. K. S. Singwi and A. Sjölander : Phys. Rev. **120**, 1093 (1960) [181](#), [184](#), [185](#), [189](#)
2. W. M. Visscher : Ann. Phys. **9**, 194 (1960) [181](#)
3. P. B. Moon : Proc. Phys. Soc. **63**, 1189 (1950) [181](#)
4. G. Endres, F. Strohkendl, H. Langhoff, and F. Gmelin : Z. Phys. B - Condensed Matter **44**, 253 (1981) [181](#)
5. H. Weiss and H. Langhoff : Phys. Lett. **69A**, 448 (1979) [181](#), [182](#)
6. H. Weiss and H. Langhoff : Z. Phys. B **33**, 365 (1979) [181](#)
7. M. Köfferlein, W. Potzel, M. Steiner, H. Karzel, W. Schiessl, and G. M. Kalvius : Phys. Rev. B **52**, 13332 (1995) [181](#)
8. W. Sturhahn and A. I. Chumakov : Hyperfine Interact. **123/124**, 809 (1999) [181](#), [186](#)
9. A. I. Chumakov, R. Rüffer, H. Grünsteudel, H. F. Grünsteudel, G. Grübel, J. Metge, O. Leupold, and H. A. Goodwin : Europhys. Lett. **30**, 427 (1995) [181](#)
10. M. Seto, Y. Yoda, S. Kikuta, X. W. Zhang, and M. Ando : Phys. Rev. Lett. **74**, 3828 (1995) [181](#)

11. W. Sturhahn, T. S. Toellner, E. E. Alp, X. Zhang, M. Ando, Y. Yoda, S. Kikuta, M. Seto, C. W. Kimball, and B. Dabrowski: Phys. Rev. Lett. **74**, 3832 (1995) [181](#), [182](#), [225](#)
12. T. S. Toellner, M. Y. Hu, W. Sturhahn, K. Quast, and E. E. Alp: Appl. Phys. Lett. **71**, 2112 (1997) [181](#), [187](#)
13. E. Burkhardt: *Inelastic Scattering of X-Rays with Very High Energy Resolution* (Springer, Berlin 1991) [182](#), [225](#)
14. E. Burkhardt: Rep. Prog. Phys. **63**, 171 (2000) [182](#), [225](#)
15. A. I. Chumakov, A. Barla, R. Rüffer, J. Metge, H. H. Grünsteudel, H. Grünsteudel, J. Plessel, H. Winkelmann, and M. M. Abd-Elemegeed: Phys. Rev. B **58**, 254 (1998) [183](#), [190](#)
16. M. Y. Hu, W. Sturhahn, T. S. Toellner, P. M. Hession, J. P. Sutter, and E. E. Alp: Nucl. Instrum. Methods Phys. Res. A **428**, 551 (1999) [183](#), [186](#)
17. A. I. Chumakov, R. Rüffer, A. Q. R. Baron, H. Grünsteudel, H. F. Grünsteudel, and V. G. Kohn: Phys. Rev. B **56**, 10758 (1997) [185](#)
18. V. G. Kohn, A. I. Chumakov, and R. Rüffer: Phys. Rev. B **58**, 8437 (1998) [185](#)
19. L. van Hove: Phys. Rev. **95**, 249 (1954)
20. W. Marshall and S. W. Lovesey: *The Theory of Thermal Neutron Scattering* (Oxford University Press, London 1971) [185](#)
21. H. J. Lipkin: Ann. Phys. **9**, 332 (1960) [185](#)
22. H. J. Lipkin: Phys. Rev. B **52**, 10073 (1995) [185](#), [223](#)
23. V. G. Kohn and A. I. Chumakov: Hyperfine Interact. **125**, 205 (2000) [186](#), [189](#)
24. W. Sturhahn: Hyperfine Interact. **125**, 149 (2000) [186](#), [189](#)
25. V. J. Minkiewicz, G. Shirane, and R. Nathans: Phys. Rev. **162**, 528 (1967) [187](#), [195](#), [221](#)
26. D. W. Johnson and J. C. H. Spence: J. Phys. D **7**, 771 (1974) [188](#)
27. A. I. Chumakov and W. Sturhahn: Hyperfine Interact. **123/124**, 781 (1999) [189](#)
28. K. Achterhold, C. Keppler, A. Ostermann, U. van Bürck, W. Sturhahn, E. E. Alp, and F. G. Parak: Phys. Rev. E **65**, 051916 (2002) [190](#), [213](#), [220](#), [221](#)
29. B. Roldan Cuanya, W. Keune, W. Sturhahn, T. S. Toellner, and M. Y. Hu: Phys. Rev. B **64**, 235321 (2001) [190](#)
30. A. I. Chumakov and R. Rüffer: Hyperfine Interact. **113**, 59 (1998) [191](#), [205](#), [225](#)
31. A. I. Chumakov, R. Rüffer, A. Q. R. Baron, H. Grünsteudel, and H. F. Grünsteudel: Phys. Rev. B **54**, 9596 (1996) [191](#), [225](#)
32. W. Sturhahn and T. S. Toellner: Phys. Rev. B, **65** 134305 (2002) [191](#)
33. B. Fultz, T. A. Stephens, E. E. Alp, M. Y. Hu, J. P. Sutter, T. S. Toellner, and W. Sturhahn: Phys. Rev. B **61**, 14517 (2000) [192](#)
34. A. van de Walle and G. Ceder: Rev. Mod. Phys. **74**, 11 (2002) [192](#)
35. U. Kürpick, A. Kara, and T. S. Rahman: Phys. Rev. Lett. **78**, 1086 (1997) [192](#)
36. B. Fultz, T. A. Stephens, W. Sturhahn, T. S. Toellner, and E. E. Alp: Phys. Rev. Lett. **80**, 3304 (1998) [192](#)
37. M. A. Stroscio and M. Dutta: *Phonons in Nanostructures* (Cambridge University Press, Cambridge, England 2001) [192](#), [198](#)
38. B. Jusserand and M. Cardona, in: M. Cardona and G. Güntherodt (eds.), *Topics in Applied Physics: Light Scattering in Solids V* (Springer, Berlin 1989) [193](#), [226](#)
39. H. Xia, G. X. Cheng, A. Hu, and X. K. Zhang: Solid State Commun. **77**, 631 (1991) [193](#)
40. M. Grimsditch, J. E. Mattson, C. H. Sowers, S. D. Bader, and M. J. Peters: Phys. Rev. Lett. **77**, 2025 (1996) [193](#)

41. M. I. Flik, B. I. Choi, and K. E. Goodson : J. Heat Transfer **114**, 666 (1992) **193**, **198**
42. B. Bushan, J. N. Israelachvili, and U. Landman : Nature **374**, 607 (1995) **193**
43. J. Krim, *Reibung auf atomarer Ebene*, Spektrum der Wissenschaft, December 1996 (in German) **193**
44. M. V. Gandhi and B. S. Thompson : *Smart Materials and Structures* (Chapman and Hall, London 1992) **194**
45. W. Kress and F. W. de Wette : *Surface Phonons* (Springer, Berlin 1991) **194**, **226**
46. A. V. Khotkevich and I. K. Yanson : *Atlas of Point Contact Spectra of Electron-Phonon Interactions in Metals* (Kluwer Academic Publishers, Amsterdam 1995) **194**, **226**
47. F. Nizzoli and J. R. Sanderock : *Dynamical Properties of Solids*, Vol. 6 (North-Holland, Amsterdam 1990) **194**, **226**
48. R. Röhlsberger, W. Sturhahn, T. S. Toellner, K. W. Quast, P. Hession, M. Hu, J. Sutter, and E. E. Alp : J. Appl. Phys. **86**, 584 (1999) **194**, **195**, **196**, **197**, **203**, **204**
49. H. R. Schober and P. H. Dederichs, in: *Phonon States of Elements, Electron States and Fermi Surfaces of Alloys*, ed. by K. H. Hellwege and J. L. Olsen, Landolt Börnstein, New Series, III/13a (Springer, Berlin 1981) **196**, **198**, **202**, **212**
50. B. Fåk and B. Dorner: Institut Laue Langevin Technical Report No. 92FA008S, 1992 (unpublished) **196**
51. B. Fultz, C. C. Ahn, E. E. Alp, W. Sturhahn, and T. S. Toellner : Phys. Rev. Lett. **79**, 937 (1997) **196**, **197**, **198**, **200**
52. H. R. Glyde and E. C. Svensson, in: *Methods of Experimental Physics*, Vol. 23 B, edited by D. L. Price and K. Sköld (Academic Press, New York 1987) **196**
53. B. Dorner: *Coherent Inelastic Neutron Scattering in Lattice Dynamics* (Springer, New York 1982) **196**
54. C. Masciovecchio, G. Monaco, G. Ruocco, F. Sette, A. Cunsolo, M. Krisch, A. Mermet, M. Soltwisch, and R. Verbeni : Phys. Rev. Lett. **80**, 544 (1998) **196**
55. E. Bonetti, L. Pasquini, E. Sampaolesi, A. Deriu, and G. Cicognani : J. Appl. Phys. **88**, 4571 (2000) **198**
56. H. Frase, B. Fultz, and J. L. Robertson : Phys. Rev. B **57**, 898 (1998) **198**, **200**
57. B. Fultz, L. Anthony, L. J. Nagel, R. M. Nicklow, and S. Spooner : Phys. Rev. B **52**, 3315 (1995) **198**
58. B. Fultz, J. L. Robertson, T. A. Stephens, L. J. Nagel, and S. Spooner : J. Appl. Phys. **79**, 8318 (1996) **198**
59. U. Stuhr, H. Wipf, K. H. Andersen, and H. Hahn : Phys. Rev. Lett. **81**, 1449 (1998) **198**
60. J. Trampenau, K. Bauszuz, W. Petry, and U. Herr : Nanostruct. Mater. **6**, 551 (1995) **198**
61. A. B. Papandrew, A. F. Yue, B. Fultz, I. Halevy, W. Sturhahn, T. S. Toellner, E. E Alp, and H. K. Mao : Phys. Rev. B **69**, 144301 (2004) **198**
62. L. Pasquini, A. Barla, A. I. Chumkov, O. Leupold, R. Rüffer, A. Deriu, and E. Bonetti : Phys. Rev. B **66**, 073410 (2002) **198**, **199**, **200**
63. A. Kara and T. S. Rahman : Phys. Rev. Lett. **81**, 1453 (1998) **198**, **200**
64. R. Meyer, L. J. Lewis, S. Prakash, and P. Entel : Phys. Rev. B **68**, 104303 (2003) **198**, **203**
65. D. Y. Sun, X. G. Gong, and X. Q. Wang : Phys. Rev. B **63**, 193412 (2001) **198**, **200**
66. D. Wolf, J. Wang, S. R. Phillpot, and H. Gleiter : Phys. Rev. Lett. **74**, 4686 (1995) **198**

67. C. G. Granqvist and R. A. Buhrman : J. Appl. Phys. **47**, 2200 (1976) [198](#)
68. P. M. Derlet, R. Meyer, L. J. Lewis, U. Stuhr, and H. V. Swygenhoven : Phys. Rev. Lett. **87**, 205501 (2001) [200](#)
69. R. Rüffer and A. I. Chumakov : Hyperfine Interact. **97/98**, 589 (1996) [201](#)
70. E. E. Alp, W. Sturhahn, and T. S. Toellner : Hyperfine Interact. **135**, 295 (2001) and J. Phys.: Condens. Matter **13**, 7645 (2001) [202](#), [213](#)
71. J. Jäckle in: *Amorphous Solids - Low Temperature Properties*, edited by W. A. Philips (Springer, Berlin 1981) [203](#), [204](#), [209](#)
72. W. A. Phillips (ed.): *Amorphous Solids - Low-Temperature Properties* (Springer, Berlin 1981) [203](#)
73. W. Schirmacher, G. Diezemann, and C. Ganter : Phys. Rev. Lett. **81**, 136 (1998) [203](#), [204](#), [209](#)
74. W. Schirmacher, G. Diezemann, and C. Ganter : Physica B **284**, 1147 (2000) [203](#), [204](#)
75. J. B. Suck and H. Rudin, in: *Glassy metals II - Topics in Applied Physics* 53, ed. H. Beck and H. J. Güntherodt, Topics in Applied Physics, Vol. 53 (Springer, New York 1983) [203](#), [206](#), [225](#), [226](#)
76. T. Ruckert, J. Tappert, R. A. Brand, and W. Keune : J. Magn. Magn. Mater. **165**, 411 (1997) [204](#)
77. T. Ruckert, W. Keune, B. Sahoo, W. Sturhahn, T. S. Toellner, E. E. Alp, and R. Röhlsberger : Hyperfine Interact. **144/145**, 65 (2003) [205](#), [206](#), [207](#)
78. J. P. Eymery, A. Findiki, R. Krishnan, M. Tessier, and J. P. Vitton : Phys. Rev. B **38**, 11931 (1988) [204](#)
79. N. Heiman, K. Lee, and R. J. Potter : J. Appl. Phys. **47**, 2634 (1976) [204](#)
80. M. Ghafari, U. Gonser, H. G. Wagner, and M. Naka : Nucl. Instrum. Methods **199**, 197 (1982) [204](#)
81. K. M. Unruh and C. L. Chien : Phys. Rev. B **30** 4968 (1984) [204](#)
82. W. Keune : private communication (2002) [205](#)
83. W. Keune, T. Ruckert, B. Sahoo, W. Sturhahn, T. S. Toellner, E. E. Alp, and R. Röhlsberger : J. Phys. : Condensed Matter **16**, 379 (2004) [207](#)
84. W. Kress : *Phonon Dispersion Curves, One Phonon Density of States and Impurity Vibrations of Metallic Systems*, Physics Data Vol. 26-1 (Fachinformationszentrum Karlsruhe, Karlsruhe, Germany, 1987) [205](#)
85. J. A. Krumhansl and G. R. Barsch : Proc. of the Internat. Conf. on Martensitic Transformations 1992, p. 25 (Monterey Inst. of Advanced Studies, Carmel 1992) [208](#)
86. S. M. Shapiro, B. X. Yang, G. Shirane, Y. Noda, and L. E. Tanner : Phys. Rev. Lett. **62** 1298 (1989) [207](#)
87. M. Matsui, H. Yamada, and K. Adachi : J. Phys. Soc. Jpn. **48**, 2161 (1980) [208](#), [209](#)
88. E. F. Wassermann in: *Ferromagnetic Materials*, edited by K. H. J. Buschow and E. P. Wohlfarth (North Holland, Amsterdam 1990) [208](#)
89. F. E. Fujita in: *Physics of New Materials*, edited by F. E. Fujita (Springer, Berlin 1994) [208](#)
90. N. Wiele, H. Franz, and W. Petry : Physica B **263-264**, 716 (1999) [209](#)
91. S. R. Elliott : *Physics of Amorphous Materials* (Longmans, New York 1990) [209](#)
92. S. N. Taraskin, Y. L. Loh, G. Natarajan, and S. R. Elliott : Phys. Rev. Lett. **86**, 1255 (2001) [209](#)

93. V. V. Struzhkin, H.-K. Mao, J. Hu, M. Schwoerer-Böhning, J. Shu, R. J. Hemley, W. Sturhahn, M. Y. Hu, E. E. Alp, P. Eng, and G. Shen : Phys. Rev. Lett. **87**, 255501 (2001) [210](#), [216](#)
94. A. A. Maradudin, in: *Solid State Physics*, edited by F. Seitz and D. Turnbull (Academic Press, New York, 1966) [210](#)
95. M. Seto, Y. Kobayashi, S. Kitao, R. Haruki, T. Mitsui, Y. Yoda, S. Nasu, and S. Kikuta : Phys. Rev. B **61**, 11420 (2000) [210](#), [211](#)
96. P. D. Mannheim : Phys. Rev. **165**, 1011 (1968) [210](#)
97. P. D. Mannheim and S. S. Cohen : Phys. Rev. B **4**, 3748 (1971) [210](#)
98. P. D. Mannheim : Phys. Rev. B **5**, 745 (1972) [210](#)
99. W. Sturhahn, R. Röhlsberger, E. E. Alp, T. Ruckert, H. Schrör, and W. Keune : J. Magn. Magn. Mater. **198-199**, 590 (1999) [212](#)
100. M. Y. Hu, W. Sturhahn, T. S. Toellner, P. D. Mannheim, D. E. Brown, J. Zhao, and E. E. Alp : Phys. Rev. B **67**, 094304 (2003) [212](#), [213](#), [214](#), [219](#)
101. G. Simmons and H. Wang: *Single Crystal Elastic Constants and Calculated Aggregate Properties* (MIT Press, Cambridge 1971) [214](#)
102. A. M. Dziewonski and D. L. Anderson : Phys. Earth Planet. Inter. **25**, 297 (1981) [215](#), [218](#)
103. P. Söderlind, J. A. Moriarty, J. M. Wills : Phys. Rev. B **53**, 14063 (1996) [215](#)
104. C. S. Yoo, J. Akella, A. J. Campbell, H. K. Mao, and R. J. Hemley : Science **270**, 1473 (1995) [215](#)
105. K. C. Creager : Nature **356**, 309 (1992) [215](#)
106. L. Stixrude and R. E. Cohen : Science **267**, 1972 (1995) [215](#)
107. R. Lübbbers : PhD Thesis (Universität Paderborn, 2000) [215](#)
108. G. Wortmann, K. Rupprecht, and H. Giefers : Hyperfine Interact. **144/145**, 103 (2002) [216](#), [219](#)
109. H. Giefers, R. Lübbbers, K. Rupprecht, G. Wortmann, D. Alfé, and A. I. Chumakov : High Press. Res. **22**, 451 (2002) [216](#), [219](#)
110. R. Lübbbers, H. F. Grünsteudel, A. I. Chumakov, and G. Wortmann : Science **287**, 1250 (2000) [216](#), [219](#)
111. H. K. Mao, J. Xu, V. V. Struzhkin, J. Shu, R. J. Hemley, W. Sturhahn, M. Y. Hu, E. E. Alp, L. Vocadlo, D. Alfé, G. D. Price, M. J. Gillan, M. Schwoerer-Böhning, D. Häusermann, P. Eng, G. Shen, H. Giefers, R. Lübbbers, and G. Wortmann : Science **292**, 914 (2001) [216](#), [217](#), [218](#)
112. H. K. Mao, P. M. Bell, J. Shaner, and D. Steinberg : J. Appl. Phys. **49**, 3276 (1978) [216](#)
113. H. K. Mao and Y. Wu and L. C. Chen and J. Shu, and A. P. Jephcoat : J. Geophys. Res. **95**, 21737 (1990) [216](#)
114. L. Vocadlo, J. Brodholt, D. Alfé, and G. D. Price : Geophys. Res. Lett. **26**, 1231 (1999) [216](#)
115. G. Steinle-Neumann, L. Stixrude, and R. E. Cohen : Phys. Rev. B **60**, 791 (1999) [216](#)
116. G. Fiquet, J. Badro, F. Guyot, H. Requardt, and M. Krisch : Science **291**, 468 (2001) [218](#)
117. F. Birch, in: *Solids under Pressure*, edited by W. Paul and D. M. Warschauer (McGraw-Hill, New York 1963), pp. 137 - 162 [218](#)
118. W. Sturhahn : private communication (2003) [218](#)

119. H. R. Wenk, S. Matthies, R. J. Hemley, H. K. Mao, and J. Shu : Nature **405**, 1044 (2000) [219](#)
120. J. T. Sage, C. Paxson, G. R. A. Wyllie, W. Sturhahn, S. M. Durbin, P. M. Champion, E. E. Alp, and W. R. Scheidt : J. Phys.: Condens. Matter **13**, 7707 (2001) [219](#), [220](#), [221](#), [222](#), [224](#), [226](#)
121. B. K. Rai, S. M. Durbin, E. W. Prohofsky, J. T. Sage, M. K. Ellison, W. R. Scheidt, W. Sturhahn, and E. E. Alp : Phys. Rev. E **66**, 051904 (2002) [219](#), [220](#)
122. M. Perutz : Nature **228**, 726 (1970) [219](#)
123. B. K. Rai, S. M. Durbin, E. W. Prohofsky, J. T. Sage, M. K. Ellison, A. Roth, W. R. Scheidt, W. Sturhahn, and E. E. Alp : J. Am. Chem. Soc. **125**, 6927 (2003) [220](#), [221](#), [224](#)
124. R. H. Austin, M. W. Roberson, and P. Mansky : Phys. Rev. Lett. **62**, 1912 (1989) [220](#)
125. L. Zhu, J. T. Sage, and P. M. Champion : Science **226**, 629 (1994) [220](#)
126. B. K. Rai, S. M. Durbin, E. W. Prohofsky, J. T. Sage, G. R. A. Wyllie, W. R. Scheidt, W. Sturhahn, and E. E. Alp : Biophys. J. **82**, 2951 (2002) [220](#), [224](#)
127. K. Achterhold , C. Keppler, U. van Bürck, W. Potzel, P. Schindelmann, E. W. Knapp, B. Melchers, A. I. Chumakov, A. Q. R. Baron, R. Rüffer, and F. Parak : European Biophys. J. Lett. **25**, 43 (1996) [220](#), [226](#)
128. J. T. Sage, S. M. Durbin, W. Sturhahn, D. C. Wharton, P. M. Champion, P. M. Hession, J. P. Sutter, and E. E. Alp : Phys. Rev. Lett. **86**, 4966 (2001) [220](#), [224](#)
129. H. Paulsen, H. Winkler, A. X. Trautwein, H. Grünsteudel, V. Rusanov, and H. Toftlund : Phys. Rev. B **59**, 975 (1999) [221](#), [224](#)
130. H. J. Lipkin : Ann. Phys. **18**, 182 (1962) [223](#)
131. T. S. Rush, P. M. Kozlowski, C. A. Piffat, R. Kumble, M. Z. Zgierski, and T. G. Spiro : J. Phys. Chem. B **104**, 5020 (2000) [224](#)
132. B. Delley, J. Schefer, and Th. Woike : J. Chem. Phys. **107**, 10067 (1997) [225](#)
133. P. Gülich, A. Hauser, and H. Spiering : Angew. Chem. **106**, 2109 (1994) [225](#)
134. P. Brüesch : *Phonons: Theory and Experiment II* (Springer, Berlin 1985) [225](#)
135. N. W. Ashcroft and N. D. Mermin : *Solid State Physics* (Holt-Saunders, Philadelphia 1976) [225](#)
136. R. A. Brand, G. Coddens, A. I. Chumakov, and Y. Calvayrac : Phys. Rev. B **59**, 14145 (1999) [226](#)
137. C. Keppler, K. Achterhold, A. Ostermann, U. van Bürck, W. Potzel, A. I. Chumakov, A. Q. R. Baron, R. Rüffer, and F. Parak : European Biophys. J. Lett. **25**, 221 (1996) [226](#)

6 Advanced Scattering Techniques

Nuclear resonant scattering of synchrotron radiation can be used to extend the energy resolution and the time resolution of x-ray scattering techniques into regimes that have not been accessible so far. The essential idea is to manipulate the resonantly scattered photon fields by controlled motion of the nuclei during the scattering process. This has led to the development of x-ray monochromators with μeV resolution and the invention of the nuclear lighthouse effect that has the potential to achieve time resolutions in the ps range. These developments promise new spectroscopic techniques (elastic and inelastic) in the x-ray regime.

6.1 Resonant Scattering from Moving Matter

In a coherent scattering process, the motion of the scatterer leads to a phase shift of the scattered radiation field. In a single scattering process of a photon with wavevector \mathbf{k}_0 at time t_0 into a photon with wavevector \mathbf{k} at time t , the phase change of the scattered photon is given by $\psi = \mathbf{k} \cdot \mathbf{r}(t) - \mathbf{k}_0 \cdot \mathbf{r}(t_0)$ that can be written as:

$$\psi = [\mathbf{k} - \mathbf{k}_0] \cdot \mathbf{r}(t) + \mathbf{k}_0 \cdot [\mathbf{r}(t) - \mathbf{r}(t_0)] \quad (6.1)$$

The left term that is proportional to the momentum transfer $\mathbf{q} = \mathbf{k} - \mathbf{k}_0$ contains information about the instantaneous dynamics of the atom in the sample as revealed through coherent inelastic neutron or x-ray scattering [1, 2]. The right term in (6.1) becomes relevant if the scattering process takes place during a finite time interval $\Delta t = t - t_0$. This applies in the case of nuclear resonant scattering and will therefore be discussed extensively in the following. Interesting new possibilities are thus introduced through resonant scattering if the state of the sample undergoes changes during the lifetime of the excited state. Since the corresponding spatial phase is a product of a quantity describing the probe, i.e. the photon wavevector \mathbf{k} , and a quantity characterizing the sample, i.e. the spatial position of the scatterer $\mathbf{r}(t)$, scattering experiments can be divided into three classes:

- For a known wave vector \mathbf{k}_0 or momentum transfer \mathbf{q} , the scattered amplitude contains information about the motional state of the scatterers

described by $\mathbf{r}(t)$. This has been exploited, e.g., in the study of diffusion processes in crystalline solids and glasses [3, 4, 5].

- If the time dependence $\mathbf{r}(t)$ is known, the scattering process can be used to study properties of the incident radiation field like transverse coherence [6].
- The knowledge of both quantities \mathbf{k} and $\mathbf{r}(t)$ can be used to tailor the properties of the scattered radiation. For example, the energy of the radiation can be tuned over a range of several meV if scattered from a fast rotating sample [7, 8]. Another example is the controlled manipulation of the temporal evolution of the nuclear decay by ultrasonic vibration [9, 10].

Nuclear resonant absorption in rotating systems has a distinguished history amongst the applications of the Mössbauer effect. Rotational motion of sources and absorbers was used in the early days of Mössbauer spectroscopy for Doppler tuning of the photon energy [11, 12]. Later, high-speed rotational motion was applied to study relativistic time-dilation effects via measurement of the transverse Doppler shift [13, 14, 15] and to determine upper bounds for an ether drift as a test of Lorentz invariance [16, 17, 18]. All these experiments were relying on the *incoherent* process of nuclear resonant absorption by individual nuclei. *Coherent* scattering processes, on the other hand, are sensitive to phase differences between all nuclei in the scattering volume, thus revealing structural properties of the sample through interference effects. Coherent nuclear resonant scattering has gained enormous momentum in recent years through the availability of high-brilliance synchrotron radiation sources. However, only a few studies so far were devoted to the influence of rotational motion on the process of coherent nuclear resonant scattering [6, 7, 19, 21].

6.2 The Nuclear Lighthouse Effect

Elastic nuclear resonant scattering proceeds via creation of a collectively excited state, where a single excitation is coherently distributed over the nuclei in the sample [20]. If the scattering process takes place in a rotating sample, the excited state is rotated during its lifetime. Consequently, the direction of the radiative decay $\mathbf{k}(t)$ deviates from the direction of \mathbf{k}_0 by the rotation angle φ that has developed during the lifetime of the excited state. As a result, the quantum-beat spectrum of the nuclear decay is mapped to an angular scale. Due to its apparent analogy with a sweeping ray of light, this effect was called the *Nuclear Lighthouse Effect* (NLE) [21, 22].

6.2.1 Basic Principles

Formally, the Nuclear Lighthouse Effect can be described in terms of angular momentum conservation: In a fixed laboratory coordinate system, a rotating

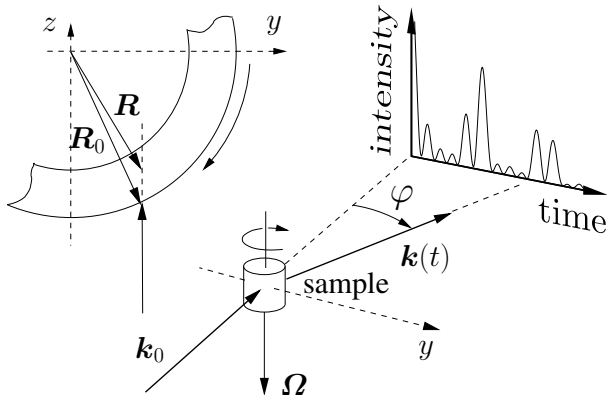


Fig. 6.1. Scattering geometry of the Nuclear Lighthouse Effect at a sample rotating with angular velocity Ω . The time spectrum of the nuclear decay is mapped to an angular scale [21]

quantum state acquires a dynamical phase factor that accounts for the motion during its time evolution:

$$\mathbf{A}(\mathbf{r}, t) = e^{i\mathbf{J} \cdot \boldsymbol{\Omega} t / \hbar} \mathbf{A}_0(\mathbf{r}, t) \approx e^{i(\mathbf{k}_0 \times \boldsymbol{\Omega} t) \cdot \mathbf{r}} \mathbf{A}_0(t). \quad (6.2)$$

The first exponential constitutes the operator for finite rotations about an angle $\varphi = |\boldsymbol{\Omega}|t$. $\boldsymbol{\Omega}$ is the angular velocity of the rotation and t is the time after excitation. $\mathbf{J} = -i\hbar \mathbf{r} \times \nabla + \mathbf{S}$ is the operator of the total angular momentum of the radiation field, consisting of orbital and spin angular momentum. The spin angular momentum operator \mathbf{S} as a matrix operator acts on the components of the polarization vector. Since the detectors in the experiments performed here are not polarization sensitive, their influence can be neglected here. The orbital angular momentum as a differential operator acts on spatial components of the radiation field and therefore affects geometrical phase factors. $\mathbf{A}_0(\mathbf{r}, t)$ describes the amplitude of the scattered radiation field from the sample at rest. In the last step in (6.2) it was assumed that this quantity can be described by a plane wave, i.e., $\mathbf{A}_0(\mathbf{r}, t) = \mathbf{A}_0(t) e^{i\mathbf{k}_0 \cdot \mathbf{r}}$.

The mapping to an angular scale is described most conveniently by a one-dimensional transformation of (6.2) into reciprocal space. Assuming fully coherent illumination, which is a good approximation for the experiments performed here, the time response is then given by

$$\mathbf{A}(\mathbf{q}, t) = \mathbf{A}_0(t) \delta(\mathbf{q} - \mathbf{k}_0 \times \boldsymbol{\Omega} t). \quad (6.3)$$

Expressing the modulus of the momentum transfer by $|\mathbf{q}| = q = k_0 \varphi$, integration over time t then yields the scattered amplitude as a function of spatial coordinate only (see Sect. 6.2.3):

$$\mathbf{A}(\varphi) = \mathbf{A}_0(\varphi/\Omega). \quad (6.4)$$

This means that the angular distribution of the scattered radiation can be described by the theory of time-resolved nuclear forward scattering using the mapping $t = \varphi/\Omega$. In order to conveniently record time spectra on an angular scale, rotational frequencies of several kHz have to be applied, equivalent to angular velocities in the range of 0.1 mrad/ns. Such high-frequency rotational motion is routinely used in the magic-angle spinning (MAS) technique of solid-state NMR [23, 24]. Samples are contained in hollow rotor cylinders with a diameter of a few mm. These rotors are driven by pressurized air up to frequencies of 35 kHz (Bruker Analytical GmbH, Rheinstetten, Germany). Such a device was modified for x-ray transmission to study nuclear resonant scattering from a ^{57}Fe foil.

6.2.2 Observation of the Nuclear Lighthouse Effect

In the first experiment with such a rotor system at the beamline BW4 at HASYLAB (DESY, Hamburg) the angular mapping of the time spectra could be confirmed [25]. The incident radiation was monochromatized to an energy width of 6.5 meV by a high-resolution nested monochromator [26]. The time spectrum of the delayed radiation was recorded with a position-sensitive detector. In the following experiment it was intended to demonstrate that such experiments can be performed even without using high-resolution crystal optics. This experiment was performed at the beamline 3-ID of the Advanced Photon Source, Argonne National Laboratory, USA. The experimental setup is shown schematically in Fig. 6.2. The radiation was monochromatized to a bandwidth of 1 eV by a water-cooled high-heat-load monochromator employing two symmetric diamond (111) reflections. A subsequent slit system was adjusted to define a beam cross section of $500 \times 30 \mu\text{m}^2$ (horizontal \times vertical),

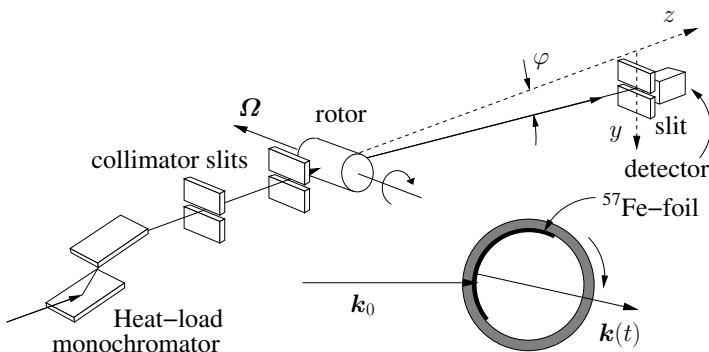


Fig. 6.2. Experimental setup at the beamline 3-ID of the Advanced Photon Source for observation of the Nuclear Lighthouse Effect. The scattered radiation from the rotor was guided through an evacuated flight tube to the detector. The coordinates refer to the same frame as introduced in Fig. 6.1. In the *bottom right* a cross sectional view of the scattering at the rotor is shown [21]

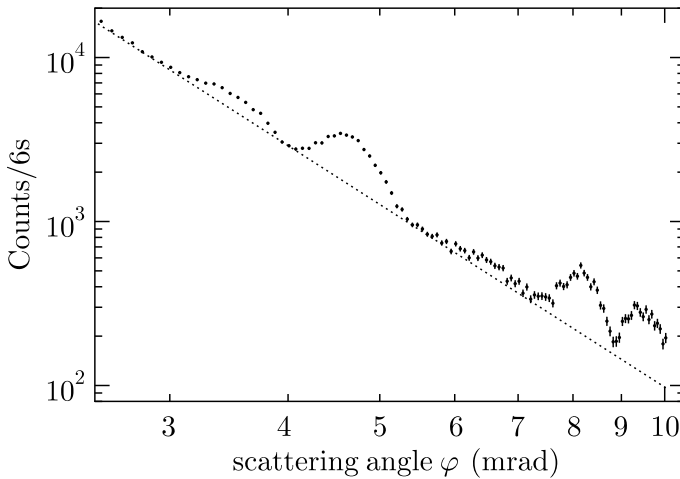


Fig. 6.3. Measured angular distribution of 14.4 keV photons scattered from a 5.7 μm thick foil of ^{57}Fe spinning at 18 kHz. The resonantly scattered quanta appear on top of a background that mainly results from small-angle x-ray scattering (SAXS) at the rotor material. The angular distribution of the SAXS was measured independently and fitted with a $\varphi^{-3.89}$ dependence [21]

resulting in a typical flux of $2 \cdot 10^{10} \text{ s}^{-1}$ on the sample. After transmission through the rotor, the beam was guided through an evacuated flight tube to minimize small-angle scattering in air. The detector assembly consisted of an avalanche photodiode with an aperture of the same cross section as defined by the upstream slit system. It was used in a distance of 3.0 m downstream of the rotor in vertical-scan mode to record the distribution of the radiation scattered from the rotor. No time discrimination as typically used in the technique of time-resolved nuclear resonant scattering was applied. The sample was a 5.7 μm thick foil of polycrystalline $\alpha - ^{57}\text{Fe}$ that covered less than one half of the inner circumference of the rotor (see Fig. 6.2). This was done to avoid interference effects resulting from the beam passing the resonant absorber twice. The sample was spun around a horizontal axis with a rotational frequency of 18 kHz, corresponding to an angular velocity of 0.11 mrad/ns. The angular distribution of the scattered radiation was recorded up to a scattering angle of 10 mrad relative to the primary beam, as shown in Fig. 6.3. Quantum beats of nuclear resonant scattering are clearly visible on top of a background (dotted line) caused mainly by small-angle scattering from the rotor material. The angular distribution of this background was measured independently with the energy tuned off resonance. Then the angular distribution of resonant scattering from the rotating ^{57}Fe foil was obtained after background subtraction, shown in Fig. 6.4a. In this experiment, the transverse coherence length was $\xi \approx 16 \mu\text{m}$ [27] at the position of the rotor, leading

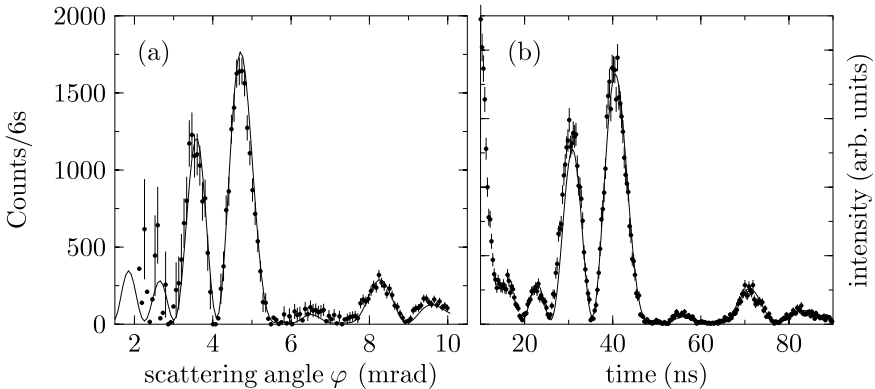


Fig. 6.4. (a) Angular distribution of the radiation scattered from the $5.7 \mu\text{m}^{57}\text{Fe}$ foil rotating at 18 kHz, obtained after background subtraction of the data in Fig. 6.3. The *solid line* is a fit according to (6.14). (b) Time spectrum of nuclear forward scattering obtained by the conventional timing technique from the same foil at rest

to a value of $\Delta t \approx 12$ ps for the width of the resolution function at a rotational frequency of 18 kHz. This justifies using (6.14) for evaluation of the data. The result of the theoretical calculation is shown in Fig. 6.4a as a solid line. Figure 6.4b shows a time spectrum of nuclear resonant forward scattering that was measured with the foil at rest using the conventional timing technique. The agreement between both sets of data confirms that the radiative nuclear decay proceeds on an angular scale according to $\varphi = \Omega t$. The Nuclear Lighthouse Effect thus allows one to obtain time spectra of nuclear resonant scattering by purely geometrical means.

6.2.3 Space-Time Description

In this section a theoretical description of nuclear resonant scattering from a rotating medium will be given. The treatment is based upon the formalism developed in Sect. 2.3.1. A central element of this formalism is the evaluation of the two-point correlation function that describes the propagation or evolution of the system between the space-time coordinates (\mathbf{r}', t') and (\mathbf{r}, t) . First, the transformation properties of the two-point correlation function under rotations have to be developed. As a result, the propagator transforms under rotations as follows:

$$\mathcal{N}(t, t') = \mathcal{M}_-(\mathbf{R}, t) \mathcal{N}_0(t, t') \mathcal{M}_+(\mathbf{R}, t') , \quad (6.5)$$

where the nomenclature introduced in Fig. 6.1 has been used. The subscript 0 indicates that this quantity has to be evaluated for the sample at rest, i.e. in the nuclear center-of-mass system (CMS). The functions $\mathcal{M}_\pm(\mathbf{R}, t)$ are

expectation values of the operator that generates the motion of the nuclei. In case of rotary motion with constant angular velocity $\boldsymbol{\Omega}$ they are given by

$$\mathcal{M}_{\pm}(\mathbf{R}, t) = \langle \gamma | e^{\pm i\boldsymbol{\Omega} \cdot \mathbf{J} t} | \gamma \rangle e^{\pm i\mathbf{k}_0 \cdot \mathbf{R}}, \quad (6.6)$$

where \mathbf{R} is the position vector of the nucleus relative to the center of rotation, as sketched in Fig. 6.1¹. $\mathbf{J} = \mathbf{R} \times \mathbf{P} + \mathbf{S}$ is the operator of the total angular momentum of the system, including the electromagnetic field, consisting of orbital and spin angular momentum. \mathbf{P} is operator of the total linear momentum of the system. For the photon state vectors we assume $|\gamma\rangle = \mathbf{a}_{k_0, \varepsilon}^\dagger |0\rangle$, where $\mathbf{a}_{k_0, \varepsilon}^\dagger$ is a creation operator of the photon field with wavevector \mathbf{k}_0 and polarization ε , and $|0\rangle$ represents the electromagnetic vacuum. This ansatz contains the assumption that the radiation field does not contain more than one photon per mode, which is a good approximation even for present-day high-brilliance synchrotron radiation sources. Neglecting the action of the spin operator \mathbf{S} on the state vectors², evaluation of (6.6) yields:

$$\mathcal{M}_{\pm}(\mathbf{R}, t) = \mathbf{1} e^{\pm i\mathbf{k}(t) \cdot \mathbf{R}} \quad (6.7)$$

with³:

$$\mathbf{k}(t) = \mathbf{k}_0 - \mathbf{k}_0 \times \boldsymbol{\Omega} t + \frac{1}{2} (\mathbf{k}_0 \times \boldsymbol{\Omega}) \times \boldsymbol{\Omega} t^2 - \dots \quad (6.8)$$

Accordingly, $\mathcal{M}_{\pm}(\mathbf{R}, t)$ is a (matrix-valued) function with the properties

$$\mathcal{M}_-(\mathbf{R}, t) \mathcal{M}_+(\mathbf{R}, t) = \mathbf{1} \quad \text{and} \quad \mathcal{M}_{\pm}(\mathbf{R}, 0) = e^{\pm i\mathbf{k}_0 \cdot \mathbf{R}}. \quad (6.9)$$

Inserting now (6.5) into (2.27), taking (6.9) into account, yields:

$$\mathbf{A}(z, t) = [\mathbf{1}\delta(t) - \mathcal{M}_-(\mathbf{R}, t) \mathbf{G}_0(z, t) \mathcal{M}_+(\mathbf{R}, 0)] \mathbf{A}_0 \quad (6.10)$$

Evaluation of this result and comparison with (2.28) results in the following expression for the delayed response of the rotating nuclear ensemble:

$$\mathbf{G}(z, t) = \mathbf{G}_0(z, t) e^{-i(\mathbf{k}(t) - \mathbf{k}_0) \cdot \mathbf{R}}, \quad (6.11)$$

where $\mathbf{G}_0(z, t)$ denotes the delayed time response from the sample at rest. The phase factor indicates that the nuclear exciton is carried with the rotating sample during its lifetime and that its radiative decay proceeds into the rotated direction given by $\mathbf{k}(t)$. Note that the first-order term in the expansion of $\mathbf{k}(t) \cdot \mathbf{R}$ implies that the scattering process takes place at an

¹ Note that the dependence of \mathcal{N} on \mathbf{R} does not violate the previous assumption of the sample to be homogeneous, because $\mathbf{k}_0 \cdot \mathbf{R} = \text{const.}$ along the direction of \mathbf{k}_0 .

² \mathbf{S} leads to a rotation of the polarization vectors and may introduce energy shifts of the nuclear levels in the order of $\hbar\Omega$ [28]. The present experiment is not sensitive to such effects since $\hbar\Omega$ is very small compared to the natural linewidth.

³ Note that the series expansion for $\mathbf{k}(t)$ is the solution of the equation of motion for a vector precessing with constant angular velocity: $d\mathbf{k}/dt = \boldsymbol{\Omega} \times \mathbf{k}$ with $\mathbf{k}(0) = \mathbf{k}_0$.

energy that is Doppler shifted by $\Delta E = -\hbar(\mathbf{k}_0 \times \boldsymbol{\Omega}) \cdot \mathbf{R} = -\hbar\mathbf{v} \cdot \mathbf{k}_0$ where $\mathbf{v} = \boldsymbol{\Omega} \times \mathbf{R}$ is the instantaneous linear velocity of the rotating sample. Thus, at sufficiently high rotational speeds the deflected radiation can be tuned over a range of several meV which may provide the basis for x-ray spectroscopy with μ eV-resolution [7], as described in Sect. 6.3.

The mapping to an angular scale is described most conveniently by a one-dimensional transformation into reciprocal space based on the geometry shown in Fig. 6.1. In this step we have to consider that the incident radiation is not a plane wave but a superposition of waves spread over a range of directions. This leads to a finite degree of transverse coherence at the sample position, that is described by the mutual coherence function (MCF) $W(y)$ [29, 30, 31]. Taking the phase factor in (6.11) up to first order in t , the delayed response in reciprocal space is then given by

$$\mathbf{G}(\mathbf{q}, t) = \mathbf{G}_0(t) \int e^{-i(\mathbf{q}-\mathbf{k}_0 \times \boldsymbol{\Omega} t) \cdot \mathbf{R}} W(y) dy . \quad (6.12)$$

$W(y)$ is often represented by a Gaussian with standard deviation ξ , which is then taken as definition of the transverse coherence length. Based on the geometry sketched in Fig. 6.1 we now write $|\mathbf{q}| = k_0 \varphi$ and $(\mathbf{k}_0 \times \boldsymbol{\Omega}) \cdot \mathbf{R} = -k_0 \Omega y$. Evaluation of (6.12) then leads to the following expression for the scattered intensity as a function of angular coordinate φ only (integrating over all times):

$$I(\varphi) = \int_0^\infty |\mathbf{G}_0(t) \mathbf{A}_0|^2 e^{-k_0^2 \xi^2 \Omega^2 (t - \varphi/\Omega)^2} dt . \quad (6.13)$$

Thus, the effect of the finite degree of transverse coherence is to introduce a resolution function as represented by the Gaussian in the above equation. If the half-width of this function, given by $\Delta t = 2\sqrt{\ln 2}/(k_0 \xi \Omega)$ is much smaller than the typical quantum-beat period to be resolved, (6.13) can be well approximated by

$$I(\varphi) = |\mathbf{G}_0(\varphi/\Omega) \mathbf{A}_0|^2 . \quad (6.14)$$

This result expresses the direct mapping of the time scale to an angular scale as described by $t = \varphi/\Omega$. It allows to evaluate the angular distribution of the scattered intensity according to the theory of time-resolved nuclear forward scattering.

6.2.4 Imaging the Temporal Evolution of Nuclear Resonant Scattering

The Nuclear Lighthouse Effect offers a conceptually new approach to observe nuclear forward scattering of synchrotron radiation. However, an unwanted source of background that constrains experiments so far is the small-angle x-ray scattering (SAXS) from the rotor material. In this section it is

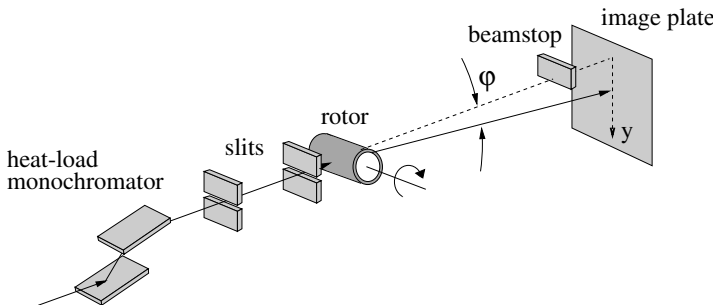


Fig. 6.5. Experimental setup to record the temporal evolution of nuclear resonant scattering on an image plate. The scattered beam from the rotor was guided through an evacuated flight tube to the detector [32]

demonstrated that the use of single-crystalline rotor materials leads to a significant improvement of the signal-to-noise ratio in such experiments. As a result, the temporal evolution of the resonant scattering process can be conveniently recorded with a position sensitive detector (PSD). This has been demonstrated in an experiment performed at the 14.4-keV resonance of ^{57}Fe ($\tau_0 = 141\text{ ns}$) with an image plate serving as a PSD [32]. Image plates provide a number of properties that make them very attractive as area detectors for x-rays, i.e., a high quantum efficiency, a high spatial resolution, a wide dynamic range, a large active area, and a high count-rate capability [33]. Thus, this kind of detector became very attractive for use in scattering and diffraction experiments with synchrotron radiation.

The experiment was performed at the undulator beamline 3-ID of the Advanced Photon Source with the experimental setup shown in Fig. 6.5. The storage ring was filled to a current of 100 mA with 36 evenly spaced triplet bunches with the buckets separated by 2.8 ns. The heat-load monochromator delivered a 1-eV wide beam, resulting from two diamond (111) reflections in a dispersive setting. A subsequent slit system defined a beam cross section of $500 \times 30\text{ }\mu\text{m}^2$ (horizontal \times vertical), resulting in a typical flux of $2 \cdot 10^{10}\text{ s}^{-1}$ on the sample. For sample rotation, a MAS system was used that allowed spinning rates of up to 10 kHz. The rotor was a cylindrical tube made of single-crystalline sapphire with an outer and inner diameter of 4 mm and 3 mm, respectively. As a sample, a $5.7\text{ }\mu\text{m}$ thick foil of $\alpha-^{57}\text{Fe}$ was wrapped once around the inner circumference of the rotor. After transmission through the rotor, the beam was guided through an evacuated flight tube to minimize small-angle x-ray scattering in air. To reduce this source of background radiation further, not only the rotor, but most of the components along the beam path (tungsten slit-blades, Si-windows) were made of single-crystalline materials. The image plate was placed at the end of the flight tube in a distance of 3.3 m from the rotor where a 1-mm thick lead beamstop blocked the direct beam. The spatial distribution of the radiation scattered from the

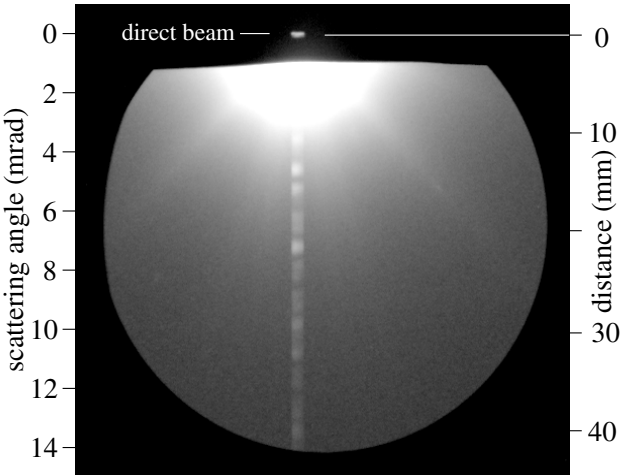


Fig. 6.6. Image plate picture of the spatial distribution of photons scattered from a $5.7\text{ }\mu\text{m}$ thick ^{57}Fe foil spinning at 10 kHz, based on the geometry shown in Fig. 6.5. The circular area marks the cross section of the flight tube through which the radiation was guided. Resonantly scattered photons appear as a vertical stripe with the quantum beats showing up as bright-dark modulation. The direct beam is marked by high-energy photons that have passed through the beamstop [32]

rotating sample is shown in Fig. 6.6, obtained in a 1-min exposure. Resonantly scattered photons appear as vertical stripe with the quantum beats visible through the bright-dark modulation of its intensity. The origin of the angular scale was marked by high-energy photons in the direct beam that passed through the beamstop. The residual small-angle scattering appears as a dark halo around the direct beam. For recording the angular distribution of this background, the heat-load monochromator was tuned off resonance. After calibration with the signal from a Si avalanche photodiode, the readout of the image plate was converted into the actual photon count. Fig. 6.7 shows the time spectrum of the resonantly scattered quanta that has been obtained after background subtraction and conversion of the angular scale to a time scale via the mapping $t = \varphi/\Omega$. The SAXS background prevents a reliable extraction of the resonant signal before $t \approx 25\text{ ns}$. The delayed response extends to times beyond 170 ns that is almost twice the bunch separation of 96 ns. The solid line is a simulation [34], assuming a magnetically polycrystalline sample with a 60% unidirectional texture perpendicular to the rotation axis. As a remarkable result arising from the simulation, the effective thickness of the rotating foil is reduced by a factor of 2.2 compared to the foil at rest. A similar observation has been made in nuclear resonant scattering from a rotating foil of stainless steel [35]. This behavior is related to interference effects that originate from the beam passing through the rotating foil twice, although the detailed mechanism is not fully understood yet. These effects

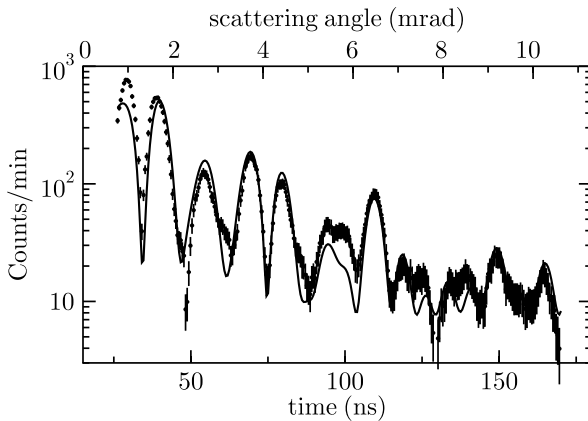


Fig. 6.7. Time spectrum of the radiation scattered from the ^{57}Fe foil rotating at 10 kHz, obtained after background subtraction of the image-plate data in Fig. 6.6. Note that the time range of the spectrum exceeds the bunch separation of 96 ns. The solid line is a simulation [32]

become negligible for samples with a very small effective thickness or when the foil covers less than half of the circumference of the rotor [21].

This experiment shows that no high-resolution crystal optics is necessary to observe coherent nuclear resonant scattering when the level of SAXS is sufficiently low. This would be particularly true for long-lived resonances like in ^{157}Gd or ^{181}Ta with lifetimes of 660 ns and 9.8 μs , respectively, where large deflection angles of a few degrees can be expected. On the other hand, if monochromators with meV-resolution are available the SAXS background can be further reduced by 2–3 orders of magnitude. Then a good signal-to-noise ratio can be obtained also with samples that contain only a small fraction of the resonant isotope.

Since this technique does not rely on a particular time structure of the exciting radiation, it has the potential to overcome existing limits for the time resolution. In the conventional method the time resolution cannot be below the bunch length that is typically in the range of 50–200 ps. In the present experimental setup the time resolution is about 150 ps. Since rotational frequencies of up to 70 kHz seem to be feasible in the near future, time resolutions in the range of 10 ps can be expected.

6.2.5 Observation of the 22.5-keV Resonance of ^{149}Sm

It is the virtue of the Nuclear Lighthouse Effect that it can be applied to many isotopes without specialized instrumentation like high-resolution crystal optics. To demonstrate this, we have applied the effect to observe the 22.5-keV nuclear resonance in ^{149}Sm . ^{149}Sm is an attractive element for

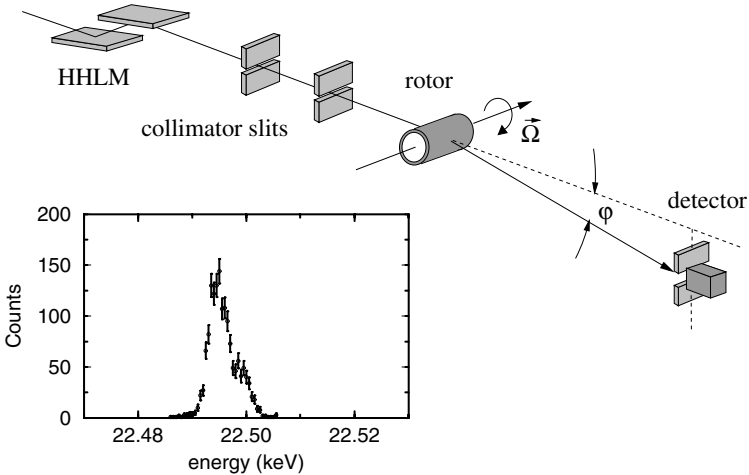


Fig. 6.8. Experimental setup with high-heat-load monochromator (HHL M), slit system, rotor and detector. In the geometry sketched here the resonantly scattered radiation is deflected downwards and guided through an evacuated flight tube to the detector. The *bottom* inset shows the resonance curve of delayed quanta while tuning the energy of the HHL M [38]

investigation of hyperfine interactions because its compounds exhibit interesting properties like relaxation phenomena, valence fluctuations and magnetic magnetic phase transitions at low temperatures [36]. The 22.5 keV resonance is a $7/2 \rightarrow 5/2$ transition with a lifetime of $\tau = 10.3$ ns, corresponding to a natural linewidth of $\Gamma_0 = 62.2$ neV [37]. Conventional Mössbauer spectroscopy involving Sm, however, is difficult because of significant broadening of the emission lines of radioactive sources. This disadvantage, which applies also for other Mössbauer isotopes within the rare earths like Dy, can be overcome by using synchrotron radiation as a source. It will be shown here that the Nuclear Lighthouse Effect can be employed to perform nuclear resonant forward scattering from this isotope [38].

The experimental setup at the undulator beamline 3-ID of the Advanced Photon Source is shown schematically in Fig. 6.8. A powder sample consisting of Sm_2O_3 enriched to 90% in ^{149}Sm was prepared as a thin sheet with an area density of 35 mg/cm^2 , corresponding to a thickness of approximately $40 \mu\text{m}$. The sample was wrapped along the inner circumference of the rotor cylinder and spun with a frequency of 15 kHz during the experiment. A collimator slit system defined a beam cross section of $500 \times 30 \mu\text{m}^2$ (horizontal \times vertical), resulting in a typical flux of $2 \cdot 10^{10} \text{ s}^{-1}$ on the sample. After transmission through the rotor, the beam was guided through a 3 m long evacuated flight tube to avoid small-angle scattering in air. To detect resonantly scattered quanta, the center of the detector aperture was placed at a scattering angle of $\varphi = 2 \text{ mrad}$, as schematically shown in Fig. 6.8. At

this angular position, the nonresonant background was on the order of 10^5 s^{-1} , mainly due to small-angle scattering from the powder sample. Because this count rate did not overload the detector system, the resonantly scattered quanta could be discriminated against the prompt background by time gating. In this setup the energy of the monochromator was tuned until the detection of delayed quanta indicated the excitation of the ^{149}Sm resonance. The resonance curve is shown in Fig. 6.8. Calibration of the photon energy was performed by scanning over the absorption K-edges of Mo at 20000.4 eV and Rh at 23222.0 eV⁴. After this calibration the transition energy of the ^{149}Sm resonance was determined from the first moment of the resonance curve to 22496(4) eV. The relatively large uncertainty is mainly due to a mosaicity of the diamond monochromator crystals that leads to the half width of 4 eV of the energy transmission curve in Fig. 6.8. The nominal width for two diamond (111) reflections in nondispersive setting would be 2.6 eV, assuming a divergence of the incident radiation of 15 μrad . Values for the ^{149}Sm resonance energy reported in the literature so far are 22494(11) eV [40] and 22507(6) eV [41]. In addition, the resonance energy was determined by incoherent nuclear resonant scattering of synchrotron radiation to be 22496(22) eV [42]. With the heat-load monochromator tuned to the resonance energy, a time spectrum of the scattered radiation was recorded. Background suppression was achieved by time gating until 18 ns after excitation. The bunch structure of the storage ring, especially parasitic bunches around the main bunches, prevented a closer approach to $t = 0$. The detector aperture covered a range of scattering angles from 1.6 to 2.6 mrad, corresponding to a time interval from 17 ns to 28 ns. In this time window a delayed count rate of about 3 Hz was observed. The measured time spectrum is shown in Fig. 6.9. The solid line is a simulation according to the theory of NFS, taking into account the triplet bunch structure of the incident radiation. ^{149}Sm in Sm_2O_3 exhibits a slight quadrupole splitting of $\Delta E \approx 1\Gamma_0$ [43]. The coherent radiative coupling of the nuclei in the sample results in a broadening of the energy response, as explained in Sect. 2.2.5. For the given sample this broadening exceeds the hyperfine splitting of the resonance line by a factor of 3.2, resulting in a significant speed-up of the nuclear decay. To illustrate this, the natural decay of the transition with a lifetime of 10.2 ns is shown here for comparison (dotted line). The inset in Fig. 6.9 shows the calculated time spectrum of the sample over an extended time range where the shaded region corresponds to the angular range covered by the detector. For simulation of the data (solid line) we have assumed a Debye temperature of $\Theta_D = 210 \text{ K}$ for Sm_2O_3 , corresponding to a recoilless fraction of $f = 0.42(6)$ at room temperature. Although the detector in this experiment covered only a limited time range we can state that our data are at variance with the value of $\Theta_D = 150 \text{ K}$ as reported in [43]. Instead, our result is more consistent with the other rare-earth oxides like

⁴ We used high-purity foils from EXAFS MATERIALS, Danville, CA, USA. The values for the energy of the absorption edges was taken from [39].

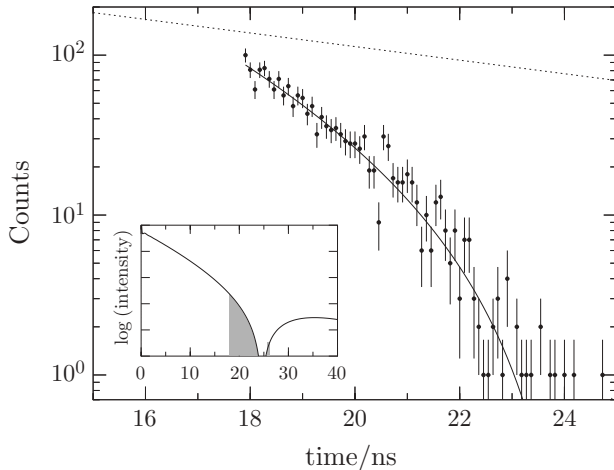


Fig. 6.9. Time spectrum of the delayed radiation scattered from a $^{149}\text{Sm}_2\text{O}_3$ sample rotating at 15 kHz, recorded with an avalanche photodiode by time gating of the prompt background. The detector aperture covered a range of deflection angles from 1.6 mrad to 2.6 mrad. The *solid line* is a simulation according to the theory of nuclear resonant forward scattering, and the *dashed line* displays the natural decay of the nuclear level. In the inset the calculated time spectrum over an extended range is shown, where the *shaded region* corresponds to the angular range covered by the detector aperture [38]

Eu_2O_3 [44, 45] that is comparable in mass and chemical binding to Sm_2O_3 . In the evaluation we have taken into account that the effective thickness of the rotating sample is reduced by about a factor of two compared to the sample at rest [35]. This effect is attributed to interference effects that arise from the beam passing through the rotating foil twice.

6.2.6 Practical Considerations

The NLE exhibits properties that seem to be attractive for nuclear resonant scattering experiments:

- Time resolutions below 100 ps,
- independence of the bunch structure in the storage ring, and
- no high-resolution optics necessary.

The applicability of the Nuclear Lighthouse Effect mainly depends on the relative magnitude of small-angle scattering. These dependencies are summarized in Fig. 6.10. In case of very low SAXS background, all of the above listed properties can be used to advantage. This is the case for well ordered (e.g., single-crystalline) rotors and samples, where a significant reduction of SAXS has been observed [32]. Similarly, a strong background reduction is

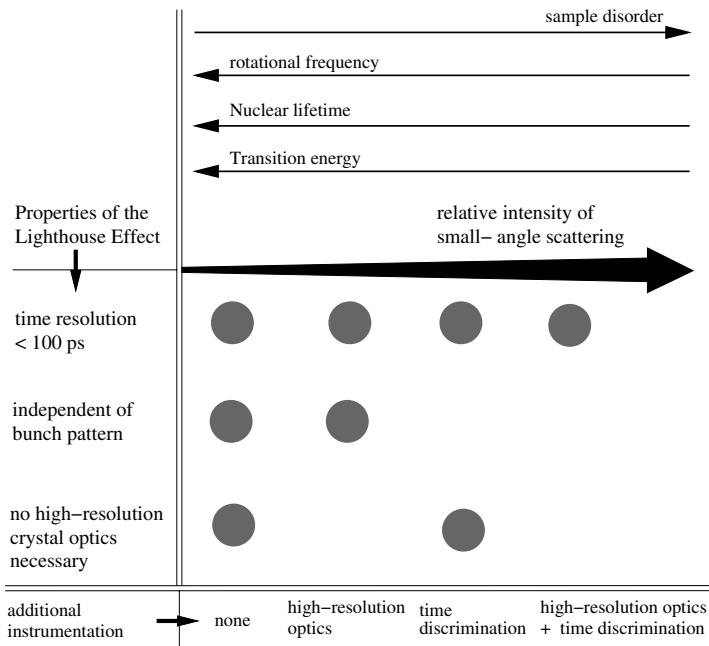


Fig. 6.10. Properties of the Nuclear Lighthouse Effect and their use depending on the experimental conditions. The *upper section* of this graph lists the factors that determine the relative intensity of the SAXS background. The quantities increase in the direction of the arrow. The *bottom line* lists the additional instrumentation that could be used. A full circle then indicates that the property of the NLE can be utilized

achieved by switching to high transition energies, because the angular dependence scales with q^{-4} . The signal-to-noise ratio increases further with increasing rotational frequencies and/or longer nuclear lifetimes: Deflection angles are then large and the resonantly scattered radiation is well separated from the SAXS halo. Future rotors may allow rotational frequencies of up to 70 kHz [46].

A significant gain in signal-to-noise ratio is achieved by use of high-resolution crystal optics with a bandwidth of a few meV. Compared to the bandwidth of the premonochromator, this should yield a reduction of the nonresonant background by 2–3 orders of magnitude. If the bunch pattern in the storage ring allows for time discrimination techniques, then the data can be recorded practically free of background. This does not imply that the time spectra are recorded by the conventional timing technique. The data are still recorded on a spatial scale where outstanding time resolutions can be reached; time discrimination is just used to gate out the prompt background. Therefore, even in less favorable situations where high-resolution optics and

time-discrimination have to be applied, time-resolved measurements can be performed that are not limited by the length of the bunches.

The NLE opens the possibility to perform time-resolved NRS without the equipment described in Sects. 3.2 and 3.3. This allows one to perform such measurements at beamlines that are not specially equipped with such instrumentation. On top of that, the effect can be applied with any bunch pattern in the storage ring, thus lifting the restrictions for special timing modes imposed by the conventional technique. Possible future applications in elastic as well as inelastic nuclear resonant scattering experiments are discussed in Chap. 7.

6.3 High-Resolution Filtering of Synchrotron Radiation

Currently, there is no x-ray spectroscopic technique available that allows one to investigate low-energy excitations with μeV resolution. For instance, vibrational spectra of disordered solids exhibit a universal feature in the range of 1–10 meV, the so-called boson peak that is not fully understood yet and is thus the subject of a lively debate [47]. Further examples are magnons [48, 49], two-level systems [50], phasons in quasicrystals [51, 52], soft phonons [53], etc. Presently, inelastic x-ray spectroscopy relies on the properties of Bragg reflections from perfect single crystals. This limits the energy resolution to values of a few hundred μeV . To overcome this limit, other scattering mechanisms have to be employed. A new approach is the use of nuclear resonant scattering techniques where the energy resolution is determined by the width of the nuclear resonance. New techniques aiming at this goal are outlined in this section.

According to the previous section, radiation resonantly scattered from a magnetized sample that rotates with angular velocity $\boldsymbol{\Omega}$ exhibits the following properties:

- **Doppler shift**

The scattering takes place at an energy $E = E_0 - \hbar(\boldsymbol{\Omega} \times \mathbf{r}) \cdot \mathbf{k}_0$, where \mathbf{r} is the radius vector relative to the center of rotation [7].

- **Lighthouse Effect**

The wavevector of the scattered radiation is $\mathbf{k}(t) = \mathbf{k}_0 + \mathbf{k}_0 \times \boldsymbol{\Omega} t$ [21].

- **Orthogonal Scattering**

The optical activity associated with magnetic hyperfine interactions leads to rotation of the plane of polarization in the scattering process. Polarization components generated as a result of orthogonal scattering (e.g. $\sigma \rightarrow \pi$) can be filtered out by crystal analyzers [54, 55, 56].

These properties provide the possibility to perform nuclear resonant filtering of synchrotron radiation that leads to a μeV wide beam, tunable over several meV. The unique properties of the resonant scattering process, e.g., the time

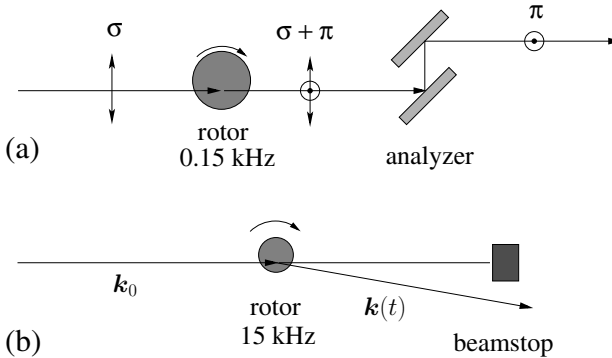


Fig. 6.11. Two schemes to extract a μeV -wide beam, resonantly scattered at a rotating sample, with a tunability over a few meV around the resonance energy. (a) Rotating-mirror spectrometer, (b) Lighthouse spectrometer [57]

scale of the nuclear decay and its polarization characteristics, allow one to separate the resonantly scattered radiation from the nonresonant radiation.

Taking these properties into account, it turns out that the highest throughput can be reached in grazing incidence reflection from thin films magnetized in Faraday geometry: $\mathbf{B} \parallel \mathbf{k}_0$. This geometry requires flat mirrors of several cm radius that are coated with a layer system containing the resonant isotope in a ferromagnetic matrix. Due to the large size of these rotors, rotational frequencies are limited to 100–200 Hz. In that case the Nuclear Lighthouse Effect can be (almost) neglected. This approach is shown schematically in Fig. 6.11a.

The second approach to high-resolution filtering relies entirely on the time scale of the nuclear decay that manifests in the Nuclear Lighthouse Effect. At sufficiently high rotational speeds, the resonantly scattered radiation is spatially separated from the nonresonant background which can be blocked out by placing a beam stop at the primary beam, see Fig. 6.11b. No high-resolution crystal optics is necessary. The high rotational frequencies of a few kHz imply small rotor diameters. Therefore, grazing incidence reflection is not appropriate in this case. Instead, forward scattering has to be employed.

6.3.1 Energetic Bandwidth

The choice of the material and the magnetization geometry determine the integrated intensity T of $\sigma \rightarrow \pi$ scattering. The magnitude of T finally determines the photon flux on the sample under study. Therefore it is an important figure-of-merit for optimization of a spectrometer. We define T by

$$T = \int_{-\infty}^{\infty} |A_{\sigma\pi}(\omega) - A_0|^2 d\omega \quad (6.15)$$

where $A_{\sigma\pi}$ is the amplitude of $\sigma \rightarrow \pi$ scattering, either given by $R_{\sigma\pi}$ in the case of grazing-incidence reflection or $T_{\sigma\pi}$ in the case of forward scattering. A_0 is the amplitude scattered off-resonance. An alternative criterion is the intensity of delayed quanta measured in a certain time interval:

$$T_t = \int_{t_1}^{t_2} |A_{\sigma\pi}(t)|^2 dt . \quad (6.16)$$

Both expressions are equivalent for $t_1 = 0^+, t_2 = \infty$. Equation 6.16 is more appropriate if certain regions of the time spectrum are excluded from detection, e.g. in the presence of strong prompt electronic (charge) scattering. It will be used for evaluation of the Nuclear Lighthouse Effect.

The purpose of this section is to discuss various scattering geometries with respect to the value of T that can be obtained. As a general rule, the maximum values of T are obtained for scattering from ferromagnetic samples that are magnetized parallel to \mathbf{k}_0 (Faraday geometry). In this case, the nondiagonal elements of the scattering matrix are largest [54, 58]. Then the circular polarizations are eigenpolarizations of the sample and incident linear polarization experiences strong orthogonal scattering.

While the Faraday geometry is difficult to realize in transmission through thin foils due to the large demagnetization field, it can be easily realized in grazing incidence geometry at thin ferromagnetic films. Fields of a few mT are sufficient to achieve a complete in-plane magnetization of the film. For various layer systems, T has been plotted as a function of angle of incidence, see Fig. 6.12. The largest values of T are obtained if the ^{57}Fe layer is coated on a total reflecting substrate layer, i.e., a layer of higher electron density, because the radiation then passes the ^{57}Fe at least twice. This becomes evident by comparison with a single ^{57}Fe layer coated directly on a substrate of lower electron density. In this case T assumes a maximum value of $30\Gamma_0$ at $\varphi = 3.8$ mrad, the critical angle for electronic scattering by Fe (a). Values more than twice as large are obtained for 10 nm ^{57}Fe coated on Pd, where $T = 65\Gamma_0$ is reached at $\varphi = 4.2$ mrad, close to the critical angle of Pd (b). In general, large values for T are found if the ^{57}Fe is coated on a substrate with a high reflectivity. This can be also a multilayer with the angle of incidence adjusted to one of its Bragg peaks. As an example, a multilayer consisting of $40 \times (1.5 \text{ nm Mo}/2.5 \text{ nm Si})$ has been assumed with 30 nm ^{57}Fe coated on top of it. In this case, $T = 55\Gamma_0$ is achieved at $\varphi = 11$ mrad (c). Such a solution becomes attractive when a large beam cross section has to be reflected. The largest value of T was found for a Pd/C/Pd x-ray waveguide structure, where a 3.5 nm thick ^{57}Fe layer was embedded in the center of the C spacer layer, so that the actual layer sequence (as seen from the top) was 2 nm Pd/10 nm C/3.5 nm $^{57}\text{Fe}/10 \text{ nm C}/30 \text{ nm Pd/Si}$. At a certain angle, a guided mode inside the waveguide is excited. The radiation is reflected several times at the internal C/Pd boundaries and constructive interference

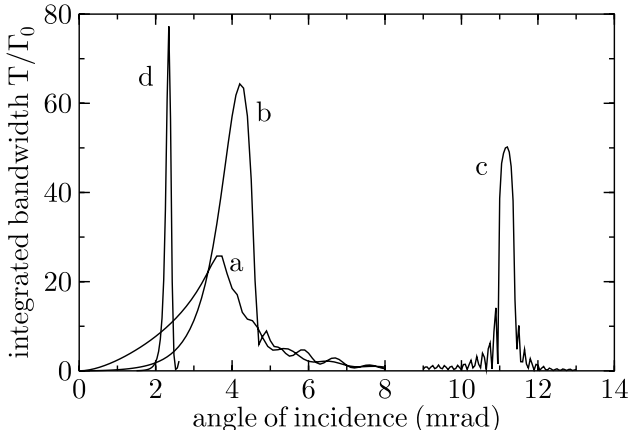


Fig. 6.12. Energy-integrated reflectivity curves $|R_{\sigma\pi}|^2$ of various layer systems: (a) 30 nm ^{57}Fe , (b) 10 nm ^{57}Fe on Pd, (c) 40 nm ^{57}Fe on a Mo/Si multilayer with $d_{Si} + d_{Mo} = 4$ nm, (d) 3.5 nm ^{57}Fe embedded in the center of a Pd/C/Pd waveguide structure. The energetic bandwidth is measured in units of the natural linewidth $\Gamma_0 = 4.7 \text{ neV}$ of the ^{57}Fe resonance [57]

between all these waves leads to a strong intensity buildup inside the spacer layer [59, 60, 61]. Here a value of $T = 78 \Gamma_0$ is reached at $\varphi = 2.2 \text{ mrad}$ (d).

In case of the lighthouse effect, the resonantly scattered radiation is selected via the angular deflection of the delayed quanta. For use of the deflected radiation in a subsequent experiment, a certain angular range (equivalent to a certain time interval) can be gated out by placement of a slit. In case of scattering from a polycrystalline ^{57}Fe foil, the maximum flux can be obtained by selecting the most intense quantum beats in the spectrum. Figure 6.13 displays the thickness dependence of the energy-integrated flux, as defined by (6.16), that is contained in the quantum beats around 30 ns and 40 ns. A maximum value of T close to $30 \Gamma_0$ is found for a foil thickness of about $8 \mu\text{m}$. T peaks at $17 \Gamma_0$ if only the quantum beat around 40 ns is taken (dotted line).

6.3.2 Spectrometer Types

Rotating-Mirror Spectrometer

The schematic setup of the rotating-mirror spectrometer is shown in Fig. 6.14. The reflecting layer system consists of 11 nm ^{57}Fe on 20 nm Pd, coated on an annular region of a superpolished mirror close to its circumference. The ^{57}Fe film is magnetized by a permanent-magnet structure that produced an almost homogeneous field along the footprint of the beam with a strength of approximately 50 mT. The mirror is mounted on an air lubricated bearing that provided an angular accuracy during rotation of better than $10 \mu\text{rad}$. The

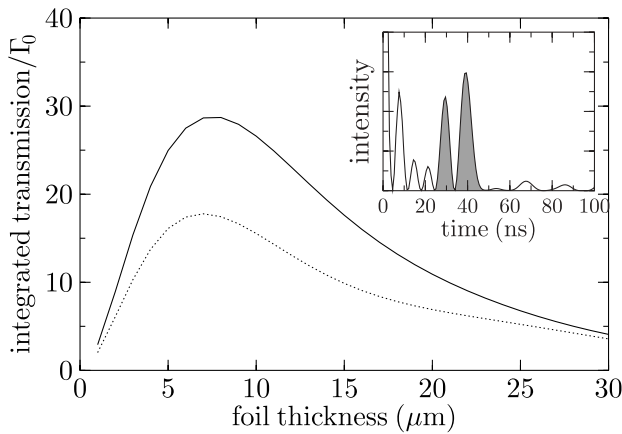


Fig. 6.13. Thickness dependence of the time integrated intensity T_t (6.16) of a ^{57}Fe foil a) in the time interval 24–46 ns (shaded area in the inset) and b) in the time interval 34–46 ns [57]

surface normal of the mirror was adjusted parallel to the rotation axis with about the same angular accuracy by employing interferometric techniques. In order to reach rotational frequencies of up to 8000 min^{-1} , the mirror has to be carefully balanced. With the magnetic field used here, no warming of

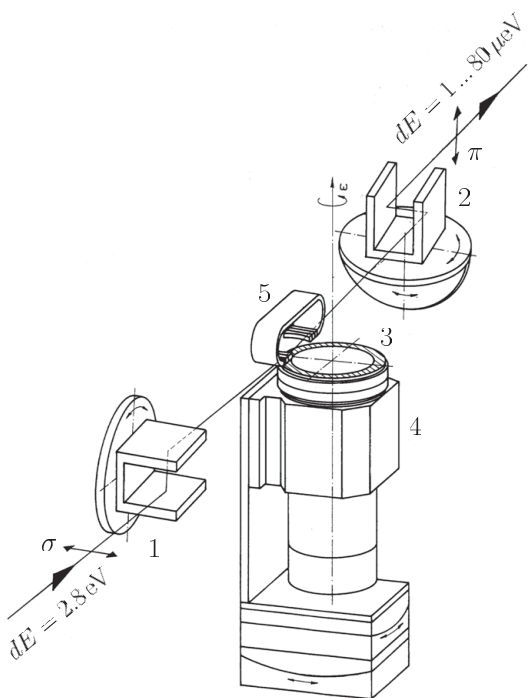


Fig. 6.14. Schematic setup of a spectrometer for μeV -resolved x-ray scattering based on elastic nuclear resonant scattering. 1: Si(840)-Polarizer, 2: Si(840)-Analyzer, 3: Superpolished mirror coated with ^{57}Fe , 4: Drive for mirror rotation with up to 8000 min^{-1} , 5: Permanent magnet for magnetization of the Fe-film parallel to k_0 . Polarizer and analyzer are channel-cut crystals with scattering planes tilted by 90° (crossed polarizers) [7]

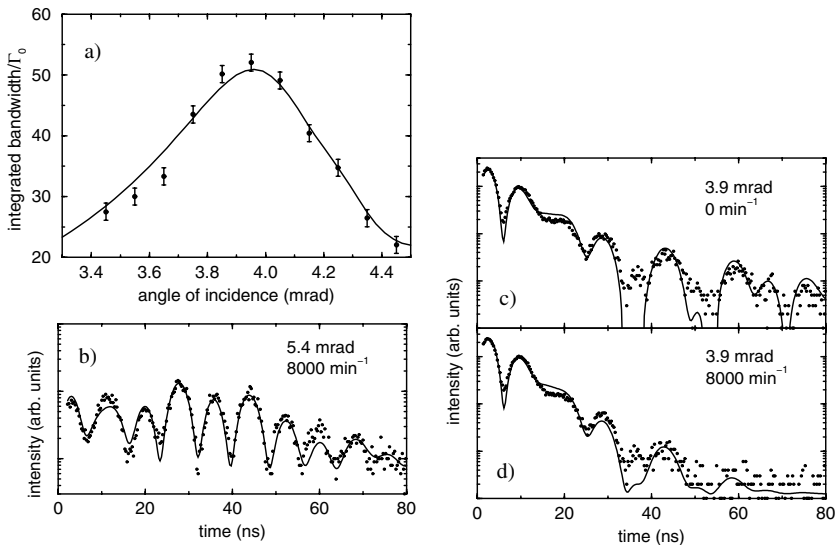


Fig. 6.15. Characterization of the rotating-mirror spectrometer. (a) Energy integrated $\sigma \rightarrow \pi$ reflectivity of the $^{57}\text{Fe}/\text{Pd}$ film, recorded with delayed quanta in a time window from 1 ns to 300 ns. (b) Time spectrum of the $^{57}\text{Fe}/\text{Pd}$ film at 5.4 mrad and a rotational frequency of 8000 min^{-1} , indicating that the magnetization is parallel to \mathbf{k}_0 [57] (c, d) Time spectra of the $^{57}\text{Fe}/\text{Pd}$ film at 3.9 mrad with the mirror rotating at 0 and 8000 min^{-1} , respectively, indicating the influence of the lighthouse effect at late times

the mirror holder due to Eddy currents could be detected during rotation. The experimental results obtained from characterization of this spectrometer [7] are summarized in Fig. 6.15. Figure 6.15a shows the angular dependence of the $\sigma \rightarrow \pi$ reflectivity $|R_{\sigma\pi}(\varphi)|^2$. It was recorded by counting delayed quanta in the time window from 2–100 ns. Since $R_{\sigma\pi}$ vanishes off resonance, the time spectrum $|R_{\sigma\pi}(t)|^2$ starts with zero intensity at $t = 0$. Therefore the measured signal is equivalent to the energy integrated reflectivity and can be directly compared with curve b) in Fig. 6.12. As expected, the reflectivity peaks at approximately 4.0 mrad close to the critical angle of the Pd substrate layer. The solid line is a theoretical simulation. Here the maximum integrated reflectivity is $50 I_0$. The deviation from the expected value of $65 I_0$ is caused by boundary roughness and layer inhomogeneities. Based on this value, a photon flux in the range 10^4 – 10^5 s^{-1} can be expected at undulator beamlines of 3rd-generation synchrotron radiation sources.

Figures 6.15c,d display the time response of the reflection at an angle of incidence of 4.0 mrad. The intensity at late times has important implications for the signal-to-background ratio in future experiments, as will be discussed below. Figure 6.15d shows the time response at a rotational frequency of 8000 min^{-1} . Due to the lighthouse effect the signal at late times is

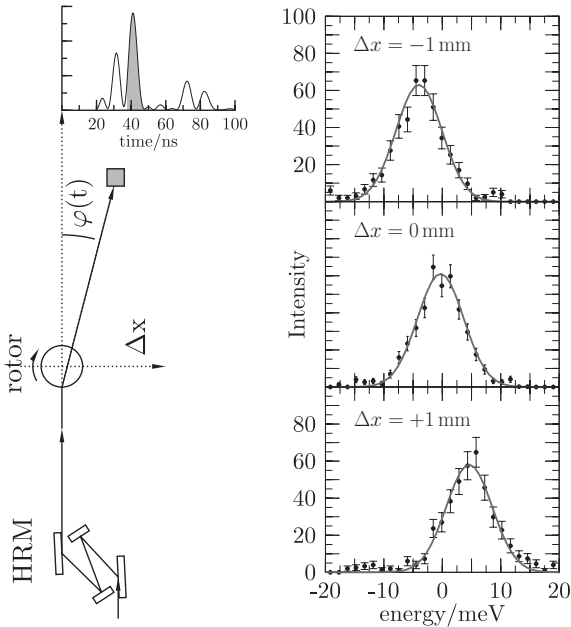


Fig. 6.16. μeV bandpass filtering and meV energy tuning of synchrotron radiation by the nuclear lighthouse effect. Energy tuning proceeds via transverse displacement Δx of the rotor relative to the beam [8]

significantly suppressed: Delayed quanta are deflected by $0.1 \mu\text{rad}/\text{ns}$, so that with increasing time they fall out of the angular acceptance of the analyzer.

Figure 6.15c displays the time spectrum recorded at 5.4 mrad and a rotational frequency of 8000 min^{-1} . The angle of incidence is far beyond the critical angle, so that the scattering is kinematical. Correspondingly, the speedup is strongly reduced. The shape of the quantum beat spectrum indicates that the film is indeed magnetized parallel to \mathbf{k}_0 , even at the maximum rotational speed.

Lighthouse Spectrometer

The linear velocity at the circumference of the rotor is 140 m/s , resulting in a tunability range of $\pm 6.8 \text{ meV}$ around the resonance. To demonstrate this, an APD was placed to record only delayed deflected quanta from the strongest quantum beat in the spectrum. Then this signal was monitored while tuning the energy of the high-resolution monochromator. The result of these scans is shown in Fig. 6.16 for offsets $\Delta x = -1, 0$ and $+1 \text{ mm}$ relative to the center of rotation, clearly demonstrating the corresponding energy shifts of $-4.5, 0.0$ and $+4.5 \text{ meV}$, respectively.

6.3.3 Considerations on Inelastic Spectroscopy

The radiation leaves the spectrometer in Fig. 6.14 with an energy bandwidth of $1\text{--}80 \mu\text{eV}$ and a tunability of $\pm 3 \text{ meV}$ around the 14.4 keV resonance of

^{57}Fe . One class of applications of this instrument will be inelastic nuclear resonant scattering experiments from samples containing ^{57}Fe . Therefore, time discrimination techniques have to be applied for detection of inelastic events. This requires that the incident radiation should exhibit a pulse-like time structure to define the time of excitation. In this spectrometer, however, this condition is deteriorated due to the fact that the radiation is generated in a nuclear resonant scattering process. In spite of the strong speedup, the intensity at late times may generate background events on the order of the inelastic signal. Here the nuclear lighthouse effect leads to a reduction of those late quanta and therefore is a welcome background suppression.

In case of the lighthouse spectrometer shown in Fig. 6.16 the time structure of the incident radiation is defined by the placement of the slit. If the slit is centered on a strong quantum-beat, the temporal width of the filtered radiation is determined by the width of the quantum beat. Accordingly, there are no events at late times so that contaminations of this kind are negligible.

For an estimate of the count-rates that can be expected in future experiments, the delayed fluorescence yield has to be calculated. The flux of K-fluorescence photons emitted in the full solid angle is given by (5.6):

$$I(E) = I_0 \varrho \sigma_0 \frac{\eta_K \alpha_K}{1 + \alpha} \frac{\pi}{2} \Gamma_0 S(E) =: C I_0 S(E) \quad (6.17)$$

where σ_0 is the nuclear resonance cross section, ϱ is the number density of resonant atoms, η_K the K-fluorescence yield, α and α_K the total and partial coefficient of internal conversion, and Γ_0 is the natural linewidth. $C = 1.4 \cdot 10^{-6}$ eV in case of ^{57}Fe . I_0 is the incident flux on the sample, and $S(E)$ is the absorption probability per unit of energy as given by (5.7). Values for $S(E)$ of $10\text{--}100\text{ eV}^{-1}$ can be found in materials with low-energy excitations [50]. Taking into account corrections for absorption in the sample, as well as coverage of solid angle and detector efficiency, one arrives at count rates of $0.1\text{--}1\text{ s}^{-1}$ at present-day sources. These values have to be compared with the flux of background events that dominantly arise from photoelectric absorption of delayed incident photons. Since the time response of this spectrometer is fast compared to the natural decay, the background can be substantially reduced by proper time gating. Ratios of $10^{-6}\text{--}10^{-7}$ can be achieved between the number of quanta emitted for $t > 60\text{ ns}$ and the total photon flux delivered by this spectrometer. A further increase in flux of almost an order of magnitude can be gained, if the collimation of the source can be matched to the angular acceptance of the polarizer/analyzer of $\approx 10 \times 10\text{ }\mu\text{rad}^2$ [57].

6.4 Heterodyne and Stroboscopic Detection Schemes

Since the early days of NRS with synchrotron radiation, several methods were proposed to perform hyperfine spectroscopy with synchrotron radiation in an energy-resolved mode. A number of experiments were performed to extract

radiation with a sufficiently narrow energy bandwidth that could be used as a source for subsequent experiments [62, 63]. While these approaches involved pure nuclear reflections from single crystals under special conditions, they are of limited value for the application in general-purpose experiments. This situation may change by application of a ‘heterodyne’ detection scheme [64, 65, 66] which relies on a single-line reference foil that is Doppler-tuned relative to the sample at rest, as illustrated in the inset of Fig. 6.17. This method is thus a combination of conventional Mössbauer absorption spectroscopy and nuclear forward scattering. The term ‘heterodyne’ originates from the fact that the unknown transition frequencies in the sample under study are compared with this variable reference frequency [67]. When this reference frequency equals one of the unknown resonance frequencies in the sample, the time-integrated signal is much larger compared to the case where both are off resonance. Thus, the time-integrated signal as a function of the Doppler velocity of the reference sample resembles a Mössbauer spectrum obtained with a radioactive source. This is shown in Fig. 6.17. While the horizontal line represents the resonance frequency ω_s in the sample, the inclined line corresponds to the variable reference frequency $\omega_r + \Delta$. When these lines cross each other, a resonance peak is found in the heterodyne spectrum. In practice, however, it is not possible to record the time-integrated signal over

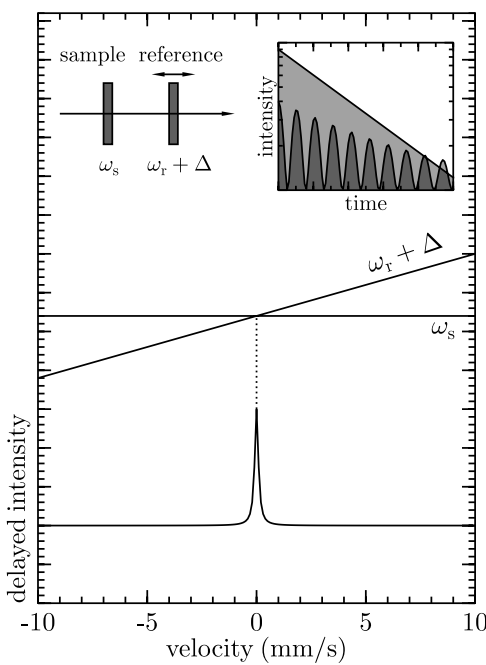


Fig. 6.17. Principle of heterodyne detection of nuclear resonant scattering of synchrotron radiation. A single-line reference absorber is moved relative to the sample at rest. When the resonance frequencies of sample (ω_s) and reference (ω_r) coincide, a resonance line is observed in the time integrated signal. The *upper-right* inset shows the time-integrated signal if both frequencies are on-resonance (*upper curve*) and off-resonance (*lower curve*)

the interval $(0, \infty)$; the signal always results from time integration over a finite time window. In the first experiment of this kind [64], photons were counted in a time window covering the whole range between two bunches, except for a narrow interval Δt after the prompt pulse. Δt is mainly given by the recovery time of the detector electronics after the arrival of the prompt radiation pulse. Typical values in forward-scattering geometry at modern synchrotron radiation sources are $\Delta t = 10\text{--}15$ ns. However, gating of the time spectra at such late times after excitation (time slicing) led to significant disturbances of the measured energy spectra, resulting from the Fourier components of the time window function [65, 68]. Only after introducing a polarizer/analyzer setup in crossed setting, the prompt nonresonant intensity could be reduced by several orders of magnitude, so that time gating of the prompt pulse could be restricted to $\Delta t = 1\text{--}2$ ns. Such a time gate has negligible effects on the measurement so that undisturbed energy spectra were obtained [66].

Another approach to eliminate the effect of time slicing is the method of stroboscopic data acquisition [69, 70]. In this case, a periodic set of short time windows is used instead of a single, long time window. This is illustrated in Fig. 6.18. Resonances of higher order appear at relative velocities that are given by

$$v_n = \pm n \frac{\omega_T}{\omega_r} c \quad \text{with} \quad n = 0, 1, 2, \dots, \quad (6.18)$$

where ω_T is the time-window frequency, ω_r is the resonance frequency of the single-line reference foil, and c is the velocity of light. These resonances are free of the distortions that the first-order spectrum suffers from in the heterodyne detection scheme. Due to the periodic structure of the time windows, this technique was called stroboscopic detection of NRS. For a given time window function $S(t)$, the intensity $I(\Delta)$ recorded as function of Doppler shift Δ is given by [70]:

$$I_S(\Delta) = \int_0^\infty dt S(t) D(t, \Delta), \quad (6.19)$$

where $D(t, \Delta) = |A(t, \Delta)|^2$. Since $S(t)$ is periodic with a frequency ω_T , it can be expanded in a Fourier series as:

$$S(t) = \sum_{n=-\infty}^{+\infty} s_n e^{in\omega_T t}. \quad (6.20)$$

Introducing

$$d_n(\Delta) := \int_0^\infty D(t, \Delta) e^{in\omega_T t} dt, \quad (6.21)$$

Equation (6.19) can be written as:

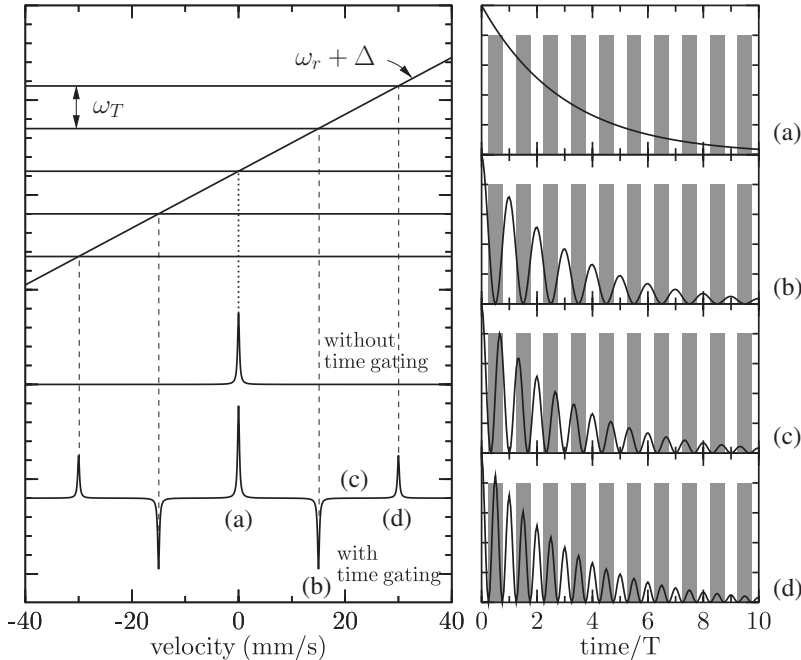


Fig. 6.18. Principle of stroboscopic detection of nuclear resonant scattering of synchrotron radiation. The *horizontal lines* in the *top part* correspond to the energetic positions of the stroboscopic resonances, shifted by ω_T relative to each other. The *inclined line* is the transition frequency in the moving reference sample. At each intersection point a resonance line on the velocity scale appears. For some selected values of the relative Doppler shift Δ , the corresponding time spectra are shown on the *right* together with the time-window function (*shaded areas*). The measured signal is the integral over the part of the time spectrum that falls into the *shaded areas*. The energy spectrum in the *middle* is obtained when no time gating is performed, which corresponds to the case of heterodyne detection

$$I_S(\Delta) = \sum_{n=-\infty}^{+\infty} s_n d_n(\Delta) = I_0(\Delta) + \sum_{n \neq 0} I_n(\Delta). \quad (6.22)$$

Thus, the total spectrum is a sum of stroboscopic resonances $I_n(\Delta)$, with $I_0(\Delta)$ being the unshifted heterodyne spectrum. Careful analysis shows that the higher order terms $I_n(\Delta)$ contain no baseline or radiative coupling terms [70]. The shape of these resonances is determined by the phase of the coefficients s_n which are complex numbers, resulting in a superposition of Lorentzian-like and dispersionlike curves with weight factors $\text{Re}(s_n)$ and $\text{Im}(s_n)$, respectively. However, if the time window is chosen symmetrically around $t_0 = T/2$, then s_n is real and one obtains purely Lorentzian-like resonances. Correspondingly, the different stroboscopic order spectra can be clearly distinguished and the interpretation of the spectra in terms

of hyperfine parameters is similar to the interpretation of a conventional Mössbauer spectrum [70].

The technique of stroboscopic detection of nuclear resonant scattering is advantageous if the bunch distance available at a synchrotron source is too short to record time spectra in a meaningful way. This is particularly interesting for experiments with long-lived isotopes like ^{181}Ta or for any other isotope when the bunch distance is much shorter than the nuclear lifetime. The technique has been applied for the determination of isomer shifts as demonstrated in the case of ^{151}Eu in EuPd_2Si_2 at pressures ranging from ambient pressure to 5 GPa [71].

6.5 Time-Domain Interferometry

6.5.1 General Considerations

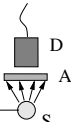
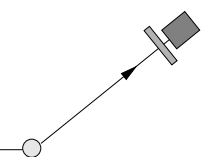
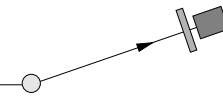
The methods of nuclear inelastic scattering described so far have in common that only samples containing resonant nuclei can be investigated. Resonant nuclei in the sample serve as energetic analyzers in an *incoherent* absorption process. While this opens a number of interesting possibilities (e.g., the use of resonant probe layers to study dynamical properties with very high spatial resolution), one may ask whether resonant absorbers could be used as energetic analyzers for coherent inelastic scattering from samples that do not contain Mössbauer isotopes. A number of possibilities how to realize this idea is summarized in Table 6.1. In general, this would enable one to investigate arbitrary samples without the restriction to dope them with specific nuclei. Such an approach has been realized for energy analysis of momentum-integrated coherent x-ray scattering [72], see Table 6.1a. In principle, this could be used for the analysis of momentum-resolved coherent inelastic scattering, too, as sketched in Table 6.1b. However, in this case even the strongest x-ray source presently available will not provide enough flux to make this method competitive with conventional inelastic x-ray scattering [2, 73]. The reason for the flux limitation is the mismatch of the narrow energy bandwidth of the analyzer compared to energetic width of the incident radiation.

A partial decoupling of the energetic resolution from the incident energy bandwidth can be achieved by measuring the time dependence of the elastically scattered radiation. However, this cannot be done by simply using the setup in Table 6.1b. The reason is that an energy transfer $\Delta\omega$ manifests in a phase factor that vanishes upon the measurement of the intensity:

$$A(\omega + \Delta\omega) = A(\omega) e^{i \Delta\omega t} \quad \text{so that} \quad |A(\omega + \Delta\omega)| = |A(\omega)|. \quad (6.23)$$

Introducing a second reference scatterer, as shown in Table 6.1c, such phase factors can be determined in interferometric experiments. In classical interferometry one would try to determine $\Delta\omega$ directly by measuring the corresponding change in the optical path length. This is usually difficult because

Table 6.1. Different approaches to use resonant absorbers as analyzers for inelastic x-ray scattering from nonresonant samples. S is the sample, A is a resonant absorber, and D is the detector.

| | Setup | Characteristics | Refs. |
|---|---|---|------------|
| A |  | Measuring the time-integrated yield of delayed quanta while scanning the photon energy. Integration over q -range given by detector aperture. | [72] |
| B |  | Measuring the time-integrated yield of delayed quanta while scanning the photon energy at a fixed momentum transfer to measure $S(\mathbf{q}, \omega)$. Strongly flux limited. | |
| C |  | Two single-line absorbers before and behind the sample. Extraction of $S(\mathbf{q}, t)$ from measured time spectra. | [74], [75] |

of high demands for the stability of such a setup. On the other hand, nuclear resonant scattering offers the advantage of using time as a coordinate for the measurement of scattering phases. This idea manifests in the method of time-domain interferometry that will be described in the following.

6.5.2 Determination of the Intermediate Scattering Function

Nuclear resonant scattering provides an interesting way to probe the dynamics in condensed matter on the time scale directly. A resonant scatterer can be viewed as a delay line to generate temporally separated photons that are correlated to each other: Photons pass through the sample either without resonant interaction or leave the sample after a certain delay time. Both paths are indistinguishable and thus they are coherently coupled. While the prompt photon probes the sample at time $t = t_0$, the delayed photon sees the sample at time $t_1 = t_0 + \Delta t$. Both paths recombine in the second resonant sample that acts as a phase-sensitive analyzer. In order to visualize the scattering process of time-domain interferometry, we extend the spacetime diagram of Fig. 2.14. The sample that is introduced between the two resonant foils introduces a phase lag between the two scattering paths, as illustrated in Fig. 6.19. Both absorbers are assumed to be identical in composition and thickness, but

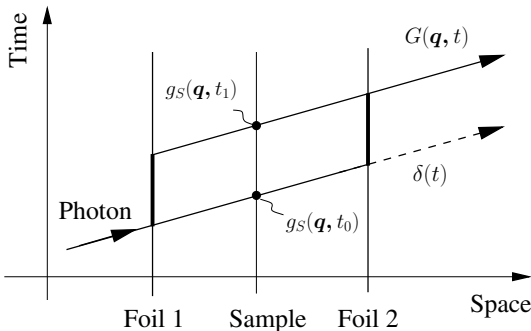


Fig. 6.19. Visualization of the scattering processes in time domain interferometry. The time evolution of the nuclear exciton that develops in the system of two foils is perturbed by the relative phases that are induced by electron-density fluctuations in the sample in-between

Doppler shifted by a value ω_D relative to each other. This means that their time responses are given by

$$f_1(t) = \delta(t) - g(t) \quad (6.24)$$

$$f_2(t) = \delta(t) - g(t) e^{i\omega_D t} \quad (6.25)$$

If $\omega_D \gg \Gamma_0/\hbar$, the radiative coupling between both absorbers is very small, so the coupling term can be neglected. Then the delayed intensity is simply given by

$$I(t) = 2g(t)^2 [1 + \cos(\omega_D t)] . \quad (6.26)$$

The time dependence of the intensity is a beat pattern with a single beat frequency that corresponds to the relative Doppler shift of the absorbers. Such interference patterns are very sensitive to small changes of the relative phase of the individual oscillations. This leads to the idea that the time-domain interference pattern should be influenced by a scattering process between both absorbers. An analysis of the perturbed time spectrum will reveal information about the dynamics in the scattering sample on the time scale of the nuclear lifetime. Such an experiment was performed with a (non-resonant) sample of glycerol placed between two resonant absorbers [74].

For a quantitative analysis we assume the scattering response from the nonresonant sample to be given by the function $g_S(\mathbf{q}, t)$, where \mathbf{q} is the momentum transfer in the scattering process. In the case of weak scattering, i.e. in the kinematical limit, the function $g_S(\mathbf{q}, t)$ is proportional to the spatial Fourier transform of the electron density $\rho_e(\mathbf{r}, t)$:

$$g_S(\mathbf{q}, t) = C \int d\mathbf{r} \rho_e(\mathbf{r}, t) e^{-i\mathbf{q} \cdot \mathbf{r}} . \quad (6.27)$$

The scattering response of the entire system is then given by

$$F(\mathbf{q}, t) = \int_0^\infty f_1(\tau) g_S(\mathbf{q}, \tau) f_2(t - \tau) d\tau =: \delta(t) - G(\mathbf{q}, t) . \quad (6.28)$$

Assuming again a large Doppler shift, we can neglect the radiative coupling term and obtain the delayed part of the scattering response:

$$G(\mathbf{q}, t) = [g_S(\mathbf{q}, t) e^{i\omega_D t} + g_S(\mathbf{q}, 0)] g(t). \quad (6.29)$$

The delayed intensity follows as:

$$\begin{aligned} I(\mathbf{q}, t) &= |G(\mathbf{q}, t)|^2 \\ &= |g(t)|^2 [|g_S(\mathbf{q}, t)|^2 + |g_S(\mathbf{q}, 0)|^2 \\ &\quad + 2 |g_S(\mathbf{q}, t) g_S(\mathbf{q}, 0)| \cos(\omega_D t + \varphi_S(0) - \varphi_S(t))], \end{aligned} \quad (6.30)$$

where $\varphi_S(t)$ is the phase of the function $g_S(t)$. Using (6.27), the function $g_S(\mathbf{q}, t) g_S(\mathbf{q}, t')$ can be rewritten via the convolution theorem as:

$$g_S(\mathbf{q}, t) g_S(\mathbf{q}, t') = C^2 \int d\mathbf{r} d\mathbf{r}' e^{-i\mathbf{q} \cdot (\mathbf{r} - \mathbf{r}')} \varrho(\mathbf{r}, t) \varrho(\mathbf{r}, t') \quad (6.31)$$

$$= C^2 \int S(\mathbf{q}, \omega) e^{i\omega(t-t')} d\omega = C^2 S(\mathbf{q}, t - t'). \quad (6.32)$$

The expression $S(\mathbf{q}, t)$ is the so-called intermediate scattering function which is the Fourier transform of the dynamic structure factor $S(\mathbf{q}, \omega)$ of the sample. Since $|g_S(\mathbf{q}, t)|^2 = |g_S(\mathbf{q}, 0)|^2 = S(\mathbf{q}, 0)$, the scattered intensity can be written as:

$$I(\mathbf{q}, t) = 2C^2 |g(t)|^2 [S(\mathbf{q}, 0) + S(\mathbf{q}, t) \cos(\omega_D t)]. \quad (6.33)$$

The intermediate scattering function typically decays monotonically with time. This is an expression of the fact that the density fluctuations in the sample destroy the phase correlation between the two interfering waves. It leads to an attenuation of the quantum beat modulation with increasing time. Therefore, from the measured time dependence of the attenuation one directly derives the intermediate scattering function. This will be shown in an experimental example below.

The range of the time spectra determines the time scale of the dynamics in the sample that can be studied with this method. In the case of high-frequency fluctuations, the damping of the quantum beats may be too fast to be observable in the time spectra. In this case, the method may be applied with both foils at rest, i.e., in the radiative-coupling regime, as proposed by Smirnov *et al.* [75]. Then the fluctuations lead to a radiative decoupling of the foils which manifests as a shift of the Bessel minima to later times. Accordingly, the dynamical range of the method is extended to shorter relaxation times. The corresponding theory of time domain interferometry for this case was worked out by Smirnov *et al.* [75].

6.5.3 Application: Dynamics at the Glass Transition

If the density fluctuations relate to relaxation around a glass transition, the intermediate scattering function is given by a stretched exponential that is often referred to as Kohlrausch function:

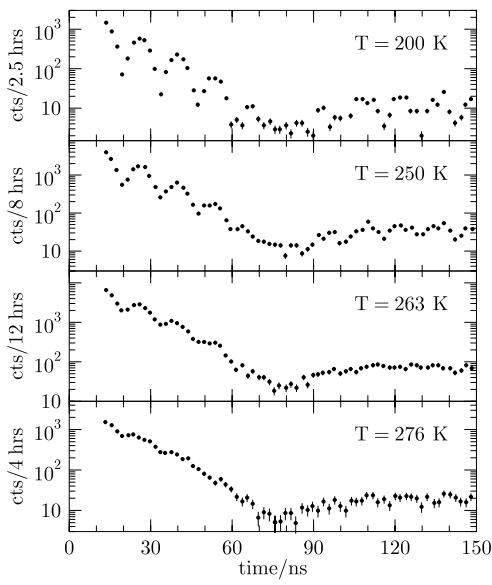


Fig. 6.20. Nuclear time-domain interferometry with a glycerol sample at different temperatures. The measurements were taken in the structure-factor maximum at a momentum transfer of $q = 1.5 \text{ \AA}^{-1}$ (Figure adopted from Baron *et al.* [74])

$$S(\mathbf{q}, t) = f_{qe}(\mathbf{q}) \exp[-(t/t_r)^\beta]. \quad (6.34)$$

For an experimental test, the method has been applied to measure the intermediate scattering function of glycerol [74]. Two ^{57}Fe stainless-steel foils with a thickness of $6 \mu\text{m}$ each were tuned to a relative velocity of 3 mm/s , leading to a beat period of $\Delta t = 16 \text{ ns}$. The setup was adjusted to the structure-factor maximum of glycerol at a momentum transfer of $q = 1.5 \text{ \AA}^{-1}$. Measurements at different temperatures were performed, shown in Fig. 6.20. One clearly sees the decreasing contrast of the beat pattern with increasing temperature. This behaviour is well described by the intermediate scattering function in (6.34) [74].

6.6 SRPAC: Perturbed Angular Correlation with Synchrotron Radiation

It is the virtue of synchrotron-based Mössbauer spectroscopy that the excited nuclear state is populated from the ground state, i.e., no radioactive parent nuclei are required. This principle can be applied also to other methods of nuclear solid state physics, in particular to time-differential perturbed angular correlation, TDPAC (For a recent review, see e.g. [76]). The synchrotron-based variant of this method is called SRPAC [77]. In SRPAC, the intermediate nuclear level is not populated from a higher-level excited state that originates from the decay of a radioactive parent like in TDPAC, but from

the ground state by resonant absorption of synchrotron radiation [78, 79], as sketched in Fig. 6.21. The direction and the arrival time of the first photon in TDPAC are replaced in SRPAC by the direction and the timing of the incident synchrotron radiation pulse. In both methods, the interference of indistinguishable paths along the hyperfine-split intermediate levels of single nuclei leads to a beat pattern in the temporal evolution of the nuclear decay. Since the absorption process is spatially incoherent, only transitions leading to the same nuclear ground state can interfere with each other. The beats in the time spectra thus reflect the excited-state splittings of single nuclei. Their observation does not require recoilless scattering. Therefore, this technique is particularly suited for materials with a small f-factor like soft matter, and involving high transition energies, high temperatures, etc. The beat pattern itself contains information about the nuclear hyperfine interaction and its time dependence. Therefore, in the static case the method can be applied to determine the orientation and magnitude of hyperfine fields in magnetic materials, for example. An interesting application is the determination of site-specific phonon density of states by recording the beat pattern of the incoherent fluorescence radiation while scanning the energy [80].

If the hyperfine fields are fluctuating during the lifetime of the intermediate state, the time evolution of the signal is damped in a characteristic way. From this damping, valuable information about the relaxation in the sample can be derived, as will be shown below.

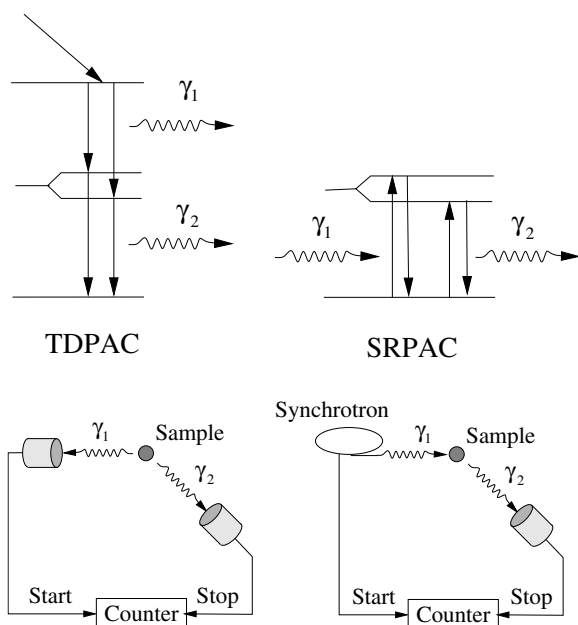


Fig. 6.21. Comparison between TDPAC and SRPAC. *Top:* Level schemes that are involved in TDPAC and SRPAC. *Bottom:* Schematic diagram of the experimental setup for both methods. In case of SRPAC, the first photon is replaced by synchrotron radiation that populates the intermediate level by excitation from the ground state

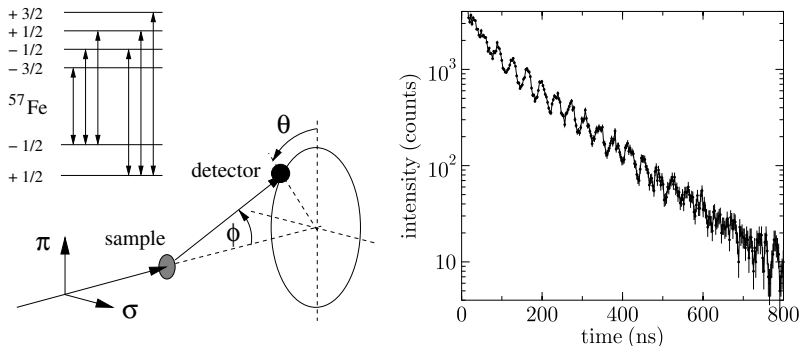


Fig. 6.22. *Left:* Generic geometry for SRPAC. Only the transitions leading to the same ground state interfere with each other, as sketched for the hyperfine-split levels of ^{57}Fe . In case of electric (magnetic) dipole transitions and incident σ polarization, the highest signal is observed for $\phi = 90^\circ$, $\Theta = 0^\circ$ ($\Theta = 90^\circ$). *Right:* Typical time spectrum recorded in SRPAC. In this case the sample was ferrocene in dibutylphthalate at $T = 160\text{ K}$. The beating originates from the quadrupole level splitting of ^{57}Fe in ferrocene

The generic experimental setup to be used in SRPAC is shown in Fig. 6.22. To avoid contributions from coherent forward scattering, the detector is set off the primary beam at a position defined by the angular coordinates (θ, ϕ) . In case of dipole transitions, the optimum geometry with highest count rate is obtained for $\theta = 90^\circ$, whereby $\phi = 0^\circ$ for electric and $\phi = 90^\circ$ for magnetic dipole transitions. To achieve a sufficient contrast in the intermediate-level quantum beats, the solid angle covered by the detector should be not too large to keep angular averaging at a minimum. In each particular case, a compromise between contrast and count rate has to be found.

In close analogy to TDPAC, the time evolution of the measured signal in SRPAC is given by

$$I(t) = I_0 e^{-t/\tau_0} (1 - A_{22} G_{22}(t)), \quad (6.35)$$

where A_{22} is the effective anisotropy coefficient, and $G_{22}(t)$ is the perturbation function. A_{22} determines the contrast of the quantum beats and is defined by the geometry of the experiment⁵. If the orientation of the hyperfine field in space does not change during the nuclear decay, the perturbation function is simply given by

$$G_{22}(t) = \cos(\Omega t/\tau_0 - 2\phi), \quad (6.36)$$

where $\hbar\Omega$ is the level splitting of the intermediate state. ϕ is the scattering angle in the vertical scattering plane as sketched for an M1 transition in Fig. 6.22. Thus, the phase of the beats changes with the detector setting

⁵ With increasing solid-angle coverage by the detector, the value of A_{22} decreases down to $A_{22} = 0$ for the full solid angle.

ϕ [78, 79]. If, however, the compound or molecule in which the nucleus is embedded moves during the nuclear decay, the function $G_{22}(t)$ is strongly affected. It should be noted that TDPAC is not affected by translational motion, therefore it is sensitive to rotational relaxation alone. This is in contrast to MS or QNFS which are sensitive to both translational and reorientational diffusion [81]. Consequently, the combination of these methods together with SRPAC allows one to separate translational and rotational relaxation [82].

In the experiment described here, SRPAC was applied to investigate the dynamics of dibutyl phthalate (DBP). DBP is a medium fragile glass former with a glass temperature of $T_g = 179\text{ K}$. It was doped by 5% (mol) of ferrocene as a probe molecule, enriched to 95% in ^{57}Fe [77]. The Fe atom in ferrocene is embedded between two cyclopentadienyl rings which produce an electric field gradient at the Fe site and, correspondingly, a quadrupole splitting of the nuclear level. This material had previously been studied by Mössbauer spectroscopy (MS) [81] and quasielastic nuclear forward scattering (QNFS) [83]. Since the latter two methods rely on coherent elastic scattering, the measured signal is proportional to f_{LM}^2 . Due to the strong decrease of the Lamb-Mössbauer factor f_{LM} with increasing temperature, these studies were limited to temperatures $T < 210\text{ K}$. Therefore, an incoherent scattering method like SRPAC, where the signal is proportional to $(1 - f_{LM})$, is well suited to extend these studies to higher temperatures.

In the experiment described here, the incident radiation was monochromatized to a bandwidth of about 6 meV at the 14.4 keV nuclear resonance of ^{57}Fe . Time spectra of the incoherent 14.4 keV fluorescence were taken with the detector aligned at $\theta = 90^\circ, \phi = 90^\circ$. The quantity $A_{22} G_{22}(t)$ as derived from the data is shown in Fig. 6.23 for various temperatures in the range of 160–300 K. At a temperature of 160 K, the elastic forward scattering is still very strong ($f_{LM} = 0.14$) and influences the time evolution of the SRPAC signal at times $t < 200\text{ ns}$. At greater times, the slowly decaying SRPAC signal can be observed without disturbances. Beyond the glass temperature, fast dynamics becomes dominating so that f_{LM} decreases rapidly. At $T = 206\text{ K}$, $f_{LM} = 0.01$, so that the NFS contribution to the SRPAC signal is negligible. Above T_g , structural relaxation dominates and causes a significant damping of the temporal beat pattern.

The theory for the influence of reorientational relaxation on TDPAC has been developed by *Blume, Tjon & Dattagupta* in a stochastic approximation, called the strong-collision model [84, 85]. There are two limiting regimes, depending on the characteristic relaxation rate λ . In the slow relaxation regime, i.e. for $\lambda \ll \Omega$, the natural decay is modulated by a pronounced quantum beat that is exponentially damped with a time constant proportional to λ :

$$G_{22}(t) \sim \frac{1}{5} e^{-4\lambda t/5} + \frac{4}{5} e^{-3\lambda t/5} \cos \Omega t . \quad (6.37)$$

In the fast relaxation regime, i.e., for $\lambda \gg \Omega$, the modulation is overdamped with a decay rate that is proportional to Ω^2/λ :

$$G_{22}(t) \sim e^{-4\Omega^2 t/5\lambda}. \quad (6.38)$$

While the solid lines in Figs. 6.23a,b are fits according to (6.37), the data in Figs. 6.23c–e were fitted using (6.38). Note that the time constant in (6.38) scales with $1/\lambda$, i.e., the decay rate of the measured intensity $I(t)$ is proportional to the relaxation time. This dependence may be somewhat counterintuitive, because it means that very short relaxation times become manifest on very long observation times. For that reason, measurements of SRPAC extending to short relaxation times should cover a large time window, as it is the case in Fig. 6.23.

The temperature dependence of the rotational relaxation rate λ_r , as derived from the SRPAC data, is shown in Fig. 6.24 together with the relaxation rate λ as determined from MS and QNFS measurements. Since these methods are sensitive to both translational and rotational relaxation, $\lambda = \lambda_r + \lambda_t$, where λ_t is the translational relaxation rate. Thus, in a temperature range where these methods are applicable, one is able to separate translational and rotational dynamics of the sample. In case of DBP, the results indicate that around and below the critical temperature of mode-coupling theory, T_c , the dynamics decouples into a translational and a rotational branch. The observed temperature dependence indicates that the rotational dynamics follows the slow β relaxation branch while the translational dynamics resembles

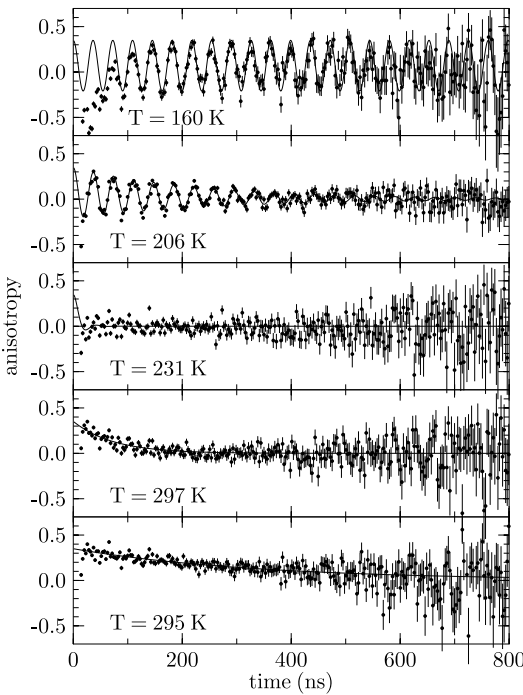


Fig. 6.23. Time evolution of the SRPAC signal $A_{22} G_{22}(t)$ of ferrocene/dibutyl phthalate at various temperatures [77]. The quantum beat in the data results from the quadrupole splitting of the nuclear levels of Fe in the ferrocene molecule. The *solid lines* are fits according to (6.37) and (6.38) as derived within the strong-collision model [84]. (Data taken from Sergueev *et al.* [82])

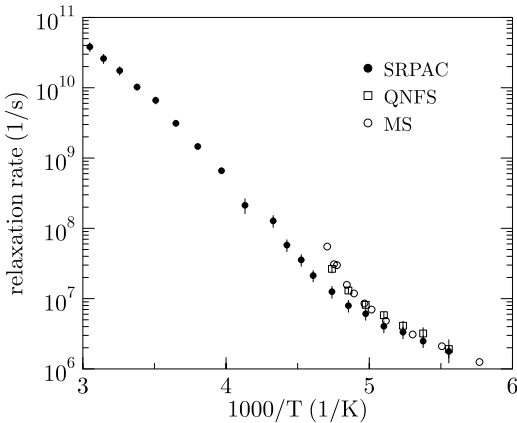


Fig. 6.24. Dependence of the characteristic relaxation rates on temperature as determined via SRPAC [82], QNFS [83], and MS [81]. In the region from 208 K–213 K, one observes a discrepancy between the data sets because MS and QNFS are sensitive to both translational and rotational relaxation, while SRPAC is sensitive to the latter one only

the structural α relaxation. These results support the concept of the decoupling of the different modes of motion below the critical temperature of mode-coupling theory.

In the experiment described here, SRPAC experiments have covered relaxation times ranging from beyond 1 μ s down to 20 ps [82]. This demonstrates the extended dynamical range of SRPAC compared to other methods. SRPAC has the intrinsic advantage not to require a radioactive parent. This avoids chemical and electronic aftereffects due to the decay of the parent nucleus that may disturb the local environment. Moreover, SRPAC can be applied to elements that are hardly accessible for TDPAC like isotopes with non-existing or very short-lived parents or isotopes with inconvenient or missing cascades. This applies, e.g., in the case of ^{57}Fe where the $5/2 \rightarrow 3/2 \rightarrow 1/2$ cascade gives a contrast of only 2% in TDPAC, while in SRPAC the maximum contrast is 50%. Exploiting the high brilliance of modern synchrotron radiation sources, SRPAC can be applied to systems that have not been accessible so far, like thin films and nanostructures, for example.

References

1. B. Dorner: *Coherent Inelastic Neutron Scattering in Lattice Dynamics* (Springer, New York 1982) 233
2. E. Burkert: *Inelastic Scattering of X-Rays with Very High Energy Resolution* (Springer, Berlin 1991) 233, 259
3. V. G. Kohn and G. V. Smirnov: Phys. Rev. B **57**, 5788 (1998) 234
4. B. Sepiol, A. Meyer, G. Vogl, R. Rüffer, A. I. Chumakov, and A. Q. R. Baron: Phys. Rev. Lett. **76**, 3220 (1996) 234
5. G. V. Smirnov and V. G. Kohn: Phys. Rev. B **52**, 3356 (1995) 234
6. A. Q. R. Baron, A. I. Chumakov, H. F. Grünsteudel, H. Grünsteudel, L. Niesen, and R. Rüffer: Phys. Rev. Lett. **77**, 4808 (1996) 234

7. R. Röhlsberger, E. Gerdau, R. Rüffer, W. Sturhahn, T. S. Toellner, A. I. Chumakov, and E. E. Alp: Nucl. Instrum. Methods Phys. Res. A **394**, 251 (1997) 234, 240
8. R. Röhlsberger, E. E. Alp, E. Gerdau, O. Leupold, K. W. Quast, R. Rüffer, W. Sturhahn, T. S. Toellner, and E. Burkel: Physica B **263-264**, 574 (1999) 234, 254
9. H. Jex, A. Ludwig, F. J. Hartmann, E. Gerdau, and O. Leupold: Europhys. Lett. **40**, 317 (1997) 234
10. G. V. Smirnov, U. van Bürck, J. Arthur, S. L. Popov, A. Q. R. Baron, A. I. Chumakov, S. L. Ruby, W. Potzel, and G. S. Brown: Phys. Rev. Lett. **77**, 183 (1996) 234
11. R. L. Mössbauer: Z. Naturforsch. **14a**, 211 (1959) 234
12. G. de Pasquali, H. Frauenfelder, H. Margulies, and R. N. Peacock: Phys. Rev. Lett. **4**, 71 (1960) 234
13. D. C. Champeney, G. R. Isaak, and A. M. Khan: Proc. Phys. Soc. **85**, 583 (1965) 234
14. H. J. Hay, J. P. Schiffer, T. E. Cranshaw, and P. A. Egelstaff: Phys. Rev. Lett. **4**, 165 (1960) 234
15. W. Kündig: Phys. Rev. **129**, 2371 (1963) 234
16. G. R. Isaak: Phys. Bull. **21**, 255 (1970) 234
17. C. Møller: Proc. Roy. Soc. A **270**, 306 (1962) 234
18. M. Ruderfer: Phys. Rev. Lett. **5**, 191 (1960) 234
19. A. Q. R. Baron: Hyperfine Interact. **123/124**, 667 (1999) 234
20. J. P. Hannon and G. T. Trammell: Physica B **159**, 161 (1989) 234
21. R. Röhlsberger, T. S. Toellner, W. Sturhahn, K. W. Quast, E. E. Alp, A. Bernhard, E. Burkel, O. Leupold, and E. Gerdau: Phys. Rev. Lett. **84**, 1007 (2000) 234, 235
22. R. Röhlsberger: Hyperfine Interact. **126**, 425 (2000) 234
23. F. D. Doty, in: D. M. Grant and R. K. Harris (eds.), *Encyclopedia of Magnetic Resonance* (Wiley, Chichester 1996), p. 4475. 236
24. F. D. Doty and P. D. Ellis: Rev. Sci. Instrum. **52**, 1868 (1981) 236
25. R. Röhlsberger, A. Bernhard, E. Burkel, K. W. Quast, O. Leupold, and E. Gerdau: HASYLAB annual report, 1997. 236
26. T. M. Mooney, T. S. Toellner, W. Sturhahn, E. E. Alp, and S. D. Shastri: Nucl. Instr. Methods Phys. Res. A **347**, 348 (1994) 236
27. E. Gluskin, E. E. Alp, I. McNulty, W. Sturhahn, and J. Sutter: J. Synchrotron Rad. **6**, 1065 (1999) 237
28. I. Bialynicki-Birula and Z. Bialynicka-Birula: Phys. Rev. Lett. **78**, 2539 (1997) 239
29. J. W. Goodman: *Statistical Optics* (John Wiley, New York 1985) 240
30. L. Mandel and E. Wolf: *Optical Coherence and Quantum Optics* (Cambridge University Press, Cambridge 1995) 240
31. S. K. Sinha, M. Tolan, and A. Gibaud: Phys. Rev. B **57**, 2740 (1998) 240
32. R. Röhlsberger, K. W. Quast, T. S. Toellner, P. Lee, W. Sturhahn, E. E. Alp, and E. Burkel: Appl. Phys. Lett. **78**, 2970 (2001) 241, 242, 243, 246
33. Y. Amemiya: J. Synchrotron Rad. **2**, 13 (1995) 241
34. W. Sturhahn and E. Gerdau: Phys. Rev. B **49**, 9285 (1994) 242
35. R. Röhlsberger, A. Bernhard, H. Sinn, Yu. V. Shvyd'ko and E. Burkel: HASYLAB annual report 1998, p. 939. 242, 246
36. K. H. J. Buschow and E. J. Wohlfahrt (eds.): *Handbook of Magnetic Materials*, Vol. 1 (Elsevier, Amsterdam 1975) 244

37. J. G. Stevens and V. E. Stevens : *Mössbauer Effect Data Index* (Plenum Press, New York 1973) **244**
38. R. Röhlsberger, K. W. Quast, T. S. Toellner, P. Lee, W. Sturhahn, E. E. Alp, and E. Burkel : Phys. Rev. Lett. **87**, 047601 (2001) **244, 246**
39. S. Kraft, J. Stümpel, P. Becker, and U. Kuettgens : Rev. Sci. Instrum. **67**, 681 (1996) **245**
40. C. M. Lederer and V. S. Shirley : *Table of Isotopes*, 7th ed. (John Wiley, New York 1978) **245**
41. R. B. Firestone and V. S. Shirley : *Table of Isotopes*, 8th ed. (John Wiley, New York 1996) **245**
42. S. Kitao, T. Mitsui, and M. Seto : J. Phys. Soc. Jpn. **69**, 683 (2000) **245**
43. S. Ofer, E. Segal, I. Nowik, E. R. Bauminger, L. Grodzins, A. J. Freeman, and M. Schieber : Phys. Rev. **137**, A627 (1965) **245**
44. G. W. Dulaney and A. F. Clifford in : *Mössbauer Effect Methodology*, Vol.5, edited by I. J. Gruverman (Plenum Press, New York 1970), p. 65. **246**
45. A. H. Zaheer, I. B. Liss, N. B. Keck, W. G. Bos, and P. J. Ouseph : J. Inorg. Nucl. Chem. **36**, 2515 (1974) **246**
46. Bruker Analytical GmbH, Rheinstetten, Germany (private communication) **247**
47. A. J. Dianoux, W. Petry, and D. Richter (eds.) : *Proceedings of the International Workshop on Dynamics of Disordered Materials II* (North-Holland, Amsterdam 1993) **248**
48. M. G. Cottam and D. J. Lockwood : *Light Scattering in Magnetic Solids*, (Wiley, New York 1986) **248**
49. P. A. Grünberg : Prog. Surf. Sci. **18**, 1 (1985) **248**
50. W. A. Phillips (ed.) : *Amorphous Solids – Low-Temperature Properties* (Springer, Berlin 1981) **248, 255**
51. V. Elser : Phys. Rev. Lett. **54**, 1730 (1985) **248**
52. J. E. S. Socolar, T. C. Lubensky, and P. J. Steinhardt : Phys. Rev. B **34**, 3345 (1986) **248**
53. J. A. Krumhansl and G. R. Barsch : Proc. of the Internat. Conf. on Martensitic Transformations 1992, p. 25 (Monterey Inst. of Advanced Studies, Carmel 1992) **248**
54. E. E. Alp, W. Sturhahn, and T. S. Toellner : Hyperfine Interact. **125**, 45 (2000) **248, 250**
55. D. P. Siddons, J. B. Hastings, U. Bergmann, F. Sette, and M. Krisch : Nucl. Instrum. Methods Phys. Res. B **103**, 371 (1995) **248**
56. T. S. Toellner, E. E. Alp, W. Sturhahn, T. M. Mooney, X. Zhang, M. Ando, Y. Yoda, and S. Kikuta : Appl. Phys. Lett. **67**, 1993 (1995) **248**
57. R. Röhlsberger : Hyperfine Interact. **125**, 69 (2000) **249, 251, 252, 253, 255**
58. R. Röhlsberger : Hyperfine Interact. **123/124**, 301 (1999) **250**
59. Y. P. Feng, S. K. Sinha, H. W. Deckman, J. B. Hastings, and D. P. Siddons : Phys. Rev. Lett. **71**, 537 (1993) **251**
60. A. Krol, C. J. Sher, and Y. H. Kao : Phys. Rev. B **38**, 8579 (1989) **251**
61. Y. Wang, M. Bedzyk, and M. Caffrey : Science **258**, 775 (1992) **251**
62. A. I. Chumakov, M. V. Zelepukhin, G.V. Smirnov, U. van Bürck, R. Rüffer, R. Hollatz, H. D. Rüter, and E. Gerdau : Phys. Rev. B **41**, 9545 (1990) **256**
63. G. V. Smirnov, U. van Bürck, A. I. Chumakov, A. Q. R. Baron, and R. Rüffer : Phys. Rev. B **55**, 5811 (1997) **256**
64. R. Coussement, S. Cottenier, and C. L'abbé : Phys. Rev. B **54**, 16003 (1996) **256, 257**

65. R. Coussement, J. Odeurs, C. L'abbé, and G. Neyens : Hyperfine Interact. **125**, 113 (2000) **256**, **257**
66. C. L'abbé, R. Coussement, J. Odeurs, E. E. Alp, W. Sturhahn, T. S. Toellner, and C. Johnson : Phys. Rev. B **61**, 4181 (2000) **256**, **257**
67. R. Callens : PhD thesis (Katholieke Universiteit Leuven, 2003) **256**
68. J. Odeurs, R. Coussement, C. L'abbé, G. Neyens, G. R. Hoy, E. E. Alp, W. Sturhahn, T. S. Toellner, and C. Johnson : Hyperfine Interact. **113**, 455 (1998) **257**
69. R. Callens, R. Coussement, C. L'abbé, S. Nasu, K. Vyvey, T. Yamada, Y. Yoda, and J. Odeurs : Phys. Rev. B **65**, 180404 (2002) **257**
70. R. Callens, R. Coussement, T. Kawakami, J. Ladrière, S. Nasu, T. Ono, I. Serdons, K. Vyvey, T. Yamada, Y. Yoda, and J. Odeurs : Phys. Rev. B **67**, 104423 (2003) **257**, **258**, **259**
71. I. Serdons, S. Nasu, R. Callens, R. Coussement, J. Ladrière, T. Kawakami, S. Morimoto, T. Ono, K. Vyvey, T. Yamada, Y. Yoda, and J. Odeurs : Phys. Rev. B **70**, 014109 (2004) **259**
72. A. I. Chumakov, A. Q. R. Baron, R. Rüffer, H. Grünsteudel, H. F. Grünsteudel, and A. Meyer : Phys. Rev. Lett. **76**, 4258 (1996) **259**, **260**
73. E. Burkel : Rep. Prog. Phys. **63**, 171 (2000) **259**
74. A. Q. R. Baron, H. Franz, A. Meyer, R. Rüffer, A. I. Chumakov, E. Burkel, and W. Petry : Phys. Rev. Lett. **79**, 2823 (1997) **260**, **261**, **263**
75. G. V. Smirnov, V. G. Kohn, and W. Petry : Phys. Rev. B **63**, 144303 (2001) **260**, **262**
76. T. Butz : Z. Naturforsch. A **51**, 396 (1996) **263**
77. I. Sergueev, U. van Bürck, A. I. Chumakov, T. Asthalter, G. V. Smirnov, H. Franz, R. Rüffer, and W. Petry : Ann. Report, Technische Universität München, Physik - Dep. E13, 39 (2001); ESRF Highlights 2002. **263**, **266**, **267**
78. A. Q. R. Baron, A. I. Chumakov, R. Rüffer, H. Grünsteudel, H. F. Grünsteudel, and O. Leupold : Europhys. Lett. **34**, 331 (1996) **264**, **266**
79. G. T. Trammell and J. P. Hannon : Phys. Rev. B **18**, 165 (1978); erratum : Phys. Rev. B **19**, 3835 (1979) **264**, **266**
80. M. Seto, S. Kitao, Y. Kobayashi, R. Haruki, Y. Yoda, T. Mitsui, and T. Ishikawa : Phys. Rev. Lett. **91**, 185505 (2003). **264**
81. S. L. Ruby, B. J. Zabransky, and P. A. Flinn : J. Phys. C6 **37**, 745 (1976) **266**, **268**
82. I. Sergueev, U. van Bürck, A. I. Chumakov, T. Asthalter, G. V. Smirnov, H. Franz, R. Rüffer, and W. Petry : ESRF Highlights (2003) **266**, **267**, **268**
83. A. Meyer, H. Franz, J. Wuttke, W. Petry, N. Wiele, R. Rüffer, and C. Hübsch : Z. Phys. B **103**, 479 (1997) **266**, **268**
84. S. Dattagupta : *Relaxation phenomena in condensed matter physics* (Academic Press, Orlando 1987) **266**, **267**
85. S. Dattagupta : Hyperfine Interact. **11**, 77 (1981) **266**

7 Outlook and Perspectives

7.1 Future Synchrotron Radiation Sources

Nuclear resonant scattering has significantly benefitted from the development of third-generation synchrotron radiation sources. This trend will certainly continue with the further evolution of these sources. For that reason, a brief outlook on the future development of synchrotron radiation sources relevant for NRS experiments will be given here.

Third-Generation Sources

An important quantity for NRS experiments is the brilliance of the radiation source. It is the spectral flux per phase space volume defined as

$$B = \frac{F}{4\pi^2 \Sigma_x \Sigma_y \Sigma_{x'} \Sigma_{y'}} , \quad (7.1)$$

where F is the spectral photon flux in photons/(s·0.1% BW); Σ_x and Σ_y are the total photon source sizes in horizontal and vertical direction, respectively. $\Sigma_{x'}$ and $\Sigma_{y'}$ are the total beam divergences in horizontal and vertical direction. Usually, all flux and brilliance values are given for a 0.1% energy bandwidth (BW). The total photon source sizes and divergences are given by the convolution of the sizes σ_x and σ_y and divergences $\sigma_{x'}$ and $\sigma_{y'}$ of the electron beam with the intrinsic radiation characteristics of a single electron. For that reason, the horizontal emittance

$$\varepsilon_x = \sigma_x \sigma_{x'} \quad (7.2)$$

of a storage ring is of crucial importance for the properties of the photon beam. The vertical emittance is given by $\varepsilon_y = \kappa \varepsilon_x$ with the so-called coupling factor κ that depends mainly on the precision of the alignment of the storage ring. Typical values for κ at present synchrotron radiation storage rings are in the range of 0.01. Thus, the lower the emittance of a storage ring, the larger the brilliance of the photon beams. Undulator sources at modern 3rd generation storage rings are very well suited to produce high brilliance due to the small source size and the low divergence of the emitted radiation.

Another important quantity that scales linearly with the brilliance is the coherent flux F_c that is given by

$$F_c = B \left(\frac{\lambda}{2} \right)^2, \quad (7.3)$$

where λ is the photon wavelength. With decreasing divergence, the coherent flux is distributed over a larger spatial range, corresponding to an increase of the transverse coherence length that is given by

$$\xi_{t(x,y)} = \frac{\lambda L}{2\Sigma_{(x,y)}}, \quad (7.4)$$

where L is the distance from the radiation source.

Thus, a low emittance and a correspondingly high brilliance is beneficial for NRS experiments in several ways:

- The efficiency of x-ray optical elements improves with increasing brilliance: The angular acceptance of high resolution crystal optics is better matched due to the low divergence.
- The smaller the source size, the smaller the focal spots to which the radiation can be focused to. Correspondingly, small samples can be illuminated very efficiently and the small beamsize allows one to perform spatially resolved experiments.
- The high coherent flux allows to merge nuclear resonant scattering with coherence applications like speckle interference and correlation spectroscopy.

A significant step towards an improvement in these directions will be made at the storage ring PETRA-III (DESY, Hamburg) that will emerge from an upgrade of the existing PETRA storage ring. 1/8 of the storage ring will be equipped with up to 13 undulators and corresponding experimental stations to become operational in 2009. A comprehensive outline of this new facility can be found in the Technical Design Report (TDR) [1]. Table 7.1 lists a number of the relevant parameters in comparison with existing radiation sources. The main figure of merit is a horizontal emittance of 1 nmrad which is about a factor of 3-4 smaller than that of existing 3rd-generation sources. A striking feature for NRS experiments is a 20-m long undulator. To facilitate count-rate estimates for future experiments, Fig. 7.1 displays the spectral flux delivered by this device through a $1 \times 1 \text{ mm}^2$ aperture in a distance of 40 m from the source.

The X-Ray Free Electron Laser (XFEL)

The interaction of ultrarelativistic electrons traveling through long undulators with the emitted radiation field leads to the generation of very short coherent light pulses with an extremely high brilliance. The underlying mechanism is self-amplified stimulated emission (SASE) [2]: The radiation emitted by the individual electrons overtakes the electrons flying ahead of them. Thus, the electric field of the radiation interacts with these electrons along the way,

Table 7.1. Overview of typical β functions, photon source sizes $\Sigma_{x,y}$ and divergences $\Sigma'_{x,y}$ for various ID positions at PETRA-III compared to other storage rings [1]. The photon source parameters are rms values for a photon energy of 12 keV. To calculate the values for PETRA III, SPring-8 and APS an emittance (coupling) of 1 nmrad (1%), 3.4 nmrad (0.2%) and 3 nmrad (1%) was assumed, respectively (Data taken from [1])

| | β_x [m] | β_y [m] | Σ_x [μm] | Σ_y [μm] | $\Sigma_{x'}$ [μrad] | $\Sigma_{y'}$ [μrad] | ID-length [m] |
|--------------------|------------------|------------------|---------------------------------|---------------------------------|--------------------------------------|--------------------------------------|------------------|
| low- β | 1.3 | 3 | 36 | 6.0 | 28 | 3.7 | 5 |
| high- β | 20 | 2.4 | 141 | 5.5 | 7.7 | 3.8 | 5 |
| 20 m-ID | 16 | 5 | 126 | 7.9 | 8.2 | 2.7 | 20 |
| ESRF low- β | 0.5 | 2.73 | 59 | 8.3 | 90 | 3 | 5 |
| ESRF high- β | 35.2 | 2.52 | 402 | 7.9 | 10.7 | 3.2 | 5 |
| SPring-8 | 22.6 | 5.6 | 277 | 6.4 | 13 | 5 | 4.5 |
| APS | 15.9 | 5.3 | 217 | 12.6 | 15.3 | 5.7 | 4 |

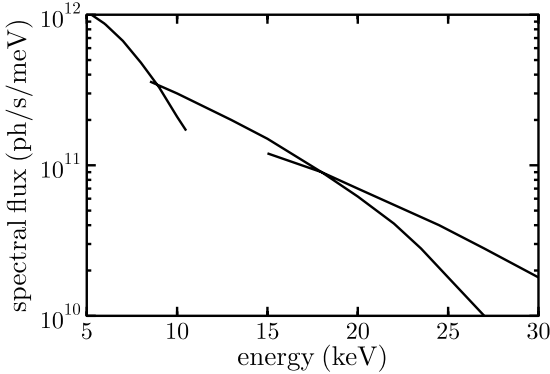


Fig. 7.1. Spectral photon flux as delivered by the 20-m undulator at the planned PETRA-III facility (DESY, Hamburg) through a $1 \times 1 \text{ mm}^2$ pin-hole at 40 m from the source. The lines are tuning curves for the 1st, 3rd and 5th harmonic of the undulator spectrum

accelerating some of them and slowing others down. As a result, the electrons gradually organize themselves into a multitude of thin disks, separated by a distance equal to the wavelength of the emitted radiation. The electron density modulation leads to a higher radiation intensity, and the higher intensity causes stronger density modulation. The result is an exponential growth in the radiation intensity. By the time the electrons reach the end of the undulator, this process has saturated and the layered structure is fully developed, as shown schematically in Fig. 7.2a,b. The key property of this bunch structure is the fact that all electrons in a given layer emit their light in synchrony. This produces extremely short and intense x-ray pulses with the properties of laser light. The realization of this SASE process requires electron bunches

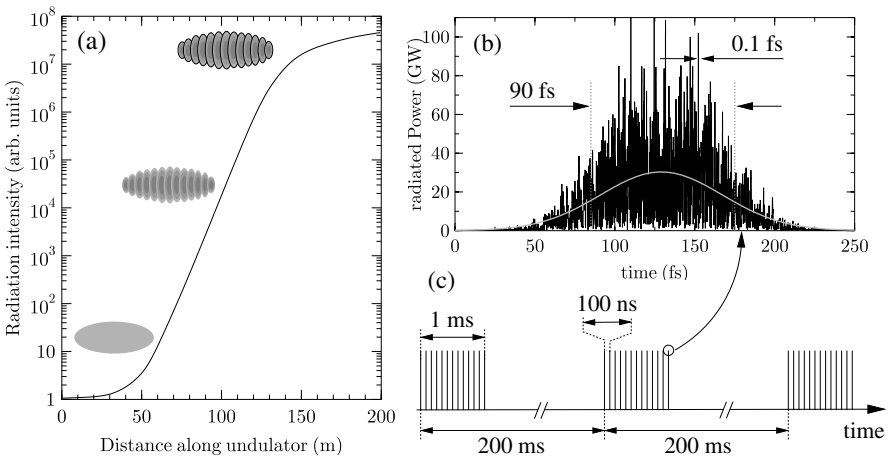


Fig. 7.2. (a) Exponential growth of the radiation intensity and longitudinal microbunching during the SASE process [4]. (b) Temporal structure of the radiation pulse from the SASE XFEL operating at a wavelength of 0.1 nm [5]. The statistical distribution of peak heights is due to the fact that the SASE process starts from noise. The grey solid line marks the average bunch shape. (c) Possible bunch pattern at the XFEL. Each bunch train is about 1 ms long and consists of 10000 bunches with a spacing of 100 ns

with a very small emittance, a high charge density as well as a very accurate magnetic structure in the undulator. While the SASE principle has been demonstrated already for radiation from the visible up to the VUV [3, 4], it is a challenge to push the limit towards shorter and shorter wavelengths into the hard x-ray regime. This is the goal at two sites worldwide, namely the LCLS at SLAC, Stanford (USA) and the European XFEL Laboratory under construction at DESY, Hamburg (Germany). The brilliance of the radiation expected at such sources is shown in Fig. 3.3.

The SASE process leads to an amplification of about 10⁷ in the intensity of the first harmonic of the corresponding undulator radiation. SASE FEL radiation will be available for a wide photon energy range up to 14.4 keV which is relevant for NRS experiments at the resonance of ⁵⁷Fe. Table 7.2 lists the expected flux values for SASE radiation and for spontaneous radiation that are based on the undulator configurations and machine parameters at the XFEL as given in the Technical Design Report [5]. The bandwidth of the SASE line is 0.2% (FWHM) and the radiation is fully transversely coherent. Due to the SASE process the photon bunch length reduces to 90 fs (FWHM) whereas for spontaneous radiation it will be 188 fs. Within these SASE FEL photon bunches a microbunch structure develops with about 1000 spikes of 0.1 fs length. A possible bunch pattern at the XFEL is shown in Fig. 7.2c.

Table 7.2. Parameters for the photon beam at the XFEL obtained from SASE radiation (first column) and spontaneous radiation (second column)

| | | |
|-------------------------|---------------------------------|-------------------|
| Photon energy E | 0.62–14.4 keV | 14–1000 keV |
| Photon wavelength | 10–0.86 Å | 0.85–0.01 Å |
| Photons per bunch | $(0.3\text{--}7.0)\cdot10^{13}$ | $3.5\cdot10^8$ |
| | ph/0.1% BW | ph/0.1% BW |
| Average flux | $(0.2\text{--}4.0)\cdot10^{18}$ | $2.0\cdot10^{13}$ |
| | ph/s/0.1% BW | ph/s/0.1% BW |
| Line width $\Delta E/E$ | 0.2% | few % |
| Bunch length | 90 fs | 188 fs |
| Photon beam size | 66–40 μm | few μm |
| Photon beam divergence | 14–1.8 μrad | few μrad |

Nuclear resonant scattering will benefit from SASE radiation mainly due to the increase in flux compared to present-day sources. The small divergence will be important in experiments using tiny sample volumes, like thin films and high-pressure cells. For the SASE radiation it is expected to obtain about 10000 resonant photons per bunch within the natural linewidth of ^{57}Fe sample, thus a few bunches will provide enough counts for a time spectrum. For inelastic scattering still average count rates of $10^4 \text{ Ph}/\text{meV}$ in the phonon lines can be expected. The short photon bunch length of less than 100 fs will enable measurements of isotopes with very short life times. The time resolution of present day detectors has to be largely improved for these experiments, but experimental methods like the Nuclear Lighthouse Effect can already achieve a time resolution in the picosecond range [6], as explained in Sect. 7.2.2. Due to the short data acquisition times external parameters may be changed at high speed, thus allowing for the investigation of non-equilibrium states. Focusing the beam will enable one to investigate dynamic magnetic properties in thin layers that accompany ordering, reorientation or phase transitions. With the SASE radiation it might be possible to exploit the coherence for nuclear photon correlation spectroscopy.

However, SASE radiation will be useful only for nuclear excitation energies below or equal to 14.4 keV. Higher energy levels have to be excited by radiation out of the continuum of spontaneous emission with its smaller flux. For those cases only applications will benefit which need very high photon energies, the time structure or the brilliance of the radiation.

An obvious problem in the application of high-power SASE radiation for NRS experiments is the monochromatization to a bandwidth of ΔE around the nuclear resonance. While conventional monochromators may not stand the high peak power loads, an elegant solution is a monochromatization already during the SASE process. For this purpose a two-stage SASE FEL

[7] was proposed, consisting of two undulators with a high-resolution x-ray monochromator in-between [8]. This leads to a ‘seeding’ of the amplification process in the second undulator stage that acts as a coherent amplifier of photons at the seeding energy. As a result, one obtains transform-limited pulses with a duration Δt that is determined by the relation $\Delta E \Delta t = h$ with $h = 4.13 \mu\text{eV}\cdot\text{ns}$ being Planck’s constant.

7.2 Elastic Nuclear Resonant Scattering

7.2.1 Lighthouse Filtering

A strong source of unwanted background arises from the small-angle x-ray scattering (SAXS) from the rotor and the sample itself. It has been shown that SAXS can be significantly reduced by the use of single-crystalline materials like Al_2O_3 (sapphire) [6]. An additional effect can be used for background reduction that relies on the spatial displacement of the nuclear exciton during its lifetime. Due to the motion of the nuclear exciton, the radiation sources of the small-angle scattering and the delayed resonant radiation are spatially separated. This is illustrated in Fig. 7.3. While the prompt small-angle scattering arises from point A , the sources of the resonant photons emitted at times t_1 and t_2 are points B_1, B_2 , respectively.

To demonstrate the feasibility of this approach, we want to consider a specific example. We assume a resonant absorber mounted on the circumference of a rotor with a diameter of 10 mm, rotating with a frequency of 3200 Hz, corresponding to a deflection of resonant photons by $20 \mu\text{rad}/\text{ns}$. During a time of 40 ns, corresponding to the position of the strongest quantum beat in the time spectrum of polycrystalline α -Fe, the nuclear exciton is rotated by an angle of 0.8 mrad. This corresponds to a spatial displacement of $4 \mu\text{m}$ at the position of the absorber. Two slits with a width of $1 \mu\text{m}$ and $10 \mu\text{m}$ that are placed behind the rotor as sketched in Fig. 7.3 select radiation from within a 10 ns wide time window. The realization of this setup requires a focusing of the radiation to a spotsize below $1 \mu\text{m}$. This can be achieved at modern high-brilliance synchrotron radiation sources.

7.2.2 Picosecond Time-Resolution

While the time resolution in conventional NFS experiments is in the range of 0.5–1.0 ns, the Nuclear Lighthouse Effect has the potential to go significantly below this limit. This can be achieved by recording the deflected radiation on a spatial scale with a position-sensitive detector (PSD). Because the deflection of resonantly scattered quanta depends only on the time difference between excitation and reemission, the NLE is independent of the time structure of the exciting radiation. Consequently, the time resolution is not even limited by the electron bunch length. Instead, it is determined by geometric effects.

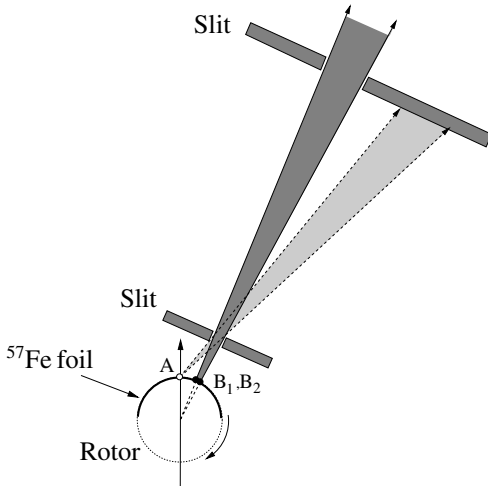


Fig. 7.3. Resonant x-ray scattering from a rotating medium is subject to the Nuclear Lighthouse Effect. The angular deflection of the radiation and the spatial displacement of the nuclear exciton during the rotation can be used to discriminate the resonantly scattered photons from the prompt background that originates from small-angle scattering. The *light-grey* beams represent the non-resonant small-angle scattering from the absorbers. A numerical example is given in the text

Firstly, the transverse coherence length ξ of the radiation introduces a finite resolution function as it is encountered in any diffraction of partially coherent radiation [9]. In case of the NLE, the width of this resolution function on the time scale is given by $\Delta t_i = 1/(k_0 \xi \Omega)$ [10]. Typically, $\xi = \lambda S / (\pi a)$, where S is the distance from the source and a is the source size [11]. Secondly, for an unfocused beam the dominating contribution to the time resolution arises from the finite angular resolution of the setup. It is determined by the angle $\Delta\varphi$ that the beam spot on the detector subtends as seen from the rotor and thus given by $\Delta t_e = \Delta\varphi / \Omega$. This contribution can be significantly decreased by focusing the beam to the detector plane, as shown in Fig. 7.4. In such a focusing scheme, $\Delta\varphi = h/L = a/S$, so that $\Delta t_e = a/(S \Omega)$. Finally, both contributions lead to an effective time resolution of¹:

$$\Delta t \approx \Delta t_i + \Delta t_e = \frac{3}{2} \frac{a}{S \Omega}. \quad (7.5)$$

Typical values at third-generation sources are $a = 60 \mu\text{m}$ and $S = 35 \text{ m}$. At $\Omega/(2\pi) = 15 \text{ kHz}$ we obtain $\Delta t = 27 \text{ ps}$. The time resolution improves the more pointlike the radiation source appears. Thus, in the case of a very long beamline with $S = 1 \text{ km}$, (available at Spring8, Japan), and rotational frequencies up to 35 kHz , time resolutions in the sub-ps range can be expected. Currently, there is no x-ray detector available that could reach such values.

7.2.3 Metrology

The wavelength of the 14.4 keV radiation from ^{57}Fe has been measured with unprecedented precision employing x-ray diffraction in backscattering

¹ It was assumed that the distance between the lens and the rotor is small compared to L , and that the width of the detector resolution function is much smaller than h .

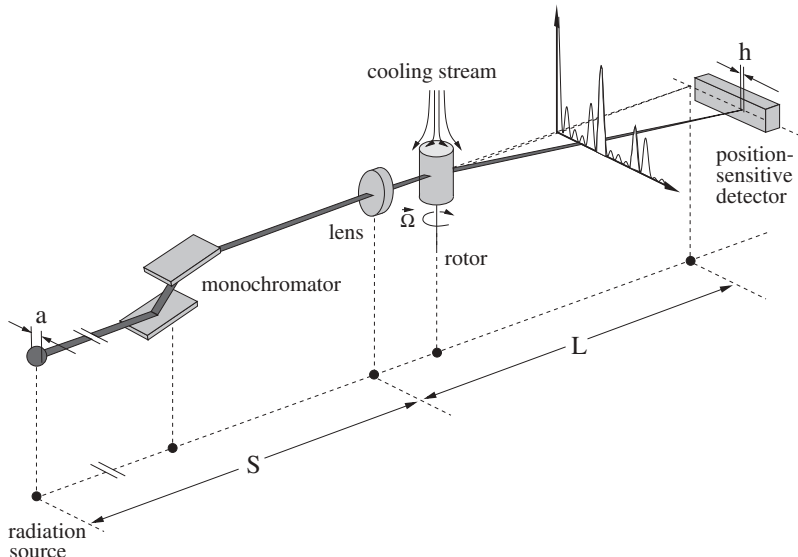


Fig. 7.4. Experimental setup to obtain picosecond time resolution in nuclear resonant scattering by employing the Nuclear Lighthouse Effect. The radiation is focused to the plane of a position-sensitive detector (PSD)

geometry [12]. Radiation resonantly scattered from ^{57}Fe thus provides a length standard for atomic scales because it can be reproduced with extreme accuracy. Nuclear resonant scattering from a rotating sample offers a convenient way to reproduce such a length standard. It has to be ensured, however, that the deflected radiation does not suffer a Doppler shift due to the high linear velocity of the rotating foil. This can be achieved by passing the beam exactly through the center of the rotor, which can be mechanically realized via an aperture in the stator with an accuracy better than $10\text{ }\mu\text{m}$. In the present experimental arrangement the energy uncertainty would be less than $30\text{ }\mu\text{eV}$, which is sufficient for reproduction of the wavelength. This procedure can be easily applied to other isotopes.

7.3 Inelastic Nuclear Resonant Scattering

7.3.1 Nuclear Inelastic Pump-Probe Experiments

A unique future application of inelastic nuclear resonant scattering will be the field of time-resolved (non-equilibrium) lattice dynamics: Since the incoherent signal reflects the phonon occupation number *at the very moment of excitation* this method is very suitable to be applied in pump-probe experiments, as sketched in Fig 7.5. A pump pulse creates a high occupation

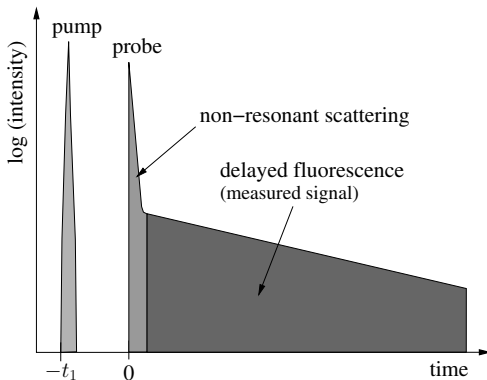


Fig. 7.5. Inelastic nuclear resonant scattering in a pump-probe arrangement. If a pump pulse hits the sample at a time $-t_1$, the x-ray pulse probes the phonon states that have developed during the time interval between pump and probe pulse

number of phonons, where the coupling mechanism is crucial for the spectral distribution of the phonons and their corresponding lifetime: A simple heat pulse will create thermal phonons with lifetimes in the ps range or below. Highly monochromatic phonons with lifetimes of several 100 ns can be created by coupling the laser pulse to impurity resonances that decay via electronic relaxation [13]. The decay of such non-equilibrium phonon states provides valuable information about the thermal transport properties of the sample.

The spectral and temporal evolution of these phonon states can be determined as follows: If the photon energy of the probe pulse is tuned around the nuclear resonance for a fixed delay between pump and probe pulses, one obtains the phonon spectrum that has developed during this time interval. On the other hand, tuning the time delay between the pump and probe pulse at a fixed off-resonance x-ray energy allows one to monitor the time evolution of particular vibrational states. The time resolution is given by the length of the pulse. It should be noted, though, that energy resolution ΔE and time resolution Δt are mutually transform-limited, related by the condition $\Delta E \Delta t > \hbar = 0.66 \text{ meV} \cdot \text{ps}$. Thus, using a meV monochromator, it should be possible to study non-equilibrium lattice dynamics on a ps time scale. For this purpose, however, conventional synchrotron radiation sources are not suited anymore. Instead, x-ray free electron lasers (XFEL) based on linear accelerators with SASE undulators are promising candidates to deliver femtosecond pulses of x-rays (see Sect. 7.1). Time resolutions well below 1 ps can be obtained by relaxing the energy resolution, taking full advantage of the short-pulse time structure of such XFELs. An immediate application would be the study of the dynamics of heat-transfer on nanoscopic length scales, for example. Due to the isotopic sensitivity of the absorption process an extremely high spatial resolution can be obtained by the use of probe layers, making this technique a rather unique application of the XFEL.

References

1. K. Balewski, W. Brefeld, W. Decking, H. Franz, R. Röhlsberger and E. Weckert (eds.) : *PETRA III: A Low-Emissance Synchrotron Radiation Source*, Technical Design Report (DESY 2004-035) 2004 **274**, **275**
2. A. M. Kondratenko and E. L. Saldin : Part. Accel. **10**, 207 (1980) **274**
3. V. Ayvazyan et al. : Phys. Rev. Lett. **88**, 104802 (2002) **276**
4. S. V. Milton et al. : Science **292**, 2037 (2001) **276**
5. TESLA Technical Design Report, Part V: The X-ray Free Electron Laser, edited by G. Materlik and Th. Tschentscher (DESY 2001 - 011, ECFA 2001 - 209, TESLA Report 2001 - 23, TESLA - FEL 2001 - 05) **276**
6. R. Röhlsberger, K. W. Quast, T. S. Toellner, P. Lee, W. Sturhahn, E. E. Alp, and E. Burkel : Phys. Rev. Lett. **87**, 047601 (2001) **277**, **278**
7. J. Feldhaus, E. L. Saldin, J. R. Schneider, E. A. Schneidmiller, and M. V. Yurkov : Opt. Commun. **140**, 341 (1997) **278**
8. E. L. Saldin, E. A. Schneidmiller, Yu. V. Shvyd'ko, and M. V. Yurkov : Nucl. Instrum. Methods Phys. Res. A **475**, 357 (2001) **278**
9. S. K. Sinha, M. Tolan, and A. Gibaud : Phys. Rev. B **57**, 2740 (1998) **279**
10. R. Röhlsberger, T. S. Toellner, W. Sturhahn, K. W. Quast, E. E. Alp, A. Bernhard, E. Burkel, O. Leupold, and E. Gerdau : Phys. Rev. Lett. **84**, 1007 (2000) **279**
11. E. Hecht : *Optics*, 3rd ed. (Addison - Wesley, New York 1998), p. 569. **279**
12. Yu. V. Shvyd'ko, M. Lerche, J. Jäschke, M. Lucht, E. Gerdau, M. Gerken, H. D. Rüter, H. C. Wille, P. Becker, E. E. Alp, W. Sturhahn, J. Sutter, and T. S. Toellner : Phys. Rev. Lett. **85**, 495 (2000) **280**
13. W. A. Tolbert, W. M. Dennis, and W. M. Yen : Phys. Rev. Lett. **65**, 607 (1990) **281**

8 Concluding Remarks

Advanced x-ray scattering techniques will play an important role for the characterization of materials with increasing degree of complexity. This does not only apply for structural and electronic properties but also for dynamical properties that often constitute the basis for new functionalities. The enormous brilliance of modern synchrotron radiation sources has opened new avenues for the characterization of low-dimensional systems like thin films and nanoparticles. In this field, nuclear resonant scattering enjoys a growing interest with applications in many disciplines of natural sciences. It is the virtue of this technique to probe magnetic order as well as dynamical properties in basically the same experimental setup. The use of isotopic probe layers, for example, allows one to determine these properties with very high spatial resolution; focusing techniques and x-ray interference effects lead to a very high sensitivity for smallest amounts of material. Therefore, the method becomes more and more powerful with increasing brilliance of modern synchrotron radiation sources.

This book was intended to give a basic introduction into this technique and to review particular applications as well as new developments. Special emphasis was given to the field of low-dimensional systems like thin films, small particles and clusters as well as high-pressure physics, diffusion and relaxation phenomena. This includes aspects like magnetism as well as lattice dynamics and thermoelastic properties. It can be expected that research will continue and intensify in these areas.

The coherence of the scattering process and the narrow resonance width imply a high sensitivity to atomic motion. On the one hand, the corresponding dephasing and loss of coherence can be used as an indicator for dynamical processes in the sample like diffusion or relaxation phenomena. On the other hand, controlled atomic motion like rotation can be used to manipulate the scattered radiation. This led to the discovery of the *Nuclear Lighthouse Effect*. The lighthouse effect should be observable for any medium in which the group velocity of light is sufficiently low; therefore it is not restricted to nuclear resonances. This may trigger ideas for applications of the effect in other areas.

Finally, the small natural linewidth of Mössbauer transitions allows the development of spectrometers for μeV -resolved x-ray spectroscopy. First

prototypes have been developed and characterized. However, in all these methods the available flux is limited by the narrow bandwidth of the scattered radiation. For that reason, such spectroscopies will require the strongest available x-ray sources. Unfortunately, for x-rays there is presently no technique available that decouples the energy resolution of the scattering process from the bandwidth of the incident radiation, as in the technique of neutron spin-echo. Since it has not been proven that similar techniques are not possible for x-rays, one should not stop to think of unconventional and exotic experiments. Any finding in that direction can open new areas for fascinating research in the future.

A Appendix

A.1 Hyperfine Interactions

This section deals with the calculation of the energy eigenvalues of the nuclear hyperfine interaction that are required for determination of the nuclear scattering amplitude $\mathbf{N}(\omega)$ in (4.12), (4.14), (4.15) and the functions $F_M(\omega)$ in (4.78).

The energies $E_n = \hbar\omega_n$ and the eigenstates $|\varepsilon\phi_n\rangle$ of the ground and excited states of the Mössbauer nuclei, which are needed for the evaluation of the matrix elements of the nuclear scattering operator, are determined by the hyperfine interactions of the nuclei. Here ε has been introduced to denote the set of electronic quantum numbers. In terms of the eigenstates, the Hamilton operator of the system is diagonal:

$$\langle\varepsilon\phi_n|\mathbf{H}_{em}|\varepsilon'\phi_{n'}\rangle = \delta_{\varepsilon\varepsilon'}\delta_{nn'}E_{\varepsilon n}. \quad (\text{A.1})$$

The Hamilton operator \mathbf{H}_{em} of the electromagnetic interaction between the nucleus and the electrons is given by

$$\mathbf{H}_{em} = -\frac{e^2}{c^2} \int \frac{\tilde{\mathbf{J}}_e(\mathbf{r}) \cdot \tilde{\mathbf{J}}_n(\mathbf{r}')}{|\mathbf{r} - \mathbf{r}'|} d^3r d^3r'. \quad (\text{A.2})$$

$\tilde{\mathbf{J}}_e$ and $\tilde{\mathbf{J}}_n$ are the 4-vectors of the electronic and nuclear current density. Since the nuclear states are superpositions of states with well defined spin, it is useful to perform a multipole expansion of $1/|\mathbf{r} - \mathbf{r}'|$. The result is:

$$\mathbf{H}_{em} = \mathbf{H}_0 + \mathbf{H}^{(0)} + \sum_{L>0} \mathbf{H}^{(L)} \quad (\text{A.3})$$

$$\text{with } \mathbf{H}^{(L)} = e \sum_M (-1)^M \tilde{\mathbf{Q}}_{L,M} \cdot \tilde{\mathbf{V}}_{L,-M}. \quad (\text{A.4})$$

\mathbf{H}_0 and $\mathbf{H}^{(0)}$ are contributions to the Hamiltonian which do not depend on the nuclear quantum numbers. They arise from the Coulomb interaction between the nuclear and the electronic charge. \mathbf{H}_0 represents the Coulomb interaction for the nucleus being a point charge. Since this is the same for all nuclear levels, it cannot be observed in a Mössbauer experiment and will therefore be omitted in the following considerations. $\mathbf{H}^{(0)}$ originates in evaluation of the $L = 2$ term in the multipole expansion. It describes the electric monopole

interaction which arises due to the spatial extent of the nucleus. Since in general the nuclear size is different for the ground and excited states, a shift in the transition energy appears, the isomer shift.

$\tilde{\mathbf{Q}}_{L,M}$ is the tensor operator of the nuclear multipole moments and $\tilde{\mathbf{V}}_{L,-M}$ is the tensor operator of the external fields, which arise from the surrounding electrons. Since $\tilde{\mathbf{Q}}_{L,M}$ and $\tilde{\mathbf{V}}_{L,-M}$ are operators in 4-vector representation, each $\mathbf{H}^{(L)}$ consists of an electrostatic and a magnetostatic part. Because the nuclear states are states of well defined parity, the expectation values of the electrostatic multipole moments with odd L and the magnetostatic multipole moments with even L vanish. Furthermore, the coupling rules of the angular momenta contained in the Clebsch-Gordan coefficients imply that the multipole moments are restricted to orders $L \leq 2I_n$ where I_n is the nuclear spin. Nuclei like ^{57}Fe and ^{119}Sn have a spin of $I_n = 1/2$ in the ground state and a spin of $I_n = 3/2$ in the excited state. The magnetic octupole moments which are possible in the excited state are too small to give rise to a significant contribution and will be neglected.

Since the hyperfine splitting of the nuclear levels has only minor influence on the electronic wavefunctions, \mathbf{H}_{em} is already diagonal with respect to the electronic quantum numbers. For solution of the eigenvalue problem (A.2), we need to calculate the matrix elements of the magnetic dipole interaction and the electric quadrupole interaction. The magnetic dipole interaction arises from the interaction of the nuclear magnetic moment μ_n with the magnetic hyperfine field \mathbf{B}_{hf} at the site of the nucleus. The matrix elements are given by

$$\langle \varepsilon I_n m | \mathbf{H}^{(1)} | \varepsilon I_n m' \rangle = -\mu_n B_{hf} (-1)^{m-m'} \frac{C(I_n 1 I_n; m, m' - m)}{C(I_n 1 I_n; I_n 0)} \times \mathcal{D}_{0,m-m'}^{(1)}(0, \theta, \varphi), \quad (\text{A.5})$$

where the rotation matrices $\mathcal{D}_{mm'}^{(L)}$ are used in the nomenclature of Rose [1].

The polar angle θ and the azimuthal angle φ define the orientation of \mathbf{B}_{hf} relative to the quantization system of the nuclear spins. If $\theta = 0$, i.e. the nuclear quantization system coincides with the direction of \mathbf{B}_{hf} , the Hamilton operator of the magnetic interaction diagonalizes with $\langle \varepsilon I_n m | \mathbf{H}^{(1)} | \varepsilon I_n m' \rangle = -\delta_{mm'} m \mu_n B_{hf} / I_n$.

The electric quadrupole interaction is caused by the interaction of the nuclear quadrupole moment Q_n with the electric field gradient (EFG) at the nucleus. The EFG tensor is a tensor of rank 2. After transformation into the system of principal axes, it is usually characterized by the largest principal axes element V_{zz} and the asymmetry parameter $\eta = (V_{xx} - V_{yy})/V_{zz}$, where $V_{\mu\mu} = \partial^2 V / \partial \mu^2$. The matrix element of the electric quadrupole interaction is given by

$$\langle \varepsilon I_n m | \mathbf{H}^{(2)} | \varepsilon I_n m' \rangle = \frac{eQ_n V_{zz}}{2} (-1)^{m-m'} \frac{C(I_n 2I_n; m, m' - m)}{2C(I_n 2I_n; I_n 0)} \times \\ \left[\mathcal{D}_{0,m-m'}^{(2)}(\alpha, \beta, \gamma) + \frac{\eta}{\sqrt{6}} [\mathcal{D}_{2,m-m'}^{(2)}(\alpha, \beta, \gamma) + \mathcal{D}_{-2,m-m'}^{(2)}(\alpha, \beta, \gamma)] \right]. \quad (\text{A.6})$$

The Euler angles (α, β, γ) transform the system of principal axes of the EFG into the nuclear quantization system.

Written for convenience in matrix form, the eigenvalue equation (A.1) appears now to be:

$$\hat{U} \hat{H} \hat{U}^* = \hat{D}, \quad (\text{A.7})$$

where the matrices \hat{D} , \hat{U} and \hat{H} are given by

$$[\hat{D}]_{mj} = \delta_{mj} (E_{nj} - E_n^{(0)}) \\ [\hat{U}]_{mj} = \langle m | \phi_{nj} \rangle \\ [\hat{H}]_{mm'} = \langle \varepsilon I_n m | \mathbf{H}^{(1)} | \varepsilon I_n m' \rangle + \langle \varepsilon I_n m | \mathbf{H}^{(2)} | \varepsilon I_n m' \rangle, \quad (\text{A.8})$$

where $E_n^{(0)} = \langle \varepsilon I_n m | \mathbf{H}^{(0)} | \varepsilon I_n m' \rangle$. The dimension of these matrices is $2I_n + 1$. The index j , which runs from $-I_n$ to I_n , labels the $2I_n + 1$ energy eigenvalues E_{nj} and the eigenvectors $|\phi_{nj}\rangle$. Since \hat{H} is hermitian, the diagonalizing matrix \hat{U} is unitary. The column vectors of \hat{U} contain the components of $|\phi_{nj}\rangle$ in the basis formed by the eigenstates $|m\rangle$ of the spin projection operator:

$$|\phi_{nj}\rangle = \sum_m |m\rangle [\hat{U}]_{mj}. \quad (\text{A.9})$$

The diagonalization problem can be solved analytically only in a few cases:

- For nuclear states with $I_n = 1/2$, which exhibit no quadrupole moment or for the states with $I_n > 1/2$ and vanishing EFG at the nucleus we obtain:

$$E_{nj} = E_n^{(0)} - \mu_n B_{hf} \frac{j}{I_n} \quad (\text{A.10})$$

$$\text{and } \langle m | \phi_{nj} \rangle = \mathcal{D}_{jm}^{(I_n)}(0, \theta, \varphi)$$

- If the EFG is axially symmetric and the magnetic hyperfine interaction vanishes, the solution is:

$$E_{nj} = E_n^{(0)} + \frac{eQ_n V_{zz}}{2} \frac{3j^2 - I_n(I_n + 1)}{2I_n(2I_n - 1)} \quad (\text{A.11})$$

$$\text{and } \langle m | \phi_{nj} \rangle = \mathcal{D}_{jm}^{(I_n)}(\alpha, \beta, \gamma)$$

- An analytic solution also appears in the special case that \mathbf{B}_{hf} is aligned parallel to the main axis of the EFG with $\eta = 0$, like in Fe₂O₃:

$$E_{nj} = E_n^{(0)} - \mu_n B_{hf} \frac{j}{I_n} + \frac{eQ_n V_{zz}}{2} \frac{3j^2 - I_n(I_n + 1)}{2I_n(2I_n - 1)} \quad (\text{A.12})$$

$$\text{and } \langle m | \phi_{nj} \rangle = \mathcal{D}_{jm}^{(I_n)}(0, \theta, \varphi) \quad (\text{A.13})$$

In general, the diagonalization problem has to be solved numerically. A very efficient algorithm has been developed by Eberlein [2].

A.2 Structure Function and Propagation Matrix

The purpose of this section is the derivation of the propagation matrix \mathbf{F} that was introduced in (4.6). This matrix describes how the field amplitudes in depth $z + dz$ are related to the amplitudes in depth z . The solution of this problem goes back to the propagation equation

$$\mathbf{A}_S(\mathbf{k}) = -c \frac{\delta_+(k)}{(2\pi)^3} \int \mathbf{M}(\mathbf{k}, \mathbf{k}') \mathbf{A}_0(\mathbf{k}') d\mathbf{k}' . \quad (\text{A.14})$$

The scattering process from the incident wavevector \mathbf{k}' to the outgoing wavevector \mathbf{k} can be read from right to left: The incident wave $\mathbf{A}_0(\mathbf{k}')$ hits the sample that is described by the total scattering amplitude $\mathbf{M}(\mathbf{k}, \mathbf{k}')$. The integral sums over all possible paths, and finally the outgoing wave is described by the photon propagator $\delta_+(k)$:

$$\delta_+(k) = -\frac{4\pi c}{\omega_0^2 - k^2 c^2 + i\varepsilon} . \quad (\text{A.15})$$

The first step is now the calculation of the scattering amplitude $\mathbf{M}(\mathbf{k}, \mathbf{k}')$ of the sample. Lets assume the sample to consist of identical atoms which are characterized by the atomic scattering amplitude $\mathcal{M}(\mathbf{k}, \mathbf{k}')$. Each outgoing wave carries the geometrical phase factor $e^{i(\mathbf{k}' - \mathbf{k})\mathbf{R}_j}$ which accounts for the position \mathbf{R}_j of the atom in space. The scattering amplitude of the whole sample is then given by a coherent sum over the scattered waves from all atoms:

$$\mathbf{M}(\mathbf{k}, \mathbf{k}') = S(\mathbf{k}' - \mathbf{k}) \mathcal{M}(\mathbf{k}, \mathbf{k}') \quad (\text{A.16})$$

$$\text{with } S(\mathbf{k}' - \mathbf{k}) = \sum_j e^{i(\mathbf{k}' - \mathbf{k})\mathbf{R}_j} .$$

All information about the arrangement of the atoms is contained in the structure function $S(\mathbf{q}) = S(\mathbf{k} - \mathbf{k}')$. Assuming that the atoms are continuously distributed in space, like in a disordered sample, the sum in (A.16) can be converted into an integration over the volume V of the scatterer:

$$S(\mathbf{q}) = \int_V \varrho(\mathbf{r}) e^{i\mathbf{q} \cdot \mathbf{r}} d^3r , \quad (\text{A.17})$$

where $\varrho(\mathbf{r})$ is the number density of the atoms. Thus, the structure function appears to be the Fourier transform of the atomic density. From this relationship one can derive a very handy physical interpretation: If one multiplies (A.17) with $i\mathbf{q}$, observes that $i\mathbf{q}e^{i\mathbf{q} \cdot \mathbf{r}} = \text{grad}_r(e^{i\mathbf{q} \cdot \mathbf{r}})$ and integrates by parts, taking into account that $\varrho(\mathbf{r}) = 0$ outside the scatterer, one obtains:

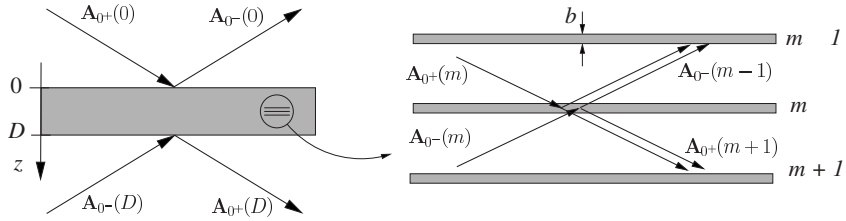


Fig. A.1. Wavefields in the dynamical theory of X-ray diffraction. The task is to determine the field amplitudes $A_{0-}(0)$ and $A_{0+}(D)$ under the boundary conditions $A_{0+}(0) = A_0$ and $A_{0-}(D) = 0$. This problem is solved by subdividing the layer into thin platelets of thickness b and to sum up the scattered waves from all platelets

$$S(\mathbf{q}) = -\frac{1}{i\mathbf{q}} \int_V [\mathbf{u}_q \cdot \text{grad}_r \varrho(\mathbf{r})] e^{i\mathbf{q} \cdot \mathbf{r}} d^3 r, \quad (\text{A.18})$$

with $q = |\mathbf{q}|$ and $\mathbf{u}_q = \mathbf{q}/q$. This expression shows that contributions to the structure function are generated by gradients in the atomic density. These contributions are largest if the density gradient is parallel to the scattering vector \mathbf{q} . The proportionality to $1/q$ reveals that in the case of x-ray scattering from disordered samples, significant values of $S(\mathbf{q})$ can only be expected at grazing angles of incidence $\varphi \ll 1$, where $q \approx 2k_0\varphi$. Under these conditions the scattered field reaches the magnitude of the incident field and multiple scattering cannot be neglected. The 1st-order Born approximation is no longer valid. For solution of this problem it is a recommended recipe to divide the scatterer into pieces for which the 1st-order Born approximation is valid and sum up the contributions of all these pieces. In the following we want to calculate the scattering from thin film structures.

We start with a single film of thickness D as shown in Fig. A.1, and divide it into M platelets of infinitesimal thickness b ($D = Mb$) and homogenous density $\varrho(\mathbf{r}) = \varrho$ which are extending to infinity in the in-plane directions.

The structure function of such a platelet is given by

$$S(\mathbf{q}) = \varrho \int_{-\infty}^{\infty} dx dy e^{i\mathbf{q}_{xy} \cdot \mathbf{r}} \int_0^b dz e^{iq_z z} = (2\pi)^2 \varrho \delta^2(\mathbf{q}_{xy}) \frac{e^{iq_z b} - 1}{iq_z} \quad (\text{A.19})$$

$$\text{with } \mathbf{q}_{xy} = \mathbf{k}_{xy} - \mathbf{k}'_{xy} \quad \text{and} \quad q_z = k_z - k'_z.$$

Very often the incident wave is to a good approximation a plane wave:

$$\mathbf{A}_0(\mathbf{k}') = (2\pi)^3 \delta^3(\mathbf{k}' - \mathbf{k}_0) \mathbf{A}_0. \quad (\text{A.20})$$

After inserting (A.16), (A.19), and (A.20) into (A.14), one obtains the following expression for the scattered wave in phase space:

$$\mathbf{A}_S(\mathbf{k}) = -c(2\pi)^2 \delta_+(k, \omega_0) \delta^2(\mathbf{q}_{xy}) \frac{e^{iq_z b} - 1}{iq_z} \varrho \mathcal{M}(\mathbf{k}, \mathbf{k}_0) \mathbf{A}_0. \quad (\text{A.21})$$

The scattered wave in real space is obtained by Fourier transformation of (A.21):

$$\mathbf{A}_S(\mathbf{r}) = \frac{1}{(2\pi)^3} \int d^3 k \mathbf{A}_S(\mathbf{k}) e^{i\mathbf{k}\cdot\mathbf{r}}. \quad (\text{A.22})$$

The integration over the δ -distributions is easy to perform and the remaining integral over k_z is solved via the residue theorem. The two poles of the photon propagator lead to two solutions for $z > 0$ (below the platelet) and $z < 0$ (above the platelet). These solutions correspond to a transmitted wave in forward direction (the 0^+ channel), and a reflected wave in specular direction (the 0^- channel). The wave in forward direction reads:

$$\mathbf{A}_{0+}(\mathbf{r}) = e^{i\mathbf{k}_{0+}\cdot\mathbf{r}} (\mathbf{1} + i b \mathbf{f}_{0+0+}) \mathbf{A}_0$$

$$\text{with } \mathbf{f}_{0+0+} := \frac{\varrho}{k_{0+z}} \mathcal{M}(\mathbf{k}_{0+}, \mathbf{k}_{0+}) \quad (\text{A.23})$$

and the wave in the specular direction reads:

$$\mathbf{A}_{0-}(\mathbf{r}) = e^{i\mathbf{k}_{0-}\cdot\mathbf{r}} i b \mathbf{f}_{0-0-} \mathbf{A}_0$$

$$\text{with } \mathbf{f}_{0-0-} := \frac{\varrho}{k_{0-z}} \frac{e^{2ik_{0-z}b} - 1}{2ik_{0-z}b} \mathcal{M}(\mathbf{k}_{0-}, \mathbf{k}_{0+}) \quad (\text{A.24})$$

$\mathbf{k}_{0+} =: (k_{0x}, k_{0y}, k_{0z}) = \mathbf{k}_0$ is the photon wavevector in the 0^+ channel and $\mathbf{k}_{0-} =: (k_{0x}, k_{0y}, -k_{0z})$ the photon wavevector in the 0^- channel. The (2×2) matrices \mathbf{f}_{0+0+} and \mathbf{f}_{0-0-} describe the scattering from the incident 0^+ channel into the 0^+ and 0^- channels, respectively. $\mathbf{1}$ is the (2×2) unit matrix. If we look at three subsequent boundaries within the layer, we find the situation that is sketched in Fig. A.1: The waves $\mathbf{A}_{0+}(m)$ and $\mathbf{A}_{0-}(m)$ are incident upon platelet m . Each of these incident waves generates two waves traveling in the 0^+ and 0^- channels that arrive at platelets $(m-1)$ and $(m+1)$, respectively. The response to the incident field $\mathbf{A}_{0+}(m)$ is given by (A.23) and (A.24). The response to the incident field $\mathbf{A}_{0-}(m)$ is obtained by exchanging 0^+ and 0^- channels in (A.23) and (A.24). Both contributions in the outgoing channels are added to result in:

$$\mathbf{A}_{0+}(m+1) = e^{ik_{0+z}b} \{ (\mathbf{1} + i b \mathbf{f}_{0+0+}) \mathbf{A}_{0+}(m) + i b \mathbf{f}_{0+0-} \mathbf{A}_{0-}(m) \} \quad (\text{A.25})$$

$$\mathbf{A}_{0-}(m-1) = e^{-ik_{0-z}b} \{ (\mathbf{1} - i b \mathbf{f}_{0-0-}) \mathbf{A}_{0-}(m) - i b \mathbf{f}_{0-0+} \mathbf{A}_{0+}(m) \},$$

where we have dropped the phase factor $e^{i\mathbf{k}_{0xy}\cdot\mathbf{r}}$. In the continuous limit $b \rightarrow 0$, i.e. $k_{0z}b \ll 1$, we expand the exponentials, make the substitutions $\mathbf{A}_{0\pm}(m) \rightarrow \mathbf{A}_{0\pm}(z)$, $\mathbf{A}_{0\pm}(m \pm 1) \rightarrow \mathbf{A}_{0\pm}(z \pm b)$ and expand the last expression around z . Then the system of coupled difference equations converts into a system of coupled differential equations:

$$\begin{aligned}\frac{d\mathbf{A}_{0+}(z)}{dz} &= i [(\mathbf{f}_{0+0+} + \mathbf{k}_{0z})\mathbf{A}_{0+}(z) + \mathbf{f}_{0+0-}\mathbf{A}_{0-}(z)] \\ \frac{d\mathbf{A}_{0-}(z)}{dz} &= i [\mathbf{f}_{0-0+}\mathbf{A}_{0+}(z) + (\mathbf{f}_{0-0-} - \mathbf{k}_{0z})\mathbf{A}_{0-}(z)],\end{aligned}\quad (\text{A.26})$$

with $\mathbf{k}_{0z} = k_{0z} \mathbf{1}$. By combining $\mathbf{A}_{0+}(z)$ and $\mathbf{A}_{0-}(z)$ into one vector \mathbf{A} , these equations can be written in matrix style:

$$\frac{d\mathbf{A}(z)}{dz} = i\mathbf{F}\mathbf{A}(z) \quad \text{with} \quad \mathbf{F} = \begin{pmatrix} \mathbf{f}_{0+0+} + \mathbf{k}_{0+z} & \mathbf{f}_{0+0-} \\ \mathbf{f}_{0-0+} & \mathbf{f}_{0-0-} + \mathbf{k}_{0-z} \end{pmatrix}. \quad (\text{A.27})$$

This is (4.24) in Sect. 4.1 if one observes that $\mathbf{k}_{0+z} = -\mathbf{k}_{0-z} = \mathbf{k}_{0z}$ and the scattering matrices $\mathbf{f}_{ss'}$ are replaced by the forward scattering matrix \mathbf{f} .

A.3 Calculation of the Matrix Exponential $e^{i\mathbf{F}z}$

This section outlines the calculation of the matrix exponential $e^{i\mathbf{F}z}$ from its introduction in (4.24) to its evaluation in (4.29). The matrix exponential relates the field amplitudes in depth z to the field amplitudes at the surface of a layer system ($z = 0$):

$$\mathbf{A}(z) = e^{i\mathbf{F}z} \mathbf{A}(0) \quad \text{with} \quad \mathbf{F} = \begin{pmatrix} \mathbf{f} + \mathbf{k}_{0z} & \mathbf{f} \\ -\mathbf{f} & -\mathbf{f} - \mathbf{k}_{0z} \end{pmatrix}. \quad (\text{A.28})$$

The matrix \mathbf{F} is a (4×4) matrix with the (2×2) submatrices \mathbf{f} and \mathbf{k}_{0z} :

$$\mathbf{f} = \begin{pmatrix} f_{xx} & f_{xy} \\ f_{yx} & f_{yy} \end{pmatrix} \quad \text{and} \quad \mathbf{k}_{0z} = \begin{pmatrix} k_{0z} & 0 \\ 0 & k_{0z} \end{pmatrix}, \quad (\text{A.29})$$

where k_{0z} is the z -component of the incident wavevector. The particular symmetry of the (4×4) matrix \mathbf{F} allows one to reduce this problem to the calculation of a (2×2) matrix exponential, as will be shown in the following.

As a first step, one transforms into the system of eigenpolarizations. This proceeds by diagonalization of the scattering amplitude matrix \mathbf{f} :

$$\mathbf{f} = \mathbf{g} \mathbf{f}_D \mathbf{g}^{-1}. \quad (\text{A.30})$$

The eigenvalues of \mathbf{f} are given by

$$f_{I,II} = \frac{1}{2}(f_{xx} + f_{yy}) \pm \frac{1}{2}\sqrt{(f_{xx} - f_{yy})^2 + 4f_{xy}f_{yx}}. \quad (\text{A.31})$$

The eigenpolarizations are the eigenvectors of \mathbf{f} . They are given by the column vectors of the diagonalizing matrix \mathbf{g} :

$$\mathbf{g}_{I,II} = \frac{1}{\sqrt{1 + |(f_{I,II} - f_{xx})/f_{xy}|^2}} \begin{pmatrix} 1 \\ \left[\frac{f_{I,II} - f_{xx}}{f_{xy}} \right] \end{pmatrix}. \quad (\text{A.32})$$

The eigenvalues of \mathbf{f} are the scattering amplitudes for the eigenpolarizations. Note, that f_I and f_{II} are independent of the choice of the special orthogonal basis, in which \mathbf{f} is represented. The matrix \mathbf{g} is now used to convert the matrix \mathbf{F} into blockdiagonal shape:

$$\mathbf{F}_D = \begin{pmatrix} \mathbf{g}^{-1} & 0 \\ 0 & \mathbf{g}^{-1} \end{pmatrix} \begin{pmatrix} \mathbf{f} + \mathbf{k}_{0z} & \mathbf{f} \\ -\mathbf{f} & -\mathbf{f} - \mathbf{k}_{0z} \end{pmatrix} \begin{pmatrix} \mathbf{g} & 0 \\ 0 & \mathbf{g} \end{pmatrix}.$$

Thus, \mathbf{F}_D can be written as direct product of two (2×2) matrices, as indicated by the dotted lines in the following equation:

$$\mathbf{F}_D = \mathcal{F}_I \times \mathcal{F}_{II} = \begin{pmatrix} f_I + k_{0z} & \cdots & 0 & \cdots & f_I & 0 \\ \vdots & & & & \vdots & \\ 0 & & f_{II} + k_{0z} & & 0 & f_{II} \\ \vdots & & & & \vdots & \\ -f_I & \cdots & 0 & \cdots & -f_I - k_{0z} & 0 \\ 0 & & -f_{II} & & 0 & -f_{II} - k_{0z} \end{pmatrix}. \quad (\text{A.33})$$

This means, that the eigenpolarizations are decoupled from each other and can be treated independently by (2×2) matrices of the following shape:

$$\mathcal{F} = \begin{pmatrix} f + k_{0z} & f \\ -f & -f - k_{0z} \end{pmatrix} \quad \text{with } f = f_I, f_{II}. \quad (\text{A.34})$$

The two eigenvalues of \mathbf{F} are given by

$$k_{\pm} = \pm k_{0z}\beta \quad \text{with} \quad \beta = \sqrt{1 + \frac{2f}{k_{0z}}}. \quad (\text{A.35})$$

The eigenvalues have an intuitive explanation: They are the z -components of the photon wavevector in the material for both scattering channels. The diagonalizing matrix is given by

$$\mathbf{h} = \frac{1}{t_{01}} \begin{pmatrix} 1 & r_{01} \\ r_{01} & 1 \end{pmatrix} \quad \text{with} \quad r_{01} = \frac{1 - \beta}{1 + \beta} \quad \text{and} \quad t_{01} = \frac{2}{1 + \beta}, \quad (\text{A.36})$$

where r_{01} and t_{01} are the Fresnel reflection and transmission coefficients for the boundary between the layer and the adjacent vacuum. The matrix \mathcal{F} can now be written as:

$$\mathcal{F} = \mathbf{h} \mathcal{F}_D \mathbf{h}^{-1} = \frac{1}{t_{01}} \begin{pmatrix} 1 & r_{01} \\ r_{01} & 1 \end{pmatrix} \begin{pmatrix} k_{0z}\beta & 0 \\ 0 & -k_{0z}\beta \end{pmatrix} \begin{pmatrix} 1 & r_{10} \\ r_{10} & 1 \end{pmatrix} \frac{1}{t_{10}} \quad (\text{A.37})$$

and its n th power is given by

$$\mathcal{F}^n = (\mathbf{h} \mathcal{F}_D \mathbf{h}^{-1})^n = \mathbf{h} \mathcal{F}_D^n \mathbf{h}^{-1}. \quad (\text{A.38})$$

Finally, we obtain for the exponential matrix the result:

$$\begin{aligned} e^{i\mathcal{F}z} &= \sum_{n=0}^{\infty} \frac{(i\mathcal{F}z)^n}{n!} = \mathbf{h} \left[\sum_{n=0}^{\infty} \frac{(i\mathcal{F}_D z)^n}{n!} \right] \mathbf{h}^{-1} = \mathbf{h} e^{i\mathcal{F}_D z} \mathbf{h}^{-1} \\ &= \frac{1}{t_{01}} \begin{pmatrix} 1 & r_{01} \\ r_{01} & 1 \end{pmatrix} \begin{pmatrix} e^{ik_{0z}\beta z} & 0 \\ 0 & e^{-ik_{0z}\beta z} \end{pmatrix} \begin{pmatrix} 1 & r_{10} \\ r_{10} & 1 \end{pmatrix} \frac{1}{t_{10}}. \end{aligned} \quad (\text{A.39})$$

This equation is a direct description of the layer structure, where the outer matrices describe the transition through the boundary and the middle matrix describes the propagation through the layer of thickness z . The matrix elements are the transition amplitudes between the scattering channels.

A.4 Transverse Coherence of X-rays

The result of x-ray scattering processes crucially depends on the coherence properties of the incident radiation field. Many experimental techniques like x-ray photon correlation spectroscopy (XPCS), for example, rely on the use of transversely coherent x-ray beams. Thus, an important question is, how coherence develops in the radiation field of an incoherent source¹. The answer is that the radiation field of a incoherent source acquires coherence in the propagation process since every point in the field receives light from all points of the same source. Hence, dependent on the degree of monochromasy and the spatial extent of the source and the distance from the source, every radiation field possesses certain longitudinal and transverse coherence properties.

Coherence is a prerequisite for the observation of interference effects in scattering. Transverse coherence is necessary for interference to occur between waves scattered from points \mathbf{r}_1 and \mathbf{r}_2 that are not aligned along the forward direction given by \mathbf{k}_0 . This is sketched in Fig. A.2. For these points the condition $\mathbf{k}_0 \times (\mathbf{r}_1 - \mathbf{r}_2) \neq 0$ holds. Thus, transverse coherence has to be considered if the translational invariance along a reflecting surface is broken, as in the case of rough surfaces, for example.

As derived in detail below, the transverse coherence depends on the source size h and the distance D from the source. In a quasimonochromatic beam with an average wavelength $\bar{\lambda}$ the transverse coherence length for a circular source is given by

$$L_T = \frac{\bar{\lambda}D}{\pi h}. \quad (\text{A.40})$$

Thus, the more pointlike a radiation source appears as seen from the sample position, the larger the transverse coherence length L_T . If we consider a synchrotron radiation source with $\bar{\lambda} = 1 \text{ \AA}$, $D = 30 \text{ m}$ and $h = 1 \text{ mm}$, we

¹ In an incoherent source the emission processes of individual photons are not correlated to each other. This is in contrast to coherent sources like lasers where the emitting atoms are coherently coupled through the radiation field.

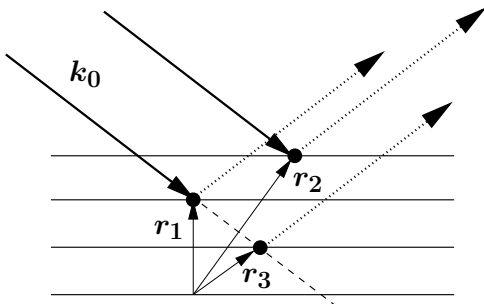


Fig. A.2. The transverse coherence of the radiation has to be considered for points r_1 and r_2 that are not aligned along the forward direction as it is the case for r_1 and r_3 . The waves scattered from the latter points are always coherently coupled which forms the basis for interference fringes in specular reflection from layered systems

obtain a value of $L_T = 1 \mu\text{m}$. L_T will be significantly larger at 3rd generation synchrotron radiation sources that are specially designed for low emittance and high brilliance like ESRF, APS, SPring8 and in particular PETRA-III (DESY, Hamburg) [3].

If the lateral spacing of scattering centers is small compared to the transverse coherence length, then interference effects can be observed in the detector plane. However, in most cases the coherence will not be complete and one has to deal with partial coherence: Let P_1 and P_2 be two points on a sample which is illuminated by an extended quasimonochromatic source. Since both points receive waves from the same source, we expect, especially when P_1 and P_2 are very close to each other, that the temporal development of the field amplitudes in these points will not be independent and waves reflected from these points may interfere. Therefore, the sharpness or visibility of the fringes obtained in an interference experiment involving P_1 and P_2 gives a measure for the correlation existing between the field amplitudes in these points. The normalized reflected intensity resulting from this interference is given by

$$|R|^2 = |R_1|^2 + |R_2|^2 + 2|R_1||R_2|\gamma_{12}(\tau)\cos(\alpha_{12}(\tau) - \Delta\Theta), \quad (\text{A.41})$$

where $\tau = \Delta s c$ with Δs the longitudinal separation of P_1 and P_2 . R_1 and R_2 are the amplitude reflection coefficients of the sample at P_1 and P_2 . $\gamma_{12}(\tau) = |\gamma_{12}(\tau)|e^{i\alpha_{12}(\tau)}$ is the complex degree of coherence between the field amplitudes A_1 and A_2 in P_1 and P_2 . It is related to the mutual coherence function $\Gamma_{12}(\tau)$ of the radiation field generated by the source:

$$\gamma_{12}(\tau) = \frac{\Gamma_{12}(\tau)}{|A_1||A_2|} \quad \text{where} \quad \Gamma_{12}(\tau) = \langle A_1(t + \tau) A_2^*(t) \rangle_t. \quad (\text{A.42})$$

A detailed derivation is given e.g. in [4]. From the viewpoint of stationary random processes, $\Gamma_{12}(\tau)$ is the cross correlation function between the field amplitudes A_1 and A_2 . The phase shift $\Delta\Theta$ takes into account the phase difference of the reflection coefficients at the angle of incidence φ as well as the geometrical phase due to the spatial separation h of P_1 and P_2 along the surface normal:

$$\Delta\Theta = 4\pi \frac{h}{\lambda} \sin \varphi + (\phi_1(\varphi) - \phi_2(\varphi)). \quad (\text{A.43})$$

$\phi_1(\varphi)$ and $\phi_2(\varphi)$ are the phases of the reflection coefficients $R_1(\varphi)$ and $R_2(\varphi)$, which are defined via:

$$R(\varphi) = |R(\varphi)| e^{i\phi(\varphi)} . \quad (\text{A.44})$$

It can be shown that $0 \leq |\gamma_{12}(\tau)| \leq 1$. If $|\gamma_{12}(\tau)| = 1$ the amplitudes $A_1(t)$ and $A_2(t)$ are said to be coherent, if $|\gamma_{12}(\tau)| = 0$ then the amplitudes are said to be incoherent. In general neither of these extreme situations is realized and we speak of partial coherence between both amplitudes with $|\gamma_{12}(\tau)|$ representing their degree of coherence.

Equation (A.41) may also be written in the form:

$$\begin{aligned} |R|^2 &= |\gamma_{12}(\tau)| ||R_1 + R_2 e^{i(\alpha_{12}(\tau) - \Delta\Theta)}|^2 \\ &\quad + (1 - |\gamma_{12}(\tau)|) (|R_1|^2 + |R_2|^2) . \end{aligned} \quad (\text{A.45})$$

Thus the intensity may be regarded as a mixture of a part resulting from completely coherent superposition and a part resulting from incoherent superposition of the amplitudes.

Note that $\gamma_{12}(\tau)$ contains the longitudinal as well as the transverse coherence properties of the field. However, if the time delay τ of the interfering beams is small compared to the coherence time $t_c = \hbar/\Delta E$ of the radiation, equivalent to that the path difference $c\tau$ between the beams is small compared to the longitudinal coherence length, then we can make the replacements $\gamma_{12}(\tau) = \gamma_{12}(0) =: \gamma_{12}$ and $\alpha_{12}(\tau) = \alpha_{12}(0) =: \alpha_{12}$, which simplify the following considerations.

According to the van Cittert–Zernike theorem, the complex degree of coherence is given by

$$\gamma_{12} = \frac{1}{|A_1| |A_2|} \int_S I_S(x, y) \frac{e^{i\mathbf{k}(\mathbf{r}_1(x, y) - \mathbf{r}_2(x, y))}}{r_1(x, y) r_2(x, y)} dx dy . \quad (\text{A.46})$$

The integration is carried out over the area S of the source aperture which is assumed to lie in the (x, y) -plane. $I_S(x, y)$ is the intensity distribution across the source aperture and $\mathbf{r}_1(x, y), \mathbf{r}_2(x, y)$ are the vectors connecting a point on the aperture with P_1 and P_2 , respectively.

For a source of rectangular shape, e.g., radiation passing through a slit, one obtains:

$$\gamma_{12} = \frac{\sin y}{y} = \operatorname{sinc} y \quad \text{with} \quad y = \frac{\pi x h}{D \lambda} , \quad (\text{A.47})$$

where x is the separation between two points along the direction in which the width h of the slit is measured. This function is shown in Fig. A.3. From this expression for γ_{12} the transverse coherence length L_T is defined as the value of x for which $y = 1$. This results in the expression given in (A.40). The value $\gamma_{12}(x = L_T) = \operatorname{sinc}(1) = 0.84$ is sufficiently large to speak of ‘good’ coherence, making the above a meaningful definition.

In the case that a sample is illuminated under an angle of incidence φ relative to the surface, the transverse coherence length in the plane of the

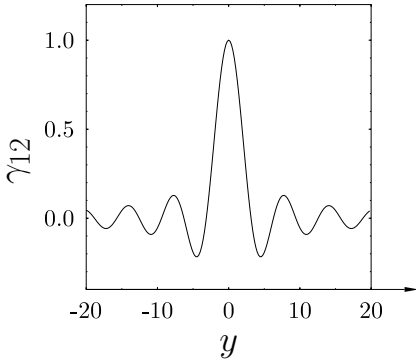


Fig. A.3. Mutual coherence function γ_{12} for a radiation source of rectangular shape

sample (the in-plane coherence length $L_{T_{ip}}$) is obtained by modifying (A.40) with the projection factor $1/\sin \varphi$:

$$L_{T_{ip}} = \frac{L_T}{\sin \varphi} = \frac{\bar{\lambda}D}{\pi h \sin \varphi}. \quad (\text{A.48})$$

Thus in grazing incidence geometry, the in-plane coherence length along the projection of \mathbf{k}_0 on the surface may exceed L_T by orders of magnitude.

A.5 Derivation of the Roughness Matrix

This appendix explains the derivation of the roughness matrix given by (4.69).

In a simple model, let us first assume that the rough boundary is represented by a transition layer with thickness d , centered around the common boundary between two layers of thickness D each, see Fig. A.4. The scattering matrices of these layers are given by \mathbf{F}_1 and \mathbf{F}_2 , respectively, the scattering matrix of the transition region is $(\mathbf{F}_1 + \mathbf{F}_2)/2$. With the above ansatz, the product \mathbf{P} of the exponential matrices is then given by

$$\begin{aligned} \mathbf{P} &= e^{i\mathbf{F}_1(D-d/2)} e^{\frac{1}{2}i(\mathbf{F}_1+\mathbf{F}_2)d} e^{i\mathbf{F}_2(D-d/2)} \\ &= e^{i\mathbf{F}_1 D} e^{-\frac{1}{2}i\mathbf{F}_1 d} e^{\frac{1}{2}i(\mathbf{F}_1+\mathbf{F}_2)d} e^{-\frac{1}{2}i\mathbf{F}_2 d} e^{i\mathbf{F}_2 D} \\ &= e^{i\mathbf{F}_1 D} e^{-\frac{1}{8}i[\mathbf{F}_1, \mathbf{F}_2]d} e^{i\mathbf{F}_2 D} \\ &=: e^{i\mathbf{F}_1 D} e^{\mathbf{W}} e^{i\mathbf{F}_2 D}, \end{aligned} \quad (\text{A.49})$$

where we have made use of the Campbell-Baker-Hausdorff (CBH) relation:

$$e^{\mathbf{A}} e^{\mathbf{B}} = e^{\mathbf{A} + \mathbf{B} + \frac{1}{2}[\mathbf{A}, \mathbf{B}]}. \quad (\text{A.50})$$

$[\mathbf{A}, \mathbf{B}] = \mathbf{AB} - \mathbf{BA}$ is the commutator between \mathbf{A} and \mathbf{B} . Commutators of higher than second-order have been neglected, which is reasonable, if the thickness of the transition region is small. Moreover, in this approximation every matrix exponential with second-order exponents commutes with matrices of first-order exponents. The simple calculation above yielded for the

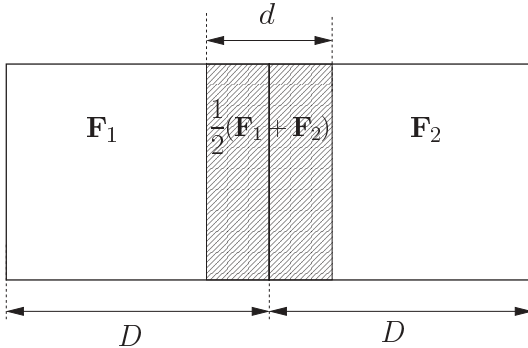


Fig. A.4. Simplest representation of a rough boundary by a transition layer. Its scattering matrix is given by the average of the adjacent scattering matrices

roughness matrix $\mathbf{W} = -i[\mathbf{F}_1, \mathbf{F}_2]d/8$. This shows that \mathbf{W} is expected to contain commutators of various orders between \mathbf{F}_1 and \mathbf{F}_2 .

For an exact derivation of the roughness matrix the density transition region is subdivided into thin slices of constant density. Then the layer matrices of all these layers are multiplied along the procedure outlined above. A detailed outline of the computational procedure is given in [5]. The result is:

$$\begin{aligned} \mathbf{W} &= \frac{1}{2} [\mathbf{F}_1, \mathbf{F}_2] \int_{-\infty}^{\infty} z^2 h(z) dz + \frac{1}{24} [[[\mathbf{F}_1, \mathbf{F}_2], \mathbf{F}_1], \mathbf{F}_2] \int_{-\infty}^{\infty} z^4 h(z) dz + \dots \\ &= \sum_{n=1}^{\infty} \frac{\langle h(z) \rangle_{2n}}{(2n)!} [\mathbf{F}_1, \mathbf{F}_2]_{2n}, \end{aligned} \quad (\text{A.51})$$

where $\langle h(z) \rangle_{2n}$ is the $(2n)$ th moment of the height distribution function $h(z)$ and $[\mathbf{F}_1, \mathbf{F}_2]_{2n}$ is the commutator of order $2n$ between \mathbf{F}_1 and \mathbf{F}_2 , i.e. $[\mathbf{F}_1, \mathbf{F}_2]_2 = [\mathbf{F}_1, \mathbf{F}_2]$, $[\mathbf{F}_1, \mathbf{F}_2]_4 = [[[F_1, F_2], F_1], F_2]$, and so on.

A.6 The Projected and the Total Phonon Density of States

In this section we show in which cases inelastic nuclear resonant scattering yields the total phonon density of states in its original definition as integrated over the full momentum space.

In general, inelastic nuclear resonant absorption yields the partial phonon density of states, projected on the direction of the photon wavevector:

$$\tilde{D}(E, \mathbf{s}) = \frac{1}{(2\pi)^3} \frac{V}{N} \sum_m \sum_j \int d\mathbf{q} \delta(E - \hbar\omega_j(\mathbf{q})) |\mathbf{s} \cdot \mathbf{e}_{j,m}(\mathbf{q})|^2. \quad (\text{A.52})$$

This differs from the exact phonon density of states that is defined as [6]:

$$D(E) = \frac{1}{(2\pi)^3} \frac{V}{3N} \sum_j \int d\mathbf{q} \delta(E - \hbar\omega_j(\mathbf{q})) . \quad (\text{A.53})$$

Here, V is the volume of the unit cell and N and N_R are the total number of atoms and the number of resonant atoms in the unit cell, respectively. The indices m and j are used to label the resonant atoms in the unit cell and the vibrational modes, respectively. Accordingly, $\mathbf{e}_{j,m}(\mathbf{q})$ is the polarization vector of the vibrations of the m th resonant atom and the j th vibrational mode with wavevector \mathbf{q} . \mathbf{s} is the unit vector along the direction of the incident beam. One notices that $\tilde{D}(E, \mathbf{s})$ differs from the exact density of states $D(E)$ because the contributions from the vibrational modes of the resonant atoms are weighted by the projections of their polarization vectors on the direction of the incident beam. However, there are two important cases where inelastic nuclear scattering yields the total phonon density of states of the sample. These are:

- Single crystals with a cubic Bravais lattice, and
- Polycrystals with an arbitrary monoatomic lattice.

In these cases the inelastic absorption appears to be isotropic. This is shown in detail in the following.

A.6.1 Single-Crystalline Systems

To discuss the general anisotropic case we introduce the second-rank Cartesian tensor:

$$T^{\mu\nu}(E) = \frac{1}{(2\pi)^3} \frac{V}{N_R} \sum_m \sum_j \int d\mathbf{q} \delta(E - \hbar\omega_j(\mathbf{q})) (\mathbf{e}_{j,m})_\mu (\mathbf{e}_{j,m})_\nu^* . \quad (\text{A.54})$$

With this definition the projected DOS can be simply written as a quadratic form:

$$\tilde{D}(E, \mathbf{s}) = \sum_\mu \sum_\nu s_\mu T^{\mu\nu}(E) s_\nu . \quad (\text{A.55})$$

Any such tensor can be decomposed into its trace T , an antisymmetric part A_κ and a traceless, symmetric part $S_{\mu\nu}$ [1], i.e.,

$$T^{\mu\nu} = \frac{1}{3} \delta_{\mu\nu} T + A_\kappa + S_{\mu\nu} . \quad (\text{A.56})$$

The three quantities T , \mathbf{A} and \mathbf{S} transform in the same way as the spherical harmonics of order 0, 1, and 2, respectively. As the antisymmetric part \mathbf{A} does not contribute to the quadratic form in (A.55), we have to consider just two contributions. While the trace T is invariant under rotations in space, the symmetric part \mathbf{S} contains the anisotropies, so that

$$\tilde{D}(E, \mathbf{s}) = \frac{1}{3} T(E) + A^{(p)}(E) Y_{20}(\Theta, \varphi) + A^{(a)}(E) \operatorname{Re}[Y_{22}(\Theta, \varphi)] \quad (\text{A.57})$$

where the angles Θ and φ describe the direction of the incident radiation with respect to the main axes of the tensor. The polar anisotropy $A^{(p)}$ and the azimuthal anisotropy $A^{(a)}$ are determined by the rotational symmetry of the crystal [7]. These anisotropies vanish for all cubic Bravais lattices. In the other Bravais lattices these anisotropies are nonzero, so that inelastic nuclear absorption is generally anisotropic, as has been shown in the case of FeBO₃ [8]. However, an anisotropic crystal structure does not necessarily imply anisotropic nuclear absorption; the anisotropy may still vanish due to the specific basis of the unit cell. For example, no anisotropy in NIS has been found for Fe₂O₃ (hematite), although it has the same space group as FeBO₃ [9].

A.6.2 Polycrystalline Systems

In polycrystalline samples without texture one averages over all directions of the incident beam:

$$\overline{D(E)} = \frac{1}{4\pi} \int d\mathbf{s} \tilde{D}(E, \mathbf{s}) = \sum_{\mu} \sum_{\nu} T^{\mu\nu}(E) \frac{1}{4\pi} \int d\mathbf{s} s_{\mu} s_{\nu}. \quad (\text{A.58})$$

The integral over all directions vanishes for the nondiagonal components of the tensor, while it is 1/3 for the diagonal components. This allows to partly separate the summation over the vibrational modes from the sum over the resonant atoms in the unit cell [10], so that (A.52) then turns into:

$$\overline{D(E)} = \frac{1}{(2\pi)^3} \frac{V}{3N} \sum_j \int d\mathbf{q} \delta(E - \hbar\omega_j(\mathbf{q})) \sum_m |\mathbf{s} \cdot \mathbf{e}_{j,m}(\mathbf{q})|^2. \quad (\text{A.59})$$

For a monoatomic lattice the sum over all resonant atoms is of course identical to the sum over all atoms in the unit cell. That sum equals unity, by definition. Then the above expression merges into the exact definition of the total DOS as given by (A.53).

A.7 Table of Resonant Isotopes

The following tables contain naturally abundant, stable nuclei with energy levels below 100 keV and lifetimes between 100 ps and 1 s. This list goes beyond isotopes that have been used in Mössbauer spectroscopy so far, because the excitation by synchrotron radiation proceeds from the ground state and thus does not require a radioactive parent. Isotopes with energy levels above 100 keV (below 200 keV, though) were included, however, if their half lifetime exceeded 10 ns. In that case, they may be accessible via timing methods. Even if their Lamb-Mössbauer factor will be low, they may be potentially interesting for the technique of SRPAC as outlined in Sect. 6.6.

The data listed here have been extracted from various sources: A general overview can be obtained from the table of Mössbauer isotopes published in

the *Mössbauer Effect Data Index* (MEDI) [11]. This compilation, however, is more than 30 years old. The actual values for the nuclear moments were taken from the most recent edition of the *Table of Isotopes* [12] and the values for the conversion coefficients were taken from the data base published by the *National Nuclear Data Center* at Brookhaven National Laboratory (USA)². From these data the resonant cross section σ_0 was calculated via

$$\sigma_0 = \frac{2\pi}{k_0^2(1+\alpha)} \frac{2I_e + 1}{2I_g + 1}, \quad (\text{A.60})$$

where $k_0 = E/(\hbar c)$ is the wavenumber of the radiation. For comparison, the total cross section σ_{ph} for photo absorption is given, as well as the ratio σ_0/σ_{ph} that determines the relative photon yield of coherent nuclear resonant scattering.

The resonance energies have been taken from the *Table of Isotopes* [12]. However, the most precise values for the resonance energies of ^{57}Fe , ^{151}Eu , ^{119}Sn , and ^{161}Dy have been obtained via backscattering of synchrotron radiation [13]. They are given by

$$\begin{array}{ll} ^{57}\text{Fe}: E_0 = 14.412497(3) \text{ keV} & ^{119}\text{Sn}: E_0 = 23.879478(18) \text{ keV} \\ ^{151}\text{Eu}: E_0 = 21.541418(10) \text{ keV} & ^{161}\text{Dy}: E_0 = 25.651368(10) \text{ keV} \end{array}$$

Moreover, it should be mentioned here that the nuclear moments of the excited states may exhibit a relatively large error. This is true even for the most widely used Mössbauer isotope, ^{57}Fe , where the value of the excited-state quadrupole moment Q_e quoted in the literature was floating between -0.19 b and 0.44 b [14], and it was a subject of controversy for a long time. However, this debate has been settled after high-precision nuclear and atomic structure calculations have been performed [14, 15]. The recommended value is now $0.15(2)$ b.

For convenience, the table is given in two versions, where the isotopes are sorted according to different criteria:

- **Table of Resonant Isotopes A:**
Isotopes are sorted after their **atomic number** Z .
- **Table of Resonant Isotopes B:**
Isotopes are sorted after their **resonance energy** E_0 .

These tables extend over two adjacent pages. While on the even pages the parameters E_0 , τ_0 , Γ_0 , a , I_g , I_e and the multipolarity are listed, the odd pages continues with the parameters μ_g , μ_e , Q_g , Q_e , α , σ_0 , σ_{ph} , and the ratio σ_0/σ_{ph} .

² This database is accessible via <http://www.nndc.bnl.gov/nndc/nudat/>. A more recent version is <http://www.nndc.bnl.gov/nudat2/>.

Table A.1. Following pages: List of all stable, naturally abundant isotopes with nuclear resonances below 100 keV that exhibit natural lifetimes between 100 ps and 1 s

E_0 is the resonance energy,

τ_0 is the natural lifetime,

Γ_0 is the natural linewidth,

a is the natural abundance of the isotope,

I_g and I_e are the spins of the ground and excited state,

μ_g and μ_e are the magnetic moments of the ground and excited states, given in units of the nuclear magneton $\mu_N = 5.0508 \cdot 10^{-27} \text{ J/T} = 0.03153 \mu\text{eV/T}$. The moments are related to the g-factors via $g = \mu/I$.

Q_g and Q_e are the quadrupole moments of the ground and excited states, given in barn ($1 \text{ b} = 10^{-28} \text{ m}^2$),

α is the factor of internal conversion,

σ_0 is the nuclear resonance absorption cross section, and

σ_{ph} is the total electronic absorption cross section at the energy of the nuclear resonance, including contributions from photo absorption and Compton scattering.

The entry N.N means that the corresponding quantity was not available at the time of publication of this book.

List of Resonant Isotopes A $E_0 < 100$ keV, $0.1 \text{ ns} < \tau_0 < 1 \text{ s}$

| Z | Isotope | E_0 keV | τ_0 | Γ_0 | a % | I_g | I_e | Multi-polarity |
|----|-------------------|--------------|---------------------|---------------------|--------|---------|---------|----------------|
| 19 | ^{40}K | 29.834 | 5.96 ns | 0.11 μeV | 0.012 | 4^- | 3^- | (M1) |
| 21 | ^{45}Sc | 12.40 | 458.78 ms | 1.4 aeV | 100.0 | $7/2^-$ | $3/2^+$ | (M2) |
| 26 | ^{57}Fe | 14.4125 | 141.11 ns | 4.66 neV | 2.14 | $1/2^-$ | $3/2^-$ | M1+E2 |
| 28 | ^{61}Ni | 67.408 | 7.60 ns | 86.57 neV | 1.19 | $3/2^-$ | $5/2^-$ | M1+E2 |
| 30 | ^{67}Zn | 93.312 | 13.22 μs | 49.8 peV | 4.11 | $5/2^-$ | $1/2^-$ | E2 |
| 32 | ^{73}Ge | 13.275 | 4.26 μs | 0.15 neV | 7.76 | $9/2^+$ | $5/2^+$ | E2 |
| 32 | ^{73}Ge | 68.752 | 2.51 ns | 0.26 μeV | 7.76 | $9/2^+$ | $7/2^+$ | M1+E2 |
| 32 | ^{73}Ge | 66.716 | 719.90 ms | 0.9 aeV | 7.76 | $9/2^+$ | $1/2^-$ | NN |
| 36 | ^{83}Kr | 9.396 | 212.08 ns | 3.10 neV | 11.55 | $9/2^+$ | $7/2^+$ | M1+E2 |
| 44 | ^{99}Ru | 89.68 | 29.58 ns | 22.26 neV | 12.72 | $5/2^+$ | $3/2^+$ | E2+M1 |
| 50 | ^{119}Sn | 23.871 | 25.61 ns | 25.70 neV | 8.58 | $1/2^+$ | $3/2^+$ | M1+E2 |
| 51 | ^{121}Sb | 37.133 | 4.99 ns | 0.13 μeV | 57.25 | $5/2^+$ | $7/2^+$ | M1 |
| 52 | ^{125}Te | 35.4919 | 2.14 ns | 0.31 μeV | 6.99 | $1/2^+$ | $3/2^+$ | M1+E2 |
| 53 | ^{127}I | 57.606 | 2.76 ns | 0.24 μeV | 100.0 | $5/2^+$ | $7/2^+$ | M1+E2 |
| 54 | ^{129}Xe | 39.578 | 1.40 ns | 0.47 μeV | 26.44 | $1/2^+$ | $3/2^+$ | M1+E2 |
| 54 | ^{131}Xe | 80.1853 | 692.4 ps | 0.95 μeV | 21.2 | $3/2^+$ | $1/2^+$ | M1+E2 |
| 55 | ^{133}Cs | 80.997 | 9.05 ns | 72.77 neV | 100.0 | $7/2^+$ | $5/2^+$ | M1+E2 |
| 57 | ^{138}La | 72.57 | 167.35 ns | 3.93 neV | 0.09 | 5^+ | 3^+ | E2 |
| 60 | ^{145}Nd | 67.25 | 42.42 ns | 15.52 neV | 8.30 | $7/2^-$ | $3/2^-$ | E2 |
| 60 | ^{145}Nd | 72.50 | 1.04 ns | 0.63 μeV | 8.30 | $7/2^-$ | $5/2^-$ | M1 |
| 62 | ^{149}Sm | 22.494 | 10.27 ns | 64.08 neV | 13.83 | $7/2^-$ | $5/2^-$ | M1+E2 |
| 62 | ^{154}Sm | 81.976 | 4.36 ns | 0.15 μeV | 22.7 | 0^+ | 2^+ | E2 |
| 63 | ^{151}Eu | 21.532 | 13.99 ns | 47.03 neV | 47.82 | $5/2^+$ | $7/2^+$ | M1+E2 |
| 63 | ^{153}Eu | 83.3671 | 1.14 ns | 0.58 μeV | 52.18 | $5/2^+$ | $7/2^+$ | M1+E2 |
| 63 | ^{153}Eu | 97.4297 | 285.6 ps | 2.30 μeV | 52.18 | $5/2^+$ | $5/2^-$ | E1 |
| 64 | ^{158}Gd | 79.5104 | 3.64 ns | 0.18 μeV | 24.84 | 0^+ | 2^+ | E2 |
| 64 | ^{155}Gd | 60.0087 | 278.4 ps | 2.36 μeV | 14.73 | $3/2^-$ | $5/2^-$ | M1+E2 |
| 64 | ^{155}Gd | 86.546 | 9.13 ns | 72.08 neV | 14.73 | $3/2^-$ | $5/2^+$ | E1 |
| 64 | ^{156}Gd | 88.9666 | 3.19 ns | 0.21 μeV | 20.47 | 0^+ | 2^+ | E2 |
| 64 | ^{157}Gd | 54.533 | 269.7 ps | 2.44 μeV | 15.68 | $3/2^-$ | $5/2^-$ | M1+E2 |
| 64 | ^{157}Gd | 63.917 | 663.64 ns | 0.99 neV | 15.68 | $3/2^-$ | $5/2^+$ | E1 |
| 64 | ^{160}Gd | 75.26 | 3.88 ns | 0.17 μeV | 21.86 | 0^+ | 2^+ | E2 |
| 66 | ^{162}Dy | 80.660 | 3.27 ns | 0.20 μeV | 25.5 | 0^+ | 2^+ | E2 |
| 66 | ^{164}Dy | 73.392 | 3.45 ns | 0.19 μeV | 28.2 | 0^+ | 2^+ | E2 |
| 66 | ^{161}Dy | 25.65135 | 41.98 ns | 15.68 neV | 18.9 | $5/2^+$ | $5/2^-$ | E1 |
| 66 | ^{160}Dy | 86.7882 | 2.91 ns | 0.23 μeV | 2.34 | 0^+ | 2^+ | E2 |
| 66 | ^{161}Dy | 74.56668 | 4.53 ns | 0.15 μeV | 18.9 | $5/2^+$ | $3/2^-$ | E1 |

| Isotope | μ_g | μ_e | Q_g | Q_e | α | σ_0 | σ_{ph} | σ_0/σ_{ph} |
|-------------------|---------|---------|---------|-------|----------|------------|---------------|------------------------|
| | μ_N | μ_N | barn | barn | | kbarn | kbarn | |
| ⁴⁰ K | -1.298 | -1.29 | -0.061 | N.N | 6.6 | 281.3 | 0.21 | 1336.74 |
| ⁴⁵ Sc | 4.756 | N.N | -0.22 | N.N | 632. | 12.6 | 4.00 | 3.15 |
| ⁵⁷ Fe | 0.0906 | -0.1553 | 0.0 | 0.16 | 8.56 | 2464.0 | 5.75 | 428.58 |
| ⁶¹ Ni | 0.750 | 0.480 | 0.162 | -0.2 | 0.139 | 709.1 | 0.10 | 7046.05 |
| ⁶⁷ Zn | 0.8756 | 0.587 | 0.15 | N.N | 0.873 | 50.0 | 0.06 | 861.49 |
| ⁷³ Ge | -0.8795 | -0.0941 | -0.173 | -0.4 | 1.1E3 | 7.4 | 15.11 | 0.49 |
| ⁷³ Ge | -0.8795 | N.N | -0.173 | N.N | 0.227 | 337.5 | 0.16 | 2120.64 |
| ⁷³ Ge | -0.8795 | N.N | -0.173 | N.N | N.N | N.N | 0.17 | N.N |
| ⁸³ Kr | -0.9707 | -0.943 | 0.253 | 0.495 | 17.09 | 1225.5 | 8.08 | 151.71 |
| ⁹⁹ Ru | -0.641 | -0.284 | 0.079 | 0.231 | 1.498 | 81.2 | 0.26 | 315.04 |
| ¹¹⁹ Sn | -1.0473 | 0.633 | 0.0 | 0.094 | 5.22 | 1380.5 | 2.45 | 562.59 |
| ¹²¹ Sb | 3.3634 | 2.518 | -0.36 | -0.48 | 11.11 | 195.4 | 4.85 | 40.26 |
| ¹²⁵ Te | -0.8885 | 0.605 | 0.0 | -0.31 | 14.0 | 259.0 | 5.87 | 44.11 |
| ¹²⁷ I | 2.8133 | 2.54 | -0.79 | -0.71 | 3.77 | 206.1 | 1.72 | 120.11 |
| ¹²⁹ Xe | -0.7780 | 0.58 | 0.0 | -0.41 | 12.31 | 234.7 | 4.97 | 47.24 |
| ¹³¹ Xe | 0.6919 | N.N | -0.120 | 0.0 | 1.57 | 74.0 | 0.75 | 99.00 |
| ¹³³ Cs | 2.5820 | 3.45 | -0.0037 | -0.33 | 1.72 | 102.8 | 0.78 | 131.62 |
| ¹³⁸ La | 3.7136 | 2.886 | 0.45 | N.N | 6.41 | 39.9 | 1.19 | 33.43 |
| ¹⁴⁵ Nd | -0.654 | N.N | -0.254 | N.N | 9.61 | 25.5 | 1.75 | 14.55 |
| ¹⁴⁵ Nd | -0.656 | -0.320 | -0.33 | N.N | 3.64 | 75.2 | 1.44 | 52.40 |
| ¹⁴⁹ Sm | -0.672 | -0.624 | 0.075 | 1.01 | 29.2 | 120.1 | 6.94 | 17.29 |
| ¹⁵⁴ Sm | 0.0 | 0.784 | 0.0 | -1.87 | 4.94 | 306.5 | 1.17 | 262.93 |
| ¹⁵¹ Eu | 3.472 | 2.591 | 0.903 | 1.28 | 28.0 | 242.6 | 8.35 | 29.06 |
| ¹⁵³ Eu | 1.5330 | 1.81 | 2.41 | 0.44 | 3.82 | 97.4 | 1.18 | 82.77 |
| ¹⁵³ Eu | 1.5330 | 3.22 | 2.41 | N.N | 0.307 | 197.2 | 0.78 | 251.42 |
| ¹⁵⁸ Gd | 0.0 | 0.762 | 0.0 | -2.01 | 6.02 | 275.6 | 1.40 | 196.36 |
| ¹⁵⁵ Gd | -0.2591 | N.N | 1.30 | -0.44 | 9.36 | 98.4 | 2.97 | 33.17 |
| ¹⁵⁵ Gd | -0.2591 | -0.525 | 1.30 | 0.11 | 0.434 | 341.7 | 1.12 | 304.61 |
| ¹⁵⁶ Gd | 0.0 | 0.774 | 0.0 | -1.93 | 3.93 | 313.5 | 1.04 | 300.60 |
| ¹⁵⁷ Gd | -0.340 | N.N | 1.36 | -0.46 | 12.4 | 92.1 | 3.83 | 24.07 |
| ¹⁵⁷ Gd | -0.340 | -0.464 | 1.36 | 2.45 | 0.971 | 455.7 | 2.51 | 181.79 |
| ¹⁶⁰ Gd | 0.0 | 0.72 | 0.0 | -2.08 | 7.44 | 255.9 | 1.62 | 157.57 |
| ¹⁶² Dy | 0.0 | 0.686 | 0.0 | N.N | 6.22 | 260.4 | 1.52 | 171.16 |
| ¹⁶⁴ Dy | 0.0 | 0.70 | 0.0 | -2.08 | 9.0 | 227.1 | 1.95 | 116.31 |
| ¹⁶¹ Dy | -0.4803 | 0.594 | 2.507 | 2.506 | 2.35 | 1109.9 | 6.30 | 176.22 |
| ¹⁶⁰ Dy | 0.0 | 0.725 | 0.0 | 1.76 | 4.69 | 285.4 | 1.25 | 227.55 |
| ¹⁶¹ Dy | -0.4803 | -0.403 | 2.507 | 1.45 | 0.679 | 174.7 | 1.87 | 93.31 |

List of Resonant Isotopes A (cont'd) $E_0 < 100 \text{ keV}$, $0.1 \text{ ns} < \tau_0 < 1 \text{ s}$

| Z | Isotope | E_0 keV | τ_0 | Γ_0 | a % | I_g | I_e | Multi-polarity |
|----|-------------------|--------------|--------------------|---------------------|--------|---------|---------|----------------|
| 66 | ^{161}Dy | 43.8211 | 1.20 ns | 0.55 μeV | 18.9 | $5/2^+$ | $7/2^+$ | M1+E2 |
| 68 | ^{166}Er | 80.574 | 2.63 ns | 0.25 μeV | 33.6 | 0^+ | 2^+ | E2 |
| 68 | ^{168}Er | 79.804 | 2.71 ns | 0.24 μeV | 26.8 | 0^+ | 2^+ | E2 |
| 68 | ^{167}Er | 79.3219 | 165.9 ps | 3.97 μeV | 22.95 | $7/2^+$ | $9/2^+$ | M1+E2 |
| 68 | ^{170}Er | 78.68 | 2.73 ns | 0.24 μeV | 14.9 | 0^+ | 2^+ | E2 |
| 68 | ^{164}Er | 91.40 | 2.12 ns | 0.31 μeV | 1.61 | 0^+ | 2^+ | E2 |
| 69 | ^{169}Tm | 8.4103 | 5.89 ns | 0.11 μeV | 100.0 | $1/2^+$ | $3/2^+$ | M1+E2 |
| 70 | ^{170}Yb | 84.2551 | 2.32 ns | 0.28 μeV | 3.05 | 0^+ | 2^+ | E2 |
| 70 | ^{171}Yb | 66.721 | 1.17 ns | 0.56 μeV | 14.31 | $1/2^-$ | $3/2^-$ | M1+E2 |
| 70 | ^{171}Yb | 75.878 | 2.37 ns | 0.28 μeV | 14.3 | $1/2^-$ | $5/2^-$ | E2 |
| 70 | ^{172}Yb | 78.7435 | 2.38 ns | 0.28 μeV | 21.9 | 0^+ | 2^+ | E2 |
| 70 | ^{174}Yb | 76.471 | 2.58 ns | 0.25 μeV | 31.84 | 0^+ | 2^+ | E2 |
| 70 | ^{176}Yb | 82.13 | 2.54 ns | 0.26 μeV | 12.7 | 0^+ | 2^+ | E2 |
| 72 | ^{180}Hf | 93.326 | 2.16 ns | 0.30 μeV | 35.1 | 0^+ | 2^+ | E2 |
| 72 | ^{178}Hf | 93.180 | 2.14 ns | 0.31 μeV | 27.3 | 0^+ | 2^+ | E2 |
| 72 | ^{176}Hf | 88.351 | 2.06 ns | 0.32 μeV | 5.21 | 0^+ | 2^+ | E2 |
| 73 | ^{181}Ta | 6.238 | 8.73 μs | 75.4 peV | 99.99 | $7/2^+$ | $9/2^-$ | E1 |
| 74 | ^{183}W | 46.4839 | 271.2 ps | 2.43 μeV | 14.3 | $1/2^-$ | $3/2^-$ | M1+E2 |
| 74 | ^{183}W | 99.0793 | 1.11 ns | 0.59 μeV | 14.3 | $1/2^-$ | $5/2^-$ | E2 |
| 76 | ^{187}Os | 75.04 | 3.12 ns | 0.21 μeV | 1.6 | $1/2^-$ | $5/2^-$ | E2 |
| 76 | ^{189}Os | 36.202 | 764.6 ps | 0.86 μeV | 16.1 | $3/2^-$ | $1/2^-$ | M1+E2 |
| 76 | ^{189}Os | 69.537 | 2.34 ns | 0.28 μeV | 16.10 | $3/2^-$ | $5/2^-$ | M1+E2 |
| 76 | ^{189}Os | 95.254 | 331.8 ps | 1.98 μeV | 16.10 | $3/2^-$ | $3/2^-$ | M1+E2 |
| 76 | ^{187}Os | 9.746 | 3.43 ns | 0.19 μeV | 1.6 | $1/2^-$ | $3/2^-$ | M1(+E2) |
| 77 | ^{193}Ir | 73.041 | 8.79 ns | 74.92 neV | 62.70 | $3/2^+$ | $1/2^+$ | M1+E2 |
| 77 | ^{191}Ir | 82.407 | 5.89 ns | 0.11 μeV | 37.3 | $3/2^+$ | $1/2^+$ | M1+E2 |
| 78 | ^{195}Pt | 98.85 | 245.2 ps | 2.68 μeV | 33.80 | $1/2^-$ | $3/2^-$ | M1+E2 |
| 79 | ^{197}Au | 77.351 | 2.76 ns | 0.24 μeV | 100.0 | $3/2^+$ | $1/2^+$ | M1+E2 |
| 80 | ^{201}Hg | 1.556 | 144.27 ns | 4.56 neV | 13.2 | $3/2^-$ | $1/2^-$ | M1+E2 |
| 80 | ^{201}Hg | 32.138 | 288.5 ps | 2.28 μeV | 13.2 | $3/2^-$ | $3/2^-$ | M1+E2 |
| 80 | ^{201}Hg | 26.269 | 865.6 ps | 0.76 μeV | 13.2 | $3/2^-$ | $1/2^-$ | M1+E2 |
| 92 | ^{238}U | 44.915 | 324.6 ps | 2.03 μeV | 99.27 | 0^+ | 2^+ | E2 |

| Isotope | μ_g | μ_e | Q_g | Q_e | α | σ_0 | σ_{ph} | σ_0/σ_{ph} |
|-------------------|----------|---------|-------|--------|----------|------------|---------------|------------------------|
| | μ_N | μ_N | barn | barn | | kbarn | kbarn | |
| ^{161}Dy | -0.4803 | -0.141 | 2.507 | 0.53 | 8.0 | 188.7 | 1.47 | 128.21 |
| ^{166}Er | 0.0 | 0.632 | 0.0 | -1.9 | 6.88 | 239.1 | 1.69 | 141.59 |
| ^{168}Er | 0.0 | 0.642 | 0.0 | -2.17 | 7.14 | 236.0 | 1.73 | 136.24 |
| ^{167}Er | 0.564 | N.N | 2.827 | N.N | 6.06 | 68.8 | 1.76 | 39.12 |
| ^{170}Er | 0.0 | 0.633 | 0.0 | -1.94 | 7.59 | 230.0 | 1.80 | 127.95 |
| ^{164}Er | 0.0 | 0.697 | 0.0 | N.N | 4.2 | 281.6 | 1.21 | 232.18 |
| ^{169}Tm | -0.2316 | 0.534 | 0.0 | -1.2 | 285.0 | 241.9 | 32.91 | 7.35 |
| ^{170}Yb | 0.0 | 0.674 | 0.0 | 2.12 | 6.37 | 233.8 | 1.66 | 141.21 |
| ^{171}Yb | 0.49367 | 0.350 | 0.0 | 1.59 | 13.0 | 78.5 | 3.05 | 25.72 |
| ^{171}Yb | 0.49367 | 1.015 | 0.0 | 2.16 | 9.73 | 118.8 | 2.18 | 54.54 |
| ^{172}Yb | 0.0 | 0.669 | 0.0 | 2.16 | 8.4 | 209.9 | 1.98 | 106.17 |
| ^{174}Yb | 0.0 | 0.676 | 0.0 | 2.12 | 9.43 | 200.6 | 2.13 | 93.96 |
| ^{176}Yb | 0.0 | 0.675 | 0.0 | 2.22 | 7.06 | 225.0 | 1.77 | 127.10 |
| ^{180}Hf | 0.0 | 0.533 | 0.0 | -2.00 | 4.71 | 246.0 | 1.40 | 175.68 |
| ^{178}Hf | 0.0 | 0.48 | 0.0 | -2.02 | 4.74 | 245.5 | 1.41 | 174.60 |
| ^{176}Hf | 0.0 | 0.539 | 0.0 | -2.10 | 5.86 | 228.4 | 1.61 | 141.47 |
| ^{181}Ta | 2.3705 | 5.28 | 3.28 | 3.71 | 70.5 | 1099.2 | 89.40 | 12.30 |
| ^{183}W | 0.11778 | -0.10 | 0.0 | 1.77 | 8.63 | 235.2 | 2.00 | 117.75 |
| ^{183}W | 0.11778 | 0.912 | 0.0 | 1.95 | 4.12 | 146.0 | 1.32 | 110.52 |
| ^{187}Os | N.N | N.N | N.N | N.N | 14.8 | 82.5 | 2.98 | 27.68 |
| ^{189}Os | 0.6599 | 0.226 | 0.856 | 0.0 | 21.0 | 42.4 | 4.39 | 9.67 |
| ^{189}Os | 0.6599 | 0.988 | 0.856 | -0.629 | 8.48 | 80.1 | 0.76 | 105.24 |
| ^{189}Os | 0.6599 | -0.320 | 0.856 | N.N | 6.59 | 35.5 | 1.61 | 22.07 |
| ^{187}Os | 0.0647 | N.N | N.N | N.N | 264. | 194.4 | 33.29 | 5.84 |
| ^{193}Ir | 0.1637 | 0.519 | 0.751 | 0.0 | 6.24 | 31.7 | 0.70 | 45.12 |
| ^{191}Ir | 0.1507 | 0.600 | 0.816 | 0.0 | 10.9 | 15.1 | 2.44 | 6.20 |
| ^{195}Pt | 0.60952 | -0.62 | 0.0 | N.N | 7.12 | 61.7 | 1.60 | 38.43 |
| ^{197}Au | 0.1457 | 0.420 | 0.547 | 0.0 | 4.36 | 38.1 | 0.68 | 56.22 |
| ^{201}Hg | -0.56022 | N.N | 0.385 | N.N | 4.7E4 | 10.7 | 658.43 | 0.02 |
| ^{201}Hg | -0.56022 | N.N | 0.385 | 0.3 | 41.9 | 55.2 | 7.43 | 7.44 |
| ^{201}Hg | -0.56022 | N.N | 0.385 | N.N | 76.7 | 22.8 | 12.67 | 1.80 |
| ^{238}U | 0.0 | N.N | 0.0 | -3.23 | 618.0 | 9.8 | 3.53 | 2.78 |

List of Resonant Isotopes B $E_0 < 100$ keV, $0.1 \text{ ns} < \tau_0 < 1 \text{ s}$

| Isotope | E_0 keV | τ_0 | Γ_0 | a % | I_g | I_e | Multi-polarity |
|-------------------|--------------|--------------------|---------------------|----------|---------|---------|----------------|
| ^{181}Ta | 6.238 | 8.73 μs | 75.4 μeV | 99.99 | $7/2^+$ | $9/2^-$ | E1 |
| ^{169}Tm | 8.4103 | 5.89 ns | 0.11 μeV | 100.0 | $1/2^+$ | $3/2^+$ | M1+E2 |
| ^{83}Kr | 9.396 | 212.08 ns | 3.10 neV | 11.55 | $9/2^+$ | $7/2^+$ | M1+E2 |
| ^{187}Os | 9.746 | 3.43 ns | 0.19 μeV | 1.6 | $1/2^-$ | $3/2^-$ | M1(+E2) |
| ^{45}Sc | 12.40 | 458.78 ms | 1.4 aeV | 100.0 | $7/2^-$ | $3/2^+$ | (M2) |
| ^{73}Ge | 13.275 | 4.26 μs | 0.15 neV | 7.76 | $9/2^+$ | $5/2^+$ | E2 |
| ^{57}Fe | 14.4125 | 141.11 ns | 4.66 neV | 2.14 | $1/2^-$ | $3/2^-$ | M1+E2 |
| ^{151}Eu | 21.532 | 13.99 ns | 47.03 neV | 47.82 | $5/2^+$ | $7/2^+$ | M1+E2 |
| ^{149}Sm | 22.494 | 10.27 ns | 64.08 neV | 13.83 | $7/2^-$ | $5/2^-$ | M1+E2 |
| ^{119}Sn | 23.871 | 25.61 ns | 25.70 neV | 8.58 | $1/2^+$ | $3/2^+$ | M1+E2 |
| ^{161}Dy | 25.65135 | 41.98 ns | 15.68 neV | 18.9 | $5/2^+$ | $5/2^-$ | E1 |
| ^{201}Hg | 26.269 | 865.6 ps | 0.76 μeV | 13.2 | $3/2^-$ | $1/2^-$ | M1+E2 |
| ^{40}K | 29.834 | 5.96 ns | 0.11 μeV | 0.012 | 4^- | 3^- | (M1) |
| ^{201}Hg | 32.138 | 288.5 ps | 2.28 μeV | 13.2 | $3/2^-$ | $3/2^-$ | M1+E2 |
| ^{125}Te | 35.4919 | 2.14 ns | 0.31 μeV | 6.99 | $1/2^+$ | $3/2^+$ | M1+E2 |
| ^{189}Os | 36.202 | 764.6 ps | 0.86 μeV | 16.1 | $3/2^-$ | $1/2^-$ | M1+E2 |
| ^{121}Sb | 37.133 | 4.99 ns | 0.13 μeV | 57.25 | $5/2^+$ | $7/2^+$ | M1 |
| ^{129}Xe | 39.578 | 1.40 ns | 0.47 μeV | 26.44 | $1/2^+$ | $3/2^+$ | M1+E2 |
| ^{161}Dy | 43.8211 | 1.20 ns | 0.55 μeV | 18.9 | $5/2^+$ | $7/2^+$ | M1+E2 |
| ^{238}U | 44.915 | 324.6 ps | 2.03 μeV | 99.27 | 0^+ | 2^+ | E2 |
| ^{183}W | 46.4839 | 271.2 ps | 2.43 μeV | 14.3 | $1/2^-$ | $3/2^-$ | M1+E2 |
| ^{157}Gd | 54.533 | 269.7 ps | 2.44 μeV | 15.68 | $3/2^-$ | $5/2^-$ | M1+E2 |
| ^{127}I | 57.606 | 2.76 ns | 0.24 μeV | 100.0 | $5/2^+$ | $7/2^+$ | M1+E2 |
| ^{155}Gd | 60.0087 | 278.4 ps | 2.36 μeV | 14.73 | $3/2^-$ | $5/2^-$ | M1+E2 |
| ^{157}Gd | 63.917 | 663.64 ns | 0.99 neV | 15.68 | $3/2^-$ | $5/2^+$ | E1 |
| ^{73}Ge | 66.716 | 719.90 ms | 0.9 aeV | 7.76 | $9/2^+$ | $1/2^-$ | NN |
| ^{171}Yb | 66.721 | 1.17 ns | 0.56 μeV | 14.31 | $1/2^-$ | $3/2^-$ | M1+E2 |

List of Unstable Resonant Isotopes $E_0 < 100$ keV, $0.1 \text{ ns} < \tau_0 < 1 \text{ s}$

| Z | Isotope | E_0 keV | τ_0 | Γ_0 | lifetime years | I_g | I_e | Multi-polarity |
|----|-------------------|--------------|-----------|---------------------|-------------------|---------|---------|----------------|
| 53 | ^{129}I | 27.78 | 24.24 ns | 27.16 neV | 1.57E7 | $7/2^+$ | $5/2^+$ | M1+E2 |
| 56 | ^{133}Ba | 12.322 | 10.10 ns | 65.18 neV | 10.52 | $1/2^+$ | $3/2^+$ | M1 |
| 57 | ^{137}La | 10.56 | 128.40 ns | 5.13 neV | 6.0E4 | $7/2^+$ | $5/2^+$ | E1 |
| 62 | ^{151}Sm | 4.821 | 50.49 ns | 13.04 neV | 90. | $5/2^-$ | $3/2^-$ | M1+E2 |
| 95 | ^{243}Am | 84.0 | 3.38 ns | 0.19 μeV | 7370. | $5/2^-$ | $5/2^+$ | E1 |

| Isotope | μ_g | μ_e | Q_g | Q_e | α | σ_0 | σ_{ph} | σ_0/σ_{ph} |
|-------------------|----------|----------|--------|-------|----------|------------|---------------|------------------------|
| | μ_N | μ_N | barn | barn | | k barn | k barn | |
| ^{181}Ta | 2.3705 | 5.28 | 3.28 | 3.71 | 70.5 | 1099.2 | 89.40 | 12.30 |
| ^{169}Tm | -0.2316 | 0.534 | 0.0 | -1.2 | 285.0 | 241.9 | 32.91 | 7.35 |
| ^{83}Kr | -0.9707 | -0.943 | 0.253 | 0.495 | 17.09 | 1225.5 | 8.08 | 151.71 |
| ^{187}Os | 0.0647 | N.N | N.N | N.N | 264. | 194.4 | 33.29 | 5.84 |
| ^{45}Sc | 4.756 | N.N | -0.22 | N.N | 632. | 12.6 | 4.00 | 3.15 |
| ^{73}Ge | -0.87947 | -0.0941 | -0.173 | -0.4 | 1120. | 7.4 | 15.11 | 0.49 |
| ^{57}Fe | 0.090604 | -0.15532 | 0.0 | 0.16 | 8.56 | 2464.0 | 5.75 | 428.58 |
| ^{151}Eu | 3.472 | 2.591 | 0.903 | 1.28 | 28.0 | 242.6 | 8.35 | 29.06 |
| ^{149}Sm | -0.672 | -0.624 | 0.075 | 1.01 | 29.2 | 120.1 | 6.94 | 17.29 |
| ^{119}Sn | -1.0473 | 0.633 | 0.0 | 0.094 | 5.22 | 1380.5 | 2.45 | 562.59 |
| ^{161}Dy | -0.4803 | 0.594 | 2.507 | 2.506 | 2.35 | 1109.9 | 6.30 | 176.22 |
| ^{201}Hg | -0.56022 | N.N | 0.385 | N.N | 76.7 | 22.8 | 12.67 | 1.80 |
| ^{40}K | -1.298 | -1.29 | -0.061 | N.N | 6.6 | 281.3 | 0.21 | 1336.74 |
| ^{201}Hg | -0.56022 | N.N | 0.385 | 0.3 | 41.9 | 55.2 | 7.43 | 7.44 |
| ^{125}Te | -0.8885 | 0.605 | 0.0 | -0.31 | 14.0 | 259.0 | 5.87 | 44.11 |
| ^{189}Os | 0.6599 | 0.226 | 0.856 | 0.0 | 21.0 | 42.4 | 4.39 | 9.67 |
| ^{121}Sb | 3.3634 | 2.518 | -0.36 | -0.48 | 11.11 | 195.4 | 4.85 | 40.26 |
| ^{129}Xe | -0.7780 | 0.58 | 0.0 | -0.41 | 12.31 | 234.7 | 4.97 | 47.24 |
| ^{161}Dy | -0.4803 | -0.141 | 2.507 | 0.53 | 8.0 | 188.7 | 1.47 | 128.21 |
| ^{238}U | 0.0 | N.N | 0.0 | -3.23 | 618.0 | 9.8 | 3.53 | 2.78 |
| ^{183}W | 0.11778 | -0.10 | 0.0 | 1.77 | 8.63 | 235.2 | 2.00 | 117.75 |
| ^{157}Gd | -0.340 | N.N | 1.36 | -0.46 | 12.4 | 92.1 | 3.83 | 24.07 |
| ^{127}I | 2.8133 | 2.54 | -0.79 | -0.71 | 3.77 | 206.1 | 1.72 | 120.11 |
| ^{155}Gd | -0.2591 | N.N | 1.30 | -0.44 | 9.36 | 98.4 | 2.97 | 33.17 |
| ^{157}Gd | -0.340 | -0.464 | 1.36 | 2.45 | 0.971 | 455.7 | 2.51 | 181.79 |
| ^{73}Ge | -0.8795 | N.N | -0.173 | N.N | N.N | N.N | 0.17 | N.N |
| ^{171}Yb | 0.49367 | 0.350 | 0.0 | 1.59 | 13.0 | 78.5 | 3.05 | 25.72 |

| Isotope | μ_g | μ_e | Q_g | Q_e | α | σ_0 | σ_{ph} | σ_0/σ_{ph} |
|-------------------|----------|---------|--------|--------|----------|------------|---------------|------------------------|
| | μ_K | μ_K | barn | barn | | k barn | k barn | |
| ^{129}I | 2.6210 | 2.8045 | -0.553 | -0.685 | 5.0 | 396.3 | 2.04 | 194.18 |
| ^{133}Ba | -0.77167 | 0.51 | 0.0 | N.N | 70.3 | 452.0 | 23.45 | 19.27 |
| ^{137}La | 2.695 | N.N | 0.24 | 0.24 | 122.3 | 133.5 | 38.07 | 3.51 |
| ^{151}Sm | -0.363 | N.N | 0.67 | N.N | 920. | 76.2 | 89.22 | 0.85 |
| ^{243}Am | 1.53 | 2.74 | 4.30 | 4.20 | 0.22 | 284.2 | 0.67 | 424.00 |

List of Resonant Isotopes B (cont'd) $E_0 < 100 \text{ keV}$, $0.1 \text{ ns} < \tau_0 < 1 \text{ s}$

| Isotope | E_0 keV | τ_0 | Γ_0 | a % | I_g | I_e | Multi-polarity |
|-------------------|--------------|-----------|---------------------|----------|---------|---------|----------------|
| ^{145}Nd | 67.25 | 42.42 ns | 15.52 neV | 8.30 | $7/2^-$ | $3/2^-$ | E2 |
| ^{61}Ni | 67.408 | 7.60 ns | 86.57 neV | 1.19 | $3/2^-$ | $5/2^-$ | M1+E2 |
| ^{73}Ge | 68.752 | 2.51 ns | 0.26 μeV | 7.76 | $9/2^+$ | $7/2^+$ | M1+E2 |
| ^{189}Os | 69.537 | 2.34 ns | 0.28 μeV | 16.10 | $3/2^-$ | $5/2^-$ | M1+E2 |
| ^{145}Nd | 72.50 | 1.04 ns | 0.63 μeV | 8.30 | $7/2^-$ | $5/2^-$ | M1 |
| ^{138}La | 72.57 | 167.35 ns | 3.93 neV | 0.09 | 5^+ | 3^+ | E2 |
| ^{193}Ir | 73.041 | 8.79 ns | 74.92 neV | 62.70 | $3/2^+$ | $1/2^+$ | M1+E2 |
| ^{164}Dy | 73.392 | 3.45 ns | 0.19 μeV | 28.2 | 0^+ | 2^+ | E2 |
| ^{161}Dy | 74.56668 | 4.53 ns | 0.15 μeV | 18.9 | $5/2^+$ | $3/2^-$ | E1 |
| ^{187}Os | 75.04 | 3.12 ns | 0.21 μeV | 1.6 | $1/2^-$ | $5/2^-$ | E2 |
| ^{160}Gd | 75.26 | 3.88 ns | 0.17 μeV | 21.86 | 0^+ | 2^+ | E2 |
| ^{171}Yb | 75.878 | 2.37 ns | 0.28 μeV | 14.3 | $1/2^-$ | $5/2^-$ | E2 |
| ^{174}Yb | 76.471 | 2.58 ns | 0.25 μeV | 31.84 | 0^+ | 2^+ | E2 |
| ^{197}Au | 77.351 | 2.76 ns | 0.24 μeV | 100.0 | $3/2^+$ | $1/2^+$ | M1+E2 |
| ^{170}Er | 78.68 | 2.73 ns | 0.24 μeV | 14.9 | 0^+ | 2^+ | E2 |
| ^{172}Yb | 78.7435 | 2.38 ns | 0.28 μeV | 21.9 | 0^+ | 2^+ | E2 |
| ^{167}Er | 79.3219 | 165.9 ps | 3.97 μeV | 22.95 | $7/2^+$ | $9/2^+$ | M1+E2 |
| ^{158}Gd | 79.5104 | 3.64 ns | 0.18 μeV | 24.84 | 0^+ | 2^+ | E2 |
| ^{168}Er | 79.804 | 2.71 ns | 0.24 μeV | 26.8 | 0^+ | 2^+ | E2 |
| ^{131}Xe | 80.1853 | 692.4 ps | 0.95 μeV | 21.2 | $3/2^+$ | $1/2^+$ | M1+E2 |
| ^{166}Er | 80.574 | 2.63 ns | 0.25 μeV | 33.6 | 0^+ | 2^+ | E2 |
| ^{162}Dy | 80.660 | 3.27 ns | 0.20 μeV | 25.5 | 0^+ | 2^+ | E2 |
| ^{133}Cs | 80.997 | 9.05 ns | 72.77 neV | 100.0 | $7/2^+$ | $5/2^+$ | M1+E2 |
| ^{154}Sm | 81.976 | 4.36 ns | 0.15 μeV | 22.7 | 0^+ | 2^+ | E2 |
| ^{176}Yb | 82.13 | 2.54 ns | 0.26 μeV | 12.7 | 0^+ | 2^+ | E2 |
| ^{191}Ir | 82.407 | 5.89 ns | 0.11 μeV | 37.3 | $3/2^+$ | $1/2^+$ | M1+E2 |
| ^{153}Eu | 83.3671 | 1.14 ns | 0.58 μeV | 52.18 | $5/2^+$ | $7/2^+$ | M1+E2 |
| ^{170}Yb | 84.2551 | 2.32 ns | 0.28 μeV | 3.05 | 0^+ | 2^+ | E2 |
| ^{155}Gd | 86.546 | 9.13 ns | 72.08 neV | 14.73 | $3/2^-$ | $5/2^+$ | E1 |
| ^{160}Dy | 86.7882 | 2.91 ns | 0.23 μeV | 2.34 | 0^+ | 2^+ | E2 |
| ^{176}Hf | 88.351 | 2.06 ns | 0.32 μeV | 5.21 | 0^+ | 2^+ | E2 |
| ^{156}Gd | 88.9666 | 3.19 ns | 0.21 μeV | 20.47 | 0^+ | 2^+ | E2 |
| ^{99}Ru | 89.68 | 29.58 ns | 22.26 neV | 12.72 | $5/2^+$ | $3/2^+$ | E2+M1 |
| ^{164}Er | 91.40 | 2.12 ns | 0.31 μeV | 1.61 | 0^+ | 2^+ | E2 |
| ^{178}Hf | 93.180 | 2.14 ns | 0.31 μeV | 27.3 | 0^+ | 2^+ | E2 |

| Isotope | μ_g | μ_e | Q_g | Q_e | α | σ_0 | σ_{ph} | σ_0/σ_{ph} |
|-------------------|---------|---------|---------|--------|----------|------------|---------------|------------------------|
| | μ_N | μ_N | barn | barn | | kbarn | kbarn | |
| ^{145}Nd | -0.654 | N.N | -0.254 | N.N | 9.61 | 25.5 | 1.75 | 14.55 |
| ^{61}Ni | 0.750 | 0.480 | 0.162 | -0.2 | 0.139 | 709.1 | 0.10 | 7046.05 |
| ^{73}Ge | -0.8795 | N.N | -0.173 | N.N | 0.227 | 337.5 | 0.16 | 2120.64 |
| ^{189}Os | 0.6599 | 0.988 | 0.856 | -0.629 | 8.48 | 80.1 | 0.76 | 105.24 |
| ^{145}Nd | -0.656 | -0.320 | -0.33 | N.N | 3.64 | 75.2 | 1.44 | 52.40 |
| ^{138}La | 3.7136 | 2.886 | 0.45 | N.N | 6.41 | 39.9 | 1.19 | 33.43 |
| ^{193}Ir | 0.1637 | 0.519 | 0.751 | 0.0 | 6.24 | 31.7 | 0.70 | 45.12 |
| ^{164}Dy | 0.0 | 0.70 | 0.0 | -2.08 | 9.0 | 227.1 | 1.95 | 116.31 |
| ^{161}Dy | -0.4803 | -0.403 | 2.507 | 1.45 | 0.679 | 174.7 | 1.87 | 93.31 |
| ^{187}Os | N.N | N.N | N.N | N.N | 14.8 | 82.5 | 2.98 | 27.68 |
| ^{160}Gd | 0.0 | 0.72 | 0.0 | -2.08 | 7.44 | 255.9 | 1.62 | 157.57 |
| ^{171}Yb | 0.49367 | 1.015 | 0.0 | 2.16 | 9.73 | 118.8 | 2.18 | 54.54 |
| ^{174}Yb | 0.0 | 0.676 | 0.0 | 2.12 | 9.43 | 200.6 | 2.13 | 93.96 |
| ^{197}Au | 0.1457 | 0.420 | 0.547 | 0.0 | 4.36 | 38.1 | 0.68 | 56.22 |
| ^{170}Er | 0.0 | 0.633 | 0.0 | -1.94 | 7.59 | 230.0 | 1.80 | 127.95 |
| ^{172}Yb | 0.0 | 0.669 | 0.0 | 2.16 | 8.4 | 209.9 | 1.98 | 106.17 |
| ^{167}Er | 0.564 | N.N | 2.827 | N.N | 6.06 | 68.8 | 1.76 | 39.12 |
| ^{158}Gd | 0.0 | 0.762 | 0.0 | -2.01 | 6.02 | 275.6 | 1.40 | 196.36 |
| ^{168}Er | 0.0 | 0.642 | 0.0 | -2.17 | 7.14 | 236.0 | 1.73 | 136.24 |
| ^{131}Xe | 0.6919 | N.N | -0.120 | 0.0 | 1.57 | 74.0 | 0.75 | 99.00 |
| ^{166}Er | 0.0 | 0.632 | 0.0 | -1.9 | 6.88 | 239.1 | 1.69 | 141.59 |
| ^{162}Dy | 0.0 | 0.686 | 0.0 | N.N | 6.22 | 260.4 | 1.52 | 171.16 |
| ^{133}Cs | 2.5820 | 3.45 | -0.0037 | -0.33 | 1.72 | 102.8 | 0.78 | 131.62 |
| ^{154}Sm | 0.0 | 0.784 | 0.0 | -1.87 | 4.94 | 306.5 | 1.17 | 262.93 |
| ^{176}Yb | 0.0 | 0.675 | 0.0 | 2.22 | 7.06 | 225.0 | 1.77 | 127.10 |
| ^{191}Ir | 0.1507 | 0.600 | 0.816 | 0.0 | 10.9 | 15.1 | 2.44 | 6.20 |
| ^{153}Eu | 1.5330 | 1.81 | 2.41 | 0.44 | 3.82 | 97.4 | 1.18 | 82.77 |
| ^{170}Yb | 0.0 | 0.674 | 0.0 | 2.12 | 6.37 | 233.8 | 1.66 | 141.21 |
| ^{155}Gd | -0.2591 | -0.525 | 1.30 | 0.11 | 0.434 | 341.7 | 1.12 | 304.61 |
| ^{160}Dy | 0.0 | 0.725 | 0.0 | 1.76 | 4.69 | 285.4 | 1.25 | 227.55 |
| ^{176}Hf | 0.0 | 0.539 | 0.0 | -2.10 | 5.86 | 228.4 | 1.61 | 141.47 |
| ^{156}Gd | 0.0 | 0.774 | 0.0 | -1.93 | 3.93 | 313.5 | 1.04 | 300.60 |
| ^{99}Ru | -0.641 | -0.284 | 0.079 | 0.231 | 1.498 | 81.2 | 0.26 | 315.04 |
| ^{164}Er | 0.0 | 0.697 | 0.0 | N.N | 4.2 | 281.6 | 1.21 | 232.18 |
| ^{178}Hf | 0.0 | 0.48 | 0.0 | -2.02 | 4.74 | 245.5 | 1.41 | 174.60 |

List of Resonant Isotopes B (cont'd) $E_0 < 100 \text{ keV}$, $0.1 \text{ ns} < \tau_0 < 1 \text{ s}$

| Isotope | E_0 keV | τ_0 | Γ_0 | a % | I_g | I_e | Multi-polarity |
|-------------------|--------------|---------------------|---------------------|----------|---------|----------|----------------|
| ^{67}Zn | 93.312 | 13.22 μs | 49.8 peV | 4.11 | $5/2^-$ | $1/2^-$ | E2 |
| ^{180}Hf | 93.326 | 2.16 ns | 0.30 μeV | 35.1 | 0^+ | 2^+ | E2 |
| ^{189}Os | 95.254 | 331.8 ps | 1.98 μeV | 16.10 | $3/2^-$ | $3/2^-$ | M1+E2 |
| ^{153}Eu | 97.4297 | 285.6 ps | 2.30 μeV | 52.18 | $5/2^+$ | $5/2^-$ | E1 |
| ^{195}Pt | 98.85 | 245.2 ps | 2.68 μeV | 33.80 | $1/2^-$ | $3/2^-$ | M1+E2 |
| ^{183}W | 99.0793 | 1.11 ns | 0.59 μeV | 14.3 | $1/2^-$ | $5/2^-$ | E2 |
| ^{155}Gd | 121.05 | 46.17 ms | 14.2 aeV | 14.8 | $3/2^-$ | $11/2^-$ | E1 |
| ^{19}F | 197.143 | 128.83 ns | 5.11 neV | 100.0 | $1/2^+$ | $5/2^+$ | E2 |

| Isotope | μ_g | μ_e | Q_g | Q_e | α | σ_0 | σ_{ph} | σ_0/σ_{ph} |
|-------------------|---------|---------|-------|--------|----------|------------|---------------|------------------------|
| | μ_N | μ_N | barn | barn | | kbarn | kbarn | |
| ^{67}Zn | 0.8756 | 0.587 | 0.15 | N.N | 0.873 | 50.0 | 0.06 | 861.49 |
| ^{180}Hf | 0.0 | 0.533 | 0.0 | -2.00 | 4.71 | 246.0 | 1.40 | 175.68 |
| ^{189}Os | 0.6599 | -0.320 | 0.856 | N.N | 6.59 | 35.5 | 1.61 | 22.07 |
| ^{153}Eu | 1.5330 | 3.22 | 2.41 | N.N | 0.307 | 197.2 | 0.78 | 251.42 |
| ^{195}Pt | 0.60952 | -0.62 | 0.0 | N.N | 7.12 | 61.7 | 1.60 | 38.43 |
| ^{183}W | 0.11778 | 0.912 | 0.0 | 1.95 | 4.12 | 146.0 | 1.32 | 110.52 |
| ^{155}Gd | -0.2591 | N.N | 1.30 | N.N | 13.0 | 35.8 | 0.47 | 76.67 |
| ^{19}F | 2.6288 | 3.607 | N.N | -0.072 | N.N | N.N | 0.00 | N.N |

References

1. M. E. Rose : *Elementary Theory of Angular Momentum* (Wiley, New York 1957) **286**, **298**
2. P. J. Eberlein : Numer. Math. **14**, 232 (1957) **288**
3. K. Balewski, W. Brefeld, W. Decking, H. Franz, R. Röhlsberger and E. Weckert (eds.) : *PETRA III: A Low-Emissance Synchrotron Radiation Source*, Technical Design Report (DESY 2004-035) 2004 **294**
4. M. Born and E. Wolf: *Principles of Optics*, 7th ed. (Cambridge University Press, Cambridge 1999) **294**
5. R. Röhlsberger : Hyperfine Interact. **123/124**, 301 (1999) **297**
6. N. W. Ashcroft and N. D. Mermin: *Solid State Physics* (Holt-Saunders, Philadelphia 1976) **297**
7. W. Sturhahn and V. G. Kohn : Hyperfine Interact. **123/124**, 367 (1999) **299**
8. A. I. Chumakov, R. Rüffer, A. Q. R. Baron, H. Grünsteudel, H. F. Grünsteudel, and V. G. Kohn : Phys. Rev. B **56**, 10758 (1997) **299**
9. P. M. Hession, W. Sturhahn, E. E. Alp, T. S. Toellner, P. Metcalf, M. Y. Hu, J. P. Sutter, and J. P. Mullen : unpublished. **299**
10. A. I. Chumakov, R. Rüffer, O. Leupold, A. Barla, H. Thiess, J. M. Jil, H. V. Alberto, R. C. Vilão, N. Ayres de Campos, V. G. Kohn, M. Gerken, and M. Lucht : Phys. Rev. B **63**, 172301 (2001) **299**
11. J. G. Stevens and V. E. Stevens : *Mössbauer Effect Data Index* (Plenum Press, New York 1973) **300**
12. R. B. Firestone and V. S. Shirley : *Table of Isotopes*, 8th ed. (John Wiley, New York 1996) **300**
13. Yu. V. Shvyd'ko, M. Lucht, E. Gerdau, M. Lerche, J. Jäschke, M. Lucht, E. E. Alp, W. Sturhahn, J. Sutter, and T. S. Toellner : J. Synchrotron Rad. **9**, 17 (2002) **300**
14. G. Martínez-Pinedo, P. Schwerdtfeger, E. Caurier, K. Langanke, W. Nazarewicz, and T. Söhnle : Phys. Rev. Lett. **87**, 062701 (2001) **300**
15. P. Dudek, P. Blaha, and K. Schwarz : Phys. Rev. Lett. **75**, 3545 (1995) **300**

Index

- α -relaxation 161
- β -relaxation 161
- ε -Fe 215
- Anharmonicity 190
- Anisotropic absorption 297
- Anisotropic optics 67
- Anisotropy constant 127
- Anomalous scattering 17
- Antiferromagnetic coupling 117
- Antiferromagnetism 31
- Asymmetric Bragg reflection 48
- Atomic scattering amplitude 16
- Avalanche photodiodes 59
- Backscattering geometry 280
- Beamlines 61
- Bessel function 28
- Bessel minimum 152, 262
- Biomolecules 219
 - Normal mode analysis 222
- Blocking temperature 143
- Blume-Tjon model 164
- Bose-Einstein condensates 20
- Boson peak 205, 209, 248
- Bragg reflection
 - acceptance 49
 - asymmetric 48
 - Darwin width 49
 - emittance 49
 - energy width 49
- Bravais lattice 299
- Brightness 42, 45
- Brilliance 43, 45, 273
- Brillouin light scattering 2
- Campbell-Baker-Hausdorff relation 296
- Causality 13, 24
- Chasman – Green lattice 38
- Circular dichroism 45, 72
- Circular polarization 45, 103
- Clebsch-Gordan coefficients 90, 286
- Clusters 139, 164
- Coherence length
 - longitudinal 30
 - transverse 85, 107, 293
- Coherent enhancement 22
- Commutator 297
- Compound refractive lens 54
- Constant-fraction discriminator 57
- Conventional Mössbauer Spectroscopy 104
- Conversion electron Mössbauer spectroscopy 10, 168, 204
- Conversion electrons 183
- Correlation function 155
- Critical angle 75, 98, 110
- Crossed polarizers 252
- Curie temperature 140
- Damped harmonic oscillator 196
- Darwin width 49, 54
- Data analysis
 - elastic scattering 166
 - inelastic scattering 189
- Data inversion 98, 117, 166
- Debye temperature 216, 245
- Debye-Scherrer rings 33
- Density fluctuations 262
- Density of states 189
- Density transition 86
- Dephasing 165
- Depth-selective hyperfine spectroscopy 115
- Detailed balance 189, 190

- Time-reversal invariance 190
- Detectors 56–61
 - avalanche photodiodes 59
 - fast-slow coincidence 58
 - timing electronics 57
- Diamond anvil cell 151
- Dichroism
 - circular 45, 72
 - linear 72, 96
 - magnetic 168
- Dicke superradiance 21
- Diffraction 1
- Diffusion
 - α -relaxation 161
 - crystalline Systems 156
 - glasses 160
 - jump function 157
 - Markovian 156
 - orientational dependence 158
- Domain formation 145, 150
- Domain wall 146
- Doppler shift 240, 248, 256, 261
- DuMond-diagrams 50
- Dynamic structure factor 155, 262
- Dynamical beats 20
- Dynamical theory 68
 - Forward scattering 73
 - Propagation matrix 68
 - roughness 85
- Eigenpolarizations 92
- Electric field gradient 90, 95, 286
- Electric hyperfine interaction 94, 286
- Electron-energy loss spectroscopy 2
- Euler angles 287
- Evanescence waves 115
- Exchange constant 127
- Exchange coupling 117
- Exchange Spring Effect 123
- Extinction depth 46
- f-factor *see* Lamb-Mössbauer factor
- Faraday geometry 55, 249
- Faraday rotation 55
- Fast-slow coincidence 58
- Fe islands
 - 2-dimensional 139
 - 3-dimensional 130, 201
 - lattice dynamics 201
- spin structure 130, 139
- FePd 208
- FePt 123
- Ferrocene/dibutylphthalate 162
- FeTb 203
- First-order Born approximation 26
- Fluorescence
 - atomic 183
 - nuclear 183
- Force constants 186, 195, 210, 224
- host-impurity 210
- Forward scattering 25, 73
- Energy domain 28
- Separated Targets 29
- Single resonance 27
- Time domain 26
- transmission matrix 73
- Fourier analysis 99
- Fourier spectra 107, 132
- Fourier transformation 13, 14, 24, 84, 85, 97, 99, 100, 156, 188, 288, 290
- Fourier-Log decomposition 188
- Fresnel coefficients 78
- g-factor 89, 301
- Geophysics 214
- GIAR films 110
- Glass transition 161, 262
- Glycerol 262
- Grain boundaries 198
- Grazing incidence reflection
 - layer systems 76
 - surfaces 74
- Guided modes 110, 195
- Hamilton operator 285
- Hard-magnetic materials 125
- Harmonic approximation 186, 191
- Heavy-fermion compounds 154
- Height distribution function 86, 297
 - Gaussian 87
- Heterodyne detection 256
- High pressure
 - lattice dynamics 214–219
 - magnetism 150–155
- High-pressure cell 151, 216
- High-resolution monochromators 47
 - designs 53
 - DuMond-diagrams 50

- nested monochromator 53
 Huygens principle 26
 Hybrid beat 24
 Hyperfine interactions 285
 Hysteresis loop 125
- Image plates 241
 Imaging 1
 Impurity modes 210
 Index of refraction 15–19, 67, 74
 Inelastic neutron scattering 2, 225
 Inelastic nuclear scattering 11,
 181–226
 Inelastic x-ray scattering 2, 225
 Inner-shell resonances 17
 Interface phonons 193
 Interferometry 167
 Intermediate scattering function 156,
 260
 Internal conversion 301
 Invar effect 208
 Isomer shift 286
 Isotopes
 ¹¹⁹Sn 190
 ¹⁴⁹Sm 154, 243
 ¹⁵⁹Tb 181
 ¹⁶¹Dy 61
 ¹⁸¹Ta 24, 31
 ⁵⁷Fe 66–243
- Jones-matrix formalism 54
 Jump diffusion 157
- Kiessig fringes 125
 Kinematical approximation 26
 Kinetic energy
 average 186, 223
 Kohlrausch function 161, 262
 Kondo-lattice compounds 153
- Lamb-Mössbauer factor 138, 152, 181,
 185, 186, 189
 Laminar grating 70
 Laplace transform 115
 Larmor precession 163
 Lattice dynamics 181
 Lattice instabilities 194, 207
 Lattice misfit 140
 Lighthouse effect 234–248
- Lighthouse spectrometer 254
 Linear dichroism 72
 Liouville's theorem 49
 Lipkin's sum rules 185, 223
 Low-energy excitations 190, 204, 220
- Mössbauer isotopes 3, 25, 299
 Mach-Zehnder interferometer 30
 Magic-angle spinning 236
 Magnetic anisotropies 134
 Magnetic hyperfine interaction 91
 Magnetic moment 301
 Magnetic shape anisotropy 94
 Magnetic spin structure *see* Spin
 structure
 Magnetic superstructure 119
 Magnetic switching 26, 167
 Magnetic x-ray scattering 168
 Magneto-optical Kerr effect 124
 Magneto-volume instabilities 208
 Magnetoresistance 123
 Magnons *see* Spin waves
 Matrix exponential 70, 73, 77, 85, 296
 Metrology 279
 Micro-channel plates 59
 Micromagnetic simulation 127
 Misfit *see* Lattice misfit
 Mode-coupling theory 160, 267
 Moiré pattern 9
 MOKE 124
 Moments
 of energy distribution 185
 of height distribution 297
- Monochromators 47
 Cryogenic cooling 47
 DuMond-diagrams 50
 polarization filtering 52
- Multi-phonon excitations 185
 Multi-slit interference 24
 Multilayers 117
 Fe-Cr 119
- Multiphonon excitation 188, 189
 Multiphoton scattering 13
 Multipole expansion 285
 Mutual coherence function 240, 294
 Myoglobin 219
- Nanocrystals 194
 Nanoparticles 198

- Nanostructures
 - Fe islands (2D) 139
 - Fe islands (3D) 130
 - self-organized 130
- Native oxide 129
- Nested monochromators 53
- Neutron reflectometry 80, 119
- Neutron scattering
 - elastic 168
 - inelastic 2, 191, 203, 225
- Non-Debye behaviour 206
- Nonlinear optics 13
- Normal mode analysis 222
- Nuclear exciton 14
- Nuclear lighthouse effect 4, 234–248
- Nuclear resonant scattering
 - Coherent elastic 66
 - coherent elastic 8
 - coherent inelastic 9
 - elastic 2
 - incoherent elastic 10
 - Incoherent inelastic 181
 - incoherent inelastic 11
 - inelastic 3
- ODIN 158
- Optical activity 52, 96
 - Faraday rotation 55
 - Orthogonal scattering 72, 248
- Orientational distribution 109
- Orthogonal scattering 72, 248
- Oxide layer 115, 129, 197
- Parratt formula 80
- Partial coherence 279
- Penetration depth 75
- Perpendicular magnetization 139
- Perturbed angular correlation 263
- PETRA-III 274
- Phase contrast 149
- Phase problem 166
- Phase transitions 207
- Phonon confinement 193
- Phonon damping 194
- Phonon density of states 186, 189
 - projected 297
- Phonon engineering 194, 203
- Phonon folding 193
- Phonon lifetime 198
- Phonon softening 207
- Phonon spectrum 4, 182, 186, 195, 201
- Phonons
 - lifetime broadening 203
- Photon correlation spectroscopy 2
- Photon propagator 288
- Polariton 15
- Polarization dependence 91
 - Electric hyperfine interaction 94
 - Magnetic hyperfine interaction 91
- Polarization factor 49
- Polarization filtering 52
- Polarized neutron reflectometry 168
- Polarized neutron scattering 124
- Polarizer-Analyzer 52, 252, 257
- Position-sensitive detector 236, 241
- Powder diffractometry 33
- Probe layers 81, 115, 212
- Program packages *see* Software packages
- Propagation matrix 68
- Propagation quantum beats 16, 20
- Propagator 28, 238, 288
- Pulse propagation 19
- Pure nuclear reflections 30, 119
- Quadrupole moment 90, 286, 301
- Quantum beats 16, 22
- Quantum efficiency 56
- Quantum optics 13
- Quarter-wave plate 45, 103
- Quasicrystals 33
- Quasielastic scattering 155, 262
- Raman scattering 2
- Rare earths 243
- Recoil energy 186, 222
- Recoilless fraction *see* Lamb-Mössbauer factor
- Reconstruction Methods 117
- Reflection coefficient
 - phase of 75
- Reflectivity
 - electronic 75
 - grazing incidence 75
 - nuclear 75, 96
- Refractive index *see* Index of refraction

- Refractive lens *see* Compound refractive lens
- Relaxation 162
- α -relaxation 161
 - β -relaxation 161
 - rotational 266
 - superparamagnetic 140, 142, 164
- Resolution function 188
- RKKY interaction 118, 153
- Rotating-mirror spectrometer 251
- Roughness 84
- dynamical theory 85
 - kinematical approximation 85
- Roughness matrix 86, 296
- SASE principle 274
- Seeding 278
- Scattering amplitude
- electronic 71
 - general 70
 - nuclear 90
- Scattering geometry 73
- Scattering matrix 93, 95
- Scattering processes
- classification 7
 - coherent elastic 8
 - coherent inelastic 9
 - incoherent elastic 10
 - incoherent inelastic 11
- Scintillation detectors 58
- Second-order Doppler shift 181
- Self-correlation function 156
- Self-intermediate scattering function 185
- Shape anisotropy, magnetic 134
- Shape memory effect 208
- Single-photon counting 56
- Small-angle neutron scattering 146
- Small-angle x-ray scattering
- electronic 240
 - nuclear 144
 - forward scattering 145
 - grazing incidence 147
- Smart materials 194
- Snell's law 78
- Soft phonons 207
- Software packages
- CONUSS 166
 - DOS 189
- MOTIF 166
- PHOENIX 189
- Sound velocity 197, 205, 212, 217
- Measurement 212
- Specific heat 192
- Spectrometer 249
- Lighthouse 254
 - Rotating-Mirror 251
- Spectroscopy 1
- Specular reflection 76
- Speedup 20, 98
- Spherical harmonics 71, 91
- Spin flip 8
- Spin flop transition 120
- Spin structure
- determination of 98
 - exchange spring 123
 - Fe islands 130, 139
- Spin waves 135
- Spontaneous magnetization 136
- Sputter deposition 124
- SRPAC 263
- Standing waves 110
- in multilayers 119
 - in thin films 110
 - in waveguides 110
- Stokes parameters 88
- Stoner criterion 152
- Stoner excitations 135
- Storage rings 45
- β -functions 275
 - Source sizes 275
- Stratified media 76
- Stroboscopic data acquisition 257
- Sum rules 185
- Superlattice *see* Multilayers
- Superparamagnetic relaxation 140, 164
- Superstructure Bragg reflection 30
- Superstructure reflections 117
- Surface anisotropy, magnetic 134
- Surface roughness 84
- Synchrotron radiation
- Brightness 42
 - Brilliance 43, 273
 - Critical energy 41
 - Historical development 37
 - Polarization 45

- Spectral flux 41
Total flux 40
Synchrotron radiation sources 37
 Buckets 44
 Chasman - Green lattice 38
 Coupling constant 43
 Emission characteristics 40
 Emittance 42
 Insertion devices 38
 Spurious bunches 44
 Time structure 43
- Table of isotopes 299
TDPAC 263
Thermal transport 193
Thin-film interference 111
Thomson scattering 17
Time resolution 56
Time-domain interferometry 259
Tomography 167
Total reflection 74
Transmission matrix 74
Transverse coherence 107, 293
 coherence length 238, 279, 295
 detector aperture 107
 mutual coherence function 294
Transverse coherence length 279, 295
Tribology 193
Two-point correlation function 26
Ultrathin films 96
Undulator 38, 42
Unstable isotopes 306
van Cittert - Zernike theorem 295
van-Hove singularities 196
Vector spherical harmonics *see*
 Spherical harmonics
Velocity of sound *see* Sound velocity
Vibrational entropy 192
Waveguides 110
 exchange-coupled films 126
 field intensity in 110
 intensity enhancement 112
 nuclear energy bandwidth 250
Wiggler 38
X-ray diffraction 204
X-ray standing waves *see* Standing
 waves
X-ray waveguide *see* Waveguides
XFEL 274
Zeeman-splitting 89

R. Röhlsberger
**Nuclear Condensed
Matter Physics
with Synchrotron Radiation**

This book provides a comprehensive introduction to the growing field of nuclear condensed matter physics with synchrotron radiation, a technique which finds numerous applications in fields such as magnetism, physics of surfaces and interfaces, lattice dynamics and more. Due to the enormous brilliance of modern synchrotron radiation sources, the method is particularly suited for the investigation of low-dimensional structures such as thin films and nanoparticles. The use of isotopic probe layers, for example, allows one to determine magnetic and vibrational properties with very high spatial resolution; focusing techniques and x-ray interference effects lead to a very high sensitivity for smallest amounts of material. The book is written on an introductory level with many examples employed to illustrate the special experimental possibilities.

ISSN 0081-3869

ISBN 3-540-23244-3



Available online at
SpringerLink.com